UNIVERSITA' DEGLI STUDI DI MILANO

DOTTORATO DI RICERCA IN SCIENZE DELLA TERRA

Curriculum Sistema Terra: Processi e Modellazione
XXXVI Ciclo

DIPARTIMENTO DI SCIENZE DELLA TERRA "ARDITO DESIO"

FROM EAST TO NORTH-WEST AFRICA: MAGNETOCHRONOLOGY OF THE OLDEST AFRICAN ACHEULEAN SITES

PhD Thesis:

Serena PERINI

R13077

Tutor: Prof. Giovanni MUTTONI

Co-Tutor: Dr. Rosalia GALLOTTI

Coordinatore di Dottorato: Maria Iole SPALLA

A.A. 2022/2023

Acknowledgments

With these words I want to thank the people I met in this three-year journey.
A special thank goes first of all to my supervisor Prof. Giovanni Muttoni, thanks for believing in me investing in my training as a paleomagnetist, for the long days spent in the laboratory and in the field.
Many thanks to my co-supervisor Dott. Rosalia Gallotti, for guiding me in the last few years through the meanders of the African Lower Paleolithic, the support, and the long phone calls.
Thank you both for the insightful discussion, for encouraging the development of my ideas without setting limits, for being always present and giving me so much.
All my gratitude goes to the French-Moroccan archaeological mission of Casablanca, in particular to David Lefèvre, Abderrahim Mohib, Jean-Paul Raynal and Mohssine El Graoui for welcoming me to Thomas Quarry and for the support in the field and after and for the useful discussion.
Thanks to the reviewers of this Thesis Dott. Mattia Marini, Dott. Edoardo Dallanave and Prof. Jean-Paul Raynal for helping me improve the manuscript.
Thanks to my beloved Edo, for being always close to me in this journey, for exchanging ideas and also for making me forget about work when it was necessary.
Thanks to all the PhD students met in this path: Alessandro, Federica, Jacopo, Luca, Sara, Tommaso and many others. We’ve been a great team.
Thank you all for making this experience unforgettable. It was the best time of my life.

Contents

Abstract

In this thesis are presented the chronologies, obtained through magnetostratigraphy, of two key sites of archaeological and paleoanthropological interest, Melka Kunture (Upper Awas Valley, Ethiopia) and Thomas Quarry I (Casablanca, Morocco). These sites of Pleistocene age document the emergence and developments of the Acheulean lithic technology thought to be a major turning point in human evolution, representing over the last two decades a highly debated issue in the study of early technologies.

In East Africa at Melka Kunture, located in the Ethiopian highlands, a time-diagnostic sequence of normal and reverse polarity magnetozones was obtained, representing a magnetochronologic record extending from the Brunhes Chron (<0.773 Ma) to the top of Reunion Subchron (2.116 Ma). The new data were then integrated with $^{40}Ar/^{39}Ar$ dating from the literature to establish age models of deposition that were used to estimate the mean ages of the main archeological levels contained. In North-West Africa at Thomas Quarry I, located in the outskirts of Casablanca (Morocco), magnetostratigraphy coupled with geochemistry provided a chronostratigraphic framework extending from the Brunhes Chron (<0.773 Ma) to the Matuyama pre-Cobb Mountain (>1.210 Ma) subchron.

Research conducted in the last decade revealed that the Acheulean emergence in East Africa should have occurred around 1.7 Ma. This datum is testified by a few key archeological sites such as Kokiselei 4 (1.76 Ma; West Turkana, Kenya), KGA6-A1 (~1.75 Ma; Konso-Gardula, Ethiopia), FLK West (~1.7-1.65 Ma; Olduvai Gorge, Tanzania). The new magnetostratigraphic results obtained from Melka Kunture archeological area of Ethiopia pushed back the first occurrence of the Acheulean at 1.95 (-0.025; +0.1) Ma, some 200 ka before what previously known, and it also provided evidence of the earliest high-altitude peopling of East Africa at 2.02 (-0.095; +0.096) Ma.

The peculiarity of the Acheulean as a cultural phenomenon lies in the first appearance of Large Cutting Tools (LCTs) representing the most evident novelty relative to the pre-existing Oldowan technology. However, the timing and modes

of the technical innovation(s) leading to the Acheulean, their relationship with the pre-existing Oldowan technology and their dispersion across the African continent are still unclear. The age models established for Melka Kunture archeological area allowed also to date other more recent Acheulean sites documenting the continuity of this technology trough time, such as GAR XIIJ at 1.13 (-0.06; +0.05) Ma, GOM II OAM, yielding two fragmentary *Homo heidelbergensis* fossils (GOM II1-576 and GOM II1-6169), dated to 1.03±0.04 Ma and GOM II "Butchery site" at 0.75 (-0.1; +0.02) Ma. On the other hand, for the two sites GOM Iγ and GOM Iδ only minimum ages were proposed, respectively of ~1.41 and ~1.51 Ma, for lack of chronological constraints in their stratigraphic interval.

Beginning from the new results from Melka Kunture, a chronostratigraphic record was assembled through a critical review of data from the literature of key archaeological and paleoanthropological sites from East Africa in order to infer about the dynamics of origin(s) and dispersal(s) of the Acheulean across the African continent, as well as the potential toolmaker(s) of this innovation. The reconstructed record spans between 2.0 and 1.6 Ma, across the Olduvai normal polarity subchron (1.925-1.770 Ma), which represents a fundamental magnetostratigraphic constraint in this field of research. The new data provided by this thesis suggest that in this time-interval, not one but several Acheulean techno-economic innovations appeared in the East African record emerging in a non-linear evolutionary path. This analysis suggests as novel scenario that there were several early Acheuleans that emerged in East Africa at different times, in different places and with different technical peculiarities derived from a common Oldowan background.

As for Thomas Quarry I (Casablanca, Morocco), the age of ~1.3 Ma obtained for the archeological site ThI-L expanded our knowledge on the Acheulean emergence in Atlantic Morocco. This new age estimate based on magnetostratigraphy coupled to geochemistry makes the Acheulean of ThI-L the earliest of North-West Africa. The dynamics of dispersal and spreading of the Acheulean from its cradle in East Africa to North Africa are not yet clear because of the inherently discontinuous nature of the stratigraphic and archeological records. The wide gap between the Oldowan in Algeria, currently dated ~1.77 Ma, and the early Acheulean of Morocco, dated in this thesis at ~1.3 Ma, does not allow to infer about the origin of the early Acheulean of ThI-L but only further discoveries will clarify the emergence of the North African Acheulean in a whole pan-African perspective.

Furthermore, the new data presented in this thesis allowed to constrain in time the site ThI-GH of Thomas Quarry I, located in a higher stratigraphic unit with respect to ThI-L, yielding *Homo* fossils associated to faunal remains and Acheulean tools. This site was constrained with magnetostratigraphy to the Brunhes/Matuyama boundary at 0.773±0.004 ka. The human remains from ThI-GH, currently under investigation, will shed light on the critical period of divergence between the Middle Pleistocene archaic lineages of Western Eurasia and Africa, one of which gave rise to the evolutionary line of *Homo sapiens*.

Riassunto

In questa tesi vengono presentate le cronologie di due siti d'interesse archeologico e paleoantropologico, Melka Kunture (Valle superiore dell'Awash, Etiopia) e Thomas Quarry I (Casablanca, Marocco), ottenute attraverso l'applicazione della magnetostratigrafia. Questi siti di età Pleistocenica documentano emergenza ed evoluzione della tecnologia litica Acheuleana, considerata tra i maggiori salti cognitivi nell'ambito dell'evoluzione umana, argomento al centro del dibattito scientifico degli ultimi vent'anni sulle prime tecnologie.

In Africa orientale a Melka Kunture, collocata sull'altipiano etiopico, è stata identificata una sequenza di magnetozone a polarità normale e inversa che rappresenta un record magnetostratigrafico che si estende dal Chron Brunhes (<0.773 Ma) al top del subchron Reunion (2.116 Ma). I dati ottenuti sono stati integrati con le datazioni $^{40}Ar/^{39}Ar$ disponibili in letteratura al fine di produrre modelli per stimare le età medie dei siti archeologici contenuti.

In Africa nord-occidentale a Thomas Quarry I, che si trova nell'area suburbana di Casablanca, i dati magnetostratigrafici hanno fornito un impianto cronologico che si estende dal Brunhes Chron (<0.773 Ma) al subchron Matuyama pre-Cobb Mountain (>1.210 Ma).

Le ricerche condotte negli ultimi decenni hanno rivelato che l'emergenza della tecnologia Acheuleana in est Africa è avvenuta intorno a 1.7 Ma. Questo dato è supportato da alcuni siti archeologici quali Kokiselei 4 (1.76 Ma; West Turkana, Kenya), KGA6-A1 (~1.75 Ma; Konso-Gardula, Ethiopia), FLK West (~1.7-1.65 Ma; gola di Olduvai, Tanzania).

I risultati magnetostratigrafici ottenuti presso l'area archeologica di Melka Kunture (Etiopia) hanno fornito un'età più antica per la prima occorrenza dell'Acheuleano a 1.95 (-0.025; +0.1) Ma, circa 200 ka prima di quanto noto in precedenza, ed hanno fornito la prova del primo popolamento di alta quota est africano datato 2.02 (-0.095; +0.096) Ma. La peculiarità del fenomeno culturale Acheuleano è costituita dalla comparsa di Large Cutting Tools (LCTs), strumenti litici di grandi dimensioni (>10 cm), i quali rappresentano la più evidente novità

rispetto alla preesistente tecnologia Olduvaiana. Tuttavia, i tempi e modalità della o delle innovazioni tecniche che condurranno all'Acheuleano, il loro rapporto con la preesistente tecnologia Olduvaiana e la loro dispersione all'interno del continente africano sono ancora poco chiari. I modelli di età costituiti per l'area archeologica di Melka Kunture hanno permesso inoltre di datare altri siti Acheuleani più recenti che documentano la continuità di questa tecnologia nel tempo, quali GAR XIIJ a 1.13 (-0.06; +0.05) Ma, GOM II OAM, che ha restituito due fossili di *Homo heidelbergensis* (GOM II1-576 and GOM II1-6169), a 1.03±0.04 Ma e il sito GOM II "Butchery site" datato 0.75 (-0.1; +0.02) Ma. D'altro canto, per i due siti GOM Iγ e GOM Iδ è stato possibile fornire solo età di minimo, rispettivamente ~1.41 e ~1.51 Ma, per mancanza di vincoli cronologici all'interno dell'intervallo stratigrafico in cui si trovano.

Al fine di investigare le dinamiche di origine e dispersione dell'Acheuleano nel continente africano, i risultati ottenuti a Melka Kunture sono stati integrati nel record cronostratigrafico generale dell'Africa orientale ottenuto attraverso la revisione critica della bibliografia esistente riguardante i siti archeologici che documentavano le più antiche occorrenze di tale tecnologia litica. Il record ottenuto risulta compreso tra 2.0 e 1.6 Ma, e comprende l'intervallo magnetostratigrafico a polarità normale Olduvai subchron (1.925-1.770 Ma), il quale rappresenta un vincolo cronostratigrafico fondamentale in questo ambito di ricerca. Questa analisi ha fornito elementi a supporto del fatto che in questo intervallo temporale diverse innovazioni tecniche Acheuleane comparvero in Africa orientale seguendo un percorso evolutivo non lineare, manifestandosi in epoche e luoghi diversi e con peculiarità tecniche differenti ma comunque derivanti da un background Olduvaiano comune.

Per quanto riguarda Thomas Quarry I (Casablanca, Marocco) l'età di ~1.3 Ma ottenuta per il sito archeologico ThI-L permette di contestualizzare meglio le dinamiche di emergenza dell'Acheuleano nel Marocco Atlantico. Questa attribuzione cronologica ottenuta integrando i dati magnetostratigrafici con analisi geochimiche ha reso l'Acheuleano di ThI-L il più antico dell'Africa nord-occidentale. Le dinamiche di dispersione ed espansione dell'Acheuleano a partire dal suo luogo di origine in Africa orientale verso il resto del continente non sono chiare a causa della natura discontinua dei record stratigrafici ed archeologici. L'ampio divario tra l'Olduvaiano rinvenuto nei siti algerini, attualmente datato ~1.77 Ma, e il primo Acheuleano marocchino, datato in questa tesi a ~1.3 Ma, non permette di discutere le origini dell'industria di ThI-L ma solo ulteriori scoperte potranno chiarire le dinamiche di emergenza dell'Acheuleano in nord Africa in una prospettiva pan-Africana.

Inoltre, I dati forniti da questa tesi hanno permesso di datare il sito ThI-GH di Thomas Quarry I, collocato in un'unità stratigrafica superiore rispetto a ThI-L, il quale ha restituito fossili umani associati a faune e strumenti litici Acheuleani. Tale sito è stato vincolato cronologicamente alla transizione Brunhes/Matuyama datata 0.773±0.004 ka. I fossili umani di ThI-GH, attualmente in fase di studio, chiariranno le dinamiche di divergenza tra i lignaggi archaici dell'Eurasia occidentale e Africa, uno dei quali darà seguito alla linea evolutiva di *Homo sapiens*.

Chapter 1

Introduction

The history of human evolution is a topic that has fascinated people and scholars for centuries. Several still unresolved questions concerning our past are currently being targeted by different disciplines. Establishing an accurate timeline for paleoanthropological- and archeological-bearing sites is a fundamental step for understanding human evolution and dispersals.

The East African Rift Valley represents an invaluable archive of the biological and cultural evolutionary history of hominin species. Despite its geochronological potential linked to the presence of extended stratigraphic sequences bearing datable volcanic deposits, the timing of many stages of this long process are unclear. Regarding the history of cultural evolution, the earliest lithic tools first occur in East Africa around 3.3 (Lomekwi, West Turkana, Kenya) to disappear soon after and reappear at about 2.8 Ma (Gona, Ethiopia). From this moment the lithic production becomes continuous, giving rise to the first human culture, the Oldowan. It took about 1 million years for a new technological leap to occur, leading to the Acheulean, that is considered the longest and widest dispersed human culture, mainly characterized by the production of Large Cutting Tools (LCTs).

The origin of the Acheulean and its relationship with the Oldowan represents a major topic in current Early Stone Age research as well as its dispersal through Africa. Over the last two decades, a considerable effort has been made to date the emergence of the Acheulean in Africa. In East Africa, earliest Acheulean industries appeared at 1.76 million years ago (Ma) at Kokiselei 4 in West Turkana, Kenya (Lepre et al., 2011), around 1.75 Ma at KGA6-A1 in Konso-Gardula, Ethiopia (Beyene et al., 2013; Suwa et al., 2015), at ~1.7-1.65 Ma at FLK West in Olduvai, Tanzania ~1.7-1.65 Ma (Diez-Martín et al., 2015;

Stanistreet et al., 2018) and at Melka Wakena, Ethiopia, around 1.6 Ma (Hovers et al., 20212). In South Africa the earliest Acheulean seems to be nearly as old as in some East African sites and is reported between ~1.6 and >1.0 Ma (Lotter and Kuman, 2018). North Africa is also rich in Acheulean sites, but most of them are out of stratigraphic context (Mohib et al., 2019). The only North African Acheulean sites in clear stratigraphic context are Tighennif near Mascara in Algeria and Thomas Quarry I (ThI) in Morocco (Geraads et al., 1986; Mohib et al., 2019; Geraads et al., 1986; Gallotti et al., 2021, 2023; Raynal et al., 2023).

In East Africa, the continental stratigraphic sequences hosting sites of archaeological and/or paleoanthropological interest are characterized by the deposition of volcanoclastic/clastic sediments intercalated with primary volcanic deposits. The depositional architecture is generally complicated by rapid lateral variations of sedimentary facies and the frequent development of unconformities, typical of continental deposition. In this context, providing reliable ages for archeological levels and performing correlations among distant sections are rather complicated tasks. Identifying an appropriate dating technique plays therefore a critical role. In South Africa, efforts to date the sequences were considerable, but the complicated sequences characterized mostly by cave infill reworked deposits often limit their validity (Gallotti, 2022). In North Africa, the long sedimentary sequences of Casablanca emplaced in coastal transitional to continental environment require specific dating methods due to the lack of datable volcanic horizons.

The contribution of this thesis is to provide reliable chronologies through magnetostratigraphy for two key archaeological and paleoanthropological areas of Africa, that will allow to discuss the implications of the Acheulean emergence and development during the Early/early Middle Pleistocene. The sites chosen for this purpose are Melka Kunture (Ethiopia) and Thomas Quarry I (Morocco) representing almost complete archives of the origin and evolution of the Acheulean, accompanied by human fossils and faunal remains (Figure 1.1).

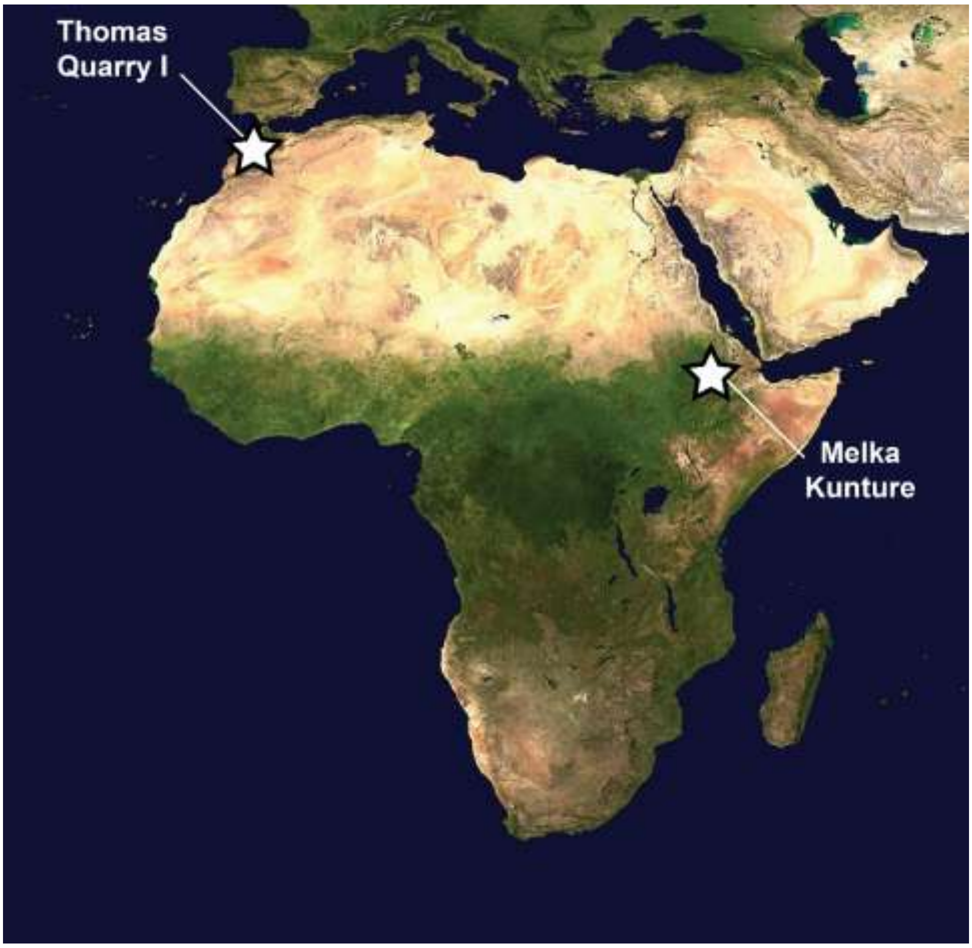

Figure 1.1 Geographical location of the sites object of this thesis.

Even though those sites are in a clear stratigraphic context, characterized by expanded stratigraphic sequences suitable for magnetostratigraphy, their chronological attributions were poorly constrained. Prior dating at Melka Kunture established through K-Ar, $^{40}Ar/^{39}Ar$ and magnetostratigraphy led to an uncertain attribution due to the high errors of radiometric results, often exceeding 20% (Morgan et al., 2012), and the incompleteness of magnetostratigraphic data (Tamrat et al., 2014). At Thomas Quarry I (Morocco) several dating attempts were made with biostratigraphy (Geraads et al., 2002; 2010), optically stimulated luminescence (OSL) and electron spin resonance (ESR) providing contrasting results (Rhodes et al., 2006).

The magnetostratigraphic method was applied to provide chronological constraints based on the globally synchronous and aperiodic polarity reversals of

Earth's magnetic field, and therefore identify the peculiar pattern of magnetozones of each stratigraphic sequence, also offering the opportunity to date geological material in situations where other methods are not effective (e.g., absence of tephra or speleothems).

The Quaternary Period, extending from 2.595 Ma to the present day (Gradstein et al., 2020), was characterized by several magnetic polarity reversals which proved particularly useful when applied to dating sections of archaeological and/or paleoanthropological relevance. Two main magnetic polarity intervals were defined for the Quaternary, the Brunhes Chron (<0.773 Ma) of prevailing normal polarity and the Matuyama Chron (0.773-2.595 Ma) of predominant reverse polarity. During the Matuyama Chron, corresponding to the Lower Pleistocene, several intervals of shorter duration (subchron) characterized by normal magnetic polarity occurred, known as Jaramillo, Cobb Mountain, Olduvai and Reunion subchrons, representing fundamental chronostratigraphic markers in this time-interval.

In this thesis the reference geomagnetic polarity timescale (GPTS) for Quaternary used throughout is the one from Channell et al., (2020) which provides the following ages for the magnetostratigraphic constraints, with acronyms according to Gee and Kent (2007) (Figure 2.1):

- Brunhes normal polarity Chron (C1n) <0.773 Ma;
- Matuyama reverse polarity subchron (C1r.1r) 0.773-0.990 Ma;
- Jaramillo normal polarity subchron (C1r.1n) 0.990-1.070 Ma;
- Matuyama reverse polarity subchron (C1r.2r·) 1.070-1.180 Ma;
- Cobb Mountain normal polarity subchron (C1r.2r-1n) 1.180-1.210 Ma;
- Matuyama reverse polarity subchron (C1r.2r ·) 1.210-1.770 Ma;
- Olduvai normal polarity subchron (C2n) 1.770-1.925 Ma;
- Matuyama reverse polarity subchron (C2r.1r) 1.925-2.116 Ma;
- Reunion normal polarity subchron (C2r.1n) 2.116-2.137 Ma;
- Gauss/Matuyama boundary (base of the Quaternary) 2.595 Ma.

Magnetostratigraphic analyses were conducted to reconstruct the magnetic polarity stratigraphy of each site for dating through correlation to the reference geomagnetic polarity time scale (GPTS). The ages obtained from the magnetic polarity reversal recognized in the stratigraphic sequences were used in combination with the available radiometric ages from the literature to perform age-depth modelling useful to derive the interpolated ages of the archeological/paleoanthropological horizons of interest.

After establishing a robust chronology for the Acheulean sequences at Melka Kunture (Ethiopia) and Thomas Quarry I (Morocco), which provided surprising results, the focus passed to an overall review of the East African chronological, archeological and paleoanthropological records. Establish high resolution-chronologies have allowed the archaeologists to interpret the origin of the Acheulean and its relationship with the crowd of hominids (Foley, 1997) that populated East Africa.

1.1 Quaternary geochronology

Quaternary geochronology represents a complex field of scientific research as continental sequences are frequently laterally discontinuous, often characterized by unconformities, difficult to correlate due to the wide variability of depositional facies even at short distances, and they frequently lack reliable biostratigraphic constraints. These issues become even more crucial when it comes to dating sites documenting human presence, because on these chronologies, the history of our species is built. Therefore, the choice of the most appropriate dating method is a fundamental aspect in the process of reconstructing our past.

Different dating methods have been implemented in the last decades in the study of the Quaternary, based mostly on radioisotopes decay, such as $^{40}Ar/^{39}Ar$ on tephra layers, U-Th or U-Pb on zircons and speleothems (Richard et al., 1998), and cosmogenic nuclides ^{26}Al and ^{10}Be (Schaefer et al., 2022). Moreover, other techniques have been developed like electron spin resonance (ESR) (Grün, 1989), optically stimulated luminescence (OSL) (Galbraith and Roberts, 2012) and Thermoluminescence (TL) (Wintle and Huntley, 1982) conceived in order to date sedimentary sequences without volcanic input. For example, ESR dating is based on the time dependent accumulation of electrons in the crystal lattice of certain minerals exposed to surrounding radiation. The age is obtained by calculating the dose received compared to the dose rate generated by the surrounding environment (Grün, 1989). These 'trapped charge' dating methods of undisputable value require careful knowledge of environmental dose rates in the past, which can be difficult to determine, leading to experimental errors sometimes exceeding 30%. Mammal biostratigraphy is also frequently applied to the study of the Quaternary, but the chronostratigraphic relationships between faunal units dispersed on a continent the size of e.g., Africa characterized by wildly different regional-scale environmental conditions and geographical barriers between them, are frequently difficult to assess.

In this thesis, Quaternary chronology is investigated through the application of magnetostratigraphy, which allows to date and correlate stratigraphic sequences at global scale across different depositional environments. Magnetostratigraphy is a branch of stratigraphy that utilizes the record of the magnetic polarity reversals of the Earth's magnetic field to date and correlate rock sequences by means of magnetic parameters. The method involves the study of the paleomagnetic direction of the field whose orientation is recorded by sedimentary and volcanic rocks through their ferromagnetic mineral content. These minerals are capable to maintain the signal registered at the time of rock emplacement over time. Due to the randomness with which the Earth's magnetic field flips polarity, a sequence of geomagnetic reversals identified along a stratigraphic sequence is characteristic of a specific time-interval. When the magnetic reversal sequence is correlated to a reference geomagnetic polarity timescale (GPTS) (Figure 2.1) and is possibly provided other chronological tie-points from, e.g., radiometric dating, an age-model of deposition can be developed for dating levels of interest. The main advantage of this technique is that stratigraphic sequences are dated and correlated through the recognition of isochronous global signals, therefore each magnetic reversal represents a synchronous timeline at global scale. Intensity and direction of the field are registered at the time of rock formation through different natural processes by ferromagnetic minerals (Muttoni, 2010). Suitable mineral phases in magnetostratigraphy are magnetite, hematite, phases of the solid solutions of the titanomagnetite and titanohematite, maghemite, greigite and greigite/pyrrhotite, while iron hydroxides such as goethite and lepidocrocite, that are usually produced by weathering reactions, are generally associated with secondary phenomena and tend to record post depositional overprint signals. Among these minerals magnetite and hematite are usually the most reliable recorders of the primary paleomagnetic signal carrying polarity reversals. They originate in magmatic contexts and acquire magnetic properties during cooling below the Curie temperature of ~580°C for magnetite or Néel temperature of ~675°C for hematite. These unlocking temperatures have been estimated as approximations by Dunlop and Özdemir (1997) for magnetite and by O'Reilly (1984) for hematite. In sedimentary environments, the erosion of pre-existing rocks provides the supply of these minerals which are then involved in transport and can be incorporated in sedimentary deposits through different processes. In marine and lacustrine realms, magnetite can also be produced biologically by magnetotactic bacteria living both in marine and freshwater environment within the sediments near the sediment-water interface and in the water column. Those are the ones that more likely contribute to magnetic remanence (e.g., Zhao et al., 2016).

Rocks containing stable ferromagnetic minerals can record a signal parallel to the direction of the ambient geomagnetic field, acquiring a natural remanent magnetization, or NRM (Muttoni, 2010). The measurement and laboratory treatment of the NRM in samples taken throughout a stratigraphic sequence is used to subdivide the sequence in intervals of alternating normal or reverse polarity, generating a magnetic reversal sequence for correlation to the reference GPTS.

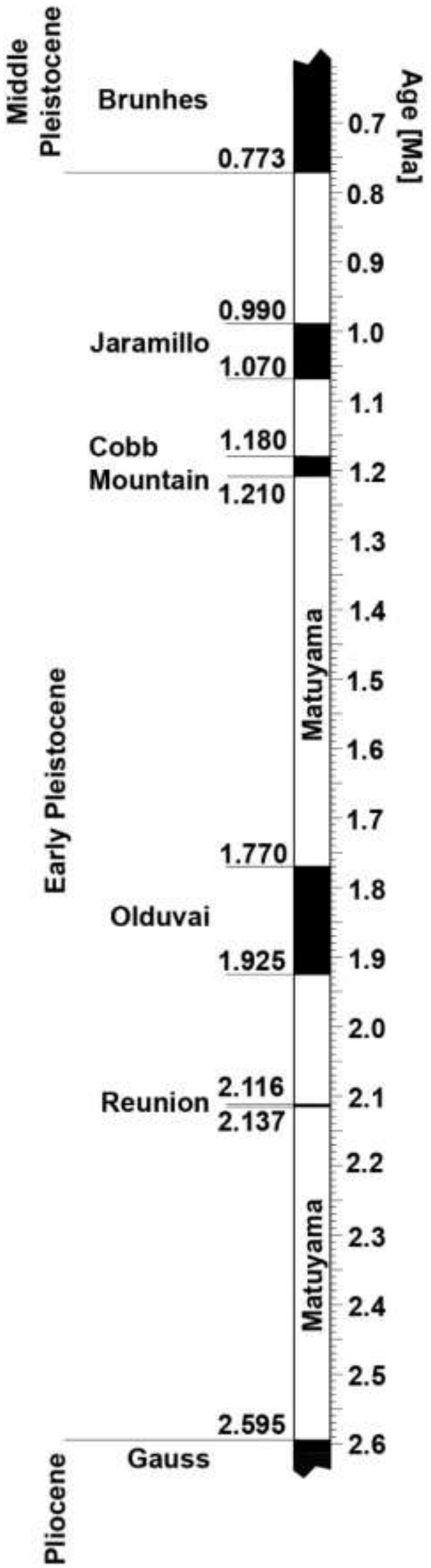

Figure 2.1 Reference GPTS according to Channell et al., (2020) used in this thesis.

1.2 Research approach

As stated above, one of the main aims of this thesis is to clarify and refine the chronologies of Melka Kunture (Ethiopia) and Thomas Quarry I (Morocco) through magnetostratigraphy. The approach used in order to reach this goal began with a careful analysis of the literature concerning the stratigraphic and chronologic frameworks of the targeted areas as well as their archaeological and paleoanthropological content. Extensive field activity was conducted at Thomas Quarry I involving outcrop description and evaluation of the stratigraphic relationships, followed by the generation of reference stratigraphic logs used for facies analysis and, finally, magnetostratigraphic sampling. With the aim of proposing age-depth depositional models integrated with chronological data, to explain the sedimentary evolution of the area, an attempt of interpretation in terms of sequence stratigraphy was proposed.

All samples collected for magnetostratigraphy for both localities were processed in the laboratory following experimental protocols illustrated in chapter 4. Then, the obtained results were integrated, where possible, with radiometric dating from the literature and used to generate age models of deposition for the sites of interest. The resulting ages were subsequently compared with selected results after a detailed review of the literature regarding the East African archeological and paleoanthropological record to delineate the dynamics of emergence of Acheulean in East Africa and eventually identify the possible toolmaker(s).

After a general introduction about the geological setting and archeological relevance for each area (chapter 3) the presentation of results in this thesis is organized from the more ancient archeological area, Melka Kunture (Ethiopia) (chapters 5, 6 and 7) to the more recent, Thomas Quarry I (Casablanca, Morocco) (chapters 8 and 9). The first manuscript of each area presents the general magnetostratigraphy and chronological interpretation for the entire sequence, followed by the chronological refinement of specific stratigraphic intervals of interest, such as Kella Valley for Melka Kunture (chapter 6) and ThI-GH site for Thomas Quarry I (chapter 9). Also, the data obtained from Melka Kunture have been used to discuss the archaeological implications regarding the Acheulean emergence in a broader East African perspective (chapter 7).

Most of the results have been published on peer-review journals and presented in international meetings, while the remainder are being processed for submission.

Chapter 2

African Early Pleistocene archeological record

The African continental record contains the oldest evidence of lithic productions, often associated with faunal and/or hominin remains. Lithic industries represent the most consistent evidence of human activity in the most ancient periods of prehistory. They provide information on the technical behaviors of prehistoric men, especially when they come from indisputable stratigraphic contexts investigated through systematic excavations. The study and interpretation of the different types of artefacts and their technical characteristics allows the identification of specific cultures in a specific space and time and, more generally, to trace human cultural evolution.

In Africa, the most ancient technologies owe their names to the type locality where they were first discovered, for example the term Oldowan derives from the Olduvai Gorge archeological area (Tanzania) where the first Oldowan stone tools were discovered in the ‘30s by Louis Leakey (Leakey, 1934; 1936), while the term Acheulean belongs to the type site of St. Acheul (France) discovered by de Mortillet (1872) at the end of XIX century.

Oldowan and Acheulean may have been produced and used by hominin species through time over wide geographical area.

2.1 Oldowan

The Oldowan represents a technocomplex broadly spanning between ~2.8 to ~1.4 Ma. However, the discovery of stone artefacts dated to ~3.3 Ma at Lomekwi 3 in West Turkana (Kenya) claims for an older origin for stone tool technology (Harmand et al., 2015).

Oldowan lithic activities mainly focus on the production of small-medium sized flakes (small flaking) with sharp edges from cobbles or angular clasts, which are rarely retouched. Flaking methods are characterized by a variety of methods strongly dependent on the raw material constraints (e.g., size, geometry, and lithology). Several Oldowan sites yielded also percussive material used both for knapping and other activities as food-processing (Kuman, 2019). Initially interpreted as a single period lasting more than one million years of technological stasis (Semaw et al., 1997; Semaw 2000; Stout et al., 2010), in the current state of knowledge it is considered as comprised of two distinct periods: early Oldowan (from 2.8 to 2.3 Ma) and late Oldowan (≤2.0 Ma). They do not correspond to two evolutionary technological steps, but the distinction between those assemblages has a chronological significance (e.g., Delagnes and Roche, 2005). The only difference so far detected in late Oldowan assemblages (≤2.0 Ma) is the rather systematic intra-site coexistence of a panoply of flaking methods and practices, which at earlier sites were only tested and experienced at inter-site scale. Accordingly, the difference is not in the final product, but it concerns more with the ability to vary the technical operations by adapting to the different raw materials, which in time generated a wide variability of flaking methods. This means that since 2.0 Ma knappers were able to simultaneously apply several technical solutions to exploit all the available lithic resources of a specific micro-region (Gallotti, 2018).

2.2 The origin of the Acheulean and the Oldowan/Acheulean transition

The disappearance of the earliest human culture, the Oldowan, and its substitution by a new technology, the Acheulean, is one of the main topics in modern Paleoanthropology. The Acheulean was the first human culture to be widely spread across the Old World and persisted for 1.5 million years. Due to these worldwide implications, much effort has been invested in recent years to trace the earliest Acheulean. However, the biological and cultural processes that led to the emergence of the Acheulean are still poorly understood (de la Torre, 2016; Gallotti and Mussi, 2018[a]). Traditionally, it has been assumed that this major cultural change was ignited by the emergence of a new human species, *Homo ergaster/erectus*. However, these assumptions are not grounded in the current available evidence, but rooted in cultural history paradigms that should now be superseded. It is therefore, at present, unclear whether there are effective causal links between the appearance of a new species, *Homo erectus*, and the emergence of the Acheulean as a technology, and their relation to the extinction of *Homo habilis* and the disappearance of the Oldowan culture (Gallotti and Mussi, 2018[a]).

Cultural mechanisms that led to the emergence of the Acheulean are also poorly understood. In the first place, it is unclear how and why core-and-flake methods of knapping, typical of the Oldowan, gave way to Acheulean technology based on the production of huge flakes made into Large Cutting Tools. Further complicating the issue is the presence of stone tool industries that lack handaxes after the emergence of the Acheulean (de la Torre, 2016; Gallotti and Mussi, 2018[a]). Summarizing, it is not clear whether the Acheulean is a technological evolution of the Oldowan or an intrusive phenomenon (e.g. de la Torre and Mora, 2016; Gallotti and Mussi, 2018[a]). Recent research has gradually provided new data on the timing of emergence of technical innovations, on the relationship with the Oldowan and on the diversity of its technical behaviors. And exactly this diversity among African Acheulean industries allows to think that there may have been not just one but several African Acheuleans (see chapter 7; Gallotti, 2022).

2.3 The developments of the Acheulean in the Early/early Middle Pleistocene

The development of the Acheulean after 1.4 Ma is poorly understood. From then onwards and up to 0.7 Ma, the long stratigraphic sequences in East Africa are from a limited number of sites, and several are of uncertain age (e.g. Leakey, 1971; Isaac and Isaac, 1997; Roche et al., 2003; de la Torre, 2011; Beyene et al., 2013; McHenry et al., 2016). Descriptions of the corresponding late Early Pleistocene lithic series are generally limited to the LCTs and their morphological or aesthetic patterns (Gallotti and Mussi, 2017, 2018[b]). Accordingly, no direct comparison can be made with the record of the earlier Acheulean.

In addition, there are very few human fossils in this period (e.g., Antón, 2013; Antón et al., 2014; Baab, 2014; Profico et al., 2016; Antón and Middleton, 2023), and their association with lithic artefacts and faunal remains has usually been taken for granted, not proved.

This fragmented evidence found in the East African record has frequently been underestimated in large-scale syntheses involving Acheulean technical behaviours. It is often taken for granted that the Early Pleistocene is a uniform cultural entity closely related to the evolutionary history of *Homo erectus* (e.g., Leakey, 1975; Sharon, 2007; Beyene *et al.*, 2013). The Acheulean industries often described as “remarkably static and lacking innovation over thousands of years and across a number of varied environmental settings” (Nowell & White, 2009, p. 76).

Recent research at Melka Kunture has instead demonstrated the existence of two Acheuleans at Melka Kunture: an early Acheulean dated to 1.6 Ma and a second Acheulean dated to 1 Ma, respectively associated with *Homo* aff. *erectus* and an ancestor of *Homo heidelbergensis* (Gallotti and Mussi, 2017, 2018).

The existence of two different Acheuleans has also been proposed for the Casablanca region (Raynal et al., 2017; Mohib et al., 2019; Gallotti et al., 2022), the first dated to 1.3 Ma at Thomas Quarry I-Unit L, the second dated to 0.5 Ma at the *Grotte à Hominidés* (Raynal et al., 2010, 2011, 2023) and to 0.7 Ma at the *Grotte des Rhinocèros* (Raynal et al., 2023). In both East and North Africa, the two Acheuleans are separated by an important chronological gap. The main question is what this poor information depends on, if it is the outcome of incomplete fieldworks or if it is related to geological, climatic, and/or paleo-environmental mechanisms.

One of the aims of this thesis is to refine the uncertain chronology of the Acheulean sequence of the Melka Kunture Formation (Ethiopia) and of Thomas Quarry I (Casablanca, Morocco), L-sites and Grotte à Hominidés, to try to better define chronologically this gap.

Figure 2.3.1 Acheulean artefacts from ThI-L archeological site.

Chapter 3

Sites and geological contexts

3.1 East Africa

The Pleistocene volcano-sedimentary archives of East Africa documents the oldest and most varied archeological and paleoanthropological record in the world. A milestone of human cultural evolution documented in this macro-region is the emergence of the Acheulean testified by several localities located across the African Rift Valley, from the Ethiopian Highlands (Melka Kunture and Melka Wakena) to the Ethiopian Mid-Lowlands (Konso-Gardula and Gona), the Lowlands of Kenya (Turkana Basin) and the Midlands of Tanzania (Olduvai Gorge). As previously stated, a main aim of this thesis is to refine the chronology of the key archeological area of Melka Kunture (Ethiopia) in order to provide an age estimate for the ten archeological sites hosted in the Melka Kunture Formation (MKF) with particular emphasis to sites registering the Oldowan-Acheulean transition.

Since the origin of the Acheulean is a highly debated topic, several questions regarding the implications of such an old age for the earliest Acheulean raised. What is the meaning of such an early appearance of the Acheulean on the Ethiopian Highlands? How did it originate and what was the dynamics of its dispersal? Is there one single Acheulean with different technology that appeared and invasively expanded through East Africa as a single event, or there are more Acheuleans with different characters appearing at different times and places across East Africa? Moreover, the timing of the development of this earliest Acheuleans is poorly understood, but the sedimentary sequence of Melka

Kunture offers the opportunity to investigate also the later stages after the Acheulean emergence.

To attempt responding these questions, a whole East African chronological framework was assembled through careful and critical review of the existing bibliography to place the earliest occurrences of the Acheulean in the various East African regions in a common temporal framework. This chronological approach was accompanied by a critical archeological discussion on the techno-economic behaviors to understand when and what type of technical innovations emerged in each region, and how they relate to the human biological variability recorded in this time period. Despite the fragmentary nature of the East African continental record, it has been possible to set a general overview based on the current state of knowledge to contextualize better the Acheulean in a broader scenario finding unexpected outcomes.

3.2 Melka Kunture (Ethiopia) state of the art: geological setting, archeological relevance and chronology

Melka Kunture is an archeological site-complex located in the Upper Awash Valley of the Ethiopian highlands (8°420N; 38°350E), about 50 km southwest of Addis Ababa at 2000-2200m above sea level (a.s.l.). The investigated area, characterized by a relatively continuous volcano-sedimentary sequence, extends over some tens of km^2 on the two banks of the Awash River, and hosts a dense concentration of archaeological and paleoanthropological sites (Fig. 6.1).

The Melka Kunture stratigraphic sequence, mainly composed of fluvial/alluvial siliciclastic and volcaniclastic deposits variably intercalated with tuff/cinerite, informally known as Melka Kunture Formation (e.g., Bardin et al., 2004; Kieffer et al., 2002, 2004; Raynal et al., 2004; Raynal and Kieffer, 2004; Gallotti and Mussi, 2017; Pioli et al., 2023), is exposed along a network of gullies incised by tributaries of the Awash River. Different stratigraphic levels of archeological and paleoanthropological interest have been discovered throughout this sequence in the last decades, spanning from the Oldowan to the Late Stone Age (Chavaillon et al., 1974; Chavaillon et al., 1979; Chavaillon and Coppens, 1986; Chavaillon and Berthelet, 2004; Chavaillon and Piperno, 2004; Gallotti et al., 2010, 2014; Gallotti and Mussi, 2015, 2017, 2018; Gallotti et al., 2010; Mussi and Gallotti, 2014; Mussi et al., 2014, 2016).

Previous magnetostratigraphic studies (Westphal et al., 1979; Tamrat et al., 2014), combined with radiometric dating of tuff/cinerite using K/Ar (Schmitt et al., 1977; Chavaillon and Piperno, 2004) and $^{40}Ar/^{39}Ar$ (Morgan et al., 2012), suggested that the Melka Kunture sequence deposited in a magnetochronologic interval spanning from the early Brunhes Chron (<0.773 Ma; geomagnetic polarity time scale of Channell et al., 2020 used throughout) at the top to the Olduvai Subchron (1.770 Ma to 1.925 Ma) at the base. These valuable magnetostratigraphic data (Tamrat et al., 2014) are however difficult to integrate in the ever-growing inventory of archeological levels described at Melka Kunture (e.g., Gallotti and Mussi, 2017, 2018) because of the laterally discontinuous nature of the stratigraphic sequence. The aim of this work was to provide new magnetochronological constraints on the deposition of the Melka Kunture sedimentary sequence and related archeological/paleoanthropological layers. Sampling for magnetostratigraphy has been conducted along nine stratigraphic sections outcropping along two adjacent gullies termed Gombore and Garba. In these sections we identified the main archeological sites from the literature including, from younger to older, Gombore II-2 Butchery site, Gombore II Open Air Museum, Gombore Iδ, Gombore Iγ, and Gombore IB for the Gombore gully, and Garba III, Garba XIIJ, Garba IVD, Garba IVE, and Garba IVF for the Garba gully. Our new magnetostratigraphic data have been integrated with $^{40}Ar/^{39}Ar$ age data from Morgan et al. (2012) in order to generate age models of deposition for the Gombore and Garba gullies sequences and derive (interpolated or extrapolated) best-fit ages of the main archeological levels therein contained.

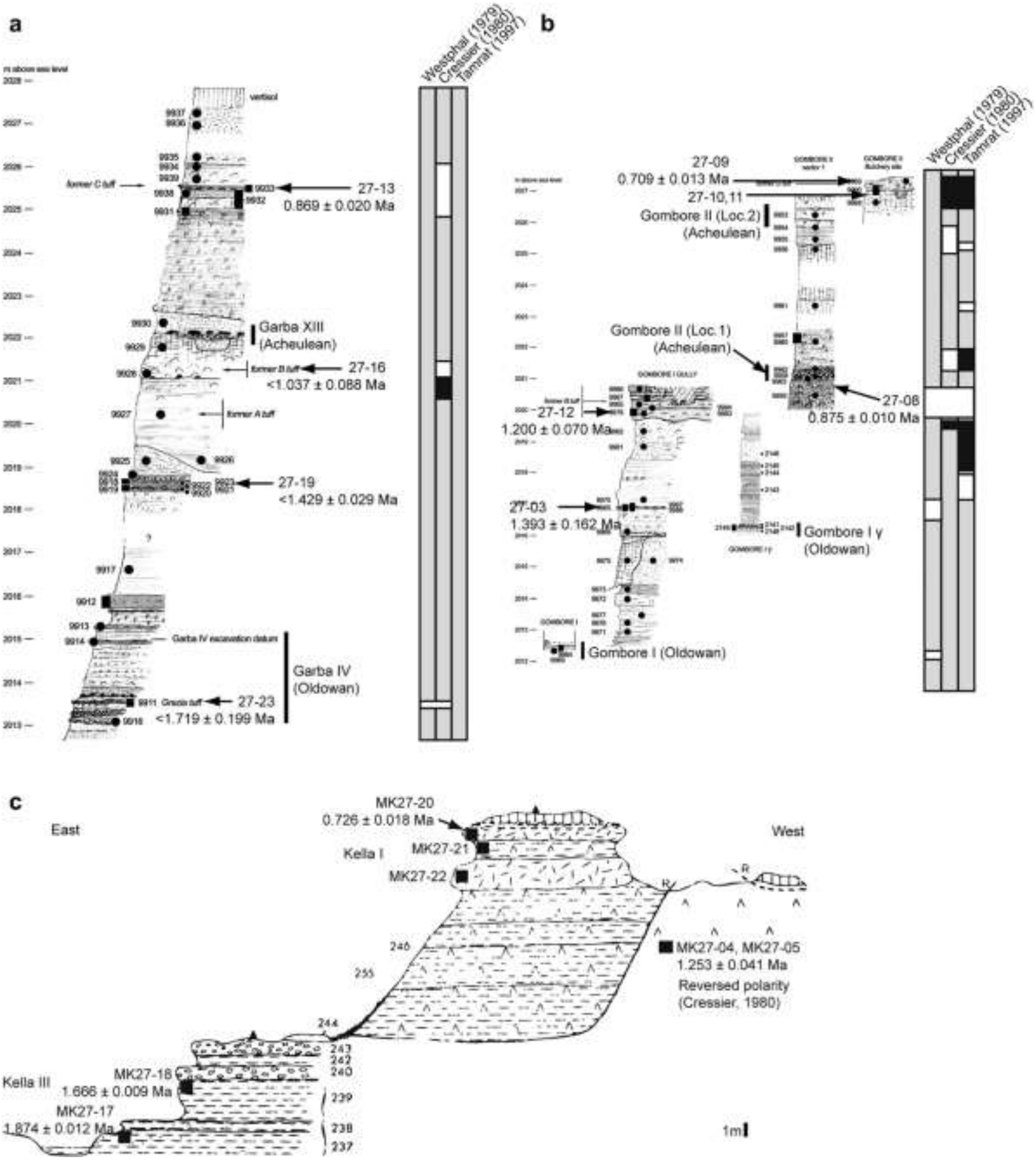

Figure 3.2.1 General stratigraphy of the Melka Kunture Formation outcropping in the tributary gully of the Awash River at Garba (a), Gombore (b) (reported in m a.s.l., after Raynal et al., 2004) and Kella localities (c) (modified from Taieb (1974)). Preliminary magnetostratigraphic results are reported according to Westphal et al. (1979), Cressier (1980), and Tamrat et al., (2014). Also, K-Ar and $^{40}Ar/^{39}Ar$ ages are reported from Schmitt et al., (1977) from Morgan et al. (2012) respectively.

Following the establishment of this first chronostratigraphic background, the focus passed to improving the chronological resolution across the critical Olduvai subchron interval using two sections located on the left bank of the Awash River in the nearby Kella valley: Kella III bis and Kella Bridge, where the basal part of the Melka Kunture Formation is documented and provided with published $^{40}Ar/^{39}Ar$ ages (Morgan et al., 2012). The oldest one, Tuff MK 27-17, 1.874 ± 0.024 Ma, suggests that the Olduvai subchron should be present in these levels. These data from Kella were used in conjunction with data from Garba IV to propose a regional correlation of the basal part of the Melka Kunture Formation around the base of the Olduvai subchron. This is relevant for the secure placement in time of both the earliest human presence so far recorded at Melka Kunture, which is also the earliest documented on the Ethiopian highlands and the Oldowan-Acheulean transition as represented by Oldowan levels Garba IVF-E and early Acheulean level Garba IVD.

3.3 North Africa

The North African record is characterized by few archeological localities that document human presence albeit devoid of accurate dating. Although many archaeological investigations have been carried out in Morocco since the beginning of the nineteenth century, only a few purported pre-Acheulean sites were reported, and all are in disputable stratigraphic contexts (Gallotti et al., 2021, 2023).

The only pre-Acheulean evidence recorded from a stratigraphic context belongs to the Ain Hanech Formation in Algeria, where Oldowan occurrences dates to 2.4 and 1.9 Ma (Shanouni et al., 2018), but their age is controversial (Geraads et al., 2006). Another possible Early Pleistocene Algerian site with a similar age is Mansourah, which yielded a lithic industry without LCTs (Chaid-Saoudi et al., 2006). In this context, the only North African Acheulean sites in known stratigraphic context are located in Algeria, Tighennif, and in Morocco, Thomas Quarry I (ThI) (Geraads et al., 1986; Gallotti et al., 2022, 2023; Raynal et al., 2023). This sporadic and low-resolution evidence, the absence of pre-Acheulean sites in Morocco, and the wide gap between the Oldowan in Algeria and the early Acheulean of Morocco don't allow a discussion hinting at a local origin of this technical innovation.

Thomas Quarry I (Morocco), targeted in this thesis, belongs to the Casablanca Sequence which represents the most complete sedimentary successions of raised marine terraces and associated continental deposits of North-West Africa, and contains key Lower Paleolithic assemblages originally discovered and studied by Biberson (1961), as well as relevant hominin remains. At Thomas Quarry I, key archeological findings are represented by Acheulean lithic tools retrieved from site ThI-L, mainly bifacial artefacts obtained from blocks of raw material and large flakes associated with poorly preserved faunal remains. At a higher stratigraphic level, site ThI-GH, yielded several human fossils including mandibles and vertebrae attributed to genus *Homo* associated with lithic tools and faunal remains (Raynal et al., 2010; Raynal et al., 2023).

3.4 Thomas Quarry I (Morocco) state of the art: geological setting and archeological relevance

In order to provide age constraints for the archeological and paleoanthropological findings, previous attempts to date this sedimentary sequence were performed through OSL and ESR dating obtaining an approximate age of ~0.9 Ma for ThI-L and ~0.5 Ma for ThI-GH respectively (Rhodes et al., 2006), with wide uncertainties and incompatible with biostratigraphic data (Geraads et al., 2002; 2010). These uncertainties prompted to conduct a thorough magnetostratigraphic study of the sequence.

The geological substratum of the South-Western side of Casablanca, area where Thomas Quarry I is located, characterized by a Late Miocene-Pleistocene sedimentary sequence emplaced above either Cambrian Quartzites or Cretaceous Limestones. This so-called Casablanca Sequence consists of a complex and extensive system of longitudinal dune ridges parallel to the actual

Atlantic coastline and recording the succession of paleo-shorelines since the end of the Miocene (Lecointre 1952; Biberson, 1961; Stearns, 1978; Lefèvre & Raynal, 2002; Lefèvre et al., 2021).

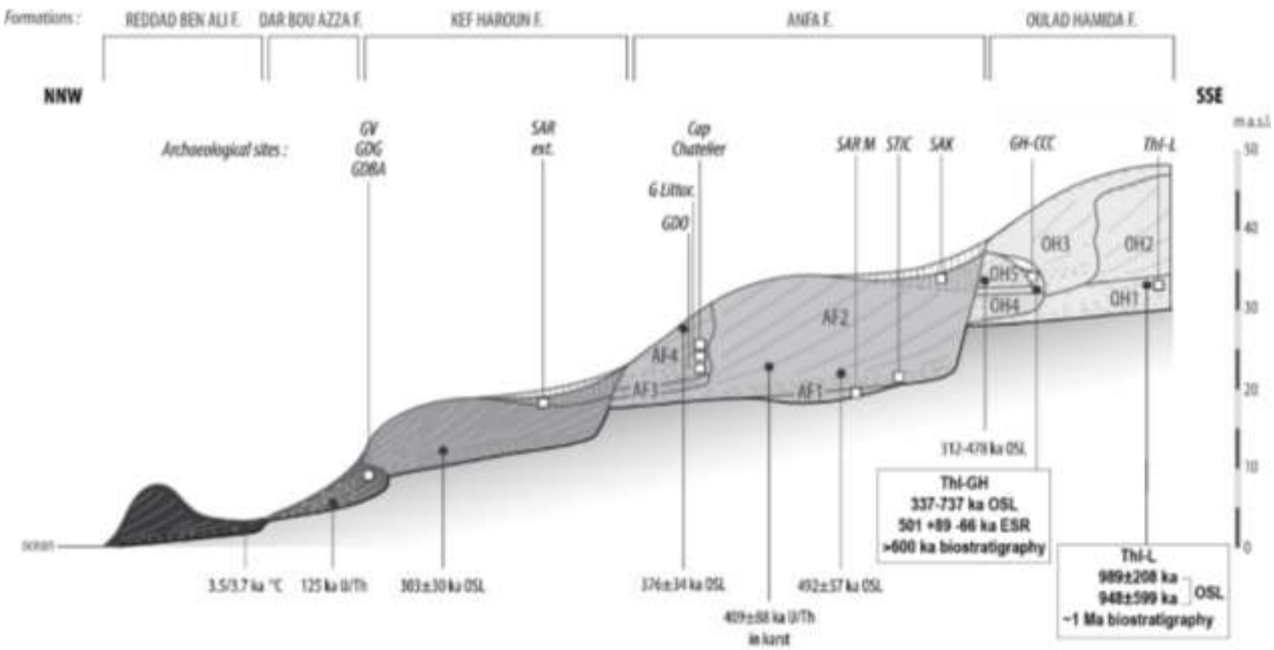

Figure 6.1.1 Sketch stratigraphic section showing the inferred relationships and relative altitudes of the Formations above present sea level: Reddad Ben Ali F., Dar Bou Azza F., Kef Haroun F., Anfa F., and Oulad Hamida F (Thomas Quarry I) (drawing from David Lefèvre). Age estimates obtained through biostratigraphy, OSL and ESR are reported according to the literature (Geraads, 2002; Geraads et al., 2010; 2022; Rhodes et al., 2006; Raynal et al., 2010). Archeological sites: GDBA: *Grotte de* Dar Bou Azza; GDG: *Grotte des Gazelles*; GDO: *Grotte des Ours;* GH-CCC: *Grotte à Hominidés*-complex of continental deposits; G Littor.: *Grotte des Littorines;* GV: *Grotte Velozzo*; SAR ext.: *Sidi Abderrahmane-Extension*; SAK: *Sidi Al Khadir*; SAR M: *Sidi Abderrahmane*-Unit M; S.T.I.C.: *Société de Transformation Industrielle et de Construction* Quarry; ThI-L: Thomas Quarry I-Unit L.

Its emplacement reflects eustatic oscillations on a passive continental margin under low uplift rates and takes the form of depositional cycles usually beginning with calcarenites marking marine transgression followed by regressive facies such as aeolianites and paleosols. Intense quarrying activities and urban exposed the Casablanca Sequence extensively. Four Formations associated with four raised platforms have been defined from the late Early to the Late Pleistocene (Figure 6.1.1): Oulad Hamida Formation (late Early Pleistocene-early

Middle Pleistocene), Anfa Formation (Middle Pleistocene), Kef Haroun Formation (Middle Pleistocene), and Dar Bou Azza Formation (Late Pleistocene) (Lefèvre, 2000; Lefèvre and Raynal 2002). The sedimentary sequence outcropping at Thomas Quarry I (hereafter ThI) was firstly described by Biberson (1961) and after recent stratigraphic revision was attributed to the Oulad Hamida Formation (hereafter OHF).

OHF lies above includes five allostratigraphic members OH1, OH2, OH3, OH4, comprising GH-continental cave complex (GH-CCC), and OH5, as described in detail in chapter 8 and supplementary material 8.

I. OH1 Member: Bed 1 is composed of coarse calcirudite at the base and a stratified coarse-grained biocalcarenite followed by Bed 2 characterized by bioclastic sands more or less bioturbated, partially decarbonated and cemented. A limestone unit within Bed 2 (ThI-L site), hosts several levels containing early Acheulean lithic artefacts, as well as the remains of large mammals;

II. OH2 Member: overlying an unconformity developed above OH1 Member, OH2A deposits comprises coarse biocalcarenites with a curved cross-bedding followed by a finer inclined planar-bedding biocalcarenites, vertically followed by massive coarse bioclastic aeolianites of OH2B, the upper part of which is affected by pedogenesis;

III. OH3 Member deposits are composed of blocs and pebbles produced by the dismantling of Members OH1 and OH2, passing to coarse and/or coquinoid biocalcarenites with inclined planar bedding, overlaid by aeolian calcarenites;

IV. OH4 Member is associated with a palaeoshoreline marked with cliff and deep coastal notch cut into OH1 and OH3. This unit begin at the base as a calcirudite with a coarse coquinoid matrix and plurimetric collapsed blocks of calcarenites from OH3 Member which constitutes the cavity ceiling and blocks of calcirudite coming from earlier units. The lower infilling of the cavity is a marine deposit passing upward to continental deposits labelled GH-Continental Cave Complex

(GHCCC). GH-CCC (SU 4-3) lies conformably above OH4 and is composed of bioclastic and quartzose sands containing lithic artefacts, macro and micro-fauna and hominin fossils, passing to GH-CCC (Su 2-1) is composed from bottom to top of a multilayer dripstone interbedded with loose red, laterally linking with a speleothem, overlying by massive bedded, rubefied sands rich in microfauna and fragments of gasteropods shells, originating from reworked superficials red soils. At the entrance of the cavity, the wide cross-bedding “gray” sands of Member OH5 are intercalated between the lower (3-4) and the upper units (1-2) of the GH-CCC;

V. Member OH5, overlying Member OH4, is composed of fine, weakly cemented calcarenites, characterized by a pronounced large scale cross-bedding. This unit partially fills GH and represent the more recent unit of the Oulhad Hamida formation.

Chapter 4

Materials and methods

4.1 Field activity

At Melka Kunture (Ethiopia), 273 stratigraphically superposed core samples were retrieved in 2017 and made available for this thesis. These analyses were conducted in order to reconstruct the general magnetostratigraphy of the sequence and date ten archeological horizons therein contained. A total of 248 samples were drilled at Thomas Quarry I in two different field campaigns with the aim to establish the general magnetostratigraphy of the sequence and date two key archeological bearing sites termed ThI-L and ThI-GH (see chapters 8, 9).

Field work at Thomas Quarry I (Casablanca, Morocco) was carried out with a detailed stratigraphic approach consisting of a first phase of evaluation of the stratigraphic context and relationships between units, followed by detailed lithological descriptions and drafting of logs. The sampling densities were decided based on the specific resolution needed for the investigated interval and also depending on the lithologies as the availability of fine granulometries that are usually the most favourable for paleomagnetism.

Sampling was performed using a water-cooled electric drill, for the more cohesive lithologies, or small plastic cylinders (5 cc volume) gently pushed into the outcrop, for soft lithologies, to obtain core-samples which were then oriented with a magnetic compass. The orientation parameters obtained are expressed as declination relative to the magnetic north and inclination with respect to the horizontal, by convention positive downward and negative upwards.

4.2 Laboratory procedure

The oriented core-samples obtained were then cut in standard sized samples, 2.5 cm diameter per 2.5 cm in length (10 cc volume) and subsequently weighted. The analyses were performed mostly at the LASA paleomagnetics Laboratory (Segrate, Italy) and also at ALP paleomagnetic Laboratory (Peveragno, Italy).

4.2.1 Rock magnetic analyses

Rock magnetic analyses were performed to investigate the magnetic mineralogy carrying the primary paleomagnetic signal. These include, magnetic susceptibility, anisotropy of magnetic susceptibility (AMS), acquisition of backfield isothermal remanent magnetization (IRM), hysteresis loops, thermal demagnetization of a three-components IRM and thermomagnetic cycles.
The initial magnetic susceptibility was measured using a MS2B (Bartington) susceptibility bridge or a KLY-2 Kappa-Bridge (Agico) followed by the measurement of the anisotropy of magnetic susceptibility (AMS) using a KLY-3 Kappa-Bridge (Agico).
The AMS was measured at room temperature to verify whether the magnetic grains had preferred orientations. These analyses allowed to define the maximum (kmax), intermediate (kint), and minimum (kmin) axes of the AMS ellipsoid of samples and the related standard parameters of foliation F = kint/kmin, lineation L = kmax/kint, degree of anisotropy P = kmax/kmin, and shape parameter T = 2ln(kint/kmin)/ln(kmax/kmin) − 1.

Backfield IRM acquisition, imparted fields from -1.5 T up to 1 T and hysteresis loops, imparted in fields between -1 T to 1 T or -0.5 T to 0.5 T, were performed with a vibrating sample magnetometer (VSM) model EZ7 (Microsense). Hysteresis plots of magnetization [Am^2/Kg] versus applied field [T] were used to determine values of saturation magnetization (Ms), saturation remanence (Mr), and coercivity (Hc), after correction for paramagnetic or diamagnetic components. The coercivity of remanence (Hcr) was determined on the same samples from IRM backfield experiments. The resulting diagram of Hc/Hcr versus Ms/Mr (Day et al., 1977; Dunlop, 2002), was used to infer about the domain state (~granulometry) of the magnetite particles, whether multi-domain (MD), pseudo-single domain (PSD) or single domain (SD). On the other hand, when samples contain a mixture of minerals with contrasting coercivities, backfield IRM acquisition curves were rescaled and analyzed using the unmixing coercivity method (Maxbauer et al. 2016) to identify each ferromagnetic phase contributing to the magnetic remanence as function of its specific coercivity spectrum and deriving the percentage in which it occurs.

Thermal demagnetization of three-component IRM (Lowrie, 1990) imparted in fields of 0.12 T, 0.4 T and 1.5 T or 2.5 T using a pulse magnetizer IM-10-30 (ASC Scientific), was performed in steps of 50°-25°C to detect ferromagnetic mineral phases by analyzing their maximum unblocking temperatures and coercivities. A selection of rock fragments was also subjected to thermomagnetic cycles using the VSM to study again the maximum unblocking temperatures of the ferromagnetic phases contained in the samples.

A selection of fragments from Thomas Quarry I was studied also using the S-Ratio = −IRM −0.3 T/SIRM2.5 T, obtained by applying a saturation IRM at 2.5 T followed by an antipodal IRM at 0.3 T, and the parameter HIRM = (IRM−0.3 T + SIRM2.5 T)/2 to investigate in detail rock magnetic variability along the section. S-Ratio approaching +1 reveals the occurrence of dominant low coercivity magnetic phases (e.g. magnetite) while S-Ratio approaching − 1 high coercivity phases (e.g., hematite, goethite), while the higher the HIRM the higher the content of high coercivity phases (e.g., hematite, goethite) relative to low coercivity phases (e.g. magnetite).

4.2.2 Magnetostratigraphy

To reconstruct the magnetic polarity stratigraphy thermal and alternating field (AF) demagnetization techniques were conducted with the purpose of isolate the characteristic (primary) component (termed ChRM) of the natural remanent magnetization (NRM) signal by removing secondary overprints usually of diagenetic origin.

Thermal demagnetization analyses were performed on oriented core-samples in increasing temperature steps from room temperature up to ~690° C with a TD48 furnace (ASC Scientific), while AF demagnetization was imparted on samples in fields from 0 mT up to 85 mT with steps of 5-10 mT with an AF demagnetizer (2G Enterprise). The residual NRM signal was measured after each demagnetization step mostly with a 755 DC-SQUID cryogenic magnetometer (2G Enterprises) located in a magnetically shielded room or with a spinner magnetometer Jr-6 (Agico).

Magnetic component directions were extracted using least-square analysis (Kirshvink, 1980) to calculate the ChRM component directions from standard vector end-point demagnetization diagrams, and standard Fisher statistics was applied to analyze the mean component directions. These ChRM component directions were transformed into virtual geomagnetic poles (VGPs). VGP latitudes were plotted versus stratigraphic depth in order to reconstruct the magnetic polarity stratigraphy for comparison with the reference timescale of Channell et al., (2020)

4.3 Age Modeling

Chronologies provide timeframes for events, allowing to derive rates of processes and making possible to compare and correlate different stratigraphic sequences. Many fields of application can profit from different kind of dating methods exploiting different principles to describe the same depositional system that could be used jointly through age modeling.

Age-depth modeling represents a useful tool to describe the depositional history of a sequence by considering different input data, for example numerical dating (e.g. ^{14}C, $^{40}Ar/^{39}Ar$) and magnetochronology, as function of depth. These are obtained by applying a mathematical function on a number of dated depths to derive a curve and the associated confidence interval used to estimate the ages of undated depths (targets) and related errors. There are several approaches to define age-depth relationships with different degrees of complexity but, generally, since ages are the result of measurements influenced by uncertainties, age modelling solutions must consider the treatment of these uncertainties (Lacourse and Gajewski, 2020). The chronological control, expressed as dating density (number of ages per time interval) represents a fundamental constraint before choosing which one to apply. Moreover, different modeling techniques are able to handle the age reversals by incorporating them increasing the uncertainty range. An age-depth model without age reversals is defined as *minimal adequate model* (Blaauw and Heegaard, 2012).

Until now, there is not a unique procedure on how to select which age-depth model to perform, what are acceptable values of age densities, and what are good quality input data. From these aspects derive precision and accuracy of the chronological model (Blaauw et al., 2018). How to mediate between these to constitute a good model is a choice that is based on the experience of the operator. Different age modeling techniques have been implemented in the last two decades (e.g. *Clam* (Blaauw, 2010), *OxCal* (Bronk Ramsey, 2008), *Chrono* (Haslett and Parnell, 2008), *Bacon* (Blaauw and Christen, 2011) and *Undatable* (Lougheed and Obrochta, 2019)) in particular for ^{14}C age modeling, that could be subdivided in different main categories according to Blaauw and Heegaard (2012):

- Linear interpolation

among the most frequently used model, represent the simpler way to build and age-depth model. In this case the age-depth model equation is a straight line interpolating the tie-points as best-fit line. The fitting quality is expressed by the correlation coefficient r^2, a value comprised between 0 (no fit) and 1 (perfect fit). The assumptions of linear interpolation presuppose that ages are accurate and that there are no variations in sedimentation rates through the investigated time-interval. The limitations in this approach lie in the inability to manage uncertainty and that changes in accumulation rates generally occur. Even though considered a crude method to establish age-depth models, it could provide fair estimates producing a fit that is hardly conflicting with more complex models (see Figure 8 in Chapter 5 for two examples of simple linear interpolation).

- Polynomial regression

returns age-depth model equations expressed as polynomial functions (e.g. quadratic curve for second-order polynomial regression, cubic curve for third-order polynomial regression etc.) and associated regression coefficient χ^2 (0= perfect fit; fitted curve passes through all the given data points).

- Splines

are polynomial curves fitted between each pair of points whose coefficients are non-locally determined, producing an overall smoothing effect and no abrupt changes in correspondence of each data point. Depending on the type of polynomial regression applied between pairs of points different models will be produced, such as cubic spline, smooth spline, or locally weighted splines (LOESS or LOWESS splines), where the smoothing terms are adjusted to constrain the bending of the curve and data could also be weighted according to their uncertainty.

Usually, smooth sedimentation rates are more realistic representations of the depositional dynamic through time especially when the sediment type does not change abruptly. Another approach would be to use one of the classes of smoothing functions which use all the available chronological information from the whole analyzed sequence to generate an age-depth model of deposition.

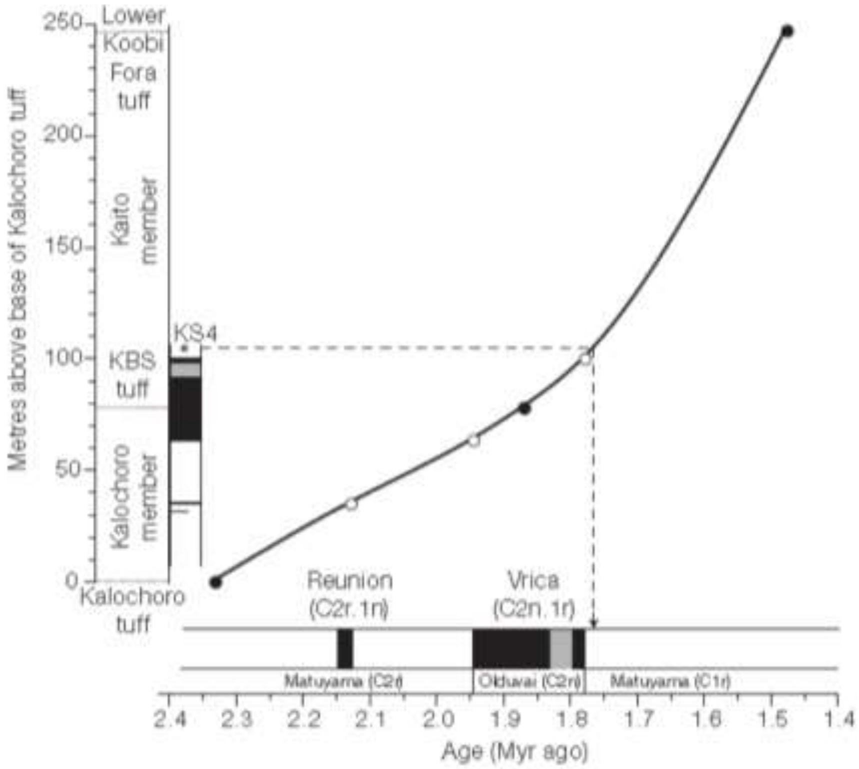

Figure 4.2.1 Example of cubic spline curve used to obtain the age of Kiselev 4 archeological site at 1.76 Myr ago (Lepre et al., 2011).

- Other models

A wide variety of age-depth models is based on the application of power functions (Campbell, 1996) as they can handle a greater degree of compaction increasing downward, which is one of the model parameters. Subsequently Bernstein polynomial (Bezier curve) regression is applied producing smoothing through or near all the points and fitted by approximation, and at the same time it is constrained to pass through the endpoints.

- Mixed-effects models

This approach involves the consideration of errors occurring in the whole age modeling system, such as the variance in age determination of a target level located at a particular depth, the numerical ages could be displaced from their true age (e.g. incorporation of older or younger material, contamination etc.) by a random value. The age-depth relationship is then obtained through any regression procedure chosen by the operator.

- Bayesian age-depth modeling

Gaining popularity in the last decade, Bayesian approaches offer an attractive alternative to the classic age-depth modeling methods, based on the principles of Bayesian statistics, which systematically combines data with all the other available information during the modeling process. The combination of prior information and data leads to the posterior distribution while the model incorporate assumptions about accumulation rates and/or how they vary, although in each program these are based on different depositional models associated to different parameters. For example, when a classical (e.g. linear, polynomial) age-depth modeling routine is applied, exploring different settings and the preferred one is chosen among the outcomes of these tests because not containing age reversals, such decision is arbitrary, while the Bayesian model is construct with a prior assumption of positive accumulation rates. Even though Bayesian techniques combines different approaches in the construction of age models, the best-fit model can resemble simple linear interpolation (Lacourse and Gajewski, 2020) and consequently, in the absence of many ages, these techniques can result in a best-fit model that resembles linear interpolation, albeit with improvements in uncertainty estimation (Blaauw et al., 2018). The main difference between Bayesian and classical models, especially linear interpolation, lies in the estimation of age uncertainties: in Bayesian models, age uncertainties tend to increase between chronological control points, while polynomial regression and smooth splines typically have uncertainties that are relatively constant between dated levels, and uncertainties in linear interpolation models could even decrease between ages. The precision of Bayesian age-depth models take advantage from chronological ordering continuing to improve by adding more dates. Bayesian models can be also supplemented by a deterministic approach (e.g. *Undatable*, Lougheed and Obrochta, 2019), but in general, this method provide better uncertainties estimations for any predicted ages for a given depth compared to the other kind of modeling routines. The accuracy of age models generally increases with higher dating densities providing reasonably accurate ages.

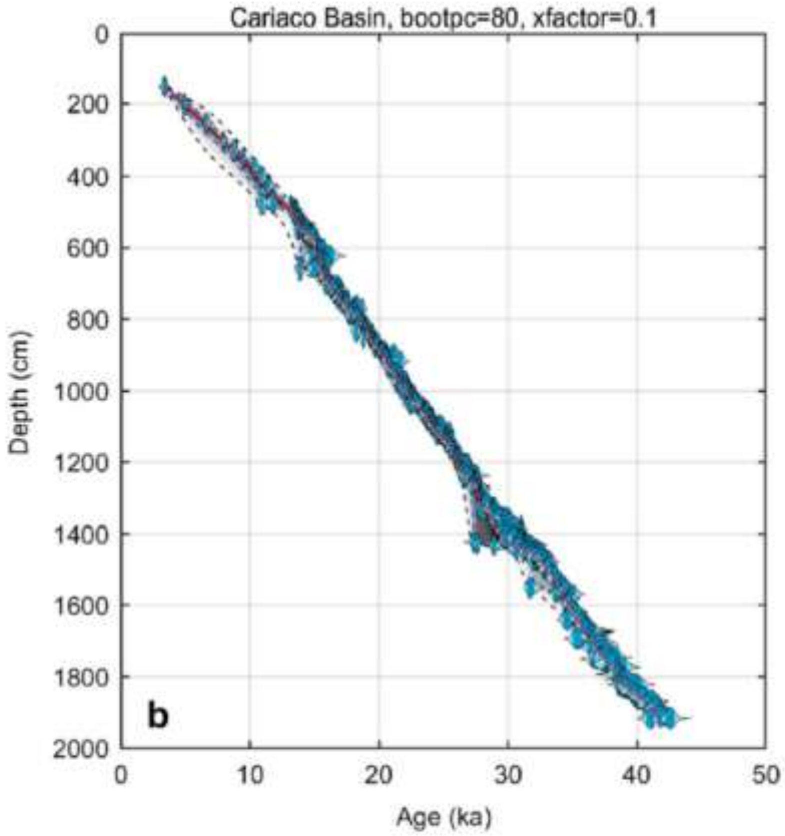

Figure 4.2.2 Example of age model of the Cariaco Basin obtained with the *Undatable* software (Lougheed and Obrochta, 2019)

Many age-depth models in literature contain long temporal gaps between ages or are affected by the age spacing problem, implying a poor chronological control in specific portions of the record. Therefore, to construct and age model besides the sufficient available ages is fundamental to consider how closely spaced the ages are in time (Blaauw et al., 2018; Lacourse and Gajewski, 2020). The tolerable gap lengths are strictly dependent on the research question, but in general long temporal gaps should be avoided (e.g. gaps of more than 20% compared to the total length of the record), even though in some cases long temporal gaps may be inevitable.

The construction of a robust age model begins by choosing the target(s) to date, the stratigraphic positions from which obtain ages (to obtain a good distribution of tie-points along the sequence), how many ages are needed and what material to date. As a general rule, extrapolating an age-depth model beyond the dated range of a sediment sequence should be avoided, as it assumes that the relationship between depth and time holds for sediments lacking chronological control.

Since most of the proposed rules for performing good age modelling refer to the field of radiocarbon dating (Blaauw et al., 2018, Lacourse and Gajewski, 2020) which has a temporal resolution bound to the last ~50 ka, it is not easy to reconcile them when dealing with more ancient geological archives (e.g. Lower-Middle Pleistocene). Since in these conditions the age modeling exploits other kinds of input data, such as magnetic reversals and numerical dating that are generally much more dispersed along a stratigraphic sequence, the best approach would be to carry out the age modeling trying several solutions in order to find the one that best describes the depositional history of a sequence.

Chapter 5

Magnetostratigraphy of the Melka Kunture Archeological Area (Ethiopia)

This chapter is presented according to

Magnetochronology and age models of deposition of the Melka Kunture stratigraphic sequence (Upper Awash, Ethiopia) and age assessments of the main archeological levels therein contained

Published on

Quaternary Science Reviews 274 (2021) 107259

https://doi.org/10.1016/j.quascirev.2021.107259

Serena Perini [a*], Giovanni Muttoni [a], Edoardo Monesi [b], 1, Rita T. Melis [c], Margherita Mussi [d]

[a] Dipartimento di Scienze della Terra 'Ardito Desio', Università degli Studi di Milano, via Luigi Mangiagalli 34, 20133, Milan, Italy; [b] via Mecenate 76, 20138, Milan, Italy; [c] Dipartimento di Scienze Chimiche e Geologiche, Università di Cagliari, Cittadella Universitaria, 09042, Monserrato, Italy; [d] Dipartimento di Scienze dell'Antichità, Università di Roma Sapienza, Piazzale Aldo Moro 5, 00185, Rome, Italy.

Abstract

We present new magnetostratigraphic results from the Melka Kunture sedimentary sequence outcropping along the Gombore and Garba gullies in the Upper Awash Valley of Ethiopia that provide a new temporal framework for human presence in this area of the Ethiopian plateau in the Pleistocene. We obtained a time-diagnostic sequence of normal and reverse polarity magnetozones representing a relatively continuous magnetochronologic record extending from the Brunhes Chron at the top to the Olduvai Subchron or possibly the Reunion Subchron at the base, assembled from 9 stratigraphic sections

correlated in a regional lithostratigraphic context. By integrating our chronology provided by paleomagnetism with $^{40}Ar/^{39}Ar$ dating from the literature, we generated simple yet reliable and testable age models of deposition for the Melka Kunture sedimentary sequence that we used to estimate the mean ages of the main archeological levels therein contained that resulted ranging from ~0.6 Ma to ~2.1 Ma thus representing altogether one of the most persistent and prolonged records of human presence of the entire African continent.

Geological setting

Gombore gully, we studied, from top to bottom, stratigraphic sections GX, GII2 - G2SAG, GII6, GOAMII, GIISag17I, GXIS, and Gombore I, this latter subdivided into four portions GG, GIG, GIS, and GIC (Figs. 1, 2 and acronyms therein described), while at Garba gully, we studied sections GBIII, GBXIIC - GBXIIB - GBXIIA, GBIVO, and GBIV (Fig. 2). The prevalent lithologies (Fig. 2) are litoquartzarenites and reworked volcanoclastic material, sometimes cross-laminated and often containing lapilli or tuff chips, as well as silts, silty clays, and conglomerates, which are variably intercalated with cinerite and tuff in primary position, some of which have been dated with K/Ar and $^{40}Ar/^{39}Ar$ (Schmitt et al., 1977; Morgan et al., 2012), as well as massive lahar deposits.

Altogether, the sedimentary succession deposited in an alluvial/fluvial plain context characterized by occasional but persistent volcanogenic input (see Raynal et al., 2004; Raynal and Kieffer, 2004; Chavaillon, 1979 for further details). These lithologies are particularly favourable for paleomagnetic analyses because of the general presence of fine-grained sediments (fine sand, silt), occurring even within the coarsest fractions either as matrix or as individual layers or pockets, as well as for the virtually ubiquitous presence in these sediments of a volcaniclastic fraction enriched in ferromagnetic minerals (as testified by the relatively high remanent magnetization values of the investigated samples; see also below).

Figure 1 Google Earth map of the Melka Kunture archeological area in Ethiopia. Gombore and Garba are the main gullies where we studied a total of 9 stratigraphic sections to assess the chronology of deposition of the Melka Kunture sequence and main archeological levels present therein. Numbers refer to georeferenced points reported also in the stratigraphic scheme of Fig. 2.

In the studied sections (Fig. 2), we identified the following tuff levels provided with what we initially considered acceptable $^{40}Ar/^{39}Ar$ ages (after Morgan et al., 2012), with errors here expressed at 2σ level: at Gombore gully, Former D tuff 27-09 at 0.709 ± 0.026 Ma, Tuff 27-08 at 0.875 ± 0.020 Ma (but see below in Paragraph 4 for the reliability of this datum), Former B tuff 27-12 at 1.200 ± 0.140 Ma, and Tuff 27-03 at 1.393 ± 0.324 Ma, while at Garba gully, Tuff 27-23, informally termed also “Grazia Tuff”, at 1.719 ± 0.398 Ma (but see below in Paragraph 4 for the reliability of this datum) (Fig. 2). As stated in the Introduction, several archeological and/or paleoanthropological levels have been described in this sequence.

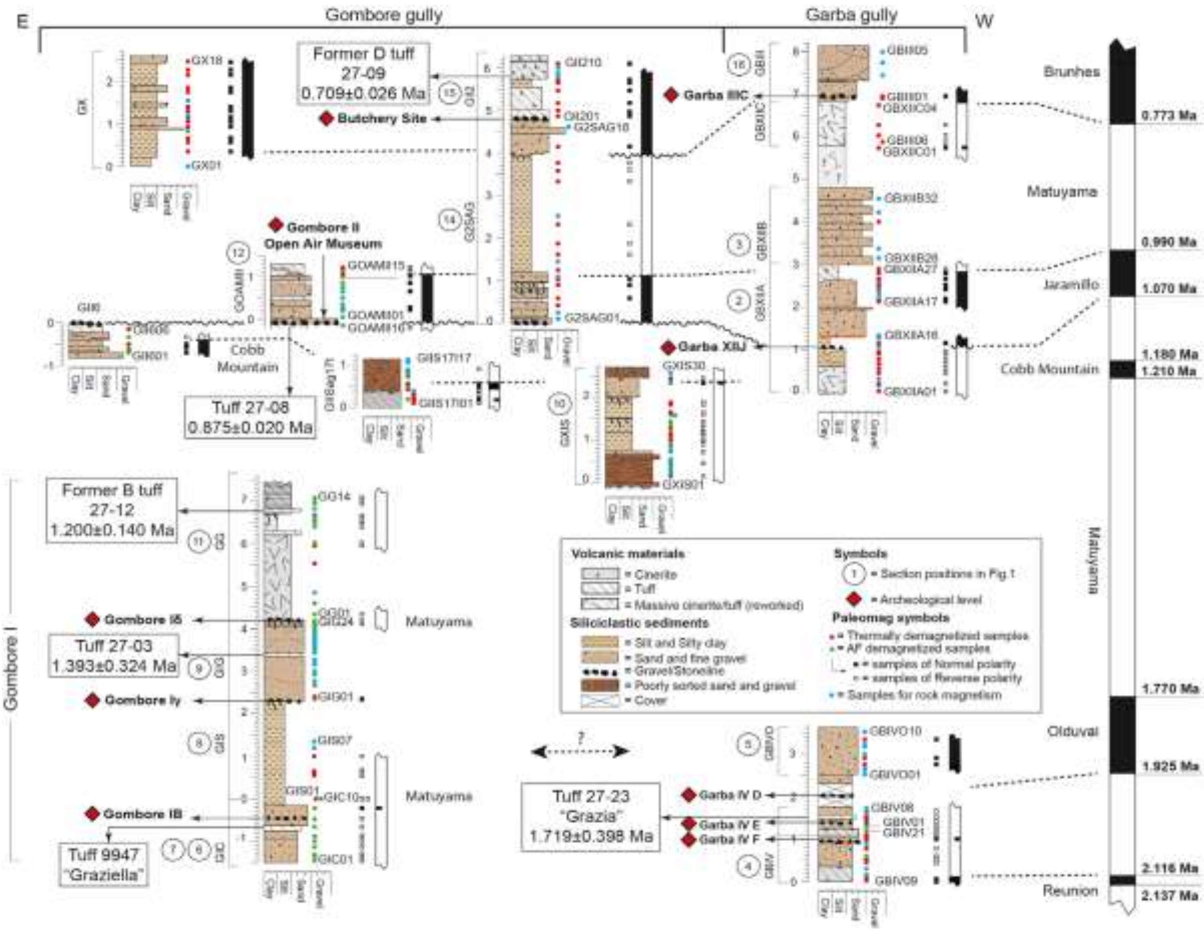

Figure 2 Stratigraphic scheme of the Melka Kunture sedimentary succession constructed using a total of 9 lithological logs from Gombore and Garba gullies correlated using essentially magnetostratigraphy in conjunction with the available radiometric dating of tuff levels. Circled numbers to the side of the logs refer to georeferenced points in Fig. 1. Samples for paleomagnetic and rock-magnetic analyses are listed next to the logs (see legend for symbols). The characteristic remanent magnetization component (ChRM) vectors extracted from samples that yielded suitable results upon thermal or alternating field (AF) treatment (see legend for symbols) were used to develop a magnetic polarity stratigraphy (white squares for reverse polarity and black squares for normal polarity) that is correlated to the geomagnetic polarity time scale of the Pleistocene with ages from Channell et al. (2020). In the Gombore I log, GIC is Gombore I Sondaggio Chavaillon, GIS is Gombore I Scalinata, GIG is Gombore I Gamma and GG is Gombore I Gully. Other acronyms are as follows: GIISag17I is Gombore II Saggio 2017 I, GXIS is Gombore XI "Sol", GOAMII is Gombore II Open Air Museum. See text for additional information.

At Gombore gully (Fig. 2), these include the Gombore II-2 Butchery site, containing Acheulean lithic tools as well as faunal remains and associated ichnological evidence (Altamura et al., 2020; Mendez-Quintas et al., 2019), Gombore II Open Air Museum, with middle Acheulean lithic tools and remains possibility pertaining to early *Homo heidelbergensis* (Royer and Coppens, 1975; Profico et al., 2016), Gombore Iδ and Gombore Iγ with additional Acheulean evidence, and Gombore IB with remains of *Homo ergaster* associated with Early Acheulean lithic tools (Di Vincenzo et al., 2015; Gallotti and Mussi, 2017; Mussi et al., 2021). In the Garba gully sequence (Fig. 2), main archeological levels are Garba IIIC, with an Acheulean lithic industry, above which lies an early Middle Stone Age level that yielded three cranial fragments attributed to archaic Homo sapiens (Mussi et al., 2014), Garba XIIJ, which yielded Early Acheulean lithic tools and faunal remains (Piperno, 2001; Chavaillon and Berthelet, 2004), Garba IVD, which yielded a rich Early Acheulean assemblage (Gallotti, 2013), Garba IVE, located immediately below the "Grazia Tuff" (tuff 27-23 of Morgan et al., 2012) and containing a partial mandible attributed to Homo erectus (Condemi, 2004; Zilberman et al., 2004a, 2004b; Zanolli et al., 2016) associated with Oldowan lithic artefacts (Gallotti and Mussi, 2018[a]), and Garba IVF, which yielded Oldowan lithic tools (Piperno et al., 2009).

The studied sections with their archeological levels have been placed in a virtually continuous stratigraphic framework by integrating magnetostratigraphy and $^{40}Ar/^{39}Ar$ geochronology (Morgan et al., 2012) as described in detail further below.

Paleomagnetism

Rock magnetic analyses

Hysteresis plots of magnetization (Am^2/kg) versus applied field (Tesla, T) (representative examples in Fig. 3A; additional examples in Supplementary Figs. 1-3) were used to determine values of saturation magnetization (M_s), saturation remanence (M_r), and coercivity (H_c), after correction for the ubiquitous occurrence of paramagnetic components. The coercivity of remanence (H_{cr}) was determined on the same samples from IRM backfield experiments.

The resulting H_c/H_{cr} versus M_s/M_r plot (Day et al., 1977) show that 65% of the studied samples fall in the pseudo-single domain (PSD) range of magnetite (Fig. 3B). The reminder 35% of the data falls above ranges defined for multidomain (MD) magnetite and tend to display wasp-waisted hysteresis loops (e.g., samples GG10 and GBIV20 in Fig. 3A) suggesting the occurrence of ferromagnetic phases with contrasting coercivities (e.g., magnetite and hematite; see also below).

Thermal demagnetization experiments of a three-component IRM show a dominant signal carried by the 0.12 T curves with maximum unblocking temperatures of about 550°-575°C, interpreted as due to magnetite, coexisting with a subsidiary higher coercivity component with maximum unblocking temperatures of about ~650°C, interpreted as hematite (Fig. 4). From all the above, we conclude that magnetite is the main ferromagnetic phase of the studied samples coexisting with hematite, in substantial agreement with previous findings (Tamrat et al., 2014).

Magnetostratigraphy

The NRM values of the investigated samples are well within ranges of instrumental measurability. The thermal or AF demagnetization of the NRM show the presence, in most of the samples, of a scattered initial component oriented northerly and down (normal polarity) and termed A component, removed either between room temperature and ~200°C or between 0 mT and 20 mT. A characteristic remanent magnetization (ChRM) component interpreted as representing the primary magnetic signal was isolated in 140 samples at higher temperatures, between ~200°C and 575°C, rarely up to 625°C, or higher alternating fields, from 20 mT to 80-85 mT (Fig. 5; thermal or AF demagnetization data in Supplementary Table 1). Considering also the results of the rockmagnetic experiments, the ChRM component directions appear to be carried essentially by the dominant magnetite fraction, whereas the subsidiary hematite fraction contributes very little to the ChRM (rare ‘tails’ above 575°C in thermal demagnetization experiments). The ChRM component directions are dipolar and oriented either downward (positive inclinations) with northerly declinations, representing normal polarity, or upward (negative inclinations) with southerly declinations, representing reverse polarity (Fig. 5). No relationships have been observed between magnetic mineralogy, which is essentially magnetite-dominated, and magnetic polarity. Standard Fisher statistics revealed that the ChRM component directions are rather scattered around a mean of Dec.= 353.7°E, Inc.= 9.2° (k=6, α95=5.3°, n=140) calculated by flipping reverse polarity data to normal polarity.

The values of declination and inclination of the ChRM component directions (Supplementary Table 2) were used to calculate virtual geomagnetic pole (VGP) latitudes (Supplementary Table 2) and derive magnetic polarity stratigraphy whereby positive VGP values (ideally approaching +90°) should represent normal magnetic polarity and negative values (approaching -90°) reverse polarity. The maximum angular deviation (MAD) values of the ChRM component directions resulted generally lower than 20°.

These data have been used to delineate the magnetic polarity stratigraphy of the Melka Kunture sequence described hereafter from top to base (see Fig. 6 for data from Gombore gully, Fig. 7 for data from Garba gully, and Fig. 2 for a general overview):

- A clear normal magnetic polarity interval has been detected in sections GII2, upper part of G2SAG, and GX (Fig. 6) as well as in GBIII base (Fig. 7). The transition to reverse polarity occurs in section G2SAG between samples G2SAG17 and G2SAG16 (Fig. 6), as well as in correlative section GBXII between samples GBIII01 and GBIII02 (Fig. 7). Taking into account also the $^{40}Ar/^{39}Ar$ age of 0.709 ± 0.026 Ma from the Former D tuff 27-09 in section GII2 (Morgan et al., 2012), this magnetic polarity reversal is interpreted as a record of the Brunhes/Matuyama boundary (0.773 Ma).
- A consistently reverse magnetic polarity interval has been recognized in the central part of the section G2SAG and at the top of GOAMII (Fig. 6), as well as in the upper portion of GBXII (Fig. 7). A transition from reverse to normal magnetic polarity is recorded between samples G2SAG06 and G2SAG10 in section G2SAG (Fig. 6), samples GOAMII11 and GOAMII12 in section GOAMII (Fig. 6), and samples GBXIIA25 and GBXIIA26 in section GBXIIA (Fig. 7) and has been interpreted as the Matuyama/Jaramillo boundary (0.990 Ma).

- A well-expressed normal polarity interval attributed to the Jaramillo Subchron has been identified in sections GOAMII and G2SAG (Fig. 6), and GBXIIA (Fig. 7), with appreciable lateral continuity. The normal-reverse polarity transition, which marks the base of the Jaramillo Subchron (1.070 Ma), lies at GOAMII between samples GOAMII16 and GOAMII03 (Fig. 6), and at GBXIIA between samples GBXIIA11 and GBXIIA13 (Fig. 7). Tuff 27-08 with an $^{40}Ar/^{39}Ar$ age of 0.875 ± 0.020 Ma (Morgan et al., 2012) should fall in Jaramillo normal polarity strata, but in section GOAMII it is located in reverse polarity strata shortly below the base of the Jaramillo (Figs. 2 and 6), and it thus appears ~200 ky younger relative to its inferred magnetochronological age (>1.070 Ma), with important consequences on the age of the Gombore II Open Air Museum archeological site resting immediately above this level (see also further below). On this ground, the age of Tuff 27-08 has been excluded from the age model of deposition of the Gombore gully sequence as described below in Paragraph 4.
- Section GII6 is characterized by reverse polarity at its top and normal polarity at its base, with the polarity transition situated between samples GII604 and GII605 (Fig. 6). This thin normal polarity interval is a possible record of the Cobb Mountain Subchron (1.180-1.210 Ma). A similar polarity excursion has been detected also in sections GIISag 2017I and GXIS (samples GIIS17I11, GIIS17I09, and GXIS27; Fig. 6).
- Proceeding down-section, a clear reverse polarity interval interpreted as a record of the (pre-Cobb Mountain?) Matuyama characterizes sections GXIS, GIISag17, as well as GG, GIG and GIS (Fig. 6), although several samples from these sections especially GIG e could not be analyzed for magnetostratigraphy as they crumbled in the laboratory.
- Section GBIVO (Fig. 7) shows a clear normal polarity signal which has been interpreted as a partial record of the Olduvai Subchron. The transition from normal to reverse polarity observed between samples GBIV07 and GBIVO04 (Fig. 7) should therefore correspond to the Olduvai/Matuyama boundary (1.925 Ma).

- Mainly reverse polarity characterizes the central-lower portion of section GBIV (Fig. 7). Tuff 27-23 “Grazia” with a mean $^{40}Ar/^{39}Ar$ age of 1.719 Ma (and large analytical errors of ±0.398 Ma at 2σ; Morgan et al., 2012)

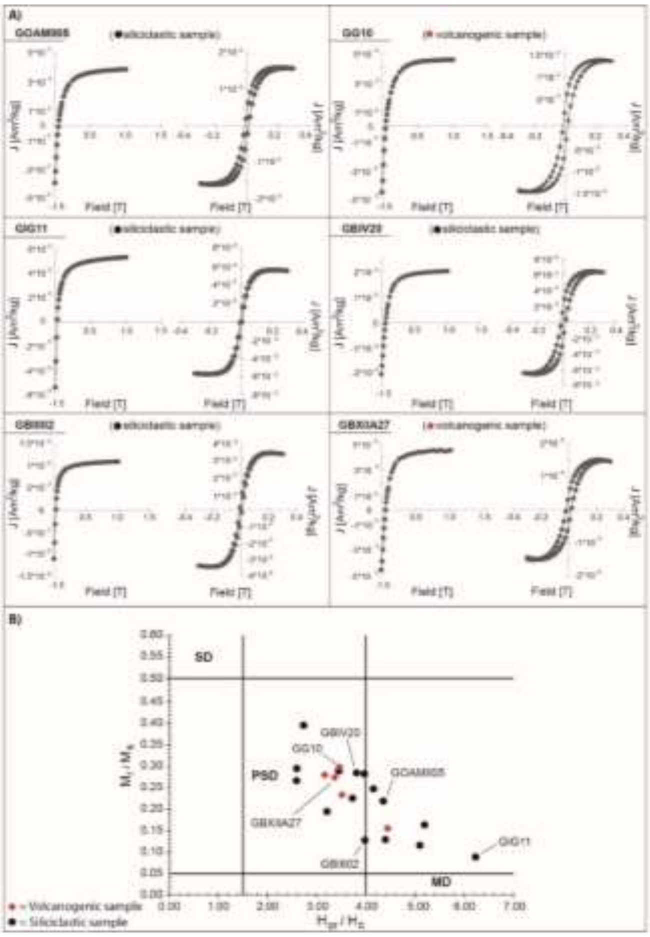

Figure 3 Isothermal remanent magnetization (IRM) backfield acquisition curves and hysteresis loops (corrected for paramagnetic components) have been performed on a total of 20 samples of volcanogenic and mainly siliciclastic lithologies (6 representative examples in panel A); additional examples in Supplementary Figs. 1-3). From these experiments, we extracted the values of saturation magnetization (Ms), remanent magnetization (Mr), coercivity (Hc), and coercivity of remanence (Hcr), which we plotted on the Day et al. (1977) diagram of panel B) reporting the ranges of existence of multi-domain (MD), pseudo-single domain (PSD), and single domain (SD) magnetite grains. About 65% of the analyzed samples fall in the PSD range while the reminder of the samples falls above the MD range, reflecting the existence of a complex mineralogy with contrasting coercivities, as reflected also by the wasp-waisted shapes of the corresponding hysteresis loops (e.g., sample GOAMII05).

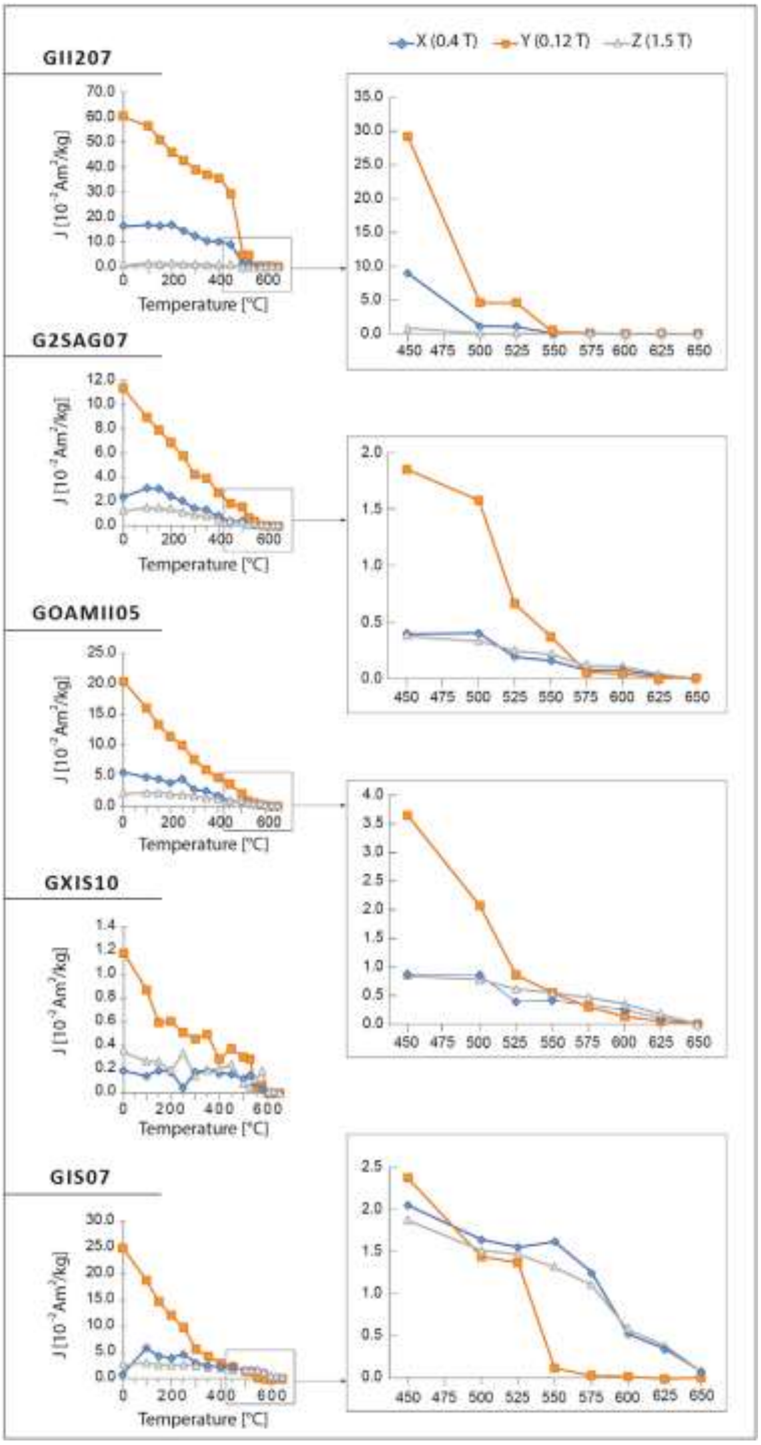

Figure 4 Thermal decay of a three-component IRM (acquired in 1.5 T, 0.4 T, and 0.12 T fields) of selected samples of volcanogenic and mainly siliciclastic lithologies. Exploded-view panels on the right illustrate the existence in the studied samples of a magnetite phase with maximum unblocking temperatures of 550e575 _C variably coexisting with a magnetic phase with maximum unblocking temperature of 650°C interpreted as hematite. The wasp-waisted shapes of some of the studied samples (Fig. 3) confirm the occurrence of a mixed-coercivity magnetic mineralogy.

should fall above or within Olduvai normal polarity strata, but in section GBIV it is located in reverse polarity strata shortly below the base of the Olduvai (Figs. 2 and 7), and it thus appears some ~200 ky younger On Paragraph 4. Finally, the base of section GBIV contains two superposed samples of normal magnetic polarity, with the reverse-normal polarity transition placed between samples GBIV10 and GBIV13 (Fig. 7). We tentatively interpret this lowermost normal polarity interval as a partial record of the Reunion Subchron (2.116-2.137 Ma), albeit we acknowledge model of deposition of the Garba gully sequence described below ground, the age of Tuff 27-23 “Grazia” has been excluded from the age in relative to its inferred magnetochronological age (>1.925 Ma). this the overall complexity of the VGP polarity pattern in section GBIV (Fig. 7).

Age models of sedimentation

In an attempt to establish best-fit age models of sedimentation of the Melka Kunture succession, two virtually continuous stratigraphies have been reconstructed, one for Gombore gully and the other for Garba gully, by piecing together in a common metric scale the constituent stratigraphic sections according to the correlation scheme of Fig. 2. Onto these continuous stratigraphies, we placed key age-depth tie points for sedimentation rate modelling, as described hereafter.

The age model for Gombore gully has been constructed by adopting seven age-depth tie-points represented by (i) the Brunhes/Matuyama boundary (0.773 Ma), (ii) top Jaramillo (0.990 Ma), (iii) base Jaramillo (1.070 Ma), (iv) top Cobb Mountain (1.180 Ma), as well as the $^{40}Ar/^{39}Ar$ ages of (v) Former D tuff 27-09 (0.709 ± 0.026 Ma), (vi) Former B Tuff 27-12 (1.200 ± 0.140 Ma), and (vii) Tuff 27-03 (1.393 ± 0.324 Ma) from Morgan et al. (2012; with errors at 2σ level) (Fig. 8A; see also Supplementary Table 3). Similarly, the age model for Garba has been constructed by adopting five recorded chronologic tie-points: (i) the Brunhes/ Matuyama boundary (0.773 Ma), (ii) top Jaramillo (0.990 Ma), (iii) base Jaramillo (1.070 Ma), (iv) base Olduvai (1.925 Ma), and (v) top Reunion (2.116 Ma) (Fig. 8B; see also Supplementary Table 3). As stated above, we excluded from the inventory of tie-points the $^{40}Ar/^{39}Ar$ ages of Tuff 27-08 from Gombore and Tuff 27-23 “Grazia” from Garba because they are in contradiction relative to

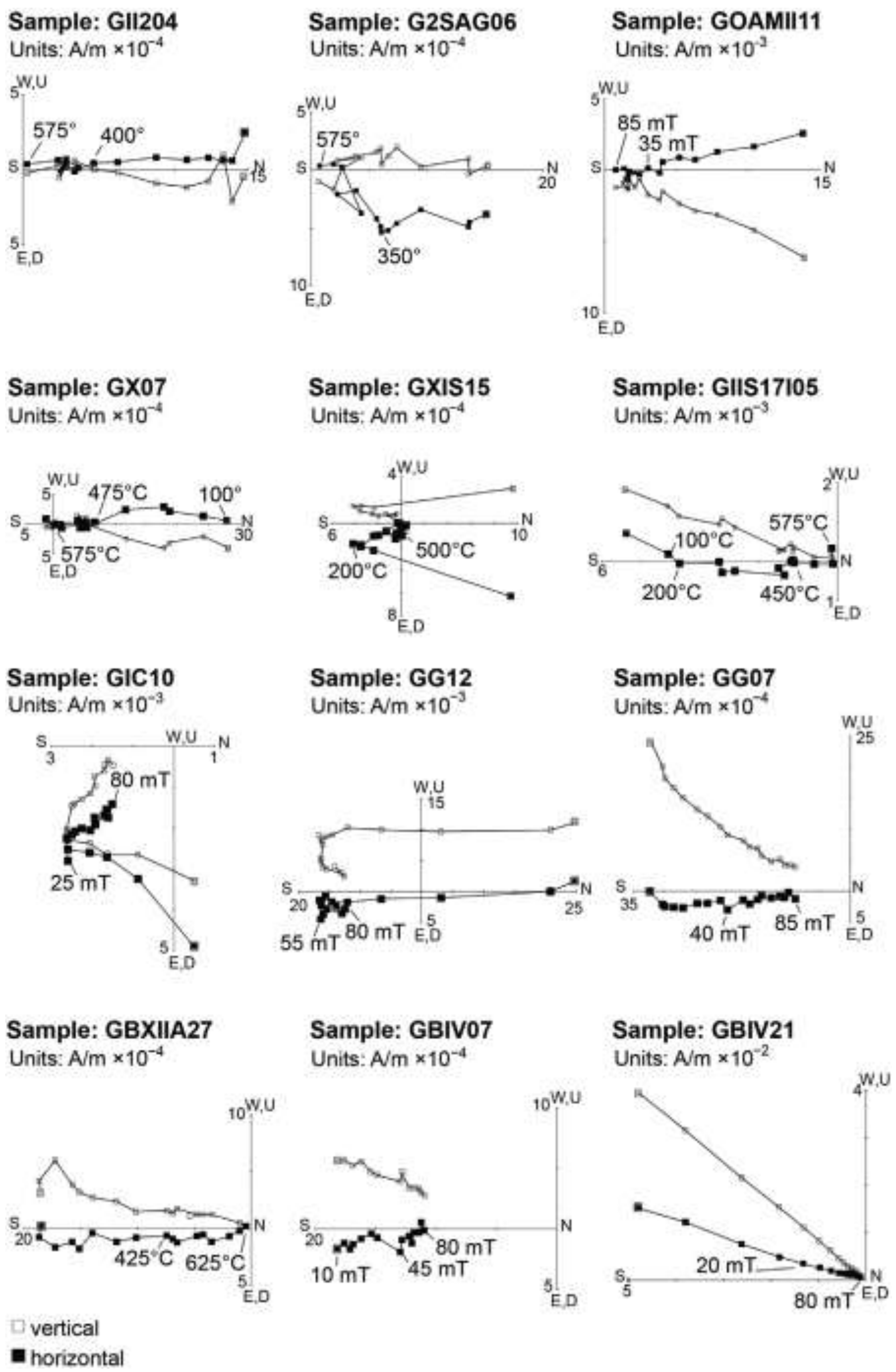

Figure 5 Vector end-point demagnetization diagrams of representative samples showing the presence of northerly-and-down or southerly-and-up characteristic remanent magnetization component (ChRM) directions indicating respectively normal or reverse polarity. Transitional directions are observed in some cases (e.g., sample GIC10). Closed symbols are projections onto the horizontal plane and open symbols onto the vertical plane in geographic (in situ) coordinates (equivalent to tilt-corrected coordinates as bedding is essentially horizontal). Demagnetization steps are expressed in °C or mT.

the overall magnetostratigraphy of the levels in which they are found (see above). Best-fit interpolations of these chronologic tie-points with associated envelopes of 95% confidence have been obtained using software PAST (Hammer et al., 2001). For Gombore gully, we generated a simple linear age model of deposition that takes the form of Depth(m) = 18.6*Age (Ma) + 32.6 (correlation coefficient r^2=0.93), where Depth(m) represents the depth in meters of the composite stratigraphy and Age (Ma) the corresponding age in Ma. The average sedimentation rate, represented by the slope of the best-fit line, is thus of 18.6 m/Ma (Fig. 8A). The basal part of the Gombore gully composite sequence, lacking direct magnetochronological and/or geochronological constraints, was tentatively dated by linear extrapolation of the best-fit line dashed line in Fig. 8A). Incidentally, this part of the sequence contains (undated) Tuff 9947 “Graziella” in section GIC (Fig. 2) that Raynal and Kieffer (2004) correlated using geochemistry to Tuff 27-23 “Grazia” (1.719 ± 0.398 Ma) from section GBIV (but see above about the reliability of this datum).
We found that several other tuffs present throughout the Melka Kunture sequence share similar compositions (see details in Supplementary Figs. 4 and 5), and hence we consider geochemistry hardly diagnostic for correlating and dating of the basal part of the Gombore sequence. Regarding the Garba sequence, the linear best-fit age model (and associated envelope of 95% confidence) that interpolates the selected chronologic tiepoints takes the form of Depth(m) = 13.2*Age(Ma) + 27.8 (correlation coefficient r^2=0.99), implying an average sediment accumulation rate of 13.2 m/Ma (Fig. 8B) that is slightly lower than at Gombore (18.6 m/Ma) because of the lateral variability in thickness of the investigated sedimentary bodies. We tested also alternative and more complex age models, including models based on second-order polynomials, which, although sometimes producing high correlation indexes, often violated the magnetic polarity recognized throughout the stratigraphy, and have therefore been discarded. We stress that the linear age models we applied, with outstanding correlation coefficients of r^2=0.93 for Gombore gully and r^2=0.99 for Garba gully, are in their simplicity very robust, and provide interpolated ages that do not violate the magnetochronological constraints used for the construction of

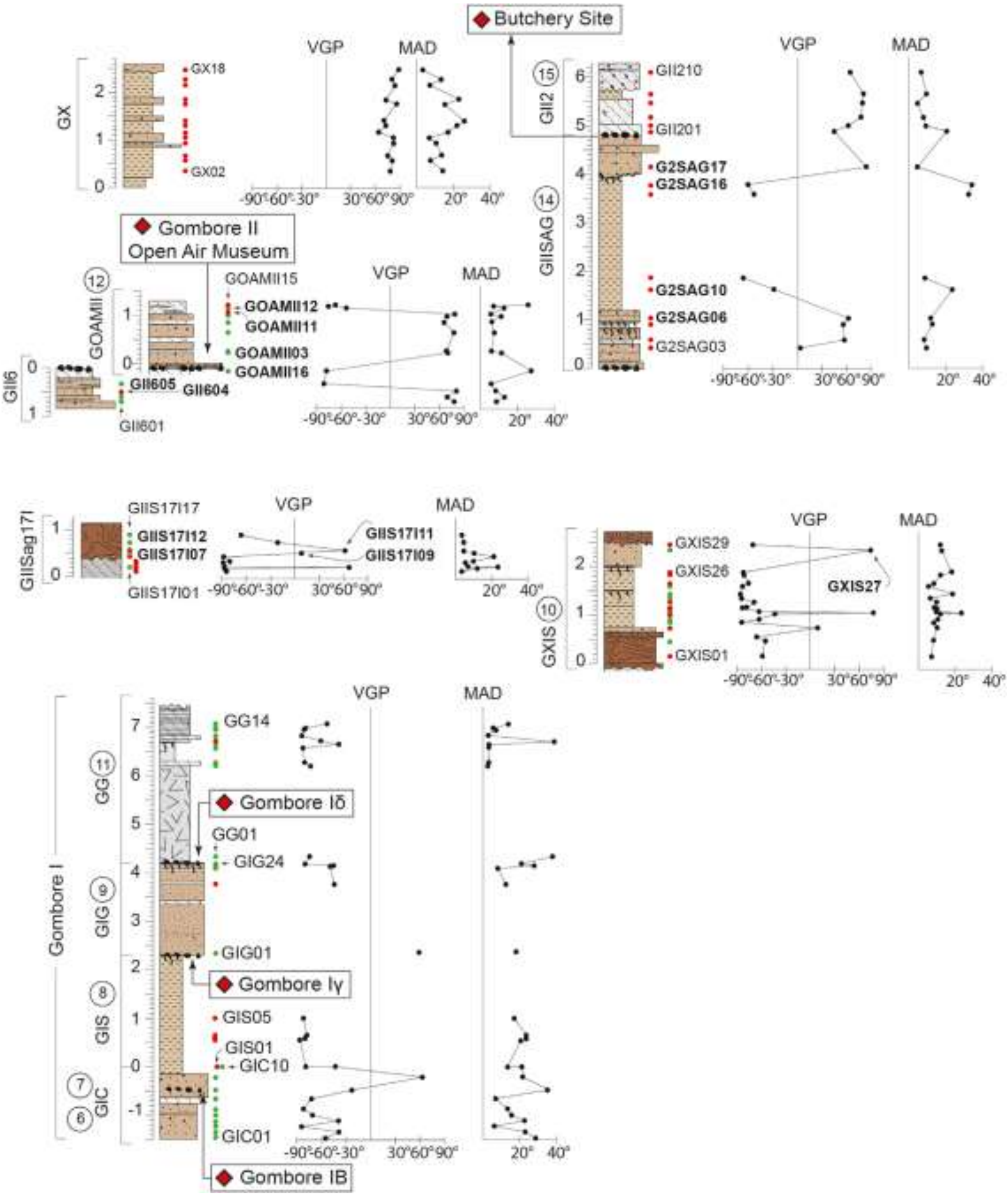

Figure 6 Magnetostratigraphic data of Gombore gully lithological sections reporting the virtual geomagnetic pole (VGP) latitudes obtained from the characteristic remanent magnetization component (ChRM) directions and used to erect the magnetic polarity stratigraphy (VGPs approaching +90° representing normal polarity and approaching -90° representing reverse polarity). The maximum angular deviation (MAD) angles (°) of the ChRM directions are also reported. See also Fig. 2 and text for discussion.

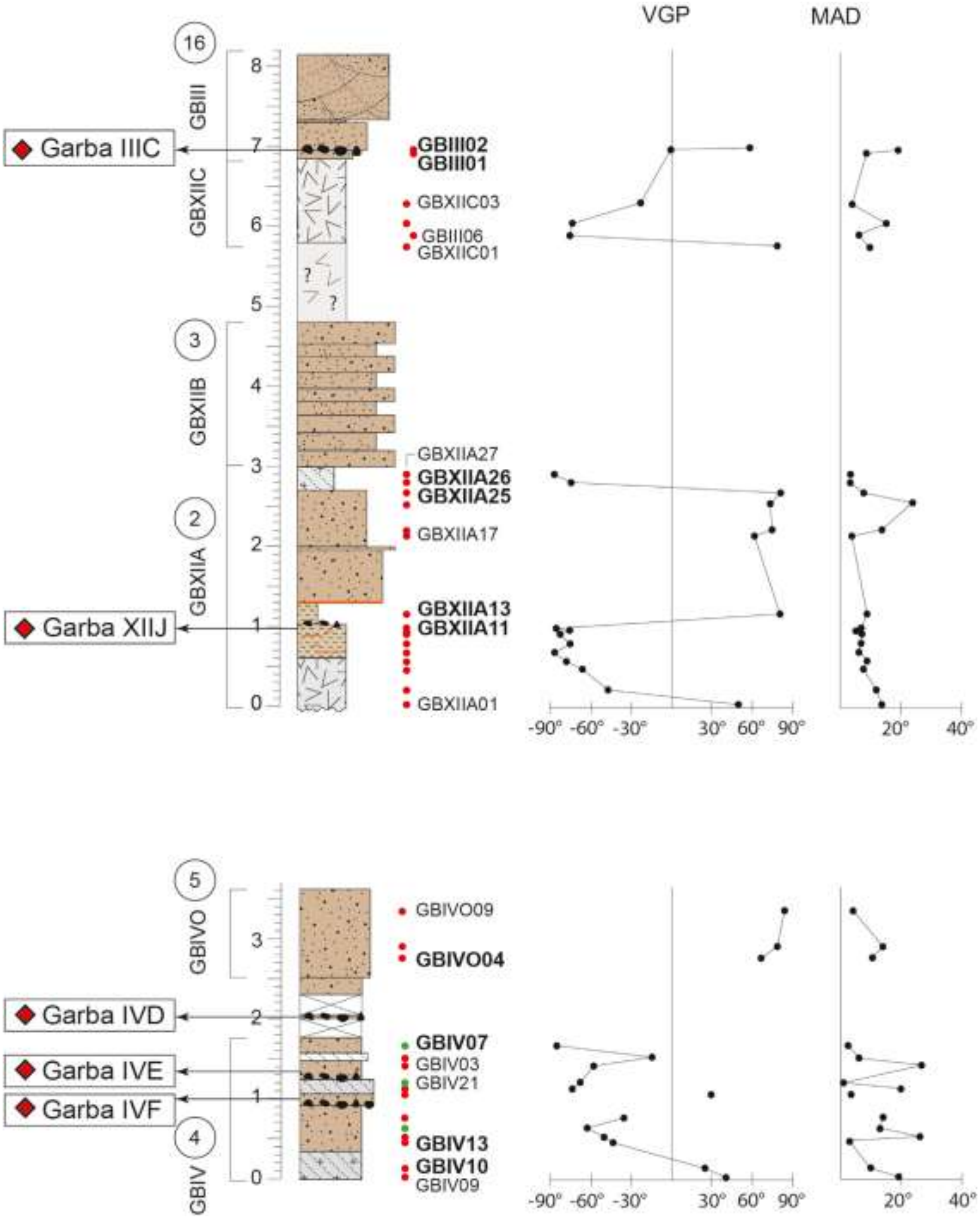

Figure 7 Magnetostratigraphic data of Garba gully lithostratigraphic sections. Symbols and parameters as in Fig. 6. See also Fig. 2 and text for discussion.

the models (Fig. 8). In any case, alternative age models can be constructed by using data in Supplementary Table 3.

Inferred ages of the main archeological levels

The linear best-fit age models described above have been used to assess the ages of the main archeological levels at Gombore gully (Fig. 8A) and Garba gully (Fig. 8B), as described hereafter (see also Fig. 2). The ± errors attached to the mean ages have been derived from the 95% confidence intervals of the best-fit lines, and are therefore symmetrical, but in some cases it was necessary to truncate them on the positive (+) and/or negative (-) side in order to avoid violating the magnetochronology; for example, the mean age of a level of reverse polarity cannot embrace with its ± error bar normal polarity levels located below and/or above it, and hence the error bar must be truncated at the appropriate age allowed by the magnetochronology, producing asymmetrical errors. The following ages of archeological levels have been derived:

- The extrapolated mean ages of the archeological levels Gombore II Butchery site (Fig. 8A) and Garba IIIC (Acheulean level) (Fig. 8B), both located in the early Brunhes Chron, are of 0.75 (-0.1; +0.02) Ma and 0.68 (-0.1; +0.09) Ma, respectively.
- The interpolated mean age of the archeological level Gombore II Open Air Museum is of 1.03 (±0.04) Ma (Fig. 8A). In particular, this level, represented by a basal fluvial lag deposit (stoneline), is of normal (Jaramillo) magnetic polarity, while the tuff level immediately below the base of the lag deposit is of reverse (Matuyama) polarity, and hence the base of the stoneline falls at the Jaramillo/Matuyama boundary at a nominal age of 1.070 Ma. As stated above, the 40Ar/39Ar age of tuff level 27-08, located immediately below the stoneline in reverse polarity (pre-Jaramillo) sediments, appears ~200 ky younger than its inferred magnetochronological age (and has been excluded from age modelling).
- The age of the Garba XIIJ archeological site (Fig. 8B), which lies in reverse polarity sediments immediately below the base of the Jaramillo/Matuyama

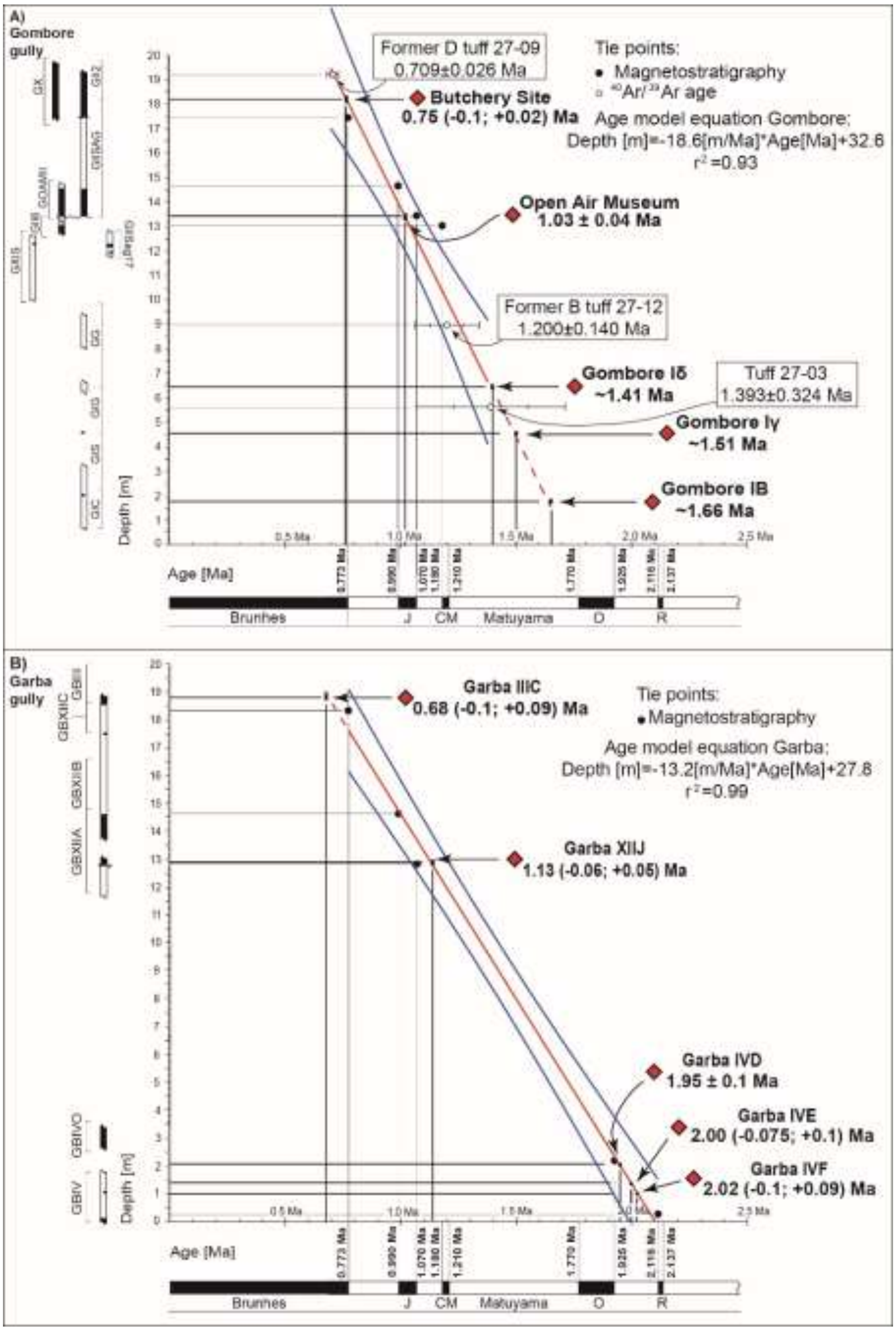

Figure 8 Composite stratigraphic sequences of Gombore gully (A) and Garba gully (B), in meters from base, correlated to the geomagnetic polarity time scale of Channell et al. (2020) using magnetochronologic and radiometric tie-points (Supplementary Table 3) fitted by simple linear regression models with associated envelopes of 95% confidence. These linear age models of sedimentation are used to derive interpolated or extrapolated mean ages and associated ± errors of the main archeological levels present at Gombore gully and Garba gully (ages reported in bold in figure). J is Jaramillo Subchron, CM is Cobb Mountain Subchron, O is Olduvai Subchron, and R is Reunion Subchron. See text for discussion.

boundary (1.070 Ma), is estimated at 1.13 (-0.06; +0.05) Ma.

- The extrapolated ages of ~1.41 Ma, ~1.51 Ma and ~1.66 Ma for archeological levels Gombore Iδ, Gombore Iγ and Gombore IB (Fig. 8A), respectively, should be taken with caution, lacking the basal Gombore sequence of robust direct chronological constraints.
- The mean ages of the Garba IV archeological levels (Fig. 8B), magnetostratigraphically comprised between the base of the Olduvai Subchron and the top of the (inferred) Reunion Subchron, resulted of 1.95 (-0.025; +0.1) Ma for Garba IVD, 2.00 (-0.0075; +0.1) Ma for Garba IVE, and 2.02 (-0.095; +0.096) Ma for Garba IVF (Fig. 8B).

Conclusions

We identified the stratigraphic positions of the main polarity reversals of the Earth's magnetic field in the Melka Kunture sedimentary succession at the Gombore and Garba gullies. The new magnetostratigraphic data allowed us to contribute dating the several archeological levels therein contained that are of exceptional relevance for understanding the patterns of human evolution in Africa during the Pleistocene. Rock magnetic analyses indicate that the main magnetic mineral that carries the primary magnetostratigraphic signal is magnetite, mostly in the pseudo-single domain range, variably associated with a higher coercivity hematite fraction. Magnetochronological tie-points (e.g., Brunhes/Matuyama boundary, top Jaramillo, base Jaramillo, base Olduvai, etc.; ages after Channell et al., 2020) derived from the reconstructed magnetic polarity pattern have been used in conjunction with a critical selection of $^{40}Ar/^{39}Ar$ ages from the literature (Morgan et al., 2012) to build accurate e and simple e age models of sedimentation for the Melka Kunture sequence from which we derived the mean age estimates of the main levels of archeological significance, from Garba IIIC with Acheulean lithic industry at 0.68 (-0.1; +0.09) Ma to Garba IVF with Oldowan tools at 2.02 (-0.095; +0.096) Ma.

From these analyses, it appears that the Melka Kunture succession covers in relatively stratigraphic continuity a time interval spanning from the Brunhes Chron at the top to the Reunion Subchron at the base, or from ~0.6 to ~2.1 Ma.

More problematic resulted the age assessments of archeological levels Gombore Id, Gombore Ig and Gombore IB because of extensive gaps in the magnetostratigraphic record and absence of direct geochronologic dating of tuff levels in the lower part of the Gombore sequence. Future work will involve filling-in the lower Gombore magnetostratigraphic gap and attempt dating critical tuff 9947 “Graziella” at Gombore I as well as redating Tuff 27-23 ‘‘Grazia’’ at Garba IV.

Credit author statement

Serena Perini: Data analyses, Conceptualization, Manuscript writing and figures preparation.
Giovanni Muttoni: Conceptualization, Data curation, Field-work and sampling, Manuscript writing.
Edoardo Monesi: Field-work and sampling, Data analyses.
Rita Melis: Supervision.
Margherita Mussi: Supervision.

Acknowledgements

We would like to thank Giuseppe Lembo for total station data used to construct Fig. 1, and Rosalia Gallotti for help in the field and insightful discussions. Giovanni Muttoni would like to thank the Rector of the Universit_a degli Studi di Milano for fundings and support. The Italian Archeological Mission at Melka Kunture was funded in 2017 by Università di Roma La Sapienza (Grandi Scavi grant SA11715C7C936C01) and by Ministero degli Affari Esteri e della Cooperazione Internazionale (grant ARC-001666). The research permits where provided by the Authority for Research and Conservation of the Cultural Heritage which also helped in many ways, together with the authorities of the Oromyia Federal Republic.

Chapter 6

Chronology of the earliest peopling of the Ethiopian highlands

---

This chapter is presented according to

Chronology of the earliest peopling of the Ethiopian highlands at Melka Kunture pre-dating the 1.925 Ma base of the Olduvai subchron

Published on

Quaternary Science Reviews 319 (2023) 10833
https://doi.org/10.1016/j.quascirev.2023.108330

Giovanni Muttoni[a], Serena Perini[a], Rita T. Melis[b,c], Margherita Mussi[c,d,e].

[a] Dipartimento di Scienze della Terra 'Ardito Desio', Università degli Studi di Milano, via Luigi Mangiagalli 34, 20133 Milan, Italy [b] Dipartimento di Scienze Chimiche e Geologiche, Università di Cagliari. Cittadella Universitaria, 09042 Monserrato, Italy. [c] Italo-Spanish Archaeological Mission at Melka Kunture and Balchit, Italy-Spain. [d] Dipartimento di Scienze dell'Antichità, Sapienza Università di Roma. Piazzale Aldo Moro 5, 00185 Roma, Italy. [e] ISMEO - The International Association for Mediterranean and Oriental Studies. Corso Vittorio Emanuele II, 244, Palazzo Baleani, 00186 Roma, Italy.

Abstract

Melka Kunture on the highlands of Ethiopia has provided evidence for the early peopling of the Ethiopian highlands (>2000 m asl). At site Garba IV, an Oldowan technocomplex was retrieved in levels E-F located shortly below the base of the Olduvai subchron, with a currently accepted age of 1.925 Ma, while the early Acheulean was found in level D located close to the base of the Olduvai subchron. The base of the Olduvai subchron becomes therefore a prime chronostratigraphic marker for the study of the early peopling of the Ethiopian plateau in the Early Pleistocene. Here we report new magnetostratigraphic data from two sections from the Kella valley located close to Garba IV, namely Kella

III bis and Kella Bridge. We document in these sections the occurrence of the Olduvai subchron, confirmed also by $^{40}Ar/^{39}Ar$ ages from the literature. We correlate these new data to previous data from Garba IV, establishing a robust registry of the critical Olduvai subchron in the lower part of the Middle Succession (part of the former Melka Kunture Formation), spanning from ~2 Ma to ~1.2 Ma, and we also point to a regional basal unconformity marking its onset of deposition. The better constrained magnetochronology provides firm evidence that the hominins were peopling areas at 2000 m of altitude at least 2 million years ago.

Introduction

Melka Kunture is a site-complex extending over some tens of km^2 at 2000-2200m above sea level in the Upper Awash Valley of the Ethiopian highlands (Fig. 1). It hosts a dense concentration of archaeological and palaeontological sites embedded in a complex volcano-sedimentary sequence, with levels extending in time from the early Holocene to around 2 million years ago (Ma) in the Early Pleistocene (Gallotti and Mussi 2015; Gallotti and Mussi, 2018[a]; Mussi et al., 2014; Mussi et al., 2016; Mussi et al., 2022). Here we summarize previous results on the chronostratigraphy of the Garba and Gombore gullies (Perini et al., 2021, Morgan et al., 2012), located on the right bank of the Awash River, and present new chronostratigraphic data from the nearby Kella valley on the left bank of the same river (Figs. 1,2), in order to better constrain the age of onset of deposition of the archaeological-bearing volcano-sedimentary sequence.

State of the Art of the Garba and Gombore Chronostratigraphy

The Garba and Gombore gullies run more or less parallel to each other at a distance of ~300 m and are incised by seasonal streams cutting through Pleistocene deposits. Both have been thoroughly researched across various geological sections (Raynal et al., 2004; Pioli et al., 2023; Perini et al., 2021). In Figure 2, we report a chronostratigraphic scheme for the Garba and Gombore gully sections that is closely derived from Perini et al. (2021) with the addition of new data from two sections from the nearby Kella valley (circled numbers associated with sections acronyms – GB for Garba and G for the Gombore – refer to locations in Figure 1; see also Perini et al., 2021). These sections are altogether comprised of a sedimentary sequence starting at the base with green silty-clays, informally termed 'basal clays' (hereafter BC) by Bonnefille et al. (2018), unconformably overlain by a volcano-sedimentary sequence subdivided into the Middle Succession (hereafter MS) (Pioli et al. 2023), first described by Raynal et al. (2004) as part of the now superseded Melka Kunture Formation, capped by the Upper Succession (US) (Pioli et al. 2023). The archaeological levels, named after the gully where they are located followed by Roman numerals, are represented by red hexagons in Figure 2.

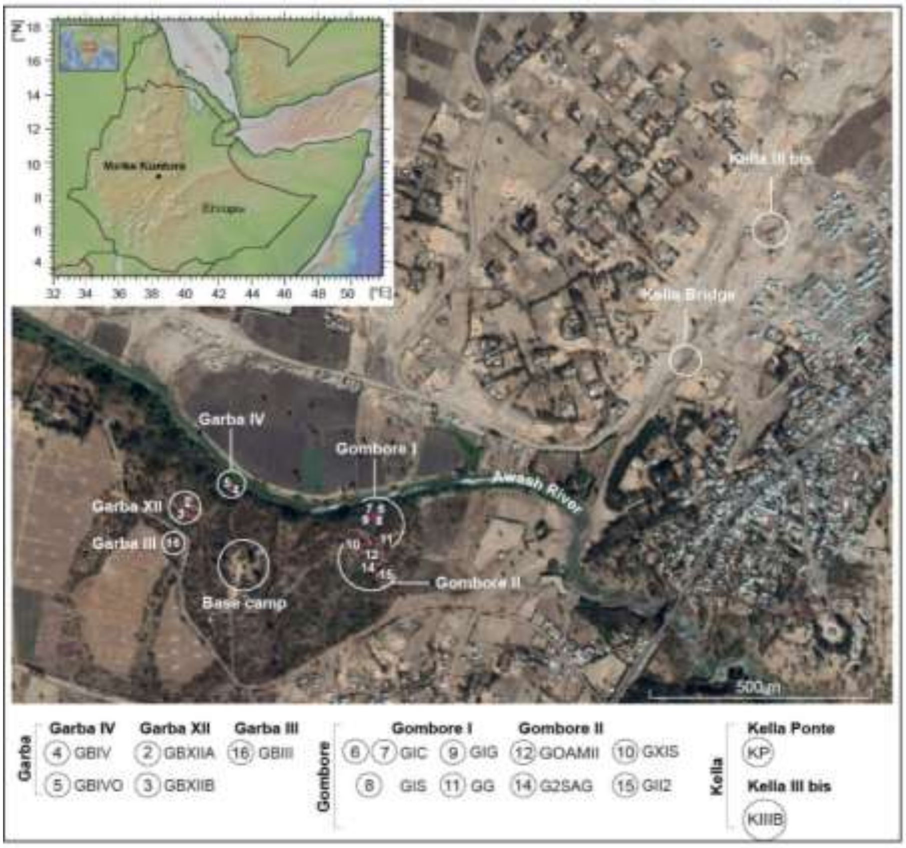

Figure 1 Location map of the Melka Kunture area (Google Earth™) in Ethiopia where Garba, Gombore and Kella represent the main localities hosting sections of the Upper Succession (US) and Middle Succession (MS, formerly Melka Kunture Formation). Numbers refer to individual sections from the Garba and Gombore gullies (acronymized using prefix GB for Garba and G for Gombore) studied by Perini et al. (2021) and reported in Figure 2. Reported are also the new sections from the basal MS of this study: Kella III bis at 8.7148°N 38.61182°E and Kella Bridge at 8.7090194°N 38.6078584°E.

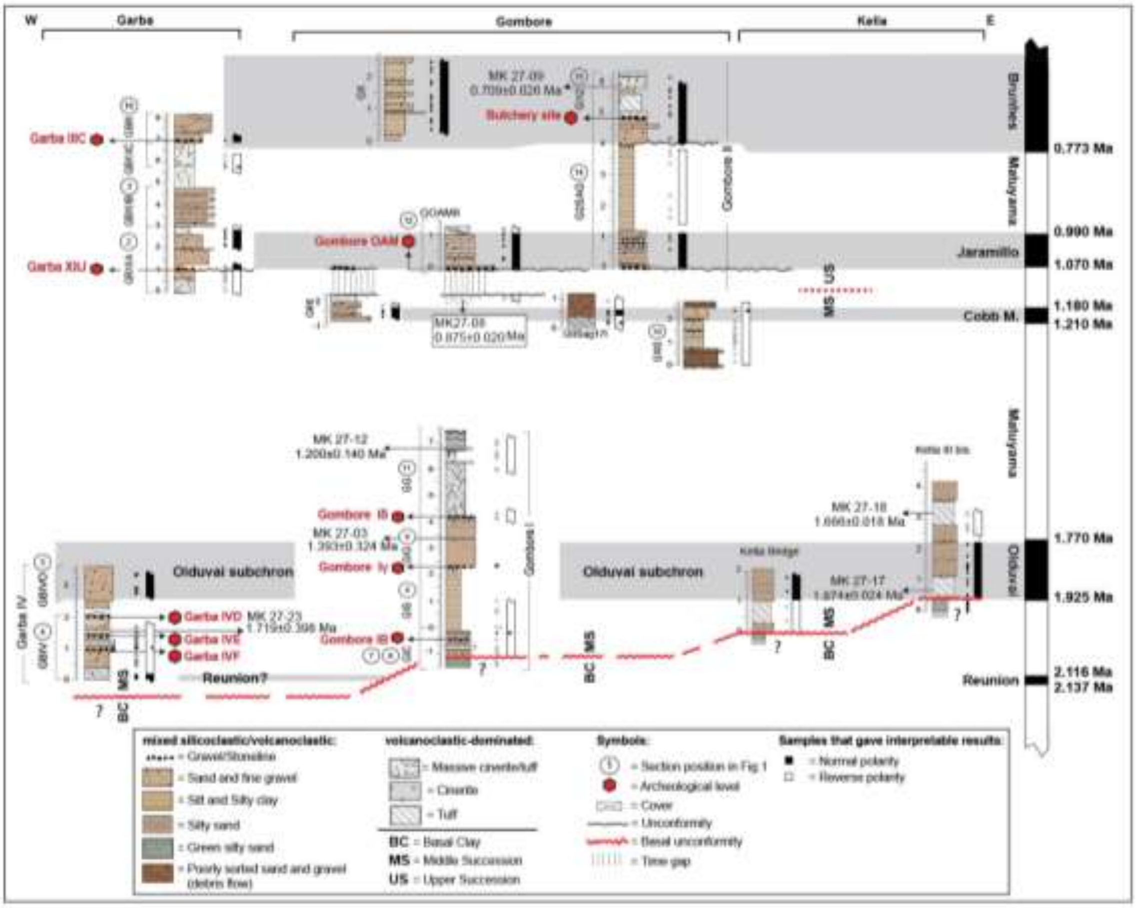

Figure 2 General litho-magnetostratigraphy of the Melka Kunture area. Stratigraphic sections across the Upper Succession (US), Middle Succession (MS, formerly Melka Kunture Formation), and 'basal clays' (BC) from the Gombore and Garba gullies are from Perini et al. (2021) while those from the Kella valley (Kella III bis and Kella Bridge; details in Figure 3) are from this study. The individual geological sections constituting the Garba and Gombore gully sequences are acronymized using prefix GB for Garba gully and G for Gombore gully. Circled numbers placed to the side of the acronyms refer to site locations in Figure 1. Sections are aligned relative to the geomagnetic polarity time scale of Channell et al. (2020) reported to the right together with the ages of the main polarity reversals. Following Perini et al. (2021), reported are also the available $^{40}Ar/^{39}Ar$ ages of key tuff layers (Morgan et al., 2012) together with their error bounds at ± 2s level. Red hexagons represent the main archaeological levels, the most relevant of which are, for this study, levels D and E-F at Garba IV. Circled numbers placed to the side of the acronyms refer to site locations in Figure 1. BC is 'basal clays', MS is Middle Succession, US is Upper Succession.

The chronology of the Garba and Gombore gully sequences was initially investigated through the application of $^{40}Ar/^{39}Ar$ dating on tuffs (Morgan et al., 2012). The volcano-sedimentary sequence was found to extend from

0.709±0.026 Ma at Gombore II-2 (Tuff MK 27-09 in section GII2; Fig. 2), across Tuffs MK 27-08, MK 27-12, MK 27-03 broadly comprised between 0.87 and 1.39 Ma, down to a poorly dated tuff at 1.719±0.398 Ma (Tuff MK 27-23) close to the base of the sequence in section Garba IV (Fig. 2). As in Perini et al. (2021), here we report the analytical errors of the radiometric ages of Morgan et al. (2012) at 2σ level, which is statistically more robust. Tuff MK 27-23, on which much emphasis has been placed as it lies close to key archaeological levels such as Garba IV level D, yielding an early Acheulean technocomplex (Gallotti, 2013), has a 2σ error of almost ± 0.4 Ma.

A preliminary magnetostratigraphic study of the Gombore and Garba successions (Tamrat et al., 2014) revealed a magnetic polarity pattern substantially consistent with the $^{40}Ar/^{39}Ar$ chronology, characterized by the occurrence of the Brunhes/Matuyama boundary (0.773 Ma according to the time scale of Channell et al., 2020, used throughout) toward the top of the sequence, followed down-section by the Jaramillo subchron (0.990-1.070 Ma) and, finally, the Olduvai subchron (1.770-1.925 Ma) toward the base of the sequence. Several of the archaeological and palaeontological sites could not, however, be accurately placed relative to the magnetochronology of Tamrat et al. (2014). Hence, a more detailed magnetochronological study followed (Perini et al., 2021) based on the analysis of 9 stratigraphic sections, summarized in Figure 2, that allowed a more detailed recovery of the magnetic polarity sequence of the US and MS from the Brunhes/Matuyama boundary through the Jaramillo and the Olduvai subchrons, also encompassing possible records of the Cobb Mountain (1.180-1.210 Ma) and Reunion (2.116-2.137 Ma) subchrons, the latter located at the very base of the MS (Fig. 2, modified from Perini et al. 2021). It is important to stress that magnetic polarity attributions (Brunhes, Jaramillo, etc.) were made considering the entire magnetostratigraphic sequence, from top to bottom. In this respect, the normal polarity magnetozone individuated at the base of the investigated stratigraphy was attributed to the Olduvai subchron (Perini et al., 2021; but also Tamrat et al., 2014) because it is part of a *sequence* of normal and reverse polarity magnetozones that start from the top of the overall stratigraphy with the Brunhes chron and continues down-section with the Matuyama chron straddling the Jaramillo subchron (Fig. 2). This magnetic polarity sequence was found to be in *substantial* agreement with several of the $^{40}Ar/^{39}Ar$ ages of Morgan et al. (2012) (with some exceptions), allowing Perini et al. (2021) to derive integrated long-term (simple linear) age models of deposition for the US and MS in the Gombore and Garba gullies. These age models were used to establish that Garba IV level D, yielding an early Acheulean technocomplex, should have an interpolated age of 1.95 (-0.025; +0.1) Ma, and would hence fall at or immediately below the base of the Olduvai subchron (which in section Garba IV falls in a sampling gap; Fig. 2), while Garba IV levels E and F with Oldowan technocomplexes should have pre-Olduvai and post-Reunion interpolated ages of 2.00 (-0.0075; +0.1) Ma and 2.02 (-0.1; +0.09), respectively (Fig. 2; see Perini et al., 2021 for additional information).

Refining the Chronostratigraphy

A critical aspect of the Perini et al. (2021) age model used to derive the ages of the archaeological levels of Garba IV comes from an admittedly limited recovery of the Olduvai subchron. This subchron had been originally found by Tamrat et al. (2014), but not in clear stratigraphic context, and eventually defined by Perini et al. (2021) in a clearer stratigraphic context at section Garba IV (Fig. 2). However, this was based on only three magnetostratigraphic samples of normal polarity, resting on top of several samples of reverse polarity in the immediately underlying strata followed down-section by a thin normal polarity interval possibly representing the Reunion subchron (Fig. 2). The nearby Gombore I composite section was affected by extended gaps in the magnetostratigraphic record (due to uninterpretable results and/or loose samples that did not survive laboratory treatment), which hindered the recovery of the Olduvai subchron in the stratigraphic interval where it was expected to occur from general age modeling (Fig. 2; see Perini et al., 2021 for additional information).

In order improve the chronological framework of the basal part of the MS across the critical Olduvai subchron, here we present magnetostratigraphic data from two sections located on the left bank of the Awash River in the nearby Kella valley: Kella III bis and Kella Bridge (Figs. 1-3), where the basal MS is documented and provided with published $^{40}Ar/^{39}Ar$ ages (Morgan et al., 2012). The oldest one (1.874±0.024 Ma for Tuff MK 27-17; Figs. 2-3) suggests that the Olduvai subchron (1.925-1.770 Ma) should be present in these levels. We will use these new data from Kella in conjunction with data from Garba IV of Perini et al. (2021) to propose a regional correlation of the basal MS around the base of the Olduvai subchron. This is relevant for the secure placement in time of both the earliest human presence so far recorded at Melka Kunture, which is also the earliest documented on the Ethiopian highlands, as represented at Garba IV by the Oldowan levels E-F and by the early Acheulean level D.

Magnetostratigraphy

Materials and Methods

The Kella III bis section (8.7148°N 38.61182°E; Fig. 1) consists of ~4 m of reworked tuffaceous sands and tuffs pertaining to the MS volcano-sedimentary sequence resting on top of green silty-clays, informally termed 'basal clays' (hereafter BC) by Bonnefille et al. (2018), via a centimetric reddened (weathered) layer possibly signaling the presence of a temporal gap in unconformity (Fig. 3). Two tuff intervals were respectively dated at 1.666±0.018 Ma and 1.874±0.024 Ma (Morgan et al., 2012) (Fig. 3; see also Fig. 2). The Kella Bridge section (8.7090194°N 38.6078584°E; Fig. 1) consists of 2 m of tuffaceous sands and tuff of the MS resting again on top of the BC in a similar context as observed at the base of the Kella III bis section (Fig. 3). A total of 29 oriented core samples were collected in stratigraphic order, 23 from Kella III bis and 6 from Kella Bridge, using a water-cooled electric drill and oriented with a magnetic compass. These samples were successively cut into standard (10cc) samples for magnetostratigraphic and rock-magnetic analyses. Samples for magnetostratigraphy have undergone thermal demagnetization in steps of 50-25°C from room temperature up to 625°C using a TD48SC ASC furnace.

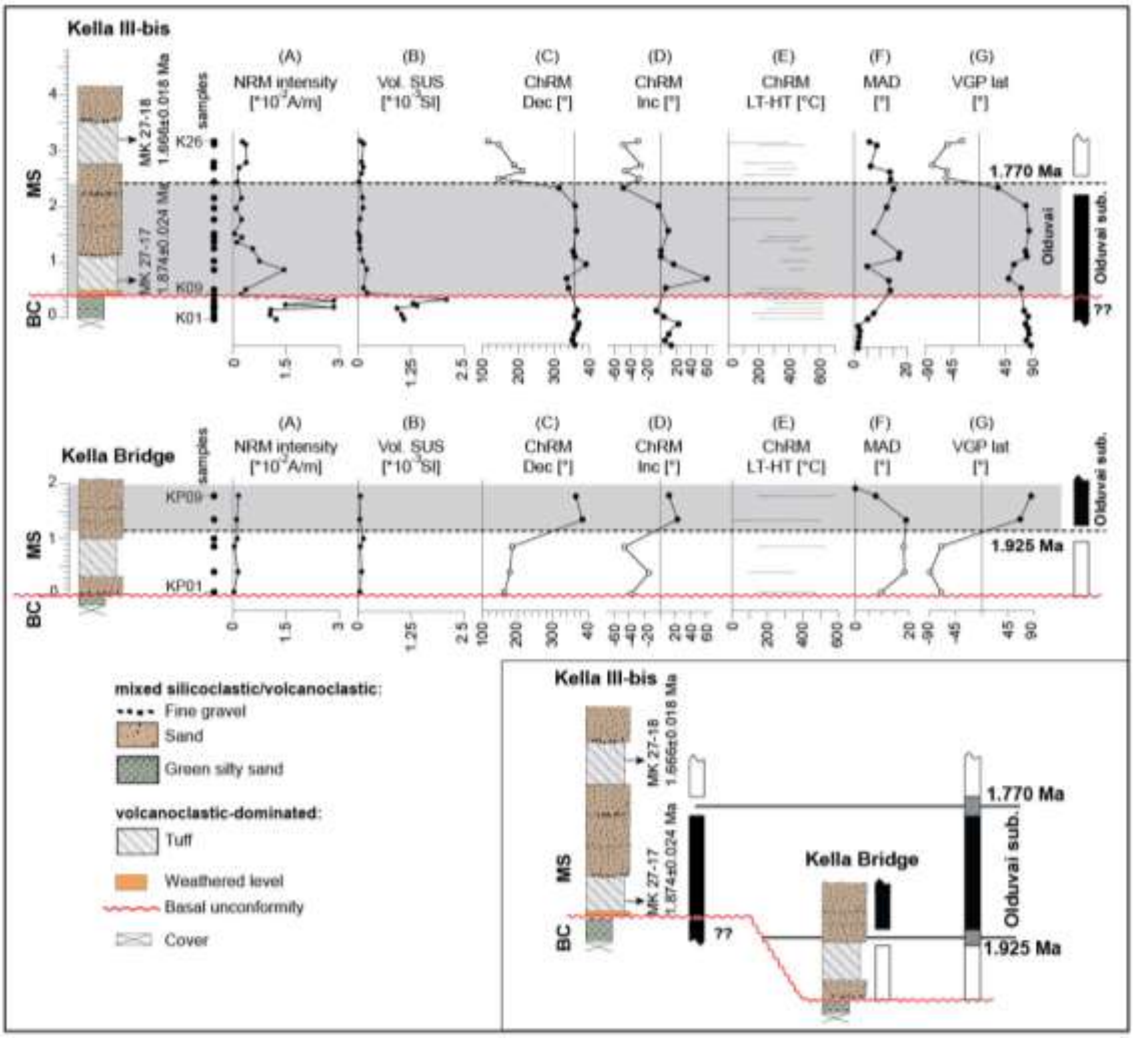

Figure 3 Magnetostratigraphic data of Kella III bis and Kella Bridge sections (see also Sup.Tab. 2) reporting, from left to the right: A) intensity of the natural remanent magnetization (NRM) at room temperature. B) Volume susceptibility at room temperature. C) Declination of the characteristic remanent magnetization (ChRM) component direction. D) Inclination of the ChRM component direction. E) Temperature range of existence of the ChRM (where LT is the minimum temperature and HT the maximum). F) Maximum angular deviation (MAD) of the ChRM component direction. G) Virtual geomagnetic pole (VGP) latitude (positive VGPs represent normal magnetic polarity and negative VGPs reverse magnetic polarity). The grey horizontal bands enclose the Olduvai normal polarity subchron, black lines represent its lower and upper limits, and the red undulated lines the position of the basal unconformity separating the 'basal clays' (BC) below from the Middle Succession (MS) above. $^{40}Ar/^{39}Ar$ ages of tuff layers of Morgan et al. (2012) are also reported with error bounds at ± 2σ.

The natural remanent magnetization (NRM) was measured after each heating-cooling cycle with a 2G Enterprises 755 DC-SQUID cryogenic magnetometer located, together with the thermal demagnetizer, an a magnetically shielded room.

The initial volume susceptibility was measured with a Bartington MS2B. Standard least-square analysis (Kirshvink, 1980) was used to calculate the characteristic magnetic component (ChRM) directions from standard vector end-point demagnetization diagrams, and standard Fisher statistics was applied to analyze the mean component directions. In order to determine the ferromagnetic mineralogy carrying the primary paleomagnetic signal, we performed thermal demagnetization of a three-component IRM imparted in fields of 0.12 T, 0.4 T and 1.5 T using a pulse magnetizer ASC IM- 10-30, and experiments of hysteresis and backfield acquisition curves of isothermal remanent magnetization (IRM) using a vibrating sample magnetometer Microsense EZ7. The hysteresis data were plotted on a modified Day diagram (Dunlop et al., 2002) while the backfield IRM curves were rescaled and analyzed using the unmixing coercivity method of Maxbauer et al. (2016) in order to identify the ferromagnetic minerals contributing to the magnetic remanence.

Results

Bulk rock-magnetic properties

Thermal demagnetization of a three-component IRM shows a dominant signal carried by the low coercivity (0.12 T) curve with maximum unblocking temperatures of ~575°C, interpreted as due to magnetite, coexisting with a higher coercivity component with maximum unblocking temperatures of ~650°C interpreted as hematite (Fig. 4A).

The backfield IRM acquisition curves (Fig. 4B), rescaled and unmixed (Maxbauer et al., 2016), reveal the existence of a magnetic phase responsible for >90% of the total remanence and characterized by B1/2 (field at which half of the remanence is acquired) of ~50-60mT, coexisting with a subsidiary higher coercivity phase responsible for the reminder <10% of the remanence and characterized by B1/2 of ~600-700mT (Fig. 4C). The hysteresis loops (Fig. 5A) yielded parameters of saturation remanence/saturation magnetization (Mrs/Ms) and coercivity of remanence/coercivity (Hcr/Hc) that plot mostly in the 'pseudo-single domain' ('PSD') range (Fig. 5B) well above the single domain (SD)-multidomain (MD) magnetite mixing line of Dunlop et al. (2002) possibly because of the presence of phases with contrasting coercivities.

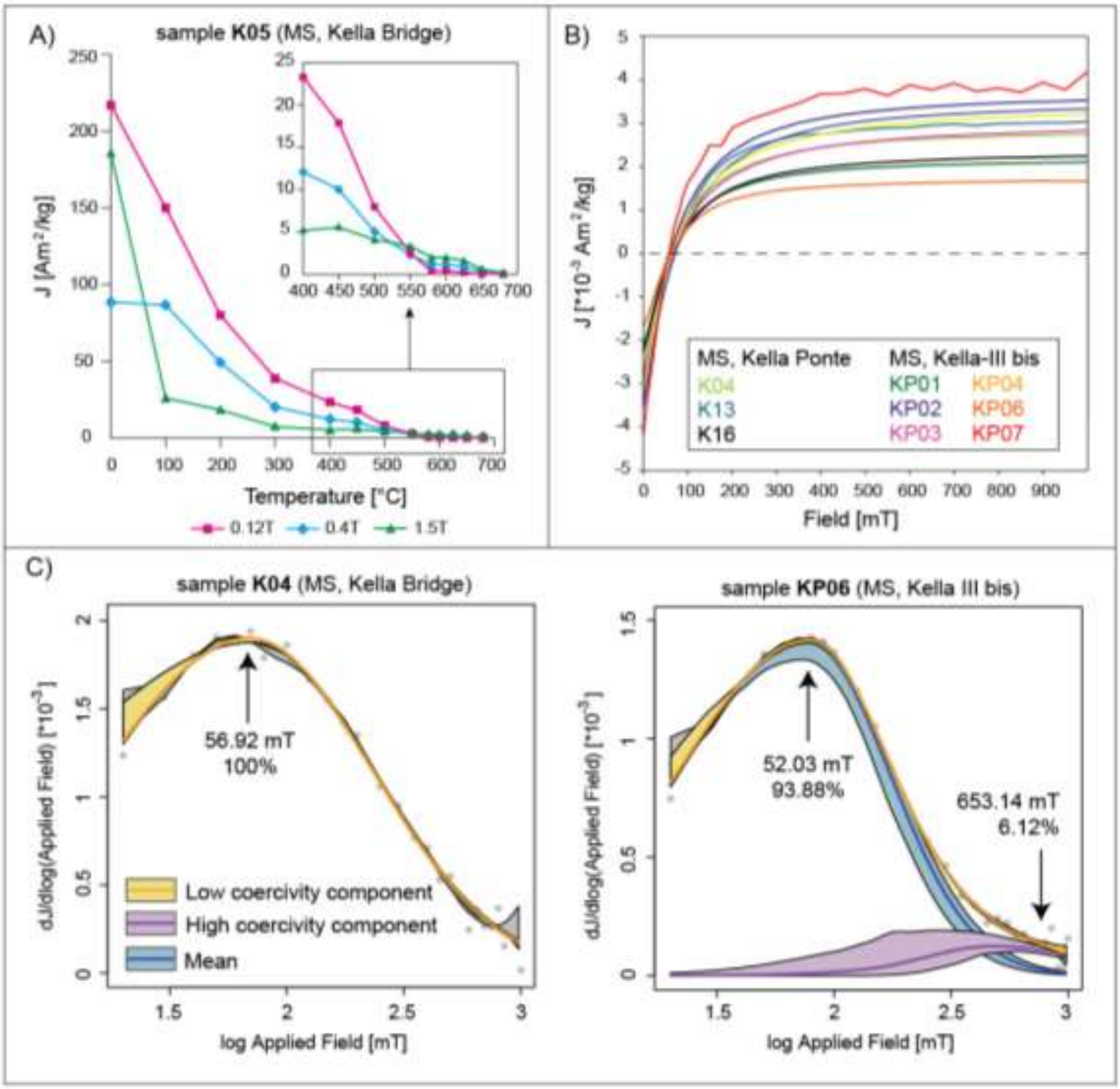

Figure 4 Rock magnetic analysis results. A) Thermal demagnetization of a three-component IRM of sample K05 from Kella Bridge acquired in applied fields of 1.5 T, 0.4 T and 0.12 T and showing the presence of a magnetite phase with maximum unblocking temperatures of ~575°C coexisting with a phase with maximum unblocking temperature of ~650°C attributed to hematite. B) Isothermal remanent magnetization (IRM) backfield acquisition curves of representative samples from Kella III bis and Kella Bridge; C) representative examples of coercivity unmixing of the IRM acquisition curves (Maxbauer et al., 2016) showing the dominant presence of a low coercivity phase (magnetite) coexisting with a subsidiary high coercivity phase (hematite).

Sample K04 is characterized by a very high Hr/Hc value and appears wasp-waisted in shape, again pointing to phases with contrasting coercivities. These results altogether suggest that the MS volcano-sedimentary sequence is characterized by low coercivity magnetite as predominant magnetic phase, coexisting with minor amounts of high coercivity hematite, in line with the previous results of Perini et al. (2021).

Magnetostratigraphy

The natural remanent magnetization (NRM) intensity is generally $<1*10^{-2}$ A/m throughout the MS volcano-sedimentary sequence to then distinctively increase in the BC as observed at Kella III bis (the modestly outcropping BC at Kella Bridge was not sampled) (Fig. 3A). This pattern is paralleled by the initial volume susceptibility, relatively low in the MS and higher in the BC (Fig. 3B). Thermal demagnetization of the NRM (Fig. 6; data in Sup. Tab. 1) reveals the occurrence in 25 samples of characteristic remanent magnetization (ChRM) component directions oriented either northernly and shallow down (generally positive inclinations), interpreted as representing normal magnetic polarity, or southerly and up (negative inclinations), representing reverse magnetic polarity, isolated between 100-150°C and 525-625°C (ChRM data in Sup. Tab. 2). The ChRM component directions, plotted on an equal-area projection, display a mean of Dec. = 356.6°E, Inc = 18.3° (α_{95} = 11.1°; Fig. 6, right panel). However, the normal and reverse ChRM directions do not pass the bootstrap reversal test (made with PmagPy; Tauxe et al., 2016) whereby the 95% confidence intervals for the normal and reverse antipodes overlap for the x and y components but not for the z component. The normal and reverse directions are antipodal in declination, but the normal polarity directions tend to be shallower in inclination (Fig. 6, equal-area projection in right panel). We stress however the paucity of data used for the reversal test, which may hinder its validity. In any case, taking into account also results of Perini et al. (2021), we are aware that the ChRM component directions extracted from these sediments are not ideal, insofar as they sometimes possess high MAD values and tend to be relatively poorly grouped. This is in fact frequently the case for remanent magnetizations acquired in medium-to-coarse grained continental sediments emplaced in high- to variable-energy depositional settings, where grains mobility and interactions may disturb the detrital remanent magnetization imparted by the (weak) Earth's magnetic field. Bearing these uncertainties in mind, we believe that the thermal demagnetization data provided sufficient information for a relatively secure polarity attribution for most of the analyzed samples (i.e., clear alignments of demagnetization steps along the N axis or the S axis for normal or reverse polarity, respectively). In addition, as observed also in Perini et al. (2021), no obvious relationship seems to exist between lithology and/or magnetic mineralogy, and magnetic polarity, and thus we are inclined to interpret these ChRM component directions as primary in origin, albeit we acknowledge that they do not display an ideal antipodal distribution. The ChRM declination and inclination values are plotted in stratigraphic order (Fig. 3C,D) together with their unblocking temperature spectra (Fig. 3E) and maximum angular deviation (MAD) values (usually ~10°; Fig. 3F). These data were used to calculate virtual geomagnetic pole (VGP) latitudes (Fig. 3G; Sup. Tab. 2) and derive the magnetic polarity stratigraphy of Kella III bis and Kella Bridge, where positive VGP values represent normal magnetic polarity and negative values reverse magnetic polarity.

The magnetostratigraphic results are described from top to bottom (Fig. 3G). At the top of Kella III bis, a reverse polarity interval was detected from sample K26 to K22, followed by a transition from reverse to normal magnetic polarity observed between samples K22 and K20, and by normal polarity down to sample K09. The reverse to normal polarity transition is interpreted as a record of the top Olduvai subchron (1.770 Ma), in agreement with the $^{40}Ar/^{39}Ar$ ages of 1.666±0.018 Ma for Tuff MK 27-18 and 1.874±0.024 Ma for Tuff MK 27-17 interbedded in the section (Morgan et al., 2012). At Kella III bis, normal magnetic polarity continues in the BC below the MS down to sample K01, but because of the presence at the MS/BC contact of a reddened surface potentially marking a hiatus in unconformity, and in absence of additional temporal constraints, we exclude from age modeling this normal polarity interval observed in the BC, and truncate the interpreted chronology of the MS at the basal unconformity marking the MS/BC contact (Figs. 2,3). The nearby Kella Bridge section is characterized by normal magnetic polarity at its top, in samples KP09 and KP07, and reverse polarity towards its base, from sample KP04 to KP01. We interpret this normal-reverse transition as the base Olduvai subchron (1.925 Ma). The BC below the MS were not sampled at Kella Bridge.

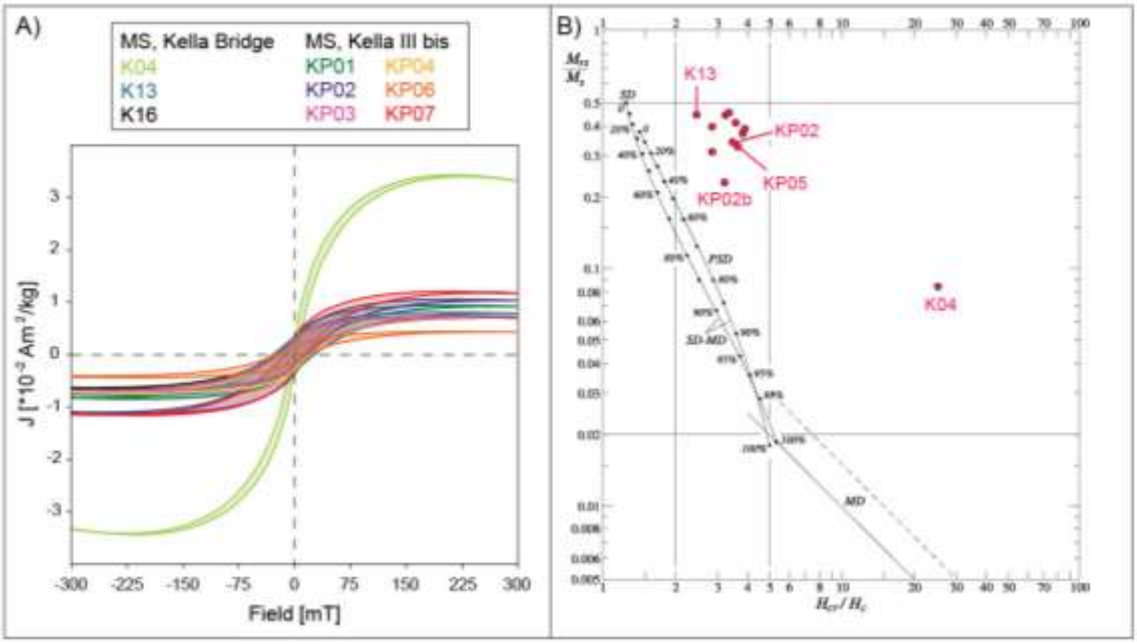

Figure 5 Rock magnetic analysis results. A) Hysteresis loops corrected for paramagnetic components performed on 9 representative samples from Kella III bis and Kella Bridge. B) Hysteresis data (Mrs/Ms *versus* Hcr/Hc) of samples from panel (A) plotted on a modified Day diagram (Dunlop, 2002) valid for variable mixtures of single domain (SD)-multidomain (MD) magnetite grains. Data plot above the SD-MD magnetite mixing line probably because controlled by mixtures of low coercivity magnetite and high coercivity hematite.

The observed magnetochronology implies that the unconformable base of the MS is diachronous between Kella III bis (younger) and Kella Bridge (older) (Fig. 3, bottom right inset). This is interpreted as due to the inherently erosive nature of the high-energy MS volcano-sedimentary sequence emplaced unconformably on top of the low-energy BC unit. End of erosion and associated onset of deposition of the MS may vary laterally depending on local energy variations, producing areas of early deposition of the MS when elsewhere erosion still prevailed and deposition of MS started only later. Hence, the age of the first sediment emplaced above the erosional basal unconformity may vary along strike, being younger at Kella III bis, where the base of the MS falls within Olduvai normal polarity, and older at Kella Bridge, where the base of the MS falls in pre-Olduvai reverse polarity (Fig. Fig. 3, bottom right inset).

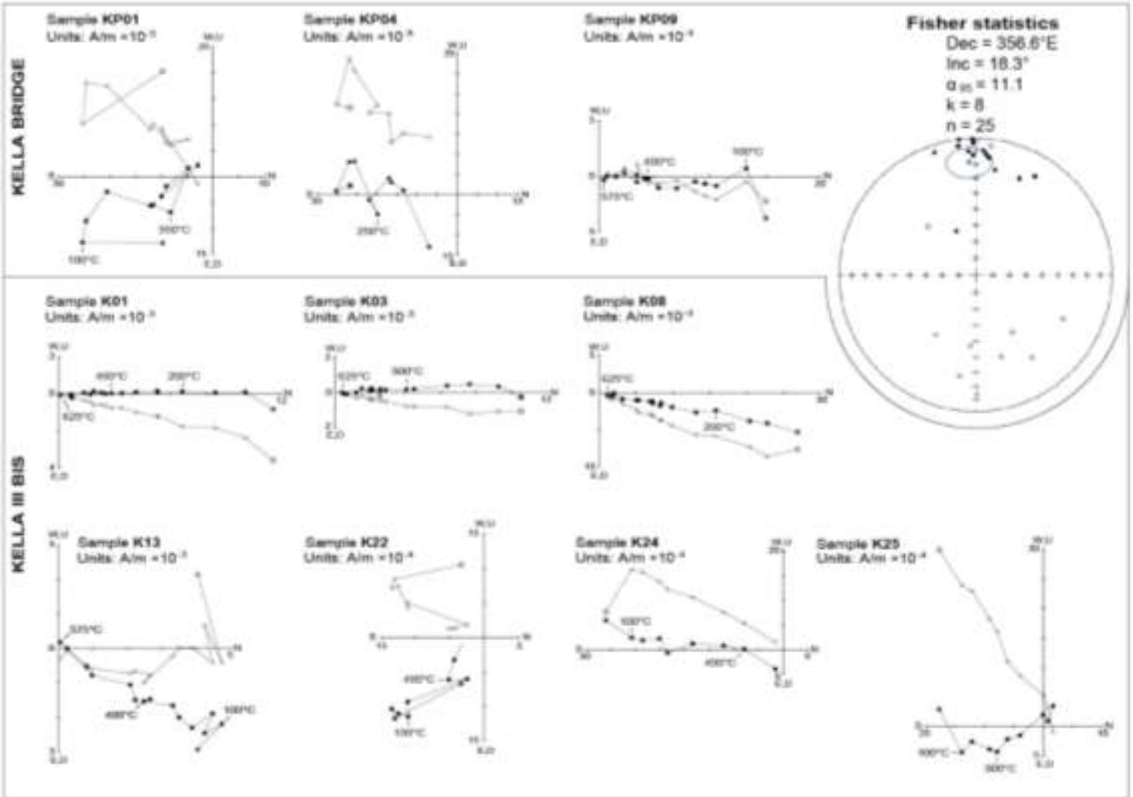

Figure 6 Vector end-point demagnetization diagrams of representative samples from Kella III bis and Kella Bridge. Demagnetization steps are expressed in °C. Closed symbols are projections onto the horizontal plane while open symbols onto the vertical plane (made with PuffinPlot; Lurcock and Wilson, 2012). Standard Fisher statistics for the northerly-and-down (normal polarity) and southerly-and-up (reverse polarity) ChRM directions is reported in top right panel (Dec = mean declination, Inc = mean inclination, α_{95} = cone of 95% of confidence around the mean, k = precision parameter of the distribution, n = number of ChRM vectors).

Discussion

At Melka Kunture there is evidence for the Olduvai subchron at the base of the volcano-sedimentary sequence (MS) above a basal unconformity with the underlying BC unit (Fig. 2). This evidence comes from the overall interpretation of the entire sequence of normal and reverse polarity magnetozones established at Garba and Gombore, aided by new data from Kella and interpreted in conjunction with selected $^{40}Ar/^{39}Ar$ ages from the literature (Fig. 2). The completeness of registry of the Olduvai subchron is however found to vary in the different sections analyzed: at Garba and Gombore, its base an top are not precisely recorded due to sampling gaps (Fig. 2), while Kella III bis and Kella Bridge register its top and base, respectively (Figs. 2; 3 bottom right inset), due to the diachronous base of the MS above the basal unconformity, as described above.

Bearing these complexities in mind, together with all the uncertainties associated with the various experimental analyses described above, the chronostratigraphic framework summarized in Figure 2, and the derived age-depth model of deposition based on magnetochronologic and selected $^{40}Ar/^{39}Ar$ age tie-points (Perini et al., 2021, figure 8), are ~~in our opinion~~ robust and valuable tools to describe the long-term age evolution of the Melka Kunture sequence and to assess the ages of the archaeological levels therein contained. The substantial linearity with which the recognized magnetozones line-up with stratigraphic depth, from the Brunhes chron at the top to the Olduvai subchron at the base, associated with the substantial agreement that this alignment has with at least some of the available $^{40}Ar/^{39}Ar$ ages (Fig. 2), imply that on the long-term, age progresses linearly with depth, allowing to interpolate ages for key archaeological levels in a simple yet statistical way (see Perini et al., 2021 for age modeling). Incidentally, simple linear age modeling does not exclude the presence throughout the sequence of high-frequency and abrupt variations in sediment accumulation rates, but these, even if present, would not change the observed linearity of the age-depth control points, which successfully describes long-term accumulation rates.

Conclusions

We established with previous and new data the occurrence of the Olduvai subchron at the base of the volcano-sedimentary Middle Succession (MS) at Melka Kunture hosting key archaeological levels. Our chronostratigraphic scheme, when considered in its entirety, indicates that archaeological levels E-F at Garba IV (Gallotti and Mussi, 2015) appear placed in reverse polarity strata shortly below the base of the Olduvai subchron, with a currently accepted age of 1.925 Ma, while level D falls close to the base of the Olduvai subchron in a magnetostratigraphic gap between normal (Olduvai) polarity above and reverse polarity below (Fig. 2). Our new results from Kella therefore confirm and substantiate previous results of Perini et al. (2021) concerning the actual age estimates of these archaeological levels obtained with long-term age-depth modeling of the MS and US sequences. Specifically, Garba IV level D yielding an early Acheulean technocomplex (Gallotti, 2013) has an interpolated age of 1.95 (-0.025; +0.1) Ma, while levels E-F with Oldowan technocomplexes have interpolated ages of 2.00 (-0.0075; +0.1) Ma and 2.02 (- 0.1; +0.09), respectively (see Perini et al., 2021 for additional information).

The $^{40}Ar/^{39}Ar$ age estimate of Tuff MK 27-23 at Garba IV, frequently used to assess the age of the aforementioned key archaeological level D at Garba IV, should be considered (like any other numerical age estimates) in its full statistical expression at 2σ (95%) level, that is, 1.719 Ma±0.398 Ma. We note that the age of this tuff expressed in this way comprises the age estimates of levels D and E-F as defined by Perini et al. (2021) and summarized above (albeit this tuff was not used in age modeling due to its large uncertainty). Obviously, this criticism is not to the detriment of the analysists who tried to date the tuff (Morgan et al., 2012). It rather serves as a reminder of the inherently imperfect and discontinuous nature of the stratigraphic record, which in this case takes the form of a 10 cm-thick, laterally discontinuous, and reworked tuff.

Finally, our chronostratigraphy has relevant implications, not explored here, for understanding the emergence of the Acheulean in East Africa (Gallotti, 2013) as well as the adaptation of *Homo* to high elevation climate vegetation, and general environmental conditions during the Pleistocene. We underline that the recorded archaeological sites at similar or higher (present-day) elevations are all later in age, as Gadeb at 2300 m asl (de la Torre, 2011), Melka Wakena at 2300-2350 m asl (Hovers et al., 2021), Kilombe at 2000 m asl (Hoare et al. 2021) and Mt. Dendi at 3000 m asl (Vogelsang et al., 2018).

Acknowledgements

We thank the Editor for handling this manuscript. Comments from three reviewers were implemented in the final version of this this manuscript. Sampling for magnetostratigraphy at Kella was performed by GM and Edoardo Monesi. GM thanks the Rector of the *Università degli Studi di Milano* for fundings for travel and laboratory expenses (*Fondi Speciali per le Ricerche Archeologiche Anno 2017*. Project: *Scavi per datazione magnetostratigrafica del sito paleolitico di Melka Kunture, Etiopia*). Archaeological excavations and fieldwork at Melka Kunture in 2017 were funded by Università di Roma Sapienza grant SA11715C7C936C01 and Ministero degli Affari Esteri e della Cooperazione Internazionale grant ARC-001666 to MM.

6.1 Confirming the presence of the Olduvai Subchron at Melka Kunture (Ethiopia)

This sub-chapter is presented according to

Reply to Gossa et al., (2024). A critical assessment of the available age constraints placed in a comprehensively described and modeled stratigraphy confirms suggestion of presence of Olduvai subchron at the base of the Melka Kunture sedimentary sequence hosting early Acheulean archeological level Garba IVD

Giovanni Muttoni[a] and Serena Perini[a]

[a] *Dipartimento di Scienze Della Terra 'Ardito Desio', Università Degli Studi di Milano, Via Luigi Mangiagalli 34, 20133 Milan, Italy*

There has been considerable turmoil in the literature (e.g., Gossa et al., 2024) after publication of inference of presence of the Olduvai subchron (1.770-1.925 Ma) at the base of the Melka Kunture (Ethiopia) volcano-sedimentary sequence that led Perini et al. (2021) and Muttoni et al. (2023) to propose an age of 1.95 (-0.025; +0.1) Ma for the early Acheulean level Garba IVD (Gallotti, 2013), *de facto* pushing back by about 200 kyr the age of the earliest Acheulean in Africa, previously dated to close to the top of the Olduvai at ~1.76 Ma (Lepre et al., 2011). Here we summarize the analyses of Perini et al. (2021) and Muttoni et al. (2023) to then proceed on with additional considerations and clarifications pertinent to the ongoing debate.

Synthesis of the results

Perini et al. (2021) studied the magnetostratigraphy of the Melka Kunture volcano-sedimentary sequence (Raynal et al., 2004) across 9 sections pertaining to the Garba and Gombore sequences, including the Garba VI section containing, among others, archeological level Garba IVD (synthesis in Fig. 1; see also fig. 2 in Perini et al., 2021). They considered the observed sequence of normal and reverse polarity intervals in relation to the available $^{40}Ar/^{39}Ar$ age data of Morgan et al. (2012). They concluded that the magnetic polarity sequence, even if fragmented, is coherent, and it was found to extend from the Brunhes/Matuyama boundary (0.773 Ma) at the top across the Jaramillo subchron (0.99-1.07 Ma), found in multiple correlative sections, down to the questioned (Gossa et al., 2024) Olduvai subchron (1.770-1.925 Ma) and even further down to a possible record of the Réunion subchron (Fig. 1; see also Perini et al., 2021). Based on these findings, Perini et al. (2021) proposed two age models, one for the Garba sequence using five magnetochronologic tie-points (see also below), and another for the Gombore sequence using 4 magnetochronologic and 3 radiometric tie-points, which resulted however poorly defined at its base. The questioned (Gossa et al., 2024) age of 1.95 (-0.025; +0.1) Ma for the early Acheulean level Garba IVD derives from the Garba sequence age model, specifically from the close proximity of this archeological level to the base of the Olduvai subchron (1.925 Ma) in the Garba IV section, as discussed in detail below. Subsequently, Muttoni et al. (2023) studied additional sections in the nearby Kella Valley, providing further data for the definition of the critical Olduvai subchron (Fig. 1), strengthening conclusions in Perini et al. (2021). We explore further some of the key elements of this chronostratigraphy in response to recent concerns about its validity (Gossa et al., 2024).

Reliability and stratigraphic continuity of the Olduvai subchron registry

Tamrat et al. (2014) first proposed the presence of the Olduvai subchron in the Garba IV section, but unfortunately, they did not provide enough information to place the archeological levels with accuracy in the observed magnetostratigraphy. Following this early attempt, the Olduvai subchron was redefined at Garba IV by Perini et al. (2021) based on three samples of interpreted normal magnetic polarity resting above several samples of reverse polarity (Fig. 2; see also fig. 2 in Muttoni et al., 2023). It was precisely the acknowledged limitation of relying on only three samples to define the critical Olduvai subchron, coupled with the fact that the Garba IV section is of limited stratigraphic extension and does not reach up to the Garba XII section located altimetrically above and containing a registry of the Jaramillo subchron and the Brunhes/Matuyama boundary (Fig. 1), that prompted Muttoni et al. (2023) to look for the Olduvai subchron at the nearby locality of Kella Valley. The studied Kella sections are located only ~1.3 km away from Garba IV and are comprised of the same volcano-sedimentary sequence unconformaby overlying the same green silty sand unit that represents a laterally continuous regional lithostratigraphic marker (Fig. 2). In the Kella sections, magnetostratigraphy (Muttoni et al., 2023) and $^{40}Ar/^{39}Ar$ dating (Morgan et al., 2012) agree well in indicating that the lowermost part of the volcano-sedimentary sequence generally hosting key archeological levels contains a record of the Olduvai subchron (Fig. 2; see Muttoni et al., 2023 for details). Incidentally, we suspect that the normal magnetic polarity interval that Tamrat et al. (2014) interpreted as the Jaramillo subchron in the Gombore-I section could in fact be a lateral equivalent of the Olduvai subchron that they observed at Garba IV, because Gombore-I overlaps altimetrically with Garba IV rather than being located above it.

In response to concerns (Gossa et al., 2024) about the quality of the magnetostratigraphic data in Perini et al. (2021) and Muttoni et al. (2023), we report in Figure 2 examples of thermal demagnetization diagrams used to interpret magnetic polarity (normal polarity for samples GBIVO04, GBIVO05, KP09, K09, K13; reverse polarity for samples GBIV21, KP04, K24) across the critical Olduvai subchron interval. Magnetic component directions of interpreted normal polarity and associated with the Olduvai subchron in the Garba IV and Kella sections, even though not always ideally defined (due to the low magnetization intensity of the investigated sediments, see below), have been isolated between ~100°C and ~425-500°C up to 600°C, well above the alleged overprint due to digenetic goethite (with Néel point of 120°C) claimed by Gossa et al. (2024), which was in any case not observed.

We take the opportunity to stress some key aspects of the procedure we commonly adopt in magnetostratigraphic data interpretation. As our analytical background is strongly anchored to stratigraphy, we interpret demagnetization data (to extract magnetic component directions of either normal or reverse polarity) in the frame of the overall stratigraphic context. Samples are interpreted not only singularly, but also in relationship with the information provided by samples located stratigraphically above and below. In this way, samples that provide the best magnetostratigraphic information (containing stable and well-defined component directions) are used to guide the interpretation of stratigraphically nearby samples (altogether defining a same magnetozone) that may be affected by higher degrees of noise. This high risk-high gain approach, aimed at augmenting the completeness of the polarity reversal sequence, necessitates a congruent inventory of samples for analyses (191 in our case), and is usually applied to stratigraphies characterized by non-ideal magnetic remanence acquisition processes and generally low magnetic intensities, like Melka Kunture. There is of course a limit whereby samples that contain less than ~3 aligned demagnetization steps are excluded from interpretation.

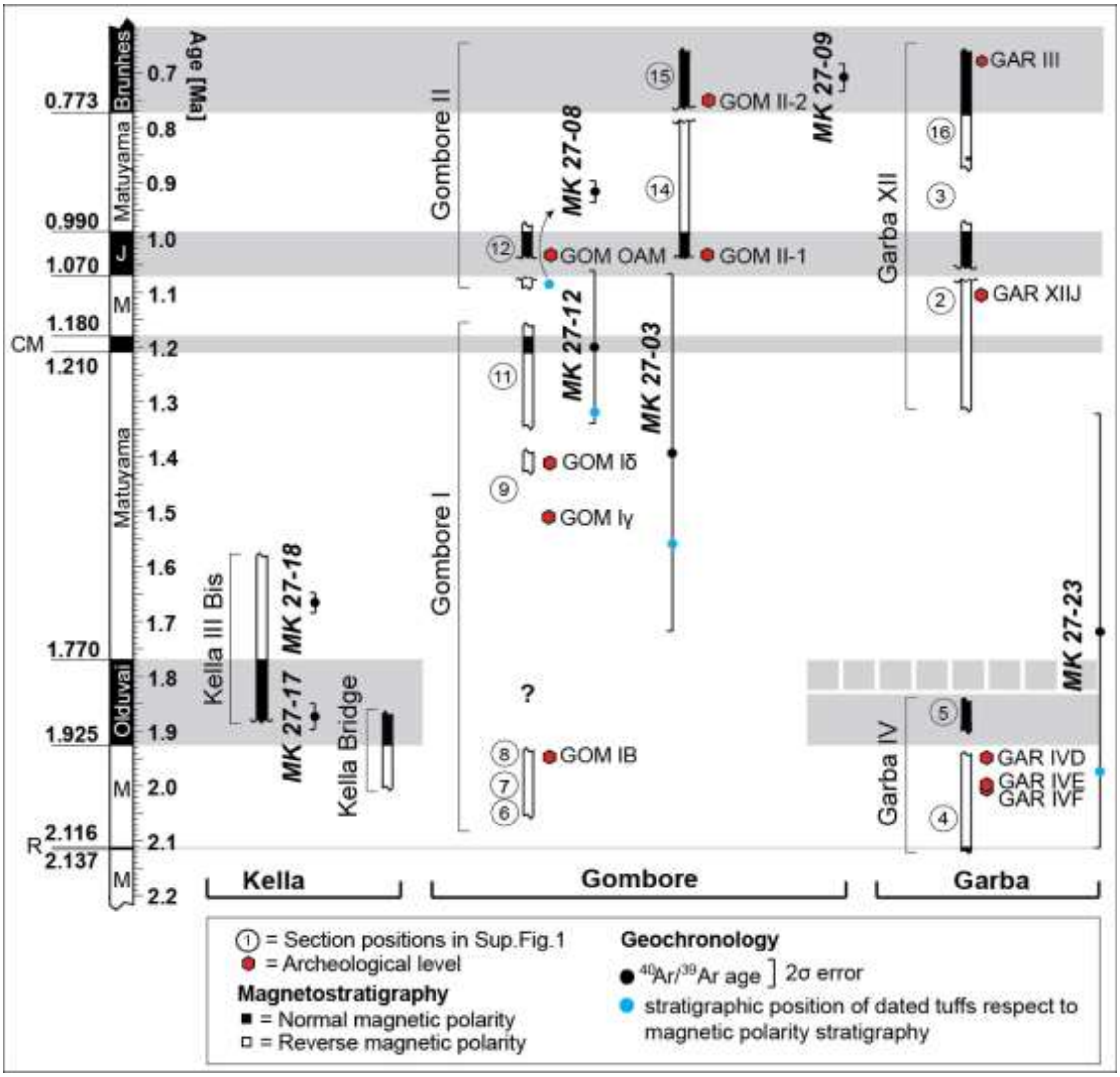

Figure 1 Synthetic chronostratigraphic scheme of the Melka Kunture sequence (Upper Awash Valley, Ethiopia) after Perini et al. (2021) and Muttoni et al. (2023). $^{40}Ar/^{39}Ar$ ages from Morgan et al. (2012) that could be relocated on the Perini et al. (2021) stratigraphy are plotted with respect to their stratigraphic position (blue dots) and numerical age (black dots with 2σ error bars).

Magnetostratigraphy and integration of magnetochronologic and radiometric age data

Gossa et al. (2024) raise concerns on the validity of the stratigraphic framework of Perini et al. (2021) and Muttoni et al. (2023) because it is '*inconsistently and selectively focused on certain dated tuff units as a basis for their correlation across sections*'. We stress that no tuffs were used for section-to-section correlations, in consideration of the acknowledged laterally discontinuous nature of the studied stratigraphy. Instead, magnetostratigraphy was applied for correlating sections across the Brunhes/Matuyama boundary, the Jaramillo subchron, and the base Olduvai (Fig. 1; see Muttoni et al., 2023). Gossa et al. (2024) raise additional concerns based on a claimed subjectivity in selecting magnetochronologic and radiometric age data in Perini et al. (2021). Seven of the 13 tuffs listed in Morgan et al. (2012; tab.1) from Garba, Gombore, and Kella could be placed in our measured stratigraphy and considered in relation to the observed sequence of magnetic polarity reversals (Fig. 1). Out of the 7 stratigraphically relocated ages, three from Gombore (MK27-09, MK27-12, MK27-03) and two from Kella (MK27-17, MK27-18) were found to be consistent with the magnetic polarity reversal sequence (Fig. 1). Two of the relocated ages were excluded after the application of selection criteria, namely (i) congruence of the radiometric age with the magnetic polarity of the hosting sediment, which led to the exclusion of tuff MK27-08 from Gombore with an age of 0.875±0.020 Ma that is slightly younger than the age predicted by the reverse polarity strata immediately below the base of the Jaramillo (>1.07 Ma) where this tuff is located (Fig. 1), and (ii) data quality, which led to the exclusion of poorly dated tuff MK27-23 from the Garba IV section (1.719±0.398 Ma at 2σ) for reasons summarized below. In retrospect, we should have probably excluded also the relocated but poorly dated tuff MK27-03 (1.393±0.324 Ma at 2σ) from Gombore (Fig. 1), albeit this tuff has limited implications for the questioned (Gossa et al., 2024) age of Acheulean level Garba IVD. The other tuffs listed in Morgan et al. (2012) were not considered because they could not be positioned with accuracy on the observed magnetostratigraphy (Tamrat et al., 2014; Perini et al., 2021; Muttoni et al., 2023) using the stratigraphic information provided in Morgan et al. (2012). This selection procedure, admittedly not fully described in Perini et al. (2021), was made objectively in preparation for age modeling, and not subjectively during age modeling to control the output, as Gossa et al. (2024) seem to suspect. In any case, we admit that there is a limitation here that could have been overcome if sampling for magnetostratigraphy and radiometric dating were done simultaneously. An invitation to cooperate in the future.

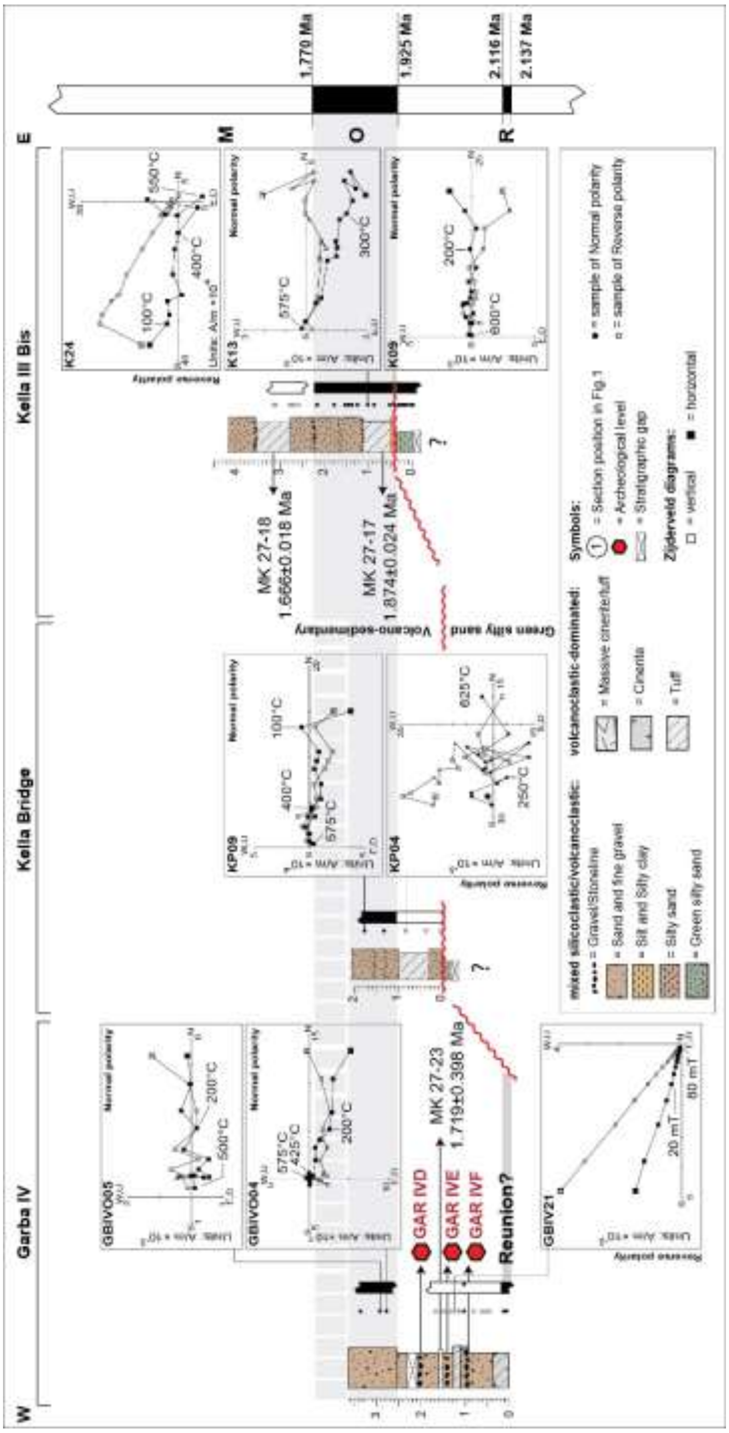

Figure 2 Detail of the stratigraphic interval in which the critical Olduvai Subchron has been identified at the base of the Melka Kunture volcano-sedimentary sequence resting unconformably on top of the green silty sand unit at Garba IV, Kella Bridge, and Kella III Bis. Next to the stratigraphic logs are reported representative examples of vector end-point demagnetization diagrams (made with PuffinPlot). Demagnetization steps are expressed in °C. Closed symbols are projections onto the horizontal plane while open symbols onto the vertical plane.

As for the conviction that magnetochronology should be routinely subjected to validation by radiometric dating [Gossa et al., 2024: '*(d)efinitive correlation of magnetostratigraphy with the geomagnetic polarity time scale depends on the existence of reliable absolute age(s)'*], we stress that the geomagnetic polarity timescale for 0-180 Ma has been constructed using magnetic anomaly data without a single absolute date on sea floor lavas but constrained using magnetostratigraphically correlated age data from land sections (e.g., Cande and Kent, 1992).

Relevance of tuff MK27-23

The $^{40}Ar/^{39}Ar$ age of MK27-23 (Morgan et al., 2012), a tuff located close to the early Acheulean level Garba IVD, is a keystone in African paleolithic archeology and reputed '*the only reliable alternative to infer the possible age for both the early Acheulian and Oldowan layers at Garba IV'* (Gossa et al., 2024). Tuff MK27-23 was however not included in the inventory of Perini et al. (2021) for its documented large experimental uncertainty. Morgan et al. (2012) clearly stressed the complicacies they encountered in dating this tuff. They listed two possible mean ages depending on grains' population – 1.57 Ma or 1.414 Ma – as well as an isochron age of 1.719 Ma, leaning in favor of the latter, sometimes quoted as a minimum age, sometimes as a maximum, while admitting that in any case, these ages, differing by over 300 kyr neglecting errors, *'are clearly not ideally determined'.* These analytical complicacies arise from the fact that tuff MK27-23 is evidently heavily reworked (Raynal et al., 2004). Perini et al. (2021) attempted to point out these limitations by elevating errors of the experimental measurements at the more robust 2σ level (a good practice that should be routinely implemented in quantitative analyses), suggesting an age range from 1.3 Ma to 2.1 Ma for this tuff, which *per se* does not violate the age model of Perini et al. (2021) while clearly indicating that this tuff cannot be considered a reliable tie-point for dating. In spite of these complicacies, tuff MK27-23 remains difficult to dislodge from the current archeological narrative. For example, Gossa et al. (2024) seem now to be fairly convinced to use, among the various possibilities discussed in Morgan et al. (2012), an age of 1.57

Ma for this tuff instead of the originally preferred (Morgan et al., 2012) isochron age of 1.719 Ma, without however presenting new experimental analyses in support of this reinterpretation.

Age modeling

Concern has been expressed on the validity of the linear age model of Perini et al. (2024), quoted as '*tied to poorly defined paleomagnetic polarity interpretations'* (Gossa et al., 2024). This concern offers the possibility to discuss age modeling in further detail. Age models implementing interpolations of various combinations of magneto-bio-geochronologic datums represent a fundamental component of advanced stratigraphic studies used to draw quantitative inferences on sediment accumulation rates and the potential occurrence of temporal gaps in unconformities. As summarized above, Perini et al. (2021) used in their age model for the Garba sequence (comprised of sections Garba III, Garba XII, and Garba IV, this latter with Acheulean level Garba IVD; Fig. 1) a set of five magnetochronologic tie-points (Fig. 3A, from Perini et al., 2021). $^{40}Ar/^{39}Ar$ age data from this sequence (Morgan et al., 2012) could not be confidently relocated on the observed magnetostratigraphy, while the questioned age of tuff MK27-23 was excluded for reasons outlined above. Perini et al. (2021) noticed that the magnetochronologic age-depth constraints of the Garba sequence (Fig. 3A) tend to follow a linear relationship ($r^2 = 0.99$) implying that on the long term, time progresses linearly with stratigraphic depth, indicating substantial regularity of deposition and most importantly, no evidence for *major* temporal gaps across the investigated stratigraphic sequence. Hence, Perini et al. (2021) applied a linear age model, implementing 95% bootstrap error analysis, to describe the *average long-term* sediment accumulation rates of the Garba sequence, finding an age for Acheulean level Garba IVD of 1.95 (-0.025; +0.1) Ma (Fig. 3A). We stress for clarity that the proposed age for Garba IVD is only moderately dependent on the age model itself because this archeological level falls at or very close to the base of the Olduvai subchron (1.925 Ma) (Fig. 2) that acts as controlling tie-point for age determination (Fig. 3A).

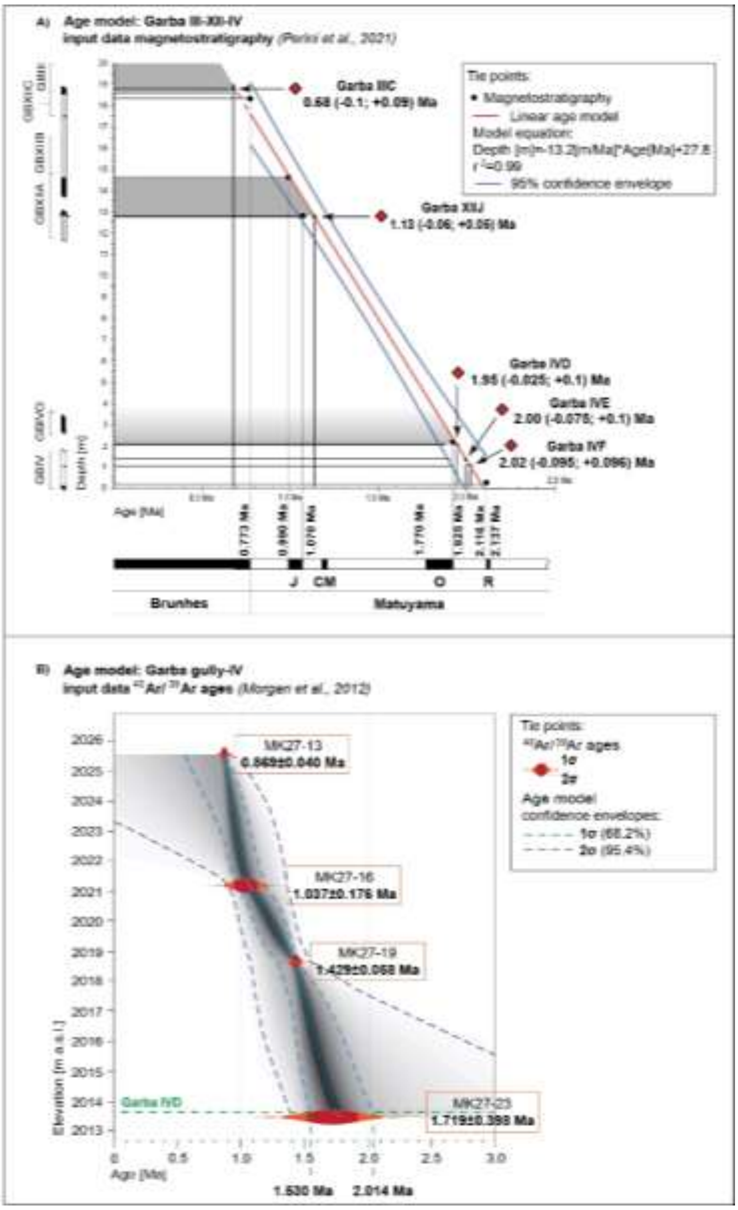

Figure 3 (A) Original age model of Perini et al. (2021) that uses a combination of $^{40}Ar/^{39}Ar$ and magnetochronologic ages from the Garba sequence at Melka Kunture. For the lower part of the sequence at Garba IV, this model takes into account the age constraints provided by the Olduvai subchron (see also Muttoni et al., 2023) while excluding the isochron age of 1.719±0.398 Ma (2σ) for tuff MK27-23. (B) Deterministic age model performed following figure 1 in Gossa et al. (2024) and using four $^{40}Ar/^{39}Ar$ tie-points from Morgan et al. (2012), including the age of tuff MK27-16 at 1.037±0.176 Ma (2σ) instead of the undisclosed tuff with mean at 1.30-1.32 Ma used in Gossa et al. (2024), not listed in Morgan et al. (2012), as well as the isochron age of 1.719±0.398 Ma (2σ) for tuff MK27-23 as preferred by Morgan et al. (2012) instead of the 'new' age of 1.57±0.300 Ma for this tuff as reinterpreted by Gossa et al. (2024). This model (B), with its large uncertainties, while not violating conclusions in Perini et al. (2021), does not allow any precise inference on the age of archeological levels, similarly to the model of figure 1 in Gossa et al. (2024). At the present state of knowledge, our preferred age model for the Melka Kunture sequence is in panel (A) (from Perini et al., 2021).

A Bayesian age model for the Garba sequence has been proposed by Gossa et al. (2024, fig. 1) as an alternative to the linear model of Perini et al.

(2021). This alternative model is based on four $^{40}Ar/^{39}Ar$ age data distributed across 12.5 stratigraphic meters and neglecting integration with the magnetochronologic data available for the sequence. Albeit not stated, we surmise that the youngest tuff plotted in figure 1 of Gossa et al. (2024) is tuff MK27-13 (0.869±0.040 Ma), followed by a tuff with a plotted mean age between 1.30 and 1.32 Ma, which is however not listed in Morgan et al. (2012), in turn followed by tuff MK27-19 (1.429±0.058 Ma) and the questionable 'new' age of 1.57±0.300 Ma for tuff MK27-23 (but see above about this age). Inspection of figure 1 in Gossa et al. (2024) confirms that Bayesian modeling based on a limited number of tie-points distributed along an extended stratigraphy (0.3 point/m) does not provide realistic outcomes, producing abnormal inflations and contractions of the error bounds proportional to the large distance between pairs of age-depth constraints. We explore this further by generating a deterministic age model implementing Bayesian principles (Lougheed and Obrochta, 2019) that uses a similar set of ages except for tuff MK27-16 at 1.037±0.176 Ma in place of the undisclosed tuff with mean at 1.30-1.32 Ma, and the isochron age of 1.719±0.398 Ma for tuff MK27-23 as originally preferred by Morgan et al. (2012) in place of the 'new' age of 1.57±0.300 Ma for this tuff now preferred by Gossa et al. (2024) (all errors expressed at 2σ, as in fig. 1 of Gossa et al., 2024). The model (Fig. 3B) allows ages of up to ~2 Ma (at a generous 1σ confidence level) for the Garba IVD archeological level, which *per se* do not violate conclusions in Perini et al. (2021) [1.95 (-0.025; +0.1) Ma], while clearly illustrating the limitations of such procedure based on a limited number of tie-points with large uncertainties that hinder the possibility to reach any testable conclusions about the age of archeological levels (e.g., Garba IVD). Fig. 3. (A) Original age model of Perini et al. (2021) that uses a combination of $^{40}Ar/^{39}Ar$ and magnetochronologic ages from the Garba gully at Melka Kunture. For the lower part of the sequence at Garba IV, this model takes into account the age constraints provided by the Olduvai subchron (see also Muttoni et al., 2023) while excluding the isochron age of 1.719±0.398 Ma (2σ) for tuff MK 27-23. (B) Deterministic age model performed following figure 1 in Gossa et al. (2024) and using four $^{40}Ar/^{39}Ar$ tie-points from Morgan et al. (2012), including the age of tuff MK 27-16 at 1.037±0.176 Ma (2σ) instead of the undisclosed tuff with mean at 1.30-1.32 Ma used in Gossa et al. (2024), not listed in Morgan et al. (2012), as well as the isochron age of 1.719±0.398 Ma (2σ) for tuff MK 27-23 as preferred by Morgan et al. (2012) instead of the 'new' age of 1.57±0.300 Ma for this tuff as reinterpreted by Gossa et al. (2024). This model (B), with its large uncertainties, while not violating conclusions in Perini et al. (2021), does not allow any precise inference on the age of archeological levels, similarly to the model of figure 1 in Gossa et al. (2024). Our preferred age model of the Melka Kunture sequence is in panel (A) (from Perini et al., 2021).

Concluding remarks and future directions

We maintain the substantial validity of our (Perini et al., 2021; Muttoni et al., 2023) integrated stratigraphic approach (summary in Fig. 1), recently misemployed by Mussi et al. (2023) but amended by Gallotti et al. (2023), which uses (i) a comprehensive understanding of the stratigraphy at a regional scale, (ii) magnetostratigraphy for section-to-section correlations across a laterally discontinuous stratigraphic landscape, (iii) an attempt to critically combine geochronology and magnetostratigraphy where possible, and (iv) a comprehensive and detailed presentation, illustration, and description of the data following agreeable analytical procedures and protocols (Langereis et al., 2010; Muttoni, 2021). We insist that it is the *overall sequence* of normal and reverse polarity magnetozones, improvable as fragmented but significant and integrated (where possible) with $^{40}Ar/^{39}Ar$ ages and correlated with the most recent Pleistocene geomagnetic polarity time scale (Channell et al., 2020), that makes our chronology testable, suggesting also that the normal polarity magnetozone detected at the base of the Melka Kunture volcano-sedimentary sequence is the best candidate to represent the Olduvai subchron (1.77-1.925 Ma).

Acknowledging by experience the extreme difficulties that experimental analysts commonly face when measuring the quantities of nature, striving for excellence as difficult as it is rare, we think that time has come to move forward with new data and scientific testing on the age of the earliest Acheulean(s) in Africa. Our suggestion is to reset the current narrative by positively introjecting the following main elements that arise from the present state of knowledge: (i) there is clear indication for the presence of the Olduvai subchron (1.770-1.925

Ma) at the base of the Melka Kunture sequence hosting Acheulean level Garba IVD, (ii) the currently proposed age of 1.95 (-0.025; +0.1) Ma for Garba IVD is primarily controlled by the age of the base of the Olduvai subchron (1.925 Ma) close to which it falls, (iii) the use of tuff MK27-23 (1.719±0.398 Ma) to approximate the age of Garba IVD should be provisionally abandoned for good, (iv) performing age modeling implies using independently determined age-depth tie-points (magnetochronologic and radiometric) conjointly and not selectively or in subordinate relationship. Finally, we would be glad to participate to the development of new age models based on critical integrations of magnetochronologic and radiometric age data in a common and shared stratigraphic reference frame. Perhaps, models might evolve from ‘simple linear’ to more ‘sophisticated Bayesian’ once a congruent inventory of well-dated tie-points (>>1/m) will be available.

Acknowledgements

We thank Rosalia Gallotti and Jean Paul Raynal for the useful discussion.

Chapter 7

A Multiple Origin for the Acheulean

Manuscript in preparation

Serena Perini [a], Rosalia Gallotti [b], Jean-Paul Raynal [c], Federica Langone [a], Francesca Forni [a], Christopher J. Lepre [d] and Giovanni Muttoni [a]

[a] Dipartimento di Scienze della Terra 'Ardito Desio', Università degli Studi di Milano, via Luigi Mangiagalli 34, 20133 Milan, Italy

[b] LabEx ARCHIMEDE and UMR 5140 Archéologie des sociétés méditerranéennes, Université Paul Valéry Montpellier 3 – CNRS, Campus Saint Charles, 34199 Montpellier, France.

[c] Université Bordeaux, CNRS, UMR 5199 PACEA-PPP, Bâtiment B18 Allée Geoffroy Saint-Hilaire CS 50023, 33615 Pessac Cedex, France.

[d] School of Earth Environment and Society Bowling Green State University, 190 Overman Hall Bowling Green, OH 43403

Keywords: Acheulean, East Africa, Early Pleistocene, Hominins, Chronostratigraphy, Magnetostratigraphy, Tephrostratigraphy.

One Acheulean or Multiple Acheuleans?

The emergence of the Acheulean is a major topic in Early Stone Age research. The production of Large Cutting Tools (LCTs) is widely considered the hallmark of the Acheulean and one of the most relevant technological leaps of humanity. Over the last two decades, a considerable effort has been made to date the emergence of the Acheulean in East Africa. Acheulean industries appeared at 1.76 Ma in West Turkana, Kenya (Lepre et al., 2011), ~1.75 Ma at Konso-Gardula, Ethiopia (Beyene et al., 2013; Suwa et al., 2015), ~1.7-1.65 Ma at Olduvai, Tanzania (Diez-Martín et al., 2015; Stanistreet et al. (2018), ~1.6 Ma at Melka Wakena and Gona, Ethiopia (Gossa and Hovers, 2022). Recent magnetostratigraphic analyses from Melka Kunture, Ethiopia (Perini et al., 2021;

Muttoni et al., 2023), combined with previous $^{40}Ar/^{39}Ar$ dating (Morgan et al., 2012), pushed the early Acheulean back to 1.95 (-0.025; +0.1) Ma (see also discussion below).

Similarly, to what occurred for the West Turkana early Acheulean (Lepre et al., 2011), the Ethiopian Acheulean gets closer in age to the late Oldowan (*sensu* Gallotti, 2018), requiring a reevaluation of the Oldowan–Acheulean transition either as a rapid change or the outcome of evolutionary trends. This also rekindled the debate about the paradigm, more taken as granted than proven, that the early Acheulean is the cultural product of *Homo erectus sensu lato*.

Several studies have addressed the very technological "nature" of the early Acheulean, trying to understand and define its characteristics. Some of them modified the previously established paradigm of a uniform and static Acheulean, partially superseding the simplistic equivalence Acheulean = handaxe while shedding new light on the high variability of these techno-economic systems (e.g., de la Torre and Mora 2005, 2016, 2018; de la Torre 2011; Chevrier, 2012; Gallotti, 2013; Diez-Martin et al., 2015; Gallotti and Mussi 2017, 2018; Texier, 2018).

Two testable hypotheses can be formulated regarding the emergence of the Acheulean. If the dates listed above, ranging broadly from 2 to 1.6 Ma, approximate reality, implying a substantially continuous stratigraphic recording of the events, then we would be inclined to conclude that the Acheulean innovation was not a single point-of-entry event, but that multiple Acheuleans, each possibly bearing its own characteristics and peculiarities, emerged across space and time in a sort of unpredictable inevitability. Alternatively, if the observed age scattering is unrealistic but rather reflects preservation issues related to the inherently discontinuous stratigraphic record, then we would expect the existence, somewhere and at some point in time, of a single point-of-entry for the Acheulean, a discrete stratigraphic level, which we may not have found yet, from which the Acheulean spread across space and time, likely preserving some of its original characteristics. Were the Acheulean innovations multiple events that had multiple origins in different localities and with different characteristics, or did they correspond to a single phenomenon that spread with similar characteristics from a single point of origin across East Africa? Multiple Acheuleans or one ‘heroic’

Acheulean? Explaining technological changes leading to innovation also requires analyzing the conceptual background present before the change occurred. Thus, we push the questions above further by asking if the late Oldowan industries constitute a cultural background, locally diversified or general, already containing all (or most of) the technical elements that eventually led to the emergence of multiple Acheuleans, each with its local characteristics, through knowledge recombination (*sensu* de Baune, 2004). Or were the late Oldowan complexes only marginally related to the Acheulean innovations, leaning in favor of a single Acheulean invention resulting from an act of genius?

A first step to tackle these questions is to go through a critical and demanding re-assessment of the chronostratigraphy of key East African localities recording the earliest occurrences of the Acheulean from late Oldowan 'precursors' broadly between 2 and 1.6 Ma. This is accompanied by a critical overview of the related techno-economic behaviors in a micro-regional perspective, to identify and describe the emerging technical innovation(s), here intended as "…the doing of new things or the doing of things that are already being done in a new way (Schumpeter, 1947)", and how they relate to the human biological variability recorded in this time period.

Assembling the East African record

We critically reviewed the chronostratigraphies of sites documenting the earliest local occurrences of the Acheulean, as well as the occurrence of the late Oldowan, in East Africa. We also included a contemporaneous record of hominin presence, following the classification and listing of Anton et al. (2014) and Anton and Middleton, (2023), to infer about potential toolmaker(s) at the times of the Acheulean innovation(s). The inventory of sites was assembled using strict chronostratigraphic criteria: (i) archeological sites should be reported in the original publications in a clear stratigraphic context, possibly accompanied by metered logs and correlative lithological descriptions; (ii) archeological sites should be provided with documented chronostratigraphies based on, e.g., magnetostratigraphy, radiometric dating (e.g., $^{40}Ar/^{39}Ar$, with uncertainties expressed in this study at 2σ level), tephrostratigraphy (applied to solve intra-site correlations), or various combinations of different experimental methods; (iii) experimental data should be presented and illustrated (e.g., demagnetization data and principal component analysis for magnetostratigraphy, mineralogy and protocols for radiometric dating, major and trace elements composition analyses for tephrostratigraphy, etc.).

Localities (with multiple sites/levels) that met these criteria, as described in detail further below, are Melka Kunture (Ethiopia), Melka Wakena (Ethiopia), Konso-Gardula (Ethiopia), Gona (DAN5; Ethiopia), West Turkana (Kenya), East Turkana (Kenya), and Olduvai Gorge (Tanzania). On the other hand, localities that according to our critical analysis resulted not well constrained chronologically were excluded, such as: Gona in Ethiopia (BSN12 and OGS12), Gadeb in Ethiopia (Gadeb2A), West Turkana in Kenya (Naiyena Engol 2), Peninj in Tanzania (ST site complex, MHS-Bayasi and RHS-Mugulud, called also Es2-Lepolosi and EN1-Noolchalai, respectively) and Nyabusosi in Uganda (NY18) (see Sup. Text 1 for these sites).

Here we provide a detailed description of the localities/sites that passed our chronostratigraphic reassessment accompanied by a critical description of their archeological (techno-economic) and human fossil content. We start our review from Melka Kunture (Ethiopia), which represents, at the present state of knowledge, the putatively oldest Acheulean site in East Africa, for which we provide also new data to refine its chronostratigraphy.

Melka Kunture

Chronology: state of the art

The overall chronostratigraphy of the Melka Kunture Formation (Pioli et al., 2023) has been recently assessed using magnetostratigraphy (Perini et al., 2021; Muttoni et al., 2023) combined with previous $^{40}Ar/^{39}Ar$ dating (Morgan et al., 2012). Results revealed a pattern of magnetic polarity reversals extending from the Brunhes Chron (<0.773 Ma; magnetochron ages used in this study are according to Channell et al., 2020) at the top in the Garba XII-Gombore II localities, to the Olduvai (1.770-1.925 Ma) and Reunion (2.116-2.137 Ma) subchrons towards the basal sequence at Garba IV (Perini et al., 2021) and at

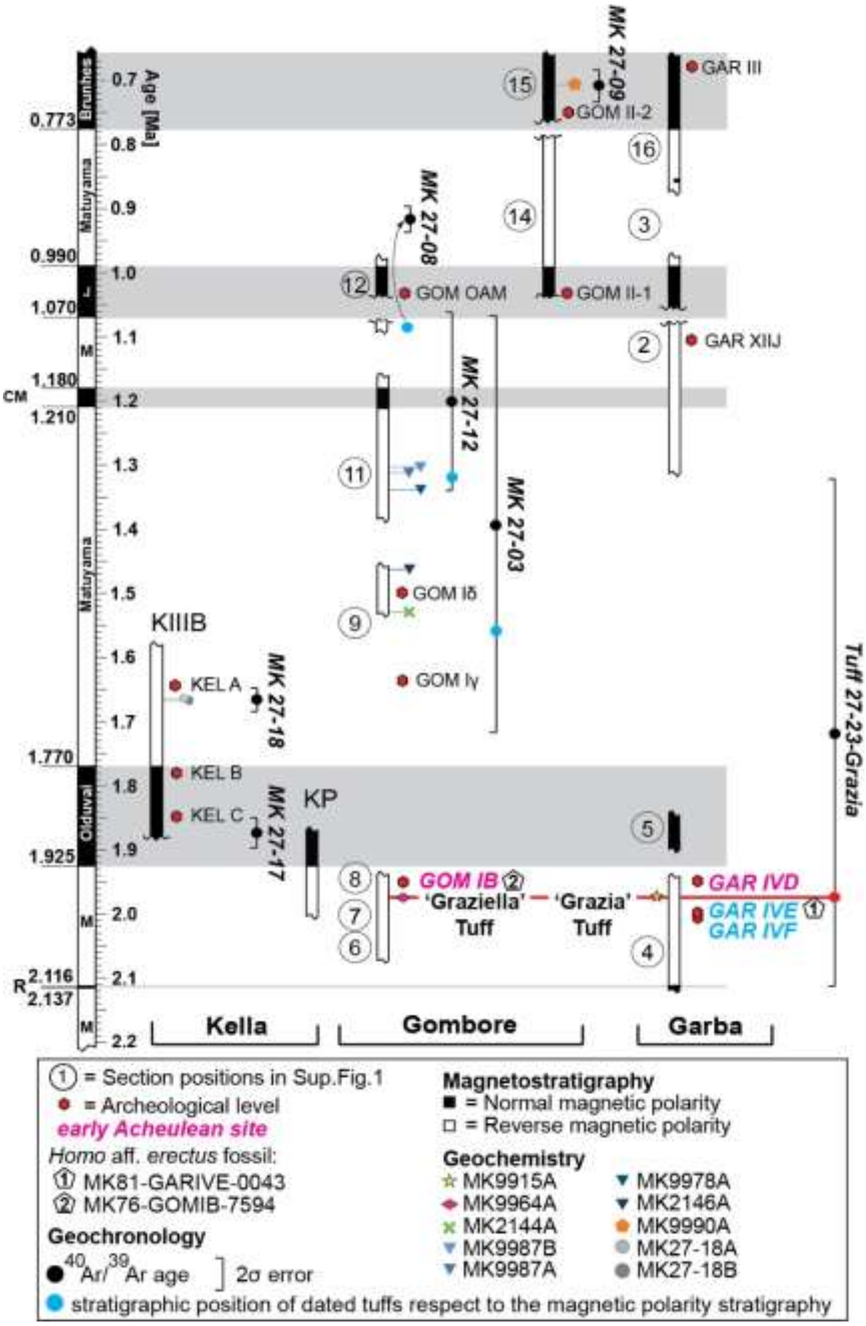

Figure 1 General chronostratigraphy of the MKF Middle-Upper successions outcropping in the archeological area, modified after Perini et al. (2021) and Muttoni et al. (2023). The sequence has been placed with respect to magnetic polarity and time. The correlation has been established using magnetostratigraphy and the available $^{40}Ar/^{39}Ar$ ages of tuff layers (Morgan et al., 2012). The magnetic polarity stratigraphy was reconstructed using the characteristic remanent magnetization (ChRM) components extracted from samples which yielded acceptable results, whereby black squares (and the grey boxes) indicate normal magnetic polarity and white squares reverse magnetic polarity, which have been correlated to the Quaternary geopolarity timescale of Channell et al. 2020. Circled numbers aside of each sampled section refer to GPS points (see Sup.Fig.1 and Sup.Tab.1).

Kella (Muttoni et al., 2023) (Fig.1; Sup.Fig.1). Archeological horizons Garba (GAR) IVE at 2.00 (-0.075; +0.1) Ma and GAR IVF at 2.02 (-0.095; +0.096) Ma (Perini et al. 2021) yielded late Oldowan assemblages (Gallotti and Mussi, 2015) associated with a *Homo* aff. *erectus* infant mandible (MK81-GARIVE-0043) at GAR IVE (Zanolli et al., 2016; Le Cabec et al., 2021). GAR IVD at 1.95 (-0.025; +0.1) Ma (Perini et al., 2021) laying above 'Grazia' Tuff (MK9915A) at Garba IV, which was crudely dated to 1.719 ± 0.398 Ma (Morgan et al., 2012; errors at 2σ), records the emergence of the Acheulean technology on the Ethiopian Highlands (Gallotti, 2013). At Gombore I, archaeological level GOM IB (Fig. 1) yielded an early Acheulean industry associated with a *Homo* aff. *erectus* fragmented humerus (MK76-GOMIB-7594; Di Vincenzo et al., 2015; Cazenave et al., 2017). The lack of the Olduvai subchron within the Gombore I magnetostratigraphy (Fig. 1) did not allow to establish a magnetostratigraphic correlation of GOM IB with archeological level GAR IVD at Garba (Perini et al., 2021). However, GOM IB lies on the (undated) 'Graziella' Tuff (MK9964A) that was repeatedly proposed (Taieb, 1974; Raynal and Kieffer, 2004), but never convincingly demonstrated, to be correlative to the Grazia Tuff at Garba IV. Here we provide new tephrostratigraphic data from the Grazia and Graziella tuffs as well as, for comparison, from other tuffs of the Melka Kunture stratigraphy, in order to verify the correlation of the Grazia and Graziella tuffs and attempt placing strict constraints on the correlation between GOM IB and GAR IVD-F archeological levels.

Tephrostratigraphy

A total of 10 samples from 10 different tuff layers throughout the Melka Kunture stratigraphy (stratigraphic position of samples in Fig. 1 and details in Sup. Fig. 1) were provided by Jean-Paul Raynal, who kindly made them available for preliminary tephrostratigraphic analyses from his private collection. These samples were collected during the field campaigns conducted under the direction of Prof. Marcello Piperno (years 1999-2007). Most of the samples contain fresh and clear glass shards with elongated vesicles except for sample MK2146A where glass shards are often strongly weathered. White elongated mm-sized pumice clasts are only present in samples MK2146A and MK9990A. The analyzed samples typically have a low crystal content, with feldspars and quartz as the main mineral phases and minor pyroxene and Fe-Ti oxides. Only sample MK2144A has a larger crystal content and contains amphibole, while MK27-18A appears completely aphyric. In a Total-alkali vs. SiO_2 classification diagram (TAS; Le Bas et al., 1986) all analyzed glasses show a rhyolitic composition with subtle variations in SiO_2 and a similar spread in alkali contents (Sup. Fig.2). The glass compositions from tephra layers MK2146A, MK2144A, MK9978A, MK9987A and MK9987B (Gombore I) plot in the comendite field (relatively low FeO* and high Al_2O_3) and have distinctively high Ba contents (Sup. Fig.2). The tuff layer from Gombore II (MK9990A) displays a very characteristic comenditic composition with the highest Al_2O_3 and Cl and the lowest TiO_2 contents among all the analyzed tuffs (Sup. Fig. 2). Compared to all the other tephra layers from Gombore I section, the Graziella Tuff (MK9964A) plots in the pantellerite field (higher FeO* and lower Al_2O_3 contents) and shows lower Cl and Ba contents and a wider spread in TiO_2 (Sup. Fig. 2). Glasses from the Grazia Tuff in Garba IV (MK9915A) overlap with those from the Graziella Tuff (MK9964A) in major and trace element compositions (Sup. Fig.2). Tephras from Kella III are also pantelleritic but exhibit higher FeO, Cl, Rb and Ba compared to the Grazia and Graziella tuffs (Sup. Fig.2). Geochemical analyses of volcanic glasses from Grazia and Graziella tuffs show that the two tuffs fully overlap in composition and are clearly distinct from the other tephras from the analyzed sections, hence they should be attributed to the same isochronous volcanic event. These results enable to contextualize chronologically the archaeological site GOM IB, lying above the Graziella tuff, so far poorly constrained, with respect to the GAR IVD archeological layer, located above the Grazia tuff (Fig. 1, Sup. Fig.1). Therefore, the age of 1.95 (-0.025; +0.1) Ma obtained for GAR IVD (Perini et al. 2021) can be extended to the archeological site GOM IB (Fig.1), with implications discussed below (see Figure 2A for a synthesis of the chronology of Melka Kunture).

Techno-economic behaviors

Lithic production at Oldowan level Garba IVF (2.02 -0.095 +0.096 Ma) with 113 artefacts, and Oldowan level Garba IVE (2.00 -0.0075 +0.1 Ma) with 718 artefacts, is devoted to small flaking, exploiting mainly obsidian cobbles collected in the nearby alluvial deposits. Small and medium-sized flakes were produced by several flaking methods developed as the most appropriate solution to exploit the different cobble geometries. Technical patterns document the efficient use of any available angle through continuous core rotation, while in some cases the surfaces were rectified to create suitable striking platforms and angles to detach flakes (Gallotti and Mussi, 2015, 2018). This intra-site variation in small flaking is well documented in other East African late Oldowan sites (Gallotti, 2018). There is also evidence of a specific technical process that has never been recorded elsewhere in the Oldowan, i.e., a systematic manufacture through retouch of small-pointed tools. This process is closely linked to obsidian exploitation, and most probably aimed to serve a specific techno-functional purpose (Gallotti and Mussi 2015; Gallotti 2018).

Several techno-economic innovations appear at 1.95 (-0.025; +0.1) Ma at Garba IVD (6986 artefacts) and correlative (see above) GOM IB (4373 artefacts) (Gallotti, 2013; Mussi et al., 2023). The small flaking methods used at Garba IVE-F persist. However, these technical solutions show a larger variation linked to a wider variety of natural blanks, i.e. all the rounded clasts available in the alluvial deposits, mainly of obsidian and aphyric cobbles, were exploited (Gallotti 2013; Gallotti and Mussi 2017, 2018b; Mussi et al., 2023). Within the panoply of flaking methods, new technical concepts and processes appeared here for the first time: preparation of the striking platform, volume/convexity management, and hierarchy among surfaces, well documented by discoid and prepared unifacial centripetal exploitations (Sup. Fig.4: 15-19). In addition, the use of obsidian angular clasts for discoid exploitation reflects a new technical skill: the incipient ability to configure the core by modifying the blank natural geometry (Sup. Fig.4: 18; Gallotti, 2013; Gallotti and Mussi, 2017, 2018). Small and medium-sized flakes were rarely modified by retouch and the pointed small tools from Garba IVE-F are no longer found in later periods (Gallotti and Mussi, 2018[a]). Along with small flaking, the production of large flakes to be turned into LCTs appears for the first time on the Ethiopian plateau at Garba IVD and GOM IB. The same innovative concepts and technical processes that emerged in small stone flaking

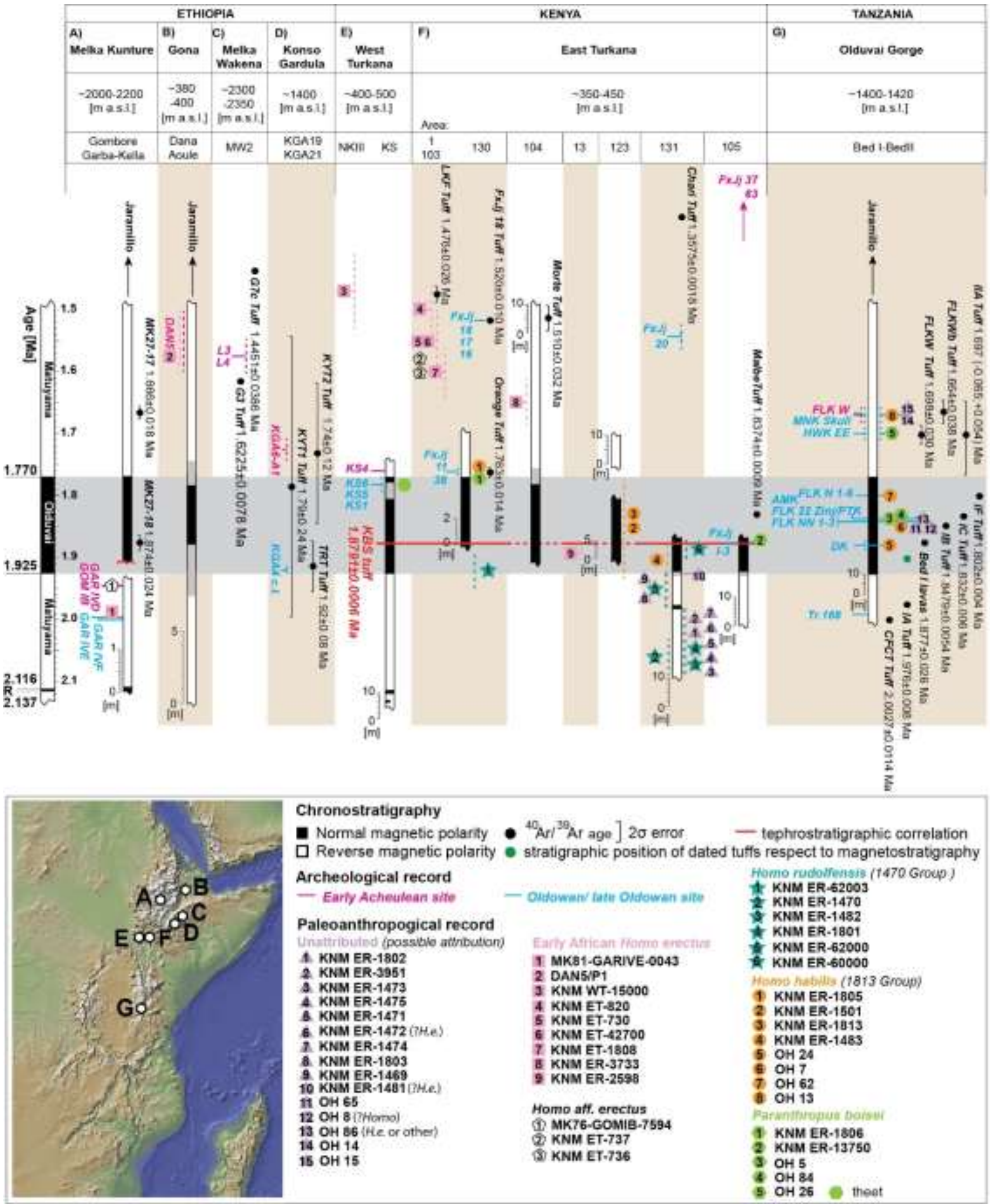

Figure 2 Chronostratigraphic scheme of the emergence of the East African Acheuleans based on the selection criteria adopted (see maintext). Each archeological site documenting Oldowan or Acheulean assemblages in a clear stratigraphic context and accompanied by a well-defined chronology has been placed in a common temporal framework, according to the available magnetostratigraphy, $^{40}Ar/^{39}Ar$ dating (reported at 2σ) and/or tephrostratigraphic correlation to trace the transition between these lithic technologies. Also, the record of hominin presence, according to the classification Anton and Middleton, (2023) and Anton et al., (2014) has been reported to discuss the possible toolmaker(s) of this innovation.

are also identified in large stone flaking. Discoid and prepared unifacial centripetal exploitation were used to produce thick flakes wider than long (Sup. Fig.4: 12, 14). Predetermination of the shapes, sizes, and technical features of large blanks are absent (Gallotti and Mussi, 2017, 2018). LCTs production is not fragmented and is quantitatively limited by the scarcity of suitable large blanks in the paleochannels, mainly large cobbles of obsidian, Melka Fault lava, porphyritic basalt, and exceptionally aphyric basalt. A systematic provision at primary sources is absent resulting in chaîne opératoire fragmentation. Scraper-like retouching was performed by modifying only the very edges of the large flakes while the overall shape of the blanks did not change (Sup. Fig.4: 3, 4, 6, 7, 9). When removals penetrated the blank volume and were
not restricted to the edges, the aim was to create a point (Sup. Fig.4: 1, 2, 5, 8, 10, 11) by thinning the butt-bulb portion without intervening on the volume balance. Absence of search for specific morphological traits does not allow the identification of shaping in LCT production (Gallotti, 2013).

Gona (Ethiopia)

Chronology

Semaw et al., (2020) reported the magnetostratigraphy of two sections from Gona, Busidima North and Dana Aoule North. We include in our inventory data from the ~60-m thick Dana Aoule North section, hosting level DAN5 with Acheulean tools and fossil remain DAN5/P1 of *Homo erectus* (for excluded sections from Gona, see Sup.Text.1). At Dana Aoule North, Semaw et al., (2020) reported five magnetic polarity reversals interpreted as, from top to bottom, the top Jaramillo (0.99 Ma), base Jaramillo (1.07 Ma), top Olduvai (1.77 Ma), base Olduvai (1.925 Ma), and top Gauss (2.595 Ma). The age of DAN5, falling ~5 m above the top Olduvai, was evaluated to about 1.6-1.5 Ma using estimates of average sediment accumulation rate through magnetostratigraphic age modeling (Fig. 2B).

Techno-economic behaviors

DAN5 yielded a very small assembly consisting of 35 artefacts *in situ* and 69 from surface collections. Artefacts include both LCTs and small flaking cores and flakes. Based on a typological list of artefacts (Semaw et al., 2020), the LCTs consist of handaxes, picks, and one retouched large flake, while the co-presence of cleavers is doubtful as they belong to surface collections. Data on small flaking is not yet available as a detailed technological study of the entire assemblage has not been published yet.

Melka Wakena (Ethiopia)

Chronology

On the eastern shoulder of the Main Ethiopian Rift, at Melka Wakena (Ethiopia) in the Webi Shebele valley at 2300–2350 m a.s.l., early Acheulean levels, dated with $^{40}Ar/^{39}Ar$ on tuffs (Hovers and Gossa 2020, Hovers et al., 2021), document the thus far oldest evidence of peopling of this area of the Ethiopian Highlands. Levels MW2-L4 and MW2-L3 crop out in section MW2 and are comprised between Tuff G3 (1.6225±0.007 Ma) below and Tuff G7c (1.4451±0.00386 Ma) above, providing an age estimate of ~1.6 Ma for these sites (Hovers et al., 2021) (Fig. 2B).

Techno-economic behaviors

MW2-L4 was excavated over only 4 m^2 and yielded a small assemblage of 104 artefacts mainly composed of flakes and lacking LCTs (Gossa and Hovers, 2022). Site MW2-L3 yielded a rich assemblage of 6064 artefacts made of volcanic rocks, predominantly ignimbrites, from an excavation area of 13 m^2. Both LCT/large flake and small flake productions are present (Gossa and Hovers, 2022). Small flaking dominates the artefact inventory, while LCTs constitute a weak percentage of the assemblage, as for Melka Kunture. Cores were usually made on cobbles and pebbles, followed by flakes and angular items. Flaking methods are mainly bifacial, peripheral, and multifacial (Gossa and Hovers, 2022). A few discoid and bifacial hierarchical centripetal cores are present (Gossa and Hovers, 2022), the bifacial ones corresponding to the prepared unifacial centripetal cores in Gallotti (2013). Large-sized angular blocks were reduced by multifacial, unifacial, and bifacial reduction methods for large flake extraction. The LCT component is characterized by very few “crude” LCTs, picks, and large scrapers mainly made on side-struck and skewed-struck large flakes. *“Typical bifacial tools are absent from the assemblage, although large flakes were produced…”* (Gossa and Hovers, 2022: 30). Given that glassy ignimbrite, of which most of LCTs are made, is rarely used for large flake production, it is possible that the LCT blanks were detached off-site and then transported into site L3. This interpretation is confirmed by the low frequency of roughing-out flakes and by the small dimensions of the large flakes, comprising those of the negative scars on large cores, which are smaller than the LCTs. On the contrary, the late stage of production was made on site, as documented by the high frequency of thinning flakes among the shaping flakes (Gossa 2020; Gossa and Hovers, 2022).

Konso-Gardula (Ethiopia)

Chronology

The Konso-Gardula archeological area, located at an elevation of ~1400 m a.s.l., yielded the Oldowan site KGA4-carbonate trench and the early Acheulean archeological site KGA6-A1, which have been dated with $^{40}Ar/^{39}Ar$ on tuff levels aided by a preliminary magnetostratigraphy (Beyene et al., 2013; Katoh et al., 2000). Since that the magnetostratigraphic data have never been formally presented, we opted to report in Figure 2C only the radiometric ages of Beyene et al. (2013). The Oldowan site KGA4-carbonate trench lies below Tuff TRT (1.92±0.08 Ma) at an estimated age of ~1.92 Ma close to the base of the Olduvai subchron (Beyene et al., 2015; 2013) (Fig. 2C), while the early Acheulean site KGA6-A1 lies stratigraphically above Tuff KYT1 (1.79±0.24 Ma) and Tuff KYT2 (1.74±0.12 Ma), and it was assigned an age estimate of ~1.75 Ma (Beyene et al., 2013). The correlation between Tuff TRT and the KBS Tuff from Koobi Fora (1.8691±0.0006 Ma; Phillips et al. 2023) proposed by Katoh et al. 2000 is no longer considered valid (Brown et al., 2006; Phillips et al., 2023).

Techno-economic behaviors

No archeological information is yet available from Oldowan site KGA4-carbonate trench (Beyene et al., 2015), therefore we opted to report it in Figure 2C without further discussion. The early Acheulean site KGA6-A1 yielded 116 artefacts, 61 of which are LCTs made of basalt. LCTs are handaxes, cleavers, picks, and massive scrapers, mainly shaped on large flakes. Most of them are unifacially modified with straight edges (Beyene et al., 2015). Data on small flaking have not been published yet.

West Turkana (Kenya)

Chronology

In the mid-lowlands of Kenya, the Kokiselei complex of West Turkana, located at ~400-500 m a.s.l., yielded several sites (KS 1, 5, 6, and 4) documenting the last occurrence of the Oldowan and the emergence of the Acheulean in a short time period (Roche et al., 2003; Lepre et al., 2011). Site KS4, the only site to be formally attributed to the Acheulean, has been dated with magnetostratigraphy integrated with radiometric age data to ~1.76 Ma shortly after the top of the Olduvai subchron (Lepre et al., 2011) (Fig. 2D). Sites KS6, KS5 and KS1, formally attributed to the late Oldowan, appear to come from stratigraphic levels ~5-10 m below the top of the Olduvai subchron of Lepre et al. (2011), and have been attributed a nominal age of ~1.8 Ma by Duke et al. (2021) (Fig. 2D). In Fig. 2 is also reported the occurrence of *Homo erectus* fossil KNM WT-15000, discovered and excavated *in situ* at the site Nariokotome III (NKIII) to which was initially assigned an age close to 1.6 Ma (Brown et al., 1985). Mcdougall et al. (2012), after providing new $^{40}Ar/^{39}Ar$ ages on six tuffaceous beds outcropping in the Omo-Turkana Basin, proposed a revised age estimate of 1.47±0.03 Ma for this fossil.

Techno-economic behaviors

Details on the lithic assemblage from KS1 are not available in the literature, except for a description of the percussive material (Arroyo et al., 2021). The systematic excavation of KS5 yielded a rich assemblage of 1766 lithic objects

(Texier et al., 2006). The lithic production is devoted to the extraction of small- to medium-sized flakes on phonolite, basalt, trachyte, and siliceous rocks. Cores are unifacial unidirectional on flat and thick cobbles and bifacial alternating on thick cobbles. The latter present alternating removals along the quasi-periphery of the blank, but they never invade the central volume of the core (Texier et al., 2006). Moreover, several refits display the ability to reconfigure the initial morphology of the raw material by creating new striking platforms during flaking after a first series of removals, rather than always using naturally serviceable ones (Texier et al., 2006). This process represents a critical technical leap because knappers were no longer strictly dependent on the natural geometry of the core blanks and were able to control in three dimensions the working volume (Texier et al., 2006, 2018). According to Texier et al. (2006), this ability to manage a three-dimensional volume is propaedeutic to the future development of the bifacial shaping. In this regard, a large and elongated artefact on split cobble shows a point manufactured by unifacial removals, heralding the LCT production of KS4 (Texier et al., 2006).

At KS6, broadly coeval to KS5 (Fig. 2D), the excavation area yielded a large corpus of 4393 artefacts. Of these, 3865 have been analyzed and published (Duke et al., 2021). Phonolite is the dominant raw material, followed by aphyric and porphyritic basalt. Three elements document technical change and innovations: (i) a strong prevalence of bifacial flaking strategies whereby flakes were extracted from two adjacent surfaces maintaining a platform edge extending around most of the perimeter of the core; (ii) knappers extracted large flakes, reused as core blanks; (iii) two artefacts, one on cobble, the other on a large flake, result more elongated with a shaped tip, documenting preliminary evidence for LCT shaping (Duke et al., 2021).

The early Acheulean site KS4 Fig. 2D) has been excavated on a limited surface (19 m^2) as the deposit was largely eroded, and yielded a lithic assemblage of 202 items, mainly made of aphyric phonolite (Texier, 2018). Of these, 28 are LCTs manufactured on large flat and elongated cobbles and slabs, on half thick cobbles splitted by bipolar percussion on anvil, and in four cases on flakes larger than long (Chevrier, 2012; Texier, 2018). Several refits document the use of blanks that reach or exceed 30 cm in length along the long axis, collected at the sources since such lithologies and such dimensions are poorly represented in the nearby conglomerates (Harmand, 2012). This raw material provisioning documents the ability to anticipate the technical requirements for LCT manufacture by selecting specific blank sizes and morphologies. A similar approach to raw material provisioning is documented since 2.34 Ma in West Turkana at Lokalalei 2c (Harmand, 2012; Texier, 2018). After the blank acquisition, LCT manufacture is performed through a limited number of unifacial alterne or alternating bifacial removals, modifying the lateral and distal edges and more rarely invading the central volume of the artefact and its proximal portion (Texier, 2018). Heavy and large hammerstones with deep percussive marks are linked to LCT production (Arroyo et al., 2020). Some small removals can retouch portions of the cutting edges (Chevrier, 2012). The result of this technical process is a large technological and morphological diversity of LCTs: picks with trihedral or square sections, unifacial or roughly shaped handaxes, as well as pieces left as rough outs (Texier, 2018). Unfortunately, data on the remaining part of the lithic assemblage, i.e., small flaking, were not published. Unfortunately, it was not possible to include in our inventory the Oldowan site Naiyena Engol 2 (NY2) (Roche et al., 2018) due to lack of chronological constraints (see Sup.Text.1).

East Turkana (Kenya)

Chronology

The Plio-Pleistocene sequence of the East Turkana Basin, located at ~350-450 m a.s.l. in the Kenyan lowlands, represents one of the richest archeological and human fossil archives in East Africa. The Koobi Fora Formation, outcropping in different numbered excavation areas, has been studied for chronostratigraphy using different methods.

Mana et al. (2019) provided the chronostratigraphy of Area 130 through $^{40}Ar/^{39}Ar$ dating of two tuff horizons accompanied by magnetostratigraphy (Fig. 2E). Area 130, where the Upper Burgi, KBS and Okote members of the Koobi Fora Formation crop out, yielded five Oldowan sites (FxJj 38, 11, 16, 17, and 18), hominin fossils KNM ER-1805 (*Homo habilis*) and KNM ER-1806 (*Paranthropus* *boisei*) (Fig. 2E). Two stratigraphic markers identified within the Okote Member, the Orange Tuff and Tuff FxJj 18, were dated to 1.763±0.014 Ma and 1.520±0.01 Ma, respectively, while oriented core-samples for paleomagnetic analyses were retrieved from the stratigraphic interval pertaining to the KBS Member to identify the top of the Olduvai subchron (1.770 Ma). According to this chronostratigraphy, Oldowan sites FxJj 38 and 11, as well as fossils KNM-ER 1805 and KNM-ER 1806, occur in correlative stratigraphic levels in the KBS Member close to top of Oduvai subchron (Mana et al., 2019) (Fig. 2E). Oldowan sites FxJj17 and 18 are constrained in age to 1.52 Ma as they are closely associated to Tuff FxJj18 (1.520±0.01 Ma), while Oldowan site FxJj 16 lies a few meters below.

Lepre & Kent (2015) provided a chronostratigraphy for Area 104 through the recognition of the top of the Olduvai subchron integrated with the previously dated Morte Tuff, with an $^{40}Ar/^{39}Ar$ age of 1.51±0.032 Ma (McDougall and Brown, 2006), that allowed to obtain an interpolated age of ~1.63 Ma for the *Homo erectus* fossil KNM ER-3733 (Fig. 3E). The oldest fossil attributed to *Homo* erectus at Koobi Fora, and in East Africa in general, is KNM ER-2598. The context of discovery and the age of this fossil have a rather problematic history. Collected in 1974 from the outcrop surface of Area 15 (Leakey and Walker, 1985), it was originally reported coming from approximately the same stratigraphic level of the KBS Tuff. Later work placed the fossil-bearing layer about 4 m below the KBS Tuff at an estimate age of 1.88-1.9 Ma (Feibel et al., 1989; Gathogo and Brown, 2006). Recently, Hammond et al. (2021), combining fieldwork and historical imagery, relocated the fossil level in Area 13 toaround 3 meters below the KBS Tuff. According to the most recent $^{40}Ar/^{39}Ar$ age of 1.8791±0.0006 Ma for the KBS Tuff (Phillips et al., 2023), KNM ER-2598 may have an age close to 1.88 Ma (Fig. 2E).

Koobi Fora Area 123 yielded several hominin fossils among which *Homo habilis* KNM ER-1813 and 1501 (Fig. 2E). Feibel et al. (2009) showed the presence of the top of the Olduvai subchron (1.770 Ma) that they combined with the radiometric age of the Lower Ileret Tuff dated at 1.527±0.028 (McDougall & Brown 2006) to provide an interpolated age estimate for the *Homo habilis* fossils of 1.86±0.08 Ma below the top of the Olduvai subchron (Feibel et al. 2009) (Fig. 2E).

Joordens et al (2013) established a chronological framework for Areas 131 and 105, where several hominin fossils were found in the upper Burgi Member and Oldowan sites in the Okote Member. They identified the base of the Olduvai subchron, located 15 m (Area 131) and 21 m (Area 105) below the KBS Tuff (1.8791±0.0006 Ma after Phillips et al., 2023) cropping out at the top of both sequences (Fig. 2E). Joordens et al (2013) utilized as tie-point for age modelling a short normal polarity interval that they identified 23.7-24.6 m (Area 131) and 21.4-22.3 m (Area 105) below the KBS Tuff and that they attributed to the pre-Olduvai event found by Channell et al. (2002) in ODP Sites 983 and 984 at 1.977 Ma. The pre-Olduvai is an unconfirmed and possibly local geomagnetic event (see Channell et al., 2020), and consequently it cannot be excluded that the short normal polarity interval of Joordens et al (2013) is in fact a record of the older Reunion subchron (2.137-2.116 Ma; Channell et al., 2020), albeit Joordens et al (2013) excluded the presence of the Reunion in their sections. In any case, accepting Joordens et al (2013) interpretation, and using the updated ages for the base of the Olduvai and the top of the Reunion subchrons of Channell et al. (2020), we revised the ages of the human fossils of Joordens et al. (2013) as follows (Fig. 2E): 2.09-2.03 Ma for KNM ER-1470 (*Homo rudolfensis*); 2.09-1.98 Ma for KNM ER-1802, 3951, 1471, 1473, 1475 (early *Homo*), 1801, 1482 (*Homo rudolfensis*), 1472 (? *Homo erectus)*, and 1474 (early *Homo*); 1.98-1.925 Ma for KNM ER-1803, 1469 (early *Homo*), and 62000 (*Homo rudolfensis*); 1.925 Ma for KNM ER-1481 (? *Homo erectus*); 1.925-1.88 Ma for KNM ER-1483 (*Homo habilis*). In Figure 2E is also reported the occurrence of several *Homo erectus* (KNM ER- 730, 820 and 1808) and *Homo* aff. *erectus* (KNM ER-736 and 737) fossils uncovered in Areas 1 and 103 of Koobi For a with estimated ages broadly ranging between ~1.6 and ~1.5 Ma obtained through further refinement of the chronology and tephrostratigraphic correlations for the Omo-Turkana Basin with $^{40}Ar/^{39}Ar$ (Mcdougall et al., 2012) and K/Ar dating (Feibel et al., 1989).

Techno-economic behaviors

None of the Koobi Fora archaeological sites between ~1.9 and ~1.5 Ma have been formally attributed to the early Acheulean, which appears to emerge in a time frame broadly comprised between ~1.4 and 0.7 Ma (Isaac and Isaac, 1997). Lithic assemblages FxJj11, 16, 17, 18, and 20 (Fig. 2E) have been formally attributed by Isaac and Isaac (1997) to the Karari industry, characterized by the production of flakes from single platform thick and large unidirectional cores, known as “Karari scrapers”. They are characterized by a high standardized form and some of them are on large flake blanks. This industry has been interpreted as local facies of the Developed Oldowan from Olduvai (Leakey, 1971) bearing as peculiar characteristic a strong adaptation to the type of raw material available (Isaac 1984; Isaac and Isaac 1997). A few rather irregular scraper forms, present in the preceding Oldowan site FxJj1-3 (Fig. 2E), bear features that do not seem well-developed in the Karari assemblages (Isaac and Isaac, 1997). Semaw et al. (2009) proposed that the Karari toolmakers had the ability to detach large flakes, mastered standardization, and lacked shaping and morphological predetermination. The real question for Semaw et al. (2009) is not whether the Karari industry is transitional, because it is evidently so, but whether or not it may already be considered part of the early East African Acheulean, characterized by a variability linked to different paleoenvironmental conditions and lithospaces. Unfortunately, a detailed and comprehensive technological study of the entire lithic assemblages attributed to the Karari industry is not currently available and, although fascinating, this interpretation is based on a single artefact category and cannot be considered representative of the whole technical system.

Olduvai Gorge (Tanzania)

Chronology

The complex stratigraphy of the Olduvai archeological area (~1400-1420 m a.s.l.) has been widely investigated through lithostratigraphy, tephrostratigraphy (McHenry, 2012; 2016), ^{40}Ar/^{39}Ar dating (Deino, 2012; Deino et al., 2020), and magnetostratigraphy (Tamrat et al., 1995). We considered (Fig. 2F):

I. Oldowan site Trench 168 (Stollhofen et al., 2021), bracketed between Tuff CFCT (2.0027± 0.0114 Ma) and Tuff IA (1.976± 0.008 Ma) (Deino, 2012) and provided with a nominal age of ~2 Ma (Stollhofen et al., 2021) (Fig. 2F).

II. Oldowan site DK (Sànchez-Yustos, 2021, Stanistreet et al., 2018b) yielding also the *Homo habilis* fossil OH24, bracketed between Bed I lavas below dated to 1.877±0.0026 Ma (Deino, 2012) and Tuff IB above dated to 1.8479±0.0054 Ma (Deino et al., 2020). DK is assigned a nominal age of ~1.88 Ma (Sànchez-Yustos, 2021) (Fig. 2F).

III. Oldowan site FLK NN 3, also bearing the early *Homo* fossil OH7 (Blumenschine et al., 2012), comprised between Tuff IB (1.8479±0.0054 Ma) (Deino et al., 2020) and Tuff IC (1.832±0.006 Ma) (Deino 2012). FLK NN 3 is assigned a nominal age of ~1.84 Ma (Blumenschine et al., 2012) (Fig. 2F).

IV. Oldowan site FLK 22 Zinj, yielding also the *Paranthropus boisei* fossil OH5 (Blumenschine et al., 2012; Dominguez-Rodrigo and Cobo-Sànchez 2017), comprised between Tuff IB (1.8479±0.0054 Ma) (Deino et al., 2020) and Tuff IC (1.832±0.006 Ma) (Deino 2012). FLK 22 Zinj is assigned age of ~1.84 Ma (Fig. 2F).

V. Oldowan site PTK and the associated early *Homo* fossil OH86, constricted to the same stratigraphic level of FLK 22 Zinj (Organista et al., 2023) at ~1.84 Ma (Fig. 2F).

VI. Oldowan site FLK North Levels 1–6 (FLK N 1–6; Fig. 2F) (Blumenschine et al., 2003; 2012), that yielded also the *Homo habilis* fossil OH62 and the unattributed fossil OH65 (?*Homo erectus*; Anton and Middleton, 2023), chronologically constrained in the upper part of the Olduvai subchron (>1.770 Ma) (Blumenschine et al., 2003) above Tuff IC dated to 1.832±0.006 Ma (Deino 2012). FLK N 1–6 is assigned an age of ~1.8 Ma (Fig. 2F).

VII. Oldowan site HWK EE is assigned an age of ~1.7 Ma (Fig. 2F) following essentially Stanistreet et al. (2018) and McHenry & Stanistreet (2018) who placed the site within the Lower Augitic Sandstones of Middle Bed II between Tuff IIA dated to 1.697 (-0.065; +0.0054) Ma (Deino et al., 2020) and the undated Tuff IIB. An alternative interpretation (Uribellarea 2017, 2019) would place HWK EE at the same stratigraphic position of FLK West in the Lower Augitic Sandstones.

VIII. Oldowan site MNK Skull is assigned an age of ~1.67 Ma following de la Torre et al. (2021) (Fig. 2F). These authors placed the site at the base of the Middle Bed II between a chert-bearing unit lying above Tuff IIA, dated to 1.697 (-0.065; +0.0054) Ma (Deino et al., 2020), and the undated Tuff IIB.

IX. Finally, the earliest local evidence of the Acheulean is documented at site FLK West in Bed II, dated to ~1.7 Ma (Diez-Martin et al. 2015), even though it is stratigraphically located between the FLKW Tuff (1.698±0.03 Ma) and the FLKWb Tuff (1.664±0.038 Ma) (Diez-Martin et al. 2015). Stanistreet et al. (2018) and McHenry & Stanistreet (2018) suggested to consider an age of ~1.65 for site FLK West. We stress that the age of the Acheulean site FLK West and of the Oldowan site MNK Skull (see above) seem virtually indistinguishable, possibly indicating coexistence of the Oldowan and Acheulean at ~1.67 Ma.

Techno-economic behaviors

From an archeological viewpoint, *"Olduvai is the site where the traditional view of the Oldowan-Acheulean transition was established (…) and the emergence of the Acheulean has traditionally been linked to the origins of a new human species, Homo erectus, whereas the Oldowan was associated with Homo habilis"* (de la Torre and Mora, 2011-2012). Despite notable efforts over the last twenty years, the dynamics of the Oldowan-Acheulean transition remains unclear. From a technological perspective, it is not yet clear how and why some Oldowan sites seem to anticipate the technical innovations of the Acheulean, while others seem to document its persistence without any anagenetic relationship with the Acheulean.

I. Trench 168 (~2 Ma; Fig. 2F) yielded an Oldowan assemblage consisting of 210 lithics of quartzite mainly from archaeological Levels 2 and 3. Knappers exploited rounded cobbles and angular chunks by hard hammer percussion into unifacial, bifacial, and multifacial cores to produce undifferentiated flakes (Stollhofen et al., 2021). A reassessment of the DK industry (Fig. 2F), with 1190 lithic objects (mainly from Level 3), showed that lithic productions, classically ascribed to the Oldowan (Lekeay, 1971; de la Torre and Mora, 2005), display "the necessary technological know-how from which the Acheulean could emerge" (Sanchez-Yustos, 2021): flaked cores with platform preparation, discrete technological processes, a high frequency and diversity of retouched flakes, the production and shaping of large blanks, and the emergence of morpho-types. Based on this evidence, Sánchez-Yustos (2021) concludes that "(…) the transition from the Oldowan to the Acheulean was more gradual and complex than previously thought".

II. Site FLK 22 Zinj (~1.84 Ma; Fig. 2F), excavated over almost 300 m^2, yielded a rich assemblages composed of 2557 artefacts mainly on quartz focused on small flaking. Usually, striking platforms are not prepared, and flakes were detached from natural surfaces using unidirectional abrupt removals. Nevertheless, some cores document more elaborate flaking methods involving the bifacial management of edges and a bifacial peripheral exploitation (de la Torre and Mora, 2005). FLK 22 Zinj is not an isolated occupation floor but is rather part of a land surface utilized intensively by hominins, including sites FLK NN and PTK (Blumenshine et al. 2012), where animal bones and stone tools were strictly interdependent as the outcome of a socio-economic organization by early humans (Domínguez-Rodrigo and Cobo-Sánchez 2017).

III. At the Oldowan site FLK North Levels 1–6 (FLK N 1–6) (~1.8 Ma; Fig. 2F), percussion is the main technical activity together with minimal knapping (De la Torre and Mora, 2005). These authors draw a scenario in which hominins were mainly involved in intense percussion of a variety of organic materials, particularly long bone shafts. However, no evidence of hammerstone-broken bones has been found in FLK N 1–6 (Domínguez-Rodrigo et al., 2007). Recent investigations unearthed a new archaeological assemblage essentially from Levels 1–2 (Domínguez-Rodrigo et al. 2010). Battering is again the main activity inferred at the site. Flaking, however, displays more variable patterns than in the assemblage revised by de la Torre and Mora (2005). Freehand direct percussion is largely used; bipolar technique is also present but restricted to the knapping of quartz slabs. Flaking modalities are unifacial uni/bidirectional, bifacial uni/bi/multidirectional, trifacial, and centripetal (Diez-Martín et al. 2010).

IV. Oldowan site HWK EE (~1.67 Ma; Fig. 2F) yielded a lithic assemblage of over 18000 pieces. Short reduction sequences, low flaking productivity, and simple and expedient flaking methods characterize the lithic production (de la Torre and Mora, 2018). At the same time, raw material selectivity and the consistent presence of retouched artefacts are also present, highlighting “the kaleidoscopic nature of technological strategies at Olduvai immediately before the earliest Acheulean handaxes appear in the sequence” (de la Torre and Mora, 2018: 236).

V. At the Oldowan site MNK Skull (~1.67 Ma; Fig. 2F), 1672 artefacts have been retrieved (de la Torre et al., 2021). Lithic production is characterized by small flaking methods that show poor management of volumes, flaking series are short and they rarely exploit the entire circumference of the cores. De la Torre et al. (2021) ascribed this handaxe-free industry to the last evidence of the Oldowan in the Olduvai archeological sequence (de la Torre et al., 2021).

VI. Finally, FLK West (~1.67 Ma; Fig. 2F) yielded the earliest evidence formally attributed to the Acheulean at Olduvai (Dominguez-Rodrigo, 2015). Despite the absence/presence and frequency of LCTs in the different levels, raw material selection, core reduction and flake retouching patterns indicate similar technological traits. This assemblage variability would correspond to “different expressions of the same economic structure” (Sánchez-Yustos et al., 2018: 1). FLK West is the oldest Acheulean site in which stone tools occur spatially and functionally associated with the exploitation of fauna, documented by bone surface modifications such as percussion and tooth marks (Yravedra et al., 2017). 2790 lithics were retrieved mainly from the two lowermost levels (L5 and L6; Diez-Martín et al., 2015). Naibor Soit quartzite is the raw material mostly used at FLK West, followed by volcanic rocks. LCTs and large flakes are documented in the whole sequence with a preference for quartzite as raw material (Sánchez-Yustos et al., 2018). Regarding small flaking, the most common methods are bifacial simple and multifacial, followed by unifacial unidirectional, orthogonal, and centripetal. No evidence of core preparation has been identified at FLK West. All large flake cores are large quartzite blocks, showing feeble exploitation, except for a very heavy quartzite block showing perpendicular exploitation. LCT blanks are tabular slabs, blocks, and flakes partially shaped via marginal and abrupt removals producing pointed areas and broad cutting edges. They do not show bifacial or invasive shaping that modify volumes. However, a single specimen discovered in the lowermost level, very large and heavy, has been intensely shaped through invasive removals producing a pointed and symmetrical handaxe (Diez-Martín et al., 2015, 2019, 2023). The discovery of this tool led Diez-Martín et al. (2015) to question the "hypothesis of a gradual development of technological and cognitive qualities during the Acheulean…supporting a somewhat punctuated flourishing of the handaxe technical and cognitive conceptualization" (Diez-Martín et al., 2019: 49).

Oldowan-Acheulean transitions: a comparative analysis

The recent age of 1.95 (-0.025; +0.1) Ma for the first occurrence of the Acheulean in GAR IVD at Melka Kunture (Perini et al., 2021; Muttoni et al., 2023) and the new correlation of GAR IVD to GOM IB (this study), together with the occurrence of two late Oldowan archaeological levels very close in age (GAR IVE and F), offers the possibility to investigate the times and modes of the technical innovations leading to the Acheulean on the Ethiopian plateau.

The production of LCTs (all on large flakes) is certainly the macroscopic novelty that marks the earliest Acheulean. Large flakes to be turned into LCTs are metrically well separated from the production of small-medium flakes. A marginal retouch turned large flakes into LCTs, sometimes creating a pointed shape. A similar process is known at Melka Kunture since the late Oldowan for obsidian small pointed tool production, and is transferred to larger modules and to a larger variety of raw materials in the earliest Acheulean. A few LCTs from GOM IB show also an emergent bifacial shaping and a three-dimensional control of the volumes. The latter is also documented in small flaking (discoid on angular obsidian elements) and corresponds to a giant step in the long process of hominin emancipation from raw material constraints. A big innovation lies in concepts and methods for LCT blank production (discoid and prepared unifacial centripetal).

However, such methods and concepts do not appear for the exclusive production of LCT blanks. They represent the main innovation in the production also of small-medium flakes, characterized by a large variety of methods, inherited from the late Oldowan and amplified. Therefore, at Melka Kunture the transition from late Oldowan to early Acheulean is a cultural continuum, where innovations emerged from the variety and flexibility of the technical solutions implemented (Gallotti and Mussi, 2018[b]).

Unfortunately, we have only partial data on the evolution of the Melka Kunture earliest Acheulean. The industries immediately following, dated at Kella between ~1.9 Ma and ~1.6 Ma, have not been the subject of systematic excavations and studies. At GOM I levels γ and δ (Sup.Fig.1), tentatively attributed to the Olduvai subchron and the Matuyama immediately preceding the Olduvai subchron, respectively, yielded two small assemblages.

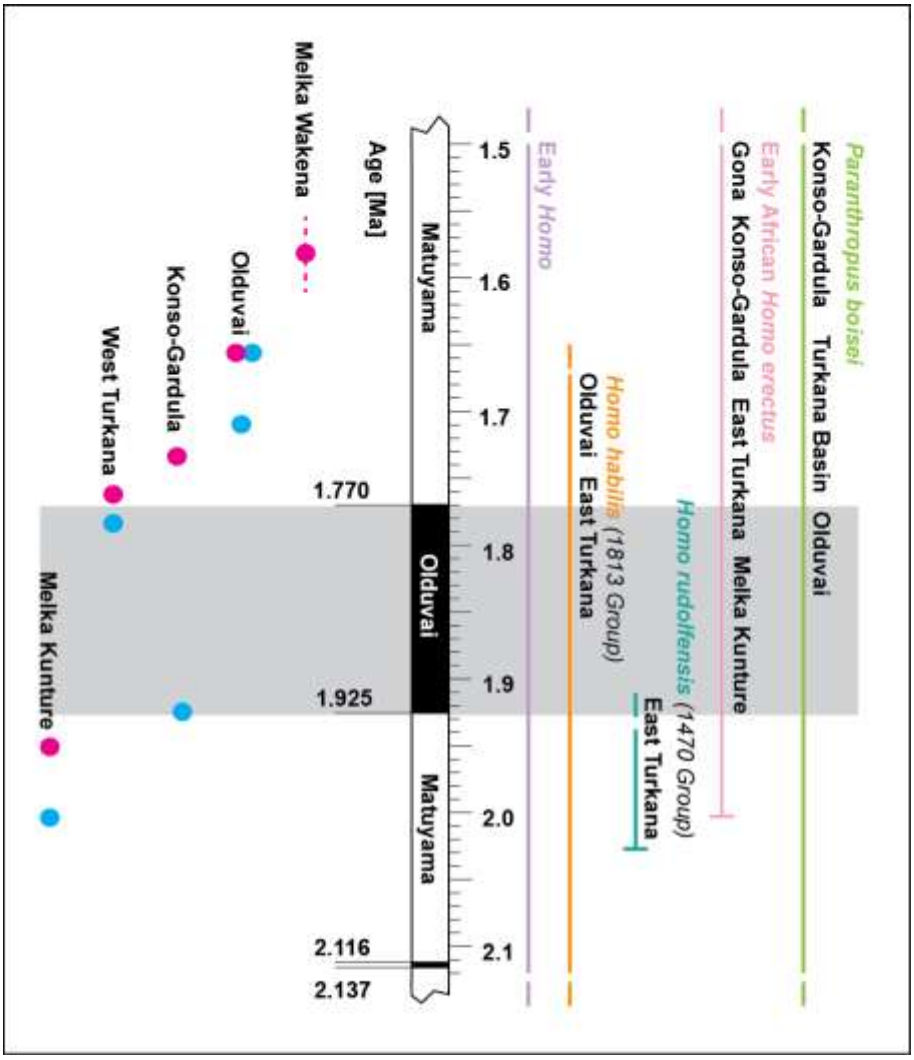

Figure 3 Synthesis of the East African record of Figure 2: chronostratigraphy, timing of Oldowan-Acheulean transition and record of hominin presence. Blue dots indicate the last occurrences of Oldowan, Pink dots indicate the first occurrences of Acheulean.

The technical innovations found in small flaking at GAR IVD persist, but LCTs are absent. However, the production of large flakes is documented by few specimens at GOM Iγ, but they are not turned into LCTs and, in some cases, are used as core blanks. Accordingly, it is unclear whether the technical processes of the earliest Acheulean persisted into the next 300 ka with or without further innovation.

When the Acheulean 'reappears' on the Ethiopian plateau at Melka Wakena at ~1.6 Ma, several technological traits recall the innovations identified at Melka Kunture: the presence, albeit sporadic, of hierarchy between surfaces and management of convexities in small flaking as well as the production of LCTs that do not document biface shaping. However, fragmentation of LCT chaînes opératoires is a new behavior appearing at Melka Wakena and is similarly documented at Melka Kunture no earlier than 1 Ma (Gallotti and Mussi, 2017, 2018; Gossa and Hovers, 2022). On the other hand, new LCTs as massive trihedral-section picks appear for the first time at Melka Wakena. This demonstrates a substantial homogeneity of the earliest Acheulean on the highlands, with further innovations occurring 300 ka after its first appearance at Melka Kunture.

The technical innovations characterizing the emergence of the Acheulean in East African low-midland sites, even if sharing some elements, show a remarkable diversity of expressions. These innovations do not represent an intrusive and sudden phenomenon, but they are deeply rooted in the late Oldowan. In these sites, the intra-site coexistence of a panoply of flaking methods and practices is rather systematic. This means that since ~2 Ma, knappers were able to simultaneously apply several technical solutions to exploit the available lithic resources (Gallotti, 2018). Although the late Oldowan technological complexes show a variety of operational expressions due to a strong dependence on local lithospaces (occurrence, frequency, lithology, geometry, and dimensions of raw materials), they share similar concepts (Gallotti, 2018). In this common conceptual background, a series of changes anticipating Acheluean innovations appear in some contexts.

In the late Oldowan of West Tukana (KS5 and KS6), these changes correspond to the ability to manage bifacially an edge along the blank periphery, and to reconfigure the initial morphology of the raw material for small flaking, controlling the working volume in three dimensions. This latter process is well documented approximately 100 ka earlier at Melka Kunture (GAR IVF-E). Both innovations are preparatory to bifacial shaping for LCT production, developed in the earliest Acheulean of KS4. However, very few large pointed and elongated tools have been recorded in late Oldowan sites, documenting preliminary evidence for LCT shaping. Bifacial shaping in the earliest Acheulean of West Turkana is not standardized, rather, it produces a wide morpho-dimensional diversity. In this diversity of LCTs, manufactured not only on flakes as at Melka Kunture, but also on large cobbles and split cobbles, massive tools such as picks emerge, which are unknown in the earliest Acheulean of Melka Kunture and which, instead, have been identified in Konso, Gona, Olduvai, and Melka Wakena.

Also at Olduvai, some sites classically attributed to the late Oldowan show innovations *“knocking on Acheulean’s door”* (Sanchez-Yustos, 2021). Some of these innovations, such as the preparation of core striking platforms (DK and HWK EE), incipient macro-tool shaping (DK), bifacial management of edges and bifacial peripheral exploitation (FLK Zinj), are known in the sub-contemporary sites of West Turkana. Others, such as the high frequency and diversity of retouched flakes (DK and HWK), are a novelty in the low-midlands, and recall the sporadic appearance of retouched flakes observed in Melka Kunture late Oldowan sites at 2 Ma, although the standardization of small-pointed tools of GAR IVE is here absent. Despite this evidence, we are still far from an unambiguous interpretation of the origin of the Acheulean at Olduvai, and the age-old question of the coexistence of two cultural traditions proposed by M. Leakey (1971, 1975) is not yet settled. If technical innovations occurred since 1.85 Ma in some late Oldowan contexts (e.g., DK) “heralding the Acheulean change" (Sanchez-Yustos, 2021), an innovation-free Oldowan persists until the first appearance of the Acheulean in other sites, as MNK Skull. Furthermore, evidence from HWK EE has called into question several attempts made in the recent years to dismiss the differences between Oldowan and Developed Oldowan A and B, and Developed Oldowan B and Acheulean, as defined by Leakey (1971) (e.g., de la Torre and Mora, 2005, 2008; Semaw et al., 2009; de la Torre, 2011, Proffitt, 2018). As well resumed by de la Torre and Mora (1971: 271) *"it appears that research on Olduvai diachronic trends may require further work before we can definitely drop terms and concepts once defined by Leakey (1971), and perhaps we should not yet tar all the non handaxe assemblages with the same brush"*.

The definition of the true nature of the technical innovations leading to the Acheulean cannot be confined to the mere presence of LCTs. It must include the entire stone assemblage intended as a system whose components are related to each other. Moreover, the definition of innovation must take into account not only the tool itself, but also its production process. The strong diversity of the technical systems of the early Acheulean seems to be strictly due to the knappers' dependence to the raw material constraints, which, being different locally, give rise to different technical expressions. Where the so-called Oldowan-Acheulean transition is preserved, this dependence is inherited from the last Oldowan. Although in some contexts, an attempt to overcome this dependence is visible in both late Oldowan and earliest Acheulean, it is nevertheless still weak to cause a reduction in technological diversity and a standardization of the tools and relative production processes. However, the absence of this transition in other contexts does not yet allow to have a unique position on the Oldowan origin for the Acheulean.

Hominin variability at the times of the Oldowan-Acheulean transitions

Is the diversity of technical innovations leading to the multiple Acheuleans as outcome of local adaptations of the conceptual capabilities and technical skills of a single hominin, e.g., *Homo erectus* sensu lato? Or is the human biological variety recorded in this period (Fig. 3) somehow linked, at least chronologically, to the observed technological diversity?

The oldest East African fossil formally attributed to *Homo erectus* is KNM ER-2598 from Koobi Fora, East Turkana. Although its discovery context posed several problems, its proposed date close to 1.88 Ma seems younger than the earliest Acheulean of Melka Kunture. It is interesting to note that East Turkana, where *Homo erectus* appeared in the stratigraphic record for the first time, is also the region where the emergence of the Acheulean occurred later (unless the interpretation proposed by Semaw et al., 2009 to consider the Karari industries as local facies of the early Acheulean is confirmed). It is also interesting to note that at Koobi Fora, where the paleoanthropological record is particularly rich, and also in other East African sites, *Homo erectus* seems to disappear from the stratigraphic record to then reappear around 1.6 Ma (Fig. 2,3) this time documented by a higher number of finds (only KNM ER-3733 is slightly older than 1.6 Ma). In this period of *Homo erectus* purported absence from the scene, the presence of *Homo habilis*/*rudolfensis* and *Parantrhopus boisei* is well documented in the fossil record of the East Africa low-midlands (Figs. 2,3). However, the hypothesis of a link between the emergence of the Acheulean and of *Homo erectus* cannot be completely ruled out. The infant mandible MK81-GARIVE-0043 found in the late Oldowan GAR IVE site, and the adult humerus MK76-GOMIB-7594 from the early Acheulean GOM IB site (Fig. 2,3) have been attributed to *Homo* aff. *erectus* (Di Vincenzo et al. 2015; Zanolli et al. 2016; Cazenave et al. 2017). Both fossils display a remarkable robustness, considered “an exaptation that became useful when early humans dispersed to high altitudes” (Di Vincenzo et al. 2015). The association of the same species with the latest Oldowan and the earliest Acheulean would validate the interpretation of continuity between the two techno-complexes at Melka Kunture. An old age for the first occurrence of *Homo erectus* in the low-midlands seems supported by two fossils (KNM ER-1472 and KNM ER-1481) tentatively attributed to *Homo erectus* at Koobi Fora (Anton and Middleton, 2023) and coming from levels slightly older than the base of the Olduvai subchron (Fig. 2,3). However, there is no Acheulean at Koobi Fora until ~0.7 Ma (Figs. 2,3). Similarly, there seems to be evidence of *Homo erectus* at Drimolen in South Africa at ~2 Ma (Herries et al., 2020), at broadly the same time of the first Acheulean at Melka Kunture, but there is no Acheulean at Drimolen.

The equivalence *Homo erectus* = emergence of the Acheulean is a paradigm that is not unequivocally supported by our chronological data. It may be true for Melka Kunture, provided that the fossils therein found do belong to *Homo erectus*, but not necessarily for the low-midlands of East Africa, where the fossil record of *Homo erectus* penecontemporaneous with the earliest Acheuleans is definitely weaker than that of *Homo habilis/rudolfensis* and *Paranthropus boisei* (Fig. 2,3). This "weakness" is further amplified by a gap of approximately 300,000 years (1.9-1.6 Ma) during which *Homo erectus* disappear from the fossil record just when the earliest Acheuleans appear in the archaeological record of West Turkana, Konso, and Olduvai (Fig. 2,3). Finally, a species attribution is difficult to establish for some of these fossils, as two of them are juvenile individuals (MK81-GARIVE-0043 and DNH 134), three are post-cranial elements (MK76-GOMIB-7594, KNM ER-737 and 736), and other three are not certainly attributed (OH86, KNM ER-1472 and 1481).

Conclusions

Faced with this overwhelming technological diversity, the idea of a uniform 'heroic' earliest Acheulean that spread from a point of origin, which we may decide to locate now at Melka Kunture at ~1.95 Ma, into the low-midlands of East Africa, should be provisionally abandoned. The idea of one single Acheulean distinguished from the Oldowan by the presence of generic LCTs, should be abandoned. Rather, multiple Acheuleans existed at different times and places. Between 2 and 1.6 Ma, several techno-economic innovations occurred in East Africa. They are not distributed along a linear evolutionary process but constitute the pieces of a puzzle that gradually and smoothly comes together (Fig. 3). In this framework, we should abandon the use of standardized labels such as "late Oldowan" and "early Acheulean" as dissolving the technological diversity in the previous typological postulates and clamors to be rethought. Acknowledging various gaps of knowledge on the path to a new and more appropriate cultural classification, it is time to talk at least of *several* earliest Acheuleans in East Africa, typologically, chronologically, and geographically distinct. The distinction of different Acheuleans certainly does not represent an ideal interpretative solution but only a precise stage in a precise historical moment and corresponds to the awareness that exists in Africa different technological entities under the great and now obsolete "Acheulean" label. Finally, the idea that *Homo erectus* was the only species capable of major cognitive leaps leading to the Acheuleans innovations is not unequivocally supported by the available chronological data.

Author contributions

Rosalia Gallotti: conceptualization, archeological interpretation, manuscript writing; **Serena Perini**: conceptualization, chronological revision, manuscript writing, figures preparation; **Federica Langone**: tephrostratigraphy, manuscript writing; **Francesca Forni**: tephrostratigraphy, manuscript writing; **Jean-Paul Raynal**: supervision, manuscript writing; **Christopher J. Lepre**: supervision, manuscript writing; **Giovanni Muttoni**: conceptualization, manuscript writing, supervision.

Chapter 8

Chronostratigraphy of Thomas Quarry I (Casablanca, Morocco)

This chapter is presented according to

First high resolution Chronostratigraphy for the early North African Acheulean at Casablanca (Morocco)

Published on

Scientific Reports (2021) 11:15340

https://doi.org/10.1038/s41598-021-94695-3

Rosalia Gallotti[1,2,3*], Giovanni Muttoni[4], David Lefèvre[1,2], Jean-Philippe Degeai[1,2], Denis Geraads[5], Andrea Zerboni[4], Valérie Andrieu-Ponel[6], Matteo Maron[7], Serena Perini[4], Mohssine El Graoui[8], Séverine Sanz-Laliberté[1,2], Camille Daujeard[9], Paul Fernandes[3,8,10], Mathieu Rué[1,10], Lionel Magoga [11], Abderrahim Mohib[8,12] & Jean-Paul Raynal[3,8,13]

1. Université Paul Valéry Montpellier 3, CNRS, UMR 5140 Archéologie des Sociétés Méditerranéennes, Campus Saint Charles, 34199 Montpellier, France. 2. LabEx Archimède, Université Paul Valéry Montpellier 3, Campus Saint Charles, 34199 Montpellier, France. 3. Université Bordeaux, CNRS, UMR 5199 PACEA-PPP, Bâtiment B18 Allée Geoffroy Saint-Hilaire CS 50023, 33615 Pessac Cedex, France. 4. Dipartimento di Scienze della Terra "Ardito Desio", Università degli Studi di Milano, Via L. Mangiagalli 34, 20133 Milan, Italy. 5. CR2P-UMR 7207, CNRS, MNHN, Sorbonne Université, CP 38, 8 rue Buffon, 75231 Paris Cedex 05, France. 6. Aix Marseille Université, CNRS, IRD, IMBE - Institut Méditerranéen de Biodiversité et d'Ecologie Marine et Continentale, Technopôle Arbois-Méditerranée, Bât. Villemin, BP 80, 13545 Aix-en-Provence Cedex 04, France. 7. Dipartimento di Ingegneria e Geologia, Università "G. d'Annunzio" di Chieti-Pescara, Via dei Vestini 31, 66100 Chieti, Italy. 8. Institut National des Sciences de l'Archéologie et du Patrimoine, Rabat-Institut, Madinat Al Irfane, Angle rue N°5 et rue N°7, BP 6828, Rabat, Morocco. 9. HNHP-UMR 7194, CNRS, MNHN, UPVD, Institut de

Paléontologie Humaine, Sorbonne Université, 1 rue René Panhard, 75013 Paris, France. 10. Paléotime, 75 avenue Jean Séraphin Achard-Picard, 38250 Villard-de-Lans, France. 11. Mission archéologique Littoral-Maroc, 5 Rue Alquié, 03200 Vichy, France. 12. Direction Provinciale de la Culture, Centre d'interprétation du Patrimoine du Gharb, Quartier administratif, Bd Mohamed V, Kenitra, Morocco. 13. Department of Human Evolution, Max Planck Institute for Evolutionary Anthropology, Deutscher Platz 6, 04103 Leipzig, Germany.

Abstract

The onset of the Acheulean, marked by the emergence of large cutting tools (LCTs), is considered a major technological advance in the Early Stone Age and a key turning point in human evolution. The Acheulean originated in East Africa at ~ 1.8–1.6 Ma and is reported in South Africa between ~ 1.6 and > 1.0 Ma. The timing of its appearance and development in North Africa have been poorly known due to the near-absence of well-dated sites in reliable contexts. The ~ 1 Ma stone artefacts of Tighennif (Algeria) and Thomas Quarry I-Unit L (ThI-L) at Casablanca (Morocco) are thus far regarded as documenting the oldest Acheulean in North Africa but whatever the precision of their stratigraphical position, both deserve a better chronology. Here we provide a chronology for ThI-L, based on new magnetostratigraphic and geochemical data. Added to the existing lithostratigraphy of the Casablanca sequence, these results provide the first robust chronostratigraphic framework for the early North African Acheulean and firmly establish its emergence in this part of the continent back at least to ~ 1.3 Ma.

Introduction

Over the last two decades, several efforts have been made to refine the chronostratigraphic framework of the Acheulean emergence in Africa. In East Africa, well-dated records place the emergence of the Acheulean at ~1.8–1.6 Ma (Lepre et al., 2011; Beyene et al., 2013; Gallotti and Mussi, 2018[b]; Semaw et al., 2020; Uribelarrea et al., 2019). The earliest Acheulean in South Africa seems to be nearly as old as in some East African sites and is reported to fall between ~ 1.6 and > 1.0 Ma (Lotter and Kuman, 2018). North Africa is also rich in Acheulean sites, but most of them are within units of unknown stratigraphic position (Mohib et al., 2019). As regards the Early Pleistocene, the only North African Acheulean sites in known stratigraphic context are Tighennif near Mascara in Algeria and Thomas Quarry I (ThI) in Morocco (Mohib et al., 2019; Geraads et al., 1986) (Fig. 1).

Thomas Quarry I is in the south-western suburbs of Casablanca (Fig. 1) and exposes an Early–Middle Pleistocene stratigraphic sequence. In this area, four formations including several members are associated with four raised marine platforms that can be assigned to the late Early to the Late Pleistocene. They revealed a rich complex of archaeological sites (Fig. 2A): the *Oulad Hamida Formation* (OHF, late Early Pleistocene-early Middle Pleistocene), the *Anfa* (AF) and *Kef Haroun Formations* (Middle Pleistocene), and the *Dar Bou Azza Form*ation (Late Pleistocene) (Lefèvre and Raynal, 2002; Texier et al., 2002).

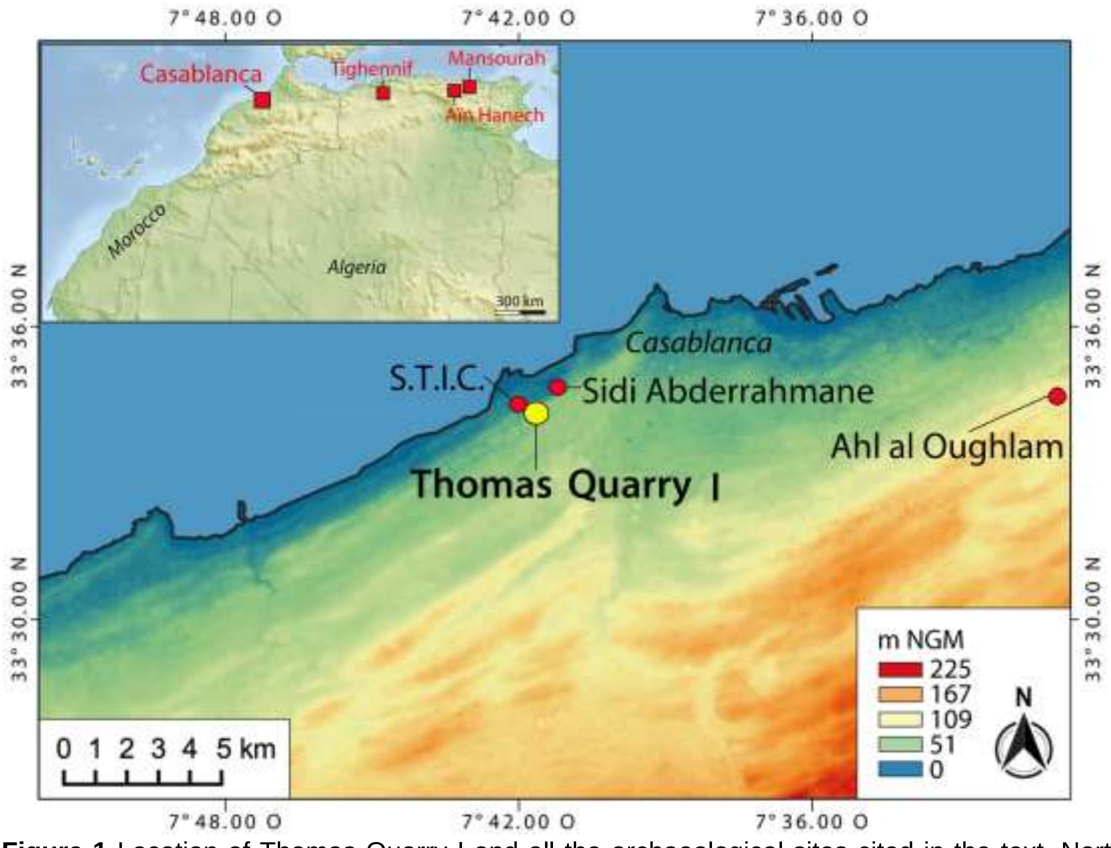

Figure 1 Location of Thomas Quarry I and all the archaeological sites cited in the text. North-Africa map: modified by R. Gallotti after NASA/JPL/NIMA, public domain, via Wikimedia Commons. Casablanca map: modified by M. Rue and R. Gallotti after NASA/SRTM, 1 arc second global elevation data, created using the free and open-source software QGIS v3.18.2 (http:// www. qgis. org).

Thomas Quarry I became famous worldwide thanks to the discovery in 1969 of a Middle Pleistocene human fossil (Mohib et al., 2019). Further research yielded more human remains and a rich archaeological complex at *Grotte à Hominidés* (GH), a cave preserved in the north-eastern wall of the same quarry (Mohib et al., 2019).

In 1985, research in the lower deposits of the quarry revealed the presence of an early Acheulean industry with a clear stratigraphic context (Unit L; ThI-L) (Raynal and Texier, 1989). Lithostratigraphy, biostratigraphy, and OSL ages placed ThI-L at approximately 1 Ma, an age similar to that of Tighennif, however, the chronology of these two sites remained poorly defined (Geraads et al., 1986; Geraads, 2016; Rhodes et al., 2006) as was the age of emergence of the Acheulean and its subsequent development in this part of the African continent. Here we present new chronostratigraphic data based on magnetostratigraphy and geochemistry for ThI-L, which constrain its age and provide a robust high-resolution framework for the earliest Acheulean in North Africa, pushing the time of its first appearance in this part of the continent back at least to ~ 1.3 Ma.

ThI-L context

The Thomas Quarry I Pleistocene deposits belong to OHF that unconformably overlies the Cretaceous and Cambro-Ordovician basement with the contact placed at a current altitude of ~ 28 m above sea level (asl) (Fig. 2A**)**. From bottom to top, OHF includes four allostratigraphic units—OH1 to OH4 Members—each having unconformities at their bases and tops (Fig. 2A,B, see Supplementary Information text and Supplementary Fig. S1) (Lefèvre and Raynal, 2002; Lefèvre et al., 2016; Raynal et al., 2011).

OH1-Bed 1, OH2, OH3, and OH4 are mainly composed of calcirudites and/or coquinoid and coarse-grained biocalcarenites overlying abrasion platforms associated either with a cliff palaeoshoreline (OH3) or a deep cavity (OH4) and pass vertically from coarse to medium-grained biocalcarenites (Mohib et al., 2019; Lefèvre and Raynal, 2002). These sedimentary sequences of genetically related intertidal, supratidal and aeolian depositional environments record sea-level high-stands associated with shoreline formation. The unconformities or sequence boundaries mark the shoreline regression due to sea-level fall. Thus, OH1 to OH4 correlate with sea-level high-stands of the main global glacio-eustatic cycles as inferred from the marine isotope stage (MIS) record and are preserved at positive elevations due to the regional tectonic uplift affecting Atlantic Morocco (Lefèvre et al., 2016; Chabli et al., 2005) et al., 2011).OHF predates the Anfa Formation (Fig. 2A) whose Members AF1 and AF2 are correlated to MIS 13 and MIS 15 (Lefèvre and Raynal, 2002; Rhodes et al., 2006; Lefèvre et al., 2016). In the GH cave, OH4 deposits are covered by a complex of continental deposits (GH-CCC) subdivided into two parts separated by an aeolianite (OH5) (Mohib et al., 2019; Lefèvre and Raynel, 2002). As GH-CCC/unit 4 overlying OH4 has been dated to 0.5–0.6 Ma (Rhodes et al., 2006; Raynal et al., 2011) in accordance with biostratigraphy (Geraads et al., 2010), the OH4 marine high-stand associated with the palaeoshoreline is undoubtedly much older than MIS 15. Thus, OH4 to OH1 Members should record sea-level high-stands from at least MIS 17 and older.

Thomas Quarry I-Unit L belongs to OH1-Bed 2 whose deposits form a 2 to 3 m-thick succession of locally cross-bedded coarse siliciclastic to bioclastic sands and calcareous mudstones-L1 to L5. In the uppermost part of the sequence, evidence of pedogenesis during warm episodes of subaerial exposure are preserved (Texier et al., 2002; Lefèvre et al., 2016) (Fig. 2E, see Supplementary Information Text, Supplementary Table S1, Supplementary Figs S2-S5). The formation of the sequence is probably related to the interplay of littoral processes that include sedimentation in low energy fluvial channels interchanged to swamps along backshore environments, alternating with periods of enhanced aeolian sedimentation. ThI-L was dated using the OSL signal of quartz grains to 989 ± 208 ka and 948 ± 599 ka (Rhodes et al., 2006), with large uncertainties.

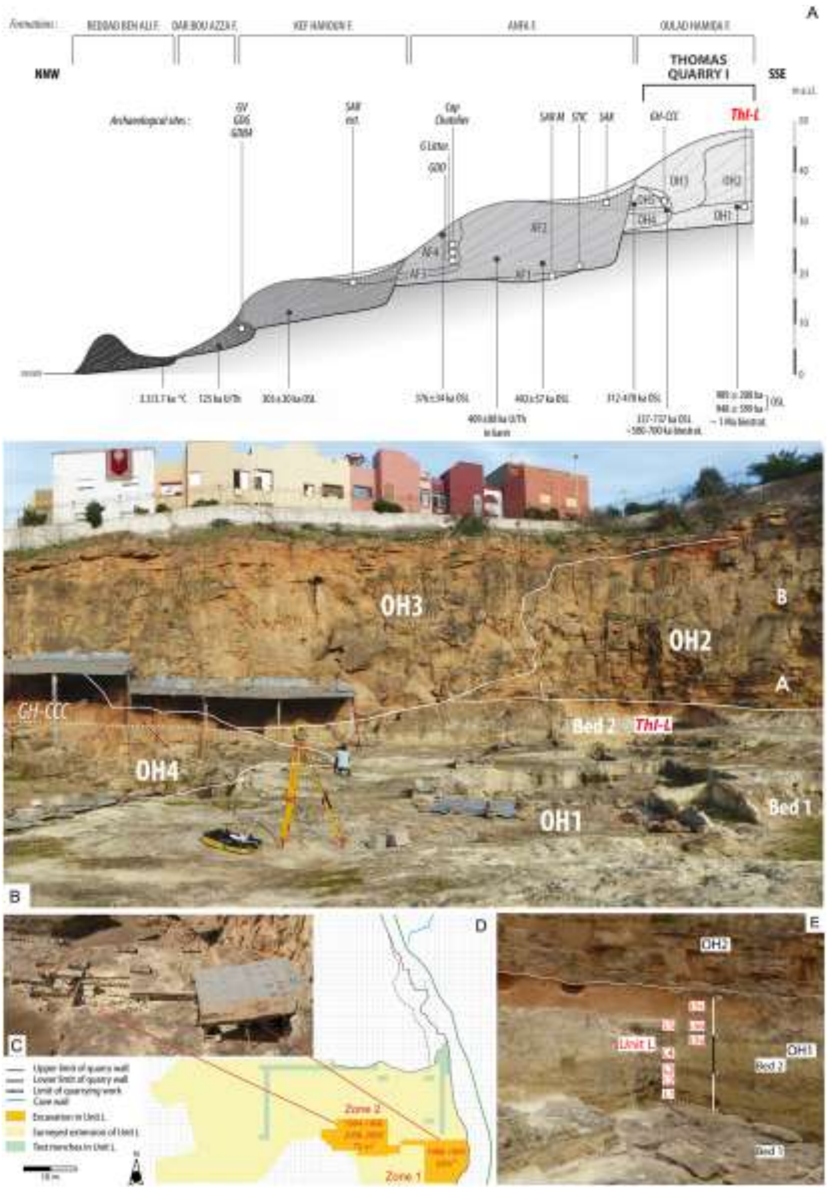

Figure 2 (A) OHF and its Members (late Early Pleistocene-Middle Pleistocene) exposed at Thomas and Sidi Abderrahmane quarries, South-West of Casablanca (drawing D. Lefevre). Archaeological sites: GDBA: *Grotte de* Dar Bou Azza; GDG: *Grotte des Gazelles*; GDO: *Grotte des Ours;* GH-CCC: *Grotte à Hominidés*-complex of continental deposits; G Littor.: *Grotte des Littorines;* GV: *Grotte Velozzo*; SAR ext.: *Sidi Abderrahmane-Extension*; SAK: *Sidi Al Khadir*; SAR M: *Sidi Abderrahmane*-Unit M; S.T.I.C.: *Société de Transformation Industrielle et de Construction* Quarry; ThI-L: Thomas Quarry I-Unit L. OSL and ESR ages, and biochronological data. (**B**) Members 1 to 4 of the OHF at ThI (photo and drawing D. Lefevre); (**C**) ThI-L1 during 2007 excavation (photo J.-P. Raynal); (**D**) map of ThI with extension of unit L and location of the excavation zones (drawing R. Gallotti); E: ThI-L, Zone 1: OH1 Bed 2—Unit L—L1 to L5 deposits. Photo and drawing D. Lefevre. Figures were generated with Adobe Photoshop CC version 2015-1, 20151114.r301 X64. Copyright 1990-2015 Adobe Systems Incorporated and its licensors. All rights reserved.

Two archaeo-stratigraphic sub-units have been recorded at ThI-L, L1 at the base and L5 at the top. About 1000 m^2 of ThI-L1 has been surveyed and systematically test-pitted, and it was excavated in 1988–1996 and 2006–2008 in two main areas of 68 m^2 (zone 1) and 75 m^2 (zone 2), respectively (Fig. 2C, D). ThI-L5 has been excavated only in zone 1. Both sub-units yielded a rich corpus of lithic artefacts together with faunal remains (Mohib et al., 2019).

The fauna from ThI-L is poor and fragmentary, and the bone surfaces are badly preserved (see Supplementary Information Text, Supplementary Figs S6, S7). Large mammals are dominated by hippos (*Hippopotamus sirensis*, akin to *H. gorgops*). Bovids include a bovin, a gazelle, a medium-sized alcelaphin, and a medium-sized *Kobus* sp. An *Equus* and a rhino are also represented, together with an elephant (Geraads et al., 2010). A tooth of the suid *Kolpochoerus* is reminiscent of *K. majus* from East Africa. Among rodents, the most significant differences from GH-CCC/unit 4 are the absence of the mole vole *Ellobius* and the presence of distinct species of *Paraethomys* and *Gerbillus* s.l. Overall, the mammalian fauna from ThI-L is too poor to be confidently dated by biochronology, but it is significantly older than GH-CCC/unit 4 and Tighennif (see Supplementary Information text).

ThI-L technical behaviours

The artefact assemblages of ThI-L1 (n = 3845) and ThI-L5 (n = 1228) are composed of Paleozoic tenacious rocks, mainly quartzites abundantly available in local primary and secondary sources, and flint derived from the phosphatic plateau in the hinterland of the Meseta and available in secondary deposits near the site (Mohib et al., 2019).

Two main quartzite production systems coexisted in both levels (Mohib et al., 2019): one is focused on the production of small to medium-sized flakes, the other is devoted to the manufacture of Large Cutting Tools (LCTs).

Small-medium sized flakes of quartzite were produced by a diversity of methods (unifacial unidirectional, bifacial partial, peripheral unidirectional, multifacial multidirectional, and discoid) and were not retouched (Fig. 3). All cores (n = 605) are on cobbles and devoted to small flaking. Cores for the extraction of large flake with a length or width > 10 cm are lacking in the excavated area.

Large Cutting Tools (n = 230) were mainly produced from large cobbles, less often from large flakes (22%) detached mainly using the *entame* core method (Sharon, 2011). At ThI-L, this method has been used to produce large flake blanks for the 12 cleavers (Tixier, 1956) identified (Fig. 4K,L) and for eight pointed handaxes (Fig. 4C). Several shaping processes are repeated on several specimens that all tend towards similar morphologies and producing several types of LCTs, the most common of which are pointed handaxes (n = 107; Fig. 4A-C). Shaping proceeds in two steps: the location of the apical portion followed by one to three series of removals that creates lateral edge convergence without further trimming. Variations of these schemes produce pointed handaxes with a skewed point (n = 18) shaped by notches that penetrate one or both edges (Fig. 4D,E) as well as various beveled handaxes (n = 16) with a transversal edge manufactured using marginal retouch (Fig. 4F, G). Other common LCTs are picks on cobbles (n = 38), mostly with a trihedral section at the tip portion, and some on flakes (n = 8; Fig. 4H). In some large specimens (n = 5) the trihedral section includes the whole object and is due to the use of a large edge flake from a block as a core (Fig. 4I,J). The remaining LCTs have broken apical parts (n = 18) or are massive scrapers on *entame* flakes (n = 7). Only one massive scraper on a Kombewa flake is present in the assemblage, but it is insufficient to document a true Kombewa strategy. Flint production (15% of the artefacts assemblage) is entirely devoted to the extraction of small flakes, adopting some of the flaking methods documented for tenacious rocks (unifacial unidirectional, bifacial partial, multifacial multidirectional) and mainly the free-hand technique. However, flint production at ThI-L1 shows evidence of one specific technical process, that of bipolar-on-anvil semi-peripheral exploitation to produce bladelet-like flakes. This technical process was hitherto unknown for periods in question and demonstrates the diversification and the flexibility within the African Acheulean (Gallotti et al., 2020).

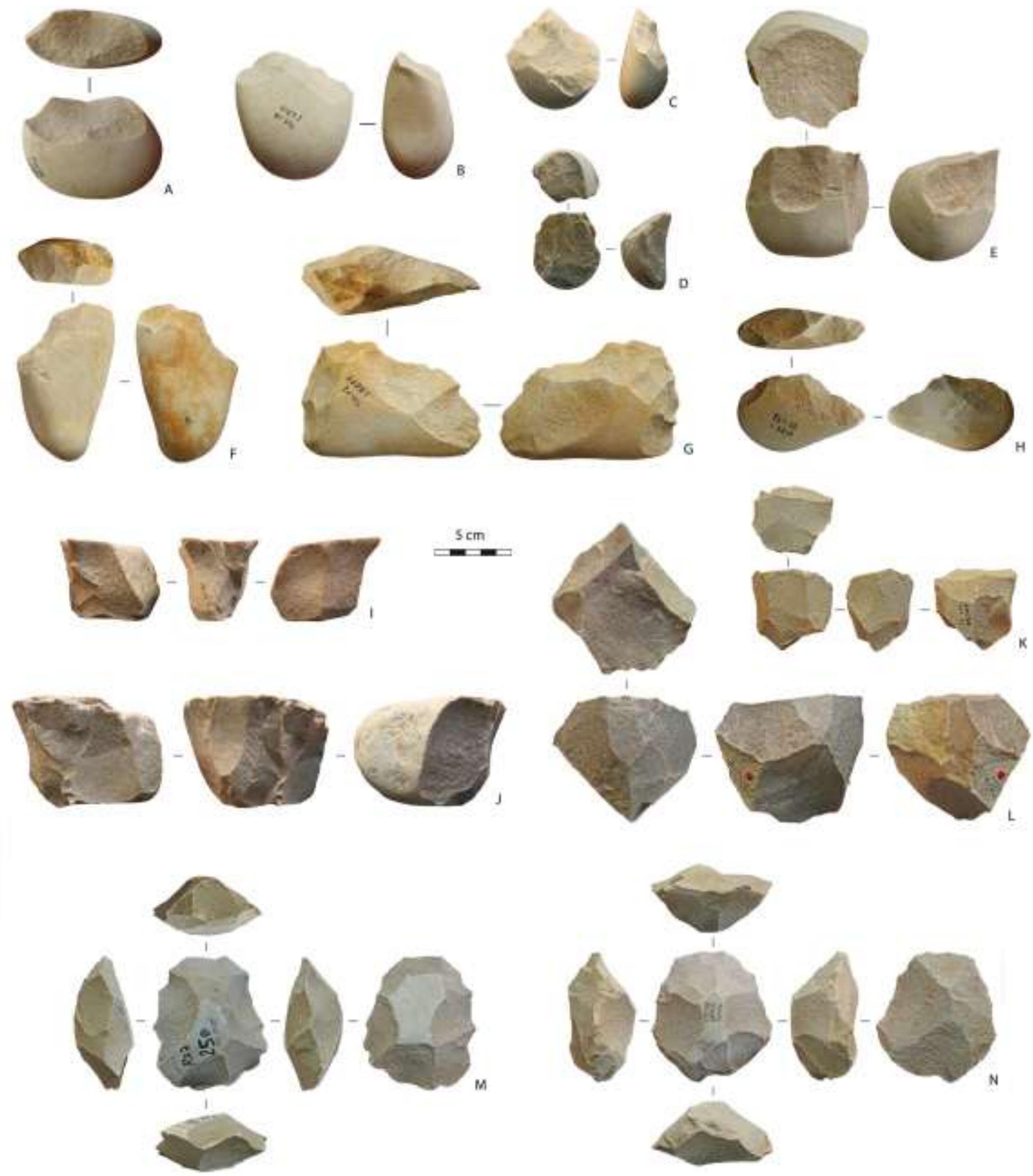

Figure 3 Quartzite cores. (A–E) unifacial unidirectional cores; (F–H) bifacial partial cores; (I,J) peripheral unidirectional cores; (K,L) multifacial multidirectional cores; (M,N) discoid cores. This figure was generated on the basis of photos made by R. Gallotti with Adobe Photoshop CC version 2015-1, 20151114.r301 X64. Copyright 1990 2015 Adobe Systems Incorporated and its licensors. All rights reserved.

Figure 4 LCTs. (A,B) pointed handaxes on cobble; (**C**) pointed handaxe on *entame* flake; (D,E) pointed handaxes on cobble with a skewed point; (F,G) beveled handaxes; (H) pick on cobble; (I,J) picks on core edge flake from block; (K,L) cleavers on *entame* flake. This figure was generated on the basis of photos made by R. Gallotti with Adobe Photoshop CC version 2015-1, 20151114.r301 X64. Copyright 1990 2015 Adobe Systems Incorporated and its licensors. All rights reserved.

Magnetochronology

Laboratory experiments have been conducted on a total of 179 oriented standard (10 cc) core samples (plus an additional suite of 20 rock chip samples) taken along stratigraphic profiles of OHF straddling OH1 Bed 1, OH1 Bed 2, OH2A and OH2B, OH3, OH4 plus GH-CCC, and OH5. We also sampled Member 2 of the Anfa Formation (AF2) at the Sidi Abderrahmane Quarry. Samples have been taken in order to establish the fundamental rock-magnetic properties of the sediments and unravel the structure and orientation of the natural remanent magnetization therein contained for magnetic polarity determination and correlation to the standard geomagnetic polarity time scale (see “Materials and methods” section, Fig. 5, Supplementary Figs S8-S14, Supplementary Tables S2, S3).

The mean initial magnetic susceptibility (SUS) of samples from OH1 Bed 1 is of ~$10*10^{-6}$ SI while that of samples from OH1 Bed 2 varies between ~$100*10^{-6}$ SI and ~$200*10^{-6}$ SI up to sample S240 to then display a progressive increasing trend up to maximum values of ~$700*10^{-6}$ SI at the top of OH1 Bed 2 (sample S314) (Fig. 5, Supplementary Table S3). This trend corresponds to a visible reddening of the sediment as observed along the south wall of the excavation trench exposing OH1 Bed 2 (Supplementary Fig. S8). The SUS then drops to ~$200*10^{-6}$ SI at the base of the coarse-grained quartz-bioclastic sandstones of OH2A to further decreases to a mean of ~$100*10^{-6}$ SI in the ensuing aeolian sandstones of OH2B (Fig. 5, Supplementary Table S3). Samples S1375 to S1701 belong to aeolian sandstones of uncertain stratigraphic attribution and will not be further discussed (OH? in Fig. 5). The mean SUS of OH3 is of ~ $50*10^{-6}$ SI, that of OH4 plus GH-CCC/unit 4 is much higher and often above $1000*10^{-6}$ SI, while the SUS of OH5 and AF2 (not shown) are on the order of ~ $350*10^{-6}$ SI and ~ $25*10^{-6}$ SI, respectively (Fig. 5, Supplementary Table S3). Units 1–2 of GH-CCC have not been sampled for magnetostratigraphy as they are attributed to the Late Pleistocene–Holocene.

Thermal demagnetization of a three-component isothermal remanent magnetization (IRM) shows for all studied samples a dominant signal carried by the 0.12 T curves with maximum unblocking temperatures of about 575°C, interpreted as due to magnetite, coexisting with a subsidiary higher coercivity (2.5 T) component with maximum unblocking temperatures of about 680°C, interpreted as hematite (Supplementary Fig. S9). IRM acquisition curves (not shown) confirm this composite mineralogy.

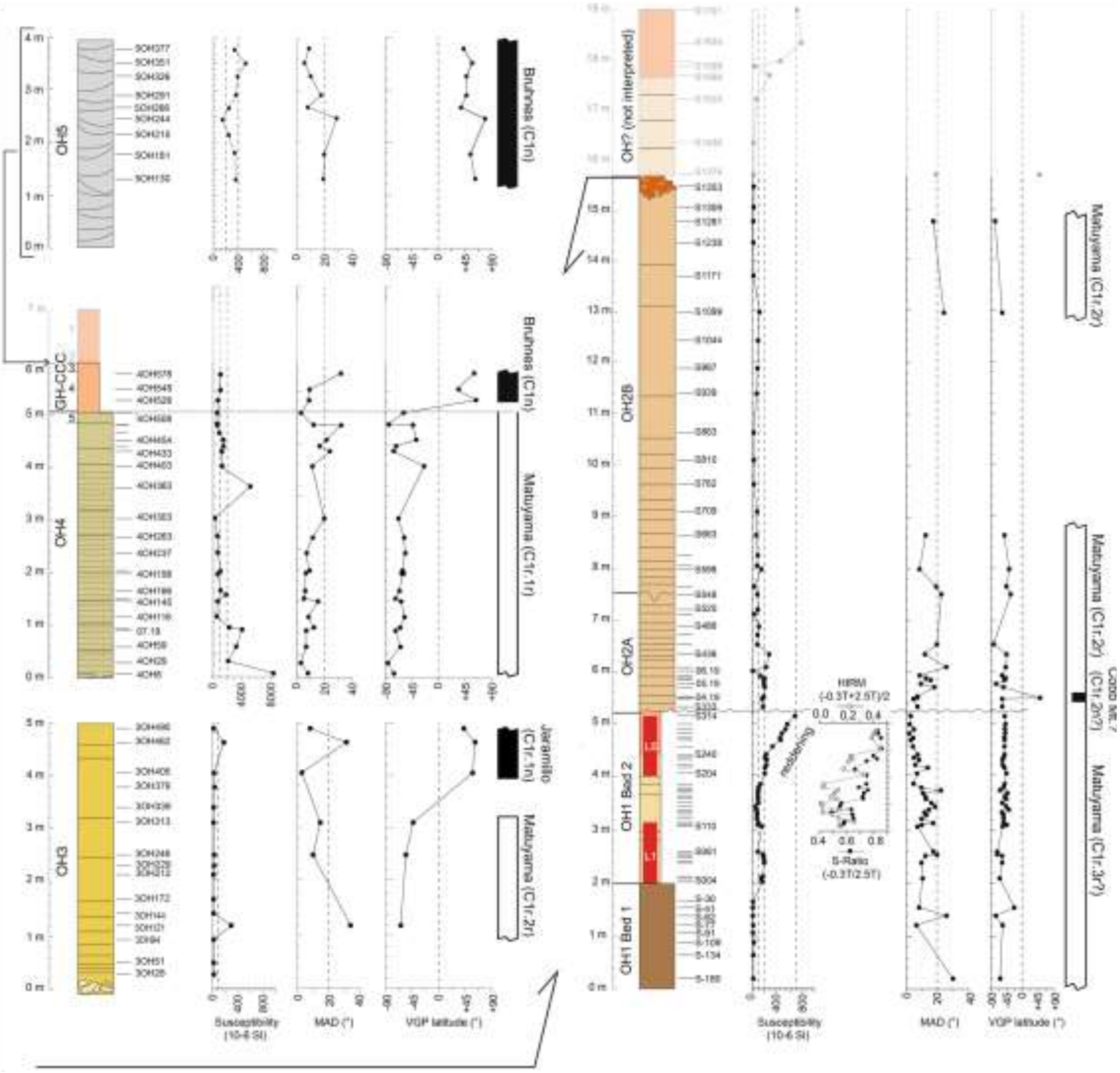

Figure 5 Generalized logs of the stratigraphic sections investigated (youngest at top left, oldest at bottom right, but see description for details) with indication of paleomagnetic samples placed aside initial magnetic susceptibility, maximum angular deviation (MAD) values of the C component directions, virtual geomagnetic pole (VGP) latitudes, and polarity stratigraphy where black bars represent normal polarity and the white bar is reverse polarity. Cobb Mt.? is a possible record of the Cobb Mountain subchron. Red bars indicate archeological units ThI-L1 (bottom) and ThI-L5 (top) within OH1 Bed 2. Drawing G. Muttoni, S. Perini, and S. Sanz-Laliberte. This figure was created with Adobe Illustrator CS6 version (http:// www. adobe. com).

The heating branches of the thermomagnetic (heating-cooling) cycles of selected samples from OH1 Bed 2 show a marked decline in susceptibility generally between 500 and 550°C attributed to magnetite to then flatten-out reaching temperatures of up to 660°C due to the presence of hematite (Supplementary Fig. S10A-E). The cooling branches of the thermomagnetic cycles generally show marked increases in susceptibility below about 550 °C due to the creation in the laboratory of new magnetite phases. Hysteresis parameters calculated on the same OH1 Bed 2 samples after correcting for paramagnetic components appear broadly compatible with dominant magnetite in the pseudo-single domain grain-size range (Supplementary Fig. S10F-L). Similar hysteresis data dominated by a low-coercivity magnetic phase (magnetite) have been obtained also for samples from OH4 and OH5 (Supplementary Fig. S11). From the analyses above, it is concluded that the main magnetic phases present in the studied rock record are magnetite in association with hematite. The reddening of the sediment observed in OH1 Bed 2 and corresponding to a marked increase in SUS (Fig. 5; see also above) correlates also to positive and progressively increasing S-ratios and HIRM values (see Materials and Methods for definition). This is tentatively interpreted as due to progressively higher contents of magnetite (S-ratios approaching +1 and high SUS values) accompanied also by higher contents of high coercivity phases such as hematite and/or goethite (high HIRM values) that are probably responsible for the (chemical) reddening of the sediment associated with soil development (see “Discussion” below).

The anisotropy of magnetic susceptibility (AMS) of the investigated samples is in general more oblate (foliation, F = kint/kmin > lineation, L = kmax/kint) than prolate (L>F) albeit the degree of anisotropy P = kmax/ kmin is in general very low (Supplementary Fig. S12). The kmin axes of these weakly anisotropic ellipsoids result broadly perpendicular to the bedding planes especially in OH1 Bed 1, OH1 Bed 2, and OH4 plus GH-CCC, a disposition interpreted as indicating a dominant sedimentary (gravitational) settling of magnetic grains, while the kmin axes of the aeolian sandstones of OH2B, OH3, and OH5 tend to lie off the normal to bedding planes, a disposition consistent with (wind-induced) imbrication of clasts (Supplementary Fig. S12).

The intensity of the natural remanent magnetization (NRM) at room temperature varies between $0.02*10^{-3}$ A/m and $40*10^{-3}$ A/m (10 cc volume). Vector end-point demagnetization diagrams of NRM thermal demagnetization data (Supplementary Table S2) show the presence of a soft component of the remanent magnetization termed A that is removed between room temperature and ~150-200°C (Supplementary Fig. S13) and is oriented downward (positive inclinations) with scattered, generally northerly declinations indicative of normal magnetic polarity (Supplementary Fig. S14 upper panel). This A component is virtually absent in samples from OH1 Beds 1 and 2 (Supplementary Fig. S13A for OH1 Bed 2) while it is variably evident in samples from OH2A-B to OH5 taking the form of an abrupt jump in remanence intensity from room temperature to 100-150 °C accompanied by a change in direction of magnetization in case the subsequent component of magnetization at higher temperatures (see below) is of reverse polarity (Supplementary Fig. S13B-E). A characteristic remanent magnetization component, termed C, was isolated in a total of 117 samples between ~200 and ~475 °C, occasionally up to 600-650 °C. These C component directions are bipolar whereby they are either oriented downward with scattered northwesterly declinations or upward with southerly declinations (Supplementary Figs S13, S14 lower panel), which especially in samples from OH1 Bed 2 (Supplementary Fig. S13A) and AF2 (Supplementary Fig. S13E) appear very shallow possibly due to post-depositional sediment compaction. These C component directions are interpreted as acquired during periods of either normal or reverse polarity of the Earth’s magnetic field (see age attribution below). The maximum angular deviation (MAD) values of these C components, generally <20°, together with the virtual geomagnetic pole (VGP) latitude they provide, are used to delineate magnetic polarity stratigraphy (Fig. 5, Supplementary Table S3).

Persistent negative VGP values interpreted as recording reverse magnetic polarity characterize OH1 Beds 1 and 2 as well as OH2A up to the base of OH2B, whereas only a few samples from the remainder part of OH2B yielded usable C component directions (Fig. 5). Sample 04.19 in OH2A contains a clear high temperature C component direction of positive VGP value attributed to normal

magnetic polarity (Fig. 5, Supplementary Fig. S13B). Next, OH3 (sampled along main section OH3-A) yielded three lower samples of reverse polarity (e.g. sample 3OH121 in Supplementary Fig. S13C) overlain by three samples of normal polarity (e.g., samples 3OH405 and 3OH490 in Supplementary Fig. S13C) (Fig. 5). Magnetic component directions from sister section OH3-B (not reported in Fig. 5) resulted mostly unstable except for two samples with C component directions of reverse polarity (e.g., sample 3BOH388 in Supplementary Fig. S13C). Samples from OH4/unit 5 yielded reverse magnetic polarity, while the three samples from GH-CCC/unit 4 as well as all samples from younger OH5 display positive VGP values interpreted as recording normal magnetic polarity (Fig. 5; examples in Supplementary Fig. S13D). Finally, 7 out of 16 samples from AF2 yielded northerly and very shallow C component directions (Supplementary Fig. S13E) interpreted as a record of normal magnetic polarity (not shown in Fig. 5).
Taking into account also the available OSL data (see also below), the observed polarity sequence is interpreted, from younger to older, as a record of the Brunhes Chron (C1n) in AF2, OH5, and GH-CCC/unit 4, with the Brunhes-Matuyama boundary (C1n-C1r) placed in the lowermost part of GH-CCC/unit 4 or at the boundary with underlying OH4. Next follows a record of the Jaramillo-Matuyama boundary (C1r.1r-C1r.1n) in OH3 (section OH3- A), and an extended record of the pre-Jaramillo Matuyama (C1r.2r) in OH2A and OH2B, OH1 Bed 2, and OH1 Bed 1 (Fig. 5). Tentatively, the one sample-based normal polarity in OH2A could represent a partial record of the Cobb Mountain subchron (C1r.2n).

The Brunhes–Matuyama boundary and the Jaramillo-Matuyama boundary -representing the two most secure magnetochronologic time-lines traced within the ThI sequence- are commonly dated to 0.781 Ma and 1.072 Ma according to the Astronomically Tuned Neogene Time Scale (ATNTS2004) (Lourens et al., 2004), used in this study, or 0.773 Ma and 1.070 using high resolution deep sea piston core data and Ar-Ar data on lavas (Channell et al., 2020). The Cobb Mountain subchron is dated to 1.186–1.221 Ma according to radioisotopic data from sections in the western U.S., or to 1.178–1.215 Ma straddling MIS 35 to 36 according to a recent record at IODP Site U1306 (Channell et al., 2020), which represents the age span adopted in this study.

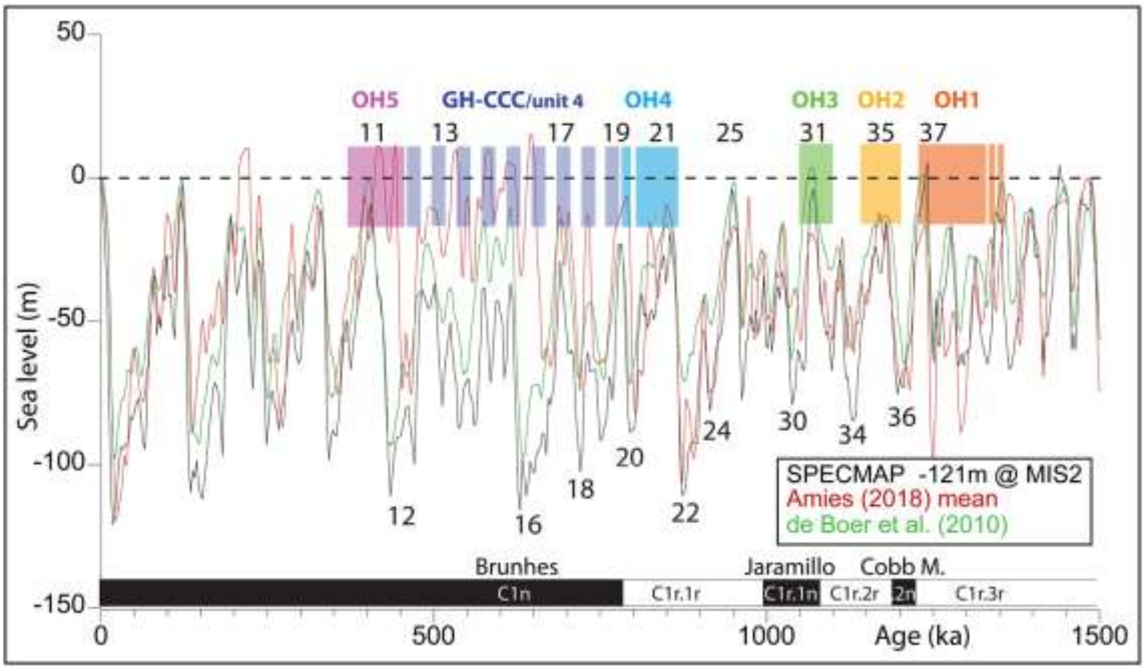

Figure 6 Various glacioeustatic solutions for the past 1.5 Myr as revealed from the ODP677/SPECMAP benthic $\delta^{18}O$ record (Shackleton, 1995) scaled to the 121 m glacioeustatic lowering at the last glacial maximum (Fairbanks, 1989), the solution of Rohling et al. (2014) based on Amies (2018) SST-corrected Mediterranean planktic $\delta^{18}O$ data [solution termed 'Amies (2018) mean' in figure], and the solution of De Boer et al. (2010) based on the benthic $\delta^{18}O$ stack of Lisiecki and Raymo (2005). Main marine isotope stages (MISs) are indicated by standard numbering whereby odd-numbered stages represent interglacials and even-numbered stages glacials. The geomagnetic polarity time scale of the Pleistocene is also reported together with the inferred ages of deposition of the studied units from OH5 to OH1. Drawing G. Muttoni. This figure was created with Adobe Illustrator CS6 version (http:// www. adobe. com).

In order to improve the age model of deposition, we consider the effects of Pleistocene glacioeustatic variability on sedimentation according to various solutions from the literature based on $\delta^{18}O$ records (Lisiecki and Raymo, 2005; Shackleton, 1995; Fairbanks, 1989) (Fig. 6). Deposition at ThI was most probably intermittent and occurring mainly during sea-level high-stands while erosional surfaces formed during sea-level falls. Therefore, considering magnetochronology, biochronology, and OSL dating, unit OH5 of normal (Brunhes) magnetic polarity with OSL ages from 370 ± 58 to 440 ± 38 ka (Rhodes et al., 2006) can be correlated to MIS 11, GH-CCC/unit 4 of early Brunhes age provided with scattered OSL ages ranging from 391 ± 32 ka to 420 ± 34 ka, a

US/ESR age of 501+ 94 -76 ka, and biochronological constraints (Raynal et al., 2011; Geraads et al., 2010), is of early Middle Pleistocene age broadly straddling MISs 12/13–19, while OH4 may have deposited during the high-stand of MIS 19 and possibly also MIS 21 (Fig. 6). Similarly, unit OH3 recording the Jaramillo–Matuyama boundary (1.072 Ma) may have deposited during MIS 31, units OH2A and OH2B during MIS 35, and OH1 (Beds 1 and 2) at least during MIS 37 (Fig. 6). A deposition of OH2A–B during MIS 35 would also be in agreement with an attribution of normal magnetic polarity sample 04.19 in OH2A to the Cobb Mountain subchron (Figs 5, 6).

Geochemistry

Pleistocene climate change impacted the chemical weathering of sediments, with higher carbonate dissolution during warmer and wetter periods (Yang et al., 2004; Profe et al., 2016). Hence, the weathering intensity of ThI-L was determined by geochemical analyses to characterize the climatic conditions of deposition (Supplementary Table S4). K/Ca and Rb/Sr elemental ratios were used to estimate the degree of decalcification of carbonate sediment (Supplementary Figs S15, S16). The high degree of weathering in subunit L1 seems to indicate a warm and humid climate, which is consistent with micropedological indicators and pollen data that suggest a woody environment or a wet depression (Supplementary Information Text, Supplementary Table S6). A shift to drier and cooler conditions could have occurred in L2-L3-L4 given the low values of the weathering index (Supplementary Fig. S17). Reddening and magnetic susceptibility increase in the upper part of OH1 Bed 2 (Fig. 5) which are typical of a soil developed in warm Mediterranean regions with seasonal contrast (Torrent et al., 2010). This also occurs in L5, which is generally characterized by a high degree of weathering, particularly in subunits L5a and L5c (Supplementary Fig. S17).

In addition, a specific group of elements composed of Si, Ti and Zr was detected by the principal component analysis of the geochemical data (Supplementary Fig. S15). These elements are typical components of Saharan dust transported by the northern branch of the Saharan Air Layers (NSAL) over

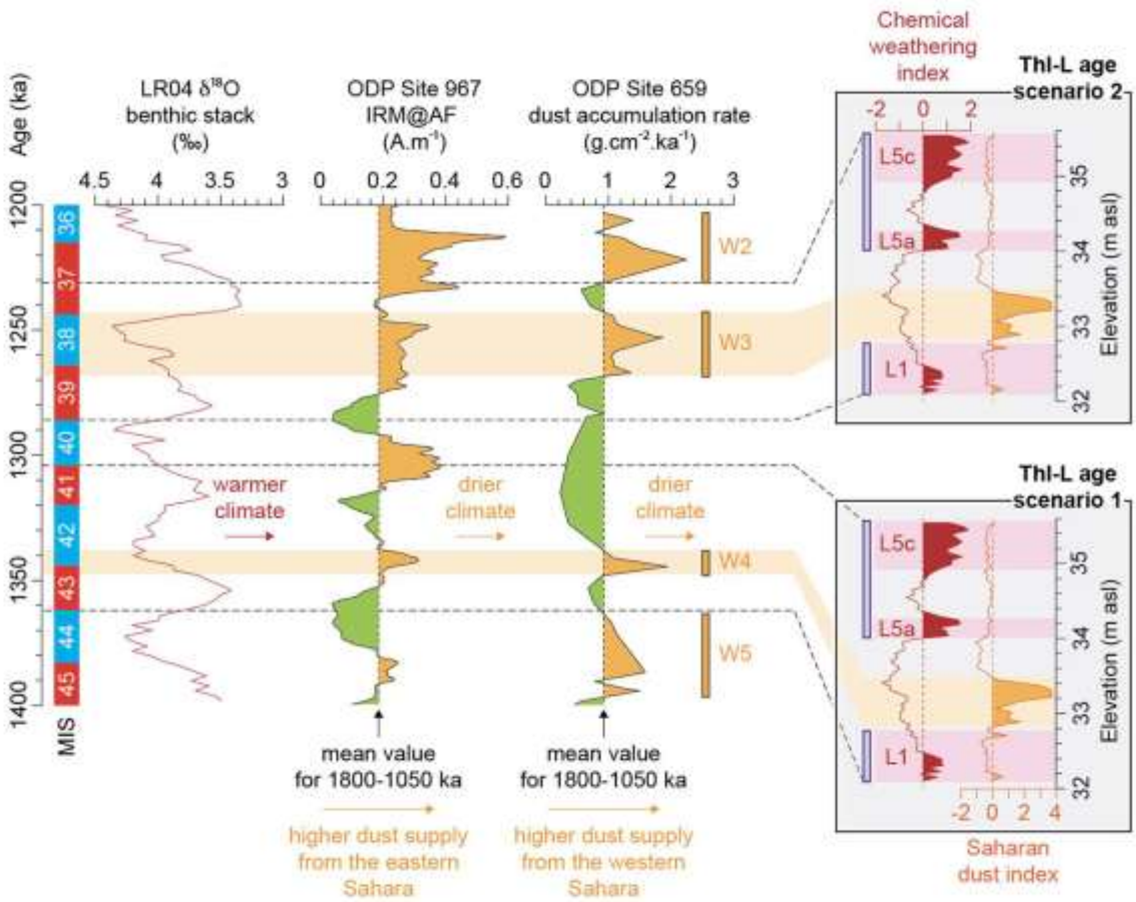

Figure 7. Age scenarios for unit L from the site of Thomas Quarry I. W2–W5: periods of higher than average dust supply from the western Sahara. L1, L5 (a,c): subunits with relatively high chemical weathering. Saharan dust proxy record from ODP Site 659 (dust accumulation rate)33. Saharan dust proxy record from ODP Site 967 (IRM@AF) (Larrasoaña et al., 2003; Grant et al., 2017). Marine Isotopic Stages (MISs) and LR04 benthic stack (Lisieki and Raymo, 2005). Drawing J.-P. Degeai. This figure was created with Adobe Illustrator CS6 version (http:// www. adobe. com).

northwestern Africa (Rodrigo-Gamiz; 2014). Therefore, the relative enrichment of Si, Ti and Zr in subunits L2-L3 is most likely be related to a period of enhanced Saharan dust flux (Supplementary Fig. S17).

Thirteen periods of above average dust supply arriving from the western Sahara (W1–W13) can be identified in marine sediments of northwestern Africa for the interval between the Jaramillo and Olduvai subchrons straddling the deposition of ThI-L (Supplementary Fig. S18). We attempt correlating the observed Si, Ti and Zr anomalies in subunits L2-L3 to this dust record by generating an integrated tectono-eustatic model (Supplementary Fig. S19, Supplementary Table S5) and palaeoelevation reconstruction (Supplementary Fig. S20) of ThI-L. Indeed, ThI-L is composed of continental sediments and therefore subunits L2–L3 cannot have been deposited when ThI was flooded by the sea. The site should not have been below sea level during W3 when considering a maximum uplift rate (Supplementary Fig. S20A), during W1, W3 and W12–W13 with a mean uplift rate (Supplementary Fig. S20B), and during W1–W4, W8 and W10–W13 with a minimum uplift rate (Supplementary Fig. S20C). Besides, dust input in subunits L2–L3 is unlikely to be related to W8–W13 because the latter are older than 1.5 Ma (Supplementary Fig. S18), while OSL dating shows that unit L was probably younger than 1.5 Ma (Rhodes et al., 2006). Moreover, if the tentative correlation of the single sample of normal polarity at the bottom of OH2A to the Cobb Mountain subchron is correct, L2 and L3 were probably not associated with W1 and W2, given that unit L was deposited during a period of reverse polarity. Hence, the most consistent periods of high dust supply from the western Sahara which could have led to the Si, Ti and Zr anomalies in subunits L2-L3 should have occurred around either 1.35–1.34 Ma (W4) or 1.27–1.24 Ma (W3). The chronology of unit L could thus range between W5 and W2, i.e., from ca. 1.36 to 1.23 Ma, while chemically weathered sediment and human settlement could date to MIS 43 or MIS 39 for subunit L1 and to MIS 41 or early MIS 37 for subunit L5 (Fig. 7).

Discussion

Bed 2 of the OHF Member 1 at Thomas Quarry I yielded in some of its sub-units rich lithic assemblages forming the L site and documenting the earliest Acheulean in North Africa. Previously, an age of c. 1 Ma falling either before or immediately after the Jaramillo sub-chronozone was the best date estimate for ThI-L. The site was dated to 989 ± 208 ka and 948 ± 599 ka, using the OSL signal of quartz grains with large uncertainties (Rhodes et al., 2006). However, the lithostratigraphy of the Casablanca sequence showed that the OHF Member 1 lies below formations representing a minimum of three sea-level high-stands older than MIS 15, ranging at least from MIS 17 to 21 (if the sedimentary record is complete, or embracing further isotope stages if the record is incomplete), suggesting an age for OHF Member 1 of at least 1 Ma into the Early Pleistocene (Lefèvre and Raynal, 2002; Texier et al., 2002). Biostratigraphy is in substantial agreement with an Early Pleistocene age older than that of Tighennif (Geraads et al., 2010). This study uses magnetostratigraphy and geochemistry to provide a mean age of ~ 1.3 Ma broadly between early MIS 37 and MIS 43 for ThI-L, and in doing so, it establishes the first well-constrained chronostratigraphic framework for the early Acheulean in North Africa.

A reliable chronology for ThI-L expands our knowledge of the emergence of the Acheulean in this part of the African continent and raises several questions on its origin. Due to the scarcity of reliable Early Pleistocene stratified and well-dated sites in North Africa, the timing and mode(s) of the first settlement(s) of this region are poorly understood and many aspects related to the "Out of East Africa" models remain open questions (Mohib et al., 2019). Although many archaeological investigations have been carried out in Morocco since the beginning of the nineteenth century, only a few purported pre-Acheulean sites were reported, and all are in disputable stratigraphic contexts (Mohib et al., 2019). The revision of the lithic collections referred to as the Moroccan Pebble Culture (Biberson, 1961) shows that all the materials are geofacts or younger reworked artefacts (Raynal and Texier, 1989; El Hajraoui, 1985; Texier, 1986; Raynal et al., 2002). Furthermore, the rich paleontological site of Ahl al Oughlam dated to ~ 2.5 Ma (Fig. 1) yielded neither lithic artefacts nor evidence of hominid actions on bones (Geraads et al., 1998). Similarly, pre-Acheulean Algerian lithic series have been mostly collected on surface and reworked deposits (Hugot, 1955; Alimen and Chavaillon, 1960; Ramendo, 1963; Roubet, 1967; Thomas, 1973; Heddouche, 1980; Sahnouni, 2006). The only pre-Acheulean evidence recorded from a stratigraphic context belongs to the Ain Hanech Formation (Sahnouni et al., 2018) in Algeria (Fig. 1), where the last Oldowan occurrence dates to 1.7 Ma (Parés et al., 2014). Another possible Early Pleistocene Algerian site with a similar age is Mansourah (Fig. 1), which yielded a lithic industry without LCTs (Chaid-Saoudi et al., 2006). This sporadic and low-resolution evidence, the absence of pre-Acheulean sites in Morocco, and the wide gap between the

Oldowan in Algeria and the early Acheulean of Morocco enable a discussion hinting at a local origin of the ThI-L early Acheulean.

However, although the ThI-L early Acheulean has been discovered in a reliable chronostratigraphic context, the other lithic assemblages of Morocco ascribed to the early Acheulean are from disputable stratigraphic contexts. In layer D of the S.T.I.C. Quarry (Figs 1, 2A), Biberson discovered a rich quartzite assemblage typologically like that of ThI-L and composed of various types of handaxes, cleavers, trihedrons, bifacial and multifacial cores (Biberson, 1961). Unfortunately, S.T.I.C. Quarry has been completely backfilled and it is impossible to establish the precise relationships between the two sites (Mohib et al., 2019; Raynal et al., 2017). Also, Biberson ascribed the industry from layer M of Sidi Abderrahmane Quarry (now destroyed by quarrying activity) to the early Acheulean (Figs 1, 2A) (Biberson, 1961). Nevertheless, this layer is younger than ThI-L because it actually belongs to the Member 1 of the Anfa Formation. This member is certainly older than 0.5 Ma (Mohib et al., 2019; Raynal et al., 2017) as confirmed by the age of 492 ± 57 Ka obtained from the bottom of Member 2 of the Anfa Formation on backshore sands (Rhodes et al., 2006) (Fig. 2A). The only other early Acheulean site recorded in a secure stratigraphic context in North Africa is Tighennif, in Algeria (Fig. 1). It is difficult to correlate ThI-L with Tighennif: paleomagnetic samples yielded a normal polarity but this site was regarded as problematic for paleomagnetic study (Geraads et al., 1986). Based on biochronology, Geraads et al. (1986) accepted an age close to 0.7 Ma, but it is becoming increasingly clear that this age was underestimated (Geraads, 2016). Pickford (2020) estimated its age at 1.4 ± 0.3 Ma, based upon his reassignment of the suid from this locality to *Metridiochoerus andrewsi* but his biochronological conclusion is debatable as the sample is similar to the Daka one, well-dated to 1 Ma (Gilbert and Asfaw, 2009).

From a technological perspective, LCTs from ThI-L show similar technical traits to those from Tighennif, such as the use of cobbles and *entame* flakes as blanks, the short shaping sequences, and the pointed forms (Sharon, 2011). On the other hand, the Kombewa strategy on entame flakes documented at Tighennif (Sharon, 2011) is absent at ThI-L as is a massive cleaver production. These technical innovations documented in the African Acheulean from 1 Ma in Algeria, introducing a next stage within the Acheulean, i.e. the Large Flake Acheulean (Sharon, 2010), are not present at ThI-L, an absence that is now explained thanks to the new ~ 1.3 Ma dating for the Moroccan site. These novelties appear later at Casablanca in several early Middle Pleistocene sites of the Second Acheulean (Mohib et al., 2019).

The late Early and Middle Pleistocene of the Late Neogene and Quaternary Casablanca sequence-now provided with a robust chronostratigraphic framework-will undoubtedly be called upon to play a major role in the understanding of the Acheulean emergence and its pan-African dynamics.

Materials and methods

Magnetochronology

We sampled a total of 179 stratigraphically superposed core samples in sections straddling the Oulad Hamida Formation as follows: one section in OH1 Bed 1 (8 samples), two sections in OH 1 Bed 2 (47 samples, see also below), one composed section in OH2A and OH2B (44 samples), two overlapping sections in OH3 (15 samples in section OH3-A and 13 samples in section OH3-B), one section in OH4 and GH-CCC (26 samples), and one section in OH5 (9 samples) (Fig. 5, Supplementary Table S2 for thermal demagnetization data and Supplementary Table S3 for data interpretation). Of the 47 samples taken in OH1 Bed 2, 37 samples were drilled along the south wall of the excavation trench (33.568445° N, 7.696421° W) from 4 to 314 cm from the exposed top of OH1 Bed 1, while an additional 10 samples were drilled along the north wall of the same trench from 7 to 82 cm from the exposed top of OH1 Bed 1. We also took 16 core samples in the Anfa Formation (AF2) at the site of Sidi Abderrhamane. 170 out of 179 core samples were taken in the field using a water-cooled electric drill and oriented with a magnetic compass, while the remainder 9 core samples derived from 6 hand samples taken in section OH2A and 3 hand samples in section OH4. All core samples were reduced in the laboratory to standard 10 cc paleomagnetic core samples for analyses.

The initial susceptibility of all standard 10 cc samples was measured with a KLY-2 Kappabridge (Fig. 5). A representative suite of samples has been subjected to backfield acquisition curves of isothermal remanent magnetization (IRM) up to 2.5 T and thermal demagnetization of a three component IRM using fields of 2.5 T, 0.4 T, and 0.12 T (three component IRM in Supplementary Fig. S9). A suite of rock fragments from OH1 Bed 2 (trench south wall) has been studied for S-Ratio = − IRM− 0.3 T/SIRM2.5 T, obtained by applying a saturation IRM at 2.5 T followed by an antipodal IRM at 0.3 T, and HIRM = (IRM−0.3 T + SIRM2.5 T)/2 in order to investigate the reddening of the sediment occurring along this section. S-Ratio approaching + 1 reveals the occurrence of dominant low coercivity magnetic phases (e.g. magnetite) while S-Ratio approaching − 1 high coercivity phases (e.g., hematite, goethite), while the higher the HIRM the higher the content of high coercivity phases (e.g., hematite, goethite) relative to low coercivity phases (e.g. magnetite). We also performed thermomagnetic (heating–cooling) cycles Sample Magnetometer (VSM) at ETH Zurich on selected samples from OH1 Bed 2 (Supplementary Fig. S10), and hysteresis analyses using a MicroSense EZ7 VSM at the University of Milan on samples from OH4, GHCCC, OH5, and AF2 (Supplementary Fig. S11). In addition, we carried out anisotropy of magnetic susceptibility (AMS) analyses on virtually all samples with a KLY-3 Kappabridge from which we defined the maximum (kmax), intermediate (kint), and minimum (kmin) susceptibility axes of samples and the related standard parameters of foliation F = kint/kmin, lineation L = kmax/kint, degree of anisotropy P = kmax/kmin, and shape parameter T = 2ln(kint/kmin)/ln(kmax/kmin) − 1 (Supplementary Fig. S12).

Samples for magnetostratigraphy have been thermally demagnetized in ~ 20 subsequent demagnetization steps from room temperature up to a maximum of 675 °C with an ASC furnace, and the natural remanent magnetization (NRM) measured after each demagnetization step with an AGICO JR-6 spinner magnetometer at the ALP paleomagnetics laboratory (Peveragno, Italy), except for samples from OH1 Bed 1 which were measured on a 2G Enterprises DC SQUID cryogenic magnetometer at ETH Zurich (thermal demagnetization data in Supplementary Table S2). Standard least-square analysis was used to calculate magnetic component directions from vector end-point demagnetization diagrams (Supplementary Fig. S13A–E), and standard Fisher statistics were used to analyze the mean component directions (Supplementary Fig. S14).

Geochemistry

Seventy-one sediment samples were collected from ThI-L for geochemical analyses with a vertical sampling step of five centimeters on average. These samples were analyzed by energy-dispersive X-ray fluorescence (ED-XRF) spectrometry with a Delta Innov-X spectrometer equipped with a 4-W Au-tube. Each sample was dried then ground into a fine powder, which was placed in a crystal polystyrene tube and covered with an ultrafine polyethylene film. The parameters of voltage, amperage and counting times were as follows: 10 kV, 0.2 mA, 10 s for Si, K and Ca; 15 kV, 0.2 mA, 45 s for Ti and Mn; 40 kV, 0.1 mA, 5 s for Fe; 40 kV, 0.1 mA, 30 s for Zn, Rb, Sr and Zr. The elemental concentrations were obtained using the Compton Normalization calibration method (EPA). The measurement uncertainty is lower than ± 5% for K, Ca, Ti, Mn, Fe, Rb, Sr, Zr, and between ± 5 and ± 10% for Si and Zn.

Acknowledgements

The study of ThI-L is part of the *Préhistoire de Casablanca* joint program led and supported by the *Institut National des Sciences de l’Archéologie et du Patrimoine* (INSAP) of the *Ministère de la Culture, de la Jeunesse et des Sports/Département de la Culture* of the Kingdom of Morocco, the *Ministère de l’Europe et des Affaires Étrangères* of France within the framework of the *Mission archéologique Littoral-Maroc* and the *Laboratoire d’Excellence Archimède - Programme Investir l’Avenir* ANR-11-LABX-0032-01 – through the *Origines* project. It is also financially supported by the Department of Human Evolution of the Max Planck Institute for Evolutionary Anthropology in Leipzig (Germany) and the *Région Aquitaine* through the *Origines* projects*.* Magnetostratigraphic analyses are supported by the *Ministero dell’Istruzione, dell’Università e della Ricerca* of Italy, through the project *‘Dipartimenti di Eccellenza 2018–2022’* awarded to the *Dipartimento di Scienze della Terra “A. Desio”* of the *Università di Milano*. We are grateful to Fatima-Zohra Sbihi-Alaoui, co-director of the French-

Morocco Casablanca project with Andre Debenath (1978-1989) then with Jean-Paul Raynal (1990-2010). J.-P. D thanks C. Skonieczny for valuable discussion on Saharan dust proxy records, V.A.P thanks Eliane Charrat, IMBE, for pollen preparation, and G.M thanks Ann Hirt for granting access to the ETH paleomagnetics facility.

Author contributions

D.L. and A.M. are co-directors of the French-Moroccan Casablanca program since 2016. J.-P.R., A.M. and R.G. made excavations at ThI-L. R.G., D.L. and G.M. design research and R.G. wrote the paper with contributions of all the authors. D.L., M.E.G., M.R. and J.-P.R. for stratigraphy; G.M., M.M. and S.P. for magnetostratigraphy; J.-P.D. for geochemistry; A.Z. for micromorphology; D.G. and C.D. for paleontology and taphonomy; V.A.P. for palynology; R.G., A.M., L.M. and J.-P.R. for lithic analysis; P.F. and J.-P.R. for petroarcheology; S.S-L. for OHF photogrammetry and CAD. All authors discussed and commented on the manuscript. All data are available in the main text or the supplementary materials. Request for materials should be addressed to R.G.

Chapter 9

Refining the chronology of ThI-GH interval yielding hominin remains, Thomas Quarry I, Casablanca (Morocco)

Since the chronostratigraphic framework delineated for Thomas Quarry I highlighted the presence of the Brunhes-Matuyama magnetic reversal (0.773 Ma) occurring within site ThI-GH, a further refinement of the chronology of this stratigraphic interval was fundamental to precisely locate and trace it laterally to anchor each finding to this magnetochronological marker. ThI-GH, located at a higher stratigraphic unit with respect to ThI-L (~1.3 Ma, Gallotti et al., 2021), yielded *Homo* fossils (mandibles and vertebrae) associated to faunal remains and Acheulean tools that were excavated in situ in 2008 and 2009 field campaigns. These hominin fossils document the critical period of divergence between the Middle Pleistocene archaic lineages of Western Eurasia and Africa and are now under study by comparing them with *Homo antecessor* fossils from Atapuerca (Spain).

Preliminary age estimates with OSL analyses on deposits from GH-CCC-SU 4 provided ages ranging between 391±32 ka to 420±34 (Rhodes et al., 2006), while ESR laser ablation ICP-MS performed on a hominin tooth yielded an age of 501 +89/-66 ka (Raynal et al*.* 2010). Biostratigraphic data suggested an older age attributing it to the early Middle Pleistocene (Geraads, 2002; Geraads et al., 2010; 2022).

In these circumstances additional samples were collected retrieving a total of 118 oriented core-samples every 2-3 cm from six sub-sections (termed A, B, C, D, E, G) from ThI-GH interval, while in Member OH3 section OH3A recording a normal magnetic polarity attributed to the Jaramillo subchron (0.990-1.070 Ma)

13 additional samples were collected to strengthen its presence in the general magnetostratigraphy.

Thomas Quarry I (ThI), located near Casablanca (Morocco; Fig. 1A), represents, together with the nearby and younger Sidi Abderrahmane Quarries (Raynal et al., 2023; Biberson, 1961), a key archaeological area of northwest Africa. ThI consists of the Oulad Hamida Formation (OHF; Lefèvre et Raynal, 2002; Lefèvre et al., 2021) and yielded, among other findings, early Acheulean tools at site ThI-L (Gallotti et al., 2021; Raynal, J.P., & Texier, J.P., 1989; Raynal et al., 1995) and hominin remains at site ThI-GH, this latter described hereafter. Philippe Beriro discovered in 1969 a hominin half-mandible attributed to *Homo mauritanicus* (Ennouchi, 1969). This fossil was however found out of stratigraphic context and was later supposed to derive from a cave opened in the ThI north-eastern wall (Sausse, 1975) together with other mammal fossils and lithics (Geraads et al., 1980). Systematic investigations in this cave conducted between 1994 and 2012 yielded quartzite and flint lithic artefacts as well as a rich faunal assemblage including several hominin fossils, and the term *Grotte à Hominidés* (ThI-GH) was coined (Raynal et al., 2010, 2023).

ThI-GH was carved by a marine high-stand in a cliffed shoreline comprised of Members OH1 and OH3 of the OHF and filled with Members OH4 and GH-CCC (Continental Cave Complex) of the OHF (SI-1.1) (Lefèvre et al, 2021). The infilling starts with calcirudites in a coquinoid matrix associated with plurimetric collapsed blocks preserved in the notch, onlapped by fine, grey, planar-bedded intertidal biocalcarenites (OH4-SU6; SU=Stratigraphic Unit). Upwards follow well-sorted bioclastic and quartzose sands interpreted as littoral deposits (OH4-SU5). Above follow, without any apparent disconformity, continental deposits of the GH-CCC-SU4 and 3, composed altogether of well-sorted bioclastic and quartzose reddish sands fed by the dismantlement of dunes and soils likely by runoff and wind transport. Altogether therefore, the sedimentation evolved from intertidal to continental (SI-1.1 and 1.2) and is attributed to a transgression of sea-level followed by high-stand normal regression, as discussed further below. Next follow the cross-bedded grey aeolianite sandstones of Member OH5 that, at the cave entrance, are interposed between SU3 described above and the continental deposits of SU2-1. OSL dating on quartz from OH5 provided an age range between 360 and 470 ka (Rhodes et al., 2006). SU2 is a multilayer dripstone interbedded with loose red sands, while SU1 consists of massively bedded, rubified sands with gastropod fragments and micro-fauna of Late Pleistocene age (Raynal et al. 2010).

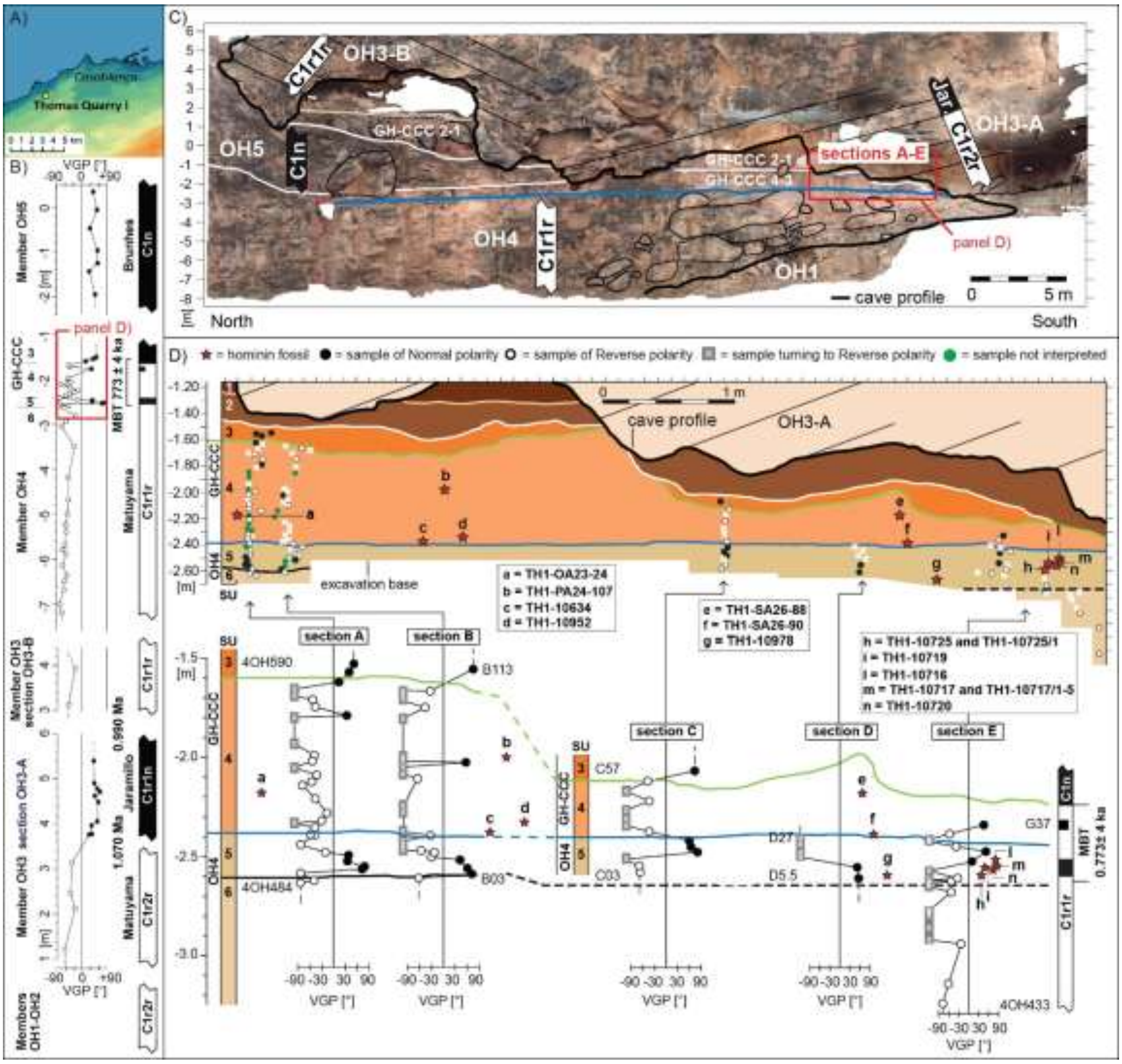

Figure 1 (A) Location map (B) Magnetostratigraphy of Members OH3A, OH3B, OH4, GH-CCC and OH5 of Gallotti et al. (2021) and this study (black bars represent normal polarity, white bars reverse polarity, VGP is Virtual Geomagnetic Pole latitude; see Fig.S1 for details). Magnetochron ages are from Channell et al., (2020). (C) Photograph of the outcrop stratigraphy with indication of magnetic polarity (Gallotti et al., 2021; this study) and lithologic members. Here we focused on sections A-E of which only section A is reported here. (D) Magnetostratigraphy of sections A-E comprised of Member OH4/SUs 6-5 and GH-CCC/SUs 4-3. MBT is the Matuyama-Brunhes Transition. The yellow stars with labels represent human remains.

SU5 and SU4 yielded lithic artefacts, a rich macro- and micro-fauna, and hominin fossils (Daujeard et al., 2016; Geraads et al., 2022; Raynal et al., 2010) (SI 1.4-1.5-1.6). SU5 yielded an adult mandible (TH1-10717), five vertebrae in connection (TH1-10717/1 to 5), two vertebrae in connection (TH1-10725/1 and 2), a child mandible (TH1-10978), and a partial femur (TH1-UA28-7). SU4 yielded six isolated teeth and a few unidentified cranial fragments. Although the precise location of the *Homo mauritanicus* half-mandible remains uncertain, sediment analysis of the matrix suggests that it is stratigraphically contemporaneous with the SU 4 and 5 hominin remains (Raynal et al., 2023). Combined Electron Spin Resonance and U-series dating directly applied to a hominid tooth from SU4 yielded an age estimate of 501+94 -76 ka (Raynal et al., 2010). OSL analyses performed on sediments collected immediately above and below the same hominin tooth yielded ages of 420 ± 34 ka and 391 ± 32 ka (Raynal et al., 2010).

Magnetostratigraphy

Gallotti et al. (2021) placed the Brunhes/Matuyama transition (773 ka; Channell et al., 2020) close to the base of GH-CCC-SU4 and, through the recognition of the Matuyama-Jaramillo-Matuyama polarity interval in Members OH4 to OH1, established an age of ~1.3 Ma for the Acheulean levels at site TH-L in OH1. Here we present new magnetostratigraphic data (Material and Methods and SI2) from 118 samples from OH3, OH4, and GH-CCC that we integrated with the 62 samples of Gallotti et al. (2021) from the same Members plus OH5 for a better definition of the Jaramillo subchron and the Brunhes/Matuyama transition (MBT) (Fig. 1B). Characteristic remanent magnetization (ChRM) component directions of samples from sections OH3-A and OH3-B yielded virtual geomagnetic pole (VGP) latitudes indicating that both the base and the top of the Jaramillo (1.07 Ma and 0.99 Ma, respectively) lie within Member OH3 (Fig. 1B). Samples from Member OH4-SU6-5 and GH-CCC-SU4-3 were taken along 5 individual sections (A–E; Fig. 1C, D). Most of these samples provided VGP latitudes of reverse magnetic polarity (or a tendency to reverse polarity visible in the demagnetization diagrams; see SI2), punctuated by a thin normal polarity excursion in Member OH4/SU5. This excursion appears laterally continuous as it was retrieved in multiple samples from three correlative sections (Fig. 2D). A reverse-to-normal polarity transition occurs in Member GH-CCC close to the SU4-3 contact, with normal polarity extending into GH-CCC-SU3 (Fig. 2D). Normal polarity then continues into younger Member OH5 (Fig. 2C).

Gallotti et al. (2021) placed a discrete, reverse-to-normal polarity MBT close to the base of GH-CCC-SU4, while our analysis from a much larger population of samples reveals a more complex scenario for the MBT occurring throughout OH4-SU6-5 and GH-CCC-SU4-3. In high sediment accumulation rate records (>15 cm/ka), the MBT is characterized by VGP excursions occurring between stable reverse (Matuyama) and stable normal (Brunhes) polarity (e.g., Channell, 2017; Haneda et al., 2020). In these records, the MBT has a mid-point at 773 ka and a transition duration of ~8ka (Channell, 2017) or ~10.8 ka (Haneda et al., 2020). We may have captured one such transitional excursions in the normal polarity interval in OH4-SU5 (Figs. 1B, D). This interpretation assumes high sediment accumulation rates for the investigated units as confirmed by sedimentological observations and an interpretation of the depositional sequence in terms of sequence stratigraphy. The intertidal biocalcarenites of OH4-SU6 and the littoral sands of OH4-SU5 are interpreted as representing the MIS20/MIS19 transgression of sea-level (starting at ~795 ka; Lisiecki and Raymo, 2005) and the following maximum flooding surface, respectively, while the ensuing continental deposits of GH-CCC-SU4-3 should be part of the subsequent regressive system tract associated with the MIS19 high-stand (~780 ka). This interpretation suggests sediment accumulation rates of 30-35 cm/ka, sufficient to capture the MBT variability. Altogether, our analysis indicates ages for the levels with hominin remains of OH4-SU5 and GH-CCC-SU4 (yellow stars in Fig. 1C, D) younger than 0.99 Ma (top of Jaramillo) and close to the MBT at a nominal age of 773 ± 4 ka (Channell, 2017). This interpretation is in agreement with biostratigraphy data but in contrast with the much younger ESR and OSL ages obtained in SU4 (see above), possibly because of loss of ESR signal after burial.

Material and methods

Magnetostratigraphy and rock magnetic properties

For magnetostratigraphy, samples were thermally demagnetized from room temperature up to a maximum of 690°C with a TD48 ASC furnace. Alternating field (AF) demagnetization up to 200mT performed on two test samples with an LDA5 AF demagnetizer resulted inadequate to resolve the magnetic remanence of the samples. After each thermal demagnetization step, the initial magnetic susceptibility was measured with a Bartington susceptibility bridge. The natural remanent magnetization (NRM) was measured on a 2G DC-SQUID cryogenic magnetometer located in a magnetically shielded room. Standard least-square analysis was used to calculate characteristic remanent magnetization (ChRM) component directions from vector end-point demagnetization diagrams, from which virtual geomagnetic pole (VGP) latitudes were derived (positive VGP values for normal polarity, negative values for reverse polarity). Great circles were used to assess qualitatively the ChRM orientation in absence of stable endpoints. The magnetic mineralogy was investigated using hysteresis experiments from -1.5T to +1.5T, low-resolution first-order reversal curves (FORCs, n=76) interpreted with FORCinel (Harrison and Feinberg, 2008), stepwise acquisition of an isothermal remanent magnetization (IRM) up to 1.5T, alternating field (AF) decay of a 1T IRM in AF peak fields from 50mT to 1.5T, and thermomagnetic decay of a 1T magnetization performed in Ar atmosphere from room temperature to 680°C. These experiments were performed with a MicroSense EZ7 Vibrating Sample Magnetometer with heating capability. Additional samples were also subjected to thermal demagnetization of a three component IRM using orthogonal fields of 1.5T, 0.4T, and 0.12T imparted with an ASC pulse magnetizer. See main text and Supplementary Information 2 for details.

Chapter 10

Discussion and Conclusions

As a whole, accurate stratigraphic reconstructions and chronologies are essential to interpret sequences bearing archeological and/or paleoanthropological sites. Unclear discovery contexts and incomplete chronostratigraphies can lead to misrepresentations of the ensuing implications. In this thesis magnetostratigraphy has provided a major contribution in dating two Acheulean stratigraphic sequences located to the antipodes of the African continent. The new magnetostratigraphic data obtained from Melka Kunture (Ethiopia) and Thomas Quarry I (Morocco) archeological areas shed new light on the debate of the Acheulean emergence in East and North Africa and also to discuss the evolution of the early Acheulean and the associated hominin fossils.

The improvement of the chronology of Melka Kunture led to an age of 1.95 (-0.025; +0.1) Ma for earliest Acheulean archeological sites GAR IVD and GOM IB as well as the earliest evidence of peopling on the Ethiopian highlands documented by archeological sites GAR IVF and GAR IVE dated to 2.02 (-0.095; +0.096) Ma and 2.00 (-0.075; +0.1) Ma. The improvement of the chronology of Thomas Quarry I provided an age of ~1.3 Ma for ThI-L, which is now the oldest well-dated Acheulean site in North Africa. Also, ThI-GH, located at Thomas Quarry I within a higher stratigraphic unit with respect to ThI-L, yielded *Homo* fossils documenting the critical period of divergence between the Middle Pleistocene archaic lineages of Western Eurasia and Africa, associated to faunal remains and Acheulean tools. This site is now dated to the Brunhes/Matuyama boundary at about 0.773 ± 0.004 Ma.

The new magnetostratigraphic data obtained provided a more accurate dating for these archeological areas. In both localities these age estimates turned out to be older compared to the available literature, and this required a thorough discussion of the archeological and paleoanthropological implications.

Regarding the Melka Kunture chronostratigraphy, the new results offered the opportunity to contextualize the modalities of the Acheulean emergence in East Africa. Two possible interpretative scenarios were discussed (Chapter 7):

I. assuming that the earliest Acheulean of Melka Kunture shared the same technical behaviors of the other East African early Acheulean sites, then it could be plausible that its origin was on the Ethiopian plateau and the innovation was produced by a single species and was spread towards the mid-lowlands as an invasive and abrupt process,

II. assuming instead that the Acheulean technical behaviors were not the same across the various East African sites, then the Acheulean was not one single entity, but several Acheuleans were conceived at different times and places, possibly emerging from variable recombinations of technical elements established in the preceding late Oldowan culture.

In order to deepen these aspects, the East African archeological and paleoanthropological records were reconsidered. It was necessary to investigate the previous Oldowan industries and then compare their technical behaviors to the early Acheulean assemblages with a well-established chronostratigraphy, such as Kokiselei 4 (1.76 Ma; West Turkana, Kenya) (Lepre et al., 2011), KGA6-A1 (~1.75 Ma; Konso-Gardula, Ethiopia) (Beyene et al., 2013), FLK West (~1.7-1.65 Ma; Olduvai Gorge, Tanzania) (Diez-Martin et al., 2015; Stanistreet et al., 2018), L3-L4 (~1.6 Ma; Melka Wakena, Ethiopia) (Hovers et al., 2021) and DAN5 (~1.5-1.6 Ma; Gona, Ethiopia) (Semaw et al., 2020).

The reconstructed record highlighted that the time interval in which the Acheulean emergence took place extends from 2.0 to 1.6 Ma, and that the presence of the Olduvai normal polarity subchron (1.770-1.925 Ma) should be considered from now on as an essential chronostratigraphic marker in this field of research.

From an archeological viewpoint, the production of LCTs represents the macroscopic novelty that marks the earliest Acheulean even though the real innovation lies in the concepts and methods for their production instead in the artefact itself. The main innovations involved mostly the manufacture of small and medium flakes produced with a large variety of methods inherited from the late Oldowan and amplified, that were not exclusive to the LCTs production. These aspects suggest that the origin of the Acheulean has its roots in the previous Oldowan culture and had multiple manifestations, meaning that the toolmakers were capable to apply several technical solutions to exploit all the available lithic resources simultaneously (Gallotti, 2018). In the case of Melka Kunture, the transition from the late Oldowan to the early Acheulean occurred as a cultural continuum (Gallotti and Mussi, 2018[b]). The comparison with the other East African archeological areas revealed a strong diversity of technical systems used in early Acheulean, giving rise to different technical expressions characterized by local differences.

Hence, there is more evidence to lean in favor of hypothesis (ii). It appears that there are several early Acheuleans in East Africa, distinguished on chronological, archeological and geographical basis. Several Acheuleans derived from local recombinations of common Oldowan background.

Also, the East African record allows to hypothesize on the relationships between lithic production and potential toolmaker(s) as several sites document the co-occurrence of hominin species in direct association with lithic artefacts. Many authors have considered the Acheulean innovation as the product of the genius of *Homo erectus* but in light of the reconstructed record (chapter 7, Fig. 2) and of hypothesis (ii) outlined above, the idea that *Homo erectus* was the only possible heroic toolmaker capable of reaching and spread the Acheulean from a point of origin as an invasive process seems to falter. If from one hand the diversity of technical innovations could be the outcome of local adaptations of the conceptual capabilities and technical skills of a single hominin, often recognized in *Homo erectus*, on the other hand, the observed hominin biological variety could also be responsible for technological diversity recorded in this period, giving rise to think that there were multiple toolmakers. Indeed, the fossil record of *Homo* *erectus* penecontemporaneous with the earliest Acheuleans is not higher than that of *Homo habilis, Homo rudolfensis* and *Paranthropus boisei*. However, the hypothesis of a link between the emergence of the Acheulean of the Ethiopian Highlands and *Homo erectus* cannot be completely ruled out as two hominin fossils attributed to *Homo* aff. *erectus* (Di Vincenzo et al. 2015; Zanolli et al. 2016; Cazenave et al. 2017; Mussi et al., 2023) are in direct association late Oldowan and early Acheulean lithic assemblages.

The chronological framework established for Melka Kunture allowed to attribute an age also to other sites documenting the continuity of the Acheulean technology through time, spanning from GAR XIIJ dated to 1.13 (-0.06; +0.05) Ma, GOM II OAM, bearing two fragmentary *Homo heildebergensis* fossils (GOM II1-576 and GOM II1-6169), now dated to 1.03±0.04 Ma and GOM II "Butchery site" dated to 0.75 (-0.1; +0.02) Ma. Unluckily, it was possible to provide only minimum ages for the two sites GOM Iγ and GOM Iδ, respectively of ~1.41 and ~1.51 Ma, for lack of chronological constraints in the stratigraphic interval hosting them. These new ages will allow a discussion on the archaeological and paleoanthropological significance of these sites in the perspective of the evolution of the Acheulean technology through time.

Considering Thomas Quarry I, the new age estimate of ~1.3 Ma based on magnetostratigraphy coupled with geochemistry makes ThI-L the oldest Acheulean site of Morocco and possibly North-West Africa. The sporadic and low-resolution evidence from North African sites such as Äin Hanech, Tighennif and Mansourah in Algeria, makes it difficult to investigate the timing and modalities of the first peopling of North Africa. The absence of Oldowan sites in Morocco, and the wide gap between the oldest Oldowan in Algeria, dated to ~1.7 Ma, and the early Acheulean of Morocco, do not allow to discuss the origin of the early Acheulean of ThI-L, but only further discoveries will clarify the emergence of the North African Acheulean in a whole pan-African perspective.

As for ThI-GH, the *Homo* fossils now dated to 0.773 ± 0.004 Ma, currently under study, document a critical period of human divergence between archaic lineages of Western Eurasia and Africa. They also show affinities with *Homo antecessor* uncovered in Atapuerca (Spain), so far considered the oldest *Homo* species in Europe. These fossils will play a major role in the comprehension of human evolution especially because this species will give rise to the evolutionary line of *Homo sapiens* in Africa and for the rarity of hominin finds between 1 and 0.6 Ma in Africa and Eurasia.

References

Amies, J. D. PhD Dissertation (The Australian National University, Research School of Earth Sciences, 2018).

Ameur, R. PhD Dissertation (Université d'Oran, 1988).

Altamura, F., Gaudzinski-Windheuser, S., Melis, R.T., Mussi, M., 2020. Reassessing hominin skills at an early middle Pleistocene hippo Butchery site: Gombore II-2 (Melka Kunture, Upper Awash Valley, Ethiopia), 2020 *Journal of Paleolithic Archeology*. 3 (2020) 1-32.

Angelucci, D. E., 2010. The recognition and description of knapped lithic artifacts in thin section. *Geoarchaeology* 25 (2010) 220-232.

Angelucci, D. E. Lithic artefacts in Archaeological Soil and Sediment Micromorphology (Nicosia, C. & Stoops, G.) 223-230 (John Wiley & Sons, 2017).

Antón, S.C., 2013. *Homo erectus* and Related Taxa. *A Companion to Paleoanthropology* (2013): 497-516.

Antón, S.C., Potts, R., Aiello, L.C., 2014. Evolution of early *Homo:* an integrated biological perspective. *Science* 345 (6192) 1236828: 1-13.

Antón, S.C., Middleton, E.R., 2023. Making meaning from fragmentary fossils: Early Homo in the Early to early Middle Pleistocene. *Journal of Human Evolution* 179 (2023) 103307.

Arroyo, A., Harmad, S., Roche, H., Tayloe, N., 2020. Searching for hidden activities: Percussive tools from the Oldowan and Acheulean of West Turkana, Kenya (2.3–1.76 Ma). *Journal of Anthropological Science* 123 (2020) 105238.

Assal, E. M., Adbel-Fattah, Z. A., El-Asmar, H. M., 2020. Facies architecture and controlling factors induced depositional model of the Quaternary carbonate eolianites in the northwestern Mediterranean coast of Egypt. *International Journal of Earth Science* 109 (2020) 1659-1682.

Baab, K.L., 2014. Defining *Homo erectus*. In: Henke, W., Tattersall, (Eds.) Handbook of paleoanthropology, 2nd ed. Heidelberg: Springer-Verlag, pp: 2189-2219.

Bardin, G., Raynal, J.P., Kieffer, G., 2004. Drainage pattern and regional morphostructure at Melka kunture (upper Awash, Ethiopia). In: Chavaillon, J., Piperno, M. (Eds.), 2004*. Studies on the Early Paleolithic site of Melka Kunture, Ethiopia.* Origines, Istituto Italiano di Preistoria e Protostoria, Florence. pp: 83-92.

Benabid, A. Flore et écosystemes du Maroc, evaluation et préservation de la biodiversité (Ibis Press, 2000).

Beyene, Y., Katoh, S., WoldeGabriel, G., Hart, W.K., Uto, K., Sudo, M., Kondo, M., Hyodo, M., Renne, P.R., Suwa, G., Asfaw, B., 2013. The characteristics and chronology of the earliest Acheulean at Konso, Ethiopia. *Proceedings of the National Acadademy of Sciences* 110 (5): 1584-1591.

Beyene, Y., Asfaw, B., Katsuhiro, S., Suwa, G., *Konso-Gardula Research Project, Vol. 2. Archaeological Collections: Background and the Early Acheulean Assemblages* (The University Museum, The University of Tokyo, Tokyo, 2015).

Biberson, P., 1961[a]. Le Paléolithique inférieur du Maroc atlantique. Publications du Service des Antiquités du Maroc 17.

Biberson, P., 1961[b]. Le cadre paléogéographique de la Préhistoire du Maroc atlantique Publications du Service des Antiquités du Maroc 16.

Blaauw, M., 2010. Methods and code for 'classical'age-modelling of radiocarbon sequences. *Quaternary geochronology* 5 (5), 512-518.

Blaauw, M., Christen, J.A., 2011. Flexible paleoclimate age-depth models using an autoregressive gamma process. *Bayesian Analyses* 6 (3), 457-474.

Blaauw, M., Christen, J.A., Bennett, K.D., Reimer, P.J., 2018. Double the dates and go for Bayes-Impacts of model choice, dating density and quality on chronologies. *Quaternary Science Reviews* 188 (2018), 58-66.

Blaauw, M., & Heegaard, E. (2012). Estimation of age-depth relationships. In: Birks, J.B., Lotter, A.F., Juggins, S., & Smol, J.P., (Eds.) *Tracking environmental change using lake sediments: data handling and numerical techniques* (Vol. 5, 2012). Springer Science & Business Media: pp. 379-413.

Blumenschine, R.J., Stanistreet, I.G., Njau, J.K., Bamford, M., Masao, F.T., Albert, R.M., Stollhofen, Andrews, P., Prassack, K.A., McHenry, L.J., Fernández-Jalvo, Y., Camlilli, E.L., Ebert, J.I., 2012. Environments and hominin activities across the FLK Peninsula during *Zinjanthropus* Times (ca. 1.84 Ma), Olduvai Gorge, Tanzania. *Journal of Human Evolution* 63 (2012): 364-383. *Journal of Human Evolution* 150 (2021) 102910.

Bonnefille, R., Melis, R.T., Mussi, M., 2018. Variability in the Mountain Environment at Melka Kunture Archeological Site, Ethiopia, During the Early Pleistocene (~1.7 Ma) and the Mid-Pleistocene Transition (0.9–0.6 Ma). In: Gallotti, R., Mussi, M., (Eds.) *The Emergence of the Acheulean in East Africa and Beyond. Contributions in Honor of Jean Chavaillon* (Springer, 2018): 93-114.

Brooke, B., 2001. The distribution of carbonate eolianite. *Earth-Science Reviews* 55 (2001) 135-164.

Bronk Ramsey, C., 2008. Deposition models for chronological records. *Quaternary Science Reviews* 27 (1-2), 42-60.

Brown, L.L., Singer, B.S., Pickens, J.C., Jicha, B.R., 2004. Paleomagnetic directions and $^{40}Ar/^{39}Ar$ ages from the Tatara-San Pedro volcanic complex, Chilean Andes: Lava record of a Matuyama-Brunhes precursor? *Journal of Geophysical Research: Solid Earth* 109 (2004) (B12).

Brown, F.H., Haileab, B., McDougall, I., 2006. Sequence of tuffs between the KBS Tuff and the Chari Tuff in the Turkana Basin, Kenya and Ethiopia. *Journal of the Geological Society of London* 163(1): 185–204.

Buggle, B., Glaser, B., Hambach, U., Gerasimenko, N., Markovic, S. 2011. An evaluation of geochemical weathering indices in loess-paleosol studies. *Quaternary International* 240 (2011) 12-21.

Campbell, I.D., 1996. Power function for interpolating dates in recent sediment. *Journal of Paleolimnology* 15 (1996): 107-110.

Cande, S.C. and Kent, D.V., 1992. A new geomagnetic polarity time scale for the Late Cretaceous and Cenozoic. Journal of Geophysical Research: Solid Earth 97(B10), 13917-13951.

Chaid-Saoudi, Y., Geraads, D., Raynal, J.-P. 2006. The fauna and associated artefacts from the Lower Pleistocene site of Mansourah (Constantine, Algeria). *C. R. Palevol* 5 (2006): 963-971.

Channell, J.E.T., Mazaud, A., Sullivan, P., Turner, S., Raymo, E., 2002. Geomagnetic excursions and paleointensities in the Matuyama Chron at Ocean Drilling Program Sites 983 and 984 (Iceland Basin). *Journal of Geophysical Research* 107 (2002): 1-14.

Channell, J.E.T., Singer, B.S., Jicha, B.R., 2020. Timing of Quaternary geomagnetic reversals and excursions in volcanic and sedimentary archives. *Quaternary Science Reviews* 228 (2020) 106114.

Chavaillon, J., 1979. Stratigraphie du site archéologique de Melka-Kunturé (Ethiopie). *Bulletin de la Société Géologique de France* 7 (I). XXI, n°3, pp: 227-232.

Chavaillon, J., Coppens, Y., 1986. Nouvelle decouverte d'Homo erectus à Melka-Kunturé. *Comptes Rendus de l'Académie des Science*, Paris. 303 (II), pp: 99-104.

Chavaillon, J., Piperno, M., 2004. Studies on the Early Paleolithic Site of Melka Kunture, Ethiopia, Origines, Istituto Italiano di Preistoria e Protostoria. Florence.

Chavaillon, J., Berthelet, A., 2004. The archaeological sites of Melka Kunture. In: Chavaillon, J., Piperno, M. (Eds.), *Studies on the Early Paleolithic site of Melka Kunture, Ethiopia.* Istituto Italiano di Preistoria e Protostoria, Florence, pp: 25-80.

Chavaillon, J., Brahimi, C., Coppens, Y., 1974. Première découverte d'Hominidé dans l'un des sites acheuléens de Melka-Kunture (Ethiopie). *Comptes Rendus de l'Académie des Science,* Paris. 278, pp: 3299-3302.

Chavaillon, J., Chavaillon, N., Hours, F., Piperno, M., 1979. From the Oldowan to the Middle Stone Age at Melka-Kunture (Ethiopia). Understanding cultural changes. *Quaternaria. Storia Naturale e Culturale del Quaternario,* Roma. 21 (1979), pp: 87-114.

Chevrier, B., PhD dissertation (Université Paris Ouest Nanterre, 2012).

Condemi, S., 2004. The Garba IV E mandible. In: Chavaillon, J., Piperno, M. (Eds.), *Studies of the Early Paleolithic site of Melka Kunture, Ethiopia.* Istituto Italiano di Preistoria e Protostoria, Florence, pp: 687-701.

Courty, M.A. Microfacies analysis assisting archaeological stratigraphy in Earth sciences and archaeology (eds. Goldberg, P., Holliday, V. T. & Ferring C.R.) 205–239 (Kluwer Academic/Plenum Publishers, 2001).

Courty, M.A., Goldberg, P., Macphail, R.I. Soils and Micromorphology in Archaeology (Cambridge University Press, 1989).

Cremaschi, M., Trombino, L., Zerboni, A. Palaeosoils and relict soils, a systematic review. In: Stoops, G., Marcelino, V., Mees, F., (Eds.) *Interpretation of micromorphological features of soils and regoliths* - Revised Edition (Elsevier, 2018): 863-894.

Cressier, P. Ph.D. Dissertation (L'Université Louis Pasteur, 1980).

Cronquist, A. An integrated system of classification of flowering plants (Columbia University Press, 1981).

Cugny, C., Mazier, F., Galop, D., 2010. Modern and fossil non-pollen palynomorphs from the Basque mountains (western Pyrenees, France): the use of coprophilous fungi to reconstruct pastoral activity. *Vegetation History and Archaeobotany*. 19 (2010) 391-408.

Day, R., Fuller, M., Schmidt, V.A., 1977. Hysteresis properties of titanomagnetites: grain-size and compositional dependence. *Physics of the Earth and Planetary Interiors* 13 (4): 260-267.

De Boer, B., van de Wal, R.S.W., Bintanja, R., Lourens, L. J., Tuenter, E., 2010. Cenozoic global ice-volume and temperature simulations with 1-D ice-sheet models forced by benthic $\delta^{18}O$ records. *Annals of Glaciology* 51 (2010): 23-33.

de la Torre, I., 2011. The Early Stone Age lithic assemblages of Gadeb (Ethiopia) and the Developed Oldowan/early Acheulean in East Africa. *Journal of Human Evolution* 60 (2011): 768-812.

de la Torre, I., Mora, R., *Technological Strategies in the Lower Pleistocene at Olduvai Beds I & II* (ERAUL, 112, Liège, Belgium, 2005).

de la Torre, I., Mora, R. 2009. Remarks on the Current Theoretical and Methodological Approaches to the Study of Early Technological Strategies in Eastern Africa. In: Hovers, E., Braun, D.R. (Eds.) *Interdisciplinary Approaches to the Oldowan. Vertebrate Paleobiology and Paleoanthropology.* Springer, Dordrecht.

de la Torre, I., 2016. The origins of the Acheulean: past and present perspectives on a major transition in human evolution. *Philosophical Transactions* 371 (2016) 20150245.

de la Torre, I., Mora, R., 2018. Oldowan technological behaviour at HWK EE (Olduvai Gorge, Tanzania). *Journal of Human Evolution* 120 (2018): 236-273.

de la Torre, I., Benito-Calvo, A., Martín-Ramos, C., McHenry, L.J., Mora, R., Njau, J.K., Pante, M.C., Stanistreet, I.G., Stollhofen, H., 2021. New excavations in the MNK Skull site, and the last appearance of the Oldowan and Homo habilis at Olduvai Gorge, Tanzania. *Journal of Anthropological Archaeology* 61 (2021) 101255.

de Mortillet, G., 1872. Classification des diverses périodes de l'âge de la pierre. *Revue d'Anthropologie* 1 (1872): 432-435.

Deino, A., Dominguez-Rodrigo, M., Luque, L., 2006. $^{40}Ar/^{39}Ar$ Dating of the Pleistocene Peninj Group, Lake Natron, Tanzania. *Eos Trans AGU* 87(52), Abstracts C1771.

Degeai, J.-P., Devillers, B., Blanchemanche, P., Dezileau, L., Oueslati, H., Tillier, M., Bohbot, H., 2017. Fluvial response to the last Holocene rapid climate change in the Northwestern Mediterranean coastlands. *Global and Planetary Change* 152 (2017) 176-186.

Degeai, J.-P., Villa, V., Chaussé, C., Pereira, A., Nomade, S., Aureli, D., Pagli, M., Nicoud, E., 2018. Chemical weathering of palaeosols from the Lower Palaeolithic site of Valle Giumentina, central Italy. *Quaternary Science Reviews* 183 (2018) 88-109.

Degeai, J.-P., Bertoncello, F., Vacchi, M., Augustin, L., da Moya, A., Ardito, L., Devillers, B., 2020. A new interpolation method to measure delta evolution and sediment flux: Application to the late Holocene coastal plain of the Argens River in the western Mediterranean. *Marine Geology* 424 (2020) 106159.

Delagnes, A., Roche, H., 2005. Late Pliocene knapping skills: The case of Lokalalei 2C, West Turkana, Kenya. *Journal of Human Evolution* 48 (2005): 435-472.

Diez-Martín, F., Sánchez-Yustos, P., Dominguez-Rodrigo, M., Mabulla, A.Z.P., Bunn, H.T., Ashley, G.M., Barba, R., Baquedano, E., 2010. New insights into hominin lithic activities at FLK North Bed I (Olduvai Gorge, Tanzania). *Quaternary Research* 74 (2010): 376-387.

Diez-Martín. F., Sánchez-Yustos, P., Uribellarea, D., Baquedano, E., Mark, D.F., Mabulla, A., Fraile, C., Duque, J., Díaz, I., Pérez-González, A., Yravedra, J., Egeland, C.P., Organista, E., Dominguez-Rodrigo, M., 2015. The Origin of The Acheulean: The 1.7 Million-Year-Old Site of FLK West, Olduvai Gorge (Tanzania). *Scientific Reports* 5 (2016) 17839.

Diez-Martín, F. Wynn, T., Sánchez-Yustos, P., Duque, J., Fraile, C., de Francisco, S., Uribellarea, D., Mabulla, A., Baquedano, E., Domínguez-Rodrigo, M., 2019. A faltering origin for the Acheulean? Technological and cognitive implications from FLK West (Olduvai Gorge, Tanzania). *Quaternary International* 526 (2019): 49-66.

Diez-Martín, F., Panera, J., Maíllo-Fernández, J.M., Santonja, M., Sánchez-Yustos, P., Pérez-González, A., Duque, J., Rubio, S., Marín, J., Fraile, C., Mabulla, A., Baquedano, E., Domínguez-Rodrigo, M., 2022. The evolution of stone tool technology at Olduvai Gorge (Tanzania): Contributions from the Olduvai Paleoanthropology and Paleoecology Project. *L'Anthropologie* 126 (2023) 103000.

Di Vincenzo, F., Rodriguez, L., Carretero, J.M., Collina, C., Geraads, D., Piperno, M., Manzi, G., 2015. The massive fossil humerus from the Oldowan horizon of Gombore I, Melka kunture (Ethiopia, >1.39 Ma). *Quaternary Science Reviews*. 122 (2015) 207-221.

Domínguez-Rodrigo, M., Barba, R., Egeland, C.P. *Deconstructing Olduvai. A taphonomic study of the Bed I sites.* Springer, New York, 2007.

Domínguez-Rodrigo, M., Mabulla, A.Z.P., Bunn, H.T., Diez-Martín, F., Baquedano, E., Barboni, D., Barba, R., Domínguez-Solera, S., Sánchez, P., Ashley, G.M., Yravedra, J., 2010. Disentangling hominin and carnivore activities near a spring at FLK North (Olduvai Gorge, Tanzania). *Quaternary Research* 74 (2010): 363-375.

Domínguez-Rodrigo, M., Baquedano, E., 2018. Distinguishing Butchery Cut Marks from Crocodile Bite Marks through Machine Learning Methods. *Scientific Reports* 8 (2018): 1-8.

Duke, H., Feibel, C., Harmand, S., 2021. Before the Acheulean: The emergence of bifacial shaping at Kokiselei 6 (1.8 Ma), West Turkana, Kenya. *Journal of Human Evolution* 159 (2021) 103061.

Dunlop, D.J., 2002. Theory and application of the Day plot (Mrs/Ms versus Hcr/Hc). Theoretical curves and tests using titanomagnetite data. *Journal of Geophysical Research: Solid Earth* 107(B3), EPM-4.

Durand, N., Monger, H. C., Canti, M. G., Verrecchia, E. P. Calcium carbonate features. In: Stoops, G., Marcelino, V., Mees, F., (Eds.) *Interpretation of micromorphological features of soils and regoliths - Revised Edition*. Elsevier (2018) pp: 205-258.

Dunlop, D.J., Özdemir, Ö., 1997. Rock Magnetism: Fundamentals and Frontiers. Cambridge University Press, Cambridge, UK.

Duval, M., Sahnouni, M., Parés, J.M., va der Made, J., Abdessadok, S., Harichane, Z., Chelli Cheheb, R., Boulaghraif, K., Pérez-González, A. 2021. The Plio-Pleistocene sequence of Oued Boucherit (Algeria): A unique chronologically-constrained archaeological and palaeontological record in North Africa. *Quaternary Science Reviews* 271 (2021) 107116.

Duval, M., Sahnouni, M., Parés, J.M., Zhao, J.X., Grün, R., Abdessadok, S., Pérez-González, A., Derradji, A., Harichane, Z., Mazouni, N., Boulaghraied, Chelli Cheheb, R., van der Made, J. 2023. On the age of Ain Hanech Oldowan locality (Algeria): First numerical dating results. *Journal of Human Evolution* 180 (2023) 103371.

El Kadiri, K., de Galdeano, C.S., Pedrera, A., Chalouan, A., Galindo-Zaldívar, J., Julià, R., Akil, M., Hlila, R., Ahmamou, M., 2010. Eustatic and tectonic controls on Quaternary Ras Leona marine terraces (Strait of Gibraltar, northern Morocco). *Quaternary Research* 74 (2010) 277-288.

El Graoui, M. PhD dissertation (Université de Bordeaux 1, 1994).

Emberger, L. Les arbres du Maroc et comment les reconnaître (Larose, 1938).

Ennouchi, E., 1969. Découverte d'un Pithécanthropien au Maroc. *Comptes rendus de l'Académie des Sciences*, Paris, 269, série D, 769-771(1969).

Fairbanks, R.G., 1989. A 17,000-year glacio-eustatic sea level record: influence of glacial melting rates on the Younger Dryas event and deep-ocean circulation. *Nature* 342 (1989) 637-642.

Feibel, C.S., Brown, F.H., McDougall, I., 1989. Stratigraphic context of fossil hominids from the Omo group deposits: Northern Turkana Basin, Kenya and Ethiopia. *American Journal of Physical Anthropology* 78 (4): 595-622.

Feibel, C.S., Lepre, C.J., Quinn, R.L., 2009. Stratigraphy, correlation, and age estimates for fossils from Area 123, Koobi Fora. *Journal of Human Evolution* 57 (2009): 112-122.

Fisher, R., 1953. Dispersion on a sphere. *Proceedings of the Royal Society of London* A217, 295-305.

Foley, R., 1997. Humans before Humanity: An Evolutionary Perspective. Wiley-Blackwell, Oxford.

Galbraith, R.F., Roberts, R.G., 2012. Statistical aspects of equivalent dose and error calculation and display in OSL dating: An overview and some recommendations. *Quaternary Geochronology* 11 (2012): 1-27.

Gallotti, R., Collina, C., Raynal, J.-P., Kieffer, G., Geraads, D., Piperno, M., 2010. The early Middle Pleistocene site of Gombore II (Melka Kunture, Upper Awash, Ethiopia) and the issue of Acheulean bifacial shaping strategies. *African Archeological Review* 27 (2010): 291-322.

Gallotti, R., 2013. An older origin for the Acheulean at Melka Kunture (Upper Awash, Ethiopia): techno-economic behaviors at Garba IVD. *Journal of Human Evolution* 65 (5): 594-620.

Gallotti, R., Mussi, M., 2015. The Unknown Oldowan: ~1.7-Million-Year-Old Standardized Obsidian Small Tools from Garba IV, Melka Kunture, Ethiopia. *PLoS ONE* 10(12): e0145101.

Gallotti, R., Mussi, M., 2017. Two acheuleans, two humankinds: from 1.5 to 0.85 Ma at Melka Kunture (Upper Awash, Ethiopian highlands). *Journal of Anthropological Sciences*. 95 (2017): 1-46.

Gallotti, R., 2018. Before the Acheulean in East Africa: An Overview of the Oldowan Lithic Assemblages. In: Gallotti, R., Mussi, M., (Eds.) *The Emergence of the Acheulean in East Africa and Beyond. Contributions in Honor of Jean Chavaillon*. (Springer, New York) pp: 13-32.

Gallotti, R., Mussi, M., 2018[a]. The Emergence of the Acheulean in East Africa: Historical Perspectives and Current Issues. In: Gallotti, R., Mussi, M. (Eds.), *The Emergence of the Acheulean in East Africa and Beyond. Contributions in Honor of Jean Chavaillon.* (Springer, New York) pp: 1-12.

Gallotti, R., Mussi, M., 2018[b]. Before, During, and After the Early Acheulean at Melka Kunture (upper Awash, Ethiopia): A Techno-economic Comparative Analysis. In: Gallotti, R., Mussi, M. (Eds.), *The Emergence of the Acheulean in East Africa and Beyond, Contributions in Honor of Jean Chavaillon*. (Springer, New York) pp: 53-92.
Gallotti, R., Muttoni, G., Lefèvre, D., Degeai, J.-P., Geraads, D., Zerboni, A., Andrieu-Ponel, V., Maron, M., Perini, S., El Graoui, M., Sanz-Laliberté, S., Daujeard, C., Fernandes, P., Rué, M.,

Magoga, L., Mohib, A., Raynal, J.-P., 2021. First high resolution chronostratigraphy for the early North African Acheulean at Casablanca (Morocco). *Scientific Reports* 11 (2021) 15340.

Gallotti, R., 2022. *Les Acheuléens africains. Stratégies techno-économiques au Pléistocène inférieur et au début du Pléistocène moyen au Maghreb.* Habilitation à diriger des recherches en Sciences humaines – Université Paul Valéry Montpellier 3.

Gallotti, R., Raynal, J.-P., Mohib, A., Fernandes, P., Magoga, L., El Graoui, M., Rué, M., Muttoni, G., Lefèvre, D., 2022. Early North African Acheulean techno-economic systems at Thomas Quarry I-L1 (Casablanca, Morocco). *Journal of Anthropological Sciences* 101 (2023).

Gallotti, R., Muttoni, G., Perini, S., Raynal, J.-P., 2023. Comment on 'EarlyHomo erectus lived at high altitudes and produced both Oldowan and Acheulean tools' by Mussi et al. (2023). *eLetter*: https://www.science.org/doi/10.1126/science.add9115

Gee, J.S., Kent, D.V., 2007. Source of oceanic magnetic anomalies and geomagnetic polarity timescale. *Treatise on Geophysics,* vol. 5: 455-507.

Geraads, D., 1980. La faune des sites à "Homo erectus" des carriers Thomas (Casablanca, Maroc). *Quaternaria* 22 (1980): 65-94.

Geraads, D., 1981. Bovidae et Giraffidae (Artiodactyla, Mammalia) du Pléistocène de Ternifine (Algérie). *Bulletin du Muséum national d'histoire naturele.* 3 (1981): 47-86.

Geraads, D., Hublin, J.-J., Jaeger, J.-J., Tong, H., Sen, S., Toubeau, P., 1986. The Pleistocene Hominid site of Ternifine, Algeria: new results on the environment, age and human industries. *Quaternary Research* 25 (1986): 380-386.

Geraads, D., 1998. Biogeography of Miocene-Pliocene circum-mediterranean rodents: a revision based upon factor analysis and parsimony analysis of endemicity. *Palaeogeography Palaeoclimatology Palaeoecology* 137 (1998): 273-288.

Geraads, D., 2002. Plio-Pleistocene mammalian biostratigraphy of Atlantic Morocco. *Quaternaire* 13 (2002): 43-53.

Geraads, D., Alemseged, Z., Reed, D., Wynn, J., Roman, D. C., 2004. The Pleistocene fauna (other than Primates) from Asbole, lower Awash Valley, Ethiopia, and its environmental and biochronological implications. *Geobios* 37 (2004): 697-718.

Geraads, D., Raynal, J.-P., Eisenmann, V., 2006. The earliest human occupation of North Africa: a reply to Sahnouni et al., (2002). *Journal of Human Evolution* 46 (2006): 751-761.

Geraads, D. Biogeographic relationships of Pliocene and Pleistocene North-western African Mammals. *Quaternary International* 212 (2010): 159-168.

Geraads, D., 2010. Biochronologie mammalienne du Quaternaire du Maroc atlantique, dans son cadre regional. *L'Anthropologie* 114 (2010): 324-340.

Geraads, D. Pleistocene Carnivora (Mammalia) from Tighennif (Ternifine), Algeria. *Geobios* 49 (2016): 445-458.

Gilbert, H., Asfaw, B., Homo erectus: Pleistocene Evidence from the Middle Awash, Ethiopia. (University of California Press, 2009) pp: 231-260.

Goldberg, P., Macphail, R. I. Practical and theoretical geoarchaeology (Blackwell Publishing, 2006).

Goldberg, P., Berna, F, 2010. Micromorphology and context. *Quaternary International* 214 (2010): 56-62.

Gossa, T., Asrat, A., Hovers, A., Tholt, A.J., Renne, P.R., 2024. Claims for 1.9-2.0 Ma old early Acheulian and Oldowan occupations at Melka Kunture are not supported by a robust age model. Comment on “Chronology of the earliest peopling of the Ethiopian highlands at Melka Kunture pre-dating the 1.925 Ma base of the Olduvai subchron” by Muttoni et al. (2023), *Quaternary Science Reviews* 319, 108330.

Gossa, T., Hovers, E., 2022. Continuity and change in lithic techno-economy of the early Acheulian on the Ethiopian highland: A case study from locality MW2; the Melka Wakena site-complex. *PLoS ONE* 17(12): e0277029.

Gossa, T., PhD dissertation (Hebrew University of Jerusalem, Jerusalem, 2020).

Gossa, T., Asrat, A., Hovers, E., Tholt, A.J., Renne, P.R., 2024. Claims for 1.9-2.0 Ma old early Acheulian and Oldowan occupations at Melka Kunture are not supported by a robust age model. Comment on ‘Chronology of the earliest peopling of the Ethiopian highlands at Melka Kunture pre-dating the 1.925 Ma base of the Olduvai subchron’ by Muttoni et al. (2023). *Quaternary Science Reviews 319* (2023) 108330.

Gradstein, F.M., Ogg, J.G., Schmitz, M., Ogg, G., 2021. The Geologic Time Scale 2020. Elsevier Science.

Grant, K.M., Rohling E.J., Westerhold, T., Zabel, M., Heslop, D., Konijnendijk, T., Lourens, L., 2017. A 3 million year index for North African humidity/aridity and the implication of potential pan-African Humid periods. *Quaternary Science Reviews* 171 (2017): 100-118.

Griffin, W.L., GLITTER: data reduction software for laser ablation ICP-MS. In: Sylvestor, P., (Eds.) *Laser Ablation ICP-MS in the Earth Sciences: Current practices and outstanding issues*. (Mineralogical Association of Canada, 40, 2008) pp: 308-311.

Grün, R., 1989. Electron spin resonance (ESR) dating. *Quaternary International* 1 (1989): 65-109.

Guilloré, P. Méthode de fabrication mécanique et en série des lames minces (Document du département des sols de l’I.N.A. Paris-Grignon, 1980).

Hammer, Ø., Harper, D.A.T., Ryan, P.D., 2001. Past: paleontological statistics software package for education and data analysis. *Palaeontologia Electronica* 4 (2001).

Hammond, A.S., Mavuso, S.S., Biernat, M., Braun, D.R., Jinnah, Z., Kuo, S., Melaku, S., Wemanya, S.N., Ndiema, E.K., Patterson, D.B., Uno, K.T., Palcu, D.V. 2021. New hominin remains and revised context from the earliest Homo erectus locality in East Turkana, Kenya. *Nature Communicattions* 12 (2021): 1939.

Harmand, S., Raw materials and techno-economic behaviors at Oldowan and Acheulean sites, in *Lithic Materials and Paleolithic Societies.* eds Adams B, Blades BS (Wiley-Blackwell, New York, 2012): 3-11.

Harmand, S., Lewis, J. E., Feibel, C. S., Lepre, C. J., Prat, S., Lenoble, A., Boës, X., Quinn, R.L., Brenet, M., Arroyo, A., Taylor, N., Clément, S., Daver, G., Brugal, J.-P., Leakey, L., Mortlock, R.A., Wright, J.D., Lokorodi, S., Kirwa, C., Kent, D.V., Roche, H. (2015). 3.3-million-year-old stone tools from Lomekwi 3, West Turkana, Kenya. *Nature* 521(7552): 310-315.

Harrison, R.J., Feinberg, J.M., 2008. FORCinel: An improved algorithm for calculating first-order reversal curve distributions using locally weighted regression smoothing, *Geochemistry Geophysics Geosystems* 9 (2008) Q05016.

Hartl, P., Tauxe, L., 1996. A precursor to the Matuyama/Brunhes transition-field instability as recorded in pelagic sediments, *Earth and Planetary Science Letters* 138 (1-4): 121-135.

Haslett, J., Parnell, A., 2008. A simple monotone process with application to radiocarbon-dated depth chronologies. *Journal of the Royal Statistical Society Series C: Applied Statistics* 57 (4): 399-418.

Hearty, P. J., 2003. Stratigraphy and timing of eolianite deposition on Rottnest Island, Western Australia. *Quaternary Research* 60 (2003): 211-222.

Hoare, S., Brink, J.S., Herries, A.I.R., Mark, D.F., Morgan, L.E., Onjala, I., Rucina, S.M., Stanistreet, I.G., Stollhofen, H., Gowlett, J.A.J., 2021. Geochronology of a long Pleistocene sequence at Kilombe volcano, Kenya: from the Oldowan to Middle Stone Age. *Journal of Archaeological Science* 125 (2021) 105273.

Hosek, J., Hambach, U., Lisá, L., Grygar, T.M., Horáĉek, I., Meszner, S., Knésl, I., 2015. An integrated rock-magnetic and geochemical approach to loess/paleosol sequences from Bohemia and Moravia (Czech Republic): Implications for the Upper Pleistocene paleoenvironment in central Europe. *Palaeogeography Palaeoclimatology Palaeoecology* 418 (2015): 344-358.

Hovers, E., Gossa, T., Asrat, A., Niespolo, E.M., Resom, A., Renne, P.R., Ekshtain, R., Herzlinger, G., Ketema, N., Martinez-Navarro, B., 2021. The expansion of the Acheulian to the Southeastern Ethiopian Highlands: Insights from the new early Pleistocene site-complex of Melka Wakena. *Quaternary Science Reviews* 253 (2021) 106763.

Inizan, M.-L., Reduron-Ballinger, M., Roche, H., Tixier, J., 1999. Technology and Terminology of Knapped Stone. Nanterre: C.R.E.P., 1999 (Préhistoire de la Pierre Taillée; 5).

Isaac, G., Curtis, G., 1974 Age of early Acheulian industries from the Peninj Group, Tanzania. *Nature* 249 (1974): 624-627.

Jarosewich, E., Nelen, J.A., Norberg, J.A., 1980. Reference Samples for Electron Microprobe Analysis. *Geostandards Newsletter* 4(1980): 43-47.

Jin, C., Liu, Q., Larrasoaña, J.C., 2012, A precursor to the Matuyama–Brunhes reversal in Chinese loess and its palaeomagnetic and stratigraphic significance, *Geophysical Journal International* 190 (2), (2012): 829-842.

Jochum, K.P., Nohl, U., Herwig, K., Lammel. E., Stoll., B., Hofmann, W., 2005 GeoReM: a new geochemical database for reference materials and isotopic standards. *Geostandards and Geoanalytical Research* 29 (3): 333-338.

Joordens, J.C.A., Dupont-Nivet, G., Feibel, C.S., Spoor, F., Sier, M.J., van der Lubbe, J.H.J.L., Kellberg Nielsen, T., Knul, M.V., Daviers, G.R., Vonhof, H.B., 2013. Improved age control on early Homo fossils from the Upper Burgi Member at Koobi Fora, Kenya. *Journal of Human Evolution* 65 (2013): 731-745.

Karkanas, P., Goldberg, P. Phosphatic features. In: Stoops, G., Marcelino, V., Mees, F., (Eds.) *Interpretation of Micromorphological Features of Soils and Regoliths* (Elsevier, 2nd ed. 2018) pp: 323-346.

Katoh, S., Nagaoka, S., WoldeGabriel, G., Renne, P.R., Snow, M.G., Beyene, Y., Suwa, G. 2000. Chronostratigraphy and correlation of the Plio-Pleistocene tephra layers of the Konso Formation, southern main Ethiopia rift, Ethiopia. *Quaternary Science Reviews* 19 (13) :1305-1317.

Kelley, S., 2002. K-Ar and Ar-Ar dating. *Reviews in Mineraolgy and Geochemistry* 47 (2002) 1: 785-818.

Kieffer, G., Raynal, J.P., Bardin, G., 2002. Cadre structural et volcanologique des sites du Paléolithique ancient de Melka Kunture (Awash, Ethiopie): premiers résultats. *Les dossiers de l'Archéologie*, Goudet, France, 2 (2002): 77-92.

Kieffer, G., Raynal, J.P., Bardin, G., 2004. Volcanic markers in coarse alluvium at Melka Kunture (Upper Awash, Ethiopia). In: Chavaillon, J., Piperno, M. (Eds.), 2004. *Studies on the Early Paleolithic site of Melka Kunture, Etiopia.* Origines, Istituto Italiano di Preistoria e Protostoria, Florence, pp: 93-101.

Kirshvink, J.L., 1980. The least-squares line and plane and the analysis of palaeomagnetic data. *Geophysical Journal International* 62 (1980) 699-718.

Krauss, L., Zens, J., Zeeden, C., Schulte, P., Eckmeier, E., Lehmkuhl, F., 2016. A Multi-Proxy Analysis of two Loess-Paleosol Sequences in the Northern Harz Foreland, Germany. *Palaeogeography Palaeoclimatology Palaeoecology* 461 (2016): 401-417.

Kruiver, P.P., Dekkers, M.J., Heslop, D., 2001. Quantification of magnetic coercivity componenst by the analysis of acquisition curves of isothermal remanent magnetisation, *Earth and Planetary Science Letters* 189 (2001): 269-276.

Kuman, K., 2019. Oldowan Industrial Complex. In: Smith, C. (eds.), Encyclopedia of Global Archaeology, Springer, pp: 5560-5570.

Lacourse, T., Gajewski, K., 2020. Current practices in building and reporting age-depth models. *Quaternary Research* 96 (2020): 28-38.

Langereis, C.G., Krijgsman, W., Muttoni, G. and Menning, M., 2010. Magnetostratigraphy-concepts, definitions, and applications. Newsletters in Stratigraphy 43 (3), 207.

Larrasoana, J. C., Roberts, A. P., Rohling, E. J., Winklhofer, M., Wehausen, R. 2003. Three million years of monsoon variability over the northern Sahara. Clim. Dyn. 21 (2003): 689-698.

Le Bas, M.L., Maitre, R.L., Streckeisen, A., Zanettin, B., IUGS Subcommission on the Systematics of Igneous Rocks (1986) A chemical classification of volcanic rocks based on the total alkali-silica diagram. *Journal of petrology* 27 (3): 745-750.

Le Cabec, A., Colard, T., Charabidze, D., Chaussain, C., Di Carlo, G., Gaudzinski-Windheuser, S., Hublin, J.-J., Melis, R.T., Pioli, L., Ramirez-Rozzi, F., Mussi, M., 2021. Insights into the palaeobiology of an early *Homo* infant: multidisciplinary investigation of the GAR IVE hemi-mandible, Melka Kunture, Ethiopia. *Scientific Reports* (2021) 11:23087.

Leakey, L.S.B., 1934. The Olduvai Cultural Sequence. *Proceedings of the 1st Congress of Prehistoric and Protohistoric Sciences*, London 1932, pp: 73-74.

Leakey, L.S.B., 1936. Stone Age Africa: An Outline of Prehistory in Africa. Oxford University Press, London.

Leakey, M.D., 1971. *Olduvai Gorge. Volume 3. Excavations in Bed I and II, 1960-1963* (Cambridge Univ Press, Cambridge, United Kingdom, 1971).

Leakey, M.D., 1975. Cultural Patterns in the Olduvai Sequence In: Butzer, K.W., Isaac, G.L., (Eds.) *After the Australopithecines. Stratigraphy, Ecology, and Cultural Change in the Middle Pleistocene.* (Mouton, Chicago, 1975): 477-493.

Leakey, R.E., Walker, A.C., 1985. Further hominids from the Plio-Pleistocene of Koobi Fora, Kenya. *Journal of Physical Anthropology* 67 (1985): 135-163.

Lecointre, G., 1952. Recherches sur le Néogène et le Quaternaire marins de la côte atlantique du Maroc. *Mémoires du Service Géologique du Maroc*, 99 (1952).

Lefèvre, D., Raynal, J.-P., 2002. Les formations plio-pléistocènes de Casablanca et la chronostratigraphie du Quaternaire marin du Maroc revisitées. *Quaternaire* 13 (2002): 9-21.

Lefèvre, D., Raynal, J.-P., El Graoui, M. Le Quaternaire d'Oulad Hamida in Préhistoire de Casablanca. I - La grotte des Rhinocéros (fouilles 1991 et 1996). Eds. Raynal, J.-P., Mohib, A. (Institut National des Sciences de l'Archéologie et du Patrimoine, VESAM volume VI, 2016) pp: 45-59.

Lefèvre, D., El Graoui, M., Geraads, D., Rué, M., Mohib, A., Raynal, J.-P. 2021. Les paléolittoraux plio-pléistocènes de Casablanca, cadre chronostratigraphique et paléogéographique de la Préhistoire ancienne du Maroc. *Bulletin d'Archéologie Marocaine* 26 (2021): 39-70.

Lepre C.J., Roche, H., Kent, D.V., Harmand, S., Quinn, R.L., Brugal, J.-P., Texier, P.-J., Lenoble, A., Feibel, C.S., 2011. An earlier origin for the Acheulian. *Nature* 477 (7362): 82-85.

Lepre, C.J., Kent, D.V., 2015. Chronostratigraphy of KNM-ER 3733 and other Area 104 hominins from Koobi Fora. *Journal of Human Evolution* 86 (2015): 99-111.

Li, R., Qiao, P., Cui, Y., Zhang, D., Liu, X., Shao, L., 2018. Composition and diagenesis of Pleistocene aeolianites at Shidao, Xisha Islands: Implications for palaeoceanography and palaeoclimate during the last glacial period. *Palaeogeography Palaeoclimatology Palaeoecology* 490 (2018): 604-616.

Lisiecki, L.E., Raymo, M.E., 2005. A Pliocene-Pleistocene stack of 57 globally distributed benthic $\delta^{18}O$ records. *Paleoceanography* 20, PA1003 (2005)

Lotter, M.G., Kuman, K., 2018.The Acheulean in South Africa, with announcement of a new site (Penhill Farm) in the lower Sundays River Valley, Eastern Cape Province, South Africa. *Quaternary International* 480 (2018): 43-65.

Lougheed, B.C., Obrochta, S.P., 2019. A rapid, deterministic age-depth modeling routine for geological sequences with inherent depth uncertainty. *Paleoceanography and Paleoclimatology* 34 (2019): 122-133.

Lourens, L., Hilgen, F., Shackleton, N.J., Laskar, J., Wilson D., *The Neogene Period* (Cambridge University Press, Cambridge. eds. 2004).

Lowrie, W., 1990. Identification of ferromagnetic minerals in a rock by coercivity and unblocking temperature properties. *Geophysical Research Letters* 17 (2): 159-162.

Lurcock, P.C., Wilson, G.S., 2012. PuffinPlot: A versatile, user-friendly program for paleomagnetic analysis. *Geochemistry, Geophysics, Geosystems* 13 (6).

Maxbauer, D.P., Feinberg, J.M., Fox, D.L., 2016. MAX UnMix: A web application for unmixing magnetic coercivity distributions. *Computers & Geosciences* 95 (2012): 140-145.

Macdonald, R., 1974 Nomenclature and petrochemistry of the peralkaline oversaturated extrusive rocks. *Bulletin volcanologique* 38 (1974): 498-516.

Macphail, R. I., Goldberg, P. Archaeological materials in Interpretation of Micromorphological Features of Soils and Regolith. Stoops, G., Marcelino, V. & Mees, F. Eds. (Elsevier, 2nd ed. 2018): 779-819.

Mana, S., Hemming, S., Kent, D.V., Lepre, C.J., 2019. Temporal Stratigraphic Framework for Paleoanthropology Sites Within East-Central Area 130, Koobi Fora, Kenya. *Frontières in Earth Science* 7 (2019): 1-13.

Martinez-Ruiz, F., Kastner, M., Gallego-Torres, D., Rodrigo-Gámiz, M., Nieto-Moreno, V., Ortega-Huertas, M., 2015 Paleoclimate and paleoceanography over the past 20,000 yr in the Mediterranean Sea Basins as indicated by sediment elemental proxies. *Quaternary Science Reviews* 107 (2015): 25-46.

McHenry, L.J., 2012. A revised stratigraphic framework for Olduvai Gorge Bed I based on tuff geochemistry. *Journal of Human Evolution* 63(2): 284-299.

Mendez-Quintas, E., Panera, J., Altamura, F., Di Bianco, L., Melis, R.T., Piarulli, F., Ruta, G., Mussi, M., 2019. Gombore II (Melka Kunture, Ethiopia): a new approach to formation processes and spatial patterns of an Early Pleistocene Acheulean site. *Journal of Archeological Science* 108 (2019) 104975.

Mesfin, I., Texier, J.-P., 2022. Prepared core technology from the Early Pleistocene site of Nyabusosi 18, Uganda. *Journal of Archaeological Science* 46 (2022) 103695.

Miller, C. E. Trampling in Encyclopedia of Geoarchaeology. Gilbert, A.S., Eds. (Springer, 2017) pp: 981–982.

Mohib, A., Raynal, J.-P., Gallotti, R., Daujeard, C., El Graoui, M., Fernandes, P., Geraads, D., Magoga, L., Lefèvre, D., Rué, M., Sbihi Alaoui, F.-Z., 2019. Forty Years of Research at Casablanca (Morocco): New Insights in the Early/Middle Pleistocene Archaeology and Geology. *Hespéris-Tamuda LIV* 54.3 (2019): 25-56.

Monger, H. C., Daugherty, L. A., Gile, L. H. A microscopic examination of pedogenic calcite in an Aridisol of southern New Mexico in Occurrence, Characteristics, and Genesis of Carbonate, Gypsum, and Silica Accumulations. In: Nettleton, W. D., (Eds.) *Soils* (Soil Science Society of America Journal Special Publication 26, 1991): 37-60.

Morgan, L.E., Renne, P.R., Kieffer, G., Piperno, M., Gallotti, R., Raynal, J.-P., 2012. A chronological framework for a long and persistent archaeological record: Melka Kunture, Ethiopia. *Journal of Human Evolution* 62 (2012): 104-115.

Mussi, M., Altamura, F., Macchiarelli, R., Melis, R.T., Spinapolice, E.E., 2014. Garba III (Melka Kunture Ethiopia): a Middle stone age site with archaic Homo sapiens remains revisited. *Quaternary International* 343 (2014): 28-39.

Mussi, M., Altamura, F., Bonnefille, R., De Rita, D., Melis, R.T., 2016. The environment of the Ethiopian highlands at the Mid Pleistocene Transition: fauna, flora and hominins in the 850-700ka sequence of Gombore II (Melka Kunture). *Quaternary Science Reviews* 149 (2016): 259-268.

Mussi, M., Altamura, F., Di Bianco, L., Bonnefille, R., Gaudzinski-Windheuser, S., Geraads, D., Melis, R.T., Panera, J., Piarulli, F., Pioli, L., Ruta, G., Sànchez-Dehesa Galàn, S., Mendez-Quintas, E., 2021. After the emergence of the Acheulean at Melka kunture (Upper Awash, Ethiopia): from Gombore IB (1.6 Ma) to Gombore Iγ (1.4 Ma), Gombore Iδ (1.3 Ma) and Gombore II OAM test pit C (1.2 Ma). *Quaternary International* 657 (2021): 3-25.

Mussi, M., Gallotti, R., 2014. The Emergence of the Acheulean in East Africa e International Workshop, Rome, “La Sapienza” University, September 12/13, 2013. *Evolutionary. Anthropology* 23 (4): 126-127.

Mussi, M., Méndez-Quintas, E., Panera, J., Altamura, F., Di Bianco, L., Bonnefille, R., Briatico, G., Brunelli, E., Geraads, D., Mutri, G., Piarulli, F., Rubio Jara, S., Ruta, G., Sánchez-Dehesa Galán, S., Serodio Domínguez, A., Melis, R.T., 2022. Une vue d’ensemble sur Melka Kunture, grand complexe de sites pléistocènes dans la vallée supérieure de l’Awash (Ethiopie). *L’Anthropologie* 126 (2022) 102999.

Mussi, M., Skinner, M.M., Melis, R.T., Panera, J., Rubio-Jara, S., Davies, T.W., Geraads, D., Bocherens, H., Briatico, G., Le Cabec, A. and Hublin, J.J., 2023. Early Homo erectus lived at high altitudes and produced both Oldowan and Acheulean tools. *Science* 382 (6671): 713-718.

Muttoni, G., Perini, S., Melis, R.T., Mussi, M., 2023. Chronology of the earliest peopling of the Ethiopian highlands at Melka Kunture pre-dating the 1.925 Ma base of the Olduvai subchron. *Quaternary Science Reviews* 319 (2023) 108330.

Nicosia, C. & Stoops, G. Archaeological Soil and Sediment Micromorphology (John Wiley & Sons, 2017).

Njau, J.K., Blumenschine, R.J, 2006. A Diagnosis of Crocodile Feeding Traces on Larger Mammal Bone, with Fossil Examples from the Plio-Pleistocene Olduvai Basin, Tanzania. *Journal of Human Evolution* 50 (2006): 142-62.

Njau, J.K., Blumenschine, R.J., 2012. Crocodylian and Mammalian Carnivore Feeding Traces on Hominid Fossils from FLK 22 and FLK NN 3, Plio-Pleistocene, Olduvai Gorge, Tanzania. *Journal of Human Evolution* 63 (2012): 408-17.

Nowell, A., White, M., 2010. Growing up in the Middle Pleistocene: Life History Strategies and Their Relationship to Acheulan Industries. In A. Nowell & I. Davidson (eds): Stone Tools and the Evolution of Human Cognition. Colorado University Press, pp: 67-81.

O'Reilly, W., 1984. Rock and Mineral Magnetism. Blackie, Glasgow, UK.

Pearce, N.J.G., Perkins, W.T., Westgate, J.A., Gorton, M.P., Jackson, S.E., Neal, C.R., Chenery, S.P., 1997. A compilation of new and published major and trace element data for NIST SRM 610 and NIST SRM 612 glass reference materials. *Geostandards newsletter* 21 (1): 115-144.

Perini, S., Muttoni, G., Monesi, E., Melis, R.T., Mussi, M., 2021. Magnetochronology and age models of deposition of the Melka Kunture stratigraphic sequence (Upper Awash, Ethiopia) and age assessments of the main archeological levels therein contained. *Quaternary Science Reviews* 274 (2021) 107259.

Phillips, D., Matchan, E., Gleadow, A., Brown, F., McDougall, I., Cerling, T., Leakey, M., Hergt, J., Leakey, L., 2023. $^{40}Ar/^{39}Ar$ eruption ages of Turkana Basin tuffs: millennial-scale resolution constrains palaeoclimate proxy tuning models and hominin fossil ages. *Journal of Geological Society of London* 180 (4).

Pickford, M., 2020. The fossil Suidae (Mammalia, Artiodactyla) from Ternifine (Tighenif) Algeria. *Münchner Geowissenschafltiche Abhandlungen* 50 (2020): 1-67.

Pioli, L., Melis, R.T., Mussi, M., 2023. Volcaniclastic sedimentation in a closed, marginal rift basin: the case of the Melka Kunture area (upper Awash, Ethiopia). *Journal of the Geological Society of London,* Special Publications, 520.

Piperno, M., 2001. The prehistory of Melka kunture (Ethiopia). *Bulletin du Centre de recherche français à Jérusalem* 8 (2001): 135-145.

Piperno, M., Collina, C., Gallotti, R., Raynal, J.-P., Kieffer, G., le Bourdonnec, F.-X., Poupeau, G., Geraads, D., 2009. Obsidian exploitation and utilization during the Oldowan at Melka Kunture (Ethiopia). In: *Interdisciplinary Approaches to the Oldowan. Vertebrate Paleobiology and Paleoanthropology*. Springer, Dordrecht, pp: 111-128.

Profe, J., Zolitschka, B., Schirmer, W., Frechen, M., Ohlendorf, C., 2016. Geochemistry unravels MIS 3/2 paleoenvironmental dynamics at the loess–paleosol sequence Schwalbenberg II, Germany. *Palaeogeography Palaeoclimatology Palaeoecology* 459 (2016): 537-551.

Proffitt, T., 2018. Is there a Developed Oldowan A at Olduvai Gorge? A diachronic analysis of the Oldowan in Bed I and Lower-Middle Bed II at Olduvai Gorge, Tanzania. *Journal of Human Evolution* 120 (2018): 92-113.

Profico, A., Di Vincenzo, F., Gagliardi, L., Piperno, M., Manzi, G., 2016. Filling the gap. Human cranial remains from Gombore II (Melka Kunture, Ethiopia; ca. 850 ka) and the origin of Homo heidelbergensis. *Journal of Anthropological Science* 94 (2016): 1-24.

Raynal, J.-P. & Texier, J.-P. Découverte d'Acheuléen ancien dans la carrière Thomas I à Casablanca et problème de l'ancienneté de la présence humaine au Maroc, *Comptes Rendus de l'Académie des Sciences* 308, (1989): 1743-1749.

Raynal, J.-P., Sbihi-Alaoui, F.Z., Geraads, D., Magoga, L. & Mohib, A. The earliest occupation of North-Africa: the Moroccan perspective. *Quaternary International* 75 (2001): 65-75.

Raynal, J.P., Kieffer, G., 2004. Lithology, dynamism and volcanic successions at Melka Kunture (Upper Awash, Ethiopia). In: Chavaillon, J., Piperno, M. (Eds.), *Studies on the Early Paleolithic Site of Melka Kunture, Ethiopia.* Origines, Istituto Italiano di Preistoria e Protostoria, Florence, pp: 115-135.

Raynal, J.P., Kieffer, G., Bardin, G., 2004. Garba IV and the Melka Kunture formation. A preliminary lithostratigraphic approach. In: Chavaillon, J., Piperno, M. (Eds.), *Studies on the Early Paleolithic Site of Melka Kunture, Ethiopia.* Origines, Istituto Italiano di Preistoria e Protostoria, Florence, pp: 137-166.

Raynal, J.-P., Sbihi-Alaoui, F.Z., Magoga, L., Mohib, A. & Zouak, M. The Lower Palaeolithic Sequence of Atlantic Morocco Revisited After Recent Excavations at Casablanca. *Bulletin d'archéologie marocaine* 20 (2004): 44-76.

Raynal, J.-P., Sbihi-Alaoui F.-Z., Mohib, A., El Graoui, M., Lefèvre, D., Texier, J.-P., Geraads, D., Hublin, J.-J., Smith, T., Tafforeau, P., Zouak, M., Grün, R., Rhodes, E.J., Eggins, S., Daujeard, C., Fernandes, P., Gallotti, R., Hossini, S., Queffelec, A., 2010. Hominid Cave at Thomas Quarry I (Casablanca, Morocco): recent findings and their context. *Quaternary International* 223-224 (2010): 369-382.

Raynal, J.-P., Sbihi-Alaoui F.-Z., Mohib, A., El Graoui, M., Lefèvre, D., Texier, J.-P., Geraads, D., Hublin, J.-J, Smith, T., Tafforeau, P., Zouak, M., Grün, R., Rhodes, E.J., Eggins, S., Daujeard, C., Fernandes, P., Gallotti, R., Hossini, S., Schwarcz, H., Queffelec, A., 2011. Contextes et âge des nouveaux restes dentaires humains du Pléistocène moyen de la carrière Thomas I à Casablanca (Maroc). *Bulletin de la Société Préhistorique Française* 108 (2011): 645-669.

Raynal, J.-P., Lefèvre, D., Gallotti, R., Geraads, D., Daujeard, C., Hublin, J.-J., El Graoui, M., Fernandes, P., Rué, M., Magoga,L., Queffelec, A., Degeai, J.-P., Muttoni, G., Perini, S., Sbihi-Alaoui, F.-Z. & Mohib, A. Thomas Quarry I (Casablanca, Morocco). In A. Beyin, D. K. Wright, J. Wilkins, A. Bouzouggar et D. I. Olszewski. *Handbook of Pleistocene Archaeology of Africa: Hominin behavior, geography, and chronology*, Volume I, Springer Nature (2023) pp: 775-793.

Reille, M., 1992. Pollen et spores d'Europe et d'Afrique du Nord. *Laboratoire de Botanique historique et de Palynologie*, 1992.

Reille, M., 1995. Pollen et spores d'Europe et d'Afrique du Nord. *Laboratoire de Botanique historique et de Palynologie*, supplément 1, 1995.

Reille, M., 1998. Pollen et spores d'Europe et d'Afrique du Nord*. Laboratoire de Botanique historique et de Palynologie*, supplément 2, 1998.

Rhodes, E.J., Singarayer, J., Raynal, J.-P., Westaway, K., Sbihi-Alaoui, F.-Z. New age estimations for the Palaeolithic assemblages and Pleistocene succession of Casablanca, Morocco. *Quaternary Science Reviews* 25 (2006): 2569-2585.

Richard, D.A., Bottrell, S.H., Cliff, R.A., Ströhle, K., Rowe, P.J., 1998. U-Pb dating of a speleothem of Quaternary age. *Geochimica et Cosmochimica Acta* 62 (1998): 3683-3688.

Roche, H., Brugal, J,-P., Delagnes, A., Feibel, C., Harmand, S., Kibunjia, M., Prant, S., Texier, J.-P., 2003. Les sites archéologiques Plio-Pléistocènes de la formation de Nachukui, Ouest-Turkana, Kenya: bilan synthétique 1997–2001. *Comptes Rendus Palevol* 2 (2003): 663–673.

Rodrigo-Gamiz, M., Martínez-Ruiz, F., Rodríguez-Tovar, F. J., Jiménez-Espejo, F.J., Pardo-Igúzquiza, E., 2014. Millennial-to centennial-scale climate periodicities and forcing mechanisms in the westernmost Mediterranean for the past 20,000 yr. *Quaternary Research* 81 (2014): 78-93.

Rohling, E.J., Foster, G.L., Grant, K.M., Marino, G., Roberts, A.P., Tamisiea, M.E., Williams, F., 2014. Sea-level and deep-sea-temperature variability over the past 5.3 million years. *Nature* 508 (2014): 477-482.

Royer, P., Coppens, Y., 1975. Découverte d'hominidé dans un site acheuléen de Melka-Kunturé (Ethiopie). *Bulletins et mémoires de la Société d'anthropologie de Paris.* Ser. XIII (1975): 125-128.

Sahle, Y., El Zaatari, S., White, T. D., 2017. Hominid Butchers and Biting Crocodiles in the African Plio–Pleistocene. *Proceedings of the National Acadademy of Sciences* 114 (2017): 13164-13169.

Sánchez-Yustos, P., (2021) Knocking on Acheulean's door. DK revisited (Bed I, Olduvai, Tanzania). *Journal of Anthropological Science*: Reports, 102763.

Sánchez-Yustos, P., Diez-Martín, F., Domínguez-Rodrigo, M., Fraile, C., Duque, J., Díaz, I., de Francisco, S., Baquedano, R., Mabulla, A., 2018. Acheulean without handaxes? Assemblage variability at FLK West (Lowermost Bed II, Olduvai, Tanzania). *Journal of Anthropological Science* 96 (2018): 1-22.

Sahnouni, M., Parés, J. M., Duval, M., Cáceres, I., Harichane, Z., Van der Made, J., Pérez-González, A., Abdessadok, S., Kandia, N., Derradji, A., Medig, M., Boulaghraif, K., Semaw, S. 2018. 1.9-million-and 2.4-million-year-old artifacts and stone tool–cutmarked bones from Ain Boucherit, Algeria. *Science* 362 (6420): 1297-1301.

Scarciglia, F., Pelle, T., Pulice, I., Robustelli, G., 2015. A comparison of Quaternary soil chronosequences from the Ionian and Tyrrhenian coasts of Calabria, southern Italy: Rates of soil development and geomorphic dynamics. *Quaternary International* 376 (2015): 146-162.

Scarciglia, F., Critelli, S., Borrelli, L., Coniglio, S., Muto, F., Perri, F., 2016. Weathering profiles in granitoid rocks of the Sila Massif uplands, Calabria, southern Italy: New insights into their formation processes and rates. *Sedimentary Geology* 336 (2016): 46-67.

Sahle, Y., El Zaatari, S., White, T.D., 2017. Hominid Butchers and Biting Crocodiles in the African Plio-Pleistocene. *Proceedings of the National Acadademy of Sciences* 114 (2017): 13164-13169.

Sahnouni, M., Hadjouis, D., van der Made, J., Derradji, A-E-K., Canals, A., Medig, M., Belahrech, H., Harichane, Z., Rabhi, M., 2002. Further research at the Oldowan site of Aïn Hanech, north-eastern Algeria. *Journal of Human Evolution* 43 (2002) 925-937.

Schaefer, J.M., Codilean, A.T., Willenbring, J.K., Lu, Z.-Y., Keisling, B., Fülöp, R.-H., Val, P., 2022. Cosmogenic nuclide techniques. *Nature Reviews Methods Primers* 2 (2022).

Schmitt, J.J., Wempler, J.M., Chavaillon, J., Andrews, M.C., 1977. Initial K-Ar and paleomagnetic results of the Melka Kunture early-man sites, Ethiopia. In: Proceedings VIII Panafrican Congress of Prehistory and Quaternary Studies, Nairobi.

Semaw, S., Renne, P., Harris, J. W. K., Feibel, C. S., Bernor, R. L., Fesseha, N., Mowbray, K., 1997. 2.5-million-year-old stone tools from Gona, Ethiopia. *Nature* 385 (1997): 333-336.

Semaw, S., 2000. The world's oldest stone artifacts from Gona, Ethiopia: Their implications for understanding stone technology and patterns of human evolution 2.6–1.5 million years ago. *Journal of Archaeological Science* 27 (2000): 1197-1214.

Semaw, S., Rogers, M., Stout, D., The Oldowan-Acheulian transition: Is there a 'Developed Oldowan' artifact tradition? in *Sourcebook of Paleolithic Transitions. Methods, Theories and Interpretations.* eds Camps M, Chauhan PR (Springer, New York, 2009), pp: 173-193.

Semaw, S., Rogers, M.J., Simpson, S.W., Levin, N.E., Quade, J., Dunbar, N., McIntosh, W.C., Cáceres, I., Stinchcomb, G.E., Holloway, R.L., Brown, F.H., Butler, R.F., Stout, D., Everett, M., 2020. Co-occurrence of Acheulian and Oldowan artifacts with Homo erectus cranial fossils from Gona, Afar, Ethiopia. *Science Advances* 6(10): eaaw4694.

Shackleton, N. J., A. Berger, and W. R. Peltier (1990), An alternative astronomical calibration of the lower Pleistocene timescale based on ODP Site 677, *Transactions of the Royal Society of Edinburgh, Earth Sciences* 81 (1990): 251-261.

Shackleton, N.J., New data on the evolution of Pliocene climate variability in Palaeoclimate and evolution, with emphasis on human origins (eds. Denton, G.H., Vrba, E., Partridge, T.C., Burckle, L.H.) (Yale University Press, 1995), pp: 242-248.

Shtienberg, G., Dix., J.K., Roskin, J., Waldmann, N., Bookman, R., Bialik, O.M., Porat, N., Taha, N., Sivan, D., 2017. New perspectives on coastal landscape reconstruction during the Late Quaternary: A test case from central Israel. *Palaeogeography Palaeoclimatology Palaeoecology* 468 (2017): 503-519.

Simpson, E. L., Eriksson, K. A., 1993. Thin eolianites interbedded within a fluvial and marine succession: early Proterozoic Whitworth Formation, Mount Isa Inlier, Australia. Sediment. Geol. 87 (1993): 39-62.

Skonieczny, C., Mcgee, D., Winkler, G., Bory, A., Bradtmiller, L.I., Kinsley, C.W., Polissar, P.J., De Pol-Holz, R., Rossignol, L., Malaizé, B., 2019. Monsoon-driven Saharan dust variability over the past 240,000 years. *Science Advances* 5 (2019) eaav1887.

Souron, A. PhD dissertation (Université de Poitiers) 2012.

Sousse, F., 1975. La mandibule atlanthropienne de la Carriere Thomas I (Casablanca). *L'Anthropologie* 79 (1975): 81-112.

Stanistreet, I.G., McHenry, L., Stollhofen, H., de la Torre, I., 2018. Bed II Sequence Stratigraphic context of EF-HR and HWK EE archaeological sites, and the Oldowan/Acheulean succession at Olduvai Gorge, Tanzania. *Journal of Human Evolution* 120 (2018): 19-31.

Stanistreet, I.G., Stollhofen, H., Njau, J.K., Farrugia, P., Pante, M.C., Masao, F.T., Albert, R.M., Bamford, M.K., 2018. Lahar inundated, modified, and preserved 1.88 Ma early Hominin (OH24 and OH56) Olduvai DK site. *Journal of Human Evolution* 116 (2018): 27-42.

Stearns, C. E., 1978. Pliocene-Pleistocene emergence of the Moroccan Meseta. *Geological Society of America Bulletin* 89 (1978): 1630-1644.

Stollhofen, H., Stanistreet, I.G., Toth, N., Schick, K.D., Rodriguez-Cintas, A., Albert, R.M., Farrugia, P., Njau, J.K., Pante, M.C., Herrmann, E.W., Ruck, L., Bamford, M.K., Blumenschine, R.J., Masao, F.T., 2021. Olduvai's oldest Oldowan. *Journal of Human Evolution* 150 (2021) 102910.

Stoops, G. Guidelines for Analysis and Description of Soil and Regolith Thin Sections (Soil Science Society of America Inc., 2003).

Stoops, G. Fluorescence microscopy in Archaeological Soil and Sediment Micromorphology (Eds. Nicosia, C. & Stoops G.), John Wiley & Sons (2017), pp: 393-397.

Stoops, G., Marcelino, V., Mees, F. Interpretation of Micromorphological Features of Soils and Regoliths (Elsevier, 2nd ed. 2018).

Stout, D., Semaw, S., Rogers, M. J., & Cauche, D., 2010. Technological variation in the earliest Oldowan from Gona, Afar, Ethiopia. *Journal of Human Evolution* 58 (2010): 474-491.

Suwa, G., Souron, A., Asfaw, B. Fossil Suidae of the Konso Formation in Konso-Gardula Research Project, Vol. 1: Paleontological Collections: Background and Fossil Aves, Cercopithecidae, and Suidae (Suwa, G., Beyene, Y. & Asfaw, B.) (The University Museum. The University of Tokyo, Bulletin N. 47, 2014), pp: 73-88.

Suwa, G., Beyene, Y., Asfaw, B., 2015. *Konso-Gardula Research Project, Vol. 1*. (The University Museum, The University of Tokyo, Tokyo).

Tamrat, E., Thouveny, N., Taieb, M., Brugal, J.P., 2014. Magnetostratigraphic study of the Melka Kunture archaeological site (Ethiopia) and its chronological implications. *Quaternary International* 343 (2014): 5-16.

Tamrat, E., Thouveny, N., Taieb, M., Opdyke, N.D., 1995. Revised magnetostratigraphy of the Plio-Pleistocene sedimentary sequence pf the Olduvai Formation (Tanzania). *Palaeogeaography Palaeoclimatology Palaeoecology* 114 (1995): 273-283.

Tauxe, L., R. Shaar, L. Jonestrask, N. L. Swanson-Hysell, R. Minnett, A. A. P. Koppers, C. G. Constable, N. Jarboe, K. Gaastra, L. Fairchild, 2016. PmagPy: Software package for paleomagnetic data analysis and a bridge to the Magnetics Information Consortium (MagIC) Database, *Geochemistry Geophysics. Geosystems*. 17 (2016).

Taieb, M., PhD dissertation (Universitè de Paris VI, France, 1974).

Texier, J.-P., Lefèvre, D., Raynal, J.-P., 1994. Contribution pour un nouveau cadre stratigraphique des formations littorales Quaternaires de la région de Casablanca (Maroc). *Comptes Rendus de l'Académie des Sciences* 318 (1994): 1247-1253.

Texier, J.-P., Lefèvre, D., Raynal, J.-P. & El Graoui, M., 2002. Lithostratigraphy of the littoral deposits of the last one million years in the Casablanca region (Maroc). *Quaternaire* 13 (2002): 23-41.

Texier, J.-P., Roche, H., Harmand, S., Kokiselei 5, formation de Nachukui, West Turkana (Kenya): un témoignage de la variabilité ou de l'évolution des comportements techniques au Pléistocène ancien? in *Actes du XIVe congrès UISPP, section 15: Préhistoire en Afrique / African Prehistory.* eds de Maret P, Cornelissen E, Ribot I. (Liege: Archaeopress, BAR International Series 1522, 2006): 11-22.

Texier, J.-P., 2018. Technological Assets for the Emergence of the Acheulean? Reflections on the Kokiselei 4 Lithic Assemblage and Its Place in the Archaeological Context of West Turkana, Kenya in *The Emergence of the Acheulean in East Africa and Beyond.Contributions in Honor of Jean Chavaillon*. eds Gallotti R, Mussi M (Springer, New York): 33-52.

Tiedemann, R., Sarnthein, M., Shackleton, N. J., 1994. Astronomic timescale for the Pliocene Atlantic $\delta^{18}O$ and dust flux records of Ocean Drilling Program Site 659. *Paleoceanography* 9 (1994): 619-638.

Trauth, M. H., Larrasoaña, J. C., Mudelsee, M., 2009. Trends, rhythms and events in Plio-Pleistocene African climate. *Quaternary Science Reviews* 28 (2009): 399-411.

Tsatskin, A., Ronen, A., 1999. Micromorphology of a Mousterian paleosol in aeolianites at the site Habonim, Israel. *Catena* 34 (1999): 365-384.

Verrecchia, E. P. Lacustrine and palustrine geochemical sediments, in Geochemical Sediments and Landscapes (eds. Nash, D. J. & McLaren, S. J.) (Blackwell, 2007), pp: 298-329.

Villagran, X. S., Huisman, D. J., Mentzer, S. M., Miller, C. E., Jans, M.M. Bone and Other Skeletal Tissues in Archaeological Soil and Sediment Micromorphology (eds. Nicosia, C. & Stoops, G.) (John Wiley & Sons, 2017), pp: 11-38.

Vogelsang, R., Bubenzer, O., Kehl, M., Meyer, S., Richter, J., Zinaye, B., 2018. When Hominins Conquered Highlands-an Acheulean Site at 3000 m a.s.l. on Mount Dendi/Ethiopia. *Journal of Paleolithic Archaeology* 1 (2018): 302-313.

Ward, W. C. Petrology and diagenesis of carbonate eolianites on northwestern Yucatan Peninsula, Mexico in Belize Shelf--Carbonate Sediments, Clastic Sediments, and Ecology (eds. Pusey, W. C. & Wantland K. F.) (AAPG Special Volumes, 1975), pp: 500-571.

Westphal, M., Chavaillon, J., Jaeger, J.J., 1979. Magnétostratigraphie des dépôts Pléistocènes de Melka-Kunturé (Ethiopie): premières données. *Bulletin de la Société Géologique de France* 7 (1979): 237-241.

Wieder, M., Yaalon, D. H., 1974. Effect of matrix composition of carbonate nodule crystallisation. *Geoderma* 11 (1974): 95-121.

Williams, M.A.J., Williams, F.M., Gasse, F., Curtis, G.H., Adamson, D.A., 1979. Plio-Pleistocene environments at Gadeb prehistoric site, Ethiopia. *Nature* 282 (1979): 29-33.

Wintle, A.G., Huntley, D.J., 1982. Thermoluminescence dating of sediments. *Quaternary Science Reviews* 1 (1982): 31-53.

Yang, S.Y., Li, C.X., Yang, D.Y., Li, X.S., 2004. Chemical weathering of the loess deposits in the lower Changjiang Valley, China, and paleoclimatic implications. *Quaternary International* 117 (2004): 27-34.

Zanolli, C., Dean, M.C., Assefa, Y., Bayle, P., Braga, J., Condemi, S., Endalamaw, M., Redae, B.E., Macchiarelli, R., 2017. Structural organization and tooth development in a Homo aff. erectus juvenile mandible from the Early Pleistocene site of Garba IV at Melka Kunture, Ethiopian highlands, 2016 *American Journal of Physical Anthropology* 162 (2017): 533-549.

Zerboni, A., 2011. Micromorphology reveals in situ Mesolithic living floors and archaeological features in multiphase sites in central Sudan. *Geoarchaeology* 26 (2011): 365-391.

Zhao, Q., Wu, S., Xu, H., Sun, Q., Wang, B., Sun, Y., Cao, F., He, X., 2011. Sedimentary facies and evolution of aeolianites on Shidao Island, Xisha Islands. *Chinese Journal of Oceanology and Limnology* 29 (2011): 398-413.

Zhao, X., Egli, R., Gilder, S.A., Müller, S., 2016. Microbially assisted recording of the Earth's magnetic field in sediment. *Nature Communications* 7 (2016): 1-7.

Zilberman, U., Smith, P., Condemi, S., 2004a. Evidence for a genetic disorder affecting tooth formation in the Garva IV child. In: Chavaillon, J., Piperno, M. (Eds.), Studies on the Early Paleolithic site of Melka Kunture, Ethiopia. Istituto Italiano di Preistoria e Protostoria, Florence, pp: 703-713.

Zilberman, U., Smith, P., Piperno, M., Condemi, S., 2004. Evidence of amelogenesis imperfecta in an early African Homo erectus. *Journal of Human Evolution* 46 (6): 647-653.

Chapter 5: Supplementary Material of
Magnetochronology and age models of deposition of the Melka Kunture stratigraphic sequence (Upper Awash, Ethiopia) and age assessments of the main archeological levels therein contained

Supplementary Table 1
Demagnetization Data

Section: sampled section (see Fig. 2,3); **Sample**: sample ID; **Treatment**: thermal demagnetization treatment [°C]; **J**: NRM intensity [10^{-2}A/m]; **Gdec**: declination in geographic coordinates [°]; **Ginc**: inclination in geographic coordinates [°].

Sample	Treatment [°C]	J [10^{-2}A/m]	Gdec [°]	Ginc [°]
GII205	0	0.142	353.9	32.0
GII205	100	0.177	349.6	20.9
GII205	150	0.209	270.7	-46.6
GII205	200	0.157	353.5	20.5
GII205	250	0.0738	346.2	15.3
GII205	300	0.0708	353.9	22.0
GII205	350	0.0266	33.2	34.3
GII205	400	0.0198	1.6	65.5
GII205	425	0.0354	337.3	42.2
GII205	450	0.0208	26.4	-7.9
GII205	475	0.0129	329.3	46.2
GII205	500	0.0265	119.9	3.0
GII205	525	0.0144	208.3	-41.8
GII205	550	0.0289	157.0	18.4
GII205	575	0.00594	183.7	-47.7
GII202	0	0.21	16.5	32.0
GII202	100	0.131	59.5	3.6
GII202	150	0.19	16.0	37.0
GII202	200	0.193	16.2	35.1
GII202	250	0.147	31.8	39.3
GII202	300	0.132	33.8	40.7
GII202	350	0.107	47.6	32.8
GII202	400	0.0163	66.9	11.3
GII202	425	0.012	65.2	26.9
GII202	450	0.0169	258.9	-17.6
GII202	475	0.0134	349.4	61.0
GII202	500	0.0162	86.0	32.3
GII201	0	0.0721	357.9	1.0
GII201	100	0.0779	341.0	5.9

GII201	150	0.0724	325.1	13.7
GII201	200	0.0635	327.8	12.1
GII201	250	0.0376	312.5	14.7
GII201	300	0.0375	301.2	20.6
GII201	350	0.0309	322.5	8.5
GII201	400	0.0211	334.8	-29.7
GII201	425	0.0576	61.6	-17.7
GII201	450	0.0177	24.0	-16.5
GII201	475	0.0144	67.3	-30.6
GII201	500	0.0136	173.6	-35.2
GII201	525	0.0223	139.1	-11.9
G2SAG17	0	0.178	202.3	29.4
G2SAG17	100	0.161	1.3	14.7
G2SAG17	150	0.154	5.3	11.5
G2SAG17	200	0.136	358.2	11.8
G2SAG17	250	0.0703	5.3	14.4
G2SAG17	300	0.0624	10.6	8.2
G2SAG17	350	0.0371	10.1	-3.3
G2SAG17	400	0.0397	41.6	16.7
G2SAG17	425	0.0366	0.1	11.8
G2SAG17	450	0.0281	16.8	12.7
G2SAG17	475	0.0108	357.8	-7.3
G2SAG17	500	0.00843	312.7	40.8
G2SAG17	525	0.109	192.0	4.2
G2SAG17	550	0.0156	127.1	30.2
G2SAG17	575	0.0188	96.8	-36.6
G2SAG15	0	0.0521	241.4	24.4
G2SAG15	100	0.0184	9.4	77.7
G2SAG15	150	0.0153	53.2	77.2
G2SAG15	200	0.0107	311.3	51.6
G2SAG15	250	0.00709	104.9	87.7
G2SAG15	300	0.00749	174.7	-14.3
G2SAG15	350	0.0166	213.2	4.0
G2SAG15	400	0.0304	188.8	27.1
G2SAG15	425	0.0248	120.3	43.7
G2SAG15	450	0.00752	218.8	-24.7
G2SAG15	475	0.0339	61.1	33.6
G2SAG15	500	0.0246	220.3	0.7
G2SAG10	0	0.0447	28.1	-71.8
G2SAG10	100	0.0348	97.3	40.4
G2SAG10	150	0.0284	118.9	18.5
G2SAG10	200	0.0255	122.3	22.3
G2SAG10	250	0.0115	107.9	13.2
G2SAG10	300	0.0154	127.6	3.5
G2SAG10	350	0.00839	183.8	41.8
G2SAG10	400	0.00748	70.1	48.3

G2SAG10	425	0.0107	74.1	65.9
G2SAG10	450	0.0111	163.6	32.3
G2SAG10	475	0.0111	130.9	-69.2
G2SAG10	500	0.0118	54.1	-52.6
G2SAG10	525	0.0115	265.4	17.0
G2SAG08	0	0.127	17.3	43.5
G2SAG08	100	0.0581	21.1	38.5
G2SAG08	150	0.0446	320.4	-46.2
G2SAG08	200	0.05	37.2	47.7
G2SAG08	250	0.0554	33.5	49.7
G2SAG08	300	0.0175	309.2	-24.8
G2SAG08	350	0.0228	54.7	2.4
G2SAG08	400	0.0952	324.5	-26.2
G2SAG08	425	0.0184	345.3	36.3
G2SAG08	450	0.0162	35.7	41.3
G2SAG08	475	0.0238	352.4	-26.0
G2SAG08	500	0.0106	15.2	-25.4
G2SAG05	0	0.107	17.8	-4.5
G2SAG05	100	0.0523	341.1	-28.3
G2SAG05	150	0.0389	350.7	-42.8
G2SAG05	200	0.0309	345.5	-38.5
G2SAG05	250	0.0287	21.4	-60.7
G2SAG05	300	0.0283	347.9	-34.0
G2SAG05	350	0.0234	245.0	-44.4
G2SAG05	400	0.0262	105.3	-22.7
G2SAG05	425	0.0188	208.4	-14.5
G2SAG05	450	0.0164	55.9	27.8
G2SAG05	475	0.0301	189.7	-23.7
G2SAG05	500	0.0241	84.6	28.1
GOAMII14	0	0.06775	65.6	65.3
GOAMII14	5	0.05836	115.2	66.8
GOAMII14	10	0.06584	161.1	43.3
GOAMII14	15	0.06767	169.7	29.4
GOAMII14	20	0.0717	172.6	25.4
GOAMII14	25	0.07346	172.4	22.2
GOAMII14	30	0.08083	180.3	18.6
GOAMII14	35	0.07397	174	17.4
GOAMII14	40	0.07432	177.1	12.4
GOAMII14	45	0.08473	180	13.1
GOAMII14	50	0.07276	180.2	17.2
GOAMII14	55	0.08016	180.4	8.8
GOAMII14	60	0.06682	187.9	17
GOAMII14	65	0.07604	182.8	9.3
GOAMII14	70	0.07458	187.9	12
GOAMII14	75	0.05982	182.2	5.9
GOAMII14	80	0.05962	176.1	10.9

GOAMII14	85	0.0628	187.6	9
GOAMII12	0	0.0986	70.4	19.0
GOAMII12	100	0.0465	151.6	-1.2
GOAMII12	150	0.0419	151.5	-6.7
GOAMII12	200	0.0495	145.1	-5.3
GOAMII12	250	0.0388	150.8	1.0
GOAMII12	300	0.0298	121.3	2.0
GOAMII12	350	0.0201	102.6	-20.3
GOAMII12	400	0.00293	155.3	-6.1
GOAMII12	425	0.00262	81.6	0.8
GOAMII12	450	0.0191	187.3	15.9
GOAMII12	475	0.0234	113.0	-39.6
GOAMII12	500	0.00688	195.7	60.6
GOAMII12	525	0.00177	151.5	7.8
GOAMII11	0	1.52457	349.3	13.7
GOAMII11	5	1.13184	350.9	12.2
GOAMII11	10	0.85245	350.6	12
GOAMII11	15	0.69293	353.4	14.8
GOAMII11	20	0.57515	350.1	14.4
GOAMII11	25	0.43253	351.7	10.7
GOAMII11	30	0.43426	1.3	20
GOAMII11	35	0.34476	356.2	20.3
GOAMII11	40	0.24904	6.5	5.7
GOAMII11	45	0.23948	3.2	20.8
GOAMII11	50	0.18317	5.1	14.1
GOAMII11	55	0.15208	353.5	12.3
GOAMII11	60	0.17936	1.7	-0.8
GOAMII11	65	0.20775	7.9	30.7
GOAMII11	70	0.15554	352	26.5
GOAMII11	75	0.17183	9.9	11.8
GOAMII11	80	0.20774	359	28.8
GOAMII11	85	0.14159	352.8	48.9
GOAMII09	0	0.20312	348.3	46.9
GOAMII09	5	0.17047	346.1	43.2
GOAMII09	10	0.13119	347.1	45.5
GOAMII09	15	0.10555	336.5	44.2
GOAMII09	20	0.08196	336	46.7
GOAMII09	25	0.06456	332.8	46.5
GOAMII09	30	0.05995	326.3	41.5
GOAMII09	35	0.05004	317.6	46.3
GOAMII09	40	0.04168	318.8	45.3
GOAMII09	45	0.03694	308.9	47.8
GOAMII09	50	0.03158	277.9	55.7
GOAMII09	55	0.03379	290.8	53.9
GOAMII09	60	0.02182	309.3	57.6
GOAMII09	65	0.02549	297.1	34.4

GOAMII09	70	0.02292	277.3	43.8
GOAMII09	75	0.02129	267.5	28.1
GOAMII09	80	0.02397	251.9	29.2
GOAMII07	0	0.33888	5	14.9
GOAMII07	5	0.27981	4.4	13.9
GOAMII07	10	0.20875	3.8	15.5
GOAMII07	15	0.16538	10.2	15.7
GOAMII07	20	0.12387	12.3	12.1
GOAMII07	25	0.10228	12.8	7.1
GOAMII07	30	0.08397	23.5	4.7
GOAMII07	35	0.07324	15.8	1.7
GOAMII07	40	0.05076	16.3	-3
GOAMII07	45	0.04985	23.9	-6.7
GOAMII07	50	0.04257	26.3	-0.9
GOAMII07	55	0.04666	29.1	-3.4
GOAMII07	60	0.0332	26.7	-7.4
GOAMII07	65	0.02865	20	-19.4
GOAMII07	70	0.0245	19.7	-41
GOAMII07	75	0.02701	349.6	-35.6
GOAMII07	80	0.0207	356.7	-8.1
GOAMII04	0	0.61238	9.4	-7.8
GOAMII04	5	0.56971	9	-5.8
GOAMII04	10	0.48518	7.1	-6
GOAMII04	15	0.39304	7.9	-4.2
GOAMII04	20	0.33568	8.2	-6.2
GOAMII04	25	0.26561	5	-3.8
GOAMII04	30	0.21974	359.7	-3.4
GOAMII04	35	0.19803	1.4	-2.5
GOAMII04	40	0.19384	355.5	-5.3
GOAMII04	45	0.18012	353.7	-14.4
GOAMII04	50	0.16364	350.5	-9.2
GOAMII04	55	0.1577	356.4	-9
GOAMII04	60	0.12808	350	-1.1
GOAMII04	65	0.10411	353.6	-0.1
GOAMII04	70	0.12168	357.7	-6.7
GOAMII04	75	0.11026	349.3	2.7
GOAMII04	80	0.09042	351.6	-8.8
GOAMII04	85	0.09994	340.9	3.1
GOAMII03	0	0.31874	13	-3.3
GOAMII03	5	0.27702	7.9	-5.1
GOAMII03	10	0.23513	1.3	-2.9
GOAMII03	15	0.19172	358.6	-3.7
GOAMII03	20	0.1635	355.7	0.2
GOAMII03	25	0.13346	353	2.4
GOAMII03	30	0.11896	351.5	0.8
GOAMII03	35	0.10517	346.9	-0.7

GOAMII03	40	0.07894	353.2	-0.1
GOAMII03	45	0.08729	345.5	-4.3
GOAMII03	50	0.08957	331.8	-1.1
GOAMII03	55	0.06572	338.8	-4.4
GOAMII03	55	0.06407	336	-1.3
GOAMII03	60	0.06753	345.9	-6.5
GOAMII03	65	0.04417	350	-1.6
GOAMII03	70	0.05123	345.3	1.2
GOAMII03	75	0.05355	357.7	-7.5
GOAMII03	80	0.04427	348.9	-23.8
GOAMII03	85	0.04674	350.5	-15.7
GOAMII02	0	0.28097	341.4	-27.2
GOAMII02	5	0.25333	339.7	-13.2
GOAMII02	10	0.17742	335.2	-11.5
GOAMII02	15	0.1029	317.9	-3.2
GOAMII02	20	0.09383	275.1	2.7
GOAMII02	25	0.08853	261.7	-3.5
GOAMII02	30	0.08728	248	14
GOAMII02	35	0.07761	254.9	-7.8
GOAMII02	40	0.10566	253.4	9.9
GOAMII02	45	0.0879	250	20.2
GOAMII02	50	0.06372	231.5	24.4
GOAMII02	55	0.0594	226.3	17.1
GOAMII02	60	0.06544	237.2	27.7
GOAMII02	65	0.06344	226.8	50.1
GOAMII02	70	0.04683	221.8	53.4
GOAMII02	75	0.02743	210.5	28.5
GOAMII02	80	0.0405	250	36.5
GOAMII16	0	0.04901	36.4	15.2
GOAMII16	5	0.02145	19.7	19.7
GOAMII16	10	0.00731	215.3	-7.6
GOAMII16	15	0.01706	201.7	-19
GOAMII16	20	0.02364	202.1	-16
GOAMII16	25	0.02416	203.1	-24.7
GOAMII16	30	0.03226	204.9	-22.9
GOAMII16	35	0.03379	206.2	-30.8
GOAMII16	40	0.03052	194	-20.3
GOAMII16	45	0.03884	207	-25.4
GOAMII16	50	0.03316	203.7	-25
GOAMII16	55	0.02988	210.8	-24.4
GOAMII16	60	0.03315	209.4	-30.8
GOAMII16	65	0.02677	215.9	-27.7
GOAMII16	70	0.02244	201.8	-33.3
GOAMII16	75	0.02306	218.4	-20.9
GOAMII16	80	0.02674	217.4	-36.3
GII606	0	0.082400	333.9	-36.8

GII606	100	0.051100	249.3	-57.4
GII606	150	0.049100	243.8	-67.8
GII606	200	0.047900	266.4	-53.4
GII606	250	0.036200	347.0	-59.7
GII606	300	0.041400	333.0	-5.9
GII606	350	0.043700	355.5	-28.0
GII606	400	0.088100	293.7	18.7
GII606	425	0.012800	53.3	-24.4
GII606	450	0.025200	185.4	-33.3
GII606	475	0.039600	211.2	-40.4
GII606	500	0.016400	66.0	45.0
GII605	0	0.0336	148.9	-13.5
GII605	5	0.04464	179.8	-21.2
GII605	10	0.06107	186.5	-19.1
GII605	15	0.06994	188.8	-16.1
GII605	20	0.07217	186.3	-16.5
GII605	25	0.07638	184.1	-13.8
GII605	30	0.07504	184.3	-11.4
GII605	35	0.06875	188.2	-9
GII605	40	0.06479	179.7	-16.8
GII605	45	0.06256	182.8	-9.1
GII605	50	0.06395	186.5	-9.2
GII605	55	0.0596	195	-9.6
GII605	60	0.06361	189.3	-9.6
GII605	65	0.0585	197.1	-14
GII605	70	0.0537	193.1	-5.9
GII605	75	0.05005	191.8	-16.1
GII605	80	0.05536	191.4	-8.2
GII605	85	0.05038	186.6	-17.7
GII603	0	0.11367	20	12.6
GII603	5	0.09124	12.8	7.5
GII603	10	0.06845	10.2	7.5
GII603	15	0.04919	11.8	11.3
GII603	20	0.03547	4.6	10.9
GII603	25	0.02094	13.6	12.8
GII603	30	0.01451	6.1	21.8
GII603	35	0.00931	31.4	17.5
GII603	40	0.00504	310.8	64.4
GII603	45	0.00892	257.1	9.4
GII603	50	0.00843	221.5	1.4
GII603	55	0.0123	223.4	22.7
GII603	60	0.01045	215	-5.8
GII603	65	0.01056	204.7	26.9
GII603	70	0.01837	213.1	9
GII603	75	0.01565	191	8.4
GII603	80	0.01385	224.4	19.4

GII603	85	0.01333	215.9	16.3
GII602	0	0.00582	308.1	19.3
GII602	100	0.0244	181.7	-21.4
GII602	150	0.0231	108.1	-13.3
GII602	200	0.0285	192.1	-9.1
GII602	250	0.0247	177.3	-0.5
GII602	300	0.0173	163.4	-18.3
GII602	350	0.0203	145.2	3.0
GII602	400	0.021	146.0	-40.6
GII602	425	0.00767	9.0	-6.2
GII602	450	0.0133	165.5	-12.2
GII602	475	0.00932	30.8	-37.1
GII602	500	0.0029	60.5	-4.3
GII601	0	0.7026	5.7	4.6
GII601	5	0.56469	1.6	5.1
GII601	10	0.38093	5.2	-0.2
GII601	15	0.27654	2.5	-5.4
GII601	20	0.2051	0.5	-8.0
GII601	25	0.1684	1.4	-9.2
GII601	30	0.1182	353.1	-11.2
GII601	35	0.10748	5.6	-0.3
GII601	40	0.10009	352.1	-24.8
GII601	45	0.07833	355.3	-4.1
GII601	50	0.06668	322.1	-20.0
GII601	55	0.03551	335.6	-10.7
GII601	60	0.03778	317.9	1.8
GII601	65	0.01519	247.2	12.1
GII601	70	0.0177	251.7	33.2
GII601	75	0.02163	280.0	5.0
GII601	80	0.02972	266.4	-32.4
GII601	85	0.04065	297.2	17.8
GIIS17I15	0	1.20997	137.4	-16.6
GIIS17I15	5	1.71702	138.4	-50.6
GIIS17I15	10	1.97972	143	-46.4
GIIS17I15	15	2.10072	146.3	-45.1
GIIS17I15	20	2.15136	149.8	-43.8
GIIS17I15	25	2.13848	153	-43
GIIS17I15	30	2.13079	155.8	-42
GIIS17I15	35	2.07251	154.9	-40.2
GIIS17I15	40	2.01085	158.7	-39.8
GIIS17I15	45	1.97580	158.9	-40
GIIS17I15	50	1.87567	161.3	-38.2
GIIS17I15	55	1.77563	162.3	-36.9
GIIS17I15	60	1.73175	161.4	-36.4
GIIS17I15	65	1.63750	159.6	-34
GIIS17I15	70	1.51989	161.9	-34.8

GIIS17I15	75	1.40254	163.6	-33.8
GIIS17I15	80	1.34620	165.1	-31.4
GIIS17I12	0	0.61296	97.1	19.8
GIIS17I12	5	0.31413	90.6	54.2
GIIS17I12	10	0.28209	102.8	58.7
GIIS17I12	15	0.26825	110	58.9
GIIS17I12	20	0.23335	114.9	57.6
GIIS17I12	25	0.2117	117.1	56.1
GIIS17I12	30	0.17884	114.5	52.5
GIIS17I12	35	0.16704	117.9	53.6
GIIS17I12	40	0.15016	115.8	49.1
GIIS17I12	45	0.14793	122	51.1
GIIS17I12	50	0.14077	125	49.1
GIIS17I12	55	0.13805	128.8	51.6
GIIS17I12	60	0.13393	123.8	53.8
GIIS17I12	65	0.12857	126.4	49.1
GIIS17I12	70	0.12658	132.5	44.7
GIIS17I12	75	0.11888	131.1	50.4
GIIS17I12	80	0.11107	131	48.9
GIIS17I09	0	0.72944	76.1	-2.2
GIIS17I09	5	0.67597	81.8	-9.6
GIIS17I09	10	0.60394	84.6	-10.9
GIIS17I09	15	0.48862	80.3	-12.7
GIIS17I09	20	0.36426	80.4	-13.3
GIIS17I09	25	0.27577	74.4	-16.9
GIIS17I09	30	0.19551	80.2	-20.4
GIIS17I09	35	0.15226	84.6	-18.1
GIIS17I09	40	0.13398	77.8	-27.8
GIIS17I09	45	0.0926	65.4	-28.4
GIIS17I09	50	0.07594	78.8	-32.8
GIIS17I09	55	0.07613	90.5	-47.7
GIIS17I09	60	0.06257	56.2	-63.5
GIIS17I09	65	0.05802	71.4	-48
GIIS17I09	70	0.05119	32.2	-56.8
GIIS17I09	75	0.05371	14.3	-55.6
GIIS17I09	80	0.03878	15.2	-66
GIIS17I07	0	0.488	41.5	14.0
GIIS17I07	100	0.294	21.2	17.8
GIIS17I07	150	0.114	281.7	-51.6
GIIS17I07	200	0.11	34.7	20.2
GIIS17I07	250	0.176	238.5	-49.7
GIIS17I07	300	0.131	196.9	-65.9
GIIS17I07	350	0.05	232.6	-24.5
GIIS17I07	400	0.0791	120.1	-13.4
GIIS17I07	425	0.0788	139.6	15.2
GIIS17I07	450	0.0796	159.6	13.1

GIIS17I07	475	0.0863	142.5	-8.8
GIIS17I07	500	0.0729	153.2	5.7
GIIS17I07	525	0.0495	68.2	29.8
GIIS17I06	0	0.316	350.0	-8.4
GIIS17I06	100	0.11	5.3	-10.7
GIIS17I06	150	0.0997	256.5	-46.4
GIIS17I06	200	0.0415	18.8	-10.3
GIIS17I06	250	0.0938	230.4	3.0
GIIS17I06	300	0.0941	227.1	-1.2
GIIS17I06	350	0.0639	158.8	-20.6
GIIS17I06	400	0.0645	133.5	-66.0
GIIS17I06	425	0.0799	185.2	-11.6
GIIS17I06	450	0.116	166.1	1.7
GIIS17I06	475	0.12	156.7	5.4
GIIS17I06	500	0.0817	146.6	4.3
GIIS17I06	525	0.0284	65.5	18.7
GIIS17I05	0	0.571	187.6	-18.7
GIIS17I05	100	0.453	182.7	-18.2
GIIS17I05	150	0.493	86.5	48.0
GIIS17I05	200	0.418	179.4	-16.1
GIIS17I05	250	0.315	179.6	-17.5
GIIS17I05	300	0.314	174.8	-20.5
GIIS17I05	350	0.276	174.9	-18.6
GIIS17I05	400	0.142	165.8	-11.9
GIIS17I05	425	0.153	173.9	-10.8
GIIS17I05	450	0.126	180.5	-20.7
GIIS17I05	475	0.116	182.6	-13.8
GIIS17I05	500	0.116	178.7	-18.8
GIIS17I05	525	0.0603	174.3	-11.6
GIIS17I05	550	0.0149	154.5	-34.7
GIIS17I05	575	0.0428	247.5	-28.9
GIIS17I03	0	0.30748	346.3	-18.6
GIIS17I03	5	0.22517	5.2	-16.9
GIIS17I03	10	0.1754	12.1	-20.7
GIIS17I03	15	0.15779	16.2	-22.5
GIIS17I03	20	0.13242	22	-25.5
GIIS17I03	25	0.11592	27.6	-28.7
GIIS17I03	30	0.10674	38.8	-29.4
GIIS17I03	35	0.10786	35.6	-29
GIIS17I03	40	0.09555	44.3	-31.8
GIIS17I03	45	0.0854	46.3	-32
GIIS17I03	50	0.08078	44	-35.5
GIIS17I03	55	0.08144	46.6	-31.1
GIIS17I03	60	0.07902	48.8	-27.3
GIIS17I03	65	0.07747	46.3	-29.5
GIIS17I03	70	0.07724	40.7	-32.4

GIIS17I03	75	0.07351	35.6	-31.5
GIIS17I03	80	0.07605	41.4	-27.8
GIIS17I02	0	0.313	150.7	-31.8
GIIS17I02	100	0.26	193.8	-22.4
GIIS17I02	150	0.307	178.8	-20.2
GIIS17I02	200	0.285	179.6	-15.1
GIIS17I02	250	0.287	178.0	-16.8
GIIS17I02	300	0.251	174.1	-19.7
GIIS17I02	350	0.18	169.6	-28.4
GIIS17I02	400	0.191	174.1	-21.9
GIIS17I02	425	0.124	179.0	31.0
GIIS17I02	450	0.169	174.6	-9.6
GIIS17I02	475	0.112	134.3	-35.7
GIIS17I02	500	0.0461	173.4	3.5
GIIS17I02	525	0.0805	195.9	-39.1
GIIS17I02	550	0.0378	140.6	-15.5
GIIS17I02	575	0.0239	78.0	8.1
GIIS17I01	0	0.7	180	-25.5
GIIS17I01	100	0.572	185	-24.0
GIIS17I01	150	0.579	185.1	-22.3
GIIS17I01	200	0.5	187.6	-22.2
GIIS17I01	250	0.478	188.4	-21.5
GIIS17I01	300	0.293	184.6	-23.9
GIIS17I01	350	0.301	185	-23.1
GIIS17I01	400	0.268	185.2	-21.0
GIIS17I01	425	0.165	190.1	-16.5
GIIS17I01	450	0.173	189.1	-11.8
GIIS17I01	475	0.173	181.5	-26.9
GIIS17I01	500	0.0793	176.7	-9.9
GIIS17I01	525	0.073	177.3	-14.0
GIIS17I01	550	0.0202	241.3	-27.7
GIIS17I01	575	0.0121	211.8	-0.6
GX18	0	0.369	356.3	18.8
GX18	100	0.261	353.7	10.8
GX18	150	0.256	358.5	16.9
GX18	200	0.212	358.7	15.9
GX18	250	0.139	358.9	15.0
GX18	300	0.111	0.1	10.5
GX18	350	0.0662	8.0	16.0
GX18	400	0.0491	4.6	13.7
GX18	450	0.0338	4.7	-1.3
GX18	475	0.0175	37.7	31.1
GX18	500	0.0875	342.9	78.9
GX18	525	0.0169	7.2	2.2
GX18	550	0.00686	88.3	0.5
GX18	575	0.00529	299.3	-15.3

GX17	0	0.115	173.0	-0.5
GX17	100	0.0675	360	6.2
GX17	150	0.0647	260.9	-50.4
GX17	200	0.0524	358.7	8.7
GX17	250	0.0288	5.3	7.5
GX17	300	0.0232	8.8	5.7
GX17	350	0.0164	32.8	-25
GX17	400	0.0154	43.8	24.3
GX17	425	0.0196	41.6	21.7
GX17	450	0.014	46.3	13.6
GX17	475	0.0108	36.3	-14.3
GX17	500	0.00928	131.9	-35.6
GX17	525	0.00671	93.9	48.1
GX16	0	0.117	23.6	51.8
GX16	100	0.256	9.0	26.2
GX16	150	0.209	355.2	5.8
GX16	200	0.207	356.9	4.7
GX16	250	0.106	356.0	14.2
GX16	300	0.0939	6.1	18.9
GX16	350	0.0727	6.6	17.2
GX16	400	0.0405	10.6	-8.0
GX16	425	0.0465	12.2	-3.9
GX16	450	0.0236	352.9	22.2
GX16	475	0.0323	350.0	-16.5
GX16	500	0.00751	231.4	9.1
GX16	525	0.0148	184.5	24.4
GX16	550	0.0127	30.4	33.0
GX16	575	0.00454	166.7	-23.5
GX12	0	0.203	127.7	37.3
GX12	100	0.159	311.3	-50.9
GX12	150	0.151	280.2	-54.1
GX12	200	0.142	276.2	-53.5
GX12	250	0.115	274.1	-55.7
GX12	300	0.116	254.6	-68.5
GX12	350	0.137	255.4	-61.9
GX12	400	0.105	251.5	-61.6
GX12	425	0.141	234.7	-59.2
GX12	450	0.131	232.1	-50.2
GX12	475	0.0972	220.2	-72.1
GX12	500	0.0126	17.5	-35.8
GX12	525	0.0103	1.6	-37.9
GX12	550	0.0148	160.6	15.7
GX12	575	0.0125	9.7	-40
GX08	0	0.125	145.7	-18.7
GX08	100	0.0911	336.2	-4.8
GX08	150	0.104	236.3	-42.3

GX08	200	0.0655	337.3	-8.7
GX08	250	0.0278	346.3	-23.6
GX08	300	0.0306	3.1	-42.2
GX08	350	0.00389	178.0	-50.5
GX08	400	0.0131	100.7	22.4
GX08	425	0.0234	344.9	-48.5
GX08	450	0.0241	315.6	-50.5
GX08	475	0.0238	0.7	-20.3
GX08	500	0.0541	127.0	37.7
GX07	0	0.339	170.6	0.1
GX07	100	0.282	358.7	7.8
GX07	150	0.243	356.7	4.8
GX07	200	0.191	353.5	9.3
GX07	250	0.185	350.6	12.8
GX07	300	0.121	348.2	11.3
GX07	350	0.0539	5.9	0.5
GX07	400	0.0432	7.8	2.3
GX07	425	0.0419	351.6	-19.7
GX07	450	0.052	357.7	-12.7
GX07	475	0.0668	356.4	-3.2
GX07	500	0.0141	25.9	-6.3
GX07	525	0.00472	24.4	-65.2
GX07	550	0.0158	214.5	15.1
GX07	575	0.00846	105.8	56.0
GX04	0	0.209	349.5	-11.7
GX04	100	0.155	357.5	-14.2
GX04	150	0.172	251.1	-45.4
GX04	200	0.122	0.9	-7.8
GX04	250	0.044	355.7	-20.4
GX04	300	0.0443	17.8	-22.3
GX04	350	0.0334	39.1	-0.1
GX04	400	0.0236	352.6	-29.5
GX04	425	0.0276	30.6	-10.8
GX04	450	0.0172	13.9	16.6
GX04	475	0.0137	7.3	-54.8
GX04	500	0.0104	334.5	-22.6
GX04	525	0.0143	152.8	-7.3
GX04	550	0.02	22.8	-19.8
GX04	575	0.0118	117.7	3.8
GXIS27	0	0.05947	54.8	61.7
GXIS27	5	0.1164	7.7	27.3
GXIS27	10	0.11458	356.1	30.2
GXIS27	15	0.09375	1.2	28.3
GXIS27	20	0.07522	354.1	36
GXIS27	25	0.05791	357.3	37.7
GXIS27	30	0.05413	333.3	53.8

GXIS27	35	0.04768	346.3	48.5
GXIS27	40	0.03784	345.5	53.6
GXIS27	45	0.03936	339.6	41.2
GXIS27	50	0.03252	324.1	36.6
GXIS27	55	0.02889	313.4	53.1
GXIS27	60	0.01997	349.8	33.1
GXIS27	65	0.01684	0.2	25.3
GXIS27	70	0.02263	331.3	57.2
GXIS27	75	0.02712	353.1	61.7
GXIS27	80	0.01762	17.7	38.1
GXIS25	0	0.166	173.8	5.8
GXIS25	100	0.163	174.4	-7.0
GXIS25	150	0.0769	85.3	4.1
GXIS25	200	0.137	173.0	1.0
GXIS25	250	0.0728	178.0	-5.5
GXIS25	300	0.0564	188.0	-17.6
GXIS25	350	0.0321	188.8	-4.9
GXIS25	400	0.0323	158.4	-10.3
GXIS25	425	0.0372	169.5	-10.1
GXIS25	450	0.0165	229.9	20.5
GXIS25	475	0.0172	238.4	16.3
GXIS25	500	0.0125	209.9	-66.4
GXIS23	0	0.19479	188.5	12.9
GXIS23	5	0.06957	183.2	2
GXIS23	10	0.07006	179.8	-3.2
GXIS23	15	0.08055	181.1	-9
GXIS23	20	0.08225	181.9	-11.9
GXIS23	25	0.08407	187	-14.5
GXIS23	30	0.08083	183.5	-9.4
GXIS23	35	0.07964	184.6	-9
GXIS23	40	0.07617	184.7	-12
GXIS23	45	0.08046	187.5	-10.5
GXIS23	50	0.07184	182.3	-9
GXIS23	55	0.07101	186.2	-7.7
GXIS23	60	0.07164	189.9	-8.1
GXIS23	65	0.06802	187.8	-10.9
GXIS23	70	0.06981	188.6	-5.2
GXIS23	75	0.06542	188.9	-7.5
GXIS23	80	0.06686	193.7	-10.1
GXIS21	0	0.0347	183.6	0.8
GXIS21	5	0.01793	276.9	-77.9
GXIS21	10	0.03222	220.3	-44.7
GXIS21	15	0.04217	189	-46.5
GXIS21	20	0.04596	199.9	-44.2
GXIS21	25	0.04439	191.2	-43.9
GXIS21	30	0.05369	188	-36.8

GXIS21	35	0.05337	185.5	-25
GXIS21	40	0.06107	190.3	-19
GXIS21	45	0.05568	159.5	-35.3
GXIS21	50	0.05807	171.1	-27.8
GXIS21	55	0.05217	188.1	7.6
GXIS21	60	0.04713	189.3	-11.6
GXIS21	65	0.04444	185.3	-7.5
GXIS21	70	0.03315	180.2	-14.4
GXIS21	75	0.03613	168.1	-14.7
GXIS21	80	0.03898	176.4	-2.5
GXIS20	0	0.09418	161.5	1.3
GXIS20	5	0.03322	136.5	-24.2
GXIS20	10	0.04063	151	-28.7
GXIS20	15	0.05018	160.3	-27.7
GXIS20	20	0.05149	161.1	-25.8
GXIS20	25	0.05143	167.4	-19.8
GXIS20	30	0.05438	172.4	-23.4
GXIS20	35	0.05167	173.2	-17.5
GXIS20	40	0.05283	173.7	-17.9
GXIS20	45	0.04858	174.9	-11.7
GXIS20	50	0.0467	178.5	-26
GXIS20	55	0.04429	181.6	-22.6
GXIS20	60	0.04303	180.3	-27.9
GXIS20	65	0.04038	194	-31.7
GXIS20	70	0.04363	194	-27.2
GXIS20	75	0.04066	189.9	-23.5
GXIS20	80	0.03937	184.2	-26.4
GXIS19	0	0.0713	130.9	20.7
GXIS19	100	0.0449	153.1	5.9
GXIS19	150	0.0416	148.0	8.2
GXIS19	200	0.0403	160.0	7.3
GXIS19	250	0.0122	118.3	60.6
GXIS19	300	0.0165	136.1	45.8
GXIS19	350	0.0358	253.7	42.2
GXIS19	400	0.0171	301.8	-7.7
GXIS19	425	0.0178	6.1	38.7
GXIS19	450	0.00789	274.7	-6.8
GXIS19	475	0.0135	311.7	38.4
GXIS19	500	0.0142	29.9	-56.4
GXIS17	0	0.0299	203.7	-50.8
GXIS17	100	0.0377	229.7	-28.3
GXIS17	150	0.14	171.4	-7.1
GXIS17	200	0.134	175.6	-0.8
GXIS17	250	0.0687	180.4	-10.4
GXIS17	300	0.0804	178.6	-17.5
GXIS17	350	0.0254	206.2	12.4

GXIS17	400	0.0252	186.1	-48.3
GXIS17	425	0.0238	199.6	-26.3
GXIS17	450	0.0146	251.1	-26.8
GXIS17	475	0.0146	170.6	-6.5
GXIS17	500	0.0127	208.4	-9.1
GXIS16	0	0.12087	68.6	7.5
GXIS16	5	0.11467	51.4	0.4
GXIS16	10	0.09897	58.3	-5.6
GXIS16	15	0.08622	67.7	-11.3
GXIS16	20	0.07425	73.7	-12.5
GXIS16	25	0.06786	86.6	-12.9
GXIS16	30	0.06924	98.3	-9.5
GXIS16	35	0.073	103.4	-11.6
GXIS16	40	0.07231	107.4	-9.9
GXIS16	45	0.06088	110.8	-8.9
GXIS16	50	0.05489	110.4	-7.9
GXIS16	55	0.06121	115.5	-7.4
GXIS16	60	0.05257	114.2	-3.5
GXIS16	65	0.05912	124.8	-6.2
GXIS16	70	0.04835	125.2	-11.4
GXIS16	75	0.04995	124.3	-4.2
GXIS16	80	0.04433	124.4	-12.9
GXIS12	0	0.09689	228.8	-81
GXIS12	5	0.07475	345.5	-77.5
GXIS12	10	0.08734	165.3	-79
GXIS12	15	0.06942	167.1	-76.1
GXIS12	20	0.08373	167.4	-60.2
GXIS12	25	0.06412	165.9	-60.5
GXIS12	30	0.05766	154	-58.9
GXIS12	35	0.06449	168.2	-60.1
GXIS12	40	0.06156	174.9	-50.7
GXIS12	45	0.05857	175	-51.5
GXIS12	50	0.07724	166.7	-53.7
GXIS12	55	0.07682	165.3	-47.8
GXIS12	60	0.06797	166.2	-45.6
GXIS12	65	0.05442	167.8	-54.5
GXIS12	70	0.05425	164.2	-62.6
GXIS12	75	0.06939	161.4	-31.2
GXIS12	80	0.07034	151.5	-34.7
GXIS11	0	0.09516	148.8	28.2
GXIS11	5	0.07349	146.1	32.3
GXIS11	10	0.07581	153.9	20.8
GXIS11	15	0.06967	163.1	8.2
GXIS11	20	0.06552	159.7	-0.8
GXIS11	25	0.0713	165.5	-6.9
GXIS11	30	0.07303	169.8	-10.1

GXIS11	35	0.07693	179.2	-15
GXIS11	40	0.0752	173.8	-2.1
GXIS11	45	0.07337	178.7	-16.1
GXIS11	50	0.05959	169.9	3
GXIS11	55	0.05595	172.5	-13.4
GXIS11	60	0.04992	179.7	-21.1
GXIS11	65	0.05414	168.3	-9.7
GXIS11	70	0.05505	181.1	-15.8
GXIS11	75	0.05556	168.9	-12.8
GXIS11	80	0.05379	178.1	-12.6
GXIS09	0	0.829	270.6	30.5
GXIS09	100	0.804	277.5	31.2
GXIS09	150	0.752	280.6	26.1
GXIS09	200	0.47	276.2	34.1
GXIS09	250	0.349	274.7	40.2
GXIS09	300	0.265	282.8	45.5
GXIS09	350	0.202	231.4	64.6
GXIS09	400	0.196	284.2	55.7
GXIS09	425	0.0874	255.3	15.4
GXIS09	450	0.135	324.3	34.5
GXIS09	475	0.0479	237.8	48.9
GXIS09	500	0.028	244.9	51.9
GXIS09	525	0.0166	305.0	22.4
GXIS09	550	0.00716	92.3	-11.7
GXIS09	575	0.00367	288.9	-10.6
GXIS06	0	1.28048	144.8	11.8
GXIS06	5	0.97731	117.1	-0.3
GXIS06	10	1.32075	136.7	3.4
GXIS06	15	1.49592	141.8	2.6
GXIS06	20	1.62132	146	5.2
GXIS06	25	1.58211	148.1	2.6
GXIS06	30	1.55370	151	1.2
GXIS06	35	1.38341	146.9	6.1
GXIS06	40	1.18756	146.9	4.8
GXIS06	45	1.02460	143.7	5.5
GXIS06	50	0.83424	147.1	7.3
GXIS06	55	0.68338	138.6	5
GXIS06	60	0.50706	139.3	12.5
GXIS06	65	0.41021	123.6	14.7
GXIS06	70	0.30495	120.9	24
GXIS06	75	0.36221	99.5	16.9
GXIS06	80	0.21317	101.5	19.4
GXIS05	0	2.84061	237.7	46.9
GXIS05	5	2.85118	238.1	47.1
GXIS05	10	2.83837	237.5	46.8
GXIS05	15	2.81243	237.3	46.7

GXIS05	20	2.78672	237	46.6
GXIS05	25	2.73165	236.4	46.9
GXIS05	30	2.65045	236	46.4
GXIS05	35	2.58718	235.8	46.2
GXIS05	40	2.50121	236	46.1
GXIS05	45	2.43450	229.3	47.8
GXIS05	50	2.29115	228.7	47.3
GXIS05	55	2.16732	228.4	47.5
GXIS05	60	2.06181	227.9	47.3
GXIS05	65	1.93167	227.6	47
GXIS05	70	1.80094	227.4	46.2
GXIS05	75	1.68419	227.2	46.5
GXIS05	80	1.56118	226.8	46.2
GXIS04	0	7.36043	80.5	-41.2
GXIS04	5	7.28262	79	-41.5
GXIS04	10	7.31310	74.9	-43.8
GXIS04	15	7.28364	74.2	-44.7
GXIS04	20	7.14901	74.2	-44.7
GXIS04	25	6.90652	73.5	-45.7
GXIS04	30	6.54453	71.9	-47.5
GXIS04	35	6.13040	71.7	-49.4
GXIS04	40	5.74827	69.9	-49.2
GXIS04	45	5.25220	68.9	-50
GXIS04	50	4.65273	69.5	-51
GXIS04	55	4.11156	68.3	-51.8
GXIS04	60	3.52805	70.1	-52.1
GXIS04	65	3.02547	70.7	-53.2
GXIS04	70	2.64536	72.5	-55
GXIS04	75	2.22709	72.5	-55
GXIS04	80	1.93724	73.2	-54.5
GG14	0	0.10289	37.8	-32.8
GG14	5	0.08599	34.7	-42.8
GG14	10	0.06765	29.1	-47.7
GG14	15	0.05716	25.5	-50.9
GG14	20	0.04762	24	-59.3
GG14	25	0.03963	34.8	-67.2
GG14	30	0.03022	52	-68.5
GG14	35	0.02735	53.2	-68.9
GG14	40	0.02521	106.9	-74.1
GG14	45	0.02129	130.2	-71.6
GG14	50	0.02703	172.5	-70.7
GG14	55	0.01937	167.4	-64.5
GG14	60	0.02055	172.8	-59.5
GG14	65	0.01778	173.4	-51.5
GG14	70	0.01673	171.9	-59.6
GG14	75	0.0153	169.1	-44.8

GG14	80	0.01856	183.8	-55.9
GG14	85	0.01584	180.1	-42.8
GG13	0	0.22747	102.4	-72.5
GG13	5	0.21076	148.8	-65
GG13	10	0.22801	162.9	-48.1
GG13	15	0.23012	164.2	-42.5
GG13	20	0.21886	164.5	-39.3
GG13	25	0.20065	164.2	-36.9
GG13	30	0.18391	163.7	-35.5
GG13	35	0.17378	166.6	-32
GG13	40	0.16463	166.7	-31.9
GG13	45	0.15834	166.8	-28.4
GG13	50	0.1434	165.2	-29.7
GG13	55	0.13687	167.8	-28.6
GG13	60	0.13435	166.5	-26.9
GG13	65	0.11849	169	-29.9
GG13	70	0.11276	165.5	-24.5
GG13	75	0.10439	165.6	-27.4
GG13	80	0.10139	169.2	-27.6
GG12	0	0.26874	2.6	-22.3
GG12	5	0.22979	6.3	-22.7
GG12	10	0.10243	44.6	-62.3
GG12	15	0.12077	149.9	-53.4
GG12	20	0.16022	159.8	-39
GG12	25	0.17369	164.5	-31.6
GG12	30	0.18027	168.9	-30.2
GG12	35	0.18424	165	-25.9
GG12	40	0.18968	167.3	-28.5
GG12	45	0.17888	168.2	-25.3
GG12	50	0.1719	170.7	-17
GG12	55	0.1786	160.6	-15.7
GG12	60	0.16915	163.9	-12.4
GG12	65	0.16165	166.5	-12.7
GG12	70	0.13792	162	-10.4
GG12	75	0.14641	166.7	-14.7
GG12	80	0.13046	164.9	-9.3
GG11	0	0.13751	248.1	-39.8
GG11	5	0.14056	207.6	-50.6
GG11	10	0.18978	181.1	-41.1
GG11	15	0.20582	178.8	-39.5
GG11	20	0.20335	178.7	-36.8
GG11	25	0.1935	172.9	-31.2
GG11	30	0.18479	175.7	-32.5
GG11	35	0.172	176.1	-31.2
GG11	40	0.1639	174.8	-27.6
GG11	45	0.15975	174.6	-28.2

GG11	50	0.14771	176.7	-27.5
GG11	55	0.13768	172.9	-31.5
GG11	60	0.12738	170.7	-27.7
GG11	65	0.12574	170.5	-28.2
GG11	70	0.11461	174.2	-25.3
GG11	75	0.11598	172.8	-26.9
GG11	80	0.10767	170.9	-26.6
GG11	85	0.1114	177	-26.3
GG09	0	0.0222	282.9	-25.5
GG09	100	0.0393	247.4	-6.9
GG09	150	0.0589	235.3	-2.4
GG09	200	0.0411	240.5	12.8
GG09	250	0.029	235.1	10.0
GG09	300	0.0367	222.4	23.5
GG09	350	0.0232	261.3	-4.5
GG09	400	0.0553	238.1	29.8
GG09	425	0.0591	220.8	15.9
GG09	450	0.062	221.1	9.5
GG09	475	0.0321	246.7	13.3
GG09	500	0.0479	251.0	1.6
GG09	525	0.0329	257.2	31.5
GG09	550	0.0403	245.7	-0.7
GG09	575	0.0368	251.4	-24.8
GG08	0	0.23901	245.5	-61.3
GG08	5	0.27032	241.9	-56.8
GG08	10	0.31656	233.7	-52.5
GG08	15	0.33844	230	-50.7
GG08	20	0.34082	228.6	-50
GG08	25	0.33607	226.6	-49.5
GG08	30	0.3209	226	-50.2
GG08	35	0.30549	224.7	-48.6
GG08	40	0.29325	223.7	-45.7
GG08	45	0.27736	221	-47.8
GG08	50	0.26342	223.8	-46.1
GG08	55	0.25088	221.2	-48.3
GG08	60	0.24126	222.5	-46.6
GG08	65	0.23262	221.7	-47.4
GG08	70	0.22203	220	-44.3
GG08	75	0.21871	234.5	-46.1
GG08	80	0.20959	233.9	-44.5
GG07	0	0.39856	167.9	-37.3
GG07	5	0.36389	166	-33.5
GG07	10	0.35074	166.1	-31.1
GG07	15	0.3308	165.9	-30
GG07	20	0.3098	166	-28.7
GG07	25	0.27993	167.4	-28.1

GG07	30	0.26077	167.2	-27.7
GG07	35	0.23407	168.4	-26.6
GG07	40	0.21986	164.7	-23.6
GG07	45	0.19146	168.1	-25.3
GG07	50	0.1783	166.1	-23
GG07	55	0.1652	168	-24.7
GG07	60	0.15434	170.9	-22.7
GG07	65	0.13635	169.5	-20.8
GG07	70	0.12487	169	-24.5
GG07	75	0.115	168.5	-21.9
GG07	80	0.1083	172.2	-24
GG07	85	0.0976	165.5	-22.8
GG06	0	0.06321	163.3	-17.3
GG06	5	0.09341	171.5	-19.5
GG06	10	0.13003	170.7	-14.3
GG06	15	0.1443	172.1	-14.2
GG06	20	0.14749	171.9	-12.4
GG06	25	0.14008	171.6	-12.4
GG06	30	0.1383	169.1	-12.6
GG06	35	0.13032	169.9	-12.6
GG06	40	0.12102	173.2	-10
GG06	45	0.12274	170.8	-9.6
GG06	50	0.12041	171	-11.7
GG06	55	0.12002	172.7	-8.7
GG06	60	0.11338	175.8	-8.8
GG06	65	0.11109	169.8	-8.8
GG06	70	0.09861	170.4	-6.7
GG06	75	0.10217	168.9	-9.4
GG06	80	0.08746	164.7	-9.2
GG05	0	0.05391	177	-3.2
GG05	5	0.06343	176.7	8.7
GG05	10	0.08225	174.9	12.1
GG05	15	0.09401	173.4	11.2
GG05	20	0.10248	171.7	13.6
GG05	25	0.10238	172.4	12.9
GG05	30	0.10181	173.7	10.7
GG05	35	0.10193	177.2	14.1
GG05	40	0.0943	176.9	12.9
GG05	45	0.09312	176	16
GG05	50	0.08549	173.5	13.1
GG05	55	0.08907	175.3	15.5
GG05	60	0.08555	176.6	14.5
GG05	65	0.08104	174.5	14.5
GG05	70	0.08011	175.1	13.2
GG05	75	0.08016	171.7	14.9
GG05	80	0.07289	177.9	15.9

GG04	0	0.0699	27.7	29.1
GG04	100	0.0251	158.3	36.9
GG04	150	0.0352	157.8	29.6
GG04	200	0.036	166.0	17.5
GG04	250	0.036	187.2	-5.3
GG02	0	0.41664	6.5	14.1
GG02	5	0.27374	3	5.5
GG02	10	0.17933	5.1	3.8
GG02	15	0.12168	359.8	-0.1
GG02	20	0.07721	356.4	-4.9
GG02	25	0.05907	352	-12.6
GG02	30	0.03121	322.6	-19.3
GG02	35	0.0224	328.6	-62.4
GG02	40	0.01229	284.8	-11.5
GG02	45	0.01782	353.9	-40.4
GG02	50	0.02849	317.5	-80.4
GG02	55	0.02926	356.3	-44.7
GG02	60	0.02634	279.7	-34.1
GG02	65	0.03107	124.3	-73
GG02	70	0.03292	297.6	-49.6
GG02	75	0.03916	311.2	-84.2
GG02	80	0.04468	278.6	-81.1
GG01	0	0.81568	1.8	27.7
GG01	5	0.37898	357.5	27.7
GG01	10	0.18447	14.5	29.3
GG01	15	0.10344	36.1	36.9
GG01	20	0.04551	40.9	56.9
GG01	25	0.04891	124.2	28.2
GG01	30	0.06328	141.5	20.8
GG01	35	0.08937	143.9	4.5
GG01	40	0.07704	150.3	11.4
GG01	45	0.06994	170.6	3.6
GG01	50	0.11068	159.8	11.7
GG01	55	0.06784	123.4	20.2
GG01	60	0.07541	161.9	26.3
GG01	65	0.07819	151.2	15.5
GG01	70	0.0894	129.5	23.7
GG01	75	0.06943	130.4	17.9
GG01	80	0.08257	126.6	52.1
GIG24	0	3.00342	66.2	-18
GIG24	5	0.51977	52.2	6.4
GIG24	10	0.1782	40.3	29.8
GIG24	15	0.13763	23.8	20.5
GIG24	20	0.06288	76.7	41.1
GIG24	25	0.07905	81.5	30.7
GIG24	30	0.05829	164.3	7.4

GIG24	35	0.04869	201.3	-12.5
GIG24	40	0.07193	226.1	33.8
GIG24	45	0.08901	238.9	68.2
GIG24	50	0.02666	19.8	-12.9
GIG24	55	0.03291	131.5	-50.8
GIG24	60	0.09141	158.9	32.9
GIG24	65	0.0563	222.6	28.8
GIG24	70	0.06198	202.3	-22
GIG24	75	0.0433	194.2	26
GIG24	80	0.07096	251.7	-12.6
GIG23	0	3.28123	290.6	-77
GIG23	5	0.60333	349.5	-34.3
GIG23	10	0.28476	4.8	2.4
GIG23	15	0.16836	15.4	21.2
GIG23	20	0.14322	23.4	27.1
GIG23	25	0.11123	65.2	15.2
GIG23	30	0.09434	113.7	22.1
GIG23	35	0.07978	144.7	-27.4
GIG23	40	0.09124	107.1	45.7
GIG23	45	0.09793	156	27.3
GIG23	50	0.1684	146	0.3
GIG23	55	0.09527	147.1	5.6
GIG23	60	0.06564	137.8	-5.3
GIG23	65	0.12558	144.5	16
GIG23	70	0.07671	142.3	9.8
GIG23	75	0.13352	170.5	19.9
GIG23	80	0.07546	135.4	-15
GIG23	85	0.06882	163.8	49.5
GIG21	0	2.16267	274.6	-18.3
GIG21	5	0.5464	323.1	-9.8
GIG21	10	0.3117	356.6	1.6
GIG21	15	0.15672	358.5	-0.8
GIG21	20	0.12877	3.6	-1.7
GIG21	25	0.08518	17.6	18.8
GIG21	30	0.03839	21.6	11.5
GIG21	35	0.02037	34.7	81.5
GIG21	40	0.02378	277.5	48.8
GIG21	45	0.038	22.2	42.9
GIG21	50	0.045	77	50.1
GIG21	55	0.0475	7.2	58
GIG21	60	0.04405	135.8	39.6
GIG21	65	0.02895	112.7	-36.3
GIG21	70	0.04553	83.4	66.3
GIG21	75	0.05318	115.3	57.3
GIG21	80	0.01859	122.4	-25.3
GIG19	0	1.466	38.7	-8.7

GIG19	5	0.50779	26.9	-6.7
GIG19	10	0.24657	37.2	-3.4
GIG19	15	0.16129	34.4	-3.5
GIG19	20	0.11647	31.9	-5.8
GIG19	25	0.07778	73.9	-10.7
GIG19	30	0.06494	79.9	-24.2
GIG19	35	0.07117	82.7	24.6
GIG19	40	0.05796	134.6	-2.9
GIG19	45	0.08945	111.2	16.5
GIG19	50	0.06803	56.1	25.5
GIG19	55	0.10155	58.5	19.5
GIG19	60	0.03409	111	52.3
GIG19	65	0.03349	72.6	8.4
GIG19	70	0.07686	125.7	53.5
GIG19	75	0.03718	168.8	9.8
GIG19	80	0.04841	97.1	31
GIG19	85	0.05023	125.9	13.9
GIG12	0	0.66097	20.8	2.8
GIG12	5	0.10951	5.3	17.9
GIG12	10	0.06381	4.3	-2.5
GIG12	15	0.03775	117	54.4
GIG12	20	0.02051	157	-68.6
GIG12	25	0.08024	326.1	58.8
GIG12	30	0.08314	298.6	25.2
GIG12	35	0.14312	22.8	43.9
GIG12	40	0.11187	16.6	33.4
GIG12	45	0.10298	43.5	25.8
GIG12	50	0.08009	30	-6.7
GIG12	55	0.03929	102.6	-2.2
GIG12	60	0.03714	324.7	-50.9
GIG12	65	0.04377	123	-64.5
GIG12	70	0.09476	55.7	-5.2
GIG12	75	0.01976	47	5.2
GIG12	80	0.07464	342.8	80.9
GIG03	0	0.4502	6.1	7.3
GIG03	5	0.24589	337.9	9.7
GIG03	10	0.15121	346.4	4.5
GIG03	15	0.09408	321.9	19.5
GIG03	20	0.1033	317.1	-8.9
GIG03	25	0.07263	338.2	0.9
GIG03	30	0.03487	6.4	-25.1
GIG03	35	0.02716	24.3	-31.2
GIG03	40	0.01625	112.4	-31.7
GIG03	45	0.02611	63	-21.5
GIG03	50	0.03935	135.9	19.1
GIG03	55	0.02763	113.2	-19.7

GIG03	60	0.03803	118.8	-7
GIG03	65	0.02874	163.1	-55.4
GIG03	70	0.04238	91.9	2.1
GIG03	75	0.02891	59.7	2.8
GIG03	80	0.01212	31.4	72
GIG01	0	0.69364	20.6	-33.7
GIG01	5	0.35953	24.3	-0.3
GIG01	10	0.22762	27.9	23.2
GIG01	15	0.20236	36.2	29.8
GIG01	20	0.15708	23.9	31.8
GIG01	25	0.14718	38.5	49
GIG01	30	0.14519	23.7	55.3
GIG01	35	0.15842	14.6	55.3
GIG01	40	0.13879	16.3	62.9
GIG01	45	0.20805	23.1	54.6
GIG01	50	0.12037	37.8	64.7
GIG01	55	0.13226	322.3	61
GIG01	60	0.12892	351.6	60.9
GIG01	65	0.12697	50.2	56.2
GIG01	70	0.086	13.9	65.8
GIG01	75	0.11738	10.9	40.2
GIG01	80	0.09344	33.4	59.3
GIG01	85	0.1091	7.5	51.5
GIS05	0	0.516	50.8	-35.2
GIS05	100	0.302	93	-38.6
GIS05	150	0.233	94.1	43.5
GIS05	200	0.35	142.4	-33.0
GIS05	250	0.335	172	-30.5
GIS05	300	0.265	170.2	-11.4
GIS05	350	0.223	165.3	-8.0
GIS05	400	0.199	168.9	-16.7
GIS05	425	0.305	192.4	-34.5
GIS05	450	0.256	188.4	-24.0
GIS05	475	0.266	148.7	-10.1
GIS05	500	0.144	170	-8.5
GIS05	525	0.0865	168.7	6.7
GIS05	550	0.057	144.4	36.6
GIS05	575	0.0408	178.7	19.8
GIS04	0	1.33	21.5	-6.9
GIS04	100	1.17	47.0	19.0
GIS04	150	0.539	270.6	-47.0
GIS04	200	0.394	30.1	-23.3
GIS04	250	0.133	120.5	-42.6
GIS04	300	0.21	175.8	-1.0
GIS04	350	0.19	159.8	-19.7
GIS04	400	0.233	168.3	-22.2

GIS04	425	0.19	168.6	24.6
GIS04	450	0.16	171.0	-11.6
GIS04	475	0.0823	128.8	-20.0
GIS04	500	0.103	198.8	-16.6
GIS04	525	0.123	180.5	19.5
GIS04	550	0.0569	150.5	10.5
GIS04	575	0.027	168.7	-61.8
GIS03	0	1.1	36.6	1.7
GIS03	100	0.747	42.9	-1.3
GIS03	150	0.412	50.0	-1.4
GIS03	200	0.31	53.0	-8.2
GIS03	250	0.0713	181.5	-46.6
GIS03	300	0.0933	173.3	-27.2
GIS03	350	0.142	173.9	7.1
GIS03	400	0.146	173.8	7.5
GIS03	425	0.115	208.8	-46.2
GIS03	450	0.0908	189.1	-2.6
GIS03	475	0.208	202.7	-18.4
GIS03	500	0.147	189.8	-6.7
GIS03	525	0.0849	176.9	41.4
GIS03	550	0.0727	163.8	-0.5
GIS03	575	0.0446	14.2	-57.2
GIS02	0	1.22	39.6	-1.3
GIS02	100	0.753	32.0	-4.4
GIS02	150	0.292	290.0	-49
GIS02	200	0.242	43.4	-7.7
GIS02	250	0.206	181.2	-25.3
GIS02	300	0.243	199.3	-16.6
GIS02	350	0.206	158.7	-16.6
GIS02	400	0.18	193.8	-5
GIS02	425	0.177	162.0	10
GIS02	450	0.132	159.0	1.7
GIS02	475	0.178	229.5	-21.6
GIS02	500	0.127	192.9	-13.4
GIS02	525	0.0748	197.5	23.9
GIS02	550	0.0141	153.3	54.8
GIS02	575	0.0234	181.3	-21.2
GIS01	0	0.62	7.6	8.2
GIS01	100	0.483	48.6	30.4
GIS01	150	0.281	23.0	0.6
GIS01	200	0.132	41.3	-7.8
GIS01	250	0.0378	97.4	-38.8
GIS01	300	0.134	192.0	-13.6
GIS01	350	0.141	176.7	-9.1
GIS01	400	0.126	180.5	-6.2
GIS01	425	0.198	180.2	-11.9

GIS01	450	0.124	186.1	-19.3
GIS01	475	0.115	151.5	13.2
GIS01	500	0.092	172.3	-17.7
GIS01	525	0.0223	169.5	20.0
GIS01	550	0.0315	165.6	-9.2
GIS01	575	0.0152	150.0	9.3
GIC10	0	0.58997	84.4	33.7
GIC10	5	0.42721	105.3	38.3
GIC10	10	0.41278	121.2	40
GIC10	15	0.40761	128.5	35.6
GIC10	20	0.42826	135.9	32.4
GIC10	25	0.43462	132.9	28.5
GIC10	30	0.40034	139.4	30.3
GIC10	35	0.36085	139.2	23.7
GIC10	40	0.34826	139.4	23.6
GIC10	45	0.32889	138.2	23
GIC10	50	0.31197	135	21.5
GIC10	55	0.27831	138.2	20.3
GIC10	60	0.28142	135.3	15.1
GIC10	65	0.24696	135.4	13.6
GIC10	70	0.23061	137.1	11.4
GIC10	75	0.23758	133.2	8.2
GIC10	80	0.21112	137.1	11.7
GIC09	0	0.25737	11.9	35.5
GIC09	5	0.24329	350	33
GIC09	10	0.20009	344.2	33.3
GIC09	15	0.19267	342.7	33
GIC09	20	0.18713	337.5	27.5
GIC09	25	0.19583	335.5	19
GIC09	30	0.20381	332.4	15.5
GIC09	35	0.19284	332	19.3
GIC09	40	0.17921	334.3	14
GIC09	45	0.17921	332.2	7.8
GIC09	50	0.16804	325.9	4.2
GIC09	55	0.14946	330.2	25
GIC09	60	0.14222	323.4	17.3
GIC09	65	0.13931	327.7	24.1
GIC09	70	0.10858	318.2	16.2
GIC09	75	0.09583	323	3.8
GIC09	80	0.09039	329.6	5.7
GIC08	0	0.22896	2	-3.5
GIC08	5	0.14783	350.5	-2.2
GIC08	10	0.07763	351.8	-20.6
GIC08	15	0.07025	353.2	-31.2
GIC08	20	0.03303	325.2	-21.4
GIC08	25	0.05317	286.9	-49.3

GIC08	30	0.04017	316.3	-43.7
GIC08	35	0.04293	269.8	-55.7
GIC08	40	0.04817	301.2	-46.1
GIC08	45	0.0351	240.8	6.8
GIC08	50	0.04217	269.8	-16.6
GIC08	55	0.05419	228.9	-29.7
GIC08	60	0.06555	240.1	-44.5
GIC08	65	0.04041	261.3	-45
GIC08	70	0.04613	287.2	-55.4
GIC08	75	0.03411	278.5	-39.6
GIC08	80	0.03206	230.1	-64.1
GIC07	0	0.0628	156.9	-26.8
GIC07	5	0.06607	159.6	-27.4
GIC07	10	0.06756	161.4	-27.2
GIC07	15	0.06992	163.3	-24
GIC07	20	0.07266	162.9	-26
GIC07	25	0.06843	164.4	-21.6
GIC07	30	0.06733	163	-21.9
GIC07	35	0.06562	165	-20.4
GIC07	40	0.06015	164.5	-21.4
GIC07	45	0.05864	160.7	-25.3
GIC07	50	0.05743	164.2	-23.1
GIC07	55	0.05275	165	-21.6
GIC07	60	0.04929	159.3	-29.1
GIC07	65	0.04861	155.8	-28.1
GIC07	70	0.05035	163	-25.1
GIC07	75	0.04161	164.5	-22.7
GIC07	80	0.0361	158.7	-24.2
GIC06	0	0.0478	263	-55.9
GIC06	5	0.04893	200.5	-15.4
GIC06	10	0.06468	191.3	-12.2
GIC06	15	0.06779	187.7	-8.3
GIC06	20	0.06556	185.5	-9.6
GIC06	25	0.06129	184.5	-10.4
GIC06	30	0.06559	186.9	-6.8
GIC06	35	0.05541	187.6	-2.7
GIC06	40	0.0574	180.6	3.1
GIC06	45	0.04547	177.9	5.6
GIC06	50	0.05284	182.5	-4.1
GIC06	55	0.0408	177.5	-5.8
GIC06	60	0.04081	180.2	-9.5
GIC06	65	0.04128	181.4	3.2
GIC06	70	0.03328	176.5	-8.3
GIC06	75	0.04282	172	-2.3
GIC06	80	0.03565	177.7	-10.4
GIC05	0	0.04376	184.8	17.6

GIC05	5	0.03703	182.9	11.8
GIC05	10	0.03914	177	11.5
GIC05	15	0.03656	184.8	10.7
GIC05	20	0.03507	184.6	14.3
GIC05	25	0.0334	187.1	11
GIC05	30	0.02952	185.3	14.4
GIC05	35	0.02797	189.8	15.8
GIC05	40	0.0273	187.4	17.3
GIC05	45	0.02296	199.4	30.1
GIC05	50	0.02351	191.8	18.4
GIC05	55	0.0267	198	12.6
GIC05	60	0.0238	189.5	12.5
GIC05	65	0.01948	193.2	23.6
GIC05	70	0.01801	179.3	25.7
GIC05	75	0.02114	173	24.2
GIC05	80	0.01888	178.3	21.5
GIC04	0	0.09088	111.2	-12.2
GIC04	5	0.08132	114.4	-13.2
GIC04	10	0.07437	120.7	-14
GIC04	15	0.06097	124.2	-21.9
GIC04	20	0.04935	129.1	-16.9
GIC04	25	0.04582	130.8	-18
GIC04	30	0.03953	129.4	-13.2
GIC04	35	0.03949	136.6	-17.2
GIC04	40	0.03636	137.3	-12
GIC04	45	0.03627	132.9	-15
GIC04	50	0.03804	137.9	-11.9
GIC04	55	0.0255	134.2	18
GIC04	60	0.0196	161.2	11.7
GIC04	65	0.02276	135.4	9.6
GIC04	70	0.02269	143.8	7.4
GIC04	75	0.02034	140.9	-6.6
GIC04	80	0.01965	111.2	-4.4
GIC03	0	0.071	207.9	-38.1
GIC03	5	0.07704	187.8	-43.1
GIC03	10	0.09276	180.7	-37.8
GIC03	15	0.09589	180.4	-36.2
GIC03	20	0.09813	183.6	-33.8
GIC03	25	0.0931	181	-31.6
GIC03	30	0.09552	179.8	-30.7
GIC03	35	0.09223	183.1	-26.5
GIC03	40	0.0899	181.9	-26.7
GIC03	45	0.08113	182.6	-26.1
GIC03	50	0.08493	178.8	-25.6
GIC03	55	0.07898	182.9	-25.1
GIC03	60	0.06952	179.8	-20.9

GIC03	65		0.06651		183.9	-28.2
GIC03	70		0.06274		179.2	-22.2
GIC03	75		0.06389		178.9	-32.1
GIC03	80		0.06456		179.8	-24.3
GIC02	0		0.10393		148.3	40.3
GIC02	5		0.09472		145.6	38.6
GIC02	10		0.08849		141.6	37.7
GIC02	15		0.08348		144.3	42.3
GIC02	20		0.07983		141.5	45.1
GIC02	25		0.06912		142.6	46.4
GIC02	30		0.06591		138.9	43.7
GIC02	35		0.06222		138.7	40.3
GIC02	40		0.05762		137.3	41.9
GIC02	45		0.05649		139.7	38.7
GIC02	50		0.05023		136.9	37
GIC02	55		0.04913		134.5	38.3
GIC02	60		0.04561		135.3	31.2
GIC02	65		0.04361		140.8	36.7
GIC02	70		0.04208		142.3	37.7
GIC02	75		0.04226		133.5	40.2
GIC02	80		0.03632		139.1	35.9
GIC01	0		0.16673		237.8	19.2
GIC01	5		0.07619		224.6	-13.7
GIC01	10		0.10401		212.5	3.7
GIC01	15		0.11998		207.5	8.4
GIC01	20		0.11308		208.2	6.2
GIC01	25		0.11305		205.4	8.3
GIC01	30		0.10352		203.4	10
GIC01	35		0.10309		203.4	8.8
GIC01	40		0.10674		202.9	11.6
GIC01	45		0.09655		205.6	4.2
GIC01	50		0.09388		203.5	9.5
GIC01	55		0.09088		204.8	13.9
GIC01	60		0.07781		199.2	15.1
GIC01	65		0.07554		201.9	4.7
GIC01	70		0.07199		203.4	6
GIC01	75		0.07423		203.5	8.8
GIC01	80		0.0908		202.3	34.3
GIC01	85		0.05748		201.4	12.5
GIC01	90		0.05987		199.7	5.1
GIC01	95		0.06104		199.1	11
GBIII06		0		0.13462	190.2	-12.2
GBIII06		100		0.14446	202.7	-12.1
GBIII06		150		0.14562	192.8	-9.6
GBIII06		200		0.13558	197.1	-10.5
GBIII06		250		0.12105	201.5	-6.5

GBIII06	300	0.10207	199.6	-11.5
GBIII06	350	0.09247	199.2	-10.2
GBIII06	400	0.05731	195.3	-9.5
GBIII06	425	0.05437	195.1	-7.1
GBIII06	450	0.0511	199.6	-11.5
GBIII06	475	0.05088	181.7	-10.1
GBIII06	500	0.04595	185.6	-11.2
GBIII06	525	0.0533	181.6	-2.4
GBIII06	550	0.03488	171.1	-1.8
GBIII06	575	0.0154	175.7	-8.4
GBIII03	0	0.93904	1.3	-5.6
GBIII03	100	0.85177	357.3	2.2
GBIII03	150	0.6914	357	-5.2
GBIII03	200	0.56627	359.3	-6.1
GBIII03	250	0.37936	4.9	-14.6
GBIII03	300	0.30505	350.5	-24.4
GBIII03	350	0.20173	331.6	-53.5
GBIII03	400	0.17781	313.7	-49.8
GBIII03	425	0.16173	336	-34.2
GBIII03	450	0.07978	310.6	-50.6
GBIII03	475	0.11422	60.9	8.9
GBIII03	500	0.12855	7.7	7.6
GBIII03	525	0.19443	30.1	-5.5
GBIII03	550	0.06575	55.7	38.5
GBIII03	575	0.09741	38	-19.9
GBIII02	0	1.4642	39.5	5
GBIII02	100	1.174	19.3	14.1
GBIII02	150	1.02659	25.8	2.7
GBIII02	200	0.79484	35.7	-2.7
GBIII02	250	0.51348	10.8	14.1
GBIII02	300	0.42503	325.5	-2.9
GBIII02	350	0.35675	324.2	-11.7
GBIII02	400	0.1937	337.8	-6.6
GBIII02	425	0.16376	296.5	11
GBIII02	450	0.19149	324.8	-16
GBIII02	475	0.15204	276.5	16.8
GBIII02	500	0.11816	242.5	63.8
GBIII02	525	0.15289	259.4	-31.2
GBIII02	550	0.13562	355.1	56.9
GBIII02	575	0.10907	279.2	6.6
GBIII01	0	0.65025	267.8	24.2
GBIII01	100	0.54786	269.2	14.9
GBIII01	150	0.47814	266.7	12.6
GBIII01	200	0.39524	266.4	10.8
GBIII01	250	0.32065	267.8	9.1
GBIII01	300	0.31087	275.7	3.7

GBIII01	350	0.20491	258.4	5.8
GBIII01	400	0.1642	268.3	-5.1
GBIII01	425	0.13524	254	-5.4
GBIII01	450	0.10701	258.3	-8.8
GBIII01	475	0.05794	293.8	-19.6
GBIII01	500	0.09667	312.1	43
GBIII01	525	0.0782	268.1	7.1
GBIII01	550	0.04466	345.4	-55.2
GBIII01	575	0.05744	232.4	12.5
GBXIIC04	0	0.34833	290.3	-6.8
GBXIIC04	100	0.31732	301.6	-4.2
GBXIIC04	150	0.28579	289.3	-10.5
GBXIIC04	200	0.24882	302.7	-7.4
GBXIIC04	250	0.23406	287.6	-11.3
GBXIIC04	300	0.21305	289.1	-4.1
GBXIIC04	350	0.1404	292.1	-9.3
GBXIIC04	400	0.05401	309.3	2.4
GBXIIC04	425	0.03822	315.1	8.6
GBXIIC04	450	0.0204	352.5	33.2
GBXIIC04	475	0.02015	326.4	27.4
GBXIIC04	500	0.0206	340.9	34.6
GBXIIC04	525	0.01603	356.5	66.8
GBXIIC04	550	0.01362	17.6	25.7
GBXIIC04	575	0.00403	314.4	5.2
GBXIIC03	0	0.40092	259.1	-12
GBXIIC03	150	0.31639	252.3	-15.9
GBXIIC03	200	0.3018	250.5	-23.3
GBXIIC03	250	0.29782	249.7	-18.5
GBXIIC03	300	0.25396	250.2	-18.8
GBXIIC03	350	0.18663	248.3	-19.2
GBXIIC03	400	0.07562	237.5	-23
GBXIIC03	425	0.03734	231.2	-17
GBXIIC03	450	0.00585	177.4	20.4
GBXIIC03	475	0.00677	165.2	-4.4
GBXIIC03	500	0.00524	132.2	-5.8
GBXIIC03	525	0.00666	204.9	-30.8
GBXIIC03	550	0.01185	93.7	-8.8
GBXIIC03	575	0.01687	99.9	26.9
GBXIIC02	0	0.13106	216	-51.8
GBXIIC02	100	0.13005	198.6	-40.9
GBXIIC02	150	0.12651	189.2	-36.9
GBXIIC02	200	0.11481	183.7	-53.6
GBXIIC02	250	0.10147	199.2	-42.9
GBXIIC02	300	0.08757	206.8	-43.3
GBXIIC02	350	0.06587	210.1	-32.6
GBXIIC02	400	0.04155	165.7	-29.1

GBXIIC02	425	0.0362	171.2	-27.5
GBXIIC02	450	0.03048	148.5	-13.6
GBXIIC02	475	0.03265	162.9	-12.3
GBXIIC02	500	0.03388	154.7	-21
GBXIIC02	525	0.02549	170	-26.5
GBXIIC02	550	0.02755	128.9	-39.5
GBXIIC02	575	0.00704	126.3	3.9
GBXIIC02	575	0.01497	100.2	20
GBXIIC01	0	0.03605	340.9	-8.7
GBXIIC01	100	0.03878	336.6	-7.7
GBXIIC01	150	0.0345	329.8	-6.3
GBXIIC01	200	0.03032	340.8	-7.9
GBXIIC01	250	0.02972	343.2	-1.9
GBXIIC01	300	0.02657	340.4	4.5
GBXIIC01	350	0.02314	351.6	-6.7
GBXIIC01	400	0.02226	353.8	5
GBXIIC01	425	0.0221	356.4	2.6
GBXIIC01	450	0.02056	347.9	10.1
GBXIIC01	475	0.01595	341.1	-2.9
GBXIIC01	500	0.01458	353.3	-5.7
GBXIIC01	525	0.00799	320.7	-8.4
GBXIIC01	550	0.0148	2.6	-8.9
GBXIIC01	575	0.00733	21.6	16.5
GBXIIB30	0	0.24705	271.5	-3.1
GBXIIB30	100	0.27301	259.1	4.5
GBXIIB30	150	0.2546	278.6	-0.1
GBXIIB30	200	0.2216	259.4	10.4
GBXIIB30	250	0.17247	265.5	15.2
GBXIIB30	300	0.19061	269.4	22.8
GBXIIB30	350	0.13039	279	9.4
GBXIIB30	400	0.10185	285	1.2
GBXIIB30	425	0.10389	255.6	40.2
GBXIIB30	450	0.09597	296.3	32.5
GBXIIB30	475	0.05204	287.2	36.6
GBXIIB30	500	0.03245	284	47.1
GBXIIB30	525	0.03335	319.4	19
GBXIIB30	550	0.02706	323.4	34.8
GBXIIB30	575	0.01717	14.7	70.2
GBXIIA27	0	0.18892	179.6	-10.6
GBXIIA27	100	0.19178	177.7	-12.7
GBXIIA27	150	0.18372	174.5	-19.1
GBXIIA27	200	0.16287	175.8	-13.8
GBXIIA27	250	0.15578	173.3	-11.9
GBXIIA27	300	0.14267	178.5	-11.1
GBXIIA27	350	0.1215	174.4	-11.4
GBXIIA27	400	0.10272	175.5	-8.5

GBXIIA27	425	0.07632	175.3	-12
GBXIIA27	450	0.07093	172.4	-11
GBXIIA27	475	0.06863	169.3	-14.9
GBXIIA27	500	0.04989	172.3	-14.5
GBXIIA27	525	0.04432	172.8	-16.1
GBXIIA27	550	0.03873	161.5	-18.7
GBXIIA27	575	0.02166	160.6	-20.9
GBXIIA26	0	0.16587	165.5	3.4
GBXIIA26	100	0.16789	165.3	1.1
GBXIIA26	150	0.15549	165.1	4.3
GBXIIA26	200	0.14348	163.4	-4.9
GBXIIA26	250	0.12905	165.9	1.5
GBXIIA26	300	0.11025	167.3	3.4
GBXIIA26	350	0.09282	31.3	17
GBXIIA26	400	0.07785	167.6	1.9
GBXIIA26	425	0.07005	168.1	-0.3
GBXIIA26	450	0.05745	165.2	4
GBXIIA26	475	0.04266	164.2	4.6
GBXIIA26	500	0.04221	164.5	-0.1
GBXIIA26	525	0.0337	168.7	3.7
GBXIIA26	550	0.02492	158.3	2.9
GBXIIA25	0	0.47129	2	23.3
GBXIIA25	100	0.40075	10.2	20.7
GBXIIA25	150	0.37076	7.4	15.4
GBXIIA25	200	0.33342	11.1	17.1
GBXIIA25	250	0.3041	14.4	12.4
GBXIIA25	300	0.26412	17.9	10.1
GBXIIA25	350	0.21601	20.8	14.4
GBXIIA25	400	0.20589	23.9	13.6
GBXIIA25	425	0.16838	34.5	9.3
GBXIIA25	450	0.13902	25.1	12.4
GBXIIA25	475	0.12287	24	27.8
GBXIIA25	500	0.08598	20.5	31.7
GBXIIA25	525	0.04756	298.2	12.4
GBXIIA25	550	0.05128	358.5	-4.8
GBXIIA25	575	0.05346	316.6	-16.7
GBXIIA23	0	0.10878	314.1	-9.1
GBXIIA23	100	0.37496	6.6	-1.9
GBXIIA23	150	0.31478	12.2	-4
GBXIIA23	200	0.22829	21.1	-7
GBXIIA23	250	0.23329	26.8	-8.7
GBXIIA23	300	0.24663	25.9	-6.6
GBXIIA23	350	0.20928	39.1	-15.8
GBXIIA23	400	0.19657	41.4	-6.6
GBXIIA23	425	0.21565	41.3	-8.8
GBXIIA23	450	0.21472	31	0.5

GBXIIA23	475	0.19658	21	-12.4
GBXIIA23	500	0.13872	20.6	2.7
GBXIIA23	525	0.08706	11.1	-9.5
GBXIIA23	550	0.09194	0.4	-3.8
GBXIIA23	575	0.03144	351	19.5
GBXIIA21	0	0.2547	48.2	7.7
GBXIIA21	100	0.27554	312.4	1.7
GBXIIA21	150	0.15068	24	55.7
GBXIIA21	200	0.09805	336.3	-62.4
GBXIIA21	250	0.16766	320.8	-61.1
GBXIIA21	300	0.13244	22.3	-31.6
GBXIIA21	350	0.04206	115.9	-53.2
GBXIIA21	400	0.16151	351.5	27.3
GBXIIA18	0	0.34858	10.7	14
GBXIIA18	100	0.25227	15.8	-3.8
GBXIIA18	150	0.23505	15.7	-8.3
GBXIIA18	200	0.21609	6.1	7.8
GBXIIA18	250	0.24717	15.4	3.4
GBXIIA18	300	0.24876	12.5	10.7
GBXIIA18	350	0.15671	34.5	22
GBXIIA18	400	0.14276	39.1	30.8
GBXIIA18	425	0.17916	34	6.4
GBXIIA18	450	0.13901	25.3	5.4
GBXIIA18	475	0.19176	12.1	-3.9
GBXIIA18	500	0.08873	31.4	-17.4
GBXIIA18	525	0.1371	13.2	5.1
GBXIIA18	550	0.08368	13.2	-31.1
GBXIIA18	575	0.05863	42.2	-3.3
GBXIIA17	0	6.26076	320.8	27.9
GBXIIA17	100	6.18477	327.4	32.5
GBXIIA17	150	5.89035	331.9	37.5
GBXIIA17	200	5.38646	326.9	30
GBXIIA17	250	4.74257	327.4	34.2
GBXIIA17	300	3.11481	335.6	32.6
GBXIIA17	350	2.16701	332.7	29.8
GBXIIA17	400	1.43624	336	30.7
GBXIIA17	425	1.33878	338.5	31.6
GBXIIA17	450	1.07484	326.1	33.4
GBXIIA17	475	0.9525	326.1	35.3
GBXIIA17	500	0.39499	334.4	35.9
GBXIIA17	525	0.39324	329	41
GBXIIA17	550	0.06792	317.5	43.3
GBXIIA17	550	0.01911	160.8	29.8
GBXIIA17	575	0.04737	287.5	26.5
GBXIIA13	0	0.14205	28.1	-7.3
GBXIIA13	100	0.07789	9.3	-10.9

GBXIIA13	150	0.05473	11.8	-11.3
GBXIIA13	200	0.04093	5.4	-8.3
GBXIIA13	250	0.03792	8.1	-18.9
GBXIIA13	300	0.02846	11.4	-30
GBXIIA13	350	0.01111	33.2	-32.1
GBXIIA13	400	0.01292	355	-73.4
GBXIIA13	425	0.01478	8.7	-78.7
GBXIIA13	450	0.00943	165.2	-51.7
GBXIIA13	475	0.01804	22.6	-21.7
GBXIIA13	500	0.00825	204.7	-74.5
GBXIIA13	525	0.01706	229	-60.1
GBXIIA13	575	0.0161	353.8	25.8
GBXIIA11	0	0.06513	186.2	-28.1
GBXIIA11	100	0.07826	190.4	-22.6
GBXIIA11	150	0.07259	185.1	-24.9
GBXIIA11	200	0.06789	186	-22.3
GBXIIA11	250	0.05494	186	-21.6
GBXIIA11	300	0.04398	191.6	-22.4
GBXIIA11	350	0.02532	182.6	-25.3
GBXIIA11	400	0.02312	183.9	-25.8
GBXIIA11	425	0.01115	146.7	-15.7
GBXIIA11	450	0.01373	285.4	-12.9
GBXIIA11	475	0.00932	210.4	-55.8
GBXIIA11	500	0.00502	116	-62.1
GBXIIA11	525	0.0078	195.3	-59.8
GBXIIA11	550	0.00819	48.4	-5
GBXIIA11	575	0.00249	182.7	6.2
GBXIIA10	0	0.08289	150.4	-40.6
GBXIIA10	100	0.08392	164.3	-28.1
GBXIIA10	150	0.0803	169.1	-23.5
GBXIIA10	200	0.06504	160.7	-27.4
GBXIIA10	250	0.05572	163.5	-28.4
GBXIIA10	300	0.04438	167.3	-27
GBXIIA10	350	0.02878	162.1	-27.7
GBXIIA10	400	0.02498	154.5	-37.5
GBXIIA10	425	0.02218	162.8	-40.4
GBXIIA10	450	0.00771	140.9	-37.9
GBXIIA10	475	0.01177	140.6	-0.1
GBXIIA10	500	0.00961	151.8	2.2
GBXIIA10	525	0.01059	86.9	-63.3
GBXIIA10	550	0.00697	256.6	4.2
GBXIIA10	575	0.00474	186.9	17.2
GBXIIA09	0	0.04603	166	-20.3
GBXIIA09	100	0.05054	175.8	-1.1
GBXIIA09	150	0.04988	173.7	-9.2
GBXIIA09	200	0.04534	174.1	-5.5

GBXIIA09	250	0.04112	171.4	-1.3
GBXIIA09	300	0.02753	170.7	0.6
GBXIIA09	350	0.02075	174.8	5.1
GBXIIA09	400	0.00999	192.3	9.4
GBXIIA09	425	0.01011	156.7	8.3
GBXIIA09	450	0.0061	167.3	7.6
GBXIIA09	475	0.00801	134.4	19.5
GBXIIA09	500	0.00535	177.6	-31.1
GBXIIA09	525	0.00753	155.2	20.8
GBXIIA09	550	0.00413	16.2	-25.3
GBXIIA08	0	0.01724	134.7	-14.8
GBXIIA08	100	0.02318	163.1	1.5
GBXIIA08	150	0.02486	163.7	3
GBXIIA08	200	0.02377	167.2	7.6
GBXIIA08	250	0.02199	167.4	4.4
GBXIIA08	300	0.01718	163.2	4.5
GBXIIA08	350	0.01181	157.3	12.4
GBXIIA08	400	0.00747	161.3	12.1
GBXIIA08	425	0.00582	173	35.7
GBXIIA08	450	0.00253	334.2	49.8
GBXIIA08	475	0.00395	112.4	61.3
GBXIIA08	500	0.0039	140.2	62.1
GBXIIA08	525	0.00224	123.3	-33.6
GBXIIA08	550	0.00521	6.9	-20.9
GBXIIA08	575	0.00558	68	-35.2
GBXIIA07	0	0.02231	166.1	-38.9
GBXIIA07	100	0.02758	180.4	-17.1
GBXIIA07	150	0.02804	176.9	-13.9
GBXIIA07	200	0.0277	177.8	-8
GBXIIA07	250	0.02274	175.2	-12.9
GBXIIA07	300	0.01776	182.6	-12
GBXIIA07	350	0.00857	167	-21.1
GBXIIA07	400	0.00623	172.3	-28.9
GBXIIA07	425	0.00377	167.3	-57.6
GBXIIA07	450	0.00384	148.6	-49.7
GBXIIA07	475	0.00506	215	-25.4
GBXIIA07	500	0.00193	60.2	-28.6
GBXIIA07	525	0.00379	145.4	-27.4
GBXIIA07	550	0.00835	29.5	-43
GBXIIA07	575	0.00224	60.8	-38.3
GBXIIA06	0	0.04213	173.8	-34.4
GBXIIA06	100	0.03918	179.2	-36.6
GBXIIA06	150	0.03812	172.7	-30.9
GBXIIA06	200	0.03222	172.1	-36.4
GBXIIA06	250	0.02378	173.3	-36.1
GBXIIA06	300	0.01852	170.6	-42.7

GBXIIA06	350	0.01207	161.6	-50.8
GBXIIA06	400	0.00971	154.9	-64.4
GBXIIA06	425	0.00727	122.1	-66.6
GBXIIA06	450	0.00408	60.2	-67.3
GBXIIA06	475	0.00243	151.7	-67.3
GBXIIA06	500	0.00424	35.5	-31.9
GBXIIA06	525	0.00518	79.2	-50.1
GBXIIA06	550	0.00456	20.1	-19.2
GBXIIA06	575	0.00223	49.7	3.2
GBXIIA05	0	0.02243	179.1	-50.9
GBXIIA05	100	0.02106	198	-46.1
GBXIIA05	150	0.01884	200.3	-43.3
GBXIIA05	200	0.01569	200.4	-44.8
GBXIIA05	250	0.01165	193.9	-42.4
GBXIIA05	300	0.01073	206.3	-48.2
GBXIIA05	350	0.00806	196.1	-37.7
GBXIIA05	400	0.00517	349.3	-70.7
GBXIIA05	425	0.00416	178.1	-63.4
GBXIIA05	450	0.00516	345.6	-60.4
GBXIIA05	475	0.0029	174	-21.1
GBXIIA05	500	0.00289	51.1	-62.1
GBXIIA05	525	0.00424	71.7	-9.4
GBXIIA05	550	0.00686	48	-32
GBXIIA05	575	0.00324	127.3	12.3
GBXIIA03	0	0.02872	120.8	-18.6
GBXIIA03	100	0.02562	138.4	-19.5
GBXIIA03	150	0.02346	134.7	-13.5
GBXIIA03	200	0.02022	143.2	-14
GBXIIA03	250	0.01462	142.6	-11.3
GBXIIA03	300	0.01347	132.9	-16.8
GBXIIA03	350	0.00858	109.3	-12.9
GBXIIA03	400	0.00716	111.4	-38.4
GBXIIA03	425	0.00523	105.1	-16.8
GBXIIA03	450	0.00341	85.6	-0.2
GBXIIA03	475	0.00687	93.5	-8.1
GBXIIA03	500	0.00392	70.1	-29.3
GBXIIA03	525	0.00321	97.1	-52.2
GBXIIA03	550	0.00527	5.1	-7
GBXIIA03	575	0.00483	116.9	16.2
GBXIIA01	0	0.02674	141.5	17.6
GBXIIA01	100	0.03077	154.8	5.4
GBXIIA01	150	0.0288	157.8	0.2
GBXIIA01	200	0.02529	155.9	0.8
GBXIIA01	250	0.02255	157.5	19
GBXIIA01	300	0.01762	163.7	15.6
GBXIIA01	350	0.0088	205.7	-19.8

GBXIIA01	400	0.01081	266.7	-6.4
GBXIIA01	425	0.00814	248.7	1.7
GBXIIA01	450	0.01838	269.5	6.3
GBXIIA01	475	0.01017	327.2	-76.7
GBXIIA01	500	0.00699	288.9	0.2
GBXIIA01	525	0.00417	92.9	38.1
GBXIIA01	550	0.01667	263.9	8.8
GBIVO09	0	1.85247	351	16.9
GBIVO09	100	1.39720	345.2	14.7
GBIVO09	150	0.9844	348	14.1
GBIVO09	200	0.7134	343.7	13.5
GBIVO09	250	0.5635	340.5	3.9
GBIVO09	300	0.3543	328	-2.7
GBIVO09	350	0.2656	319.9	-19.5
GBIVO09	400	0.2607	259.2	-38.4
GBIVO09	425	0.1741	278.6	-44.7
GBIVO09	450	0.2307	265.6	-37.7
GBIVO09	475	0.2167	270.3	-36
GBIVO09	500	0.1655	238.1	-25
GBIVO09	525	0.0350	22	-44.4
GBIVO09	550	0.0652	121.6	-67.2
GBIVO09	575	0.0383	285.5	-85.6
GBIVO05	0	0.5465	358.5	-13.3
GBIVO05	100	0.4261	359.8	-1.2
GBIVO05	150	0.3276	354.2	2.7
GBIVO05	200	0.2602	3.5	3.6
GBIVO05	250	0.1886	352	-16.6
GBIVO05	300	0.1531	20.6	8.1
GBIVO05	350	0.1246	11.2	-31.7
GBIVO05	400	0.0947	36.8	-12.5
GBIVO05	425	0.0879	357.6	-28.5
GBIVO05	450	0.0952	27.2	-30.5
GBIVO05	475	0.0888	5.9	-23.8
GBIVO05	500	0.0376	17.5	-20.6
GBIVO05	525	0.1286	27.1	-16.7
GBIVO05	550	0.0422	131.2	-11.2
GBIVO05	575	0.0433	28.9	-5.5
GBIVO04	0	1.43498	20.9	-1.2
GBIVO04	100	1.09322	15.8	7.5
GBIVO04	150	0.7901	22.1	19.2
GBIVO04	200	0.5952	26.1	15.2
GBIVO04	250	0.4578	18.1	20.5
GBIVO04	300	0.4001	12.7	34.3
GBIVO04	350	0.2419	21.9	31.8
GBIVO04	400	0.2139	55.9	74.9
GBIVO04	425	0.1812	350.4	71.6

GBIVO04	450	0.1431	167.9	76.2
GBIVO04	475	0.2396	179.8	73.4
GBIVO04	500	0.1092	216.4	84.5
GBIVO04	525	0.0288	255.4	28.3
GBIVO04	550	0.0496	30.5	68.2
GBIVO04	575	0.0553	281.2	46
GBIV07	0	0.21439	128.5	-8.3
GBIV07	5	0.1672	171.2	-16
GBIV07	10	0.18793	175.6	-17.6
GBIV07	15	0.18506	176.2	-17.9
GBIV07	20	0.1803	174.5	-17.6
GBIV07	25	0.17696	175.7	-17.3
GBIV07	30	0.17141	177.2	-19.1
GBIV07	35	0.16061	178.6	-17.1
GBIV07	40	0.15524	177.3	-16.7
GBIV07	45	0.13664	171.7	-16.6
GBIV07	50	0.13661	176	-20
GBIV07	55	0.12702	177.3	-15.6
GBIV07	60	0.12529	174.5	-16
GBIV07	65	0.12305	178.6	-16.2
GBIV07	70	0.11867	178.6	-16.3
GBIV07	75	0.11625	182.8	-14.9
GBIV07	80	0.11315	179.4	-14.3
GBIV05	0	0.0228	97.8	9.3
GBIV05	100	0.0189	105.1	7.2
GBIV05	150	0.0169	108.8	3.8
GBIV05	200	0.0146	103.4	-0.5
GBIV05	250	0.0139	116.5	3.5
GBIV05	300	0.0119	98.5	-4.7
GBIV05	350	0.0069	115.4	-5.4
GBIV05	400	0.0018	123.6	22.4
GBIV05	425	0.0047	294.3	44.1
GBIV05	450	0.0046	23.3	0.2
GBIV05	475	0.0056	231.1	15.8
GBIV05	500	0.0081	282.1	3.2
GBIV05	525	0.0023	122.6	39
GBIV05	550	0.0041	115.8	14.1
GBIV05	575	0.0031	308.7	21.6
GBIV04	0	2.14753	46	22.7
GBIV04	100	1.95298	42.6	22.7
GBIV04	150	1.82999	40.5	24.1
GBIV04	200	1.72958	38	22.5
GBIV04	250	1.67543	41.5	16
GBIV04	300	1.62821	39.8	21.3
GBIV04	350	1.58022	29.6	20.8
GBIV04	400	1.54526	24.6	16.2

GBIV04	425	1.47524	19.8	24.3
GBIV04	450	1.49995	21.7	17.1
GBIV04	475	1.55073	22.5	19.4
GBIV04	500	1.51407	21.6	18.1
GBIV04	525	1.49796	21.4	15.5
GBIV04	550	1.47778	19.4	13.1
GBIV04	575	1.11202	22.4	17.7
GBIV04	600	0.1760	27.8	23.6
GBIV04	625	0.08795	27.1	18.7
GBIV03	0	0.7116	102.3	17
GBIV03	100	0.5924	108.1	15.1
GBIV03	150	0.4502	119.6	15.8
GBIV03	200	0.3708	124.6	14.3
GBIV03	250	0.3087	128.2	17.1
GBIV03	300	0.2114	141.3	18.1
GBIV03	350	0.1880	162.1	29
GBIV03	350	0.1859	156.4	29.4
GBIV03	400	0.1605	198	17.1
GBIV03	425	0.2235	271	33.9
GBIV03	450	0.2270	250.2	23.1
GBIV03	475	0.0863	300.2	34.5
GBIV03	500	0.0405	337.9	-81.5
GBIV03	525	0.0872	29.5	-31.3
GBIV03	550	0.1173	196.3	45.4
GBIV03	575	0.0398	232.6	28
GBIV01	0	1.91688	86.4	9.8
GBIV01	5	0.346	62.6	9.6
GBIV01	10	0.17582	49.5	-4.5
GBIV01	15	0.12504	52.2	-5.3
GBIV01	20	0.09637	55.5	-3.7
GBIV01	25	0.09687	71.7	-17
GBIV01	30	0.07876	84.9	-12.6
GBIV01	35	0.06031	61.3	-32.5
GBIV01	40	0.05557	21.3	-23.3
GBIV01	45	0.04375	69.9	-18.6
GBIV01	50	0.05916	84.8	-28.4
GBIV01	55	0.02899	80.7	-67.3
GBIV01	60	0.06521	83.6	-34.1
GBIV01	65	0.03921	108.8	-37.2
GBIV01	70	0.02694	25.6	-25.6
GBIV01	75	0.05941	68.8	-58.1
GBIV01	80	0.02812	69.3	-22.7
GBIV21	0	6.35596	197.6	-38.2
GBIV21	5	5.08429	197.8	-38.3
GBIV21	10	3.47650	196.2	-38.4
GBIV21	15	2.43972	195.1	-39

GBIV21	20	1.74733	194.7	-39.3
GBIV21	25	1.30148	194.6	-39.1
GBIV21	30	0.98801	195.6	-38.6
GBIV21	35	0.75276	195.9	-37.5
GBIV21	40	0.61458	196.7	-37.1
GBIV21	45	0.49381	198.9	-36.1
GBIV21	50	0.40246	201.8	-36.3
GBIV21	55	0.32203	202.5	-36.2
GBIV21	60	0.27325	205.6	-34.5
GBIV21	65	0.23653	202.6	-32.3
GBIV21	70	0.19395	207.3	-32.3
GBIV21	75	0.17221	206.6	-27.6
GBIV21	80	0.15231	209	-28
GBIV20	0	0.1883	71.5	1.3
GBIV20	100	0.1382	65.8	-17.6
GBIV20	150	0.1717	48	-14.6
GBIV20	200	0.1384	108.2	-4.1
GBIV20	250	0.0563	113.7	-23.8
GBIV20	300	0.0648	131.9	13.1
GBIV20	350	0.1021	177.9	-4
GBIV20	400	0.1217	171.6	-5.5
GBIV20	425	0.0964	179.7	15.3
GBIV20	450	0.0440	186	21.1
GBIV19	0	0.3111	317.9	60.9
GBIV19	100	0.2517	301	67.4
GBIV19	150	0.1802	328.4	59.5
GBIV19	200	0.1604	309.8	71.3
GBIV19	250	0.1475	300	70.6
GBIV19	300	0.1016	320.6	67.8
GBIV19	350	0.0772	314.3	63.2
GBIV19	400	0.0397	185.2	51.2
GBIV19	425	0.0180	177.3	2.6
GBIV19	450	0.0213	188.8	25.3
GBIV19	475	0.0436	63.2	53.7
GBIV19	500	0.0590	43.4	33.5
GBIV19	525	0.0280	283.6	39.6
GBIV19	550	0.0362	323.3	-51.1
GBIV19	575	0.0123	16.6	-50.3
GBIV18	0	0.7566	71.5	19.8
GBIV18	100	0.6081	74.6	13.2
GBIV18	150	0.5194	80.7	16
GBIV18	200	0.4751	80.2	17.8
GBIV18	250	0.4106	83	17.1
GBIV18	300	0.2839	84.5	14.6
GBIV18	350	0.1642	86.5	-1.4
GBIV18	400	0.1013	96.9	31.6

GBIV18	425	0.1292	97.1	23.5
GBIV18	450	0.0463	70.3	23.9
GBIV18	475	0.0215	88.4	3.4
GBIV18	500	0.0445	58.1	6
GBIV18	525	0.0285	105.3	41.8
GBIV18	550	0.0230	331.1	49.9
GBIV18	575	0.0252	335.8	88.3
GBIV16	0	0.2171	110.4	65.2
GBIV16	100	0.1613	109.8	51.2
GBIV16	150	0.1356	128.4	35.1
GBIV16	200	0.1236	98.7	35.2
GBIV16	250	0.1013	106.2	31.2
GBIV16	300	0.0842	123.3	24.9
GBIV16	350	0.0558	130.5	28.1
GBIV16	400	0.0333	120.7	-36.3
GBIV16	425	0.0286	62.6	-47.1
GBIV16	450	0.0339	98.1	-31.9
GBIV16	475	0.0149	203.9	-25.1
GBIV16	500	0.0306	74.4	-49.5
GBIV16	550	0.0201	273.7	0.2
GBIV16	575	0.0083	259.3	-15.2
GBIV15	0	0.52334	44.8	6.8
GBIV15	5	0.17969	22.5	22.8
GBIV15	10	0.0908	32.4	40
GBIV15	15	0.0549	71.4	41.6
GBIV15	20	0.04906	107.4	35.4
GBIV15	25	0.05762	116.1	28.6
GBIV15	30	0.05456	125.6	26.1
GBIV15	35	0.05993	130.3	3.8
GBIV15	40	0.0512	137.3	14.7
GBIV15	45	0.06055	131.7	-1.7
GBIV15	50	0.06035	152.8	-3.8
GBIV15	55	0.04852	159.3	0
GBIV15	60	0.04708	148.5	11.6
GBIV15	65	0.04626	156.8	-19.9
GBIV15	70	0.03665	161.9	-18.6
GBIV15	75	0.02202	163.1	-10.9
GBIV15	80	0.02841	145.4	-31.8
GBIV14	0	0.5129	71.6	32.2
GBIV14	100	0.3860	70.8	33.3
GBIV14	150	0.2941	72	31.2
GBIV14	200	0.2509	81.2	39
GBIV14	250	0.2233	91.6	33.2
GBIV14	300	0.1699	89.4	21.6
GBIV14	350	0.0795	115.2	20.4
GBIV14	400	0.0341	8.2	-19.9

GBIV14	425	0.0393	337.5	23
GBIV14	450	0.0515	185.8	44.9
GBIV14	475	0.0264	287.1	-31.5
GBIV14	500	0.0309	27.4	-68.7
GBIV14	525	0.0281	296.2	-36.1
GBIV14	550	0.0214	17	-16.5
GBIV14	575	0.0348	120	-33.2
GBIV13	0	0.2541	92.4	21.9
GBIV13	100	0.1970	101.5	16.3
GBIV13	150	0.1716	106.8	17.7
GBIV13	200	0.1545	111.2	14.3
GBIV13	250	0.1528	106.5	8.3
GBIV13	300	0.1094	108	5.8
GBIV13	350	0.0447	111.1	8.2
GBIV13	400	0.0202	159.8	51
GBIV13	425	0.0442	139.1	47.1
GBIV13	450	0.0253	167.3	35.8
GBIV13	475	0.0384	159	26.1
GBIV13	500	0.0293	144.8	-7.7
GBIV13	525	0.0223	149	-7.1
GBIV13	550	0.0070	194.7	-35
GBIV13	575	0.0278	147.9	-3.4
GBIV10	0	0.1084	323.2	38.3
GBIV10	100	0.0957	339.2	20.6
GBIV10	150	0.0800	343.6	15.4
GBIV10	200	0.0789	349.5	13.5
GBIV10	250	0.0688	350.4	2.8
GBIV10	300	0.0543	358.4	-4.5
GBIV10	350	0.0381	359.6	19.9
GBIV10	400	0.0436	39.4	-20.6
GBIV10	425	0.0389	331.4	-2.4
GBIV10	450	0.0268	319.1	10.3
GBIV10	475	0.0193	229.3	52.1
GBIV10	500	0.0499	31.7	-23.6
GBIV10	525	0.0222	288.4	-20.1
GBIV10	550	0.0237	291.1	53.1
GBIV10	575	0.0112	124.6	63.8
GBIV09	0	0.1743	68.8	-46.7
GBIV09	100	0.1416	62.9	-67.4
GBIV09	150	0.1219	75.1	-76.6
GBIV09	200	0.1196	111.5	-83.9
GBIV09	250	0.1042	105.9	-81.2
GBIV09	300	0.0973	135	-80.5
GBIV09	350	0.0748	210.1	-78.7
GBIV09	400	0.0694	156.1	-65.3
GBIV09	425	0.0710	166.1	-50.2

GBIV09	450	0.1243	202.1	-60.2
GBIV09	475	0.0805	90.1	-64.4
GBIV09	500	0.0772	58.2	-53.9
GBIV09	525	0.0589	97.3	-23.7
GBIV09	550	0.0449	31.5	-35.4
GBIV09	575	0.0141	265.2	-19.2

Supplementary Table 2

A) ChRM components and VGP

Sample: sample ID; **Depth**: [cm from the base]; **LT**: minimum temperature/minimum field of the ChRM component [°C or mT]; **HT**: maximum temperature/maximum field of the ChRM component [°C or mT]; **λ_s**: site latitude [°]; **ChRM Dec**: declination of the ChRM component [°E]; **ChRM Inc**: inclination of the ChRM component [°]; **MAD**: maximum angular deviation of the ChRM component [°]; **VGP lat**: latitude of the virtual geomagnetic pole [°].

Sample	Depth [cm]	LT [°C]	HT [°C]	λs	ChRM dec [°]	ChRM inc [°]	MAD [°]	VGP lat [°]
GII210	610	150	575	8.7007	340.8	-10.0	6.9	66.4
GII205	565	200	475	8.7007	352.8	21.2	9.6	82.53
GII204	548	200	575	8.7007	355.6	3.2	4.9	81.6
GII203	517	200	525	8.7007	351.1	27.2	8.0	79.6
GII202	500	150	500	8.7007	24.2	37.5	9.3	63.7
GII201	487	150	500	8.7007	315.6	21.0	20.4	46.3
G2SAG17	415	100	500	8.7007	2.7	12.4	4.7	86.4
G2SAG16	377	150	400	8.7007	206.9	4.1	33.9	-61.15
G2SAG14	357	450	575	8.7007	216.7	-31.3	32.1	-53.4
G2SAG11	188	100	525	8.7007	163.0	13.8	8.9	-66.9
G2SAG10	162	150	475	8.7007	121.8	21.4	23.4	-28.8
G2SAG06	102	0	575	8.7007	23.7	-4.5	11.9	64
G2SAG05	89	100	300	8.7007	347.2	-37.5	12.8	57.7
G2SAG04	58	100	550	8.7007	335.3	-20.5	8.5	58.8
G2SAG03	42	200	575	8.7007	91.6	-32.3	9.7	4.1
GOAMII15	122	0	250	8.7007	159.4	-10.3	25.6	-69.3
GOAMII14	121	200	575	8.7007	179.1	5.8	7.1	-78.4
GOAMII12	114	100	425	8.7007	145.5	-13.4	12.7	-55.8
GOAMII11	101	5 mT	75 mT	8.7007	353.1	22.8	5.6	82.5
GOAMII10	99	100	500	8.7007	341.8	16.4	11.1	72
GOAMII09	86	5 mT	80 mT	8.7007	358.8	49.4	5.9	68.4
GOAMII07	67	0 mT	80 mT	8.7007	8.8	21.1	7.3	81
GOAMII04	27	5 mT	85 mT	8.7007	13.7	-6.0	5.9	72
GOAMII03	23	0 mT	85 mT	8.7007	13.5	-2.9	11.3	73.1
GOAMII16	-15	50 mT	65 mT	8.7007	171.9	-30.6	27.2	-78.9
GII605	-33	25 mT	85 mT	8.7007	187.8	-11.5	5.8	-81.8
GII604	-50	0	575	8.7007	2.3	6.4	8.2	84

GII603	-61	20 mT	85 mT	8.7007	16.5	4.3	12.9	72.3
GII601	-71	5 mT	85 mT	8.7007	1.8	0.2	8.5	81.2
GIIS17I15	90	30 mT	80 mT	8.7007	159.7	-38.0	3.8	-66.7
GIIS17I12	72	25 mT	80 mT	8.7007	122.2	51.8	4.8	-21.3
GIIS17I11	58	200	575	8.7007	4.4	-35.4	4.9	61.4
GIIS17I09	49	25 mT	80 mT	8.7007	81.0	-7.9	10.6	8.3
GIIS17I07	40	450	525	8.7007	181.2	-14.2	21.2	-88.1
GIIS17I06	33	450	525	8.7007	174.0	-0.8	10.3	-79.8
GIIS17I05	29	0	575	8.7007	181.5	-17.9	5.6	-88.4
GIIS17I04	23	200	575	8.7007	177.2	-16.1	7.1	-87.2
GIIS17I03	20	25 mT	80 mT	8.7007	10.3	-22.9	23.4	67
GIIS17I02	17	150	575	8.7007	176.2	-18.2	12.1	-86.2
GIIS17I01	11	0	575	8.7007	184.6	-23.1	3.7	-84.4
GX18	247	150	575	8.7007	359.2	15.6	3.6	88.9
GX17	227	100	525	8.7007	352.3	7.5	13.5	80.9
GX16	216	150	575	8.7007	357.7	7.2	7.5	84.4
GX15	185	150	575	8.7007	4.3	-14.4	22.9	73.4
GX14	174	100	475	8.7007	356.2	16.3	15.5	86.2
GX12	141	100	450	8.7007	345.9	-8.6	25.8	70.8
GX10	130	250	400	8.7007	16.8	14.9	22.0	73.3
GX08	114	200	350	8.7007	336.3	-3.4	17.0	64.1
GX07	104	150	575	8.7007	354.2	7.3	7.0	82.33
GX06	92	100	575	8.7007	359.5	3.3	10.8	83
GX04	68	200	575	8.7007	4.1	-10.6	13.6	75.4
GX03	57	150	575	8.7007	359.4	-0.1	7.7	81.2
GX02	35	150	450	8.7007	355.3	-3.7	14.2	78.4
GXIS29	244	150	575	8.7007	166.0	10.0	11.3	-70.4
GXIS27	233	10	80	8.7007	353.5	36.5	12.1	76.8
GXIS26	188	200	575	8.7007	176.3	-2.9	17.3	-81.9
GXIS25	184	200	500	8.7007	175.7	-3.0	11.5	-81.6
GXIS24	166	0	575	8.7007	167.6	-3.2	8.0	-75.8
GXIS23	158	5 mT	80 mT	8.7007	185.4	-8.8	5.0	-83.1
GXIS21	142	20 mT	80 mT	8.7007	182.5	-22.9	17.8	-85.9
GXIS20	134	25	60	8.7007	174.6	-20.6	6.1	-84.4
GXIS19	127	100	300	8.7007	159.2	-9.8	9.5	-69
GXIS18	115	0	575	8.7007	167.9	-14.8	8.1	-78
GXIS17	113	150	500	8.7007	175.5	-6.9	9.8	-83.1
GXIS16	108	30 mT	80 mT	8.7007	112.1	-8.8	9.2	-22.5
GXIS15	107	150	525	8.7007	152.1	-18.7	12.0	-62.5
GXIS14	102	200	550	8.7007	178.7	2.3	22.3	80.1
GXIS13	101	100	575	8.7007	227.2	-5.8	11.4	-42.7
GXIS12	91	20 mT	80 mT	8.7007	164.8	-51.5	10.4	-62.6
GXIS11	85	35 mT	80 mT	8.7007	175.3	-11.2	8.0	-84.42
GXIS09	72	100	575	8.7007	278.3	32.3	9.7	10.5
GXIS06	45	25 mT	80 mT	8.7007	146.3	4.6	7.7	-54.7
GXIS01	15	200	575	8.7007	186.9	39.3	6.8	-58.3

GG14	294	40 mT	85 mT	8.7007	195.3	-62.0	13.9	-52.9
GG13	286	15 mT	80 mT	8.7007	175.8	-34.0	5.6	-79.2
GG12	283	35 mT	80 mT	8.7007	170.8	-19.1	7.2	-80.8
GG11	268	25 mT	85 mT	8.7007	182.2	-27.3	2.8	-83.8
GG09	257	150	575	8.7007	195.1	30.9	39.0	-60.6
GG08	250	25 mT	80 mT	8.7007	231.9	-34.9	3.2	-38.7
GG07	242	10 mT	85 mT	8.7007	174.8	-27.4	3.2	-82.2
GG06	204	20 mT	80 mT	8.7007	171.0	-10.6	2.8	-80.5
GG05	198	20 mT	80 mT	8.7007	174.7	13.8	2.4	-73.4
GG01	13	25 mT	80 mT	8.7007	195.4	-25.9	38.1	-74.1
GIG24	419	30 mT	50 mT	8.7007	181.2	0.9	20.8	-80.8
GIG23	413	30 mT	85 mT	8.7007	138.2	14.6	27.7	-45.4
GIG22	411	0	425	8.7007	143.8	18.0	8.0	-49.8
GIG16	378	150	575	8.7007	134.1	-11.4	12.3	-44.4
GIG01	234	25 mT	85 mT	8.7007	24.2	47.8	17.9	59.7
GIS05	100	250	575	8.7007	172.6	-20.9	16.9	-82.4
GIS04	65	400	575	8.7007	170.4	-5.0	23.3	-78.6
GIS03	58	350	575	8.7007	181.2	0.8	23.4	-80.8
GIS02	55	250	575	8.7007	180.8	-11.8	20.3	-87.1
GIS01	0	450	575	8.7007	170.7	-7.9	21.0	-79.6
GIC10	151	30 mT	80 mT	8.7007	137.5	20.8	6.6	-43.4
GIC09	129	10 mT	80 mT	8.7007	333.1	19.7	10.9	63.4
GIC08	102	55 mT	80 mT	8.7007	248.3	-46.0	17.7	-23.2
GIC07	84	20 mT	80 mT	8.7007	162.9	-23.6	3.4	-72.8
GIC06	63	30 mT	80 mT	8.7007	181.4	-3.0	6.7	-82.7
GIC05	50	15 mT	80 mT	8.7007	187.4	16.1	7.7	-71.6
GIC04	38	10 mT	80 mT	8.7007	129.1	-13.8	11.4	-39.6
GIC03	29	35 mT	80 mT	8.7007	181.3	-25.8	3.0	-84.9
GIC02	15	15 mT	80 mT	8.7007	149.6	52.5	11.6	-39.2
GIC01	2	15 mT	95 mT	8.7007	212.4	7.4	14.5	-55.4
GBIVO09	106	0	500	8.7007	355.3	20.5	4.3	85
GBIVO05	60	100	550	8.7007	1.4	-3.0	14.0	79.7
GBIVO04	46	150	450	8.7007	22.0	4.5	10.6	67.2
GBIV07	165	10 mT	80 mT	8.7007	176.6	-17.2	2.4	-86.6
GBIV05	152	100	400	8.7007	105.4	2.6	6.0	-15
GBIV03	141	350	575	8.7007	156.5	22.4	26.5	-59
GBIV21	120	0	80	8.7007	197.2	-38.3	1.0	-69.1
GBIV20	112	400	450	8.7007	164.6	-17.8	19.9	-74.8
GBIV19	105	200	350	8.7007	309.0	69.9	3.5	29.3
GBIV16	76	300	425	8.7007	137.4	45.1	13.9	-35.6
GBIV15	62	50 mT	80 mT	8.7007	154.9	-6.6	13.1	-64.5
GBIV14	51	450	550	8.7007	178.2	49.1	25.9	-51.2
GBIV13	46	500	550	8.7007	135.2	0.9	3.1	-44.5
GBIV10	11	100	300	8.7007	293.9	54.9	9.9	24.5
GBIV09	0	150	425	8.7007	18.8	-57.1	19.0	40.4

GBIII02	0	150	625	8.7007	34.2	6.8	19.0	55.6
GBIII01	-3	100	500	8.7007	268.0	10.6	8.7	-1.2
GBIII06	-123	100	575	8.7007	195.7	-9.3	6.2	-73.9
GBXIIC03	638	300	525	8.7007	248.7	-19.2	3.9	-22.3
GBXIIC02	603	150	600	8.7007	190.3	-41.9	15.3	-71.7
GBXIIC01	575	250	625	8.7007	347.6	1.0	9.8	75.2
GBXIIA27	290	200	625	8.7007	174.8	-12.2	3.3	-84.2
GBXIIA26	280	100	550	8.7007	165.4	1.0	3.3	-72.8
GBXIIA25	268	100	500	8.7007	14.2	16.0	7.7	75.9
GBXIIA23	252	100	625	8.7007	16.7	-4.1	24.2	70.2
GBXIIA18	220	100	600	8.7007	17.6	3.3	13.9	71.2
GBXIIA17	213	200	575	8.7007	329.1	31.9	3.7	58.8
GBXIIA13	115	100	425	8.7007	8.8	-1.0	9.0	77.3
GBXIIA11	98	100	500	8.7007	187.2	-23.2	7.0	-82.2
GBXIIA10	95	150	450	8.7007	165.0	-26.9	5.2	-74.3
GBXIIA09	90	150	525	8.7007	172.7	-4.0	7.3	-80.1
GBXIIA08	79	150	450	8.7007	165.3	-1.0	6.9	-73.3
GBXIIA07	68	150	450	8.7007	179.4	-5.4	6.2	-84
GBXIIA06	55	150	475	8.7007	171.6	-36.4	9.0	-75.9
GBXIIA05	46	100	400	8.7007	199.3	-45.1	7.7	-64.4
GBXIIA03	20	100	525	8.7007	135.5	-16.2	12.0	-46.1
GBXIIA01	1	100	400	8.7007	139.1	7.6	13.7	47.4

B) A component

Sample	LT	HT	λs	ChRM dec [°]	ChRM inc [°]	MAD [°]	VGP lat [°]
G2SAG16	0	250	8.7007	359.0	-6.8	19.9	77.8
G2SAG15	100	300	8.7007	2.6	60.8	22.7	56.9
G2SAG03	0	400	8.7007	12.1	-13.9	16.4	70.1
GOAMII14	0 mT	45 mT	8.7007	18.9	31.6	7.4	69.7
GOAMII02	0 mT	45 mT	8.7007	1.1	-21.5	10.7	70.1
GOAMII16	0 mT	45 mT	8.7007	32.5	25.1	8.1	57.8
GII605	0 mT	30 mT	8.7007	25.9	10.3	14.2	64.1
GIIS17I15	0 mT	35 mT	8.7007	5.0	62.8	25.0	54.3
GIIS17I06	0	450	8.7007	356.0	-4.9	21.2	78.1
GIIS17I03	0 mT	45 mT	8.7007	334.5	-9.7	10.5	61.2
GXIS20	5 mT	35 mT	8.7007	26.6	7.1	19.2	63.1
GXIS16	5 mT	40 mT	8.7007	13.7	6.0	9.1	75.2
GXIS15	0	250	8.7007	18.5	-6.8	2.0	67.9
GXIS12	0 mT	20 mT	8.7007	346.8	0.2	18.2	74.3
GXIS06	5 mT	25 mT	8.7007	359.7	-7.0	7.0	77.8
GG13	0 mT	15 mT	8.7007	1.2	-24.7	4.9	68.3
GG12	0 mT	35 mT	8.7007	356.3	-2.2	2.9	79.5
GG11	0 mT	20 mT	8.7007	325.4	20.4	6.9	55.9

GG08	0 mT	25 mT	8.7007	32.9	13.9	7.6	57.4
GG06	0 mT	20 mT	8.7007	356.9	8.5	6.3	84.6
GG05	0 mT	30 mT	8.7007	346.9	-25.2	7.8	64.5
GG04	0	250	8.7007	16.2	17.1	11.2	74.0
GIG03	0 mT	20 mT	8.7007	15.5	7.6	13.1	73.8
GIG01	0 mT	15 mT	8.7007	15.0	-51.1	7.4	47.0
GIS05	0	200	8.7007	23.1	-39.5	35.8	51.6
GIS04	0	200	8.7007	45.1	20.3	24.4	45.6
GIC10	0 mT	20 mT	8.7007	39.4	13.7	8.6	51.0
GIC07	0 mT	20 mT	8.7007	16.1	8.9	18.0	73.4
GIC06	0 mT	20 mT	8.7007	343.8	-23.8	7.3	63.5
GIC03	0 mT	25 mT	8.7007	325.2	13.3	19.6	55.4
GIC01	0 mT	20 mT	8.7007	2.6	-33.8	3.1	62.7
GBIV20	100	200	8.7007	356.7	-12.9	5.0	74.4
GBIV16	0	200	8.7007	321.6	84.2	17.5	17.6
GBIV15	5 mT	45 mT	8.7007	5.1	18.8	9.3	84.9
GBIV14	150	250	8.7007	33.3	15.3	17.5	57.0
GBXIIC02	0	150	8.7007	319.2	-30.0	7.9	42.6
GBXIIA10	0	150	8.7007	41.9	-40.5	8.0	38.1
GBXIIA08	0	150	8.7007	23.5	-23.5	3.3	58.6
GBXIIA07	0	200	8.7007	17.4	-38.2	12.5	55.3

Supplementary Table 3
Age model input data

Description	Depth [m]	Age [Ma]	Error 2σ [Ma]
Tie Points included in Fig.8A			
Former D tuff [27-09]	19.2	0.709	±0.026
Brunhes/Matuyama	17.48	0.773	±0.002
Butchery Site mean depth	18.7		
Matuyama/Jaramillo	14.65	0.99	±0.003
Open Air Museum top	13.45		
Jaramillo/Matuyama	13.42	1.07	±0.003
Matuyama/Cobb Mountain	13.02	1.18	±0.006
Former B tuff [27-12]	8.99	1.2	±0.140
Gombore Iδ mean depth	6.45		
Tuff [27-03]	5.6	1.393	±0.324
Gombore Iγ mean depth	4.55		
Gombore IB mean depth	1.78		
Tie Points excluded in Fig.8A			
Tuff GOAMII [27-08]	13.3	0.875	±0.020

Tie Points included in Fig.8A			
Garba IIIC mean depth	18.8		
Brunhes/Matuyama	18.35	0.773	±0.002
Matuyama/Jaramillo	14.62	0.99	±0.003
Jaramillo/Matuyama	12.8	1.07	±0.003
Olduvai/Matuyama	2.2	1.925	±0.005
Garba IVD mean depth	2.1		
Garba IVE mean depth	1.4		
Garba IVF mean depth	1		
Matuyama/Reunion	0.12	2.116	±0.005
Tie Points excluded in Fig.8B			
Tuff "Grazia" [27-23]	1.5	1.719	±0.398

Chapter 6: Supplementary Material of

Chronology of the earliest peopling of the Ethiopian highlands at Melka Kunture pre-dating the 1.925 Ma base of the Olduvai subchron

Supplementary Table 1
Thermal demagnetization data of samples from Kella

Section: sampled section (see Fig. 2,3); **Sample**: sample ID; **Treatment**: thermal demagnetization treatment [°C]; **J**: NRM intensity [A/m]; **Gdec**: declination in geographic coordinates [°]; Ginc: inclination in geographic coordinates [°].

Section	Sample	Treatment [°C]	J [A/m]	Gdec[°]	Ginc [°]
Kella III bis	K26	0	0.0024942	122.2	-29.3
	K26	100	0.0019055	116.6	-32.3
	K26	150	0.0017807	117.2	-32.9
	K26	200	0.0016025	113.4	-32.3
	K26	250	0.0014518	112.7	-22
	K26	300	0.0011974	111.3	-24.9
	K26	350	0.0008788	106.2	-22.4
	K26	400	0.000407	82.7	-23.7
	K26	425	0.0006268	76.3	-21.1
	K26	450	0.000536	76	-55.7
	K26	475	0.0003774	278.9	-59.4
	K26	475	0.0001452	121.1	9.5
	K26	500	0.000419	88.1	-60.7
	K26	525	0.0004173	40.8	-38
	K26	550	0.0004508	336.9	-38.2
	K26	575	0.0001615	67.9	34.2
	K26	600	0.0001615	67.9	34.2
	K26	625	0.0002212	282.2	22.6
	K25	0	0.0034908	189.4	-59.1
	K25	100	0.0028046	162.6	-58.8
	K25	150	0.0026087	168.1	-61.6
	K25	200	0.0020708	157.2	-61.5
	K25	250	0.0018461	151.6	-60.9
	K25	300	0.0012756	160.7	-59.5
	K25	350	0.0009608	159.7	-63.7
	K25	400	0.0005693	268.4	-69.4
	K25	425	0.0003307	308.4	-68.6
	K25	450	0.0003956	294.8	13.3

	K25	500	0.0007651	321.4	0.5
	K25	525	0.0006003	356.1	24.5
	K25	550	0.0007953	192.1	-40.3
	K25	575	0.000658	336.9	24.1
	K25	600	0.0001235	48.9	51.9
	K24	0	0.0037244	189.4	-11.8
	K24	100	0.0034826	184.5	-27.7
	K24	150	0.0032571	183.8	-28.8
	K24	200	0.0028735	185.2	-28.7
	K24	250	0.0026464	178.4	-27.5
	K24	300	0.0021238	183.8	-29.9
	K24	350	0.0014247	183.9	-31.9
	K24	400	0.0009561	180.7	-34.1
	K24	425	0.0004506	111.9	-20.1
	K24	450	0.0006602	274.1	-12.9
	K24	475	0.0005397	219.7	-39.4
	K24	500	0.0010732	166	-44.2
	K24	525	0.0005199	183.9	-47.7
	K24	550	0.0004998	75.6	-0.1
	K24	575	0.0003961	160.4	-32.6
	K24	600	0.0002601	68.9	-62.8
	K23	0	0.0015382	1.7	-69.4
	K23	100	0.0015635	252.2	-65.6
	K23	150	0.0014704	253.6	-60.6
	K23	200	0.0014527	258.6	-61.1
	K23	250	0.0012501	247.3	-60
	K23	300	0.0007603	253.9	-45.7
	K23	350	0.0004588	313.9	-58.8
	K23	400	0.0005018	335.8	-30.3
	K23	425	0.0003538	333.6	-23.8
	K23	450	0.0005039	341.7	-11.7
	K23	475	0.0007974	334.2	13.6
	K23	500	0.0008567	316.9	18.7
	K23	525	0.000787	327.7	2.9
	K23	575	0.0003263	40.7	-41.8
	K23	600	0.0003023	261.8	15.1
	K22	0	0.0012948	116.7	-54.7
	K22	100	0.0019471	137.9	-25.9
	K22	150	0.0018458	142.5	-23
	K22	200	0.0018245	138.6	-24.1
	K22	250	0.0016474	134	-15.1
	K22	300	0.0015406	140.1	-19.2
	K22	300	0.003224	322.4	26.1

	K22	350	0.0006757	112.5	-15.9
	K22	400	0.0008137	130.2	-9.5
	K22	425	0.0005595	143.6	-13.6
	K22	450	0.0007336	208.1	-72.1
	K22	475	0.0004293	269.6	-10.8
	K22	500	0.0007291	125	-28.9
	K22	525	0.0003723	71.6	-8.1
	K22	550	0.0004584	106.7	-5.5
	K22	575	0.0006035	269.9	3.9
	K21	0	0.0011881	339.3	-29
	K21	100	0.0008111	323.9	-34.6
	K21	150	0.0007123	314	-47.7
	K21	200	0.0006958	306.5	-47.8
	K21	250	0.0004694	302.2	-56
	K21	300	0.0003085	278	-48.2
	K21	350	0.0002714	276.7	-57.8
	K21	400	0.0001661	320.8	-22.8
	K21	425	0.0000974	273.5	-51
	K20	0	0.0022444	6.3	-0.9
	K20	100	0.0012759	359.4	-14.2
	K20	150	0.0012826	356.2	-13.3
	K20	200	0.0012378	357.6	-7.5
	K20	250	0.0010089	359.9	-9.7
	K20	300	0.000921	357	-3
	K20	350	0.0007512	347.7	-0.8
	K20	400	0.0006618	12.7	4
	K20	425	0.0005475	7	5.4
	K20	450	0.0008607	321.5	-56.2
	K20	475	0.0006829	340.3	19.9
	K20	500	0.0006795	357.5	15.4
	K20	525	0.0004692	351.5	39.5
	K20	550	0.0006683	344.2	18.3
	K20	550	0.0002675	317.3	-33.4
	K20	575	0.0005291	343.6	52.3
	K20	600	0.0002956	56.6	3.3
	K20	625	0.0002544	73.3	0.7
	K18	0	0.0006997	254.9	-54.9
	K18	100	0.0002	138.6	-14
	K18	150	0.0000913	72.9	-69.5
	K18	200	0.0001927	11	1.9
	K18	250	0.0003403	8.7	18.4
	K18	300	0.0004804	13.9	41.4
	K18	350	0.0004327	340.3	3.8

	K18	400	0.000435	303.4	-4.9
	K18	425	0.0006381	23.1	-18.9
	K18	450	0.0006999	292.6	-42.8
	K18	475	0.0007451	295.7	-50.1
	K18	500	0.0006825	321.2	20.6
	K18	525	0.0007848	322.8	-45.8
	K18	550	0.0012673	283.9	-37.6
	K17	0	0.0023316	6	16
	K17	100	0.0012581	4.7	5.4
	K17	150	0.0011379	0.7	3.9
	K17	200	0.0010403	0.7	6.1
	K17	250	0.0008842	356.4	1.8
	K17	300	0.0006604	357.7	-1.4
	K17	350	0.0004138	359.1	-3.2
	K17	400	0.000236	346.6	0.2
	K17	425	0.0000769	7.6	2.7
	K17	450	0.0002078	232.8	-31.8
	K17	475	0.0004408	304.2	1.2
	K17	500	0.0003555	112.7	1.5
	K17	525	0.0002387	294.1	13.4
	K17	550	0.0002719	54.7	-14.6
	K17	575	0.0002274	123.4	-26.3
	K17	600	0.0000903	97.3	-8.3
	K16	0	0.0002254	339.1	-18.5
	K16	100	0.000135	329.9	-1.3
	K16	150	0.0001567	311.3	-34
	K16	200	0.0001557	305	-51.4
	K16	250	0.0000754	17.1	-51.2
	K16	300	0.0000717	359.5	-34.8
	K16	350	0.0000507	41.2	-23.1
	K16	400	0.0001212	323.9	-1.7
	K16	425	0.0000781	307.2	-13.1
	K15	0	0.0025357	336.9	-37.8
	K15	100	0.0021546	346.1	-32.7
	K15	150	0.002143	348.9	-31.6
	K15	200	0.0020676	343.9	-33.4
	K15	250	0.0018865	350.4	-37.5
	K15	300	0.0016173	347.9	-41.8
	K15	350	0.0014164	350.2	-44.8
	K15	400	0.00119	335.5	-50.2
	K15	425	0.0010942	332.9	-51.4
	K15	450	0.0012924	334.3	-55.5
	K15	475	0.0012049	41.8	-85.2

	K15	500	0.0011122	272	-72.9
	K15	525	0.0010405	193.2	-86.6
	K15	550	0.0004059	313.6	-32.9
	K15	575	0.0003295	14.3	-37.7
	K15	600	0.000374	316.6	-39.3
	K15	625	0.0001666	89.8	2.3
	K14	0	0.0009144	349.9	-5.7
	K14	100	0.0006699	4.1	-5.2
	K14	150	0.0006252	352.9	-2.4
	K14	200	0.0005793	350.4	2.5
	K14	250	0.0005134	356.4	-1.9
	K14	300	0.0004057	7.9	-5
	K14	350	0.0002827	26.9	6
	K14	400	0.0003519	21.8	0.5
	K14	425	0.0001739	350.3	23.5
	K14	450	0.000333	328.1	11.4
	K14	475	0.0002047	7	-25.2
	K14	500	0.0002904	20.2	-58.3
	K14	525	0.0001025	316.9	72.2
	K14	550	0.0001474	28.7	-13.4
	K14	575	0.0000995	355.3	-29.3
	K13	0	0.0054262	36	-23.4
	K13	100	0.0052319	24.8	4.5
	K13	150	0.0049381	30.1	-7.9
	K13	200	0.0048642	22.9	4.8
	K13	250	0.0044984	30.7	-0.4
	K13	300	0.0040193	29.8	-0.3
	K13	350	0.0037029	26.6	3.3
	K13	400	0.0030675	32	18.8
	K13	425	0.0031235	29	14.1
	K13	450	0.0027429	34	13.7
	K13	475	0.0024292	26.9	17.1
	K13	500	0.0013588	38.9	25.2
	K13	525	0.0011089	32.6	31.2
	K13	550	0.0002473	357.9	15
	K13	575	0.0003418	280.9	55.9
	K12	0	0.0073665	278.1	83.5
	K12	100	0.0061746	301.1	75
	K12	150	0.0057656	293.4	73
	K12	200	0.0052246	302.5	72.3
	K12	250	0.0042035	301.9	69.6
	K12	300	0.0034613	309.5	73.8
	K12	350	0.0026535	325.7	72.6

	K12	400	0.0019684	309.2	66.5
	K12	425	0.0016717	319.1	75.2
	K12	450	0.001645	321.9	62.3
	K12	475	0.0006557	211	69
	K12	500	0.000847	83	67
	K12	525	0.0007722	225.6	73.5
	K12	550	0.0003939	50	-15.5
	K12	575	0.0001153	74.1	58
	K12	600	0.0001632	135	-44.5
	K11	0	0.0143865	353	-10.3
	K11	100	0.0147537	356.9	-14.2
	K11	150	0.0138329	358.6	-14.9
	K11	200	0.0117879	358.7	-14.3
	K11	250	0.0093447	356.7	-12.9
	K11	300	0.0074079	356.8	-12.7
	K11	350	0.0050407	357.3	-11.6
	K11	400	0.0040099	355.9	-6.3
	K11	425	0.0030704	353.1	-15.2
	K11	450	0.0022647	347	-16.9
	K11	475	0.0017209	1.1	-17.8
	K11	500	0.0013686	69.3	-46.9
	K11	525	0.0005539	350.7	-28.3
	K11	550	0.0003591	18.4	43
	K11	575	0.0003488	8.4	-38.5
	K11	600	0.0003179	249.5	56.4
	K10	0	0.0034164	4.1	-22.5
	K10	100	0.0032461	359.5	-24.1
	K10	150	0.0030066	356	-19.3
	K10	200	0.0027605	6.7	-11.1
	K10	250	0.0023719	7.5	-11.3
	K10	300	0.0019752	9	-10
	K10	350	0.0015631	349.7	-44.4
	K10	400	0.0012555	12.4	-11.3
	K10	425	0.0010797	359.8	-33.2
	K10	450	0.0009663	357.2	-25.8
	K10	475	0.000823	8.8	-19.4
	K10	500	0.000606	17.3	-26.8
	K10	525	0.000497	19.6	-14.1
	K10	550	0.0001753	10.6	-63.3
	K10	575	0.0001284	280.6	9.5
	K10	600	0.0001438	265.2	-23.5
	K09	0	0.0020837	354.9	6.6
	K09	100	0.0018073	358	9.3

	K09	150	0.0015393	1.1	3.5
	K09	200	0.0012432	359	4
	K09	250	0.0009792	1.6	-1.7
	K09	300	0.0007814	357.8	0.8
	K09	350	0.0006394	359.2	2.3
	K09	400	0.0005524	358.2	3.2
	K09	425	0.0004622	350.9	0
	K09	450	0.0004826	355.1	-8.2
	K09	475	0.000343	0.4	-13.3
	K09	500	0.0002842	348.8	-4.8
	K09	525	0.0002029	359.4	16.9
	K09	550	0.0001968	353.6	-1.2
	K09	575	0.0000557	326.7	-33.9
	K09	600	0.0000315	336.2	-50.2
	K08	0	0.0283271	11.1	15.5
	K08	100	0.0245951	10.2	20.4
	K08	150	0.0219096	10.5	19.4
	K08	200	0.0169134	8.4	20
	K08	250	0.0144258	11.2	22.9
	K08	300	0.0109074	11	23.7
	K08	350	0.0091669	8.8	23.2
	K08	400	0.009161	11.8	23.8
	K08	425	0.0079616	10.8	22.4
	K08	450	0.0078985	8.9	22.7
	K08	475	0.0074869	9.3	22.3
	K08	500	0.0059777	10.2	25.9
	K08	525	0.0055486	10.8	24
	K08	550	0.0034733	14.1	23.3
	K08	575	0.0020237	359.8	13.5
	K08	600	0.001983	12.3	29.1
	K08	625	0.0012597	14.8	26.5
	K06	0	0.0146944	8.6	6.8
	K06	100	0.0118472	5.6	12.5
	K06	150	0.0103751	6.4	12.7
	K06	200	0.0081865	5	11.6
	K06	250	0.0060865	8	12.8
	K06	300	0.0045502	7.2	14.4
	K06	350	0.0039129	4.1	14.6
	K06	400	0.0032845	7.2	15
	K06	425	0.0032088	6.7	14.7
	K06	450	0.0028731	7.3	14.3
	K06	475	0.0026884	6.4	14.1
	K06	500	0.0022502	8.5	17.2

	K06	525	0.0017103	12.9	12.9
	K06	550	0.0014923	7.4	17.4
	K06	575	0.0007254	6.6	20.4
	K06	600	0.0009033	357.3	22.5
	K06	625	0.0004666	9	21
	K04	0	0.0283562	310.3	-32.4
	K04	100	0.0227709	311.9	-31.4
	K04	150	0.0174325	313.4	-29.6
	K04	200	0.0124225	316.3	-28.2
	K04	250	0.0083861	322.5	-23.4
	K04	300	0.0052694	327.3	-18.7
	K04	350	0.0047947	327.9	-16.4
	K04	400	0.0035346	332	-10.5
	K04	425	0.0031931	333.7	-8.7
	K04	450	0.0031203	335.1	-2.3
	K04	475	0.0019988	347.7	4.7
	K04	500	0.002084	341.1	1.9
	K04	525	0.0014433	349.3	7.6
	K04	550	0.0014981	346.2	9
	K04	575	0.001055	351.8	18.1
	K04	600	0.0007656	2.4	15.1
	K04	625	0.0003801	32.8	34.3
	K03	0	0.0105836	1.4	5.7
	K03	100	0.0093251	357.9	6.6
	K03	150	0.0077128	356.4	9
	K03	200	0.0063986	356.5	7.4
	K03	250	0.0045415	357.4	10.1
	K03	300	0.0041055	357.4	10.8
	K03	350	0.0028926	356.7	10.1
	K03	400	0.0025856	355.6	10.5
	K03	425	0.0025615	356.1	5.6
	K03	425	0.0025425	358.6	2.4
	K03	450	0.0021718	356.2	10.9
	K03	475	0.0020926	353.2	11
	K03	500	0.0019583	356.2	10.8
	K03	525	0.0015222	351	7.3
	K03	550	0.0012164	359.3	13.3
	K03	575	0.0005819	6.5	12.4
	K03	600	0.000646	8.3	5.9
	K03	625	0.000397	358.2	11.7
	K02	0	0.0103399	358.3	7.9
	K02	100	0.0087413	356.2	4.7
	K02	150	0.0071117	351.6	6.2

	K02	200	0.0054587	351.8	5.3
	K02	250	0.0043414	354.4	5.2
	K02	350	0.0024778	353	5.7
	K02	400	0.0020962	352.5	3.3
	K02	425	0.0020426	352.1	4.3
	K02	450	0.0017812	351.4	6.3
	K02	475	0.0015181	352.1	5.1
	K02	500	0.0013952	352.4	5.9
	K02	525	0.0011833	354.6	4.6
	K02	550	0.0009588	357.2	9.9
	K02	575	0.000338	10.8	17.9
	K02	600	0.0002194	292.7	12.5
	K02	625	0.0001881	17.4	-0.7
	K01	0	0.0121332	4.1	17.2
	K01	100	0.0103252	359.4	13.2
	K01	150	0.0086213	359.5	12.2
	K01	200	0.0068758	358.9	14.7
	K01	250	0.0054439	358.9	12.4
	K01	250	0.005438	358.3	13.1
	K01	300	0.004266	358.5	13.2
	K01	350	0.0034592	359.2	12.5
	K01	400	0.0029074	359	14.8
	K01	425	0.0025799	359.5	14.3
	K01	450	0.0023099	358.1	13.8
	K01	475	0.0019535	355.4	17.7
	K01	500	0.0017068	0.3	13.9
	K01	525	0.0013696	356.9	14.5
	K01	550	0.0007265	15.1	16.2
	K01	575	0.0006403	2.5	12.6
	K01	600	0.0006631	3.6	14.2
	K01	625	0.0000685	57.6	-11.4
Kella Ponte	KP09	0	0.0015624	14	8.1
	KP09	100	0.0013255	356.7	1.9
	KP09	150	0.0010757	4.5	11.2
	KP09	200	0.0009704	3.8	10.3
	KP09	250	0.0008739	2.8	8.7
	KP09	300	0.0007048	8.5	2.9
	KP09	350	0.0005448	10.6	6.7
	KP09	400	0.0004475	2.2	7.3
	KP09	425	0.0004075	2.8	1.9
	KP09	450	0.0003566	357.3	-18.3
	KP09	475	0.0003422	7.8	0.2
	KP09	500	0.0002401	351.3	-18.5

	KP09	525	0.0001474	359.4	-2.9
	KP09	550	0.0000762	356.2	-24
	KP09	575	0.0000514	41	7.5
	KP07	0	0.0010591	32	44
	KP07	100	0.0009141	19.2	51.6
	KP07	150	0.0008095	13.2	62.5
	KP07	200	0.0006775	1.9	63.8
	KP07	250	0.0006454	15.5	78.5
	KP07	300	0.0005123	10	87.9
	KP07	350	0.0005402	94.6	83.9
	KP07	400	0.0004936	125.7	83.7
	KP07	425	0.000395	162.1	70.1
	KP07	450	0.0004542	303.8	69.8
	KP07	475	0.0004859	187.3	68.5
	KP07	500	0.0003779	277.8	71.7
	KP07	525	0.0004287	235.6	65.8
	KP07	550	0.0003164	288.5	59.6
	KP07	575	0.0000944	62.1	-14.2
	KP05	0	0.0011701	313.8	-22.1
	KP05	100	0.0010619	308.2	-7.4
	KP05	150	0.001044	289.6	-4.4
	KP05	200	0.0010112	293	-5.9
	KP05	250	0.0010733	288.1	-16.8
	KP05	300	0.0009314	284.8	-8.6
	KP05	350	0.0008392	274.1	-4.3
	KP05	400	0.0009061	270.6	-8
	KP05	425	0.0007556	272.4	-22.6
	KP05	450	0.000789	266.1	-21.6
	KP05	475	0.0007198	298.3	9.6
	KP05	500	0.0008558	265.5	-22.8
	KP05	525	0.0006358	284.1	-34.3
	KP05	550	0.0005249	308	9.9
	KP05	575	0.0006063	277.8	0.9
	KP05	600	0.0003385	127.8	11.7
	KP05	625	0.0001688	131.9	-34.6
	KP04	0	0.0003435	184.7	-38.8
	KP04	100	0.0003747	181.6	-36.6
	KP04	150	0.0004386	196.7	-50.2
	KP04	200	0.0004076	197.8	-48.8
	KP04	250	0.0003006	166	-47.2
	KP04	300	0.000299	176.4	-42.6
	KP04	350	0.0002659	193.3	-48.9
	KP04	400	0.0002111	190.3	-37.7

	KP04	425	0.0002029	184.2	-48.6
	KP04	450	0.0002055	118.2	-43.8
	KP04	475	0.0001835	184	-10.1
	KP04	500	0.0002095	133	-30.7
	KP04	525	0.0001342	229	-14.1
	KP04	550	0.0001561	191.7	22.9
	KP04	575	0.0001311	206.4	-15.1
	KP04	600	0.0000875	123.9	-40
	KP04	625	0.0001146	337.3	15.9
	KP03	0	0.0013969	175.2	5.2
	KP03	100	0.0010009	178.8	-15
	KP03	150	0.0007925	180.6	-17.1
	KP03	200	0.0006346	174.7	6.3
	KP03	250	0.0003831	186.9	-38.3
	KP03	300	0.0001914	188.7	-36.4
	KP03	350	0.0003874	97.5	56.9
	KP03	400	0.000328	167.5	35.2
	KP03	425	0.0001943	214.6	-13.3
	KP03	450	0.0004715	187.5	-11.4
	KP03	475	0.0003688	26.7	-13.7
	KP03	500	0.0003232	114.6	-30.7
	KP03	525	0.0001799	275.1	44.6
	KP03	550	0.0004057	19.3	19.8
	KP03	575	0.0003623	349.4	-1.2
	KP03	600	0.0002819	349.3	-15.2
	KP03	625	0.000173	133.9	23.6
	KP01	0	0.0002603	127.4	-51.7
	KP01	100	0.0003012	153.4	-19.7
	KP01	150	0.000318	160.9	-34.9
	KP01	200	0.0002725	172.1	-40.2
	KP01	250	0.000162	155.1	-34.4
	KP01	300	0.0001642	155.2	-38.3
	KP01	350	0.0001238	140.3	-29.3
	KP01	400	0.000089	199.3	-54.8
	KP01	425	0.0001138	168.4	-35.3
	KP01	450	0.0001425	159.3	-40.9
	KP01	475	0.0000398	216.8	20.3
	KP01	500	0.0001479	204.3	-55.7
	KP01	525	0.0000735	40.5	6.2
	KP01	550	0.000132	291.5	-10.8
	KP01	575	0.0000877	289.7	-7.7
	KP01	600	0.0000863	289.8	-33.7
	KP01	625	0.0000486	252.1	7.1

Supplementary Table 2
ChRM component analysis on samples from Kella

Section: sampled section; **sample**: sample ID; **depth**: [cm from the base]; **J**: NRM intensity [A/m]; **ChRM Dec**: declination of the ChRM component [°E]; **ChRM Inc**: inclination of the ChRM component [°]; **MAD**: maximum angular deviation of the ChRM component [°]; **LT**: minimum temperature of the ChRM component [°C]; **HT**: maximum temperature of the ChRM component [°C]; **comment**; **VGP lat**: latitude of the virtual geomagnetic pole [°].

Section	Sample	Depth [cm]	J [A/m]	ChRM Dec [°]	ChRM Inc [°]	Mad [°]	LT [°C]	HT [°C]	Comment	VGP lat [°]
Kella III bis	K26	315	0.00249	116.5	-29.5	5.9	0	400		-27.8
	K25	310	0.00349	147.4	-49	8.7	200	500		-52.9
	K24	278	0.00372	189.2	-26.2	6.3	100	425		-79.6
	K23	269	0.00154	213.9	-46.44	13.7	250	450		-52.8
	K22	258	0.00130	145.5	-27.9	13.9	100	425		-55.7
	K21	243	0.00119	315.4	-48.7	15	150	425		32.5
	K20	215	0.00224	0.2	-3.1	12.4	0	550		79.7
	K18	197	0.00070						Not interpreted	
	K17	177	0.00233	3.5	10	7.7	0	450		84.9
	K16	152	0.00023						Not interpreted	
	K15	145	0.00254	353	0.4	17.2	250	525		79
	K14	137	0.00091	358.7	0.7	16.9	200	475		81.5
	K13	125	0.00543	31.1	16.9	5.1	400	550		59.3
	K12	103	0.00737						Not interpreted	
	K11	88	0.01439	341.5	6.2	13.8	400	500		70.8
	K10	53	0.00342	6.8	-5.7	7.6	200	500		76.6
	K09	44	0.00208	359	4.2	5.2	100	600		83.3
	K08	33	0.02833	10.5	23.2	1.7	250	625		79.1
	K06	26	0.01469	6.7	14.8	2.3	300	625		83.3
	K04	22	0.02836						Not interpreted	
	K03	17	0.01058	356.7	10.4	2.1	250	625		85.2
	K02	8	0.01034	352.3	5.6	1.8	150	625		80.3
	K01	0	0.01213	358.8	13.7	1.6	200	625		87.9
Kella Ponte	KP09	178	0.00156	4.8	12.6	7.6	150	575		84.7
	KP07	135	0.00106	24.3	23.6	18.9	0	500		65.8
	KP05	100	0.00117						Not interpreted	
	KP04	86	0.00034	184.4	-46.9	18.1	150	525		-70.2
	KP03	40	0.00140	179.4	-14.1	18.3	100	350		-88.3
	KP01	3	0.00026	162.4	-37.5	9.5	150	475		-69.1

Chapter 7: Supplementary Material of

A Multiple Origin for the Acheuleans

Supplementary Text 1

The following archeological sites have been provisionally excluded from our analysis based on insufficient chronostratigraphic information. In this description (as well as in the main text), the ±errors associated to the radiometric ages are always expressed at 2s level.

Gona (Ethiopia)

Semaw et al., (2020) reported the magnetostratigraphy of the ~60-m thick Dana Aoule North section, described in the main text and Figure 2B, and of the ~65-m-thick Busidima North section, hosting a fossil remain attributed to *Homo erectus* in level BSN12. At Busidima North (excluded from our inventory), they found reverse magnetic polarity embedded between a normal/reverse polarity transition at the top and a reverse/normal polarity transition at the base, interpreted respectively as the base Brunhes and the top Olduvai, with the *H. erectus* level BSN12 falling ~8 m above the top Olduvai. The low density of samples that yielded paleomagnetic results (22 samples in ~65 meters) seems to have prevented the detection of the intervening Jaramillo subchron. To improve the chronology of the section, Semaw et al., (2020) used tephrostratigraphic correlation based on major elements between the undated Boolihinan Tuff (BHT), closely associated to level BSN12, and the MK27-05 tuff from Melka Kunture, dated to 1.253±0.082 Ma (Morgan et al., 2012) (even though they report for MK27-05 an age of 1.262 ±0.068 Ma). We provisionally exclude from our inventory level BSN12 as tephrostratigraphic correlations based on major elements are in our opinion insufficient to propose an age of 1.26 ma for BSN12 (Semaw et al., 2020).

In the ~55 m-thick Ounda Gona South section, Semaw et al., (2018) reported Acheulean artefacts from level OGS12 retrieved ~18 m from section base. The Gonash-16 tuff, dated to 1.64±0.03 Ma (Quade et al., 2004), crops out ~5 meters below the archeological level. According to these data, Semaw et al., 2018) assigned an age of 1.6-1.5 Ma to OGS12, but in our opinion the lack of chronological constraints above the archeological level poses limits to this age assignment.

Gadeb (Ethiopia)

Gadeb is located at 2300 m a.s.l. in East-Central Ethiopia. Here, volcaniclastic fluvial deposits of the Mio Goro Formation bearing Acheulean artefacts Clark and Kurashina (1979), emplaced in erosional channels unconformably lying above lacustrine deposits, are stratigraphically younger than the Adaba ignimbrite dated to 2.35±0.4 Ma (Williams et al., 1979). The archaeological sites that where more in-depth analyzed are the 15 m-thick Gadeb 2 and the ~17 m-thick Gadeb 8. Most of the archeological levels therein contained are stratigraphically above a pumice deposit dated with K/Ar to ~1.48 Ma and should be older than base of the Brunhes Chron due to the presence of exclusive reverse magnetic polarity (Williams et al., 1979). The K-Ar and paleomagnetic analyses are reported in Williams et al. (1979) as personal communication from, respectively, G. H. Curtis and R. Drake, and A. Cox and L. Lee, without providing details on the experimental procedures followed and the stratigraphic positions of the studied samples. In the early 1980's, a hydropower dam was built on the Wabe River, forming an artificial lake that submerged the Gadeb archeological area (de la Torre, 2011). For the uncertainties illustrated above, we opted to exclude this entry from our inventory.

West Turkana (Kenya)

The Naiyena Engol 2 (NY2) Oldowan site, located in the mid-lowlands of West Turkana at around 400-500 m a.s.l., was positioned by Roche et al. (2018) in the middle of Kaitio Member of the Nachukui Formation. In particular, NY2 falls 34.5 m and 43.5 m above two layers of bentonite, one of which could represent the KBS Tuff (currently dated to 1.8791±0.0006 Ma; Phillips et al., 2023) based on field mapping Roche et al. (2018). No geochemical analyses of major and trace elements composition has been performed to confirm this hypothesis and additional chronological constraints are available from stratigraphic levels below NY2, which was discarded from our inventory.

East Turkana (Kenya)

In East Turkana we excluded Acheulean sites FxJj63 (area 118), FxJj33 (area 129), and FxJj37 (area 131). Isaac and Isaac (1997) reported from site FxJj63 in the Karari Escarpmen reverse magnetic polarity obtained from 8 hand samples retrieved from subunit IA of the Chari member excavated in Trench B. The samples have however been measured only at room temperature and have not been subjected to demagnetization treatment or principal component analysis. Isaac and Isaac (1997) attempted to correlate site FxJj63 to the Chari Tuff (currently dated to 1.3575±0.0018 Ma; Phillips et al., 2023). However, according to Kaufulu (1987), site FxJj63 is positioned at a higher stratigraphic level than the Chari Tuff. Sites FxJj33 and FxJj37 are reported coming from lower stratigraphic levels of the Chari member relative to FxJj63 and close to the top of the underlying Okote Member (Kaufulu, 1987; Isaac and Isaac, 1997). In a subsequent work (Presnyakova et al., 2018), these Acheulean sites as well as others from Koobi Fora (FxJj65, FxJj63, FxJj21) were attributed as coming from the Okote Member and "*likely quasi-contemporaneous"* (Presnyakova et al., 2018: 162) with an approximate age of ~1.4 Ma. For the inconsistencies illustrated above, we opted to exclude these entries from our inventory.

Peninj (Tanzania)

Peninj is an archaeological area located on the western shore of Lake Natron, Tanzania, where the Peninj Group is well exposed. The Acheulean sites therein recognized are the ST site complex and site MHS-Bayasi (Es2-Lepolosi in Diez-Martín et al., 2014[a]), which are embedded in the USC member (upper sands with clays) of the Humbu Formation, as well as site RHS-Mugulud (EN1-Noolchalai in Diez-Martín et al., 2014[b]), located at a higher stratigraphic level within the Moinik Formation. A first chronological constraint for the Peninj Group was obtained with K/Ar dating providing an age comprised between 3.5 and 1.7 Ma for the Hajaro beds at the base of the sequence, between 1.91 and 0.91 Ma for the Main Tuff located just below the archeological sites ST and MHS-Bayasi, and between 1.2 and 1.15 for the Upper Tuff located at the top of the Peninj Group, leading to a preliminary chronological attribution of 1.5-1.4 Ma for the three archeological sites (Isaac 1967; Howell, 1972; Isaac and Curtis, 1974). A subsequent magnetostratigraphic study (Thouveny and Taieb, 1987) detected five normal magnetic polarity intervals embedded within an extended interval of reverse polarity. The normal polarity intervals have been interpreted as remagnetized, providing no further constraints on the age of emplacement of the Peninj Group other than between the Jaramillo and Olduvai subchrons (Thouveny and Taieb, 1987). More recent $^{40}Ar/^{39}Ar$ age estimates, announced at the American Geophysical Union meeting in 2006 by Deino et al. (2006), depicted a younger scenario for the emplacement of the Peninj Group, constraining the Acheulean sites to around 1.2-1.1 Ma. However, to our knowledge, the analytical data were never formally presented, and considering also that according to

McHenry et al. (2011), the Peninj tuffs are affected by strong diagenetic alteration, we provisionally opted to exclude Peninj from further consideration.

Nyabusosi (Uganda)

Nyabusosi 18 (NY18) is an early Acheulean site located in the Western Rift Valley, Lake Albert plain (Uganda). Pickford et al., 1991 used a ferruginous nodule horizon, considered a regional lithostratigraphic marker bed, to place NY18 below the undated Kagusa Tuff (present in the area but not found at NY18). In turn, the undated Kagusa Tuff was correlated using major and trace elements to undated tuff K89-3335 of the Nachukui Formation in West Turkana. Then, the age of tuff K89-3335 was estimated to around ~1.5 Ma following its stratigraphic position between the Nariokotome Tuff, dated with K/Ar to 1.33±0.04 Ma (Feibel et al., 1989), and the Morutot Tuff, dated to 1.607±0.038 Ma (McDougall and Brown, 2006). In the end, both NY18 and the allegedly correlative Kagusa and K89-3335 tuffs were attributed a similar age of ~1.5 Ma (Pickford et al., 1991). Senut et al. (1994) performed large mammal biostratigraphy at Nyabusosi, but we could not access the original publication.

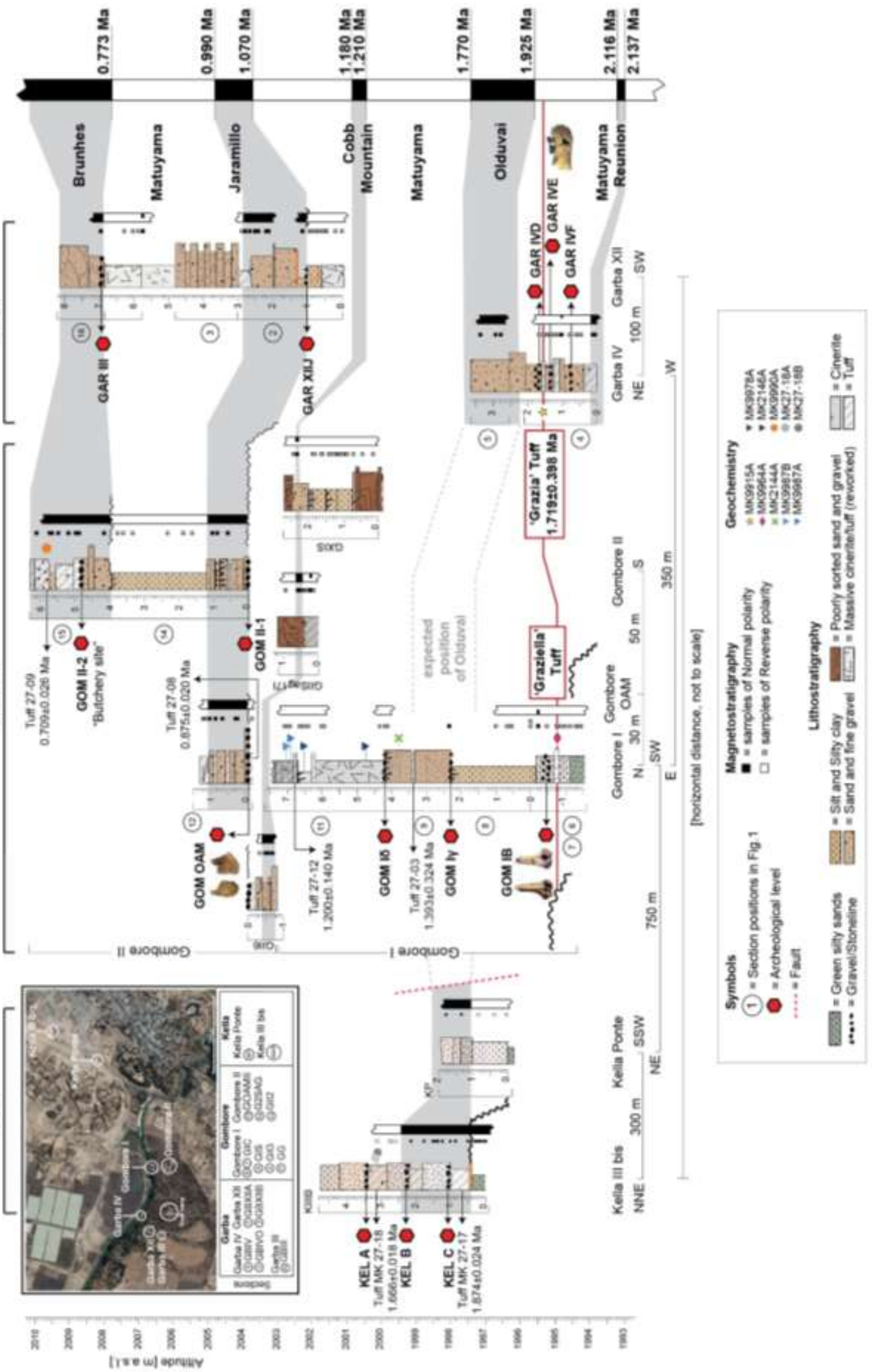
Kella
Gombore
Garba
Gombore II
Gombore I
Altitude [m a.s.l.]
KEL A
Tuff MK 27-18
1.666±0.018 Ma
KEL B
KEL C
Tuff MK 27-17
1.874±0.024 Ma
Kella III bis
Kella Ponte
NNE
NE
SSW
300 m
GOM OAM
Tuff 27-12
1.200±0.140 Ma
GOM Iδ
Tuff 27-03
1.393±0.324 Ma
GOM Iγ
GOM IB
750 m
Tuff 27-08
0.875±0.020 Ma
Tuff 27-09
0.709±0.026 Ma
GOM II-2
"Butchery site"
GOM II-1
expected position of Olduvai
'Graziella' Tuff
'Grazia' Tuff
1.719±0.398 Ma
Gombore I
Gombore OAM
Gombore II
30 m
50 m
350 m
N
SW
S
E
W
GAR III
GAR XIIJ
GAR IVD
GAR IVE
GAR IVF
Garba IV
Garba XII
100 m
[horizontal distance, not to scale]
Brunhes
Matuyama
Jaramillo
Cobb Mountain
Olduvai
Matuyama Reunion
0.773 Ma
0.990 Ma
1.070 Ma
1.180 Ma
1.210 Ma
1.770 Ma
1.925 Ma
2.116 Ma
2.137 Ma
Symbols
= Section positions in Fig 1
= Archeological level
= Fault
Magnetostratigraphy
= samples of Normal polarity
= samples of Reverse polarity
Geochemistry
Lithostratigraphy
= Green silty sands
= Gravel/Stoneline
= Silt and Silty clay
= Sand and fine gravel
= Poorly sorted sand and gravel
= Massive cinerite/tuff (reworked)
= Cinerite
= Tuff

Sup. Fig. 1 A) Location map of Melka Kunture archeological area (Google Earth), where Garba, Gombore and Kella represent the main tributaries of the Awash River along which the Melka Kunture Formation is exposed. Numbers refer to GPS points where the sampling was conducted, reported also in the general stratigraphy of Fig.1 (see Sup.Tab.1 for GPS positions). **B)** General chronostratigraphy of the MKF Middle-Upper successions outcropping in the archeological area, modified after Perini et al. (2021). The sequence has been placed with respect to the altimetry (m a.s.l.) according to Salvini et al. 2015. The correlation has been established using magnetostratigraphy, tephrostratigraphy and the available $^{40}Ar/^{39}$ Ar ages of tuff layers from literature. The magnetic polarity stratigraphy was reconstructed using the characteristic remanent magnetization (ChRM) components extracted from samples which yielded acceptable results, whereby black squares (and grey boxes) indicate normal magnetic polarity and white squares reverse magnetic polarity, which have been correlated to the Quaternary geopolarity timescale of Channell et al. 2020. Circled numbers aside of each sampled section refer to GPS points of A).

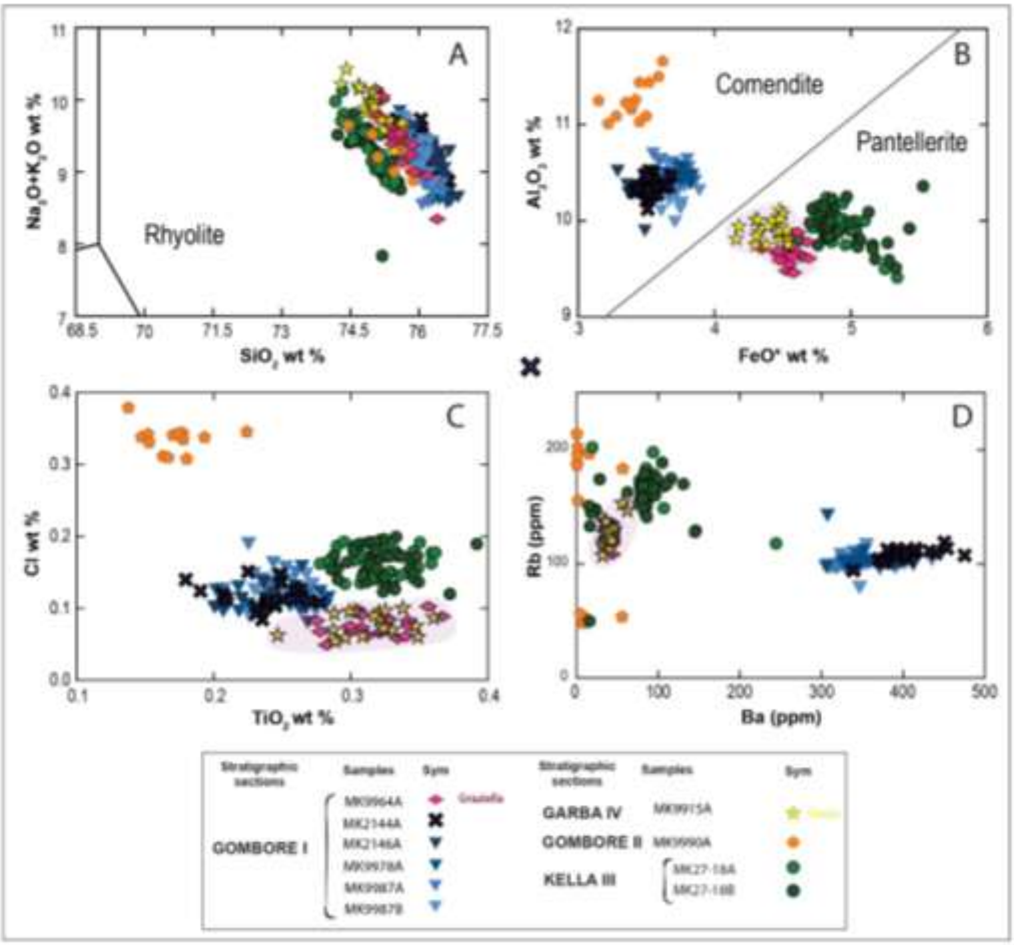

Sup. Fig. 2 Geochemical compositions of Melka Kunture tuffs – **A)** Zoom on the rhyolitic portion of the total alkali versus silica classification diagram by Le bas et al 1986. **B)** Al_2O_3 versus FeO* content (refers to total Fe as FeO) and classification of peralkaline rhyolites according to Macdonald (1974). **C)** Cl versus TiO_2 content. **D)** Rb versus Ba content.

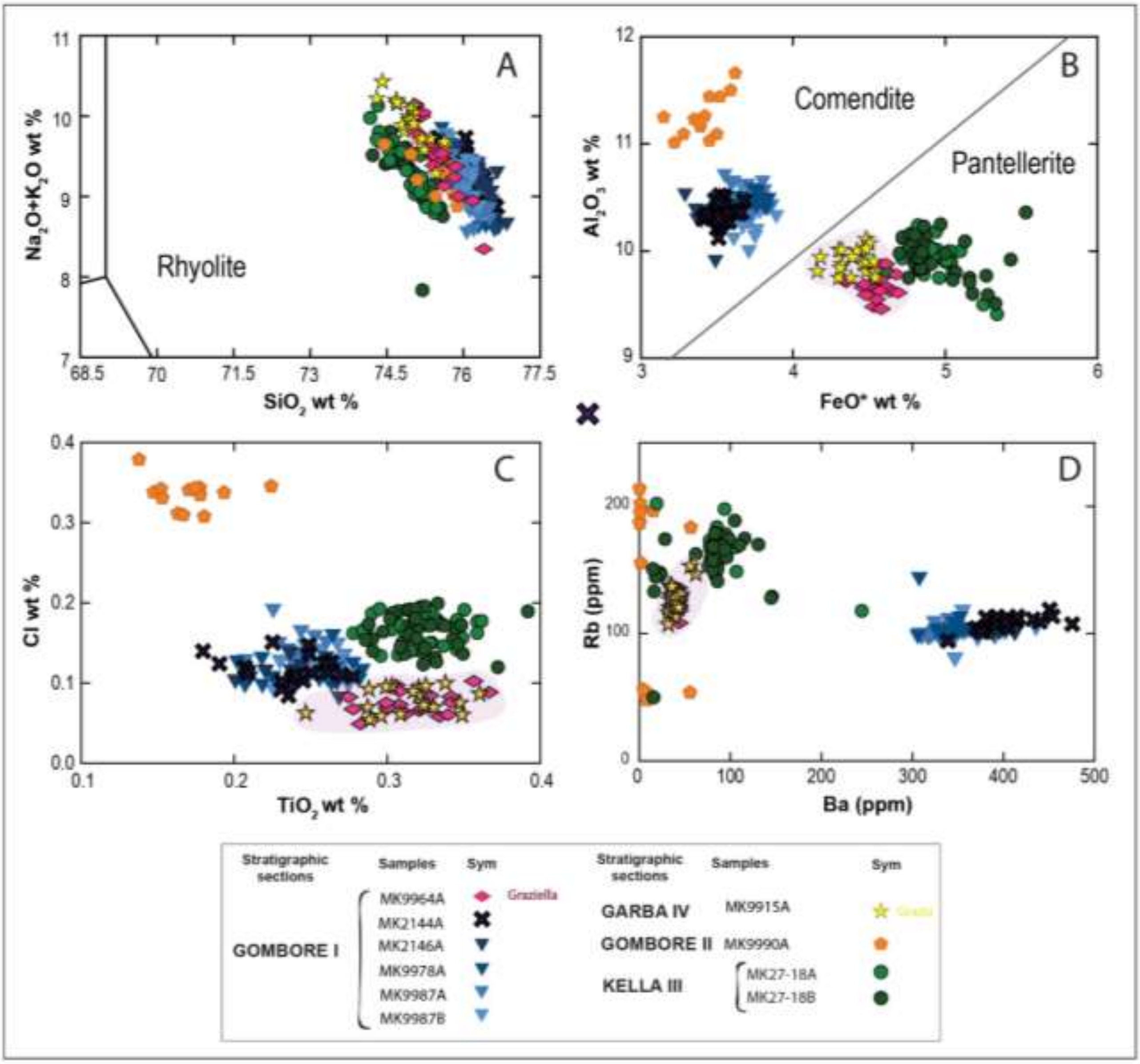

Sup.Fig. 3 Comparison between the composition of volcanic tuffs from this study and ash layers with similar ages from East Africa available in the literature (Koobi Fora, Olduvai and Konso). When compositional data from the literature were reported as average values and associated standard deviations we used the average value and added 2 standard deviations to obtain the fields represented in the figure. Data are from Katoh et al 2000 (1), Brown, 2006 (2), McHenry, 2012 (3), Beyene et al. 2013 (4) and Phillips et al. 2023 (5). **A)** Al_2O_3 vs FeO* plot highlights the comenditic and pantelleritic rhyolite compositional fields (by Macdonald, 1974) **B)** Zoom of the red dotted box area reported in A. **C)** Cl vs FeO* diagram.

Sup.Fig. 4 Artefacts from Gombore IB (1-4, 11, 13, 15, 16, 19) and Garba IVD (5-10, 12, 14, 17, 18) documenting the technical innovations characterizing the emergence of the Acheulean at Melka Kunture. LCTs of obsidian (1-7), aphyric basalt (8), porphyritic basalt (9, 11, 13), and Melka Fault lava (10). Large flake of porphyritic basalt (11). Large cores of porphyritic basalt with a large negative scar on the flaking surface and a peripheral striking platform prepared by unidirectional removals (12, 14). Unifacial prepared centripetal core of aphyric basalt (15). Discoid cores of aphyric basalt (17) and obsidian (16, 18, 19). N. 18 is a discoid core on obsidian angular element, documenting the incipient ability to configure the natural blank geometry.

Chapter 8: Supplementary Material of
First high resolution Chronostratigraphy for the early North African Acheulean at Casablanca (Morocco)

1. Litho-chronostratigraphy of Thomas Quarry I

The Casablanca hinterland shows a vast system of longitudinal dune ridges parallel to modern coast, composed of marine and aeolian calcarenites. It records an exceptional succession of palaeoshorelines since the end of the Miocene (Lefévre and Raynal, 2002; Lecointre, 1952; Biberson, 1961[a]; Stearns, 1978).
In the South-West of Casablanca, four Formations associated with four raised platforms and including several Members have been defined from the late Early to the Late Pleistocene: the Oulad Hamida Formation (late Early Pleistocene-early Middle Pleistocene), the Anfa and the Kef Haroun Formations (Middle Pleistocene), and the Dar Bou Azza Formation (Late Pleistocene) (Fig. 2A) (Lefévre and Raynal, 2002; Texier et al., 2002; Texier et al., 1994).
The sedimentary formations of ThI were succinctly described by Biberson and considered as an extension of the Sidi Abderrahmane formations even if their altitude was higher (Biberson, 1961[b]). The stratigraphic revision carried out in relation to the excavation of the Grotte à Hominidés (GH) and Thomas Quarry I-Unit L (ThI-L) archaeological sites showed that these deposits could not be continuous with those of the Sidi Abderahmane quarries, and belonged to an earlier morphostratigraphic unit that we have called the Oulad Hamida Formation (OHF) (Lefévre and Raynal, 2002; Lecointre, 1952; Texier et al., 1994; Lefévre et al., 2016).

1.1 Lithostratigraphy. OHF sits on a major unconformity formed at an altitude of ~28 m above sea level (asl) at the expense of the Cretaceous and Palaeozoic substratum, ~10 m above the platform of the Anfa Formation (AF) in the Sidi Abderrahmane quarries. OHF includes four allostratigraphic units or Members – OH1 to OH4 from bottom to top (Fig. 2B and Supplementary Fig. S1).

OH1 Member: Bed 1 is composed of a coarse calcirudite at the base and a stratified coarse-grained biocalcarenite. The lower part of Bed 2 consists of over

2 m succession of fine to coarse locally trough cross-bedded sands and calcareous mudstone, called L1 to L4. These beds form sequences into little inset channels. In the upper part of each micro-sequence, features due to hydratationdesiccation alternations (platy structure levels), to exundation (thin laminar calcareous crusts), to drying phenomena (fissural polygonal network emphasized by ferric oxides) and to bioturbation (rootlets marks associated to ferric coatings) occur. These deposits are interpreted as evidence of intermittently flowing braided streams in a nearshore fluviolacustrine hydrosystem5.

Bioclastic sands more or less bioturbated, partially decarbonated and cemented form the upper part- L5- of Bed 2. L5 is subdivided in three sub-units: 5a, light brownish grey clay with a roughly polyhedral structure; 5b, whitish to light reddish sandy clayey silt and 5c, reddish sandy silt. They probably represent aeolian deposits which accumulated in damp vegetated depressions with evidence of pedogenesis during warm episodes of subaerial exposure.

In the limestone deposits of Bed 2 (ThI-L site), several levels contain early Acheulean lithic artefacts (Raynal and Texier, 1989; Raynal et al., 2001; Raynal et al., 2004) as well as the remains of large mammals dominated by hippopotamus along with Kobus; Equus cf mauritanicus; Elephas sp. Among the microfauna, there are reptiles; amphibians and rodents, predominantly the Praomys; Paraethomys; Meriones and the Gerbillus species.

OH2 Member: Overlying an unconformity above the OH1 Member deposits, OH deposits are coarse biocalcarenites with a curved cross-bedding followed by a finer inclined planar-bedding biocalcarenites formed within intertidal depositional environments (OH2A); vertically there follows massive coarse bioclastic aeolianites about ten or so metres thick (OH2B), the upper part of which is affected by fersialsol pedogenesis.

OH3 Member is associated with a shoreline marked by a basal erosion platform and a cliff carved into OH1 and OH2 deposits, whose base is at an altitude of 37 m NGM. The OH3 deposits are composed from bottom to top of blocs and pebbles from OH1 and OH2 calcarenite and limestone, passing to coarse and/or coquinoid biocalcarenites with inclined planar bedding, overlying at the upper part by aeolian calcarenites.

OH4 Member is associated with a palaeoshoreline marked with cliff and deep cavities cut into OH1 and OH3. In the cavities, OH4 deposits are composed of i) a calcirudite with a coarse coquinoid matrix and plurimetric collapsed blocks of calcarenites originating partly from OH3 Member which constitutes the cavity ceiling and blocks of calcirudite coming from earlier formations. These deposits are associated with a well-defined notch shaped at the expense of OH1 and OH3 Members at an altitude of about 34 m asl, ii) this chaos of blocks, whose surfaces are smoothed, is drowned out by a fine, planar-bedding calcarenite which is well developed laterally, which is inserted between the blocks and covers them; upwards, these sands become more massive. OH4 marine deposits constitute the lower set of the infilling of the GH large cavity (Raynal et al., 2011; Raynal et al., 2010). The upper set of the infilling is composed of continental deposits (GH-Continental Cave Complex). Without any apparent disconformity with OH4, GH-CCC lower units 4-3 deposits are composed of bioclastic and quartzose sands containing lithic objects, macrofauna, microfauna and hominin fossils, hence the cavity's name, probably edified in several episodes. The upper part of the GH-CCC is composed from bottom to top of a multilayer dripstone interbedded with loose red sands (GH-CCC-unit 2) which laterally links up with a speleothem, overlying by massive bedded, rubefied sands rich in microfauna and fragments of gasteropods shells, originating from reworked superficials red soils (GH-CCC-unit 1) (Raynal et al., 2011; 2010). At the entrance of the cavity, the wide cross-bedding “gray” sands of an aeolianite (OH5) are intercalated between the lower (3-4) and the upper units (1-2) of the GH-CCC.

1.2 Chronostratigraphy. According to the sequence stratigraphy, OH1 to OH4 Member are allostratigraphic units defined by a sedimentary sequence characterized by a succession of genetically related deposits - intertidal, supratidal and aeolian/continental depositional environments - and bounded at its base and top by unconformities. This sequence records sea-levels high-stands associated with the formation of a shoreline marked by a cliff in the case of OH3 and OH4. The unconformities or sequence boundaries mark the regression of the shoreline due to sealevel fall and the continentalisation of the coast. Thus, OH1 to OH4 Members are correlative to sea-levels high-stands of the main global glacio-eustatic cycles as inferred from the marine isotope stage (MIS) record and are preserved at positive elevations due to the regional tectonic uplift affecting Atlantic Morocco.

OHF predates the Anfa Formation (AF) whose Members AF1 and AF2 are correlated to MIS 13 even 15 (Fig. 2A). The OH4 deposits predates the continental cave deposits of the GH (Fig. 2A). OSL analyzes on GH-CCC-unit 4 yielded ages from 391±32 ka to 420±3413. A hominin tooth provided a laser abrasion ICP-MS age of 501 +89/-66 ka13. Biostratigraphic data point towards the first part of the Middle Pleistocene (Geraads, 2002; 2010). OSL dating of quartz provided an age range between 360 ka to 470 ka (370 ± 58 to 440 ± 38 ka) for the aeolianite OH5 intercalated between the lower units (3-4) and the upper (1-2) of the GH-CCC (Rhodes et al., 2006). The stratigraphic position, the facies and the dating allow to correlate this aeolianite with MIS 11 AF3 Member of the Anfa Formation.

The OH1-Bed2 microfauna, particulary the rodents, suggest a placement of the faunal assemblage between the fauna of Aïn Hanech and that of Tighennif in Algeria, i.e, representing the second half of the Early Pleistocene, but probably not in its terminal part (Geraads, 2002; 2010). This attribution is agreement with the results of the OSL dating, which provide an age between 0.8 and 1.2 Ma (Rhodes et al., 2006). As continental infillings of the GH cavity have been dated to 0.5-0.6 Ma (Raynal et al., 2011; 2010; Rhodes et al., 2006) in accordance with biostratigraphic data (Geraads, 2002; 2010), OH4 sea-level high-stand associated with the palaeoshoreline is undoubtedly much older than MIS 15. Thus, the OH4 to OH1 Members records sea-level highstands at least MIS 17 to older, much older if the record is not complete. Nevertheless, since it is difficult to estimate what the large hiatus corresponding to the embedding of about ten meters of the Anfa formation base platform in the Oulad Hamida Formation, and the quartzitic basement, may represent in terms of unrecorded cycles, it cannot be ruled out that these sea-levels high-stands of the OH formation are much older.

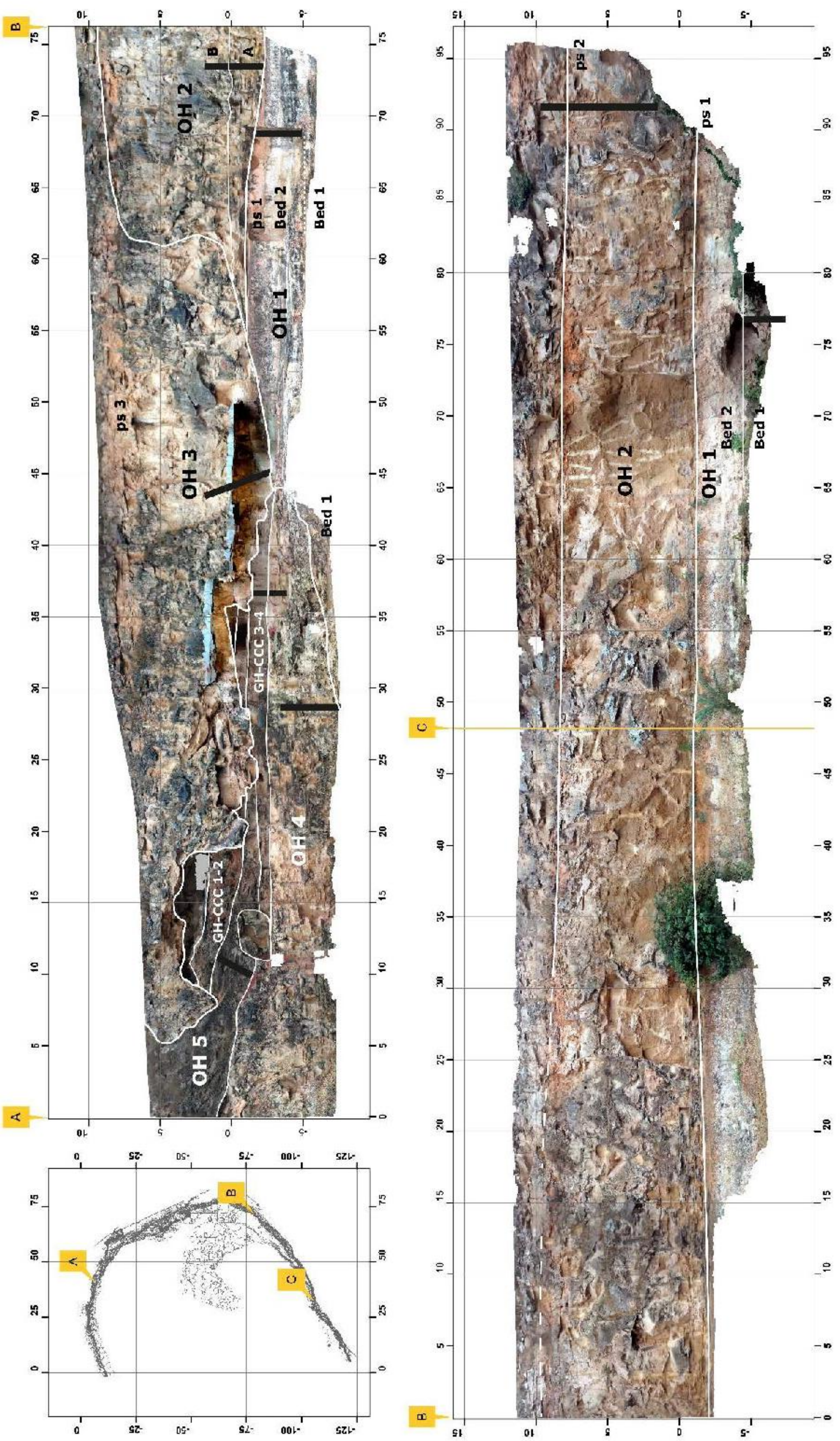

Fig. S1. Oulad Hamida Formation at ThI (photogrammetry and CAD S. Sanz-Laliberté and D. Lefèvre). The black bars indicate the location of magnetostratigraphical samples.

2. Thin sections' micromorphology of OH1 Bed2 - ThI-L

2.1 Methods. Twenty-seven samples were extracted during 1990 excavation from a test pit section in squares U25 (L1 to L5 base) and U28 (L5) of the lithic-bearing stratigraphic section of ThI-L site, OHF Member 1 (OH1), Bed 2. Five samples only were selected from archaeostratigraphic units L1 (9065), L2 (9062) and L5 (9039, 9043, 9054) to manufacture large thin sections (13,5 x 5,5 cm) at the micromorphology facility of Institut du Quaternaire from Bordeaux University (M. El Graoui). They were cut from oriented blocks of sediments vaccum-impregnated with polyester resin, following the process described by Guilloré (1980) (El Graoui, 1994).

This preliminary observation was intended first to give support to the interpretation of the field evidence about the depositional and post-depositional processes leading to the formation of each unit and second to search for the occurrence of mineral and organic anthropogenic debris related to human or animal activities (Cremaschi et al., 2018; Courty, 2001; Goldberg and Macphail, 2006; Goldberg and Berna; 2010). Micromorphological studies of thin sections employed an optical petrographic microscope Olympus BX41 equipped with a digital camera Olympus E420. Thin sections were observed at various magnifications (20x, 40x, 100x, 200x, 400x) under plane polarized light (PPL), cross-polarized light (XPL), and oblique incident light (OIL). Additionally, thin sections have been observed under oblique incident radiation (epifluorescence) of ultraviolet (UV) and blue (BLF) lights using a mercury burner (HBO lamp) 100 W, mostly to detect the occurrence of phosphatic features and to assess the degree of bone fragments preservation (Stoops, 2017). The description of thin sections is summarized in Table S1 that follows the terminology suggested by Stoops (2003). Data interpretation follows the concepts on the formation of natural and anthropogenic layers summarized in Courty et al. (1989) Nicosia and Stoops (2017), and Stoops et al. (2018).

2.2 Results. From the sedimentological point of view, Bed 2 presents distinct sedimentary environments that corresponds to facies related to the evolution of nearshore environments. The lowermost part of the sequence (L1) consists of a packed accumulation of sand-sized, subangular quartz grains with occasional occurrence of glauconite grains, and common to scarce coarse bioclasts (Supplementary Fig. S2). The latter are in part dissolved and testified by moldic voids, pseudomorphic of bioclasts. In some cases, dissolution voids are partially filled by sparitic or micritic cement (Supplementary Fig. S3). The micromass consists of a variable quantity of micrite; in the lower part of L1 the micritic groundmass is almost absent and calcite nodules are present (Supplementary Fig. S2).

The following L2 unit alternates levels consisting of carbonatic mud with interspersed scarce sand-sized quartz grains and very rare bioclasts (Supplementary Fig. S2) displaying calcitic coatings, to levels with abundant sand-sized quartz grains, ghosts of carbonatic clasts, and calcitic pedorelicts (with altered margins) in a micromass of micritic to sparitic calcite (Supplementary Fig. S2). The porosity is generally low in L2 and related to construction voids and occasionally by bioturbation voids (common to scarce channels; Supplementary Fig. S2). Occasional compact microlayers are evident (Supplementary Fig. S4). In L2 altered bone fragments and phosphatic impregnation on the groundmass are occasionally present (Supplementary Fig. S4).

The uppermost part of the sequence (L5) consists of accumulations of coarse sand, which is constituted mostly by subangular quartz grains and occasionally other minerals including glauconite (Supplementary Fig. S2), interspersed in a calcitic micromass. Unit L5 displays a weak to moderate preferential orientation of the coarse constituents, which is detectable thanks to the occurrence of aligned dissolution voids after shell fragments (Supplementary Fig. S5). In the lower part of L5, a thin layer of laminar to stromatolithic calcite is present. Bioturbation is evident in this part of the sequence and the occurrence of Fe-rich oxy-hydroxides staining mineral grains and the rim of voids and impregnating the groundmass in the lower part of L5 is a further evidence of pedogenesis (Supplementary Fig. S3). Anthropogenic debris are occasionally present; in L5 they are represented by fragments of knapped lithic artifacts and bone fragments and phosphatic impregnation of the groundmass, which can have an animal origin (Supplementary Fig. S5). A few, very small fragments of charcoal are also present, but their attribution to intentional human firing is not possible.

The sedimentary facies observed at the microscale suggest the interplay of distinct sedimentation mechanism in charge of the accumulation of Bed 2. All processes happened in nearshore environments thanks to the interplay between wind and fluvial sedimentation. The basal unit L1 formed after the accumulation of aeolian sand constituted by quartz grains, glauconite grains, and bioclasts (e.g., shell fragments, bryozoan, echinoderm, foraminifera, red algae) deflated presumably from the emerged shelf. The subsequent layer L2 shows a transition towards fluvial processes and the unit likely accreted in correspondence of a system of low to medium energy channels alternated to swamps. In such conditions, decantation of clay and precipitation of calcite occurred in swamp to lake environments, whereas coarse layers suggest increased energy of the system and the onset of a channel system. Likely, it was a braided system that accumulated carbonatic sand-sized grains, limestone fragments, and pedorelicts resulting from the dismantling of the carbonatic mud of the swamp environment. Finally, thin sections from layer L5 suggest a further shift in the sedimentary system and a new onset of wind sedimentation with the accretion of dunes. The shape and size of quartz grains is compatible with the aeolian sedimentary environment and the presence of glauconite grains and abundant bioclast moulds support the interpretation of this unit as eolianites.

All deposits identified in the L5 to L1 sequence suffered strong post-depositional modification. Evidence of bioturbation is evident along the whole sequence as much a huge mobilization and reprecipitation of calcite. Bioclasts in the L5 wind-accreted unit are completely dissolved resulting in abundant dissolution/moldic voids; the same happened to carbonatic grains from the L2 unit, which are represented by micrite envelopes28. Calcite reprecipitated as micrite cementing the micromass or occasionally as sparite; in many cases, secondary calcite formed bridges among grains and recipitated inside the voids of former mineral grains and bioclasts (Cremaschi et al., 2018; Ward, 1975). As common in carbonatic soils of the Mediterranean area, the typical calcitic crystallitic b-fabric is the combination between calcite inherited from sedimentary parent material and gradual precipitation of micrite in the micromass and filling of pore space between grains by precipitated silt- and claysize pedogenic carbonate crystals (Wieder and Yaalon, 1974; Monger et al., 1991; Verrecchia, 2007; Durand et al., 2018). Incipient formation of calcite nodules is evident in the basal part of the sequence (L1). Bioturbation is evident in deposits related to wind sedimentation suggesting a moderate vegetal cover. Also, carbonatic mud observed under the microscope display moderate to weak occurrence of bioturbation (channel voids) due to vegetation or invertebrates. L5 suffered initial pedogenesis under warm environmental conditions during episodes of subaerial exposure; this is suggested by the occurrence of Fe-oxyhydroxides impregnating the groundmass and forming coatings on grains and voids (Tsatskin and Ronen, 1999; Zhao et al., 2011; Li et al., 2018). Warm conditions after the deposition of the sand deposit of L5 are further confirmed by the occurrence of micritic ondulated laminar layers that can be interpreted as thin calcrete (Ward, 1975; Shtienberg et al., 2017). Such processes (calcite redistribution and Fe-bearing pedofeatures) are common in Pleistocene eolianites deposits from the Mediterranean region and elsewhere (Brooke, 2001; Simpson and Eriksson, 1993; Hearty, 2003; Assal et al., 2020) and likely promoted by the transpiration of dune plants (Ward, 1975; Zhao et al., 2011; Shtienberg et al., 2017).

Compact layers detected in L2 and repeated alignments of elongated constituents in L5 are syndepositional features likely related to runoff or eolian processes even if trampling associated to human occupation of the site could also be suggested (Zerboni, 2011; Miller, 2017). The accumulation of bone fragments is also due to animal and/or human accumulators. Observation of bone fragments under BLF light suggests that they are moderately altered and partially impregnated by Fe-oxyhydroxides. The fluorescence light highlighted the presence of accumulation of phosphates in the groundmass of L5 and (less abundant) L2, likely formed after weathering under warm conditions of bone fragments (Stoops, 2017; Villagran et al., 2017; Karkanas and Goldberg, 2018). Finally, the occurrence of lithic fragments (Angelucci, 2010; 2017) confirms an in situ knapping activity already revealed by the excavation.

2.3 Conclusion. The observation of thin sections from sediments of ThI-L under the microscope highlighted the major sedimentary properties of the deposit and strong post-depositional and taphonomic processes affecting the whole sequence. The final product is a sedimentary sequence alternating coarse siliciclastic to bioclastic sands and calcareous mudstones. The formation of the sequence is likely related to the interplay of littoral processes that include sedimentation in low energy channel interchanged to swamps along backshore environments, alternated to periods of enhanced aeolian sedimentation. Moreover, the whole sequence displays strong evidence of pedogenesis and diagenesis, including huge calcite mobilization and redistribution and bioturbation, resulting in layers with huge accumulation of micritic cement in the groundmass and abundant dissolution cavities related to pristine calcitic constituents (mineral grains and bioclasts). In the uppermost part of the sequence (unit L5), evidence of pedogenesis during warm episodes of subaerial exposure and increased vegetation cover are preserved. A limited human overprint on sedimentation and taphonomy of deposits is supposed in two distinct layers. In the uppermost part of L5, biogenic/anthropogenic indicators (Macphail and Goldberg, 2018) are interspersed in the groundmass and include fragments of knapped lithic artefacts and minute fragments of altered bones. In the same unit, very small charcoal fragments of unknown origin have been identified. In the same layer a weak to moderate preferential orientation and alignment of dissolution voids (mould of shell fragments) was detected but more investigations are necessary before attributing them to repeating trampling on the same surface rather to ordinary bioturbation. Moderately preserved fragments of altered bones were also identified in layer L2; under fluorescence light and the same thin section displays evidence of phosphatic impregnation of the groundmass, which is generally related to the deep weathering of bone fragments and the same unit displays occasional evidence of compaction features that could be associated to trampled surfaces. However, one must keep in mind that these low energy channels and swamps environment was at least heavily frequented by hippos and crocodiles.

Table S1.

Summary of micromorphological properties of samples.

Sample	Layer	Depth (cm)	Mineral consitutents	Micromass	Organic and anthropogenic constituents	Voids	c/f related distribution	b-fabric	Microstructure	Pedofeatures
9039	L5	-223–233	Common to abundant sand-sized quarts grains, subangular to poorly rounded; very scarce igneous grains; scarse altered bioclasts	Brownish grey clayey micromass impregnated of calcite	Scarce, small bone fragments, partially weathered; scarce fragments of knapped lithic; very rare small charcoal fragments	Common vughs; scarse channels and planes; common mouldic voids after bioclasts dissolution, occasionally aligned	Single spaced porphyric	Crystallitic to undifferentiated	Massive to complex	Common crystalline pedofeatures related to calcite dissolution and redistribution, including sparitic and micritic coatings on voids and clasts, infillings of mouldic voids, hypocoatings, and impregnation of the gorundmass; scarse phosphatic impregnation on the groundmass; weak evidence of Fe-oxyhydroxides impregnationon on the groundma and around discrete elements; weak Mn-rich oxyhydroxides impregnation on bone fragments; scarce passage features
9043	L5	-283–273	Common to abundant sand-sized quarts grains, subangular to poorly rounded; scarce glauconite clasts; very scarce igneous grains; scarce altered bioclasts	Brownish grey clayey micromass impregnated of calcite	Scarce, small bone fragments, partially weathered	Common vughs; rare to scarce channels and planes; common mouldic voids after bioclasts dissolution	Single spaced to close porphyric	Undifferentiated	Massive to complex	Common crystalline pedofeatures related to calcite dissolution and redistribution, including sparitic and micritic coatings on voids and clasts, infillings of mouldic voids, hypocoatings, and impregnstion of the gorundmass; scarce calcite nodules; weak evidence of Fe-oxyhydroxides impregnation on on the groundmass and around discrete elements; weak Mn-rich oxyhydroxides impregnation on bone fragments; scarce passage features
9054	L5-L4	-326–335	Common sand-sized quarts grains, subangular to poorly rounded; common carbonatic clasts; very scarce altered bioclasts	Brownish grey clayey micromass impregnated of calcite; in the upper part, weakly micritic ondulated laminar layers		Common vughs; scarce to common channels and planes; common mouldic voids after bioclasts dissolution	Single to double spaced porphyric; occasionally close porphyric	Crystallitic to undifferentiated	Massive to complex	Common crystalline pedofeatures related to calcite dissolution and redistribution, including sparitic and micritic coatings on voids and clasts, infillings of voids, hypocoatings, and impregntion of the gorundmass; scarce calcite nodules; common Fe-oxyhydroxides impregnationon on the groundmass and around discrete elements
9062 haut	L23	-402–414	Scarce to common sand-sized quarts grains, subangular to poorly rounded; common to scarce carbonatic clasts; very rare bioclasts	very scarce micritic micromass	Scarce, small bone fragments, partially weathered	Common vughs; scarce channels and planes; scarce mouldic voids after limestone clasts and bioclasts dissolution	Close porphyric	Crystallitic	Massive to complex	Common crystalline pedofeatures related to calcite dissolution and redistributior including sparitic and micritic coatings on voids and clasts, infillings of voids (including mouldic voids), hypocoatings, and impregnation of the gorundmass; scarce calcite nodules; ripening layers; in the lower part of the sample, calcitic pedorelicts with erosional margins and Fe-impregnation; tion of the gorundmass
9062 bas	L23	-417–429	Scarce to common sand-sized quarts grains, subangular to poorly rounded; common to scarce carbonatic clasts; scarce rock fragments (limestone); very rare bioclasts	Brownish grey clayey micromass impregnated of calcite		Common vughs; scarce channels and planes; scarce mouldic voids after limestone clasts and bioclasts dissolution	Close to sulgle spaced porphyric	Crystallitic	Massive to complex	Common crystalline pedofeatures related to calcite dissolution and redistributior including sparitic and micritic coatings on voids and clasts, infillings of voids (including mouldic voids), hypocoatings, and impregnation of the gorundmass; scarce calcite nodules; calcitic pedorelicts with erosional margins and Fe-impregnation; tion of the gorundmass; scarce lithorelicts
9065 haut	L1 top	-455–467	Common to abundant sand-sized quarts grains, subangular to poorly rounded; very scarse igneous grains; scarce altered bioclasts	Brownish grey clayey micromass impregnated of calcite		Common vughs; scarse channels and planes; common mouldic voids after bioclasts dissolution	Single spaced to close porphyric	Crystallitic to undifferentiated	Massive to complex	Common crystalline pedofeatures related to calcite dissolution and redistribution, including sparitic and micritic coatings on voids and clasts, infillings of mouldic voids, hypocoatings, and impregnstion of the gorundmass; scarce calcite nodules; very weak Fe-oxyhydroxides impregnation on the groundma
9065 bas	L1 top	-460–472	Common to abundant sand-sized quarts grains, subangular to poorly rounded; scarce glauconite clasts; very scarce igneous grains; scarce altered bioclasts	Scarce brownish grey clayey micromass impregnated of calcite		Common vughs; scarse channels and planes; common mouldic voids after bioclasts dissolution	Close porphyric	Crystallitic to undifferentiated	Massive to complex	Common crystalline pedofeatures related to calcite dissolution and redistribution, including sparitic and micritic coatings on voids and clasts, infillings of mouldic voids, hypocoatings, and impregnstion of the gorundmass; scarce calcite nodules; common abundant calcitic nodules

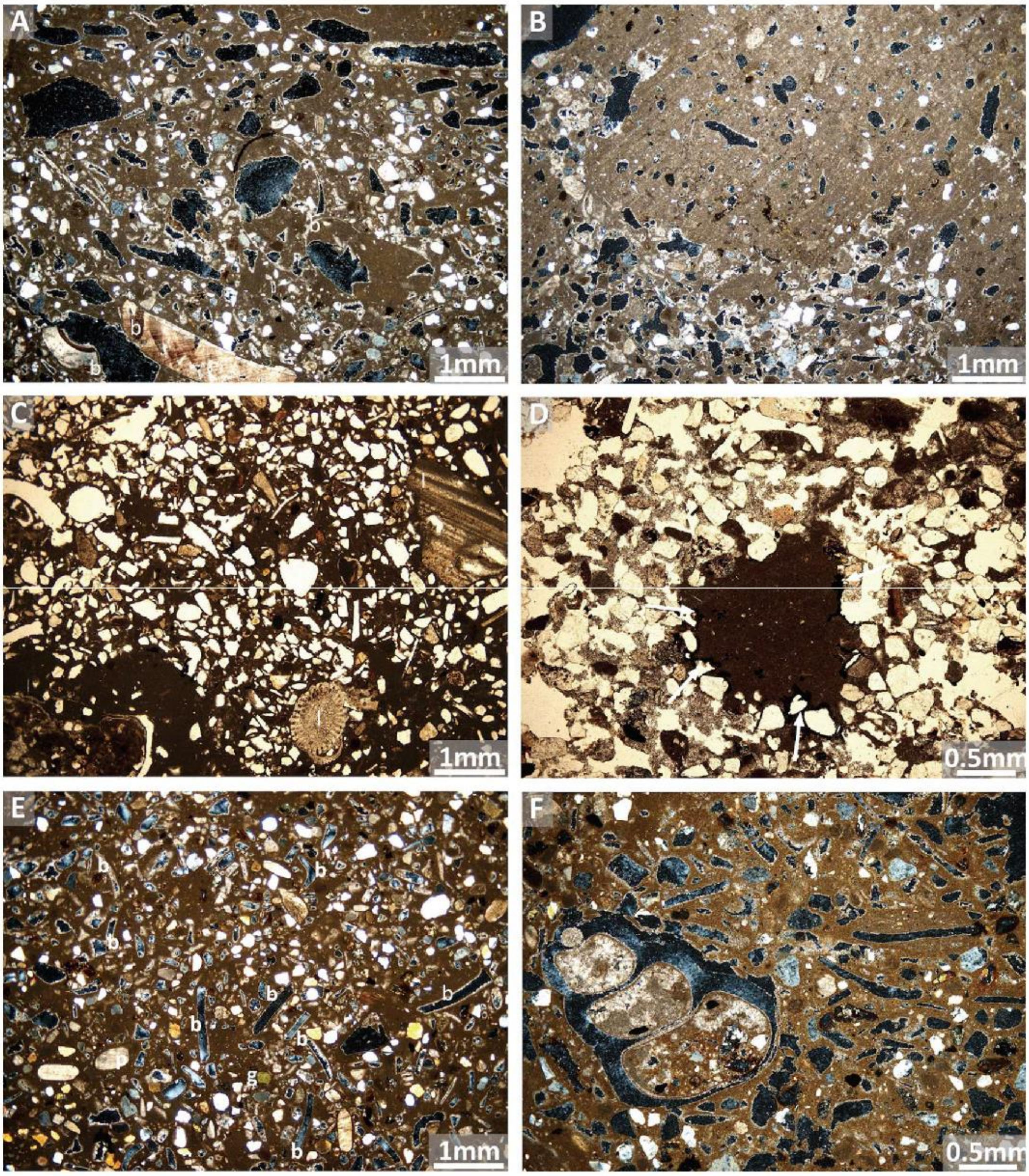

Fig. S2. General aspect of the observed thin sections from layers L1–L5 illustrating variations in the groundmass and constituents that reflects changes in sedimentary environments. (A) Single spaced porphyric c/f related distribution of the sandy L1 unit; notice the occurrence of common bioclasts (B) (XPL). (B) Open porphyric c/f related distribution of the carbonatic mud in L2 (XPL). (C) Close to single spaced porphyric c/f related distribution of the sandy layer in L1 related to moderate energy fluvial system; notice the occurrence of lithorelicts (l) (PPL). (D) A pedorelict (a micrite nodule with altered margins indicated by the arrows) in the L1 unit (PPL). (E) Close to single spaced porphyric c/f related distribution of the sandy L5 unit; notice the occurrence of subangular quartz grains, glauconite grains (g), and common bioclasts (B) (XPL). (F) A detail of the voids pseudomorphs of shell fragments with partial reprecipitation of micrite in L5 (XPL).

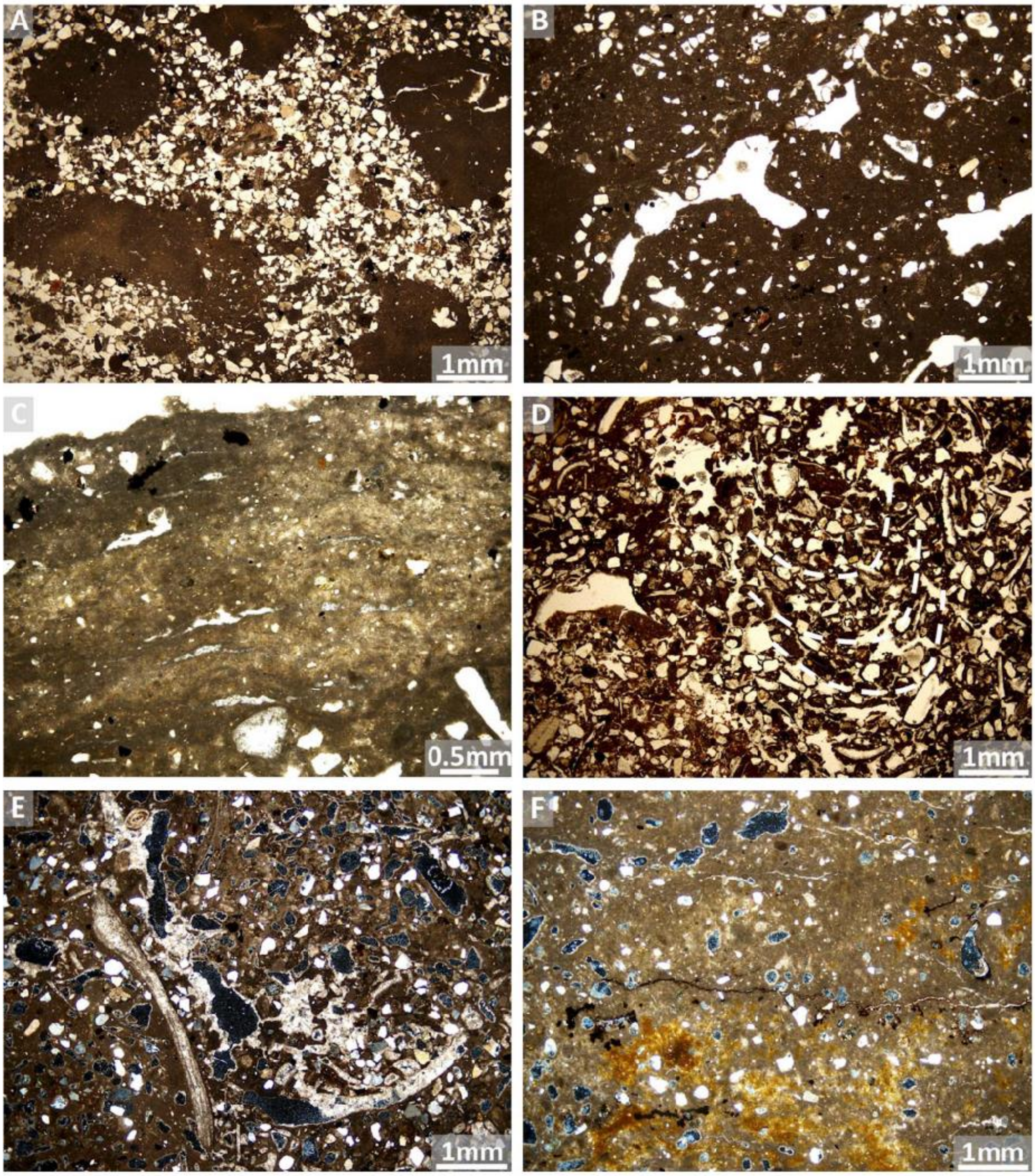

Fig. S3. Photomicrographs illustrating post-depositional processes (pedogenesis and diagenesis) affecting the sedimentary sequence of Bed 2. (A) Calcitic nodules in the sandy groundmass of L1 (PPL). (B) Channel voids due to bioturbation in the mudstone of L2 (PPL). (C) Micritic undulated laminar layer (calcrete) in L5 (PPL). (D) Dashed lines highlight a passage pedofeature (bioturbation) in L5 (PPL). (E) Strong dissolution of bioclast and reprecipitation of micrite and sparite in L5 (XPL). (F) Fe-rich oxy-hydroxides impregnating the groundmass and coating voids and grains in the lower part of L5 (XPL).

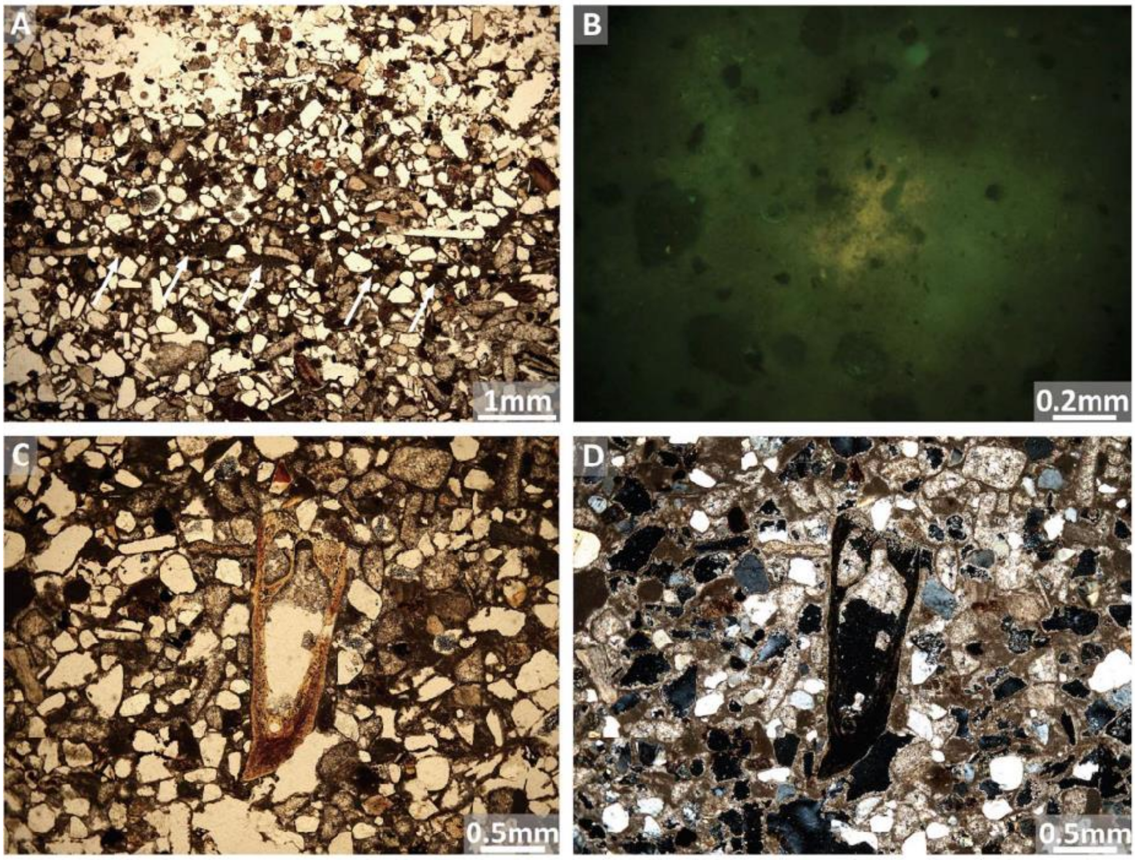

Fig. S4. Photomicrographs of some microscopic features detected unit L2. (A) Evidence of compaction (indicated by arrows) in the upper part of L1 (PPL). (B) Phosphatic impregnation on the groundmass (BLF). (C) A weakly altered bone fragment in L2; notice the abundant occurrence of moldic voids after grains dissolution with micrite envelope or secondary sparite/micrite precipitation (PPL). (D) the same of (C) in XPL.

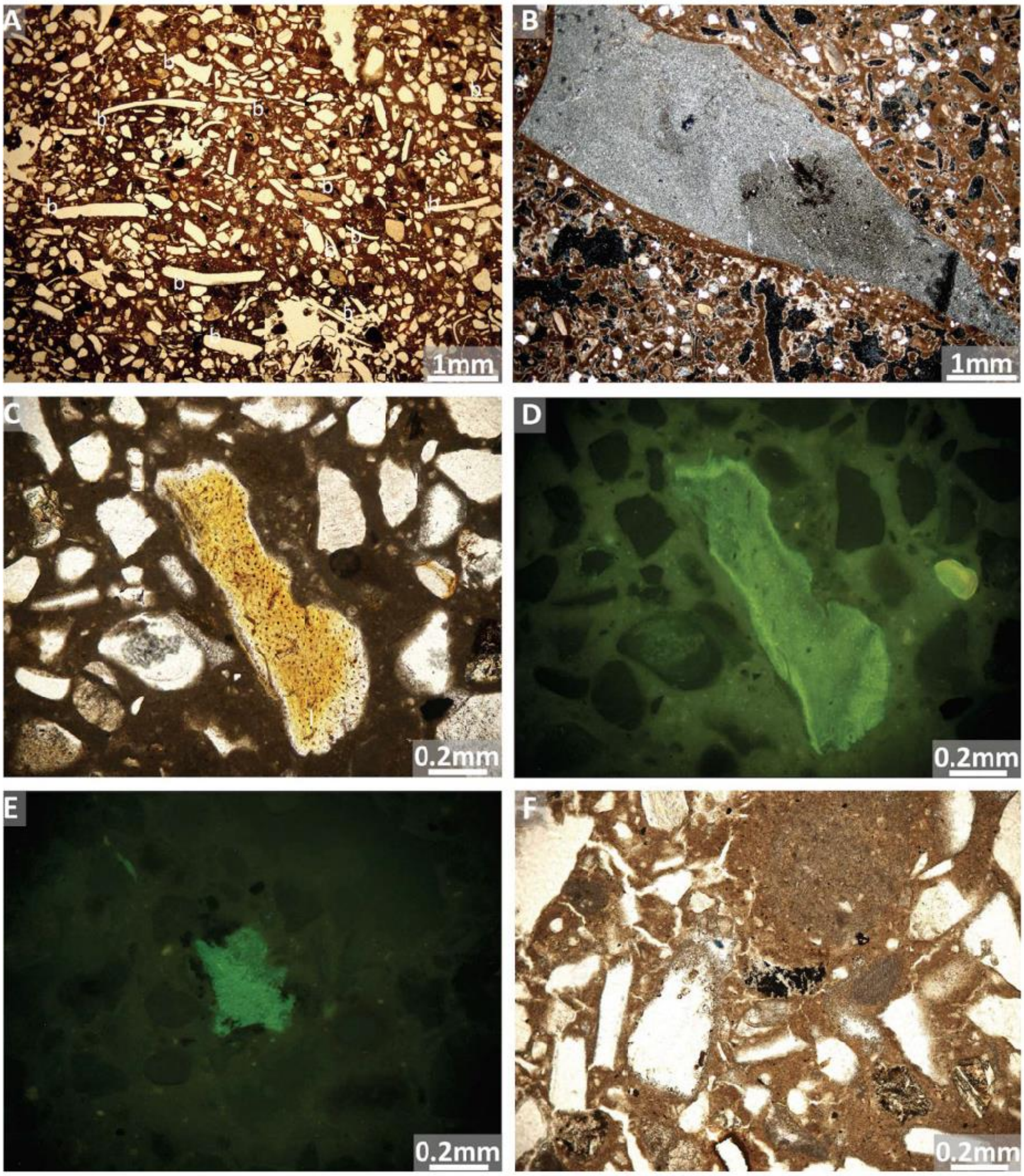

Fig. S5. Photomicrographs of some microscopic features detected in unit L5. (A) Preferential alignment of moldic voids, pseudomorphic of bioclasts (b) in the upper part of L5 (PPL). (B) A knapped lithic artifact (XPL). (C) A weakly altered bone fragment (PPL). (D) the same of (C) in BLF. (E) A bone fragment in BLF with Fe-oxyhydroxides impregnation on its margins. (F) A small fragment of charcoal (PPL).

3. Paleontology, biochronology, and zooarchaeology

3.1 Paleontology and biochronology. Large mammal remains are rare and fragmentary at ThI-L. Not unexpectedly in this environment, they are dominated by a large hippo probably identical with Hippopotamus sirensis from Tighennif (itself probably identical with *H. gorgops* from East Africa). A complete suid upper M3 was assigned to *Kolpochoerus maroccanus* by Geraads (2010), but if this species belongs in fact to *Metridiochoerus* as hypothesized by Souron (2012), this tooth must in fact belong to either *K. majus* or to *K. limnetes/olduvaiensis*, all known in the East African Early Pleistocene. It is more simply built and smaller than most *K. olduvaiensis* teeth from the Early Pleistocene, slightly larger *than K. majus* teeth from the upper Konso levels (Suwa et al., 2014), and more like teeth from Asbole (Geraads et al., 2004) or Daka (Gilbert, 2008) but we refrain from drawing biochronological conclusions from a single tooth. Bovids include a bovin, a gazelle, a medium-size alcelaphin, and a medium-size *Kobus sp*. An *Equus* and a rhino are also present, together with an *Elephantidae*, probably *Elephas*, although the poorly loxodont pattern of some *Loxodonta atlantica* teeth from Tighennif makes genus identification difficult.

A single tooth of *Crocidura sp*. is documented. An upper anterior premolar of Lagomorph (*Lepus sp*.?) is too primitive to belong to the common hare of the Middle Pleistocene of these quarries, *Trischizolagus raynali*, but could be of *Lepus*, already present at Ahl al Oughlam. Rodents are represented by 15 teeth of which only three belong to murins, and 12 to gerbillins, suggesting rather arid environment. The absence of the dormouse *Eliomys* can be due to incomplete sampling, but that of the mole vole *Ellobius* is perhaps significant, as this genus is usually common when present. This genus is an Asian immigrant that first appears at Tighennif, suggesting that this Algerian site might be younger than ThI-L. A molar fragment of the murin *Paraethomys* differs from all other *Paraethomys* found in Morocco, including the *P. tighennifae* from other levels in Thomas and Oulad Hamida Quarries, but is reminiscent of *P. mellahe* (Ameur, 1988) from Oued Mellah, an Algerian site earlier than Tighennif, according to Ameur (1988). A few teeth document two unnamed species of *Gerbillus*, both different from the species known at Grotte à Hominidés, at Grotte des Rhinoceros of the nearby Oulad Hamida 1 Quarry and at Tighennif 8. The evolutionary grade of the smaller form is intermediate between those of *G. minutus* from the Plio-Pleistocene and of *G. campestris* of the Middle Pleistocene.

On the whole, the mammalian fauna from ThI-L is too poor to be confidently dated by biochronology, but it significantly differs from those of GH-CCC-unit 4, and also from that of Tighennif. It is well-known that the rodent fauna of the northwestern African Pleistocene is highly endemic (Geraads, 1998), but the large mammals have strong affinities with Eastern Africa (Geraads, 2010), although temporal resolution is too low to estimate the dates of possible dispersal events. Most of the taxa present at ThI-L may have local ancestors, except perhaps *K. majus*, which must be of East African origin, because the earlier sites of Mansourah (Chaid-Saoudi et al., 2006) and Aïn Hanech (Sahnouni et al., 2002) yielded instead *K. olduvaiensis*, which belongs to another lineage (Souron, 2012).

3.2 Remarks on biochronology of Tighennif site (Algeria). The age of this site remains poorly supported. Geraads et al. (1986) accepted an age close to 0.7 Ma, but it is becoming increasingly clear that this age was underestimated (Geraads, 2016). Pickford (2020) estimated its age at 1.4 ±0.3 Ma, based upon his reassignment of the only suid from this locality to *Metridiochoerus andrewsi*, a species older than the South African *M. compactus*. This re-identification may be correct, but Pickford's biochronological conclusion is debatable, as the East African chronological range of *M. andrewsi* extends after 1 Ma. For instance, at Daka, a site well-dated at 1 Ma (Gilbert and Asfaw, 2009) the range of M3 length (63.7– 88.1 mm, N = 4) (Gilbert and Asfaw, 2009) is almost the same as at Tighennif (64–83.5 mm, N = 6). We agree that Tighennif cannot be much younger than 1 Ma, but on the basis of bovids (Geraads, 1981), an age older than 1.5 is very unlikely.

3.3 Taphonomy. The faunal assemblage is highly fragmented and the bone surfaces are badly preserved. The main alterations are natural abrasion striations, desquamation, fissuring and polishing (Supplementary Fig. S6). Trampling, weathering and water flowing could be the main post-depositional agents of alteration, notably in this context of open-air deposits in wetland environments. Besides, we notice a total absence of anthropogenic and carnivorous marks, possibly due to this scarcity of legible surfaces. However, crocodile tooth marks (scores and punctures) could be identified, some on hippo remains (Supplementary Fig. S7) (Domínguez-Rodrigo and Baquedano, 2018; Njau and Blumenschine, 2006; 2012; Sahle et al., 2017).

Fig. S6. Natural notches and abrasion striations on an unidentified bone fragment (ThI-L- R27-16). Digital microscope images C. Daujeard.

Fig. S7. Crocodile tooth punctures on a fragment of a hippo talus (ThI-L-5381). Photo C. Daujeard.

4. Magnetostratigraphy

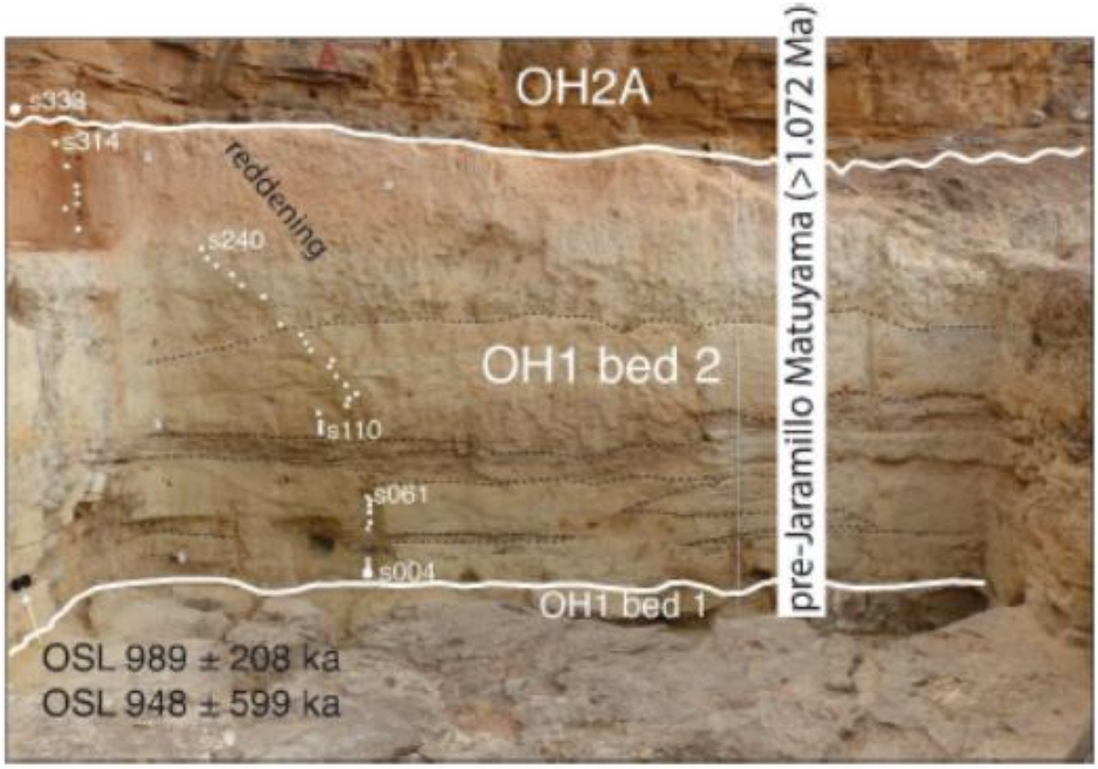

Fig. S8. Photograph of the stratigraphy of archeological section in unit OH1 Bed 2, trench south side with position of samples for magnetostratigraphy. OH1 Bed 2 is dated to the pre-Jaramillo Matuyama (>1.072 Ma) probably prior to the Cobb Mountain subchron. See main text for discussion.

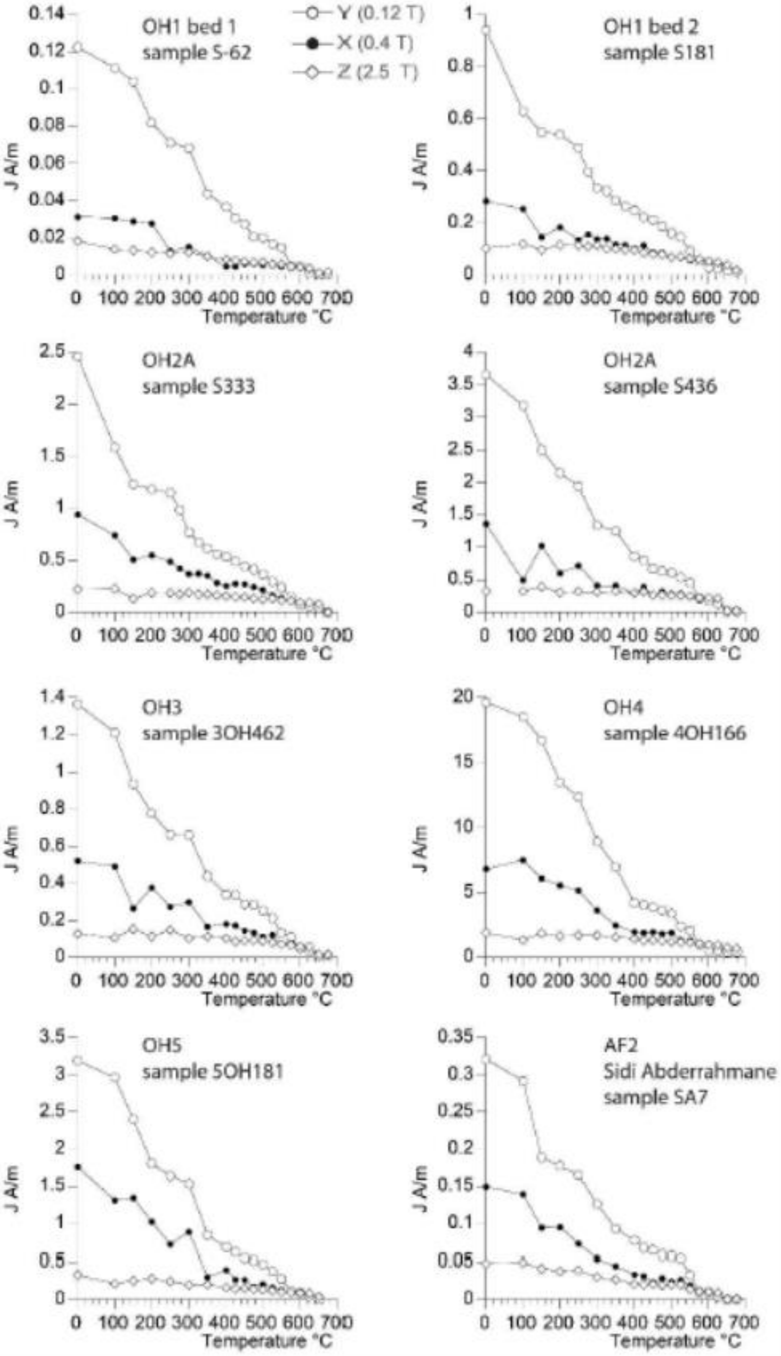

Fig. S9. Thermal demagnetization of a three-component isothermal remanent magnetization (IRM) using fields of 2.5T, 0.4T, and 0.12T of selected samples from the investigated sedimentary units showing the predominance of magnetite as the carrier of the remanence coexisting with subsidiary hematite. See text for discussion.

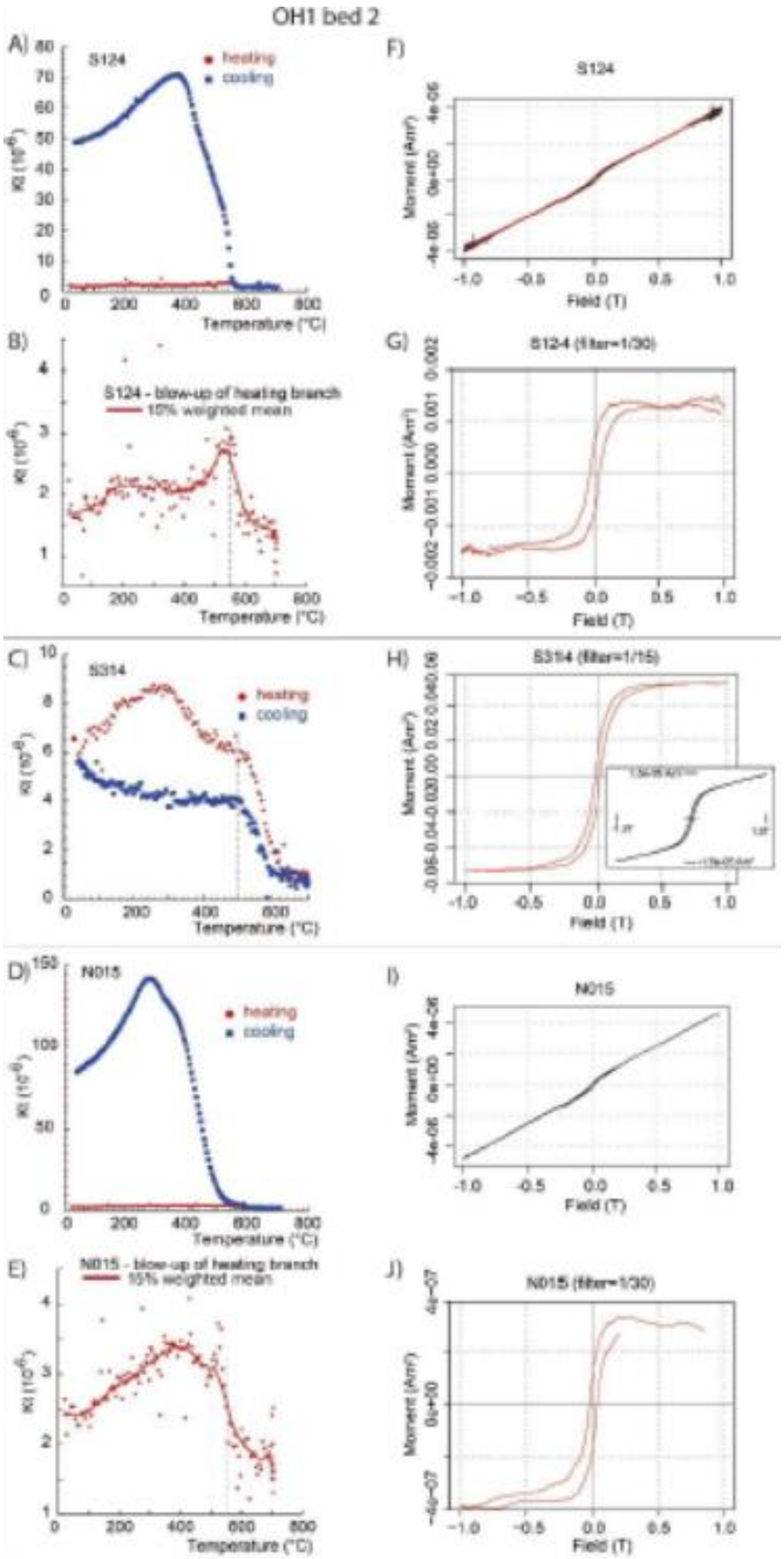

Fig. S10. Thermomagnetic (heating-cooling) cycles of magnetic susceptibility (A–E) and hysteresis experiments (F–J) on selected samples from OH1 Bed 2.

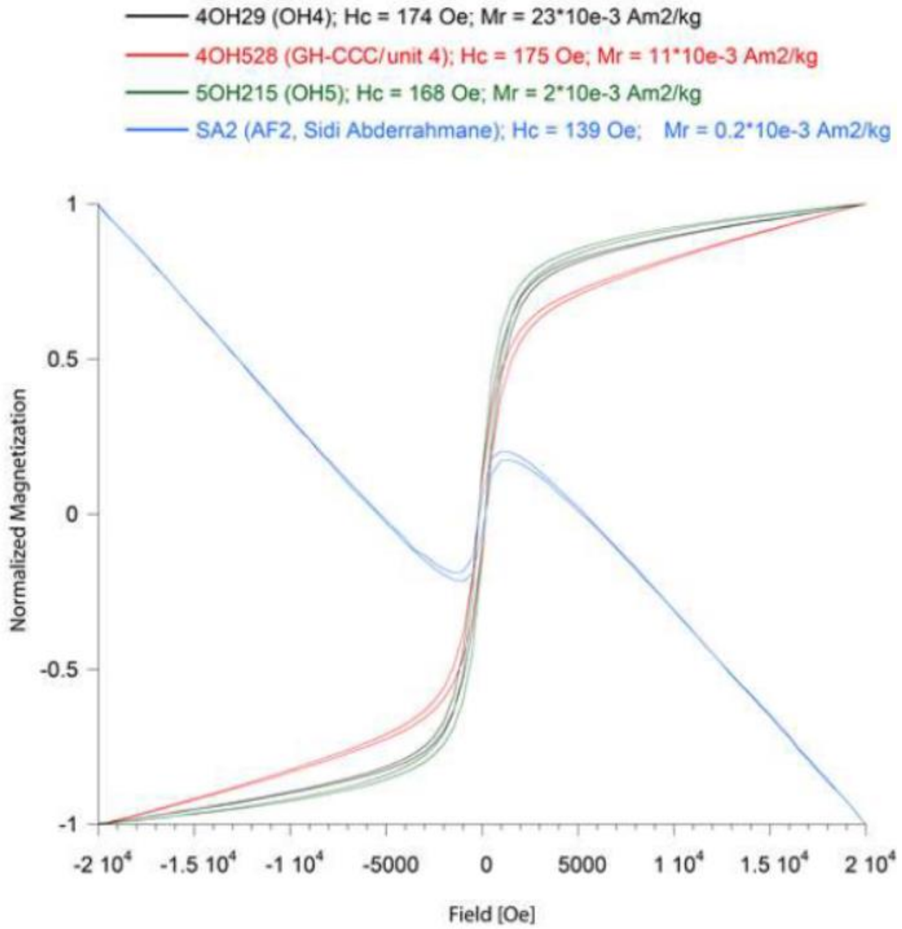

Fig. S11. Hysteresis experiments on samples from OH4, GH-CCC, OH5, and AF2 at Sidi Abderrahmane quarry. Analyses are non-corrected for paramagnetic (positive slope) or diamagnetic (negative slope) contributions.

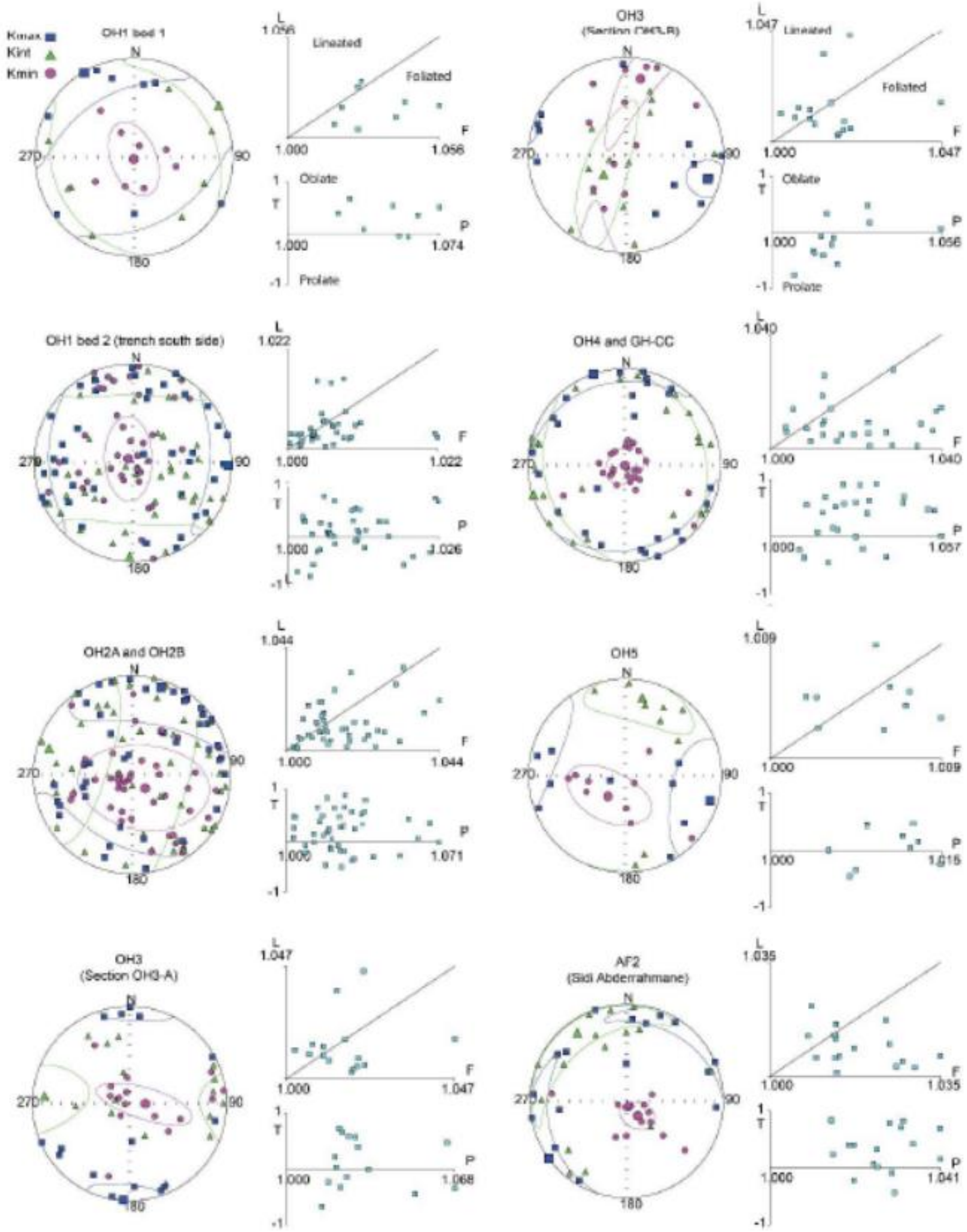

Fig. S12. Anisotropy of magnetic susceptibility data. See Material and Methods for anisotropy parameters definition and text for discussion.

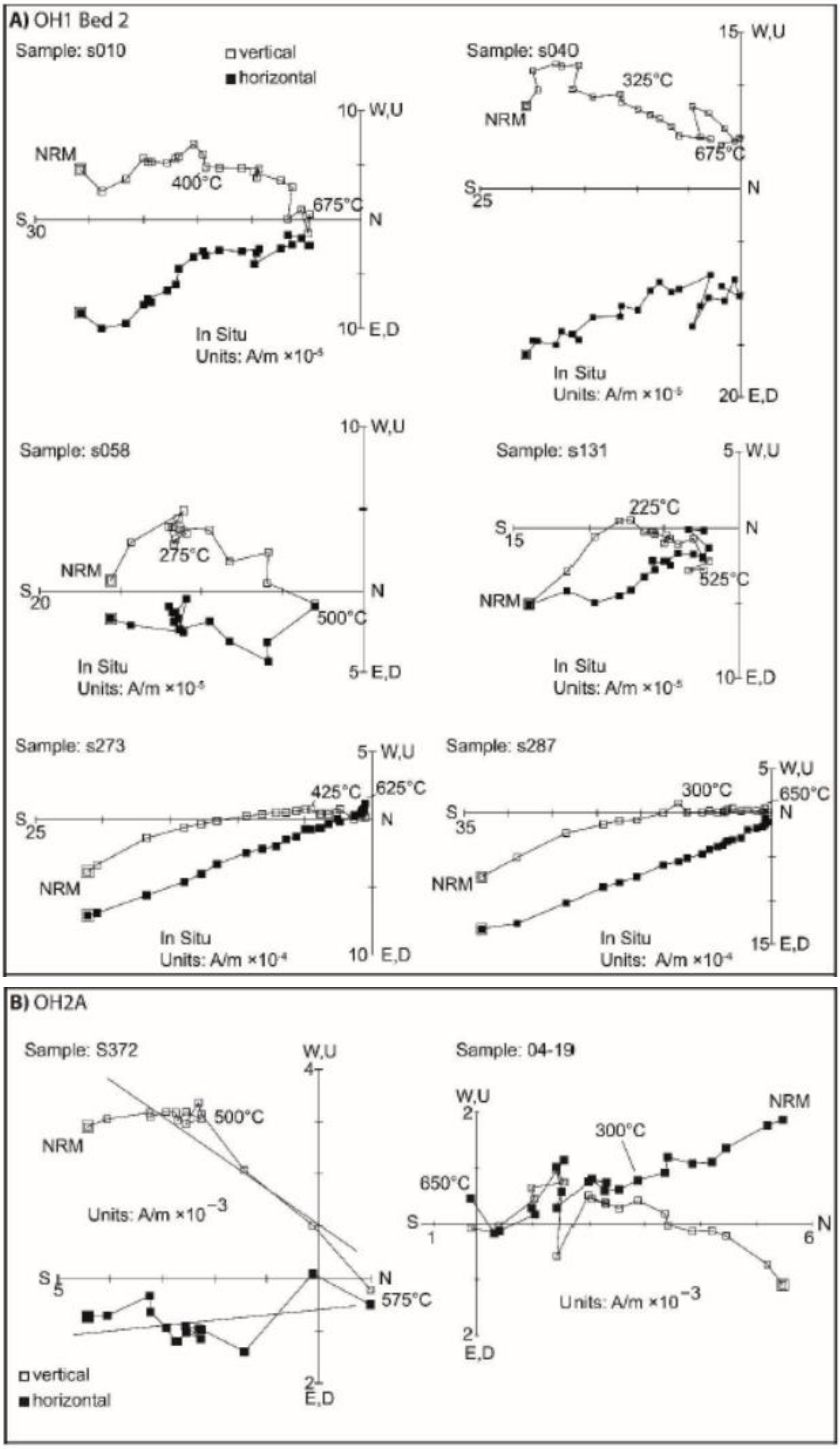

A) OH1 Bed 2
Sample: s010
vertical
horizontal
10 W,U
NRM
400°C
675°C
S 30
N
In Situ
Units: A/m ×10⁻⁵
10 E,D
Sample: s040
15 W,U
325°C
NRM
675°C
S 25
N
In Situ
Units: A/m ×10⁻⁵
20 E,D
Sample: s058
10 W,U
NRM
275°C
S 20
N
500°C
In Situ
Units: A/m ×10⁻⁵
5 E,D
Sample: s131
5 W,U
225°C
S 15
N
NRM
525°C
In Situ
Units: A/m ×10⁻⁵
10 E,D
Sample: s273
5 W,U
425°C
625°C
S 25
N
NRM
In Situ
Units: A/m ×10⁻⁴
10 E,D
Sample: s287
5 W,U
300°C
650°C
S 35
N
NRM
In Situ
Units: A/m ×10⁻⁴
15 E,D
B) OH2A
Sample: S372
W,U
4
500°C
NRM
Units: A/m ×10⁻³
S 5
N
575°C
vertical
horizontal
2 E,D
Sample: 04-19
W,U
2
NRM
300°C
650°C
S 1
N 6
Units: A/m ×10⁻³
2 E,D

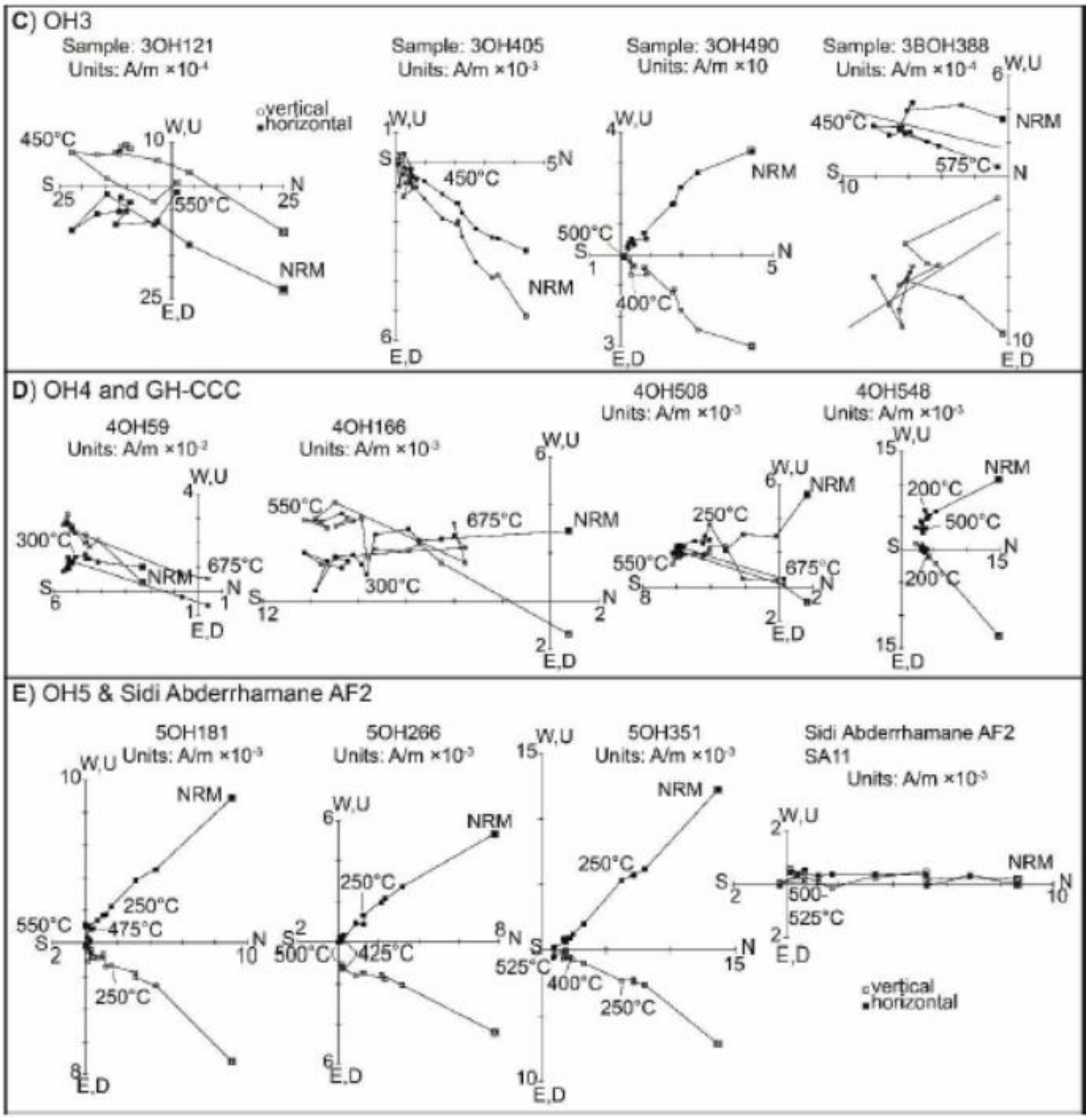

Fig. S13. Vector end-point demagnetization diagrams of representative samples from the main units investigated. (A) OH1 Bed 2, (B) OH2A, (C) OH3 (samples 3OH121, 3OH405, 3OH490 from section OH3-A, and sample 3BOH388 from section OH3-B), (D) OH4 and GH-CCC, (E) OH5, and AF2 at Sidi Abderrahmane Quarry. Filled/open symbols are projections onto the horizontal/vertical plane.

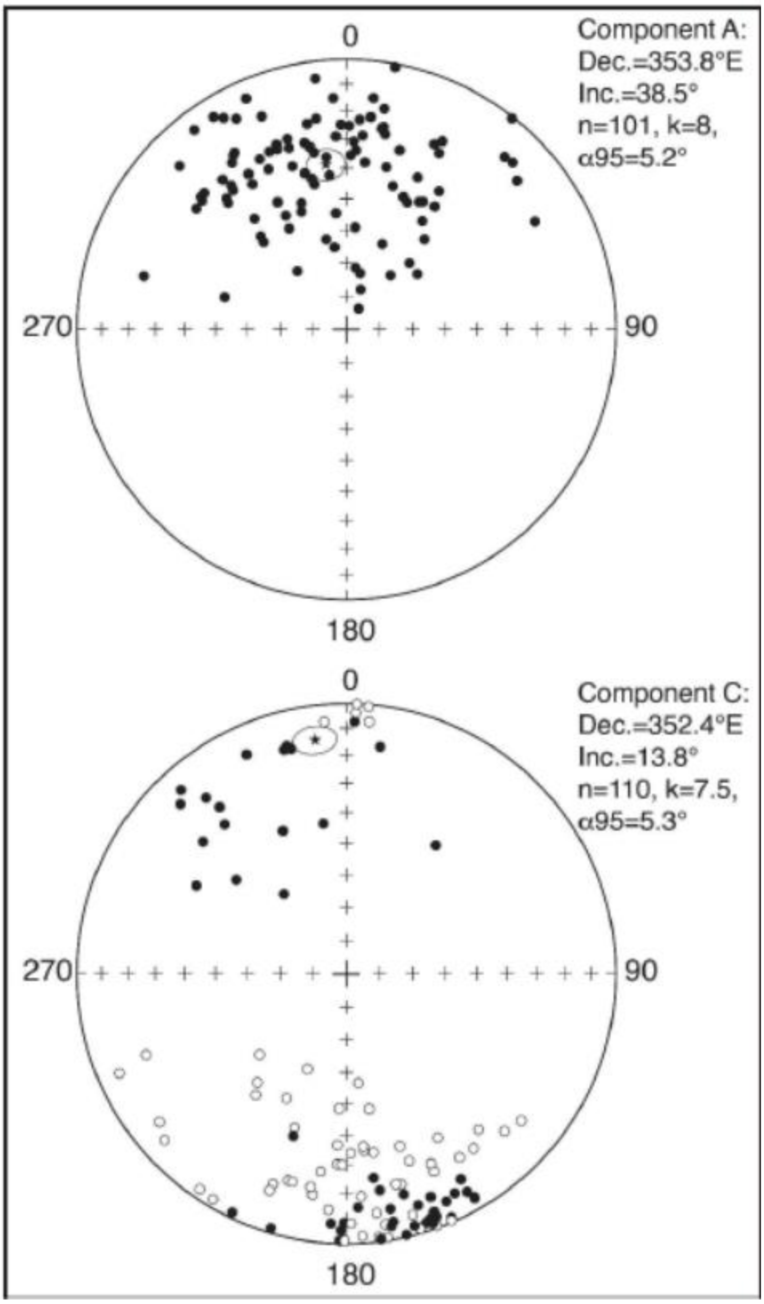

Fig. S14. Equal area plots and standard Fisher statistics of the A and C component directions from the studied sections. Filled/open symbols are projections on lower/upper hemisphere.

5. Geochemistry

Table S4. Elemental concentrations in the sediments of unit L from ThI at Casablanca.

Elevation (m asl)	Si (ppm)	K (ppm)	Ti (ppm)	Ca (ppm)	Mn (ppm)	Fe (ppm)	Zn (ppm)	Rb (ppm)	Sr (ppm)	Zr (ppm)
35.545	77149.8 ± 4067.82	16416.89 ± 454.75	3398 ± 63	208606.05 ± 3469.93	360 ± 7	21234.21 ± 492.28	18 ± 2	23.3 ± 1	362 ± 4	156 ± 3
35.495	61654.94 ± 3833.35	18513.31 ± 493.08	3155 ± 60	201851.37 ± 3463.41	393 ± 7	23105.03 ± 534.19	18 ± 2	25 ± 1	338 ± 4	180 ± 3
35.445	68138.75 ± 3944.82	17674.33 ± 495.12	2045 ± 53	196469.22 ± 3417.81	303 ± 7	21060.27 ± 508.05	18 ± 2	26.9 ± 1	328 ± 4	202 ± 3
35.395	65639.54 ± 4203.59	17522.37 ± 480.34	2196 ± 55	214413.21 ± 3831.63	300 ± 7	17829.56 ± 457.91	65 ± 3	24.7 ± 1	368 ± 5	175 ± 3
35.345	71562.66 ± 4180.67	16444.75 ± 443.28	2041 ± 51	222256.59 ± 3841.43	281 ± 6	17757.01 ± 446.39	45 ± 3	26.5 ± 1	335 ± 4	170 ± 3
35.295	73291.18 ± 4310.46	18250.44 ± 490.55	2042 ± 54	225529.04 ± 3960.91	288 ± 6	18393.48 ± 467.29	46 ± 3	26.9 ± 1	331 ± 4	156 ± 3
35.245	76411.8 ± 4437.09	16680.39 ± 469.41	1840 ± 52	242117.13 ± 4262.85	240 ± 6	16628.78 ± 442.25	34 ± 3	24.6 ± 1	287 ± 4	134 ± 2
35.195	71250.7 ± 4158.16	18223.7 ± 484.8	2412 ± 57	235223.83 ± 4003.93	287 ± 6	16789.7 ± 429.2	37 ± 3	26 ± 1	405 ± 5	191 ± 3
35.145	61735.91 ± 4047.23	17785.37 ± 474.98	2073 ± 53	226849.19 ± 3883.46	273 ± 6	15836.03 ± 409.46	36 ± 2	25.4 ± 1	394 ± 5	170 ± 3
35.095	85375.01 ± 4250.74	19196.35 ± 489.93	2655 ± 55	230325.56 ± 3780.57	309 ± 6	19004.98 ± 456.78	35 ± 2	29.4 ± 1	369 ± 5	205 ± 3
35.045	69144.83 ± 4087.91	17478.27 ± 467.2	2264 ± 53	230663.93 ± 3877	214 ± 6	17102.29 ± 428.55	33 ± 2	26.1 ± 1	363 ± 5	157 ± 3
34.995	81187.49 ± 4196.5	18866.65 ± 489.48	2321 ± 54	244832.65 ± 3989.01	243 ± 6	17188.08 ± 428.45	31 ± 2	26.6 ± 1	374 ± 5	178 ± 3
34.945	72577.81 ± 6016.02	19063.5 ± 1197.64	2772 ± 57	259247.16 ± 15383.06	212 ± 5	15912.08 ± 985.24	30 ± 2	23.2 ± 0.9	381 ± 5	193 ± 3
34.895	53970.24 ± 3686.64	14619.11 ± 416.42	1982 ± 52	233609.1 ± 3938.45	212 ± 6	16760.76 ± 423.31	32 ± 2	24.9 ± 1	421 ± 5	125 ± 2
34.845	56254.28 ± 3876.46	14940.69 ± 427.56	1834 ± 52	247159.73 ± 4125.53	188 ± 5	16612.72 ± 420.68	23 ± 2	22.9 ± 1	424 ± 5	181 ± 3
34.795	50079.35 ± 3755.99	13799.21 ± 406.97	2139 ± 54	250941.5 ± 4178.63	200 ± 5	17087.38 ± 428.19	28 ± 2	24.4 ± 1	450 ± 5	156 ± 3
34.745	63138.25 ± 4018.31	15062.47 ± 424.79	2057 ± 53	257071.37 ± 4293.22	202 ± 5	14772.7 ± 390.16	25 ± 2	19.5 ± 0.9	441 ± 5	169 ± 3
34.695	72562.14 ± 3954.18	14796.21 ± 404.27	2359 ± 54	273967.75 ± 4445.88	182 ± 5	14669.73 ± 388.22	25 ± 2	22.2 ± 0.9	413 ± 5	150 ± 3
34.645	56108.88 ± 3835.02	12333.04 ± 374.3	1945 ± 52	271541.8 ± 4449.91	235 ± 6	12835.12 ± 352.28	23 ± 2	18.6 ± 0.9	424 ± 5	119 ± 2
34.595	54404.41 ± 3946.71	11853.71 ± 384.44	2761 ± 60	257550.25 ± 4496.39	183 ± 5	13036.55 ± 374.28	19 ± 2	18.3 ± 0.9	383 ± 5	96 ± 2
34.545	47867.8 ± 3687.04	11551.96 ± 354.85	1817 ± 51	291833.43 ± 4702.12	160 ± 5	12981.48 ± 355.38	19 ± 2	17.4 ± 0.9	411 ± 5	133 ± 3
34.495	47851.17 ± 3720.12	12441.33 ± 385.55	1902 ± 52	271836.6 ± 4525.95	142 ± 5	13003.1 ± 362.12	15 ± 2	20.7 ± 0.9	413 ± 5	183 ± 3
34.445	51223.25 ± 3786.09	13629.79 ± 404.99	2408 ± 56	263789.3 ± 4394.47	165 ± 5	14133.37 ± 381.13	19 ± 2	19.7 ± 0.9	401 ± 5	148 ± 3
34.395	46083.65 ± 3708.39	11652.14 ± 364.16	1545 ± 50	310208.91 ± 4923.14	125 ± 5	10544.53 ± 312.48	9 ± 2	19.7 ± 0.9	338 ± 4	145 ± 3
34.345	58916.43 ± 3782.03	14071.73 ± 402.66	2365 ± 56	277447.71 ± 4413.26	198 ± 5	13464.38 ± 359.39	21 ± 2	21 ± 0.9	345 ± 4	112 ± 2
34.295	63029.06 ± 3895	15053.48 ± 423.93	2401 ± 54	264610.1 ± 4288.59	130 ± 4	13719.58 ± 367.28	27 ± 2	24.8 ± 1	338 ± 4	145 ± 3
34.245	76400.18 ± 4041.08	18669.82 ± 483.87	3605 ± 64	251346.5 ± 4018.19	176 ± 5	19169.66 ± 457.91	30 ± 2	26.1 ± 1	317 ± 4	184 ± 3
34.195	69586.49 ± 4049.22	18225.34 ± 483.92	2962 ± 59	220749.81 ± 3714.78	193 ± 5	17429.86 ± 433.89	24 ± 2	27.5 ± 1	355 ± 4	178 ± 3
34.145	56625.49 ± 4051.3	17720.2 ± 487.94	2861 ± 62	274342.44 ± 4728.3	223 ± 6	19274.65 ± 491.02	22 ± 2	25.7 ± 1	395 ± 5	205 ± 3
34.095	65656.26 ± 4118.57	17036.41 ± 456.4	3092 ± 62	250599.92 ± 4290.07	291 ± 6	19959.57 ± 487.9	28 ± 2	26.8 ± 1	373 ± 5	180 ± 3
34.04	61085.28 ± 4192.44	16086.67 ± 457.19	2791 ± 61	234284.74 ± 4198.3	189 ± 6	20163.59 ± 508.03	21 ± 2	25 ± 1	343 ± 4	147 ± 3
33.99	39237.62 ± 3652.39	13142.77 ± 395.43	1460 ± 53	303538.07 ± 4941.5	273 ± 6	17743.7 ± 448.03	26 ± 3	20.1 ± 1	420 ± 5	125 ± 3
33.945	30114.09 ± 3597.56	11166.22 ± 371.35	807 ± 48	324166.87 ± 5388.59	242 ± 6	12497.27 ± 365.05	15 ± 2	19.2 ± 1	470 ± 6	81 ± 2
33.895	41691.36 ± 3473.6	11536.59 ± 364.34	1387 ± 50	323067.54 ± 4690.57	302 ± 6	12549.63 ± 329.78	25 ± 3	19.3 ± 1	472 ± 6	62 ± 2
33.845	36397.94 ± 3678.23	12005.43 ± 380.9	1860 ± 53	328742.18 ± 5308.35	280 ± 6	12797.79 ± 365.02	23 ± 2	19.4 ± 1	464 ± 6	97 ± 2
33.795	30124.98 ± 3615.13	9784.15 ± 348.72	938 ± 47	292648.87 ± 5053.96	256 ± 6	11728.25 ± 351.39	23 ± 2	17 ± 0.9	531 ± 6	92 ± 2
33.745	31971.85 ± 3644.61	11057.73 ± 367.26	877 ± 46	323113.34 ± 5347.09	310 ± 6	11560.67 ± 346.35	27 ± 3	17.3 ± 0.9	499 ± 6	95 ± 2
33.695	28531.62 ± 3468.14	10085.59 ± 346.03	831 ± 46	333079.79 ± 5386.89	268 ± 6	10794.32 ± 327.55	25 ± 3	14.9 ± 0.9	506 ± 6	101 ± 2
33.645	28153.5 ± 3552.2	9800.69 ± 341.73	843 ± 47	338008.96 ± 5458.28	269 ± 6	10343.1 ± 319.85	22 ± 2	17.6 ± 0.9	481 ± 6	75 ± 2
33.595	32661.9 ± 3483.38	10754.4 ± 356.44	984 ± 49	320954.4 ± 5070.06	310 ± 7	13546.81 ± 370.38	26 ± 3	18.9 ± 1	487 ± 6	79 ± 2
33.545	32886.15 ± 3571.72	9773.29 ± 350.2	1282 ± 50	321279.69 ± 5275.27	275 ± 6	14852.34 ± 406.5	21 ± 2	15.8 ± 0.9	467 ± 6	119 ± 3
33.495	35012.26 ± 3689.57	8690.06 ± 330.69	1197 ± 51	312491.95 ± 5234.78	213 ± 6	12592.23 ± 365.53	11 ± 2	13.7 ± 0.9	450 ± 6	117 ± 2
33.445	34196.64 ± 3511.75	8652.15 ± 318.28	1505 ± 52	306086.69 ± 4880.44	238 ± 6	16860.29 ± 423.71	14 ± 2	12.8 ± 0.9	435 ± 5	163 ± 3
33.405	47082.37 ± 3728.35	6922.94 ± 292	2332 ± 55	284951.36 ± 4803.54	247 ± 6	13699.85 ± 381.05	15 ± 2	10.1 ± 0.8	456 ± 6	151 ± 3
33.215	98919.57 ± 4360.87	9230.95 ± 324.54	5323 ± 74	218609.02 ± 3452.32	283 ± 6	17043.37 ± 402.6	17 ± 2	13.1 ± 0.8	319 ± 4	236 ± 3
33.165	70075.51 ± 4202.47	10723.56 ± 366.47	2551 ± 56	254166.11 ± 4330.88	211 ± 6	16299.15 ± 428.46	18 ± 2	14.8 ± 0.9	366 ± 5	274 ± 4
33.115	61989.16 ± 4085.72	8985.1 ± 340.32	2374 ± 57	287437.53 ± 4823.63	198 ± 5	12438.15 ± 362.76	7 ± 2	13.6 ± 0.9	327 ± 4	136 ± 3
33.065	46849.6 ± 3723.74	9672.94 ± 336.66	2202 ± 54	282121.02 ± 4672.68	177 ± 5	12539.15 ± 353.14	18 ± 2	16.6 ± 0.9	382 ± 5	132 ± 3
33.015	51713.85 ± 3667.82	8603.69 ± 327.9	2555 ± 56	279524.95 ± 4480.37	216 ± 5	13059.42 ± 358.19	16 ± 2	14.1 ± 0.9	341 ± 4	185 ± 3
32.93	52122.12 ± 3750.94	8185.52 ± 324.28	2294 ± 51	266313.24 ± 4395.75	218 ± 5	11799.56 ± 338.83	16 ± 2	13.7 ± 0.8	330 ± 4	138 ± 2
32.89	68810.14 ± 3921.67	7726.63 ± 311.36	2336 ± 52	274471.22 ± 4311.88	216 ± 5	11563.78 ± 325.83	12 ± 2	13.7 ± 0.8	286 ± 4	174 ± 3
32.845	53297.93 ± 3575.37	8944.41 ± 325.19	1926 ± 51	261307.02 ± 4149.11	232 ± 6	11278.1 ± 316.14	13 ± 2	15.9 ± 0.9	303 ± 4	147 ± 3
32.795	29550.83 ± 3461.17	8065.48 ± 328.79	1668 ± 51	266992.35 ± 4659.86	239 ± 6	11143.65 ± 338.27	18 ± 2	15.9 ± 0.9	319 ± 4	90 ± 2
32.75	44504.25 ± 3636.08	10316.86 ± 363.58	1564 ± 49	263755.56 ± 4454.29	196 ± 5	11849.26 ± 343.27	20 ± 2	19.1 ± 0.9	372 ± 5	119 ± 2
32.71	67465.21 ± 3728.07	10114.22 ± 340.99	2646 ± 55	249731.71 ± 3881.04	241 ± 6	10924.58 ± 303.46	18 ± 2	16.9 ± 0.9	364 ± 4	166 ± 3
32.67	42266.4 ± 3347.5	11891.73 ± 366.58	1651 ± 50	273807.99 ± 4285.9	224 ± 6	11214.47 ± 313.77	21 ± 2	20 ± 0.9	374 ± 5	163 ± 3
32.625	34566.11 ± 3530.29	11075.77 ± 383.44	1293 ± 47	282601.74 ± 4779.88	187 ± 5	11977.91 ± 353.04	27 ± 2	20.4 ± 0.9	359 ± 5	115 ± 2
32.575	43284.87 ± 3503.23	11281.31 ± 372.16	1242 ± 49	283732.56 ± 4498.05	191 ± 5	11979.31 ± 336.53	18 ± 2	20.6 ± 1	365 ± 5	110 ± 2
32.51	48819.53 ± 3587.4	10501.44 ± 351.16	1303 ± 46	267551.51 ± 4299.8	189 ± 5	9558.9 ± 288.02	17 ± 2	19 ± 0.9	343 ± 4	116 ± 2
32.47	49366.02 ± 3493.18	12154.87 ± 379.28	1506 ± 48	261326.58 ± 4112.39	257 ± 6	11623.73 ± 321.13	31 ± 2	22.2 ± 0.9	358 ± 5	119 ± 2
32.43	44535.53 ± 3468.46	12171.74 ± 384.75	1679 ± 50	246571.75 ± 4028.43	233 ± 6	12284.46 ± 338.11	30 ± 2	26.1 ± 1	363 ± 5	207 ± 3
32.39	57649.3 ± 3612.45	13920.45 ± 408.43	1661 ± 48	248117.62 ± 3938.42	209 ± 5	14111.63 ± 365.25	26 ± 2	27.2 ± 1	358 ± 4	194 ± 3

32.35	61010.44 ± 3800.47	14798.13 ± 438.78	1660 ± 49	246037.87 ± 4042.97	268 ± 6	13639.01 ± 370.25	29 ± 2	25.9 ± 1	361 ± 5	186 ± 3
32.31	56394.36 ± 3680.83	14483.62 ± 417.91	1836 ± 49	246038.46 ± 3886.15	266 ± 6	12675.35 ± 336.91	31 ± 2	27.4 ± 1	365 ± 5	187 ± 3
32.27	52203.14 ± 3636.66	12280.72 ± 389.78	1677 ± 49	260887.9 ± 4217.13	189 ± 5	10687.31 ± 313.18	23 ± 2	22.7 ± 0.9	344 ± 4	163 ± 3
32.23	52163.37 ± 3665.88	12892.18 ± 400.77	1868 ± 49	251822.6 ± 4108.25	226 ± 5	11758.74 ± 331.48	26 ± 2	26.8 ± 1	341 ± 4	152 ± 3
32.19	54322.8 ± 3674.52	12487.89 ± 384.14	2781 ± 57	258227.44 ± 4169.5	247 ± 6	11297.98 ± 320.06	28 ± 2	21.9 ± 0.9	416 ± 5	201 ± 3
32.15	67671.32 ± 3657.86	11828.21 ± 365.69	3075 ± 57	244089.75 ± 3780.51	257 ± 6	11665.06 ± 316.19	27 ± 2	21.9 ± 0.9	285 ± 4	209 ± 3
32.11	45066.72 ± 3490.59	10334.55 ± 345.22	1651 ± 48	263743.81 ± 4132.33	198 ± 5	12401.92 ± 330.32	26 ± 2	20.8 ± 0.9	300 ± 4	151 ± 3

Table S5. Parameters of coastal deposits related to sea-level high-stands used to estimate uplift in the area of Casablanca from ca. 2.5 to 1 Ma. Coastal deposits identified from Lefèvre and Raynal1. Chronological data from this study for OH3 and from Geraads14 for AAO. Minimum and maximum sea-level high-stand estimated from minimum and maximum relative sea level in Supplementary Fig. S17A, respectively. Uplift of coastal deposits related to sea-level high-stand is calculated by subtracting the mean relative sea level from the mean elevation of intertidal deposits. Uncertainties of uplift for a sea-level high-stand = [(Maximum relative sea level – Minimum relative sea level)2 + (Maximum elevation of intertidal deposits – Minimum elevation of intertidal deposits)2]0.5.

Coastal deposits related to sea-level high-stand	Chronological data of intertidal deposits	Minimum / maximum elevation of intertidal deposits (m asl)	Minimum / maximum sea-level high-stand (m)	Estimated uplift (m)
OH3 (Oulad Hamida Formation)	1075-1070 ka (Slightly earlier than Matuyama-Jaramillo transition)	34 / 37	-15 / 0	43.0 ± 7.6
AAO (Ahl al Oughlam Formation)	2500-2400 ka (biostratigraphy)	100 / 105	-35 / 15	112.5 ± 25.1

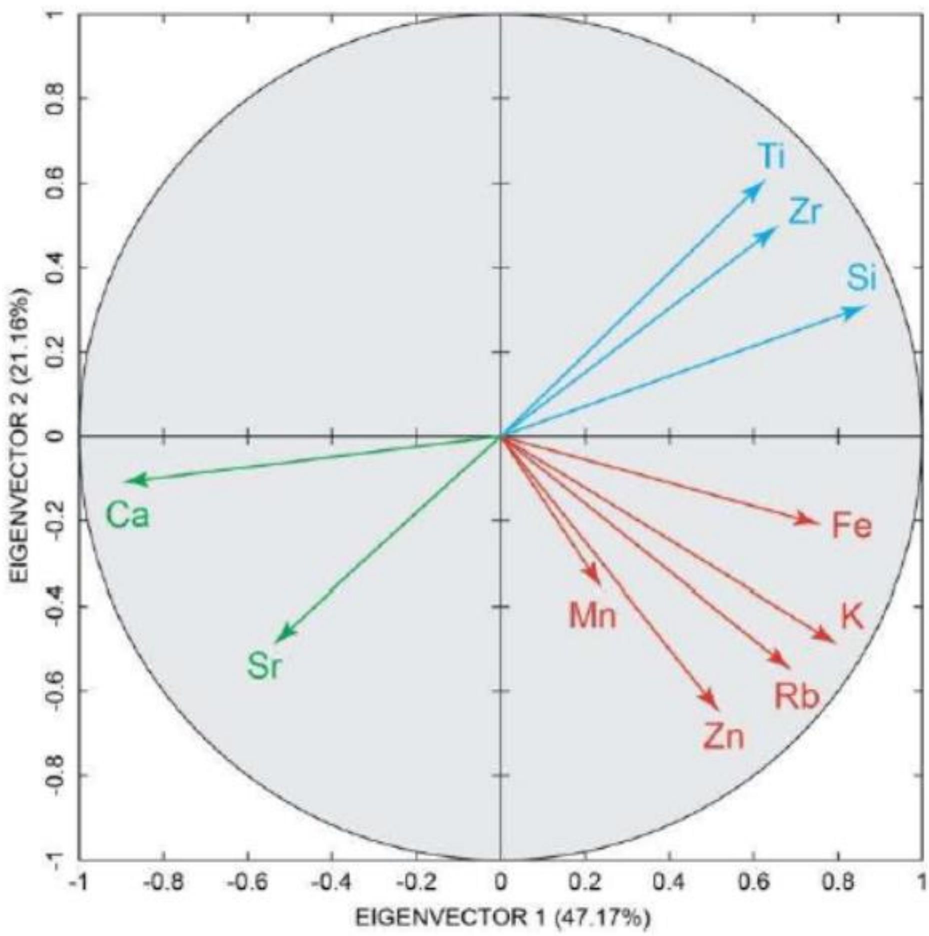

Fig. S15. Correlations between the initial variables (element concentrations) and the two first eigenvectors of the principal component analysis of geochemical data from the sediments of ThIL. The principal component analysis shows three groups of elements. The first group (Ca, Sr) can be related to detrital sediments eroded from local carbonate rocks (calcarenite). The second group (K, Mn, Fe, Zn, Rb) is representative of chemically weathered sediments, with carbonate dissolution leading to an enrichment in K and Rb relatively to Ca and Sr (Yang et al., 2004; Profe et al., 2016; Hosek et al., 2015), while Mn, Fe and Zn are typically associated with redox processes (Rodrigo-Gamiz et al., 2014; Martinez-Ruiz et al., 2015; Scarciglia et al., 2015; 2016; Krauss et al., 2016). The third group (Si, Ti, Zr) is supposed to be representative of Saharan dust input in the sediments of unit L, given that these three elements are typical of aeolian dust transported from the Sahara Desert (Rodrigo-Gamiz et al., 2014; Martinez-Ruiz et al., 2015).

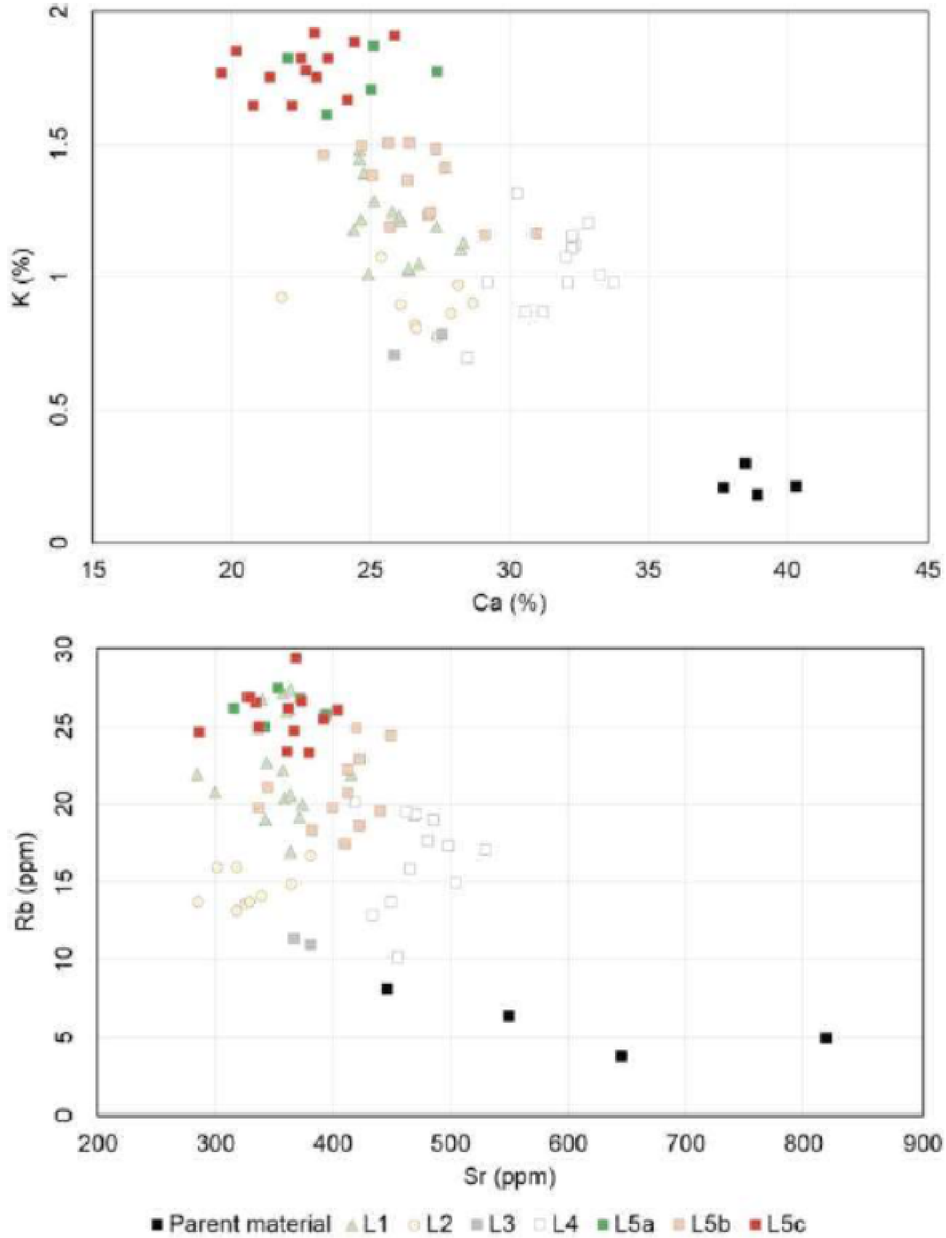

Fig. S16. Plots of K vs. Ca and Rb vs. Sr for the sediments of unit L. The samples of parent material were collected in calcarenite underlying unit L. Elements representative of parent rocks (Ca, Sr) are depleted in weathered subunits. K and Rb are increasingly enriched relatively to Ca and Sr, respectively, with an increasing degree of weathering.

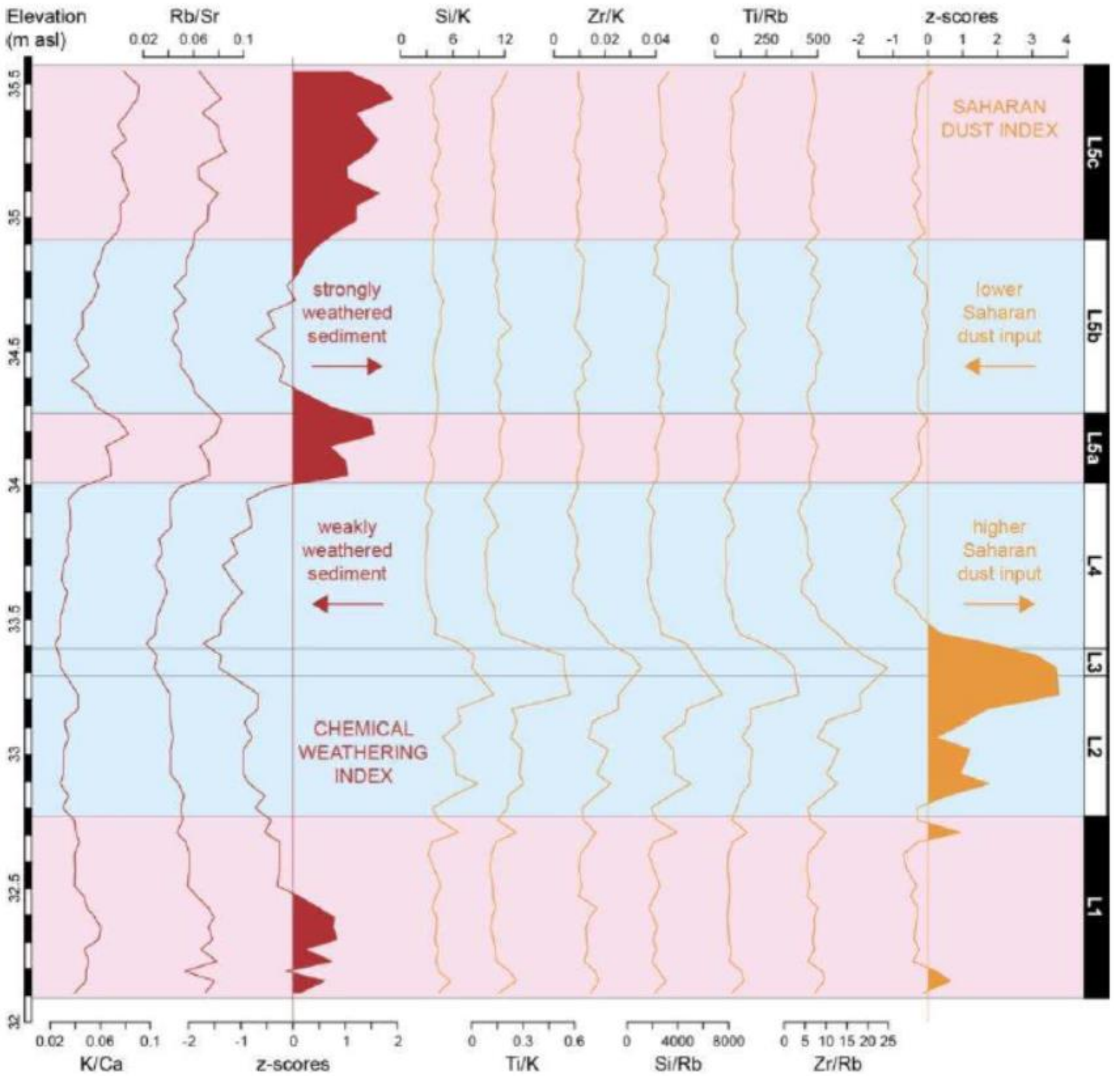

Fig. S17. Elemental ratios for the sediments of ThI-L. Rb/Sr and K/Ca ratios are useful for estimating the degree of chemical weathering of Pleistocene sediments (Yang, et al., 2004; Profe et al., 2016; Buggle et al., 2011; Degeai et al., 2018). A chemical weathering index was calculated from the average of z-scores of Rb/Sr and K/Ca ratios. The elements representative of eolian input from the Sahara (Si, Ti, Zr) were normalized to K and Rb, which can be associated with fluvial input (Rodrigo-Gamiz et al., 2014; Martinez-Ruiz et al., 2015; Degeai et al., 2017;2020). An index of Saharan dust input was calculated from the average of z-scores of Si/K, Ti/K, Zr/K, Si/Rb, Ti/Rb and Zr/Rb ratios.

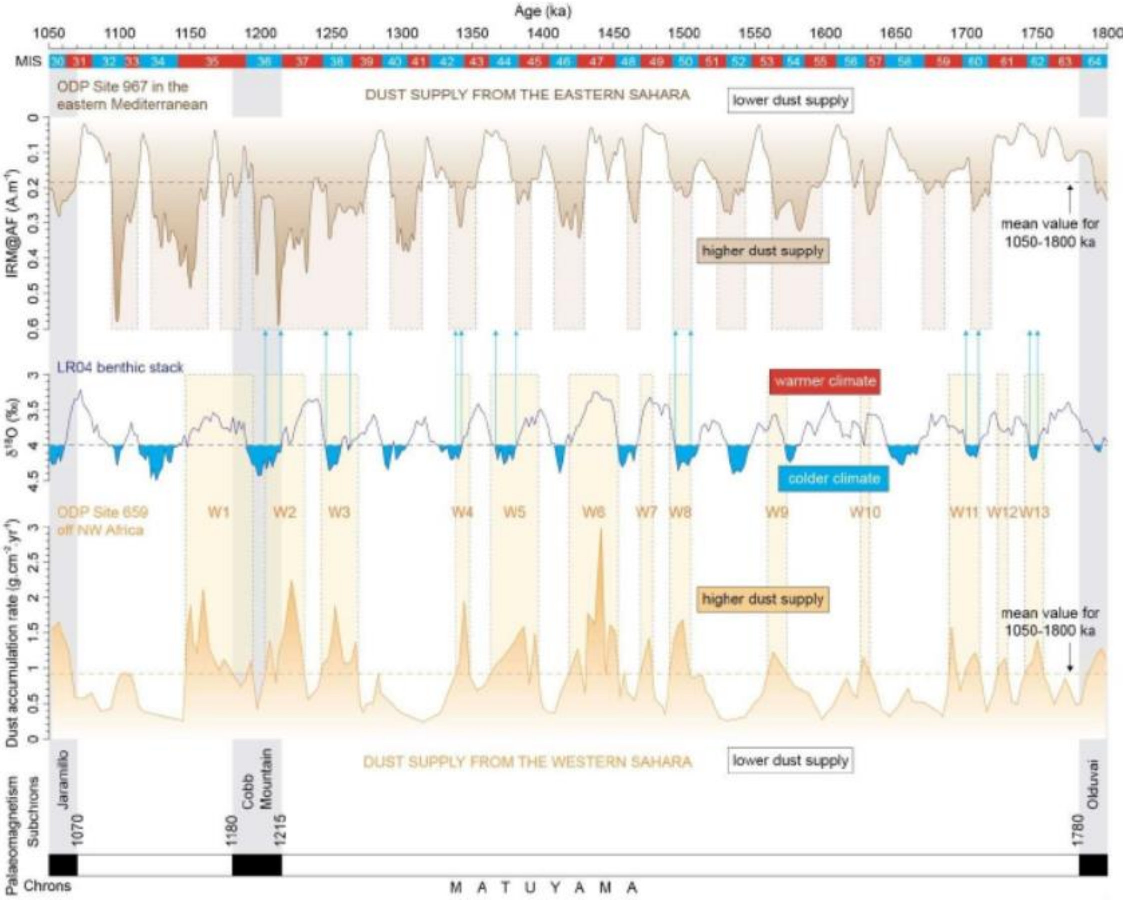

Fig. S18. Dust supply from the western and eastern Sahara between the Jaramillo and Olduvai subchrons. The most proximal marine records of Saharan dust supply around Morocco are located off northwestern Africa (ODP Site 659) and in the eastern Mediterranean (ODP Site 967), and are representative of dust flux from the western Sahara in northwestern Africa and from the eastern Sahara in northeastern Africa, respectively (Trauth e tal., 2009). Hence, the dust record from ODP Site 659 should be preferentially used for comparison of Saharan dust input in unit L with Saharan dust supply recorded in marine sediments, which allows to distinguish thirteen periods of higher than average dust supply from the western Sahara between the Jaramillo and Olduvai subchrons (W1-W13, pale yellow vertical bands). However, dust supply from this $CaCO_3$-based proxy record is potentially biased and overestimated during glacial maximum owing to deep ocean circulation changes that led to increased dissolution of calcium carbonate (Skonieczny et al., 2019). Seven periods (W2-W5, W8, W11 and W13, blue arrows) occurred partly during glacial maximum characterized by values of the LR04 $\delta^{18}O$ benthic stack higher than 4 ‰. The reliability of these periods was controlled and validated by a comparison with the periods of higher than average dust supply highlighted by the dust record from ODP Site 967 (light brown vertical bands). Amongst the seven above-mentioned periods, only W13 and the later half of W5 were not associated with periods of high Saharan dust supply at ODP Site 967 and could thus be artifacts. Saharan dust proxy record from ODP Site 659 (dust accumulatio rate) from Tiedemann et al.

(1994). Saharan dust proxy record from ODP Site 967 (IRM@AF) from Larrasoaña et al. (2003) with age model from Grant et al. (2017). Marine Isotopic Stages (MIS) and LR04 benthic stack from Lisiecki and Raymo (2005). Palaeomagnetic record from Channell et al. (2020).

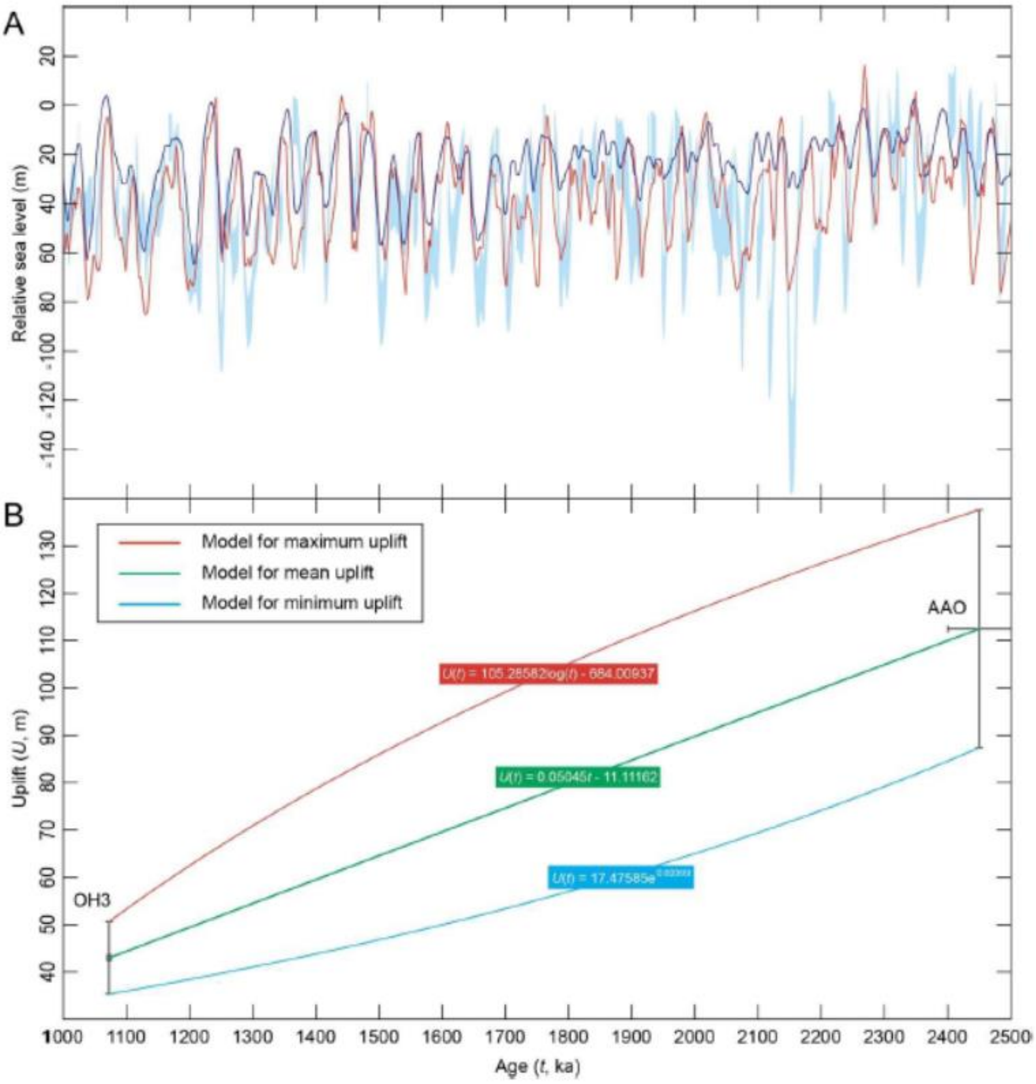

Fig. S19. Estimates of relative sea-level (RSL) changes (A) and uplift in the area of Casablanca from ca. 2.5 to 1 Ma (B). A: blue shaded area: RSL from Rohling et al. (2014) corrected by Amies (2018); dark blue line: RSL from de Boer et al. (2010); red line: RSL from SPECMAP data (Shackleton, 1995) rescaled with 121 m sea level fall at 17 ka (Fairbanks, 1989) corresponding to a $\delta^{18}O$ value of ca. 1.78. All RSL data were resampled at 1 ka interval. B: Maximum, mean and minimum uplift estimated for sea-level high-stands OH3 and AAO were used in order to test three uplift models based on logarithmic, linear and exponential regressions, respectively, assuming no subsidence during the Quaternary (Stearns, 1978; El Kadiri et al., 2010). OH3: sea-level high-stand of the Oulad Hamida formation; AAO: sea-level high-stand of the Ahl al Oughlam Formation. The parameters of sea-level high-stands are listed in Supplementary Table S5.

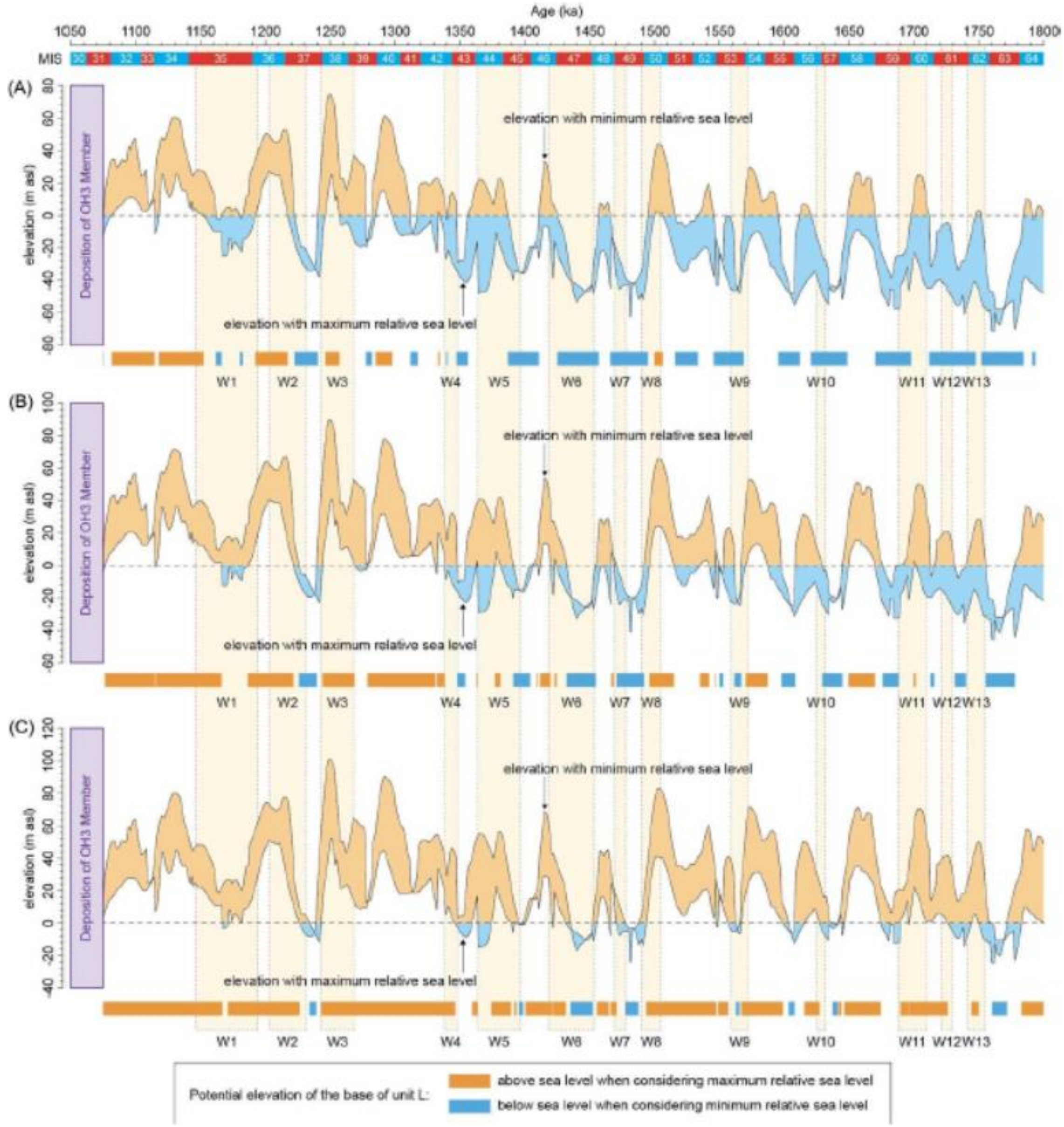

Fig. S20. Potential elevation of the base of unit L during the periods of higher than average dust supply from the western Sahara (W1-W13, pale yellow vertical bands) for different uplift models. A: Logarithmic model for maximum uplift. B: Linear model for mean uplift. C: Exponential model for minimum uplift. Elevation was calculated by subtracting relative sea level and uplift from the present elevation of the base of unit L (ca. 32 m above sea level). Maximum and minimum relative sea level were determined from Supplementary Fig. S19A. Uplift was estimated from models in Supplementary Fig. S19B. Palaeo-elevation reconstruction is supposed to give potential elevations because it does not take into account potential periods of sedimentation and erosion at the site of Thomas Quarry I before the deposition of unit L. Marine Isotopic Stages (MIS) from Lisiecki and Raymo (2005).

6. Palynology

Fossil pollen data from Th-L1 (Supplementary Table S6) show that the vegetal landscape was dominated by a steppe (66.8%) with Compositae (42.5 %), Poaceae (4 %) Chenopodiaceae (3.7 %) and varied plants: *Convolvulus*, *Helianthemum*, and *Reseda*. Regionally, an open Mediterranean forest (Arboreal Pollen: 26.7 %) was present. It consists mainly of deciduous *Quercus* (9.9 %), *Pinus* (1.2 %) and *Olea* (0.3 %). *Myrtus* (11.2%) could develop either in the oak wood undergrowth or in wet depressions (Emberger, 1938). Edible plants were identified in the pollen assemblage (Supplementary Table S6). They correspond to 76% of all the identified phanerogams. They could constitute a significant part of the potential diet of the hominins.

6.1 Methods. The Casablanca region is located in the sclerophyllous forest ecoregion (Benabid, 2000) which is nowadays degraded by human activities. Of the seven samples taken from profile 19 of the ThI-L, only sample CT 19-01 was polliniferous. The sporo-pollinic material was extracted from the sediment using chemical treatment (HCl acid, NaOH 10% and acetolysis), a flotation in heavy liquid (d = 2) and 160 + 10 µm sieving. The identification was carried out with a photonic microscope (x500 magnification). The palynological identifications were based on the pollen reference collection of IMBE (CNRS, Aix-en-Provence, France) and the bibliography (Reille, 1992; 1995; 1998; Cugny et al., 2010). The pollen percentages were calculated on a Pollen Sum (PS: 322) including only the phanerogams. The weight of the pollen sample is: 15.6 g. The analysed volume is 45 µl. The Absolute pollen Frequency is of 20.6 pollen grain/gram. The biodiversity is high: in total, 42 taxa were identified, among them 38 phanerogams et 4 non pollen palynomorphs (charcoal (very few) and unidentifiable insect, chironomid and fungi).

Table S6. Phanerogams and edible plants (in bold) of the pollen sample CT 19-1. Values are in counting values and in percentages (calculated on a pollen sum including all the phanerogams). The systematic is from Cronquist (1981).

Sample	Counting value	%	Edible organ	Sample	Counting value	%	Edible organ
Acer sp	2	0.62		***Hippophae rhamnoides***	4	1.24	Fruit
***Ammi* t.**	14	4.35	Seed	***Hypericum* sp.**	1	0.31	Leaf
Apiaceae	7	2.17	Leaf, stem, root	***Linum usitatissimum***	2	0.62	Seed
***Artemisia* sp.**	31	9.63	Leaf, shoot	***Myrtus* sp.**	36	11.18	Fruit, bud
***Aster* t.**	2	0.62	Leaf, stem	*Odontites* sp.	3	0.93	
***Atriplex* t.**	7	2.17	All	***Olea* sp**	1	0.31	Fruit
Blackstonia t.	3	0.93		***Pimpinella* sp.**	1	0.31	Seed
Bupleurum sp.	1	0.31		***Pinus sylvestris* t.**	2	0.62	Seed, young shoot
***Calendula* t.**	1	0.31	Leaf, flower	***Pinus* (mediterranean)**	2	0.62	Seed, young shoot
***Carduus* t.**	2	0.62	Leaf	**Poaceae**	13	4.04	Young shoot, leaf
Chenopodiaceae	5	1.55	Leaf	***Polygonum aviculare* sp.**	2	0.62	Seed, young leaf and plant
Cichorioideae	100	31.06	Leaf, flower, stem	***Prunus* sp.**	4	1.24	Fruit
***Cirsium* t.**	1	0.31	Leaf, flower, stem	***Quercus* sp. (deciduous)**	32	9.94	Fruit
Convolvulus sp	*1*	0.31	Leaf, young shoot	*Ranunculus* sp.	2	0.62	
Cyperaceae	3	0.93	Root	***Reseda* sp.**	5	1.55	Young shoot, leaf
Euphorbia sp.	7	2.17		*Scutellaria* t.	12	3.73	
***Galium* sp**	1	0.31	Leaf	***Sinapis* t.**	3	0.93	Seed, leaf
Gentiana sp.	3	0.93		***Urtica* sp.**	1	0.31	Leaf
Helianthemum sp.	2	0.62		***Vitis* sp.**	3	0.93	Fruit

Table2. Thermal demagnetization data
(1) Sample = sample name
(2) Temperature (°C)
(3) NRM intensity (A/m)
(4) Core Declination (°E)
(5) Core Inclination (°)
(6) Geographic Declination (°E)
(7) Geographic Inclination (°)

(1) (2) (3) (4) (5) (6) (7)

OH1 Bed 1 (samples S-)

S-30 0 6,56E-05 183,24 19,319 66,2 83,8
S-30 100 4,96E-05 221,93 25,068 28,3 49,1
S-30 150 1,43E-04 51,746 43,545 132,2 -15,6
S-30 200 1,19E-04 55,921 43,793 133,9 -13
S-30 250 1,51E-04 52,949 32,858 141,9 -21,1
S-30 300 1,02E-04 326,5 42,447 69,1 -25,7
S-30 350 2,04E-04 17,071 -49,4 257,9 -51,9
S-30 400 2,74E-04 349,31 22,508 79,8 -52
S-30 425 7,63E-05 52,903 48,666 128,6 -11,8
S-30 450 1,78E-04 286,1 55,519 63 2,7
S-30 475 1,71E-04 309,72 40,968 58,4 -18
S-30 500 1,41E-04 331,67 6,9367 40,9 -54,9
S-30 550 1,35E-04 340,67 54,428 84,2 -19,6
S-30 575 1,42E-04 264,72 22,317 26,7 10
S-30 600 1,19E-04 207,77 55,087 74,4 43,6
S-41 0 3,01E-04 35,838 27,55 138,1 -41,8
S-41 100 2,97E-04 60,544 -41,63 227,7 -25,8
S-41 150 2,26E-04 54,766 -17,978 201,8 -35,3
S-41 200 1,70E-04 45,599 -4,5613 184,5 -44,6
S-41 250 1,80E-04 23,016 38,678 117,7 -40,5
S-41 300 1,70E-04 30,743 49,216 116,4 -28,6
S-41 350 1,94E-04 31,304 63,538 108 -16,6
S-41 400 1,69E-04 19,47 46,939 110 -34,3
S-41 425 1,87E-04 357,22 61,607 92,6 -22,4
S-41 450 1,67E-04 24,624 50,912 111,5 -29,3
S-41 475 5,47E-04 279,59 58,225 62,7 0,1
S-41 500 1,57E-04 325,01 76,54 86,3 -5
S-41 525 3,05E-04 291,17 27,127 34,4 -15,8
S-41 550 4,11E-04 311,52 20,784 34,8 -35,4
S-41 575 7,77E-05 359,13 40,142 93,1 -43,9
S-62 0 3,11E-04 347,66 12,248 53,6 -61,9
S-62 100 3,90E-04 32,46 6,6232 140,6 -52,3
S-62 150 7,09E-04 26,858 9,257 131,5 -55,3
S-62 200 3,99E-04 344,08 25,226 57,9 -48,7
S-62 250 3,44E-04 356,65 5,6678 69,7 -71
S-62 300 1,86E-04 348,98 32,252 67,1 -43,5
S-62 350 2,85E-04 346,12 15,447 53,8 -58,4
S-62 400 3,89E-04 324,2 39,272 49,1 -28
S-62 425 3,95E-04 297,81 27,775 24,9 -17,3
S-62 450 4,23E-04 337,44 2,8468 23,7 -62,6
S-62 475 6,18E-04 315,29 25,295 31,4 -32
S-62 500 3,86E-04 335,91 15,459 39,3 -52,9
S-62 525 4,04E-04 292,14 39,272 33,6 -8,2
S-62 550 1,51E-04 306,56 36,28 36,6 -19,6
S-62 575 6,75E-04 279,71 16,872 8,7 -5,3
S-77 0 2,52E-04 59,271 -33,954 211,8 -31
S-77 100 3,95E-04 56,917 -21,861 197,7 -34,3
S-77 150 2,86E-04 61,18 -7,2193 180,7 -29,5
S-77 200 3,59E-04 69,463 -16,321 191,7 -22,4
S-77 250 2,72E-04 69,775 -14,28 189,5 -21,9
S-77 300 4,33E-04 20,407 -20,972 209,6 -67,5
S-77 350 4,85E-04 60,719 -40,651 219,1 -28,6
S-77 400 3,53E-04 301,93 12,773 18,4 -28
S-77 425 1,87E-04 30,735 -76,693 260,7 -21,3
S-77 450 1,13E-04 23,278 3,8441 148,3 -63
S-77 475 1,99E-04 354,78 -20,545 292,9 -78,3
S-77 500 2,51E-04 119,93 62,875 113,3 22,2
S-77 550 2,44E-04 359,52 -12,324 279,4 -87,6
S-77 575 1,42E-04 50,843 -22,097 198,5 -39,9
S-91 0 1,59E-04 15,343 14,612 119 -62,7
S-91 100 3,23E-04 9,3129 -12,696 202,9 -79,7
S-91 150 3,09E-04 8,6568 -19,06 228,7 -76,1
S-91 200 1,46E-04 351,36 7,1082 55,1 -72,6
S-91 250 1,36E-04 333,62 24,072 46,9 -48,9
S-91 300 1,27E-04 356,13 58,186 82,8 -23,7
S-91 350 1,37E-04 333,03 38,372 58,5 -37,3
S-91 400 2,28E-04 328,99 43,139 58,8 -31,6
S-91 425 4,11E-04 310,72 40,492 46 -23,6
S-91 450 3,64E-04 298,06 19,769 20,5 -23
S-91 475 3,15E-04 298,78 -32,445 322,3 -28,5
S-91 500 5,34E-04 300,13 33,376 34,9 -19,8
S-91 525 3,85E-04 328,96 4,1706 15,4 -56,7
S-91 550 2,62E-04 322,23 28,499 41,6 -38,4
S-109 0 3,35E-04 91,107 -51,79 217,5 -21
S-109 100 3,40E-04 88,882 -52,889 218,2 -22,6
S-109 150 5,13E-04 91,045 -57,73 223,6 -22,9
S-109 200 3,09E-04 123,29 -50,04 226,5 -2,8
S-109 250 3,77E-04 99,302 -51,448 219,2 -16,2
S-109 300 3,88E-04 140,85 -18,506 215,3 30
S-109 350 4,93E-04 85,477 -50,017 214,5 -23,9
S-109 400 3,78E-04 173,99 -40,758 254,1 21
S-109 425 3,57E-05 126,94 23,422 161,8 42,3
S-109 450 3,09E-04 221,05 37,019 14,4 54,5
S-109 475 2,56E-04 19,312 14,473 105,2 -43,6
S-109 500 3,07E-04 247,35 -26,128 315,4 5,7
S-109 550 3,10E-04 205,36 -15,702 291,5 39,9
S-109 575 4,07E-04 333,27 38,202 57 -19,2
S-109 600 8,29E-05 61,39 -24,964 181 -35,6
S-134 0 2,18E-04 18,034 51,409 99 -21,8
S-134 100 2,61E-04 46,121 16,861 143,8 -34,4
S-134 150 3,09E-04 53,986 -5,7505 173,1 -36,2
S-134 200 1,49E-04 21,617 48,943 102,3 -23,2
S-134 250 2,69E-04 12,615 36,973 99,6 -36,7
S-134 300 2,72E-04 113,32 48,003 130,4 26,6
S-134 350 2,12E-04 17,223 -8,4214 157,6 -71,9
S-134 400 6,97E-04 356,57 10,742 79,3 -64
S-134 425 2,94E-04 5,0883 4,0973 102,2 -70,2
S-134 450 2,01E-04 310,06 26,568 37,3 -26,1

Table2. Thermal demagnetization data

(1) Sample = sample name

(2) Temperature (°C)

(3) NRM intensity (A/m)

(4) Core Declination (°E)

(5) Core Inclination (°)

(6) Geographic Declination (°E)

(7) Geographic Inclination (°)

S-134 475 6,11E-04 298,51 32,897 37,4 -14,3
S-134 500 5,08E-04 301,83 36,221 41,8 -15
S-134 550 3,00E-04 287 22,539 23,5 -9,3
S-180 0 3,76E-04 65,695 -50,709 243 -32,1
S-180 100 3,76E-04 59,88 -36,361 225,8 -36,6
S-180 150 3,51E-04 66,83 -41,152 231,8 -31,4
S-180 200 2,90E-04 65,624 -43,352 234,4 -32,4
S-180 250 2,93E-04 72,072 -52,398 244,8 -28,1
S-180 300 2,93E-04 45 -48,294 243,6 -45,7
S-180 350 3,23E-04 62,103 -72,658 268,4 -29,1
S-180 400 2,49E-04 55,797 -51,562 245,2 -38,1
S-180 425 4,27E-04 6,6799 -38,217 268 -72,8
S-180 450 1,07E-04 12,653 -20,724 192,2 -78,2
S-180 475 2,71E-04 231,78 -67,918 303,3 -7,6
S-180 500 5,29E-04 257,35 -18,394 354,2 4,3
S-180 525 3,59E-04 235,24 4,6332 6,4 33,9
S-180 550 1,23E-04 80,518 -39,873 231,9 -20,9
N007 0 8,60E-05 187,25 -37,75 175,9 40,8
N007 100 8,59E-05 214,85 -38,8 199,4 30,5
N007 150 1,03E-04 228,52 -41,9 204,9 20,9
N007 200 9,14E-05 219,6 -39,72 201,8 27,4
N007 225 9,54E-05 225,09 -30,91 212,7 29,8
N007 250 9,18E-05 225,37 -26,04 217,5 32,4
N007 275 7,84E-05 225,12 -27,27 216,2 31,9
N007 300 7,39E-05 226,72 -30,56 214 28,8
N007 325 7,34E-05 222,15 -23,7 217,8 36,1
N007 350 7,08E-05 215,72 -20,76 216,2 42,7
N007 375 7,64E-05 231,75 -17,03 230,2 31,7
N007 400 7,98E-05 229,81 -8,79 238,5 36,6
N007 425 7,69E-05 230,58 -2,75 246 37,8
N007 450 6,10E-05 230,6 -7,56 240,3 36,3
N007 475 6,99E-05 225,86 -3,89 242,7 42
N007 500 8,25E-05 233,14 -1,02 248,9 35,8
N007 525 6,70E-05 237,11 -0,55 250,6 32,1
N007 550 7,16E-05 255,12 2,97 258,4 15,2
N007 575 8,30E-05 257,25 3,66 259,5 13,2
N007 600 5,70E-05 246,14 9 263,2 25
N007 625 4,72E-05 259,13 -19,09 237,3 6,5
N007 650 6,81E-05 238,39 -9,98 240,5 28,3
N007 675 9,95E-05 264,65 17,1 274,2 8,3
N011 0 2,06E-05 207,17 30,22 294,7 60,2
N011 100 9,20E-06 277,26 -6,7 252,5 -8,6
N011 150 1,64E-05 309,26 -18,37 245 -41,2
N011 200 1,54E-05 291,16 -23,07 238 -24,6
N011 225 1,58E-05 303,19 -12,17 252 -34,8
N011 250 2,18E-05 291,05 -14,88 246,9 -23,5
N011 275 1,91E-05 329,58 -15,09 251,3 -60,6
N011 300 3,23E-05 298,47 -12 251,4 -30,2
N011 325 3,68E-05 295,09 -19,14 242,8 -27,9
N011 350 3,76E-05 302,09 -14,48 249,1 -34
N011 375 3,75E-05 306,94 -16,46 247,3 -38,9
N011 400 3,73E-05 301,98 -19,92 242,5 -34,4
N011 425 3,69E-05 288,17 -27,7 232,7 -22,4
N011 450 4,75E-05 300,22 -36,77 222,4 -32,4
N011 475 4,12E-05 321,42 -45,32 205,5 -44,9
N011 500 3,58E-05 305,58 -31,03 228,7 -37,5
N011 525 2,98E-05 300,08 -29,7 230,7 -32,8
N011 550 4,53E-05 304,58 -27,1 233,7 -36,9
N011 575 5,45E-05 319,77 -12,84 254,1 -50,9
N011 600 2,31E-05 295,57 -16,39 245,9 -28
N011 625 2,84E-05 66,92 -22,77 96 -26,4
N011 650 1,38E-05 85,66 -26,42 102,2 -10
N011 675 4,34E-05 270,69 55 311,5 11
N015 0 1,00E-04 89,81 -62,28 141,8 -12,5
N015 100 1,39E-04 72,04 -71,63 151,8 -18,9
N015 150 1,37E-04 52,7 -74,59 157 -22,9
N015 200 1,27E-04 68,21 -75,94 156,5 -18,8
N015 225 1,23E-04 61,08 -73,7 155 -21,3
N015 250 1,25E-04 65,4 -68,15 148,9 -22
N015 275 1,21E-04 66,48 -64,49 145 -22,6
N015 300 1,17E-04 67,26 -63,39 143,7 -22,6
N015 325 1,32E-04 65,51 -57,53 137,7 -24,8
N015 350 1,33E-04 69,19 -61,99 142 -22,1
N015 375 1,22E-04 59,49 -56,52 137,6 -28,3
N015 400 1,34E-04 66,25 -63,74 144,2 -22,9
N015 425 1,28E-04 60,43 -63,7 145 -25,4
N015 450 1,25E-04 58,92 -64,89 146,5 -25,6
N015 475 1,32E-04 57,19 -61,17 143 -27,7
N015 500 1,16E-04 32,8 -61,82 151,7 -36,8
N015 525 1,20E-04 47,43 -65,71 149,9 -29,4
N015 550 1,22E-04 43,96 -60,24 145,8 -33,8
N015 575 9,52E-05 54,59 -60,66 143,1 -29,1
N015 600 1,23E-04 89,8 -63,48 143,1 -12,6
N015 625 1,12E-04 63,88 -74,42 155,4 -20,4
N015 650 1,18E-04 126,73 -61,4 147,7 3,7
N015 675 1,21E-04 90,74 -43,91 123,4 -9,1
N019 0 1,14E-04 348,52 -69,98 171,9 -32,6
N019 100 1,46E-04 334,82 -72,51 175,7 -28,7
N019 150 1,65E-04 332,56 -66,49 180 -33,5
N019 200 1,78E-04 326,59 -58,24 188,9 -38,3
N019 225 1,84E-04 319,63 -58,87 191,5 -35,2
N019 250 1,90E-04 319,12 -56,58 193,9 -36,4
N019 275 1,91E-04 315,71 -56,86 195 -34,7
N019 300 2,05E-04 319,54 -49,42 201,2 -40,8
N019 325 1,90E-04 318,13 -51,71 199,3 -38,8
N019 350 1,89E-04 317,38 -52,88 198,4 -37,7
N019 375 1,85E-04 317,36 -52,04 199,3 -38,2
N019 400 1,86E-04 309,87 -53,71 200,3 -33,4
N019 425 1,79E-04 310,77 -51,96 201,9 -34,7
N019 450 1,73E-04 307,04 -45,52 210,3 -34,9

Table2. Thermal demagnetization data
(1) Sample = sample name
(2) Temperature (°C)
(3) NRM intensity (A/m)
(4) Core Declination (°E)
(5) Core Inclination (°)
(6) Geographic Declination (°E)
(7) Geographic Inclination (°)

N019 475 2,02E-04 309,42 -48,11 206,6 -35,5
N019 500 2,01E-04 313,1 -45,05 208,9 -39
N019 525 1,78E-04 311,09 -41,37 214 -39
N019 550 1,88E-04 314,27 -46,67 206,6 -39,1
N019 575 1,88E-04 316,6 -36,7 218 -44,6
N019 600 1,66E-04 315,85 -45,97 206,7 -40,4
N019 625 1,51E-04 308,47 -45,88 209,4 -35,7
N019 650 1,67E-04 314,92 -36,51 218,8 -43,4
N019 675 1,75E-04 304,79 -35,35 222,9 -35,7
(1) (2) (3) (4) (5) (6) (7)
OH1 Bed 2 (trench North Wall, samples N)
N023 0 4,97E-05 265,99 26,3 286,3 9,3
N023 100 6,16E-05 297,34 11,49 280 -23,2
N023 150 8,03E-05 309,76 -4,55 266,2 -39,7
N023 200 8,94E-05 311,06 2,41 275,3 -39
N023 225 9,45E-05 303,91 4,2 274,6 -31,7
N023 250 1,04E-04 299,21 2,54 271,2 -27,7
N023 275 1,13E-04 301,62 10,98 281,1 -27,3
N023 300 1,22E-04 301,27 13,19 283,3 -26,2
N023 325 1,10E-04 303,15 17,88 288,9 -26
N023 350 1,11E-04 296,47 4,68 272,7 -24,5
N023 375 1,19E-04 303,14 10,93 281,7 -28,7
N023 400 1,19E-04 296,51 15,16 283,4 -21,2
N023 425 1,34E-04 295,17 18,96 286,7 -18,6
N023 450 1,45E-04 300,46 17,6 287,4 -23,8
N023 475 1,43E-04 304,41 17,06 288,6 -27,4
N023 500 1,41E-04 290,14 15,11 281,2 -15,4
N023 525 1,56E-04 295,42 16,12 284 -19,8
N023 550 1,55E-04 291,76 17,34 283,9 -16,1
N023 575 1,31E-04 301 19,01 289,1 -23,7
N023 600 1,42E-04 302,94 18,23 289,1 -25,6
N023 625 1,55E-04 298,66 22,96 292 -20
N023 650 1,37E-04 317,18 28,4 306,8 -31,4
N023 675 1,16E-04 310,81 19,15 294 -31,9
N069 0 2,50E-04 87,06 24,07 149,5 4,7
N069 100 2,27E-04 83,14 7,58 163,9 -4,1
N069 150 2,09E-04 78,42 1,42 168,3 -10,6
N069 200 1,87E-04 82,32 -12,98 183,5 -11,1
N069 225 1,72E-04 77,4 -18,37 187,6 -17,1
N069 250 1,72E-04 84,77 -23,37 194,3 -11,7
N069 275 1,70E-04 81,64 -23,8 194 -14,5
N069 300 1,54E-04 83,8 -24,54 195,2 -12,8
N069 325 1,52E-04 91,98 -31,5 204 -7,7
N069 350 1,52E-04 89,04 -32,92 204,7 -10,4
N069 375 1,52E-04 93,77 -27,99 201,1 -5,2
N069 400 1,52E-04 98 -29,62 203,8 -2,2
N069 425 1,43E-04 99,92 -33,72 208,2 -2
N069 450 1,44E-04 95,87 -37,98 211,2 -6,5
N069 475 1,36E-04 90,46 -41,63 213,6 -11,5
N069 500 1,35E-04 117,39 -46,49 225,5 4,4
N069 525 1,66E-04 95,78 -45,73 218,6 -8,9
N069 550 1,75E-04 88,91 -54,66 226,5 -15,2
N069 575 1,55E-04 104,81 -62,44 236,3 -9,3
N069 600 1,48E-04 114,22 -62,53 238,3 -5,4
N069 625 1,33E-04 117,69 -67,53 243,4 -6,7
N069 650 1,14E-04 102,87 -68,45 241,8 -12,1
N069 675 9,00E-05 155,72 -61,74 251,9 7,9
N072 0 1,39E-04 72,66 66,39 103 8,8
N072 100 1,20E-04 57,76 60,28 105,1 0,1
N072 150 8,57E-05 68,33 50 117 -0,2
N072 200 5,92E-05 41,23 42,59 111,2 -19,4
N072 225 5,19E-05 39,72 41,58 111,1 -20,9
N072 250 5,53E-05 18,02 54,19 91,2 -17,2
N072 275 4,10E-05 3,29 45,13 82,9 -27,8
N072 300 3,11E-05 332,73 63,97 68,6 -6,3
N072 325 3,58E-05 327,5 59,15 64,1 -9,4
N072 350 3,60E-05 312,25 52,2 52,9 -9,4
N072 375 3,54E-05 287,97 33,97 28 -4,7
N072 400 3,84E-05 289,06 33,84 28,2 -5,5
N072 425 3,40E-05 278,45 30,6 21,9 1,6
N072 450 4,59E-05 265,62 10,71 359,3 7,2
N072 475 3,79E-05 284,89 53,32 44,9 5
N072 500 2,47E-05 236,55 -3,32 335,7 30,6
N072 525 3,73E-05 255,04 -21,76 325 6,9
N072 550 3,04E-05 291,81 34,46 29,8 -7,3
N072 575 3,53E-05 285,04 24,19 17,9 -6,1
N072 600 3,84E-05 289,96 26,34 21,7 -9,4
N072 625 3,17E-05 260,45 4,34 351,7 10,4
N072 650 3,55E-05 1,82 36,79 82,1 -36,2
N072 675 1,97E-05 235,52 9,58 350 35,6
N074 0 1,17E-04 60,18 2,45 158,7 -28,1
N074 100 1,13E-04 44,21 -9,02 167,7 -46,5
N074 150 1,30E-04 31,93 -22,64 189,9 -58,6
N074 200 1,38E-04 70,58 -0,11 164,5 -18,8
N074 225 9,96E-05 22,34 -38,67 224,8 -58,4
N074 250 9,19E-05 23,35 -43,77 230 -54,2
N074 275 8,57E-05 13,81 -40,88 237,8 -60,5
N074 300 8,03E-05 11,37 -47,22 245,6 -55,5
N074 325 6,85E-05 8,09 -39,21 245 -63,8
N074 350 6,36E-05 1,75 -42,85 256,6 -61,1
N074 375 5,75E-05 327,61 -40,82 299,5 -51,1
N074 400 5,32E-05 355,82 -42,72 265,6 -61,1
N074 425 4,80E-05 324,13 -17,72 338,3 -55,3
N074 450 7,05E-05 306,44 -26,96 325,8 -38,6
N074 475 5,32E-05 324,81 -15,43 342,3 -56
N074 500 6,81E-05 315,54 -37,91 309,5 -44
N074 525 8,12E-05 327,53 -42,9 296,9 -49,8
N074 550 9,19E-05 312,36 -63,57 281,7 -30,5
N074 575 7,57E-05 293,2 -64,26 284,9 -22,6
N074 600 8,44E-05 298,23 -36,2 315,2 -30,9

Table2. Thermal demagnetization data

(1) Sample = sample name
(2) Temperature (°C)
(3) NRM intensity (A/m)
(4) Core Declination (°E)
(5) Core Inclination (°)
(6) Geographic Declination (°E)
(7) Geographic Inclination (°)

N074 625 4,14E-05 354,38 -75,74 260,9 -28,2
N074 650 3,76E-05 250,95 -78,36 270,4 -10
N074 675 4,89E-05 323,49 -10,78 350,2 -54,2
N077 0 1,59E-04 83,88 16,71 150,6 -1,7
N077 100 1,71E-04 81,19 17,61 149 -3,9
N077 150 1,63E-04 72,45 5,72 158,2 -15,5
N077 200 1,10E-04 30,15 -33,58 209,2 -56,4
N077 225 1,22E-04 69,45 -0,57 163,7 -20,1
N077 250 1,14E-04 70 0,57 162,7 -19,2
N077 275 1,05E-04 68,47 -11,93 175,4 -23,5
N077 300 9,75E-05 60,68 -15,03 177,5 -31,4
N077 325 8,78E-05 57,61 -10,56 171,8 -33,7
N077 350 7,83E-05 61,34 -2,22 163,2 -28,3
N077 375 6,44E-05 69 -9 172,4 -22,4
N077 400 5,30E-05 72,19 0,06 163,8 -17,2
N077 425 4,54E-05 67,86 -27,96 192,9 -25,9
N077 450 4,23E-05 68,87 -12,32 175,9 -23,2
N077 475 3,51E-05 99,85 -30,5 200,2 1,2
N077 500 4,26E-05 73,15 1,42 162,7 -16
N077 525 1,15E-05 115,64 -12,99 188,3 20,8
N077 550 2,11E-05 61,93 -57,11 225,8 -26,8
N077 575 3,64E-05 211,38 -58,43 274,5 13,2
N077 600 3,39E-05 159,62 -52,67 245,2 21,1
N077 625 7,55E-05 297,93 -72,25 275,1 -21,7
N077 650 4,78E-05 238,3 -49 292,7 8,7
N077 675 4,81E-05 235,18 -50,61 290,2 9,5
N082 0 1,55E-04 71,86 11,63 112,7 -13,7
N082 100 1,50E-04 75,02 0,15 124,9 -14,3
N082 150 1,42E-04 60,16 -10,71 132,2 -31,4
N082 200 1,29E-04 68,9 -11,4 135,1 -23,2
N082 225 1,13E-04 66,75 -4,43 127,1 -23,6
N082 250 9,58E-05 63,93 -8,15 130,3 -27,2
N082 275 8,25E-05 73,59 -8,28 133 -18
N082 300 7,37E-05 84,28 -24,43 151,6 -11,6
N082 325 7,35E-05 63,92 -24,59 148,8 -29,9
N082 350 6,10E-05 71,77 -28,9 154,4 -23,4
N082 375 5,00E-05 95,05 -19,13 149 -0,6
N082 400 6,26E-06 257,42 -9,15 296,9 9,4
N082 425 4,08E-05 62,47 -17,14 140,1 -30,4
N082 450 4,71E-05 50,86 -11,75 131,2 -40,6
N082 475 4,03E-05 86,01 -3,51 131,6 -4,8
N082 500 3,86E-05 80,85 -34,47 161,2 -16,4
N082 525 2,32E-05 65,04 -51,35 179,4 -27,9
N082 550 4,63E-05 68,82 -4,77 128,1 -21,7
N082 575 1,03E-05 46,91 -14,83 134,5 -44,9
N082 600 3,52E-05 178,41 -50,18 218,2 23,8
N082 625 3,85E-05 129,21 -28,04 170,8 24
N082 650 6,50E-05 102,46 -37,54 168,5 -0,2
N082 675 5,67E-05 96,58 -32,52 162,3 -3,2
S004 0 1,72E-04 330,87 0,15 78,6 -60,9
S004 100 1,70E-04 326,67 -4,75 69,7 -56,4
S004 150 1,88E-04 329,76 -20,6 41,5 -54
S004 200 1,80E-04 331,39 -18,48 43,4 -56,4
S004 225 1,74E-04 335,48 -17,35 41,3 -60,3
S004 250 1,70E-04 338,63 -23,02 28,9 -59
S004 275 1,57E-04 337,09 -21,12 33,5 -59,2
S004 300 1,57E-04 335,34 -26,61 28,1 -54,3
S004 325 1,44E-04 328,73 -25,22 36,1 -50,6
S004 350 1,42E-04 326,78 -27,51 34,7 -47,9
S004 375 1,27E-04 321,21 -20,72 47,2 -46,8
S004 400 1,33E-04 327,91 -12,58 55,5 -55,8
S004 425 1,33E-04 326,97 -7,92 64 -56,1
S004 450 1,39E-04 324,08 -8,97 63,2 -53,1
S004 475 1,30E-04 318,47 -10,8 62,2 -47,3
S004 500 1,10E-04 306,29 -10,25 65,6 -35,6
S004 525 1,28E-04 303,07 -16,39 58,9 -31,6
S004 550 1,19E-04 322,48 -2,35 74,4 -52,4
S004 575 1,19E-04 323,24 -22,69 43,3 -47,7
S004 600 1,48E-04 327,84 -20,92 42,6 -52,3
S004 625 1,38E-04 327,95 -30,92 29,8 -46,6
S004 650 1,42E-04 335,51 -51,45 6,6 -34,6
S004 675 1,51E-04 317,09 -43,74 23,7 -31,9
S010 0 2,76E-04 316,18 76,46 161,8 -9,7
S010 100 2,60E-04 293,42 74,97 157,4 -5,9
S010 150 2,39E-04 302,09 72,58 156,4 -9,2
S010 200 2,22E-04 321,24 70,78 159 -14,9
S010 225 2,14E-04 320,01 70,92 158,8 -14,5
S010 250 2,16E-04 322,53 71,67 159,9 -14,5
S010 275 1,97E-04 325,54 70,88 160,2 -15,7
S010 300 1,89E-04 330,75 69,85 161,1 -17,5
S010 325 1,83E-04 342,74 70,43 165,3 -18,7
S010 350 1,73E-04 352,25 65,85 167,8 -23,9
S010 375 1,60E-04 354,75 67,48 169,1 -22,4
S010 400 1,55E-04 348,35 71,22 167,4 -18,4
S010 425 1,42E-04 351,65 69,87 168,2 -19,9
S010 450 1,23E-04 346,74 66,33 165,5 -23
S010 475 1,08E-04 345,84 63,25 164,3 -25,9
S010 500 1,08E-04 339,23 67,08 162,8 -21,4
S010 525 1,15E-04 330,98 63,95 157,9 -22,6
S010 550 8,64E-05 339,05 63 161 -25,1
S010 575 7,37E-05 338,18 63,64 160,8 -24,3
S010 600 6,87E-05 301,97 87,28 169 -1,4
S010 625 5,83E-05 321,69 77,78 163,6 -9,6
S010 650 5,52E-05 232,22 68,98 154,4 12,7
S010 675 5,29E-05 290,11 71,74 154,1 -6,2
S040 0 2,72E-04 341,23 71,87 142,3 -17,1
S040 100 2,61E-04 347,22 67,98 143,2 -21,4
S040 150 2,71E-04 350,56 64,81 143,9 -24,8
S040 200 2,61E-04 344,08 61,32 139,8 -27,5
S040 225 2,49E-04 347,52 60,92 141,4 -28,3

Table2. Thermal demagnetization data

(1) Sample = sample name

(2) Temperature (°C)

(3) NRM intensity (A/m)

(4) Core Declination (°E)

(5) Core Inclination (°)

(6) Geographic Declination (°E)

(7) Geographic Inclination (°)

S040 250 2,44E-04 341,12 58,94 137,3 -29,2
S040 275 2,34E-04 340,97 64,2 139,3 -24,3
S040 300 2,08E-04 341,64 63,26 139,3 -25,3
S040 325 1,92E-04 334,95 58,37 133,7 -28,4
S040 350 1,81E-04 337,46 59,99 135,8 -27,5
S040 375 1,71E-04 328,94 58,38 130,7 -26,7
S040 400 1,49E-04 332,5 57,28 131,8 -28,7
S040 425 1,37E-04 332,86 56,12 131,3 -29,7
S040 450 1,34E-04 321,08 54,56 124,2 -26,8
S040 475 1,24E-04 315,53 54,48 121,7 -24,5
S040 500 1,00E-04 311,36 42,94 109,4 -28,9
S040 525 1,29E-04 303,88 45,61 109,2 -23
S040 550 1,61E-04 312,2 42,67 109,5 -29,6
S040 575 1,31E-04 315,34 38,29 106,6 -33,9
S040 600 1,23E-04 305,15 34,43 98,3 -28,4
S040 625 9,86E-05 303,34 31,17 94,2 -28,1
S040 650 1,14E-04 299,53 29,1 90,9 -25,5
S040 675 1,04E-04 301,44 38,57 101,3 -24,1
S054 0 1,34E-04 270,27 25,39 98,7 -0,2
S054 100 1,26E-04 274,21 23,15 96,5 -3,9
S054 150 1,18E-04 281,43 12,48 86 -11,2

OH1 Bed 2 (trench South Wall, samples S004–S314)

S054 200 1,20E-04 279,57 4,35 77,7 -9,5
S054 225 1,19E-04 279,17 4,7 78 -9,1
S054 250 1,15E-04 275,91 1 74,3 -5,9
S054 275 1,18E-04 274,44 0,24 73,5 -4,4
S054 300 1,11E-04 273,53 1,76 75 -3,5
S054 325 1,04E-04 272,52 -4,3 69 -2,5
S054 350 1,09E-04 273,8 -6,89 66,4 -3,8
S054 375 1,09E-04 267,85 -12,77 60,5 2,1
S054 400 1,07E-04 266,54 -12,16 61,1 3,4
S054 425 1,14E-04 264,99 -16,22 57 4,8
S054 450 9,75E-05 279,53 -33,57 39,3 -7,9
S054 475 1,19E-04 271,53 -34,12 39,2 -1,3
S054 500 7,58E-05 276,28 -29,8 43,3 -5,4
S054 525 1,29E-04 259,19 -19,92 53 10,2
S054 550 6,82E-05 247,45 -28,8 42,5 19,6
S054 575 6,65E-05 256,12 -35,61 36,9 11,2
S054 600 9,09E-05 204,97 -44,31 6,7 40,4
S054 625 8,10E-05 241,92 -75,97 355,7 6,6
S054 650 8,66E-05 242,88 -37,06 33 21,3
S054 675 8,71E-05 220,65 -33,31 28 39,4
S058 0 1,57E-04 55,19 85,55 173,9 -2,5
S058 100 1,48E-04 7,45 77,98 171,9 -11,9
S058 150 1,24E-04 353,32 66,35 167,4 -23,5
S058 200 1,24E-04 3,99 68,68 171,8 -21,3
S058 225 1,25E-04 10,64 71,02 173,9 -18,6
S058 250 1,27E-04 15,91 70,79 175,7 -18,4
S058 275 1,22E-04 2,65 76,04 170,9 -13,9
S058 300 1,21E-04 12,5 74,15 173,8 -15,5
S058 325 1,15E-04 21,49 70,38 177,7 -18,2
S058 350 1,22E-04 354,55 71,63 168,5 -18,3
S058 375 1,22E-04 354,83 71,05 168,5 -18,9
S058 400 1,04E-04 356,98 68,41 169,1 -21,6
S058 425 9,00E-05 318,99 74,17 159,7 -11,9
S058 450 7,65E-05 306,95 58,2 143,9 -18,5
S058 475 6,71E-05 284,6 71,46 152,3 -4,6
S058 500 3,21E-05 208,82 74,92 162,9 13,2
S058 525 6,16E-05 344,47 30,7 146 -55,9
S058 550 5,62E-05 331,81 45,85 145,6 -37,9
S058 575 5,54E-05 273,68 52,43 132,8 -2,2
S058 600 3,76E-05 41,95 28,03 221,8 -41
S058 625 3,38E-05 98,4 22,33 237,7 7,8
S058 650 3,73E-05 336,41 50,15 151,8 -36
S058 675 6,85E-05 39,89 26,27 222,7 -43,5
S061 0 1,01E-04 193,06 73,85 166,5 15,7
S061 100 9,71E-05 153,78 79,7 174,9 9,2
S061 150 7,89E-05 188,46 82,89 169,2 7
S061 200 7,89E-05 225,47 78,3 161,9 8,2
S061 225 7,88E-05 210,16 75,14 162,7 12,8
S061 250 8,28E-05 220,22 78,93 163,1 8,4
S061 275 7,39E-05 208,36 78,09 164,6 10,5
S061 300 6,66E-05 171,31 73,58 172,8 16,2
S061 325 6,00E-05 163,43 71,08 175,9 18,1
S061 350 6,64E-05 166,69 64,44 176,6 24,8
S061 375 6,63E-05 178,53 52,96 171,4 37
S061 400 5,50E-05 176,82 36,65 174,5 53,2
S061 425 6,25E-05 172,91 42,02 178,1 47,5
S061 450 5,60E-05 169,33 41,62 182,1 47,3
S061 475 5,56E-05 181,59 15,85 164,7 74,1
S061 500 4,24E-05 151,79 17,67 226,3 57,1
S061 525 6,31E-05 169,74 10,49 214,2 75,4
S061 550 5,90E-05 170,4 36,28 183,1 52,6
S061 575 4,27E-05 172,47 52,6 176 37
S061 600 5,44E-05 153,17 30,11 208,2 50,5
S061 625 5,61E-05 148,02 40,4 202,2 40,2
S061 650 4,73E-05 130,67 21,96 232,3 37,2
S061 675 4,86E-05 155,63 30,43 205,4 51,8
S110 0 2,30E-04 54,2 83,12 170,9 7,9
S110 100 2,43E-04 60,26 78,62 175,2 6,2
S110 150 2,19E-04 61,65 73,97 179,4 4,1
S110 200 2,10E-04 44,91 73,65 176,7 0,3
S110 225 2,01E-04 45,34 74,29 176,4 0,8
S110 250 1,91E-04 51,87 75,18 176,9 2,7
S110 275 1,83E-04 63,87 76,37 177,6 5,8
S110 300 1,79E-04 77,64 72,79 182,2 7,9
S110 325 1,85E-04 63,16 72,3 181,1 3,7
S110 350 1,78E-04 50,23 70,93 179,8 -0,5
S110 375 1,69E-04 52,59 70,69 180,5 0
S110 400 1,57E-04 57,32 71,77 180,6 1,8

Table2. Thermal demagnetization data

(1) Sample = sample name

(2) Temperature (°C)

(3) NRM intensity (A/m)

(4) Core Declination (°E)

(5) Core Inclination (°)

(6) Geographic Declination (°E)

(7) Geographic Inclination (°)

S110 425 1,46E-04 57,1 63,86 187 -2,7
S110 450 1,38E-04 46,47 68,94 180,4 -2,8
S110 475 1,52E-04 49,39 65,39 183,8 -4,4
S110 500 1,34E-04 76,68 63,83 190,8 5
S110 525 1,66E-04 54,54 66,19 184,5 -2,2
S110 550 1,55E-04 72,91 68,43 185,9 5
S110 575 1,42E-04 49,42 65,55 183,7 -4,2
S110 600 1,21E-04 67,47 52,63 199,5 -3,6
S110 625 8,12E-05 24,24 49,95 182,2 -24,5
S110 650 6,97E-05 146,15 47,34 197,4 44,7
S110 675 9,11E-05 36,9 32,07 202,9 -33,5
S113 0 1,40E-04 177,93 49,39 173,6 53,6
S113 100 1,12E-04 189,3 51,77 162,2 50,5
S113 150 9,47E-05 175,63 55,83 174,9 47
S113 200 8,05E-05 175,75 50,88 175,6 52
S113 225 7,03E-05 171,77 48,27 180,6 54,1
S113 250 7,29E-05 166,58 51,85 184,1 49,7
S113 275 6,66E-05 172,17 50,03 179,5 52,4
S113 300 5,84E-05 164,94 40,23 194,5 59,7
S113 325 5,26E-05 159,24 28,1 220,1 65,5
S113 350 5,42E-05 162,78 30,32 211,1 66,5
S113 375 5,08E-05 162,02 20,73 234,7 71,2
S113 400 5,38E-05 160,07 14,66 254 70,6
S113 425 5,04E-05 152,14 15,13 253,4 62,9
S113 450 4,91E-05 151,81 3,9 276,9 60,7
S113 475 4,97E-05 147,65 13,91 255,8 58,5
S113 500 5,43E-05 157,71 10,44 265,6 68
S113 525 4,35E-05 167,9 -1,5 310,8 71,2
S113 550 3,97E-05 149,25 9,14 265,4 59,6
S113 575 3,23E-05 156,16 -32,35 325,1 39,2
S113 600 2,75E-05 197,98 -9,23 30,9 61,5
S113 625 6,88E-05 166,43 -36,58 337,3 38,8
S113 650 3,76E-05 358,77 -59,63 352,1 -43,4
S113 675 5,80E-05 133,57 -26,24 302,5 30,2
S117 0 2,44E-04 141,31 67,92 182,4 25,8
S117 100 2,08E-04 143,51 66,2 183 27,6
S117 150 1,80E-04 128,59 67,58 186,1 22,3
S117 200 1,50E-04 131,45 64,14 188,5 25,2
S117 225 1,27E-04 126,97 65,86 188 22,7
S117 250 1,09E-04 123,91 57,61 196,7 25,3
S117 275 9,75E-05 117,88 51,92 203,9 24,1
S117 300 9,91E-05 124,6 53,76 200,5 27,2
S117 325 9,49E-05 120,26 47,42 208,2 26,9
S117 350 7,91E-05 122,69 46,7 208,4 28,7
S117 375 7,54E-05 111,95 39,83 217,8 22,6
S117 400 6,94E-05 117,11 40,14 216,7 26,4
S117 425 6,96E-05 118,91 36,91 220 28,4
S117 450 7,03E-05 113,29 30,81 227,4 24,6
S117 475 5,89E-05 112,2 39,87 217,7 22,7
S117 500 5,31E-05 152,87 35,25 206,5 53,9
S117 525 5,60E-05 113,77 19,8 239,6 25,3
S117 550 3,89E-05 142,33 15,55 243,4 52,7
S117 575 6,09E-05 155,38 29,09 212,9 59,4
S117 600 2,94E-05 152,12 29,56 215,2 56,8
S117 625 1,17E-04 77,84 4,56 250,8 -11,2
S117 650 7,89E-05 56,75 51,38 199,6 -12,5
S117 675 2,85E-05 231,42 13,26 87,1 39,4
S124 0 1,23E-04 256,76 84,76 163,1 10,2
S124 100 1,01E-04 302,12 80,77 160,5 4
S124 150 8,65E-05 337,65 73,3 162 -6,5
S124 200 7,54E-05 337,34 70,36 160,7 -9,1
S124 225 6,98E-05 345,01 66,21 162,1 -14
S124 250 6,82E-05 348,17 66,37 163,4 -14,1
S124 275 5,92E-05 353,09 65,21 165,3 -15,6
S124 300 5,31E-05 352,5 61,18 164,5 -19,6
S124 325 4,59E-05 355,37 54,14 165,2 -26,7
S124 350 4,17E-05 340,54 48,01 153,3 -30,4
S124 375 3,94E-05 334,5 48,73 149,5 -28,1
S124 400 4,02E-05 342,29 38,29 150,1 -39,9
S124 425 3,48E-05 341,43 32,73 146,2 -44,7
S124 450 4,20E-05 320,12 55,6 146 -17,4
S124 475 3,20E-05 285,99 72,49 151,4 3,9
S124 500 2,93E-05 311,71 46,09 134,8 -20,1
S124 525 3,03E-05 335,46 62,94 157 -15,6
S124 550 3,31E-05 272,23 30,11 108,4 2,6
S124 575 4,01E-05 337,99 27,59 138,7 -47,7
S124 600 4,33E-05 323,98 10,64 106,2 -49,1
S124 625 4,37E-05 52,22 5,2 245,1 -36
S124 650 5,05E-05 329,34 8,86 107,8 -54,6
S124 675 2,44E-05 58,18 -38,81 298,2 -30,3
S131 0 1,57E-04 219,42 74,67 160,1 18,7
S131 100 1,25E-04 237,62 78,16 160 13,2
S131 150 1,09E-04 282,97 72,28 153 2,8
S131 200 9,21E-05 297,21 68,24 151 -3,2
S131 225 8,38E-05 298,39 67,52 150,6 -3,9
S131 250 7,15E-05 287,69 72,17 153,3 1,4
S131 275 6,30E-05 282,77 73,76 154,4 3,2
S131 300 6,21E-05 295,59 78,42 159,8 1,9
S131 325 5,30E-05 268,42 71,91 152,1 7,1
S131 350 5,57E-05 256,49 76,38 156,8 10
S131 375 5,34E-05 279,02 75,48 155,9 4,5
S131 400 4,57E-05 242,64 76,64 158,1 12,9
S131 425 3,55E-05 258,38 70,94 151,3 10,4
S131 450 3,69E-05 221,8 53,63 142,3 32,5
S131 475 3,26E-05 206,02 49,74 147,8 42
S131 500 4,40E-05 167,57 56,66 179,1 39,4
S131 525 3,61E-05 173,38 47,55 177,1 49,1
S131 550 4,45E-05 127,85 43,61 212,5 31,7
S131 575 3,79E-05 152,23 42,19 200,8 47,1
S131 600 4,26E-05 125,64 -26,06 294,7 27,8

Table2. Thermal demagnetization data
(1) Sample = sample name
(2) Temperature (°C)
(3) NRM intensity (A/m)
(4) Core Declination (°E)
(5) Core Inclination (°)
(6) Geographic Declination (°E)
(7) Geographic Inclination (°)

S131 625 9,08E-05 88,48 5,22 254,9 -0,9
S131 650 2,29E-05 75,65 -58,49 318,9 -13,4
S131 675 1,42E-05 354,89 18,3 159,1 -64,2
S135 0 1,08E-04 226,04 64,82 147,7 23,8
S135 100 1,09E-04 246,22 68,8 147,3 15
S135 150 9,37E-05 257,5 68,53 145,9 11,1
S135 200 7,80E-05 270,32 63,74 140,9 6,1
S135 225 6,73E-05 269,8 66,84 144 6,5
S135 250 6,33E-05 264,04 59,57 136,6 9
S135 275 5,74E-05 262,78 59,56 136,6 9,7
S135 300 5,09E-05 259,84 54,1 131,2 11,6
S135 325 4,92E-05 263,63 51,45 128,4 9,4
S135 350 4,60E-05 267,88 53,13 130,1 6,9
S135 375 5,10E-05 269,1 47,19 124,2 5,7
S135 400 4,53E-05 285,13 43,26 122,3 -6
S135 425 4,61E-05 292,04 40,79 121,5 -11,7
S135 450 4,51E-05 290,42 30,22 110,8 -13,8
S135 475 3,29E-05 301,54 25,07 109,1 -24,7
S135 500 3,98E-05 302,77 45,54 129,3 -16,8
S135 525 2,73E-05 314,25 43,05 132 -25
S135 550 2,54E-05 312,62 35,27 124,1 -28,6
S135 575 4,32E-05 285,7 24,87 104,4 -11,1
S135 600 1,67E-05 157,74 58,36 181,5 35,8
S135 625 5,39E-05 52,15 -1,94 254,3 -37,8
S135 650 3,08E-05 265,35 -24,97 51,9 1,2
S135 675 2,62E-05 272,38 8,94 86,4 -1,2
S140 0 7,68E-05 253,12 76,8 156,6 5,8
S140 100 7,48E-05 267,08 74,01 153,3 2,7
S140 150 6,19E-05 315,87 64,2 150,9 -16,3
S140 200 4,20E-05 320,43 47,86 139,9 -29,4
S140 225 3,73E-05 330,52 48,34 146,2 -33,5
S140 250 3,37E-05 329,01 46,7 144 -34,2
S140 275 3,11E-05 336,93 18,65 122,6 -59,3
S140 300 3,35E-05 349,13 13,56 134,9 -71,1
S140 325 3,56E-05 356,22 12,7 155,1 -74,8
S140 350 3,16E-05 0,39 2,65 174,1 -85,3
S140 375 3,35E-05 9,53 -16,34 316,7 -72,9
S140 400 2,81E-05 339,28 -17,78 40,2 -64,3
S140 425 4,71E-05 354,62 -34,65 357,4 -57
S140 450 4,45E-05 17,36 -35,2 325,3 -53,1
S140 475 5,18E-05 24,85 -41,66 323,2 -44,5
S140 500 5,09E-05 1,6 -40,67 347,3 -51,3
S140 525 5,24E-05 29,23 -43,5 321,3 -41
S140 550 5,04E-05 358,04 -40,14 351,7 -51,8
S140 575 5,59E-05 4,67 -37,79 343 -54
S140 600 3,78E-05 5,15 -49,95 344,8 -41,9
S140 625 5,31E-05 33,16 -25,08 298 -50,6
S140 650 5,70E-05 28,76 -76,56 342,7 -13,7
S140 675 4,32E-05 21,31 -34,05 319,8 -52,3
S146 0 1,20E-04 237,54 75,41 156,8 9,7
S146 100 1,09E-04 262,54 75,26 154,6 3,8
S146 150 9,96E-05 296,85 75,24 156,1 -4,7
S146 200 9,00E-05 299,7 71,72 153,4 -7
S146 225 8,31E-05 317,27 67,95 154,1 -14,1
S146 250 7,98E-05 314,49 65,42 151,4 -15
S146 275 6,54E-05 321,35 64,06 152,6 -18,1
S146 300 6,45E-05 329,77 63,55 155,4 -20,7
S146 325 5,76E-05 325,38 56,82 149,2 -24,9
S146 350 4,95E-05 321,1 52,12 143,7 -26,7
S146 375 4,59E-05 338,88 47,8 151,7 -36,9
S146 400 4,14E-05 332,43 41,51 142,5 -39,8
S146 425 4,16E-05 333,86 46,98 147,5 -35,9
S146 450 4,78E-05 353,32 45,21 162,9 -42,4
S146 475 3,95E-05 337,17 40,33 145,5 -42,8
S146 500 4,54E-05 322,56 15,18 105,5 -49,2
S146 525 3,36E-05 352,72 16,93 148,8 -69,8
S146 550 4,53E-05 329,66 32,9 132,5 -44,8
S146 575 3,55E-05 350,54 13,25 137,9 -72,1
S146 600 2,34E-05 14,03 12,02 213,8 -70,2
S146 625 2,67E-05 343,82 -9,28 54,3 -72,3
S146 650 1,54E-05 305,23 -39,63 34,6 -27,8
S146 675 3,96E-05 354,81 15,39 153 -71,9
S152 0 1,97E-04 135,72 74,39 176,7 18
S152 100 1,73E-04 129,36 76,94 175,7 15,1
S152 150 1,44E-04 98,05 74,61 180,7 8,9
S152 200 1,19E-04 85,95 70,66 184,7 5,3
S152 225 1,08E-04 87,99 65,12 190,3 5,5
S152 250 1,03E-04 84,62 65,74 189,5 4,2
S152 275 9,39E-05 88,73 66,81 188,6 5,9
S152 300 9,08E-05 92,59 64,83 190,7 7,4
S152 325 8,94E-05 73,69 65,84 188,4 -0,2
S152 350 7,88E-05 78,66 64,48 190,3 1,5
S152 375 7,11E-05 80,8 60,5 194,4 1,6
S152 400 6,37E-05 136,38 60,29 188 27,5
S152 425 6,02E-05 101,39 59,49 195,8 11,8
S152 450 4,96E-05 94,54 35,02 220,8 7,7
S152 475 5,72E-05 126,97 29 224,5 35,5
S152 500 4,30E-05 94,5 1,47 254,4 4,6
S152 525 5,61E-05 101,57 -0,19 256,9 11,5
S152 550 4,16E-05 124,92 -12,11 274,3 32
S152 575 5,55E-05 140,14 -14,98 284,5 44,8
S152 600 5,85E-05 142,96 -0,28 264,9 52,3
S152 625 6,02E-05 116,35 -12,4 272,2 23,8
S152 650 4,08E-05 63,03 -3,66 255,8 -27,2
S152 675 7,16E-05 102,92 5,46 251,3 13,4
S160 0 1,83E-04 173,72 60,87 172,2 37,9
S160 100 1,56E-04 180,7 59,06 167,8 39,9
S160 150 1,12E-04 177,77 57,05 169,9 41,9
S160 200 9,19E-05 192,75 52,55 157,3 45,2
S160 225 8,35E-05 194,22 48 153,7 49,2

Table2. Thermal demagnetization data
(1) Sample = sample name
(2) Temperature (°C)
(3) NRM intensity (A/m)
(4) Core Declination (°E)
(5) Core Inclination (°)
(6) Geographic Declination (°E)
(7) Geographic Inclination (°)

S160 250 7,62E-05 185,07 38,6 160,3 60,1
S160 275 7,24E-05 178,49 34,11 171,2 64,9
S160 300 6,87E-05 168,07 23,25 205,6 71,7
S160 325 6,52E-05 159,01 2,84 273,4 68,2
S160 350 6,52E-05 161,38 6,82 263,7 71,4
S160 375 6,96E-05 157,85 3,77 270,2 67,4
S160 400 6,42E-05 169,01 0,11 296,8 75,9
S160 425 6,62E-05 170,13 -11,14 322,1 67,6
S160 450 8,17E-05 165,88 -22,99 325,1 55,2
S160 475 8,53E-05 165,65 -24,32 325,8 53,9
S160 500 8,41E-05 167,96 -10,89 317 66,8
S160 525 8,02E-05 161,8 -24,75 320,9 51,9
S160 550 8,43E-05 166,95 -38,78 334,9 40,7
S160 575 9,37E-05 183,08 -31,11 352,4 49,8
S160 600 1,02E-04 168,81 -31,24 333,8 48,4
S160 625 1,12E-04 144,54 -45,95 321,5 26,5
S160 650 1,04E-04 159,31 -47,07 332 31
S160 675 8,35E-05 168,6 -72,32 344,8 8,3
S164 0 1,17E-04 220,03 75,45 157,3 20,9
S164 100 9,68E-05 247,71 80,89 158,6 13,3
S164 150 7,19E-05 289,54 72,98 151,2 4
S164 200 5,45E-05 293,09 65,99 145,3 0,1
S164 225 4,74E-05 277,77 66,38 143,8 6,1
S164 250 4,01E-05 282,92 60,33 138,4 2,4
S164 275 3,45E-05 291,63 54,77 134,8 -3,9
S164 300 2,58E-05 330,18 60,71 152,7 -15,5
S164 325 3,11E-05 292,25 51,94 132,3 -5,3
S164 350 2,54E-05 258,76 58,3 135,1 14,4
S164 375 1,25E-05 320,93 48,62 140,6 -22
S164 400 1,45E-05 306,96 51,47 136,5 -13,5
S164 425 2,72E-05 343,1 48,7 154,6 -29,4
S164 450 1,79E-05 324,58 46,27 141 -25,4
S164 475 2,15E-05 335,24 37,07 142,4 -37,5
S164 500 4,05E-05 354,32 28,39 159,3 -51,2
S164 525 1,80E-05 336,73 5,05 109,3 -62,4
S164 550 2,55E-05 284,21 12,53 92,4 -11,4
S164 575 1,73E-05 241,61 28,32 104,3 29,6
S164 600 3,93E-05 303,88 14,17 99,9 -29,3
S164 625 2,49E-05 256,2 -10,03 64,8 11,6
S164 650 1,66E-05 235,3 12,2 85,2 35,8
S164 675 3,94E-05 218,19 4,57 71,9 51,8
S171 0 1,46E-04 226,45 78,03 163,1 19,1
S171 100 1,18E-04 267,35 79,93 162 11,3
S171 150 8,95E-05 315,35 72,81 160,3 -1,4
S171 200 7,00E-05 318,32 65,58 156,2 -7,4
S171 225 6,41E-05 326,83 65,4 158,9 -9,7
S171 250 4,86E-05 344,41 55,94 163 -21,8
S171 275 4,17E-05 18,96 57,02 183,1 -20,2
S171 300 2,96E-05 14,32 32,8 189,1 -44,1
S171 325 2,16E-05 19,15 50,4 185,8 -26,4
S171 350 2,68E-05 359,2 41,49 171,5 -37,5
S171 375 2,61E-05 359,26 39,95 171,6 -39
S171 400 2,29E-05 18,02 37,76 190,5 -38,4
S171 425 2,98E-05 13,55 20,62 195,2 -55,7
S171 450 2,35E-05 30,49 11,36 226,8 -52,3
S171 475 3,12E-05 18,43 4,15 223,7 -66,2
S171 500 4,23E-05 21,22 4,22 227,6 -64
S171 525 2,66E-05 37,91 -18,81 278,9 -52,6
S171 550 4,95E-05 42,62 -25,78 288,5 -47,2
S171 575 4,89E-05 31,84 -23,95 289,7 -57,1
S171 600 5,42E-05 64,25 -29,35 289,8 -27,7
S171 625 5,29E-05 49,15 -18,56 277,4 -42
S171 650 3,94E-05 10,62 -45,93 339,7 -53,9
S171 675 3,72E-05 311,45 -43,17 35,6 -37,2
S176 0 1,76E-04 190,01 77,84 170 25
S176 100 1,38E-04 229,78 77,17 161,8 21
S176 150 9,64E-05 270,41 71,27 153,1 12,2
S176 200 6,78E-05 267,6 59,17 140,7 12,4
S176 225 6,35E-05 276,27 51,96 134,2 6,4
S176 250 5,54E-05 287,46 53,87 138,1 0,5
S176 275 4,78E-05 267,18 49,3 130,6 11,6
S176 300 3,20E-05 251,28 51,16 132,5 21,8
S176 325 3,91E-05 248,98 40,22 120,8 24,3
S176 350 4,23E-05 253,54 27,9 107,5 20,4
S176 375 4,45E-05 247,81 25,24 104,3 25,4
S176 400 3,41E-05 243,14 22,59 101,1 29,5
S176 425 3,54E-05 259,22 18,72 98,6 14,2
S176 450 3,54E-05 233,56 -10,33 61,1 31,9
S176 475 3,80E-05 233,4 -7,24 64,5 33,2
S176 500 6,43E-05 242,44 -15,06 59,8 22,1
S176 525 5,04E-05 237,91 -33,77 40 17,8
S176 550 7,42E-05 232,8 -27,1 43,7 25
S176 575 6,69E-05 215,02 -50,95 14,8 19,1
S176 600 6,88E-05 259,79 -58,5 23,4 -5,8
S176 625 8,67E-05 229,35 -55,95 17,8 9,7
S176 650 7,95E-05 244,39 -54,31 24,1 3,6
S176 675 7,68E-05 244,59 -63,05 16,5 -0,6
S181 0 3,96E-04 159,14 68,18 175,6 35,2
S181 100 3,55E-04 139,6 66,51 184 32
S181 150 3,13E-04 136,11 65,4 186,1 31,7
S181 200 2,87E-04 132,35 62,34 190,2 32,1
S181 225 2,70E-04 138,81 62,07 188,3 34,7
S181 250 2,60E-04 127,96 62,58 191,1 30,2
S181 275 2,41E-04 137,59 60,68 190,1 35,1
S181 300 2,34E-04 131,96 59,98 192,7 33,2
S181 325 2,18E-04 134,33 58,25 193,7 35,1
S181 350 2,10E-04 138,48 56,42 194 38
S181 375 2,03E-04 140,67 53,4 196,2 40,8
S181 400 2,04E-04 141,6 55,18 193,9 40,1
S181 425 1,89E-04 137,34 52,07 199,1 39,9

Table2. Thermal demagnetization data
(1) Sample = sample name
(2) Temperature (°C)
(3) NRM intensity (A/m)
(4) Core Declination (°E)
(5) Core Inclination (°)
(6) Geographic Declination (°E)
(7) Geographic Inclination (°)

S181 450 1,91E-04 142,32 53,17 195,7 41,7
S181 475 1,83E-04 144,49 51,63 196,2 43,7
S181 500 1,72E-04 144,18 50,39 197,7 44,3
S181 525 1,72E-04 134,27 51,71 200,8 38,4
S181 550 1,74E-04 156,77 47,52 192,1 52,2
S181 575 1,51E-04 158,4 48,59 189,6 52
S181 600 5,96E-05 13,17 74,34 169,8 -0,3
S181 625 1,12E-04 149,35 44,19 201,7 50,9
S181 650 1,10E-04 157,86 40,21 199,4 58,3
S181 675 9,75E-05 185,09 54,38 161,6 50,4
S187 0 3,70E-04 264,62 74,95 161,5 17,8
S187 100 3,43E-04 276,53 75,2 162,1 14,8
S187 150 2,85E-04 303,66 72,38 162,6 6,8
S187 200 2,36E-04 297,36 68,8 158,4 6,5
S187 225 2,19E-04 305,44 66,7 158,5 2,8
S187 250 2,04E-04 295,76 66,34 156 5,8
S187 275 1,78E-04 309,54 63,98 157,5 -0,2
S187 300 1,66E-04 307,84 62,32 155,8 -0,8
S187 325 1,57E-04 308,53 60,84 154,9 -2
S187 350 1,48E-04 301,56 61,74 153,5 1,2
S187 375 1,41E-04 300,42 59,91 151,7 0,6
S187 400 1,34E-04 301,24 60,68 152,5 0,7
S187 425 1,28E-04 312,3 58,23 154,3 -5,2
S187 450 1,19E-04 324,85 60,93 160,9 -7,1
S187 475 1,17E-04 320,23 66,79 162,7 -1,2
S187 500 9,65E-05 315,32 71,78 164,6 3,7
S187 525 1,00E-04 277,82 64,43 151,4 12
S187 550 8,26E-05 274,34 65,98 152,6 13,7
S187 575 6,75E-05 263,83 56,29 141,9 17,5
S187 600 1,29E-04 160,63 58,69 191,6 45,9
S187 625 8,41E-05 282,05 56,7 144,5 7,7
S187 650 8,00E-05 183,97 65,26 175,1 41,7
S187 675 7,10E-05 315,21 50,47 150 -11,9
S204 0 5,88E-04 213,9 74,16 160,7 24
S204 100 5,10E-04 226,35 75,44 159,1 20,8
S204 150 4,13E-04 242,86 74,9 156,2 17,5
S204 200 3,29E-04 250,32 72,69 153,3 16,3
S204 225 3,00E-04 255,19 71,54 151,8 15,1
S204 250 2,83E-04 256,23 68,47 148,6 15,3
S204 275 2,36E-04 249,51 66,51 147,1 18,2
S204 300 2,07E-04 255,47 62,82 142,8 16,4
S204 325 1,86E-04 252 63,44 143,8 17,8
S204 350 1,58E-04 250,97 64,11 144,5 18,1
S204 375 1,42E-04 258,36 63,13 143 15,1
S204 400 1,18E-04 250,51 52,43 132,4 20,5
S204 425 1,11E-04 253,83 50,81 130,4 18,7
S204 450 1,05E-04 266,74 33,72 113,1 8,8
S204 475 9,93E-05 261,75 36,27 115,3 13,1
S204 500 7,76E-05 279,99 30,76 112,4 -2,8
S204 525 7,60E-05 266,07 9,96 89,4 5,7
S204 550 7,53E-05 251,43 17,21 94,7 20,8
S204 575 8,71E-05 252,4 -3,43 73,3 16,6
S204 600 8,89E-05 266,88 -0,11 79,6 3
S204 625 8,61E-05 250,81 -1,11 75,3 18,6
S204 650 6,63E-05 263,55 -28,47 51,2 0,3
S204 675 4,50E-05 300,38 -49,83 29,3 -27,8
S215 0 5,35E-04 217,96 74,52 166,4 17,1
S215 100 5,04E-04 229,75 77,4 166,4 13
S215 150 4,21E-04 245,33 79,08 166,2 9,5
S215 200 3,25E-04 235,39 81,76 169,4 9,6
S215 225 2,81E-04 255,41 78,51 165,1 7,8
S215 250 2,43E-04 213,01 87,36 174,8 7,2
S215 275 2,02E-04 253,29 81,76 168,3 7,3
S215 300 1,68E-04 251,23 81,33 168 7,7
S215 325 1,22E-04 186,03 81,59 175,4 13,4
S215 350 1,21E-04 128,5 80,81 183,6 10,7
S215 375 1,08E-04 147,61 77,54 183,2 15,5
S215 400 9,89E-05 210,51 78,42 170,2 14,9
S215 425 1,07E-04 197,73 80,92 173,4 13,6
S215 450 7,61E-05 164,24 65,8 183,5 28,2
S215 475 8,58E-05 98,73 62,15 204,1 8,5
S215 500 6,37E-05 99,02 59,24 207 8,9
S215 525 6,08E-05 66,54 62,51 201,5 -6,1
S215 550 3,48E-05 52,86 37,64 220,4 -25
S215 575 4,22E-05 79,39 16,57 248,6 -8,7
S215 600 4,21E-05 73,54 23,89 240,4 -12,9
S215 625 8,33E-05 61,77 -10,44 275,5 -28,6
S215 650 2,93E-05 50,01 -40,23 312 -33
S215 675 1,99E-05 352,33 -56,41 1,7 -38,2
S221 0 7,65E-04 208,86 79,74 165,2 13
S221 100 6,49E-04 211,06 83,52 166,9 9,5
S221 150 5,06E-04 257,45 87,62 168 4,5
S221 200 4,02E-04 311,47 87,09 168,1 2,1
S221 225 3,36E-04 343,99 85,29 169 -0,5
S221 250 2,84E-04 357,18 87,42 170,2 1,4
S221 275 2,37E-04 29,72 81,78 174,4 -3,1
S221 300 2,17E-04 25,79 80,46 174,4 -4,6
S221 325 1,83E-04 10,76 83,67 171,5 -2,2
S221 350 1,49E-04 0,34 79,6 170,3 -6,4
S221 375 1,26E-04 32,42 70,96 180,6 -12,1
S221 400 1,10E-04 33,51 71 180,9 -11,8
S221 425 9,89E-05 38,62 56,42 192,1 -21,9
S221 450 1,14E-04 57,61 54,6 200,7 -14,6
S221 475 9,32E-05 68,78 42,91 214,7 -12,5
S221 500 6,88E-05 54,19 30,77 222,2 -27,8
S221 525 5,03E-05 32,75 24,52 216,8 -47,3
S221 550 8,66E-05 55,16 10,05 245,5 -33,3
S221 575 7,72E-05 51,27 11,79 242,4 -36,6
S221 600 7,03E-05 43,45 -13,45 275,6 -46,1
S221 625 8,57E-05 73,36 -18,88 278,8 -17

Table2. Thermal demagnetization data
(1) Sample = sample name
(2) Temperature (°C)
(3) NRM intensity (A/m)
(4) Core Declination (°E)
(5) Core Inclination (°)
(6) Geographic Declination (°E)
(7) Geographic Inclination (°)

S221 650 8,72E-05 40,54 -26,78 295 -45,1
S221 675 1,11E-04 41,42 -16,98 281,2 -47,4
S230 0 7,58E-04 243,7 74,17 162,4 17,6
S230 100 7,81E-04 255,42 78,41 165,7 13,7
S230 150 5,94E-04 272,58 76,79 163,9 10,1
S230 200 4,41E-04 289,83 75,27 163,4 5,7
S230 225 3,70E-04 295,8 72,86 161,9 3,2
S230 250 3,10E-04 286,56 71,1 159,1 5,2
S230 275 2,16E-04 301,52 66,03 157 -2
S230 300 2,07E-04 307,02 63,66 156,4 -5,2
S230 325 1,51E-04 306,66 55,69 150 -9,9
S230 350 1,24E-04 300,65 46,4 140 -11,9
S230 375 1,02E-04 294,3 35,76 128 -12,5
S230 400 7,33E-05 295,75 31,02 124,1 -15,5
S230 425 6,76E-05 287,24 30,45 120,8 -8,9
S230 450 5,85E-05 314,66 30,58 132,4 -29,8
S230 475 4,21E-05 319 15,45 119,6 -41,5
S230 500 6,43E-05 318,61 -4,76 92,6 -48,6
S230 525 5,44E-05 330,4 -23,84 58,8 -59,1
S230 550 8,55E-05 333,64 -61,03 12,8 -36,4
S230 575 8,01E-05 310,27 -53,76 29,4 -31,9
S230 600 9,10E-05 290,31 -64,59 22,4 -18,6
S230 625 8,54E-05 359,66 -60,56 357,5 -40,4
S230 650 1,15E-04 256,56 -75,87 11,1 -7,4
S230 675 9,23E-05 342,95 -51,01 13,2 -47,6
S234 0 8,40E-04 241,06 80,5 168,6 16,5
S234 100 7,78E-04 245,93 81,6 169,3 15,3
S234 150 6,23E-04 267,84 82,25 169,4 12,2
S234 200 4,94E-04 273,27 82,75 169,9 11,5
S234 225 4,40E-04 274,14 83,17 170,3 11,4
S234 250 3,99E-04 266,28 85,93 173,1 12,2
S234 275 3,22E-04 263,51 83,09 170,2 12,7
S234 300 2,82E-04 216,91 86,02 174,8 15,2
S234 325 2,54E-04 237,82 83,28 171,4 15,5
S234 350 2,13E-04 240,43 82,34 170,4 15,7
S234 375 1,92E-04 253,6 80,87 168,2 14,4
S234 400 1,77E-04 264,03 82,46 169,6 12,7
S234 425 2,11E-04 214,79 85,29 174,5 15,9
S234 450 1,46E-04 3,78 88,5 177,4 10,5
S234 475 1,53E-04 51,15 87,16 179,5 10,2
S234 500 1,26E-04 206,74 85,07 175 16,4
S234 525 1,32E-04 68,82 81,5 185,3 8,8
S234 550 1,40E-04 89,29 81,34 186,1 11,8
S234 575 1,06E-04 34,9 67,42 190,1 -6,7
S234 600 1,00E-04 64,77 61,45 202,9 -1
S234 625 1,18E-04 62,37 41,87 219,6 -11,5
S234 650 9,67E-05 63,11 52,19 210,6 -6,1
S234 675 8,63E-05 38,2 68,39 190,5 -5,2
S240 0 1,10E-03 240,82 74,91 159,8 13,1
S240 100 1,09E-03 227,45 79,74 165,5 12,9
S240 150 8,99E-04 251,59 79,38 163,1 9,2
S240 200 7,14E-04 261,54 79,66 163 7,4
S240 225 6,49E-04 269,37 78,42 161,6 6
S240 250 5,85E-04 259,07 78,29 161,7 8,1
S240 275 4,96E-04 277,12 77,57 160,9 4,3
S240 300 4,55E-04 298,26 78,87 163,5 0,7
S240 325 4,19E-04 275,7 78,54 161,8 4,8
S240 350 3,47E-04 274,61 77,36 160,6 4,8
S240 375 3,25E-04 276,48 78,26 161,6 4,6
S240 400 2,77E-04 259,3 76,82 160,2 8,3
S240 425 2,62E-04 271,13 79,45 162,7 5,7
S240 450 2,41E-04 254,29 81,31 164,8 8,3
S240 475 2,34E-04 241,19 80,92 165,2 10,3
S240 500 1,71E-04 246,45 72,14 156,5 12,8
S240 525 1,83E-04 251,28 80,26 163,9 9
S240 550 1,46E-04 241,15 74,41 159,3 13,3
S240 575 1,17E-04 248,9 64,89 149,2 14,3
S240 600 9,32E-05 262,19 65,52 148,7 8,7
S240 625 4,75E-05 184,14 64,13 171,2 31,8
S240 650 8,98E-05 252,38 85,38 168,8 7,4
S240 675 5,23E-05 299,94 75,41 160,7 -1,4
S253 0 1,43E-03 312,96 83,78 163,6 12,7
S253 100 1,52E-03 317,5 82,57 163,2 11,5
S253 150 1,25E-03 338,49 79,14 164,3 6,9
S253 200 1,02E-03 343,78 78,51 165,1 5,9
S253 225 9,16E-04 347,97 77,97 165,8 5,2
S253 250 8,16E-04 346,41 78,02 165,5 5,3
S253 275 6,95E-04 339,43 77,6 163,9 5,4
S253 300 6,19E-04 346,74 78,42 165,6 5,7
S253 325 5,13E-04 7,37 76,78 170 3,9
S253 350 4,29E-04 2,41 77,42 168,8 4,4
S253 375 3,79E-04 357,85 74,2 167,7 1,2
S253 400 3,32E-04 10,07 77,05 170,5 4,2
S253 425 2,98E-04 1,84 80,71 168,6 7,7
S253 450 2,43E-04 32,95 78 174,8 6,8
S253 475 2,41E-04 32,24 79,17 174,1 7,8
S253 500 1,88E-04 69,09 82,48 175,5 14,2
S253 525 1,98E-04 72,69 81,14 177 14,2
S253 550 1,54E-04 89,07 79,48 179,3 16,5
S253 575 1,14E-04 109,36 47,88 212,8 25,4
S253 600 7,78E-05 127,95 44,01 214,9 38,8
S253 625 8,85E-05 110,31 9,44 254,8 22
S253 650 5,72E-05 101,85 17,77 244,2 16
S253 675 4,63E-05 159,31 24,49 233,6 69,3
S268 0 2,74E-03 174,33 88,2 160,5 13,8
S268 100 2,51E-03 81,44 88,77 161,5 11,8
S268 150 2,09E-03 4,53 85,93 160,6 7,9
S268 200 1,67E-03 12,14 84,68 161,4 6,8
S268 225 1,48E-03 9,44 84,67 161,2 6,7
S268 250 1,33E-03 8,86 83,47 161,3 5,5

Table2. Thermal demagnetization data
(1) Sample = sample name
(2) Temperature (°C)
(3) NRM intensity (A/m)
(4) Core Declination (°E)
(5) Core Inclination (°)
(6) Geographic Declination (°E)
(7) Geographic Inclination (°)

S268 275 1,09E-03 11,33 81,55 161,9 3,7
S268 300 9,97E-04 8,06 82,69 161,3 4,8
S268 325 8,50E-04 7,39 82,29 161,3 4,4
S268 350 7,21E-04 5,64 81,62 161,1 3,7
S268 375 6,19E-04 11,65 82,17 161,9 4,3
S268 400 5,66E-04 13,15 80,08 162,5 2,3
S268 425 5,04E-04 17,98 80,32 163,3 2,8
S268 450 4,40E-04 4,59 78,83 161,2 0,9
S268 475 4,22E-04 11,98 82,35 161,9 4,5
S268 500 3,12E-04 15,31 80,06 162,9 2,4
S268 525 3,22E-04 32,25 83,26 163,9 6,3
S268 550 2,41E-04 44,35 79,62 167,5 4,5
S268 575 1,99E-04 53,46 68,82 177,2 -0,9
S268 600 1,11E-04 26,94 64,23 171,9 -11,1
S268 625 1,43E-04 49,44 44,57 194,9 -17,9
S268 650 8,84E-05 67,63 54,7 192,6 -2,6
S268 675 1,09E-04 27,98 48,45 180,3 -24,7
S273 25 2,26E-03 304,13 84,34 161,5 9,8
S273 100 2,18E-03 310,82 83,56 161,4 8,7
S273 150 1,77E-03 331,15 80,21 161,6 4,4
S273 200 1,47E-03 337,1 78,33 161,8 2,2
S273 225 1,33E-03 342,19 77,8 162,6 1,4
S273 250 1,20E-03 350,19 77,16 164,1 0,3
S273 275 9,68E-04 356,45 75,26 165,4 -1,7
S273 300 8,48E-04 356,41 74,32 165,3 -2,7
S273 325 7,41E-04 354,45 72,79 164,6 -4,1
S273 350 6,59E-04 3,24 72,16 167,3 -4,8
S273 375 5,82E-04 3,98 70,59 167,6 -6,4
S273 400 5,09E-04 15,15 67,96 172 -8,3
S273 425 4,66E-04 12,53 67,51 171,1 -9
S273 450 3,97E-04 14,85 70,36 171,3 -6
S273 475 3,88E-04 13,34 69,91 170,9 -6,6
S273 500 3,30E-04 23,45 67,59 175,1 -7,6
S273 525 2,67E-04 32,08 62,09 180,9 -10,8
S273 550 2,53E-04 17,77 58,1 176 -17,4
S273 575 1,41E-04 63,06 58,58 194 -2,2
S273 600 9,80E-05 65,65 41,07 210,3 -8,9
S273 625 1,33E-04 79,81 7,89 246,2 -8
S273 650 1,18E-04 44,16 22,53 217,2 -34
S273 675 1,16E-04 54,74 13,74 232 -29,5
S281 0 2,68E-03 174,05 88,75 162,4 14,2
S281 100 2,74E-03 336,61 88,14 161,5 11,3
S281 150 2,25E-03 342,64 84,65 160,7 7,9
S281 200 1,81E-03 343,79 83,08 160,3 6,3
S281 225 1,60E-03 344,85 82,65 160,4 5,9
S281 250 1,41E-03 339,06 82,08 159,4 5,6
S281 275 1,20E-03 346,96 81,97 160,5 5,2
S281 300 1,09E-03 344,19 81,39 159,9 4,7
S281 325 9,44E-04 348,74 81,45 160,6 4,6
S281 350 7,61E-04 359,05 82,01 162,2 5
S281 375 6,78E-04 345,4 80,23 159,8 3,5
S281 400 6,26E-04 351,82 80,47 160,9 3,6
S281 425 5,69E-04 346 80,24 159,9 3,5
S281 450 5,37E-04 344,94 78,24 159,2 1,6
S281 475 4,99E-04 343,77 79,63 159,4 3
S281 500 3,99E-04 343,09 78,26 158,9 1,8
S281 525 3,52E-04 3,89 78,22 163,1 1,2
S281 550 2,80E-04 7,63 75,67 164,2 -1,2
S281 575 1,74E-04 346,35 77,88 159,4 1,2
S281 600 1,04E-04 314,17 70,38 148,3 -0,9
S281 625 8,19E-05 21,75 47,4 178,6 -26,6
S281 650 8,46E-05 11,17 59,31 168,2 -17,1
S281 675 1,06E-04 20,31 73,59 167,9 -2,4
S287 25 3,63E-03 296,15 84,49 158,2 11,5
S287 100 3,20E-03 305,93 81,76 156,5 9,1
S287 150 2,56E-03 321,84 78,72 156,3 5
S287 200 2,11E-03 326,66 77,48 156,4 3,5
S287 225 1,92E-03 326,03 76,21 155,6 2,5
S287 250 1,71E-03 323,47 75,88 154,9 2,5
S287 275 1,38E-03 328,01 73,52 154,6 -0,1
S287 300 1,21E-03 331,04 67,87 152,7 -5,5
S287 325 1,10E-03 322,42 71,6 152,2 -0,8
S287 350 9,24E-04 316,77 70,12 149,8 -0,7
S287 375 8,25E-04 319,7 69,19 150 -2,1
S287 400 7,30E-04 314,67 69,1 148,6 -1
S287 425 6,72E-04 312,4 67,82 147,1 -1,3
S287 450 6,21E-04 316,49 67,76 148,2 -2,4
S287 475 5,99E-04 319,89 66,48 148,3 -4,3
S287 500 5,44E-04 318,44 63,92 146,2 -5,8
S287 525 4,53E-04 306,18 62,31 141,2 -3
S287 550 3,42E-04 318,38 63,48 145,9 -6,2
S287 575 2,47E-04 305,87 56,01 136,1 -6,7
S287 600 1,88E-04 294,56 47,51 125,2 -5,4
S287 625 1,10E-04 298,61 56,06 133,9 -3,4
S287 650 1,57E-04 309,01 36,49 121,5 -20,3
S287 675 1,12E-04 290,21 40,25 117,2 -5,7
S299 25 3,94E-03 223,48 85,18 159,9 13,5
S299 100 3,74E-03 253,91 85,7 159,1 11,2
S299 150 3,02E-03 295,17 84,12 157,9 7,5
S299 200 2,56E-03 305,17 83,8 158,2 6,4
S299 225 2,28E-03 309,36 82,54 157,5 5,2
S299 250 2,02E-03 310,46 82,67 157,7 5,2
S299 275 1,56E-03 312,13 82,76 157,9 5,1
S299 300 1,39E-03 309,23 82,05 157,1 4,9
S299 325 1,27E-03 310,31 82,25 157,4 4,9
S299 350 1,04E-03 304,53 79,96 155 4,2
S299 375 9,33E-04 302,61 79,76 154,6 4,4
S299 400 7,78E-04 287,61 77,89 151,7 6,2
S299 425 1,00E-03 330,22 72,34 154,6 -5,4
S299 450 6,18E-04 285,38 79,5 153,1 7,1

Table2. Thermal demagnetization data
(1) Sample = sample name
(2) Temperature (°C)
(3) NRM intensity (A/m)
(4) Core Declination (°E)
(5) Core Inclination (°)
(6) Geographic Declination (°E)
(7) Geographic Inclination (°)

S299 475 6,22E-04 294,14 76,34 150,8 4,2
S299 500 4,68E-04 275,36 76,65 149,8 8,5
S299 525 4,18E-04 280,61 76,17 149,6 7,2
S299 550 3,74E-04 281,5 73,61 147,1 6,4
S299 575 2,40E-04 271,06 71,68 144,7 9,2
S299 600 1,30E-04 279,82 61,46 135,1 4,1
S299 625 8,44E-05 290,31 64,78 139,7 0,7
S299 650 1,16E-04 255,72 45,44 117,9 17,1
S299 675 1,45E-04 280,28 29,25 103,9 -3,9
S314 25 6,04E-03 31,25 82,48 162,2 8,5
S314 100 5,43E-03 5,19 80,61 159,1 5,6
S314 150 4,41E-03 349,63 79,38 156,4 4,5
S314 200 3,72E-03 3,28 77,59 159 2,6
S314 225 3,27E-03 0,12 77,7 158,3 2,7
S314 250 3,01E-03 352,15 77,14 156,5 2,3
S314 275 2,40E-03 342,97 77,53 154,7 3,1
S314 300 2,02E-03 345,6 75,71 154,8 1,1
S314 325 1,74E-03 342,76 75,54 154 1,2
S314 350 1,48E-03 344,94 73,99 154,2 -0,5
S314 375 1,30E-03 332,58 74,66 151,3 1,3
S314 400 1,11E-03 334,94 73,8 151,5 0,3
S314 425 6,81E-04 288,31 78,92 147,6 11,3
S314 450 8,82E-04 325,14 74,85 149,7 2,4
S314 475 8,68E-04 323,35 73,85 148,7 1,9
S314 500 6,57E-04 322,02 69,97 146,1 -1
S314 525 5,44E-04 301,07 68,33 139,8 3,2
S314 550 4,59E-04 305,36 69,22 141,4 2,5
S314 575 2,80E-04 290,39 50,26 121,5 -0,9
S314 600 1,63E-04 272,16 13,49 81,9 1,4
S314 625 1,45E-04 274,63 -2,94 66,6 -5,2
S314 650 1,85E-04 268,92 2,71 70,6 1,7
S314 675 1,98E-04 268,58 -7,66 60,5 -0,6
OH2 (samples S333– S1701; hand samples oh2_)
S333 25 7,98E-04 64 47,17 177 -2,5
S333 100 6,84E-04 60,12 42,12 179,7 -7,5
S333 150 5,86E-04 59,01 37,17 183,4 -11
S333 200 4,89E-04 51,84 36,16 180,7 -16,2
S333 225 4,43E-04 55,01 34,67 183,5 -15,1
S333 250 3,73E-04 53,01 34,6 182,6 -16,5
S333 275 3,05E-04 38,89 28,09 178,9 -29,7
S333 300 2,54E-04 44,98 24,08 186,6 -28,5
S333 325 1,98E-04 44,62 24,81 185,7 -28,3
S333 350 1,99E-04 35,93 23,27 180,5 -35,1
S333 375 1,78E-04 24,17 15,7 175,3 -47,9
S333 400 1,67E-04 29,68 8,17 189,1 -50,1
S333 425 1,58E-04 33,42 13,42 187,2 -43,8
S333 450 1,36E-04 30,93 4,93 194,2 -51,3
S333 475 1,52E-04 27,67 5,56 190 -53,3
S333 500 1,44E-04 26,49 -1,38 198,2 -58,6
S333 525 1,17E-04 10,54 -7,87 183,3 -74,9
S333 550 1,09E-04 3,61 2,15 149,2 -68,6
S333 575 1,09E-04 351,2 -9,95 94,8 -77,6
S333 600 9,71E-05 322,06 -24,67 33,2 -54,4
S333 625 1,43E-04 352,6 -25,15 6,1 -80,8
S333 650 1,18E-04 326,42 -32,78 17,9 -57
S333 675 1,37E-04 5,26 -24,72 279,8 -82,5
oh2_3 0 1,10E-02 174,5 2,4 174,5 2,4
oh2_3 100 1,04E-02 173,6 -3,2 173,6 -3,2
oh2_3 150 8,83E-03 172,3 -5,2 172,3 -5,2
oh2_3 200 7,71E-03 173 -6,1 173 -6,1
oh2_3 225 7,29E-03 173,6 -5,8 173,6 -5,8
oh2_3 250 6,66E-03 172,6 -9,4 172,6 -9,4
oh2_3 275 6,03E-03 170,1 -10,3 170,1 -10,3
oh2_3 300 5,62E-03 167,4 -10,8 167,4 -10,8
oh2_3 325 5,00E-03 170 -11,4 170 -11,4
oh2_3 350 4,76E-03 170 -7,9 170 -7,9
oh2_3 375 4,61E-03 170,4 -12,6 170,4 -12,6
oh2_3 400 4,57E-03 172,3 -8,8 172,3 -8,8
oh2_3 425 4,33E-03 172,9 -4,3 172,9 -4,3
oh2_3 450 4,10E-03 175,5 6,5 175,5 6,5
oh2_3 475 4,46E-03 168,2 -8,7 168,2 -8,7
oh2_3 500 4,40E-03 161 -14,7 161 -14,7
oh2_3 525 4,03E-03 164,1 -6,9 164,1 -6,9
oh2_3 550 3,26E-03 148,6 -2,9 148,6 -2,9
oh2_3 575 3,39E-03 163,4 -13,6 163,4 -13,6
oh2_3 600 3,05E-03 156,7 -3,4 156,7 -3,4
oh2_3 625 3,21E-03 162,1 -18,5 162,1 -18,5
oh2_3 650 3,34E-03 154,2 11 154,2 11
oh2_3 675 2,81E-03 146,5 -7,5 146,5 -7,5
oh2_4 0 5,89E-03 341,1 10,7 341,1 10,7
oh2_4 100 5,54E-03 341,2 7,5 341,2 7,5
oh2_4 150 4,66E-03 343 2,6 343 2,6
oh2_4 200 4,34E-03 345,2 1,6 345,2 1,6
oh2_4 225 4,00E-03 344,3 1,9 344,3 1,9
oh2_4 250 3,61E-03 340,6 0,3 340,6 0,3
oh2_4 275 3,49E-03 344,6 -3,1 344,6 -3,1
oh2_4 300 3,00E-03 344,7 -8 344,7 -8
oh2_4 325 2,61E-03 346,3 -6,2 346,3 -6,2
oh2_4 350 2,38E-03 345,4 -9,3 345,4 -9,3
oh2_4 375 2,24E-03 338,4 -11,5 338,4 -11,5
oh2_4 400 2,44E-03 342 -8,4 342 -8,4
oh2_4 425 2,18E-03 339,1 -13,6 339,1 -13,6
oh2_4 450 1,57E-03 348,5 21,3 348,5 21,3
oh2_4 475 1,74E-03 339,2 -20 339,2 -20
oh2_4 500 2,00E-03 324,3 -28,6 324,3 -28,6
oh2_4 525 2,08E-03 323,7 -21 323,7 -21
oh2_4 550 1,21E-03 343,6 -32,6 343,6 -32,6
oh2_4 575 1,14E-03 350,7 -22,9 350,7 -22,9
oh2_4 600 4,17E-04 17,3 5,6 17,3 5,6
oh2_4 625 3,78E-04 27,4 21,2 27,4 21,2

Table2. Thermal demagnetization data
(1) Sample = sample name
(2) Temperature (°C)
(3) NRM intensity (A/m)
(4) Core Declination (°E)
(5) Core Inclination (°)
(6) Geographic Declination (°E)
(7) Geographic Inclination (°)

oh2_4 650 4,78E-04 256,3 9,1 256,3 9,1
oh2_4 675 1,59E-03 321,7 -63,8 321,7 -63,8
S352 0 1,08E-02 98,956 36,225 181,5 7,8
S352 100 9,88E-03 103,61 31,562 185,9 12,1
S352 150 7,09E-03 98,659 32,51 185,3 7,8
S352 200 5,41E-03 92,591 35,103 182,9 2,7
S352 250 5,37E-03 92,869 35,02 183 2,9
S352 300 4,05E-03 95,277 38,851 179,1 4,7
S352 350 3,88E-03 93,479 31,88 186,1 3,5
S352 400 3,00E-03 105,76 45,689 171,4 11,7
S352 425 2,90E-03 90,225 28,421 189,6 0,7
S352 475 2,74E-03 94,217 37,34 180,6 4
S352 500 2,63E-03 99,97 42,17 175,5 8
S352 550 2,66E-03 105,02 43,246 173,9 11,6
S352 575 1,95E-03 112,34 37,567 178,5 18,2
S352 600 2,19E-03 106,99 37,307 179,6 14,1
S352 625 1,23E-03 186,73 16,591 105,3 73,1
S352 650 4,91E-04 311,91 62,958 107,3 -16,7
S352 675 6,83E-04 105,22 51,783 165,3 10,1
S372 0 6,90E-03 80,401 0,6646 168,2 -9,4
S372 100 7,30E-03 79,787 -4,2449 173 -10,6
S372 150 5,95E-03 71,596 -8,0193 176,1 -19,1
S372 200 5,37E-03 57,348 -4,5896 170,9 -32,9
S372 250 5,14E-03 53,644 -4,46 170,4 -36,6
S372 300 4,57E-03 46,253 -8,0476 174,4 -44,2
S372 350 4,54E-03 46,969 -4,1682 169,2 -43,2
S372 400 4,45E-03 43,452 0 162,7 -46,1
S372 425 4,39E-03 42,036 3,922 156,7 -46,6
S372 450 4,25E-03 42,992 4,3179 156,5 -45,6
S372 475 4,22E-03 39,806 2,1726 158,4 -49,2
S372 500 3,98E-03 37,938 4,8966 153,6 -50,3
S372 525 4,03E-03 41,882 0,99526 160,8 -47,5
S372 550 4,21E-03 35,617 1,4978 157,9 -53,5
S372 575 4,00E-03 36,87 2,2906 157,1 -52
S372 600 2,88E-03 37,036 17,141 136,2 -46,2
S372 625 1,05E-03 6,3775 -14,019 218,8 -80,6
S372 650 1,10E-03 262,45 36,953 26,4 10,2
oh2_2 0 1,97E-02 170,8 0,2 170,8 0,2
oh2_2 100 1,77E-02 169,5 0,4 169,5 0,4
oh2_2 150 1,49E-02 170,8 -2,9 170,8 -2,9
oh2_2 200 1,30E-02 168,6 -3,3 168,6 -3,3
oh2_2 225 1,24E-02 170,6 -4 170,6 -4
oh2_2 250 1,15E-02 171 -5,8 171 -5,8
oh2_2 275 1,05E-02 174,4 -7,5 174,4 -7,5
oh2_2 300 9,25E-03 172,2 -6,7 172,2 -6,7
oh2_2 325 8,36E-03 172,7 -9 172,7 -9
oh2_2 350 7,94E-03 171,9 -9,2 171,9 -9,2
oh2_2 375 7,26E-03 174,6 -13,1 174,6 -13,1
oh2_2 400 6,92E-03 173,7 -9,9 173,7 -9,9
oh2_2 425 6,54E-03 175,8 -10,2 175,8 -10,2
oh2_2 450 6,00E-03 169,9 0,7 169,9 0,7
oh2_2 475 6,03E-03 181,2 -20,4 181,2 -20,4
oh2_2 500 5,58E-03 173,8 -14,9 173,8 -14,9
oh2_2 525 4,70E-03 178,6 -19 178,6 -19
oh2_2 550 6,38E-03 173,5 -22,6 173,5 -22,6
oh2_2 575 4,14E-03 187,3 -11,6 187,3 -11,6
oh2_2 600 4,02E-03 190,8 -33,5 190,8 -33,5
oh2_2 625 2,89E-03 179 -26,3 179 -26,3
oh2_2 650 3,63E-03 205,1 -24,2 205,1 -24,2
oh2_2 675 6,48E-03 261,2 7,2 261,2 7,2
oh2_5 0 4,42E-03 204,5 14,3 204,5 14,3
oh2_5 100 4,08E-03 207,6 14,4 207,6 14,4
oh2_5 150 3,77E-03 206,6 2,2 206,6 2,2
oh2_5 200 3,47E-03 212,2 9,4 212,2 9,4
oh2_5 225 3,02E-03 212,6 6,2 212,6 6,2
oh2_5 250 2,94E-03 211,1 5,6 211,1 5,6
oh2_5 275 2,80E-03 208,7 10,3 208,7 10,3
oh2_5 300 2,40E-03 210,4 10,9 210,4 10,9
oh2_5 325 2,28E-03 211,2 15,8 211,2 15,8
oh2_5 350 2,14E-03 217,2 6,9 217,2 6,9
oh2_5 375 1,99E-03 217,6 7,4 217,6 7,4
oh2_5 400 1,67E-03 209 12,9 209 12,9
oh2_5 425 1,54E-03 212,2 1,9 212,2 1,9
oh2_5 450 1,49E-03 227,4 -30,4 227,4 -30,4
oh2_5 475 1,39E-03 201,6 5,6 201,6 5,6
oh2_5 500 1,27E-03 196,4 4,2 196,4 4,2
oh2_5 525 2,04E-03 200,6 25,9 200,6 25,9
oh2_5 550 1,31E-03 213,3 42 213,3 42
oh2_5 575 1,56E-03 166,7 44,7 166,7 44,7
oh2_5 600 7,31E-04 179 -16,3 179 -16,3
oh2_5 625 1,84E-03 144,3 53,8 144,3 53,8
oh2_5 650 1,35E-03 81,1 85,5 81,1 85,5
oh2_5 675 1,70E-03 214,6 64,1 214,6 64,1
S386 0 7,43E-03 87,982 6,183 161,6 -3,6
S386 100 7,45E-03 89,846 5,3893 161,9 -1,6
S386 150 4,97E-03 78,437 10,43 159,9 -13,9
S386 200 5,09E-03 76,929 8,3518 162,4 -14,8
S386 250 3,36E-03 78,791 6,3143 163,9 -12,5
S386 300 3,44E-03 73,333 10,552 161 -18,8
S386 350 3,00E-03 69,845 18,651 153,3 -23,7
S386 400 3,04E-03 68,235 18,222 154 -25,1
S386 450 2,93E-03 62,751 26,382 145,5 -31,1
S386 475 2,80E-03 62,534 24,018 148,2 -31,1
S386 500 1,93E-03 64,538 23,999 148,1 -29,3
S386 525 2,71E-03 69,775 26,472 144,8 -24,9
S386 550 2,66E-03 59,927 32,917 137,8 -33,7
S386 575 2,83E-03 43,819 14,506 162,9 -47,8
S386 600 2,05E-03 50,346 18,937 155,7 -42
S386 625 2,61E-03 48,932 18,643 156,2 -43,4
S386 650 2,63E-03 61,631 30,145 141,1 -32,2

Table2. Thermal demagnetization data

(1) Sample = sample name

(2) Temperature (°C)

(3) NRM intensity (A/m)

(4) Core Declination (°E)

(5) Core Inclination (°)

(6) Geographic Declination (°E)

(7) Geographic Inclination (°)

S386 675 7,16E-04 49,588 -15,637 197,5 -31,7
oh2_1 0 1,14E-02 155,1 15,4 155,1 15,4
oh2_1 100 1,05E-02 156,5 12,6 156,5 12,6
oh2_1 150 8,77E-03 158,1 12,1 158,1 12,1
oh2_1 200 7,68E-03 154,4 10,1 154,4 10,1
oh2_1 225 7,07E-03 158,5 9,6 158,5 9,6
oh2_1 250 6,07E-03 153,9 8,8 153,9 8,8
oh2_1 275 5,53E-03 153,7 8 153,7 8
oh2_1 300 5,08E-03 151,5 12,8 151,5 12,8
oh2_1 325 4,47E-03 148,2 8,2 148,2 8,2
oh2_1 350 4,06E-03 149,3 6,6 149,3 6,6
oh2_1 375 3,70E-03 149,2 9,6 149,2 9,6
oh2_1 400 3,31E-03 145,6 10,6 145,6 10,6
oh2_1 425 3,19E-03 145,8 9,7 145,8 9,7
oh2_1 450 2,88E-03 157,1 -17,7 157,1 -17,7
oh2_1 475 2,51E-03 150,5 -0,9 150,5 -0,9
oh2_1 500 3,02E-03 145,3 25,6 145,3 25,6
oh2_1 525 1,86E-03 140 4,1 140 4,1
oh2_1 550 1,42E-03 163,3 47,1 163,3 47,1
oh2_1 575 1,26E-03 189,7 -45,9 189,7 -45,9
oh2_1 600 1,38E-03 131,8 32,2 131,8 32,2
oh2_1 625 9,04E-04 144,5 0,4 144,5 0,4
oh2_1 650 1,28E-03 57,8 -46,3 57,8 -46,3
oh2_1 675 9,45E-04 81,7 31,7 81,7 31,7
oh2_6 0 3,19E-04 324 -40,5 324 -40,5
oh2_6 100 2,91E-04 333,8 -24,4 333,8 -24,4
oh2_6 150 2,28E-04 307 -55,8 307 -55,8
oh2_6 200 2,94E-04 329 -47,2 329 -47,2
oh2_6 225 2,91E-04 330,3 -51,8 330,3 -51,8
oh2_6 250 2,52E-04 329,4 -43,9 329,4 -43,9
oh2_6 275 2,80E-04 342,2 -47,7 342,2 -47,7
oh2_6 300 1,91E-04 0,6 -24,9 0,6 -24,9
oh2_6 325 2,80E-04 345,5 -49,8 345,5 -49,8
oh2_6 350 2,56E-04 334,3 -46,1 334,3 -46,1
oh2_6 375 2,51E-04 357,2 -19,5 357,2 -19,5
oh2_6 400 2,45E-04 342 -50,9 342 -50,9
oh2_6 425 4,57E-04 285,3 -46,2 285,3 -46,2
oh2_6 450 1,42E-03 215,4 60,7 215,4 60,7
oh2_6 475 3,72E-04 305,6 -23 305,6 -23
oh2_6 500 2,65E-04 19,8 15,4 19,8 15,4
oh2_6 525 1,15E-03 233,9 -57,4 233,9 -57,4
oh2_6 550 9,81E-04 239,6 -55,1 239,6 -55,1
oh2_6 575 5,94E-04 238,9 4,3 238,9 4,3
oh2_6 600 1,17E-03 204,1 -78,9 204,1 -78,9
oh2_6 625 5,25E-04 198,7 1 198,7 1
oh2_6 650 1,84E-04 168,2 -1,4 168,2 -1,4
oh2_6 675 1,51E-03 94,9 -75,1 94,9 -75,1
S409 0 3,18E-03 127,66 29,577 123,9 31,5
S409 100 2,77E-03 118,97 22,299 134,4 26,2
S409 150 1,58E-03 101,14 34,884 124,5 8,5
S409 200 1,04E-03 133,57 56,899 95,1 21,2
S409 250 1,00E-03 152,05 47,115 93,2 36
S409 300 1,78E-03 177,54 23,442 75,4 65,4
S409 350 9,79E-04 187,63 15,892 46,3 71,5
S409 400 2,81E-04 120,5 47,715 107,9 19,2
S409 400 4,07E-04 199,47 72,406 64 15,6
S409 425 1,29E-03 159,94 24,897 105,5 57,6
S409 450 1,55E-03 247,29 60,587 42,6 10
S409 475 1,18E-03 259,74 52,077 32,6 5,5
S409 500 1,52E-03 231,99 43,643 30,7 25,7
S409 550 1,23E-03 256,27 53,501 34,4 7,3
S409 575 1,58E-03 276,24 44,264 24,4 -5,2
S409 600 1,69E-03 236,2 48,664 34,1 20,8
S409 625 1,02E-03 288,31 -30,186 308,3 -15,2
S409 650 5,92E-04 181,5 -25,735 253,2 65,2
S436 0 2,85E-03 71,501 5,6375 140,5 -17,4
S436 100 2,72E-03 60,096 -8,673 154,4 -30,6
S436 150 2,82E-03 47,056 -12,267 158,3 -43,5
S436 200 2,90E-03 49,376 -22,075 171,3 -40,5
S436 250 2,81E-03 53,606 -19,749 167,7 -36,9
S436 300 2,50E-03 44,912 -22,726 173,1 -44,5
S436 350 2,39E-03 40,938 -23,304 175,1 -47,9
S436 400 2,78E-03 31,122 -27,15 185,9 -54,9
S436 450 2,89E-03 24,744 -28,761 193,9 -58,8
S436 475 2,77E-03 36,69 -23,383 176,9 -51,6
S436 500 2,96E-03 48,25 -14,091 160,8 -42,3
S436 525 2,53E-03 40,32 -16,528 165,2 -49,8
S436 550 2,84E-03 44,883 -13,289 159,9 -45,6
S436 575 2,26E-03 40,31 -22,15 173,7 -48,8
S436 600 3,55E-03 41,898 -35,884 191,5 -42,7
S436 625 3,19E-03 37,809 -17,127 166,7 -52,1
S436 650 2,43E-03 17,763 -0,23621 126,2 -70,7
S436 650 8,64E-04 202,32 0,33168 311,1 66,5
S436 675 1,00E-03 38,279 -50,697 209,6 -36,9
S453 0 1,54E-03 141,82 61,17 77,7 21,3
S453 100 1,37E-03 136,84 58,955 81,2 21,2
S453 150 9,11E-04 126,54 51,841 91,1 20,7
S453 200 8,11E-04 98,242 44,452 104,2 5,2
S453 250 6,28E-04 105,56 58,534 89,5 7,2
S453 300 7,90E-04 57,636 51,56 93 -20,3
S453 350 6,49E-04 35,142 70,289 70,7 -17
S453 400 6,18E-04 252,55 27,049 357,4 15
S453 425 4,73E-04 229,96 37,342 14,3 30,1
S453 450 4,83E-04 154,28 28,038 97,4 51,9
S453 475 6,59E-04 53,276 76,2 70,2 -9,2
S453 500 5,51E-04 171,54 57,124 64,4 31,5
S453 550 1,53E-03 1,7993 68,057 59,7 -22,9
S453 575 7,12E-04 330,96 32,346 20,9 -48,4
S453 600 7,37E-04 13,285 66,327 64,8 -24
S453 625 7,67E-04 110,65 79,56 68,8 2,7

Table2. Thermal demagnetization data
(1) Sample = sample name
(2) Temperature (°C)
(3) NRM intensity (A/m)
(4) Core Declination (°E)
(5) Core Inclination (°)
(6) Geographic Declination (°E)
(7) Geographic Inclination (°)

S453 650 3,06E-04 47,203 -16,106 171,3 -40,4
S453 675 1,58E-04 77,758 21,681 127,1 -11,7
S471 0 7,73E-04 307,2 20,441 353,1 -34,5
S471 100 7,51E-04 279,93 8,6577 336,8 -9,8
S471 150 6,62E-04 250,85 -16,763 310,3 18,3
S471 200 7,86E-04 269,92 -17,558 310,4 0,1
S471 250 7,74E-04 274,35 -27,725 300,2 -3,9
S471 300 8,43E-04 274,56 -29,962 298 -3,9
S471 350 8,36E-04 252,9 -21,985 305,1 15,8
S471 400 9,23E-04 269,4 -21,95 306 0,6
S471 450 1,02E-03 279,23 -14,844 313 -8,9
S471 475 1,02E-03 261,04 -14,185 313,6 8,7
S471 500 1,04E-03 263,56 -5,8558 322,1 6,4
S471 525 9,03E-04 261,74 -23,367 304,4 7,6
S471 550 6,52E-04 298,11 23,397 354,1 -25,6
S471 575 1,66E-03 278,54 -50,985 276,7 -5,4
S471 600 6,24E-04 245,18 -32,042 293,4 20,8
S471 625 6,22E-04 263,62 -32,912 294,9 5,3
S471 650 5,25E-04 257,15 10,198 338,5 12,6
S471 675 2,69E-04 113,63 -86,272 234,6 1,5
S486 0 1,09E-03 154,27 43,339 96,3 49,9
S486 100 7,79E-04 114,52 -2,7956 164,5 23,6
S486 150 6,48E-04 117,38 -34,307 197,3 16
S486 200 4,81E-04 117,96 -43,33 205,8 12,5
S486 250 4,81E-04 163,27 -37,382 229,6 40,1
S486 300 4,95E-04 74,148 -31,698 187,2 -18,7
S486 350 1,77E-04 86,332 -47,296 203,6 -9,8
S486 400 3,75E-04 67,949 -76,856 234,4 -14,7
S486 425 5,60E-04 154,4 -70,674 238,7 7,5
S486 450 4,51E-04 122,88 -74,837 234,3 -1,6
S486 475 7,50E-04 194,01 -39,58 260,8 38,7
S486 500 5,43E-04 246,13 -62,903 271,6 1,5
S486 525 7,03E-04 117,15 -75,563 234,2 -3,2
S486 550 5,68E-04 114,13 -57,452 217,5 4
S486 575 7,20E-04 120,14 -69,608 229,5 0,5
S510 0 1,28E-04 77,814 43,932 126,8 1,2
S510 100 1,94E-04 44,716 -35,76 208,8 -44,5
S510 150 2,62E-04 15,542 -47,88 244,3 -53,7
S510 200 3,33E-04 2,0214 -59,257 260,5 -44,7
S510 250 3,93E-04 43,264 -65,404 242,6 -30,9
S510 300 4,02E-04 36,781 -71,349 249,4 -28,5
S510 350 3,88E-04 306,32 -68,033 281,6 -26,1
S510 400 3,80E-04 343,63 -54,647 275,9 -47,4
S510 450 3,60E-04 325,45 -34,552 312,4 -52,7
S510 475 5,55E-04 309,95 -51,461 297,8 -35,3
S510 500 3,78E-04 311,16 -59,851 288,5 -32
S510 525 4,42E-04 314,82 -59,754 287,4 -33,6
S510 550 7,82E-04 337,93 18,402 47,5 -51
S510 575 7,62E-04 15,043 -5,0446 142,3 -72,7
S510 600 3,29E-04 282,99 -71,058 281,4 -17,4
S510 625 4,33E-04 10,036 -33,357 238,5 -68,6
S510 650 4,25E-04 309,88 -41,89 309 -38,7
S510 675 5,90E-04 12,48 -30,346 228,9 -70
S520 0 1,32E-03 209,34 56,629 46,1 43,7
S520 100 7,05E-04 247,01 43,708 19,4 27,5
S520 150 7,73E-04 259,25 33,699 9 17,6
S520 200 7,16E-04 255,26 33,977 8,9 20,9
S520 250 7,49E-04 254,74 29,853 4,4 20,9
S520 300 7,61E-04 264,64 23,869 359,9 11,2
S520 350 8,44E-04 266,23 17,302 353,7 8,2
S520 400 7,49E-04 267,26 18,198 354,9 7,5
S520 425 8,59E-04 273,26 10,73 349,2 -0,1
S520 450 7,55E-04 260,65 5,5521 340,8 10,5
S520 475 1,12E-03 249,83 4,8126 337,1 20,7
S520 500 6,50E-04 261,77 12,251 347,7 11,1
S520 525 5,90E-04 272,81 -14,138 325,1 -6,5
S520 550 9,74E-04 254,31 -5,4817 328,2 13,4
S520 575 6,95E-04 231,94 -6,5226 318,4 33,9
S520 600 9,82E-04 246,12 -6,6652 324,2 20,8
S520 625 6,28E-04 230,29 -31,19 293,4 22,5
S548 0 1,35E-03 189,04 4,8734 29,4 72,6
S548 100 1,00E-03 186,08 -2,4607 21,9 80,3
S548 150 8,07E-04 178,87 -19,779 234,8 80,2
S548 200 7,77E-04 197,52 -19,86 298,7 70,4
S548 250 7,75E-04 197,17 -22,698 291,2 69,2
S548 300 7,57E-04 200,5 -21,802 297,6 67,1
S548 350 7,51E-04 201,62 -15,929 313 68,1
S548 400 6,93E-04 203,65 -17,559 310,2 65,8
S548 450 7,64E-04 209,17 -7,7481 333,1 61,1
S548 475 6,72E-04 200,25 -20,459 300,4 67,9
S548 500 7,84E-04 205,48 -46,09 267,4 47,9
S548 525 8,79E-04 186,52 -25,687 261,7 73,1
S548 550 5,69E-04 214,57 -8,9948 329,7 55,9
S548 575 7,94E-04 175,86 -29,412 230,3 70,2
S548 600 4,92E-04 219,39 -13,769 321,4 51,3
S548 625 8,10E-04 196,17 -14,946 312 73,5
S548 675 4,64E-04 314,73 17,053 345,2 -45,5
S565 0 4,06E-04 77,905 -17,65 171,8 -14,4
S565 100 7,08E-04 45,135 -32,159 191 -42,9
S565 150 5,99E-04 43,888 -24,052 180,4 -46
S565 200 5,23E-04 42,205 -14,047 165,9 -48,6
S565 250 4,84E-04 26,342 -18,295 177 -63,2
S565 300 4,19E-04 48,196 1,6422 145,1 -40,6
S565 350 5,56E-04 31,285 28,448 103,3 -41,1
S565 400 1,11E-03 42,51 25,063 114,9 -35,7
S565 425 6,54E-04 238,3 -35,183 293,3 18,8
S565 450 6,06E-04 8,4652 4,1625 97,2 -73,5
S565 475 5,76E-04 14,809 3,3834 114,5 -70,1
S565 500 5,74E-04 16,236 7,5131 109,3 -66,2
S565 550 3,29E-04 54,638 36,095 110,9 -21

Table2. Thermal demagnetization data
(1) Sample = sample name
(2) Temperature (°C)
(3) NRM intensity (A/m)
(4) Core Declination (°E)
(5) Core Inclination (°)
(6) Geographic Declination (°E)
(7) Geographic Inclination (°)

S565 575 8,43E-04 21,505 11,289 111,7 -59,8
S565 600 5,97E-04 43,084 16,857 124,1 -39,6
S565 625 7,99E-04 13,942 23,077 88,3 -54,2
S565 650 4,19E-04 286,36 0,41026 339,3 -16
S598 0 5,21E-03 102,36 9,3916 189 13,3
S598 100 4,92E-03 97,502 4,2003 193,7 7,9
S598 150 2,64E-03 89,779 11,14 185,9 1,1
S598 200 2,34E-03 97,431 8,3393 189,5 8,3
S598 250 2,04E-03 97,765 11,319 186,6 8,9
S598 300 2,21E-03 90,528 10,954 186,2 1,8
S598 350 9,60E-04 114,65 8,3284 191,1 25,3
S598 400 5,15E-04 172,91 46,201 114,7 50,3
S598 400 5,25E-04 147,96 52,625 130,9 37,4
S598 425 8,07E-04 85,375 -20,445 216,9 -6,8
S598 450 6,58E-04 95,993 56,407 140,9 9,1
S598 450 3,61E-04 210,53 41,102 73,3 46,4
S598 475 6,43E-04 138,35 35,91 153,6 42,2
S598 500 7,68E-04 149,59 26,446 159,5 55,2
S598 550 6,28E-04 177,38 29,561 112,9 67,3
S598 575 4,35E-04 157,48 18,374 167,5 65,3
S598 600 4,13E-04 140,41 24,638 167,4 48,2
S598 625 3,65E-04 182,92 74,423 106,2 22,6
S598 650 4,05E-04 296,63 3,6838 24,6 -25,9
S605 0 9,57E-04 256,58 19,843 74,9 13,3
S605 100 9,00E-04 269,56 28,757 83,7 1,3
S605 150 1,16E-03 274,87 36,363 91,6 -2,7
S605 200 7,75E-04 294,8 60,905 118,4 -10
S605 250 1,05E-03 275,04 65,079 120,2 -0,3
S605 300 1,06E-03 264,01 32,185 87,2 6,1
S605 350 1,28E-03 288,08 55,357 111,9 -8,5
S605 400 1,24E-03 334,56 60,31 131,5 -24,6
S605 425 1,09E-03 286,96 9,4627 65,5 -16,4
S605 450 1,21E-03 294,02 51,261 109,1 -13,1
S605 475 1,04E-03 282,14 45,458 101,3 -7
S605 500 9,09E-04 269,46 45,935 100,9 1,8
S605 550 1,00E-03 276,24 43,492 98,8 -3,1
S605 575 1,13E-03 300,91 33,668 93,5 -24,1
S605 600 1,28E-03 290,66 39,218 96,5 -14,5
S605 625 1,35E-03 298,26 40,229 99,4 -19,8
S605 650 2,85E-04 334,56 36,694 116 -44,7
S625 0 1,18E-03 229,47 -55,916 357,2 21,4
S625 100 8,01E-04 226,1 -46,521 215,3 28,5
S625 150 5,88E-04 262,52 -70,144 349,7 2,5
S625 200 5,22E-04 260,13 -63,44 356,2 4,4
S625 250 5,86E-04 270,14 -47,213 12,8 -0,1
S625 300 3,22E-04 311,41 -10,926 45,6 -40,5
S625 350 8,06E-04 276,66 -62,64 357,2 -3,1
S625 400 4,09E-04 185,37 -19,735 338,4 67,6
S625 425 1,12E-03 238,08 -28,999 26,9 27,5
S625 450 4,32E-04 234,25 -22,024 33,5 32,8
S625 475 2,39E-04 279,46 -6,7315 53,2 -9,4
S625 500 4,17E-04 265,03 -67,176 352,7 1,9
S625 550 3,46E-04 135,13 -28,834 278 38,4
S625 575 5,30E-04 319,21 -35,147 12,9 -38,2
S625 600 5,21E-04 49,764 -51,584 298,8 -23,7
S663 0 7,70E-04 166,75 19,817 178,1 68
S663 100 6,63E-04 149,97 25,271 191,6 52,9
S663 150 6,70E-04 151,77 22,915 193,4 55,6
S663 200 5,89E-04 152,26 14,946 206,1 59,7
S663 250 5,27E-04 156,52 12,279 208 64,6
S663 300 5,42E-04 164,21 -4,5497 255,6 72,9
S663 350 5,79E-04 150,73 21,068 197,1 55,7
S663 400 4,53E-04 148,26 26,065 191,9 51,2
S663 425 4,34E-04 157,36 20,808 190,9 61
S663 450 5,52E-04 191,78 18,171 108,2 70,1
S663 475 5,92E-04 182,43 6,3025 113,6 85,1
S663 500 4,98E-04 198,07 27,502 110,5 59,2
S663 525 5,46E-04 219,48 38,742 103,6 38,6
S663 550 4,13E-04 162,36 27,42 175 59,5
S663 575 6,37E-04 220,36 8,2196 63,3 49,3
S709 0 1,07E-03 270,85 -79,036 333 -2,1
S709 100 8,08E-04 320,94 -70,74 334,5 -16,8
S709 150 7,00E-04 337,04 -42,878 352,5 -44,3
S709 200 7,53E-04 319,73 -40,312 0,2 -37,2
S709 250 7,30E-04 324,39 -41,548 356,2 -39,1
S709 300 7,13E-04 323,19 -36,799 1,8 -41,4
S709 350 9,16E-04 324,74 -38,313 359,2 -41,4
S709 400 7,94E-04 324,54 -36,813 0,9 -42,3
S709 450 7,32E-04 307,84 -23,695 24,2 -35,1
S709 475 5,25E-04 314,91 -30,313 13,7 -38,8
S709 500 8,19E-04 335,88 -16,319 19,5 -62,3
S709 525 1,02E-03 318,08 -14,603 32,7 -46,8
S709 550 1,12E-03 327,12 -10,778 35,5 -56,2
S709 575 2,33E-04 266,78 -72,238 339,7 -0,9
S709 600 5,85E-04 321,68 -30,303 10,1 -44
S709 625 9,53E-04 332,7 -18,287 18,9 -58,7
S709 650 8,45E-04 14,573 -27,257 294,4 -61,1
S709 675 6,43E-04 258,15 62,979 115,4 7,1
S762 0 7,83E-04 248,23 -3,2944 38,5 20,4
S762 100 4,16E-04 231,86 5,238 43,4 38,3
S762 150 4,89E-04 232,15 -1,7574 35 36,2
S762 200 6,40E-04 232,16 -12,552 22,8 32,3
S762 250 6,27E-04 259,05 2,7419 47,2 11,3
S762 300 6,64E-04 260,81 -2,8472 42,1 8,3
S762 350 7,09E-04 261,86 18,85 63,9 11,7
S762 400 8,11E-04 267,62 26,83 72,8 7,9
S762 425 1,25E-03 265,52 39,139 84,9 11,6
S762 450 6,31E-04 252,95 11,984 190,2 12,9
S762 450 2,78E-03 96,311 38,232 55,4 19
S762 475 6,91E-04 282,46 16,478 66 -7,9

Table2. Thermal demagnetization data
(1) Sample = sample name
(2) Temperature (°C)
(3) NRM intensity (A/m)
(4) Core Declination (°E)
(5) Core Inclination (°)
(6) Geographic Declination (°E)
(7) Geographic Inclination (°)

S762 500 7,04E-04 269,05 19,076 65,4 5,1
S762 550 6,47E-04 272,21 16,068 63,1 1,5
S762 575 8,17E-04 223,33 33,764 82,4 45,6
S762 600 9,00E-04 284,41 9,3373 59,6 -11,7
S762 625 8,04E-04 289,78 22,681 74,2 -12,6
S762 650 2,17E-04 3,4602 7,6681 146,6 -69
S762 675 3,17E-04 46,548 7,796 205,4 -39,3
S810 0 5,80E-04 324,78 -48,691 326,9 -44
S810 100 5,31E-04 343,96 -37,076 323 -62
S810 150 4,73E-04 357,93 -20,303 309,9 -82,4
S810 200 4,84E-04 353,93 -12,64 27,8 -84,1
S810 250 5,05E-04 358,82 -16,316 313,9 -86,5
S810 300 4,42E-04 2,0309 -16,826 268,1 -85,7
S810 350 3,56E-04 2,5448 -27,623 286,1 -75,2
S810 400 5,45E-04 350,61 -11,761 31,7 -80,7
S810 450 5,57E-04 316,04 -12,76 20,2 -47,2
S810 475 4,23E-04 332,24 30,266 83,8 -39,1
S810 500 5,58E-04 9,8569 -10,018 188,9 -79,9
S810 525 7,61E-04 19,071 -30,643 253,1 -65,1
S810 550 7,23E-04 355,07 18,296 106,1 -58,3
S810 575 5,20E-04 321,98 -19,91 9,1 -53
S810 600 8,05E-04 10,399 -35,714 274,4 -65,4
S810 625 3,53E-04 9,9792 -11,43 196,9 -80,1
S810 650 7,63E-04 325,93 4,8851 50,7 -51,7
S810 675 1,57E-04 120,2 56,613 147,3 27,2
S863 0 6,15E-04 90,194 -16,521 223,4 -5,9
S863 100 4,68E-04 115,29 -25,052 241,3 11,6
S863 150 4,80E-04 120,92 -14,467 234,7 21,6
S863 200 2,97E-04 117,5 -21,976 239,7 14,9
S863 250 3,69E-04 132,18 -20,766 236,5 38
S863 300 3,17E-04 33,286 29,867 151 -29,1
S863 350 7,16E-04 131,81 -50,297 269,4 6,1
S863 400 6,69E-04 153,94 -52,962 282,3 11,7
S863 425 3,56E-04 127,97 24,587 194,2 42,4
S863 425 3,80E-04 130,79 27,457 190,6 45,2
S863 450 1,39E-04 63,104 -56,298 261,8 -33
S863 475 3,14E-04 72,374 2,3728 198,9 -15,4
S863 500 1,24E-04 16,684 -53,549 280,2 -56
S863 550 3,83E-04 56,894 -5,8473 200,5 -32,8
S863 575 8,55E-04 87,996 14,012 194,3 3,4
S863 600 2,62E-04 136,58 -28,002 256,1 24,8
S939 0 7,38E-04 165,7 -3,2624 273,2 60,3
S939 100 6,76E-04 143,89 -10,837 252,8 41,1
S939 150 4,47E-04 121,52 -18,247 243,8 19,6
S939 200 4,57E-04 113,65 -10,85 233 16,8
S939 250 4,28E-04 122,09 3,3485 223,3 30,7
S939 300 5,03E-04 107,78 7,8919 212,5 19,4
S939 350 6,14E-04 125,92 -1,6801 230,6 31,9
S939 400 7,78E-04 105,75 -15,893 233,9 7,7
S939 450 6,19E-04 127,85 -0,46258 230,4 34,2
S939 475 6,17E-04 133,1 -14,944 248,1 30,5
S939 500 6,24E-04 98,587 -14,955 230,1 1,8
S939 525 8,97E-04 165,23 40,454 155,1 68,6
S939 550 7,32E-04 145,66 -4,3068 247,8 46,8
S939 575 9,77E-04 102,72 18,384 200,3 18,4
S939 600 6,80E-04 136,91 -4,4712 240,6 39,8
S939 625 6,71E-04 119,5 8,1411 217 30,3
S939 650 6,15E-04 127,52 -2,4246 232,2 32,9
S939 675 4,09E-04 165,21 4,6299 262,9 66,7
S987 0 1,08E-03 201,89 26,94 64,6 68,4
S987 100 4,49E-04 196,97 -20,316 332,8 47,3
S987 150 1,47E-04 185,67 -15,839 318,5 54,7
S987 200 4,19E-04 190,44 -8,926 330,1 60,2
S987 250 7,29E-05 191,8 -34,335 321 35,5
S987 300 1,03E-04 118,7 27,057 198,6 33,5
S987 350 4,17E-04 238,88 63,529 102,7 30,6
S987 400 5,11E-04 146,22 -5,2763 251,8 48,8
S987 400 3,56E-04 211,7 47,645 94,3 51,5
S987 425 3,30E-04 252,29 -40,714 355,2 0,3
S987 475 3,15E-04 203,42 10,793 22,4 66
S987 500 3,91E-04 196,03 15,436 28,4 74,3
S987 550 3,44E-04 161,34 44,06 156,8 60,5
S987 575 1,32E-04 184,72 51,333 123,5 57,5
S987 600 3,81E-04 200,4 -6,0287 349,7 57,9
S1044 0 1,10E-03 242,74 -25,888 18,3 16
S1044 100 8,52E-04 264,78 -30,143 21,6 -3,6
S1044 150 7,89E-04 268,58 -39,797 13,1 -9,1
S1044 200 6,61E-04 277,26 -41,998 12,1 -15,9
S1044 250 7,31E-04 280,69 -41,87 12,5 -18,5
S1044 300 7,54E-04 282,24 -38,629 16 -19,3
S1044 350 7,70E-04 279,38 -42,867 11,3 -17,6
S1044 400 7,02E-04 283,38 -31,893 23,2 -19,5
S1044 450 6,32E-04 307,91 -41,263 11,5 -38,7
S1044 475 5,84E-04 291,4 -30,884 25 -26,3
S1044 500 6,63E-04 291,76 -33,919 21,6 -26,7
S1044 525 5,75E-04 314,63 -19,494 40,4 -46,8
S1044 550 5,87E-04 278,85 -49,177 4,7 -17,8
S1044 575 4,61E-04 274,03 -22,053 31,6 -9,6
S1044 600 5,19E-04 283,83 -38,607 16,1 -20,6
S1044 625 6,60E-04 295,63 -28,9 27,5 -29,8
S1044 650 5,84E-04 317,97 -47,305 0,7 -43,4
S1044 675 6,53E-04 37,852 -10,672 228,6 -52,8
S1099 0 7,98E-04 235,71 26,266 70,8 37,1
S1099 100 6,48E-04 307,77 15,759 77,6 -29,9
S1099 150 6,33E-04 308,66 13,713 76 -31,7
S1099 200 5,05E-04 329,69 8,3186 84,8 -52
S1099 250 5,35E-04 330,72 8,1657 85,7 -52,9
S1099 300 4,86E-04 335,71 5,5485 87,7 -58,4
S1099 350 4,68E-04 333,27 -13,333 49,3 -64
S1099 400 5,03E-04 306,09 -16,028 40,2 -38,2

Table2. Thermal demagnetization data
(1) Sample = sample name
(2) Temperature (°C)
(3) NRM intensity (A/m)
(4) Core Declination (°E)
(5) Core Inclination (°)
(6) Geographic Declination (°E)
(7) Geographic Inclination (°)

S1099 425 6,54E-04 319,34 0,43815 66,4 -47
S1099 450 4,26E-04 321,19 -14,257 45 -52,5
S1099 475 5,84E-04 313,98 -28,4 23,5 -45,5
S1099 500 6,22E-04 302,14 -36,249 15 -34,6
S1099 525 7,53E-04 286,21 -25,989 26,5 -20,8
S1099 550 4,17E-04 265,46 -20,336 28,2 -1
S1099 575 5,73E-04 258,48 -23,543 23,3 4,2
S1099 600 4,78E-04 282,12 -29,879 21,9 -17,7
S1099 625 3,67E-04 203,2 -29,232 345,8 40,4
S1171 0 4,32E-04 115,5 33,575 190,7 24,5
S1171 100 4,40E-04 113,43 26,894 198,2 23,6
S1171 150 5,10E-04 105,17 16,407 209,6 16,2
S1171 200 4,84E-04 104,43 19,055 206,9 15,6
S1171 250 4,72E-04 106,56 10,995 215,3 17,3
S1171 300 4,70E-04 111,42 26,841 198,5 21,8
S1171 350 3,60E-04 128,56 -3,3444 234 37,8
S1171 400 4,27E-04 112,79 20,419 205,3 23,4
S1171 450 4,35E-04 117,29 35,605 188,2 25,6
S1171 475 3,68E-04 145,84 42,723 169 42,5
S1171 500 4,51E-04 116,15 46,453 176,9 22,2
S1171 525 3,27E-04 138,19 48,715 167,3 34,6
S1171 550 4,51E-04 163,5 60,051 144,9 34,5
S1171 575 3,93E-04 151,77 30,721 178,5 53,8
S1171 600 5,51E-04 110,52 -25,705 253,8 15,6
S1171 625 5,81E-04 297,39 80,735 126,8 1,7
S1171 650 3,23E-04 236,75 76,962 123,8 13
S1171 675 1,13E-04 13,034 14,341 167,3 -65,9
S1238 0 2,72E-04 350,28 47,585 109,2 -32,8
S1238 100 3,55E-04 351,55 38,127 108 -42,2
S1238 150 3,34E-04 359,45 51,205 116,6 -29,8
S1238 200 3,93E-04 7,9243 45,45 123,8 -35,1
S1238 250 3,81E-04 349,11 23,655 99,1 -55,7
S1238 300 3,98E-04 347,01 39,616 103,9 -39,9
S1238 350 2,74E-04 275,13 55,157 82,2 4,5
S1238 400 9,27E-04 335,01 75,813 111 -3,9
S1238 425 2,53E-04 284,42 0,22649 29,5 -14,2
S1238 450 3,98E-04 299,86 62,046 92,9 -5,3
S1238 475 6,16E-04 325,45 46,385 91,1 -26,6
S1238 500 7,44E-04 339,47 51,92 103 -26,6
S1238 550 4,75E-04 324,59 40,584 86,2 -30,6
S1281 0 4,24E-04 65,818 20,275 199,2 -18,1
S1281 100 4,90E-04 62,613 17,459 200,9 -21,9
S1281 150 5,72E-04 53,835 14,997 200,1 -30,7
S1281 200 5,92E-04 60,984 13,867 204 -24,6
S1281 250 5,28E-04 62,34 13,015 205,4 -23,6
S1281 300 5,43E-04 61,692 12,774 205,4 -24,3
S1281 350 5,35E-04 64,316 11,966 207,1 -22,1
S1281 400 5,51E-04 64,007 26,618 192,4 -17,4
S1281 450 5,13E-04 57,837 13,178 203,6 -27,7
S1281 475 4,69E-04 35,495 5,8718 201,2 -50,8
S1281 500 5,64E-04 25,044 26,223 167,8 -45,5
S1281 525 6,60E-04 28,59 4,5168 197,9 -57,6
S1281 550 3,59E-04 68,824 5,2796 215,3 -19,6
S1281 575 4,76E-04 51,746 13,115 201,2 -33,3
S1281 600 1,98E-04 86,077 27,676 197,1 1,7
S1281 625 2,05E-04 46,763 51,878 162,8 -15,4
S1281 650 5,54E-04 59,017 22,632 194,4 -23,1
S1281 675 1,48E-04 165,43 -34,479 298,7 42,5
S1309 0 2,97E-04 212,72 -5,7877 8,4 45,7
S1309 100 2,98E-04 228,01 -74,291 330 -14
S1309 150 3,16E-04 29,745 -87,079 316,4 -27,5
S1309 200 3,14E-04 25,641 -79,824 312,7 -34,1
S1309 250 2,65E-04 28,413 -74,842 308,9 -38,1
S1309 300 2,91E-04 104,88 -76,83 304,4 -21
S1309 350 2,52E-04 71,565 -82,791 310,3 -27,1
S1309 400 2,04E-04 181,97 -73,506 318,6 -8,5
S1309 425 2,17E-04 62,7 -80,741 308,6 -28,9
S1309 450 1,67E-04 194,43 -32,655 332,1 30,7
S1309 475 2,68E-04 300,4 -71,033 337,6 -33,3
S1309 500 3,51E-04 242,51 -19,444 17,9 14,7
S1309 525 3,93E-04 315,12 -34,015 24,1 -50,2
S1353 0 1,84E-04 149,23 -18,584 276,9 44,8
S1353 100 4,01E-04 116,27 64,27 165,4 24,8
S1353 150 3,77E-04 76,122 45,895 182,5 1,4
S1353 200 2,31E-04 74,784 55,854 172,9 4,1
S1353 250 3,23E-04 47,346 -24,525 249,8 -44,7
S1353 300 7,28E-04 11,388 5,6772 169,4 -66,4
S1353 350 4,27E-04 243,17 -24,168 18,3 17
S1353 400 6,17E-04 90,928 -45,522 274,7 -10
S1353 425 5,28E-04 322,79 -39,638 5,5 -49,2
S1353 450 2,13E-04 16,798 58,685 148,9 -15
S1353 475 1,49E-04 351,25 57,94 135,2 -16,7
S1353 500 2,78E-04 344,34 -36,921 349,5 -64
S1353 525 3,12E-04 345,47 3,8637 101,5 -66,3
S1353 550 5,66E-04 182,01 40,968 136,5 64
S1353 575 3,21E-04 33,838 47,84 163,5 -20,3
S1375 0 6,40E-04 211,98 -30,915 353,2 25,4
S1375 100 4,92E-04 232,25 -56,074 349,2 -3,2
S1375 150 4,04E-04 222,98 -63,508 340,8 -5,7
S1375 200 4,23E-04 236,71 -62,032 346,4 -9
S1375 250 3,92E-04 230,6 -62,497 344,1 -7,2
S1375 300 3,70E-04 250,65 -61,208 350,9 -13,9
S1375 350 3,56E-04 276,64 -57,701 358,9 -25,2
S1375 400 3,27E-04 263,53 -64,311 350,4 -20,6
S1375 450 2,58E-04 290,27 -43,332 16,4 -31,8
S1375 475 4,35E-04 265,24 -46,207 358,8 -4,7
S1375 500 4,53E-04 257,21 -68,346 345,4 -19,5
S1375 525 5,75E-04 281,13 13,468 70 -3,8
S1375 550 4,68E-04 343,97 -14,613 87,1 -71,2
S1375 575 4,10E-04 326,1 -25,121 47,1 -59,5

Table2. Thermal demagnetization data

(1) Sample = sample name

(2) Temperature (°C)

(3) NRM intensity (A/m)

(4) Core Declination (°E)

(5) Core Inclination (°)

(6) Geographic Declination (°E)

(7) Geographic Inclination (°)

S1375 600 2,26E-04 313,36 -8,9266 65,4 -42,7
S1375 625 4,42E-04 214,41 -41,523 349 15,3
S1375 650 7,26E-04 298,12 -11,683 54,3 -30,2
S1375 675 1,07E-04 84,652 -65,759 296 -25,7
S1436 0 6,34E-04 242,8 -67,49 349,2 -8,7
S1436 100 2,26E-04 292,04 -38,92 24,8 -29,3
S1436 150 2,56E-04 262,23 -17,498 39,9 1
S1436 200 3,52E-04 286,4 -33,423 30,4 -24,2
S1436 250 5,04E-04 343,17 -64,842 338,8 -43,8
S1436 300 5,04E-04 254,07 -12,716 41,4 10,2
S1436 350 5,49E-04 317,01 -72,919 342,6 -31,9
S1436 400 5,94E-04 299,53 8,0289 78,1 -24,3
S1436 425 3,28E-04 220,99 -39,419 1,5 19,3
S1436 450 4,28E-04 299,05 -30,001 35,7 -34,5
S1436 475 2,73E-04 316,23 -32,776 31,6 -49,1
S1436 500 1,94E-04 305,98 -32,497 32,8 -40,5
S1436 550 2,35E-04 290,07 -8,056 58 -21,5
S1436 575 3,75E-04 291,83 -4,2838 62,5 -22
S1436 600 2,53E-04 320,55 10,704 93,8 -40,5
S1436 625 8,45E-05 233,13 -52,452 358,3 4,2
S1525 0 1,37E-03 195,66 10,324 5 63,1
S1525 100 6,50E-04 180,35 -5,0346 329,6 52
S1525 150 5,96E-04 158,52 8,1034 285,6 58,1
S1525 200 1,24E-04 120,05 3,1486 253,7 26,7
S1525 250 2,24E-04 122,93 -13,606 269,7 18,4
S1525 300 2,17E-04 64,29 -34,158 259,3 -37,4
S1525 350 1,80E-04 146,68 -25,118 296,1 23,8
S1525 400 1,53E-04 92,265 -57,947 292,7 -26,4
S1525 450 2,28E-04 108,43 -55,265 294,5 -17,2
S1525 475 2,88E-04 350,85 -65,478 336 -57,1
S1525 500 3,40E-04 118,98 32,53 221,8 39,5
S1525 525 1,12E-03 166,7 -74,446 325,3 -17,8
S1525 550 2,46E-04 84,13 -29,153 261,5 -19,9
S1525 575 5,88E-04 131,16 -9,4875 272,5 27
S1525 600 3,84E-04 202,21 -41,372 345,9 12,9
S1525 625 3,14E-04 212,01 -21,466 2,8 27,6
S1525 650 5,24E-04 74,34 -61,701 294,7 -35,9
S1525 675 4,64E-04 266,2 -44,413 18,3 -20
S1569 0 3,59E-03 184,48 -38,35 332,4 37,5
S1569 100 1,60E-03 186,94 -52,316 332,6 23,4
S1569 150 1,48E-03 52,643 -48,124 287,6 -35
S1569 200 2,05E-03 167,43 -45,527 317,9 29,4
S1569 250 1,05E-03 148,83 -46,785 305,3 23,1
S1569 300 1,78E-03 116,88 -30,755 275,6 14,7
S1569 350 1,01E-03 345,2 -63,406 336,5 -39,5
S1569 400 1,54E-03 51,756 -70,403 311 -25,4
S1569 425 1,31E-03 254,49 -49,784 6,5 -1
S1569 450 6,69E-04 14,83 -40,643 304,9 -60,4
S1569 475 7,86E-04 42,332 -59,849 303,7 -34,7
S1569 500 1,03E-03 60,601 -64,067 303,1 -25,2
S1569 550 8,82E-04 44,268 -46,338 288,4 -40,9
S1569 575 1,20E-03 55,244 -84,271 323,1 -17,2
S1569 600 7,71E-04 69,896 -54,757 292 -23
S1569 625 9,50E-04 68,153 -60,888 298,7 -22,8
S1569 650 2,59E-04 6,2178 2,2152 169,3 -72,7
S1589 0 8,68E-04 200,44 14,824 29,3 68,7
S1589 100 8,00E-04 201,67 45,526 107,2 62,3
S1589 150 7,71E-04 205,89 46,231 104,4 59,6
S1589 200 8,30E-04 214,16 42,428 92,6 56,3
S1589 250 4,50E-04 224,78 34,536 76,8 49,9
S1589 300 7,19E-04 195,63 44,094 112,4 66,2
S1589 350 2,07E-04 201,04 61,952 125,9 49,5
S1589 400 7,95E-04 220,38 69,314 123,9 38,8
S1589 425 6,79E-04 190,32 50,738 127 62,1
S1589 450 5,03E-04 216,37 23,303 57,3 56,8
S1589 475 6,13E-04 220,57 48,913 99,6 49,7
S1589 500 6,45E-04 212,6 50,706 106,1 53,3
S1589 550 7,33E-04 221,28 45,646 94,6 50,4
S1589 575 4,05E-04 176,27 46,942 147,5 66,9
S1589 600 7,13E-04 191,18 43,648 118,7 68,3
S1599 0 1,18E-02 202,62 -19,041 359,7 40,8
S1599 100 3,06E-03 217,65 16,536 54,9 53,9
S1599 150 3,04E-03 216,07 8,5132 41,7 51,9
S1599 200 1,54E-03 254,87 35,701 90,3 26
S1599 250 1,50E-03 259,25 35,645 91,2 22,6
S1599 300 1,38E-03 258,51 36,373 91,8 23,3
S1599 350 1,34E-03 273,57 49,724 108,7 16,6
S1599 400 1,02E-03 278,9 36,027 97,3 7,8
S1599 425 1,90E-03 279,43 29,971 92 4,7
S1599 450 1,54E-03 271,04 41,307 99,8 15,5
S1599 475 1,28E-03 283,65 43,891 106 8
S1599 500 1,48E-03 284,28 31,876 95,6 1,9
S1599 525 1,45E-03 293,4 7,9048 78,7 -17,4
S1599 550 1,16E-03 301,33 40,503 110,3 -4,8
S1599 575 1,31E-03 312,17 37,991 114,2 -12,7
S1599 600 8,88E-04 256,27 44,216 99,8 26,7
S1634 0 2,01E-02 200,37 -33,391 356,8 35,1
S1634 100 5,72E-03 193,52 6,2211 25,9 72,3
S1634 150 4,51E-03 300,79 49,85 122,3 -4,5
S1634 200 4,26E-03 143,28 24,522 228,7 55,3
S1634 250 3,84E-03 129,26 48,444 197,4 39,1
S1634 300 6,54E-03 197,98 12,716 51,6 71,9
S1634 350 1,36E-03 180,59 -7,4998 330,3 62,5
S1634 400 4,18E-03 180 77,991 156 30
S1634 425 3,72E-03 180,78 78,689 155,8 29,3
S1634 450 2,53E-03 195,03 63,774 147 43,1
S1634 475 1,30E-03 203,28 34,373 108,9 63,6
S1634 500 1,16E-03 164,66 69,523 162,7 37,6
S1634 550 1,14E-03 40,397 76,189 165 7,3
S1634 575 1,04E-03 243,43 84,815 151,1 20,3

Table2. Thermal demagnetization data

(1) Sample = sample name

(2) Temperature (°C)

(3) NRM intensity (A/m)

(4) Core Declination (°E)

(5) Core Inclination (°)

(6) Geographic Declination (°E)

(7) Geographic Inclination (°)

S1634 600 9,98E-04 52,181 68,729 172,7 4,4
S1634 625 1,68E-03 52,846 77,569 166 10,3
S1634 650 1,05E-03 1,3744 8,0816 159,1 -63,9
S1701 0 1,80E-02 194,31 0,19056 13,8 67,3
S1701 100 7,29E-03 193,28 -11,632 358,8 57,6
S1701 150 3,28E-03 264,69 -55,953 8,7 -11,9
S1701 200 1,46E-03 190,41 -26,451 347,1 44,4
S1701 250 4,62E-03 216,52 -55,952 353,8 9,9
S1701 300 4,94E-03 180,94 -42,535 334,8 29,5
S1701 350 4,12E-03 172,5 -46,532 328,3 25,1
S1701 400 4,12E-03 251,9 -82,363 341,5 -15,5
S1701 425 1,82E-03 222,68 -21,308 22,6 32,6
S1701 450 8,45E-04 212,87 31,533 94,8 57,4
S1701 475 7,96E-04 187,37 -21,531 344,7 49,8
S1701 500 4,40E-04 208,08 -27,918 5,2 36,6
S1701 550 3,19E-04 141,25 17,12 239,3 53,1
S1701 575 6,18E-04 267,67 6,1302 69,1 4,1
S1701 600 4,29E-04 224,37 41,659 105,8 45,5

OH3-A

3OH28 0 6,00E-04 185,27 3,7281 278,9 69,1
3OH28 100 4,65E-04 173,39 30,668 123,9 81,1
3OH28 150 4,24E-04 169,73 37,487 114,7 73,9
3OH28 200 4,72E-04 157,99 39,275 129,4 65,9
3OH28 250 3,91E-04 155,22 54,146 109,1 54,6
3OH28 300 4,44E-04 144,38 40,41 136,5 56
3OH28 350 4,57E-04 150,61 45,895 123,8 57,8
3OH28 400 5,34E-04 171,11 26,337 155,9 81,6
3OH28 425 3,75E-04 146,47 57,233 111,1 49
3OH28 450 3,41E-04 155,71 43,342 123,9 62,2
3OH28 475 2,02E-04 55,125 78,516 93,8 17,1
3OH28 500 4,34E-04 133,88 48,312 128,1 46,5
3OH28 550 3,71E-04 170,73 36,571 114,2 75,1
3OH28 575 3,64E-04 104,4 31,795 148,3 24
3OH28 600 2,69E-04 156,44 23,172 171,4 68,4
3OH28 625 2,75E-04 189,95 65,07 77,7 48,4
3OH51 0 4,39E-04 196,21 36,951 48,6 62
3OH51 100 2,50E-04 165,07 -82,864 255,2 -6,1
3OH51 150 2,58E-04 171,38 -82,572 255,9 -5,7
3OH51 200 1,40E-04 131,69 -20,934 202 31,7
3OH51 250 2,16E-04 123,07 -24,607 201,2 22,9
3OH51 300 3,27E-04 133,33 -27,078 208,9 29,5
3OH51 350 5,72E-05 118,83 -18,234 193,1 22,1
3OH51 400 1,68E-04 102,06 -38,069 206,6 1,2
3OH51 425 7,42E-05 13,317 8,5262 109,3 -64,7
3OH51 450 1,48E-04 47,931 -35,467 203,2 -41,5
3OH51 475 1,72E-04 111,61 -4,6797 176,9 19,8
3OH51 500 2,67E-04 66,65 -41,605 207,2 -26
3OH51 525 1,53E-04 58,25 -12,047 173 -33,3
3OH94 0 8,62E-04 293,09 16,645 3 -15,2
3OH94 100 5,94E-04 308,48 5,6968 359,8 -33,6
3OH94 150 6,02E-04 308,99 2,9537 357,1 -35,3
3OH94 200 6,22E-04 307,55 -2,0262 350,8 -36
3OH94 250 7,41E-04 315,71 2,3203 0,2 -41,5
3OH94 300 6,09E-04 310,92 -5,1849 348,6 -40,3
3OH94 350 5,55E-04 311,93 3,2042 359 -37,8
3OH94 400 5,84E-04 311,18 3,3362 358,7 -37,1
3OH94 450 6,67E-04 311,9 3,1781 358,9 -37,8
3OH94 475 5,08E-04 304,25 1,3528 353 -31,6
3OH94 500 5,93E-04 302,32 -0,67646 349,9 -30,6
3OH94 525 7,26E-04 282,81 10,803 353,5 -8,3
3OH94 550 6,50E-04 300,86 27,078 16,2 -16,5
3OH94 575 8,52E-04 325,56 -13,362 343,4 -56,5
3OH94 600 3,63E-04 292,13 13,231 359,4 -15,8
3OH94 625 6,49E-04 307,26 9,1312 2,7 -30,9
3OH94 650 4,16E-04 4,1748 48,726 72 -22,2
3OH94 675 7,86E-04 338,1 6,6519 26,9 -56,5
3OH121 0 3,51E-03 284,18 73,788 42,6 16,3
3OH121 100 1,37E-03 23,252 51,906 73,6 -14,3
3OH121 150 1,02E-03 42,638 13,288 113,4 -35,9
3OH121 200 1,69E-03 63,435 -7,7961 146,9 -27,5
3OH121 250 9,20E-04 72,367 -21,088 163,8 -23,1
3OH121 300 1,49E-03 53,322 -15,894 152,7 -39,4
3OH121 350 1,65E-03 70,701 -44,706 189,5 -28,1
3OH121 400 1,46E-03 73,442 -21,234 164,2 -22,2
3OH121 425 1,32E-03 52,531 -22,048 160,4 -41,4
3OH121 450 1,47E-03 58,271 -27,913 168,8 -37
3OH121 475 1,50E-03 62,992 -15,859 155,6 -30,4
3OH121 500 1,92E-03 72,629 -18,027 160,7 -22,1
3OH121 550 2,55E-03 75,739 -13,401 156,9 -17,9
3OH121 575 1,48E-03 91,725 -26,104 174,1 -7,6
3OH121 600 2,20E-03 75,964 -7,5594 151,2 -15,8
3OH121 625 9,75E-04 98,763 36,736 46,4 -39,8
3OH121 625 1,92E-04 349,09 28,029 116 19,2
3OH144 0 3,28E-04 227,59 17,393 340,5 43,3
3OH144 100 1,94E-04 215,12 12,209 333 55,5
3OH144 150 1,68E-04 199,72 33,961 22 60
3OH144 200 2,40E-04 159,44 16,195 126,6 69,1
3OH144 250 2,68E-04 158,77 14,056 132,8 68,9
3OH144 300 2,43E-04 154,05 30,981 101,2 58,1
3OH144 350 2,21E-04 163,02 25,792 99,3 67,5
3OH144 400 1,74E-04 168,5 39,812 73 58,5
3OH144 450 1,10E-04 355,41 72,891 54,6 -7,1
3OH144 475 7,58E-05 275,39 45,409 11,6 3,4
3OH144 500 2,12E-04 265,45 57,655 23,1 10,9
3OH144 525 2,54E-04 279,46 56,578 23 3,2
3OH144 550 1,06E-04 199,73 25,303 7,8 65,8
3OH144 575 5,95E-04 203,28 61,809 42,7 35,5
3OH144 600 3,03E-04 264,78 43,543 8,7 10,6
3OH144 625 3,37E-04 204,61 -59,635 248,8 17,6
3OH144 650 2,43E-04 70,866 31,272 111,3 -10,7

Table2. Thermal demagnetization data
(1) Sample = sample name
(2) Temperature (°C)
(3) NRM intensity (A/m)
(4) Core Declination (°E)
(5) Core Inclination (°)
(6) Geographic Declination (°E)
(7) Geographic Inclination (°)

3OH144 675 1,33E-04 343,79 -7,3902 334 -73,8
3OH172 0 5,63E-04 303,86 -35,003 313,1 -23,9
3OH172 100 3,96E-04 316,26 -13,869 330,9 -42,7
3OH172 150 4,09E-04 304,07 -22,887 325,5 -28,7
3OH172 200 4,16E-04 308,57 -9,4039 339,3 -36,8
3OH172 250 3,78E-04 307,36 -29,304 317,4 -29
3OH172 300 4,06E-04 302,41 -23,21 325,7 -27,2
3OH172 350 3,32E-04 325,68 -24,751 311,7 -45,3
3OH172 400 3,64E-04 322,97 -38,231 300,2 -34,8
3OH172 425 3,93E-04 321,91 -24,331 314,9 -42,7
3OH172 450 3,97E-04 325,07 -14,309 325,4 -50,3
3OH172 475 5,53E-04 342,1 -23,339 295,9 -56,7
3OH172 500 3,88E-04 339,95 -22,282 300 -56,4
3OH172 525 4,75E-04 331,75 -16,132 317,4 -55
3OH172 550 5,32E-04 322,7 -7,0179 337,4 -50,9
3OH172 575 5,65E-04 315,98 -59,189 286,8 -17
3OH212 0 4,27E-04 210,84 -67,713 246,9 19
3OH212 100 4,68E-04 126,06 -74,191 222,1 9,2
3OH212 150 4,57E-04 104,04 -80,125 225,4 2,4
3OH212 200 7,51E-04 339,57 -81,666 237,9 -7,8
3OH212 250 7,91E-04 2,8624 -85,646 234,8 -4,3
3OH212 300 6,30E-04 341,57 -77,833 238,9 -11,5
3OH212 350 6,37E-04 284,83 -80,463 244,2 -2,4
3OH212 400 7,19E-04 24,928 -83,751 232,4 -5,7
3OH212 450 6,83E-04 272,77 -84,784 240,2 -0,3
3OH212 475 6,71E-04 309,66 -81,544 241,5 -5,4
3OH212 500 6,92E-04 228,18 -83,656 239,7 4,2
3OH212 525 7,50E-04 331,06 -50,663 256,6 -33,7
3OH212 550 7,45E-04 288,86 -69,829 254,2 -6,4
3OH212 575 6,02E-04 348,77 -76,688 237,6 -13,1
3OH212 600 9,09E-04 122,32 -86,342 231,9 2
3OH212 625 4,31E-04 33,83 -74,783 226,4 -12,6
3OH212 650 5,62E-04 152,96 -73,165 227,2 14,9
3OH212 675 3,29E-04 232,4 -0,86956 323,9 37,6
3OH229 0 1,16E-03 286,08 30,111 319,1 -11,2
3OH229 100 8,38E-04 309,5 9,475 303 -37,6
3OH229 150 8,00E-04 315,71 2,15 295,1 -45,2
3OH229 200 7,82E-04 320,93 8,9715 306,6 -48,6
3OH229 250 7,60E-04 318,09 9,8529 306,6 -45,7
3OH229 300 7,60E-04 314,68 5,4359 299,4 -43,6
3OH229 350 8,05E-04 323,2 -7,778 280,7 -53,3
3OH229 400 4,79E-04 305,76 -18,87 267,4 -35,4
3OH229 425 8,23E-04 331,61 8,7314 312,8 -58,5
3OH229 450 7,52E-04 319,75 1,0664 294,5 -49,3
3OH229 475 7,48E-04 315,87 2,5302 295,7 -45,3
3OH229 500 8,97E-04 316,54 -2,749 288,3 -46,6
3OH229 550 7,04E-04 322,05 -4,1521 286,7 -52,2
3OH229 575 9,13E-04 316,4 -18,579 265,5 -45,4
3OH229 600 8,59E-04 335,73 1,0672 300,4 -65
3OH229 625 8,79E-04 330,68 -15,913 264 -59,2
3OH229 650 2,03E-04 340,58 -7,6331 278,2 -70,5
3OH246 0 1,27E-03 139,38 -53,901 230,8 32,8
3OH246 100 1,13E-03 127,34 -52,246 224,6 27,7
3OH246 150 9,53E-04 118,01 -56,025 226,1 21,2
3OH246 200 7,64E-04 105,99 -59,751 228,1 14,1
3OH246 250 7,26E-04 84,5 -68,048 236,1 4,4
3OH246 300 7,55E-04 84,199 -65,193 233,3 3,9
3OH246 350 7,16E-04 52,741 -57,65 232,1 -12,6
3OH246 400 5,23E-04 6,3144 -62,016 254,8 -20,8
3OH246 450 5,65E-04 1,8328 -63,741 257,1 -19,2
3OH246 475 5,68E-04 1,206 -70,444 257,6 -12,6
3OH246 500 6,39E-04 312,77 -44,619 292,6 -23,2
3OH246 525 4,87E-04 295,44 -56,009 288,6 -7,9
3OH246 550 6,79E-04 340,58 -53,624 270,8 -27,2
3OH246 575 5,77E-04 328,26 -58,44 275 -19,8
3OH246 600 1,07E-03 321,13 -43,385 289,3 -28,5
3OH246 625 6,60E-04 315,38 -49,159 287,6 -21,7
3OH246 650 2,63E-04 294,97 72,145 61,3 -14,2
3OH246 675 7,74E-04 324,71 33,417 31,9 -48
3OH313 0 9,43E-04 201,07 -47,287 318,2 57,8
3OH313 100 4,63E-04 140,83 37,199 143,8 21,9
3OH313 150 4,13E-04 124,36 41,36 150 9,9
3OH313 200 3,50E-04 133,51 45,526 142,3 12,1
3OH313 250 2,63E-04 119,3 52,67 142,9 0,4
3OH313 300 9,28E-05 151,78 31,745 139,2 31,6
3OH313 350 2,41E-04 87 17,885 185,1 -8,7
3OH313 400 2,15E-04 114,62 60,546 137,7 -6
3OH313 425 2,48E-04 191,63 32,95 98,9 35,9
3OH313 450 3,16E-04 276,17 83,241 103,8 -20,6
3OH313 475 4,06E-04 1,7062 54,614 112,7 -55,4
3OH313 500 2,80E-04 159,79 51,582 123,9 16,3
3OH313 525 2,26E-04 334,73 15,399 14,3 -65,5
3OH339 0 1,25E-03 249,24 -37,245 11,3 26,5
3OH339 100 6,97E-04 264,51 -32,838 14,4 13,6
3OH339 150 7,34E-04 267,79 -35,599 11 11,5
3OH339 200 6,36E-04 281,16 -46,318 357,8 4,8
3OH339 250 6,37E-04 278,66 -41,345 3,1 4,9
3OH339 300 5,38E-04 275,46 -32,86 12 4,7
3OH339 350 6,02E-04 287,57 -12,966 27,1 -12,5
3OH339 400 6,02E-04 272,84 -25,047 20,2 4,6
3OH339 450 6,82E-04 278,7 -26,941 16,8 0,2
3OH339 475 5,17E-04 285,25 0,22156 40,7 -14,6
3OH339 500 6,31E-04 297,23 -24,425 12,4 -16,1
3OH339 525 3,33E-04 290,78 0,17225 38,8 -19,9
3OH339 550 6,30E-04 288,52 -14,066 25,7 -12,9
3OH339 575 8,43E-04 304,2 15,828 52,4 -36,6
3OH339 600 5,72E-04 277,37 -6,2218 36,9 -5,2
3OH339 625 9,20E-04 285,62 28,91 70 -21,5
3OH339 650 2,66E-04 288,06 79,537 124,4 -20
3OH339 675 2,73E-04 346,83 -3,3645 348,8 -65,8

Table2. Thermal demagnetization data

(1) Sample = sample name

(2) Temperature (°C)

(3) NRM intensity (A/m)

(4) Core Declination (°E)

(5) Core Inclination (°)

(6) Geographic Declination (°E)

(7) Geographic Inclination (°)

3OH379 0 7,48E-04 209,51 -53,503 324,7 40,5
3OH379 100 2,78E-04 177,46 -35,894 297,3 64
3OH379 150 1,30E-04 140,58 -13,886 221,8 51,3
3OH379 200 2,30E-04 117,09 30,041 175,9 17,5
3OH379 250 2,51E-04 83,29 61,535 150,9 -12
3OH379 300 2,30E-04 229,79 19,514 63,1 32,8
3OH379 350 8,91E-05 191,45 56,735 115,2 22,6
3OH379 400 4,19E-04 115,88 69,197 140,6 -0,6
3OH379 425 4,19E-04 279,4 70,37 102,1 -12,6
3OH379 450 3,85E-04 77,471 87,258 124,7 -10,6
3OH379 475 4,29E-04 12,967 68,697 127,4 -30,7
3OH379 500 3,26E-04 68,199 69,717 141,7 -16,8
3OH379 550 4,38E-04 48,211 60,675 146,5 -28,2
3OH379 575 3,90E-04 19,163 67,479 130,4 -31,1
3OH379 600 3,12E-04 102,94 75,932 135,8 -6,6
3OH379 625 2,69E-04 75,809 0,21282 214,3 -14
3OH379 650 4,41E-04 107,42 -31,912 242,5 20
3OH379 675 1,00E-04 286,04 -3,4946 25,6 -15,1
3OH405 0 7,36E-03 204,74 28,82 34,1 44,4
3OH405 100 5,70E-03 204,92 32,248 36,6 41,5
3OH405 150 5,62E-03 202,62 31,174 38 43,5
3OH405 200 4,81E-03 201,13 31,336 39,7 44
3OH405 250 3,74E-03 204,13 32,365 37,4 41,8
3OH405 300 3,16E-03 209,77 33,406 33,2 38,2
3OH405 350 3,20E-03 207,8 32,33 34 40
3OH405 400 2,64E-03 204,14 28,474 34,4 45
3OH405 450 1,67E-03 203,31 26,195 33,4 47,3
3OH405 475 8,88E-04 200,54 24,33 35 50,2
3OH405 475 1,11E-03 197,05 27,487 41,6 49
3OH405 500 1,18E-03 200,96 33,18 41,1 42,4
3OH405 525 1,22E-03 182,17 12,152 59,4 67,7
3OH405 550 7,10E-04 209,53 23,771 24,9 45,6
3OH405 575 7,56E-04 193,96 12,532 33,1 63,5
3OH405 600 8,52E-04 206,63 18,548 22,3 51,2
3OH405 625 4,53E-04 248,94 -27,767 309 23,2
3OH405 650 8,45E-04 53,093 68,387 83,6 -22,3
3OH405 675 1,24E-04 332,11 48,954 39,4 -44,6
3OH462 0 4,29E-03 276,24 9,2537 9,8 -5,3
3OH462 100 3,17E-03 278,62 8,7038 9,5 -7,7
3OH462 150 3,04E-03 279,28 -2,0725 358,7 -9,4
3OH462 200 2,54E-03 287,34 -12,49 348,5 -18
3OH462 250 2,15E-03 283,16 -16,463 344,3 -14
3OH462 300 2,00E-03 278,98 -13,126 347,5 -9,9
3OH462 350 1,95E-03 290,73 5,0274 7,2 -20,1
3OH462 400 1,92E-03 284,27 -1,0133 0,2 -14,3
3OH462 425 1,98E-03 282,99 1,6782 2,9 -12,8
3OH462 450 2,11E-03 289,98 0,27195 2,1 -19,9
3OH462 475 2,36E-03 294,83 -1,4577 0,7 -24,9
3OH462 500 2,31E-03 287,89 -0,24785 1,4 -17,8
3OH462 525 1,94E-03 290,92 -3,7897 357,9 -21,1
3OH462 550 1,81E-03 286,85 8,59 10,4 -15,8
3OH462 575 1,90E-03 281,95 0,15052 1,2 -11,9
3OH462 600 1,72E-03 303,18 -7,6999 354,1 -33,5
3OH462 625 1,07E-03 326,63 -21,349 330,1 -53,8
3OH462 650 6,61E-04 261,91 -11,966 347,3 6,8
3OH490 0 6,23E-03 235,58 -12,328 321,6 28,6
3OH490 100 4,42E-03 227,77 -16,548 313,1 33,3
3OH490 150 3,46E-03 228,83 -18,69 311,6 31,3
3OH490 200 2,67E-03 236,75 -18,129 316,3 25
3OH490 250 2,66E-03 233,99 -17,725 315,3 27,5
3OH490 300 1,14E-03 241,69 -19,675 317 20,1
3OH490 350 1,17E-03 234,17 -6,0663 327,6 32,3
3OH490 400 9,02E-04 213,91 -14,912 304,8 45,1
3OH490 425 5,06E-04 241,49 -30,624 306,6 15,4
3OH490 450 6,75E-04 230,43 -17,949 313,2 30,4
3OH490 475 6,68E-04 231,74 -10,517 321,6 32,7
3OH490 500 1,35E-04 282,15 46,512 32,7 2,7
3OH490 550 3,84E-04 8,9816 29,831 85,9 -44,3
3OH490 575 3,61E-04 41,269 -25,432 186,9 -50,1
3OH490 600 2,60E-04 30,407 18,158 118,1 -45,3
3OH490 625 4,70E-04 23,601 5,8676 125 -58,7
3OH490 650 5,09E-04 215,78 -9,0389 313,1 47,2

OH3-B

3BOH30 0 1,22E-03 197,08 48,95 331,3 44,7
3BOH30 100 7,00E-04 204,6 21,617 292,7 61,5
3BOH30 150 3,64E-04 157,43 17,761 46,9 65
3BOH30 200 4,61E-04 203,09 24,192 298,8 61,3
3BOH30 250 3,18E-04 116,65 17,74 60,1 27,2
3BOH30 300 2,25E-04 123,23 72,047 2,5 15,5
3BOH30 350 3,16E-04 244,01 64,794 323,5 16,3
3BOH30 400 3,90E-04 45,327 17,633 48,3 -39,4
3BOH30 425 3,47E-04 322,45 -21,855 229,6 -50,4
3BOH30 450 3,96E-04 224,03 -77,831 175,4 2,8
3BOH30 475 2,11E-04 265,64 1,6319 258,2 4,5
3BOH30 500 1,56E-04 296,43 14,306 275,5 -23,8
3BOH30 550 1,33E-04 289,61 3,3747 262,7 -19,1
3BOH30 575 3,58E-04 168,35 33,946 6,6 60
3BOH30 600 3,52E-04 261,8 20,478 276,8 9,8
3BOH30 625 1,04E-03 40,537 -73,801 156 -18,1
3BOH57 0 9,30E-04 189,5 67,5 337,2 17,2
3BOH58 100 5,72E-04 238,6 74,4 327,7 3,2
3BOH59 150 2,66E-04 334,8 54,4 323 -36,6
3BOH60 200 2,09E-04 328,4 68,6 329 -23
3BOH61 250 2,47E-04 333 62,4 327 -29,2
3BOH62 300 2,50E-04 329,3 67,9 328,9 -23,8
3BOH63 350 3,48E-04 204,9 74,5 334,5 9
3BOH64 400 2,40E-04 314,4 56,8 314,9 -27
3BOH65 425 3,58E-04 12,5 34,5 0,9 -58,3
3BOH66 450 4,62E-04 301 41 294,7 -26,4
3BOH67 475 3,96E-04 319,5 31,8 291,3 -43,6

Table2. Thermal demagnetization data

(1) Sample = sample name

(2) Temperature (°C)

(3) NRM intensity (A/m)

(4) Core Declination (°E)

(5) Core Inclination (°)

(6) Geographic Declination (°E)

(7) Geographic Inclination (°)

3BOH68 500 3,12E-04 310,5 29,8 285 -37,2
3BOH69 525 5,80E-04 301,9 46,2 300,4 -25,3
3BOH70 550 3,16E-04 310,5 -3,6 242,1 -39,8
3BOH71 575 4,99E-04 310,2 4,1 252,2 -40,4
3BOH72 600 6,68E-04 306,5 14,3 265,1 -36,6
3BOH73 625 3,63E-04 316,7 44,6 304,3 -35,3
3BOH94 0 1,02E-03 225,39 43,696 330 28,9
3BOH94 100 6,51E-04 236,22 56,066 337,1 16,3
3BOH94 150 5,69E-04 241,65 54,468 334,1 14,3
3BOH94 200 4,31E-04 253,93 73,441 350,1 2,6
3BOH94 250 4,02E-04 315,91 70,574 352,1 -15,8
3BOH94 300 3,23E-04 300,21 55,498 335 -18,3
3BOH94 350 3,47E-04 353,2 59,256 1,9 -32,5
3BOH94 400 4,20E-04 332,29 74,564 358,6 -15,6
3BOH94 450 3,82E-04 316,25 20,845 303,2 -43,4
3BOH94 475 6,75E-04 331,56 58,277 349,3 -29,5
3BOH94 500 6,33E-04 314,02 66,995 348,8 -17,7
3BOH94 525 1,11E-03 338,34 13,976 306,4 -65,5
3BOH94 550 3,94E-04 337,07 39,756 340 -46,9
3BOH94 575 6,85E-04 3,3558 22,669 14,7 -69,1
3BOH94 600 4,90E-04 355,66 30,269 358,2 -61,4
3BOH94 625 2,31E-04 301,01 -0,74403 273,9 -31
3BOH94 650 9,25E-04 227,03 52,822 337,4 22,6
3BOH94 675 2,89E-04 309,17 15,257 293,9 -38,2
3BOH136 0 1,67E-03 219,31 58,211 330,6 36
3BOH136 100 9,69E-04 218,32 28,484 294,6 51,2
3BOH136 150 9,87E-04 215,71 30,572 298,9 52,7
3BOH136 200 8,38E-04 232,25 21,634 282,5 39,6
3BOH136 250 4,23E-04 282,51 22,062 289,4 -6,4
3BOH136 300 4,37E-04 252,53 10,286 271,5 19,1
3BOH136 350 4,16E-04 210,06 14,462 271,4 60,8
3BOH136 400 6,37E-04 193,51 23,986 307,6 73,1
3BOH136 400 6,48E-04 202,37 17,695 280,1 67,9
3BOH136 425 4,58E-04 246,92 -4,5085 254,8 21,3
3BOH136 450 5,29E-04 231,84 9,0222 266,1 39
3BOH136 475 7,59E-04 191,13 -12,628 198,7 62,1
3BOH136 500 9,66E-04 246,35 -35,077 224,8 11
3BOH136 550 6,22E-04 255,37 -20,797 241,2 8,6
3BOH136 575 1,44E-03 157,79 -38,871 154,2 34,1
3BOH136 600 5,25E-04 190,37 10,53 252,4 79,5
3BOH136 625 5,36E-04 270 -16,034 249,4 -3,6
3BOH178 0 1,32E-03 261,73 47,777 327,6 9,3
3BOH178 100 7,09E-04 268,28 27,025 306,8 3,8
3BOH178 150 5,76E-04 267,66 26,724 306,5 4,3
3BOH178 200 4,12E-04 320,74 37,858 333,1 -33,7
3BOH178 250 4,69E-04 323,55 34,713 332 -37,5
3BOH178 300 7,56E-04 324,72 37,581 335,4 -36,2
3BOH178 350 8,85E-04 338,76 44,928 351,4 -36,6
3BOH178 400 6,01E-04 322,68 32,368 329,1 -38,5
3BOH178 425 6,34E-04 321,9 30,217 326,4 -39,3
3BOH178 450 8,75E-04 328,76 42,772 338,5 -43,2
3BOH178 475 6,64E-04 333,34 33,582 338,7 -43,9
3BOH178 500 3,74E-04 349,96 14,723 343,4 -67,9
3BOH178 525 4,22E-04 287,88 46,04 328,1 -8,6
3BOH178 550 5,15E-04 344,78 21,188 340,8 -59,9
3BOH221 0 1,52E-03 222,18 -5,8175 309,1 46,7
3BOH221 100 1,10E-03 210,53 -14,604 289,8 54,5
3BOH221 150 7,88E-04 197,47 -44,437 248 39,1
3BOH221 200 6,33E-04 178,9 -54,699 231,3 31,3
3BOH221 250 7,88E-04 148,51 -36,189 198,5 40,2
3BOH221 300 6,12E-04 140,89 -56,544 210 21,6
3BOH221 350 7,47E-04 111,99 -72,096 215,4 2,8
3BOH221 400 6,70E-04 61,119 -64,56 209 -15,7
3BOH221 425 5,11E-04 161,17 -57,328 220,7 26,8
3BOH221 450 4,84E-04 74,899 -66,16 208,7 -9,7
3BOH221 475 3,32E-04 28,896 -58,046 214,6 -31,4
3BOH221 500 3,98E-04 52,896 -42,516 189,6 -29,4
3BOH221 550 5,88E-04 49,943 -37,276 185 -33,6
3BOH221 575 6,15E-04 330,43 -48,275 257 -39
3BOH221 600 5,31E-04 29,393 -60,311 215,8 -29,4
3BOH221 625 6,66E-04 158,49 -63,742 222 20,4
3BOH221 650 4,72E-04 249,9 -19,543 300,1 17,4
3BOH221 650 8,66E-05 18,544 39,965 71,4 -42,8
3BOH281 0 8,26E-04 198,7 75,569 12,3 13,7
3BOH281 100 7,59E-04 125,11 84,084 21,8 3,4
3BOH281 150 7,94E-04 132,67 83,704 21,6 4,3
3BOH281 200 8,52E-04 49,821 82,055 23,1 -5,1
3BOH281 250 8,45E-04 38,919 75,82 26 -11
3BOH281 300 8,58E-04 18,36 73,66 22,3 -15,5
3BOH281 350 8,87E-04 17,669 72,937 22,3 -16,2
3BOH281 400 8,12E-04 2,6838 76,309 17,7 -13,7
3BOH281 450 8,34E-04 339,76 72,443 20,7 -18,4
3BOH281 475 1,07E-03 342,52 29,298 348,8 -56,3
3BOH281 500 5,23E-04 326,49 59,84 359,2 -24,8
3BOH281 525 1,39E-03 10,437 67,01 21,4 -22,6
3BOH281 550 9,96E-04 349,28 64,073 11,8 -25,4
3BOH281 575 8,43E-04 325,7 60,223 359,1 -24,2
3BOH281 600 7,86E-04 353,69 72,503 15 -17,4
3BOH281 625 1,01E-03 331,19 83,496 13,9 -5,7
3BOH281 650 5,57E-04 286,61 -11,698 274,8 -16,3
3BOH281 675 1,57E-04 328,14 32,313 337,2 -45,9
3BOH308 0 1,02E-03 141,03 27,832 58,3 42,8
3BOH308 100 6,01E-04 123,35 -22,185 124,5 31
3BOH308 150 5,68E-04 113,42 -23,547 124 21,8
3BOH308 200 5,30E-04 112,42 -18,953 119 21,5
3BOH308 250 4,65E-04 109,53 -14,969 114,5 19,1
3BOH308 300 5,97E-04 111,21 -5,5745 104,6 21,2
3BOH308 350 6,03E-04 110,85 4,1847 94,1 20,7
3BOH308 400 5,35E-04 112,26 -7,7283 106,9 22,2
3BOH308 425 5,07E-04 110,44 -2,0337 100,8 20,5

Table2. Thermal demagnetization data
(1) Sample = sample name
(2) Temperature (°C)
(3) NRM intensity (A/m)
(4) Core Declination (°E)
(5) Core Inclination (°)
(6) Geographic Declination (°E)
(7) Geographic Inclination (°)

3BOH308 450 2,03E-04 92,741 -22,25 121,2 2,9
3BOH308 475 2,81E-04 100,91 5,1011 93,6 10,8
3BOH308 500 3,42E-04 72,827 -28,107 128,4 -14,6
3BOH308 525 2,93E-04 112,98 17,497 79,7 21,5
3BOH308 550 3,12E-04 114,54 -13,529 113,4 24,1
3BOH388 0 1,00E-03 181,88 -19,332 264,1 69,6
3BOH388 100 8,87E-04 165,14 -31,53 236,9 54,5
3BOH388 150 9,57E-04 140,1 -31,214 213 40,3
3BOH388 200 9,02E-04 138,41 -36,385 217,5 36,3
3BOH388 250 1,07E-03 143,85 -22,034 204,4 47,9
3BOH388 300 1,14E-03 147,83 -20,554 205,2 51,8
3BOH388 350 1,05E-03 129,16 -25,059 200,7 34,4
3BOH388 400 1,08E-03 139,66 -20,115 199,4 45,2
3BOH388 425 8,61E-04 137,39 -25,24 204,6 41,2
3BOH388 450 9,64E-04 138,13 -23,988 203,5 42,3
3BOH388 475 7,00E-04 144,73 -21,106 203,7 49
3BOH388 500 8,62E-04 136,96 -33,049 213,2 37,1
3BOH388 550 1,14E-03 115,11 -16,603 187,6 23,7
3BOH388 575 7,42E-04 139,99 -23,082 203,4 44,2
3BOH388 600 7,81E-04 125,87 -27,711 202,5 30,7
3BOH388 625 1,12E-03 150,45 -45,597 233,5 36,6
3BOH388 650 1,57E-04 157,66 -27,306 223,5 54,5
3BOH388 675 2,75E-04 295,2 65,814 56,9 -9,1
3BOH428 0 1,06E-03 202,6 47,668 333,7 38,4
3BOH428 100 7,17E-04 221,96 65,856 336,3 17,7
3BOH428 150 5,61E-04 211,82 57,973 334,7 26,8
3BOH428 200 6,38E-04 254,77 46,175 310,2 10,5
3BOH428 250 4,15E-04 239,26 71,853 337,3 9,2
3BOH428 300 6,30E-04 245,66 72,97 337,4 6,9
3BOH428 350 6,69E-04 267,45 76,408 339,4 0,6
3BOH428 400 5,62E-04 292,09 70,939 335,2 -7,1
3BOH428 425 4,65E-04 237,34 53,308 320,9 18,8
3BOH428 450 4,54E-04 275,92 68,705 331,8 -2,1
3BOH428 475 5,38E-04 263,31 32,237 295,4 5,7
3BOH428 500 6,04E-04 319,27 54,496 328 -26,1
3BOH428 525 5,86E-04 279,96 28,63 292 -8,7
3BOH428 550 3,83E-04 281,83 47,49 311,1 -8
3BOH428 575 5,45E-04 292,53 30,431 295,5 -19,3
3BOH428 600 4,86E-04 258,58 30,4 293,9 9,8
3BOH428 625 4,23E-04 272,53 15,372 278,4 -2,4
3BOH428 650 3,72E-04 302,89 45,695 313,7 -22,3
3BOH428 675 1,93E-04 282,24 0,29626 263,3 -12,2
3BOH463 0 1,76E-03 167,74 57,555 21,7 31,6
3BOH463 100 1,07E-03 146,25 19,541 71,4 51,6
3BOH463 150 7,79E-04 135,31 2,5764 100,3 45,3
3BOH463 200 5,90E-04 138,16 -2,0412 107,1 48,1
3BOH463 250 5,83E-04 136,35 -10,882 119,6 45,3
3BOH463 300 5,65E-04 124,97 -23,123 131,5 31,8
3BOH463 350 5,67E-04 126,02 2,9317 100,4 36
3BOH463 400 5,32E-04 116,12 -29,393 136,1 22,6
3BOH463 425 4,92E-04 112,1 -43,67 149,9 15,8
3BOH463 450 5,78E-04 95,375 -37,404 141,5 4,3
3BOH463 475 6,22E-04 129,23 -16,143 124,5 37,4
3BOH463 500 5,42E-04 91,645 -44,988 149 1,2
3BOH463 525 6,24E-04 78,836 -30,546 135 -9,6
3BOH463 550 3,72E-04 60,474 -45,683 153,6 -20,1
3BOH463 575 5,13E-04 128,36 -41,355 152,3 27,8
3BOH486 0 5,10E-04 170,52 -1,4603 113,9 80,5
3BOH486 100 3,25E-04 148,25 16,616 85,1 53,5
3BOH486 150 2,79E-04 145,67 13,275 91,9 52,7
3BOH486 200 1,98E-04 126,6 -13,375 132,1 36
3BOH486 250 1,14E-04 140,42 -30,051 157,9 43,2
3BOH486 300 3,24E-04 175,75 -0,88442 102,3 85,6
3BOH486 350 7,14E-05 36,041 31,509 72,2 -45
3BOH486 400 9,00E-05 111,3 29,284 85,4 17,4
3BOH486 450 8,81E-05 5,5115 -82,534 206,3 -5,4
3BOH486 475 9,33E-05 62,994 5,2259 112,2 -27,1
3BOH486 500 3,38E-04 46,836 -49,231 175,3 -24,8
3BOH486 525 9,05E-05 7,4543 -53,38 201,6 -34,3
3BOH486 550 1,29E-04 107,39 -36,584 154,5 15,1
3BOH486 575 7,31E-04 252,1 -59,217 236,7 10,8
3BOH486 600 3,97E-04 336,5 7,6678 311,4 -65,9
3BOH486 625 1,97E-04 347,88 -8,1568 256,8 -74,2
3BOH486 650 1,88E-04 315,74 54,557 0,2 -26,3
3BOH486 675 1,32E-04 309,68 43,624 347,4 -29,1
3BOH510 0 1,33E-03 205,06 43,102 10,8 31,3
3BOH510 100 5,35E-04 207,43 52,543 14,4 22,2
3BOH510 150 6,35E-04 237,05 59,535 6,7 6,1
3BOH510 200 4,35E-04 238,5 65,286 11,1 2,4
3BOH510 250 6,36E-04 334,42 65,939 20 -32,4
3BOH510 300 3,36E-04 119,98 57,619 59,8 5,8
3BOH510 350 3,94E-04 227,66 62,377 11,8 7,9
3BOH510 400 7,02E-04 295,51 61,132 4 -21,8
3BOH510 425 4,72E-04 241,05 70,053 14,6 -1
3BOH510 450 4,97E-04 296,18 66,046 9,1 -20,5
3BOH510 475 3,19E-04 8,0091 50,981 39,8 -49,5
3BOH510 500 4,57E-04 261,6 54,272 356,6 -4,1
3BOH510 525 4,72E-04 321,8 48,907 359,6 -40,6
3BOH510 550 5,85E-04 341,62 57,872 19,2 -41,1
3BOH510 575 5,20E-04 8,9117 48,886 41,4 -51,4
3BOH510 600 6,90E-04 27,53 46,166 60,4 -47,8
3BOH510 625 7,03E-04 312,35 34,303 338,2 -40,8
3BOH510 650 9,23E-05 148,11 4,7849 97,2 54,5
3BOH510 675 4,55E-04 292,72 5,0444 302,8 -23,2

OH4

4OH8 0 4,04E-02 4,808 -37,029 230,2 -52,7
4OH8 100 9,08E-02 37,794 -34,947 195,3 -40,4
4OH8 150 1,08E-01 43,666 -35,581 192,5 -36
4OH8 200 1,08E-01 38,984 -37,44 197,1 -38,1
4OH8 250 1,08E-01 46,561 -35,341 190,8 -34,1

Table2. Thermal demagnetization data

(1) Sample = sample name

(2) Temperature (°C)

(3) NRM intensity (A/m)

(4) Core Declination (°E)

(5) Core Inclination (°)

(6) Geographic Declination (°E)

(7) Geographic Inclination (°)

4OH8 300 1,17E-01 45,042 -34,364 190,5 -35,7
4OH8 350 1,21E-01 49,363 -31,689 185,6 -33,7
4OH8 400 1,11E-01 40,819 -32,31 190,6 -39,8
4OH8 450 1,26E-01 45,111 -29,576 185,2 -37,9
4OH8 475 1,19E-01 47,866 -28,536 182,8 -36,1
4OH8 500 1,21E-01 46,23 -29,118 184,1 -37,2
4OH8 525 1,24E-01 47,425 -29,234 183,7 -36,2
4OH8 550 1,26E-01 48,804 -30,369 184,4 -34,6
4OH8 575 1,27E-01 46,695 -31,91 187,1 -35,6
4OH8 600 1,19E-01 47,303 -29,485 184,1 -36,2
4OH8 625 1,17E-01 46,229 -29,235 184,3 -37,1
4OH8 650 1,16E-01 48,16 -29,184 183,4 -35,6
4OH8 675 1,99E-02 253,01 7,2993 334,1 16,8
4OH29 0 1,57E-02 2,2546 -13,245 224,4 -79,5
4OH29 100 2,79E-02 33,376 -25,033 184 -51,1
4OH29 150 3,04E-02 31,982 -31,072 193 -48,8
4OH29 200 3,55E-02 35,961 -27,5 185,6 -47,8
4OH29 250 3,69E-02 41,072 -26,545 181,5 -44,2
4OH29 300 3,63E-02 34,774 -27,228 186 -48,9
4OH29 350 3,63E-02 37,051 -29,039 186,9 -46,2
4OH29 400 3,76E-02 36,663 -28,226 186,1 -46,9
4OH29 425 3,91E-02 38,558 -25,586 181,5 -46,6
4OH29 450 3,63E-02 33,837 -26,349 185,5 -50
4OH29 475 3,73E-02 33,548 -26,1 185,4 -50,4
4OH29 500 3,68E-02 35,077 -25,426 183,4 -49,5
4OH29 525 4,05E-02 35,754 -8,8004 157,4 -54
4OH29 550 3,67E-02 32,735 -24,969 184,4 -51,6
4OH29 575 2,89E-02 33,509 -24,555 183,3 -51,2
4OH29 600 2,83E-02 31,724 -23,786 183,5 -53
4OH29 625 3,40E-03 273,86 -58,401 268,1 -4,6
4OH59 0 2,57E-02 87,011 -14,396 203,4 -8,7
4OH59 100 4,83E-02 67,88 -14,743 196,4 -25,9
4OH59 150 5,06E-02 72,375 -13,264 196,6 -21,3
4OH59 200 5,39E-02 68,097 -14,275 196 -25,6
4OH59 250 5,33E-02 72,128 -14,797 198,1 -22,1
4OH59 300 5,83E-02 68,781 -13,693 195,7 -24,8
4OH59 350 6,03E-02 66,354 -12,459 193,4 -26,5
4OH59 400 6,24E-02 66,901 -13,443 194,7 -26,4
4OH59 450 6,38E-02 62,246 -11,576 190,8 -29,9
4OH59 475 6,16E-02 65,941 -11,703 192,5 -26,6
4OH59 500 6,30E-02 65,161 -8,1211 188,5 -25,9
4OH59 525 6,29E-02 63,559 -9,7044 189,4 -28
4OH59 550 6,27E-02 64,222 -9,5441 189,5 -27,3
4OH59 575 5,94E-02 66,918 -11,564 192,7 -25,6
4OH59 600 6,12E-02 64,455 -9,7866 189,9 -27,2
4OH59 625 6,01E-02 67,71 -11,91 193,4 -25,1
4OH59 650 1,02E-02 38,283 1,6258 161,5 -44,4
4OH59 675 8,70E-03 324,04 14,655 56,1 -37,1
oh4_7 0 1,26E-02 262,3 -34,1 262,3 -34,1
oh4_7 100 2,39E-02 209 -38,3 209 -38,3
oh4_7 150 2,58E-02 190,4 -28,5 190,4 -28,5
oh4_7 200 3,26E-02 192,9 -33,6 192,9 -33,6
oh4_7 225 3,47E-02 193,4 -31,5 193,4 -31,5
oh4_7 250 3,73E-02 192,2 -32,1 192,2 -32,1
oh4_7 275 3,97E-02 188,9 -31,7 188,9 -31,7
oh4_7 300 4,30E-02 185,7 -35,6 185,7 -35,6
oh4_7 325 4,13E-02 189,5 -28,2 189,5 -28,2
oh4_7 350 4,36E-02 189,5 -31 189,5 -31
oh4_7 375 4,25E-02 191,1 -29,5 191,1 -29,5
oh4_7 400 4,31E-02 187,1 -28,4 187,1 -28,4
oh4_7 425 4,35E-02 187,5 -31,2 187,5 -31,2
oh4_7 450 4,57E-02 181 -38,6 181 -38,6
oh4_7 475 4,48E-02 187 -27,4 187 -27,4
oh4_7 500 4,80E-02 170,5 -32,1 170,5 -32,1
oh4_7 525 4,39E-02 178,4 -29,6 178,4 -29,6
oh4_7 550 4,48E-02 181 -29 181 -29
oh4_7 575 4,52E-02 174,2 -26,9 174,2 -26,9
oh4_7 600 4,28E-02 180,5 -22,2 180,5 -22,2
oh4_7 625 4,44E-02 175,1 -28,6 175,1 -28,6
oh4_7 650 9,40E-03 171,6 0,8 171,6 0,8
oh4_7 675 9,51E-03 171,6 -25,4 171,6 -25,4
4OH96 0 1,23E-02 60,119 -70,237 210,7 -16,4
4OH96 100 2,62E-02 51,921 -61,922 204,7 -23,3
4OH96 150 3,27E-02 65,746 -52,377 192,1 -20,2
4OH96 200 3,54E-02 49,582 -54,837 198,7 -28,1
4OH96 250 4,01E-02 56,919 -58,588 200,2 -22,7
4OH96 300 4,17E-02 54,75 -52,338 194,6 -26,5
4OH96 350 3,92E-02 60,286 -54,448 195,3 -22,7
4OH96 400 4,21E-02 56,993 -48,465 190 -26,7
4OH96 425 4,09E-02 60,195 -54,514 195,4 -22,7
4OH96 450 4,04E-02 57,819 -53,135 194,6 -24,5
4OH96 475 4,11E-02 52,705 -53,843 196,7 -27
4OH96 500 3,99E-02 62,374 -52,782 193,2 -22,1
4OH96 525 4,00E-02 65,273 -51,182 191 -20,8
4OH96 550 3,98E-02 66,484 -49,109 188,6 -20,6
4OH96 575 3,85E-02 64,699 -50,765 190,6 -21,3
4OH96 600 4,03E-02 63,736 -50,701 190,8 -21,9
4OH96 625 2,23E-02 63,78 -42,929 182,6 -23,8
4OH96 650 5,56E-03 312,5 -6,4078 316,2 -42,8
4OH116 0 3,80E-03 284,46 -58,879 252 -16,9
4OH116 100 7,19E-03 349,81 -65,378 225,7 -35,2
4OH116 150 8,08E-03 4,1803 -68,053 218,6 -32,9
4OH116 200 8,18E-03 346,4 -67,044 226,8 -33,2
4OH116 250 8,44E-03 356,21 -61,011 222,9 -39,9
4OH116 300 8,58E-03 1,2575 -61,458 219,7 -39,5
4OH116 350 8,90E-03 15,893 -59,679 210,1 -39,9
4OH116 400 8,87E-03 4,4917 -57,826 217,2 -43
4OH116 450 8,78E-03 14,094 -56,828 210 -42,9
4OH116 475 8,12E-03 359,5 -55,585 220,9 -45,4
4OH116 500 8,09E-03 2,2329 -57,351 218,8 -43,6

Table2. Thermal demagnetization data
(1) Sample = sample name
(2) Temperature (°C)
(3) NRM intensity (A/m)
(4) Core Declination (°E)
(5) Core Inclination (°)
(6) Geographic Declination (°E)
(7) Geographic Inclination (°)

4OH116 525 9,39E-03 358,99 -56,865 221,3 -44,1
4OH116 550 8,62E-03 1,4354 -59,382 219,5 -41,6
4OH116 575 8,41E-03 0,8814 -57,233 219,8 -43,8
4OH116 600 7,37E-03 5,3662 -45,866 214 -54,8
4OH116 625 7,83E-03 349,38 -55,852 228,8 -44,4
4OH116 650 3,27E-03 112,17 -26,758 162 14,2
4OH116 675 1,76E-03 137,51 -53,413 195,7 16,2
4OH145 0 1,67E-03 187,26 -29,093 249,2 65,9
4OH145 100 5,10E-03 33,69 -62,645 218,1 -16,7
4OH145 150 5,79E-03 36,561 -50,181 208,5 -25,5
4OH145 200 6,53E-03 49,399 -47,325 200 -21,2
4OH145 250 6,38E-03 39,472 -46,306 204 -27
4OH145 300 8,47E-03 53,711 -43,774 195 -20,7
4OH145 350 7,92E-03 52,231 -48,714 200,1 -18,9
4OH145 400 9,10E-03 35,168 -47,677 207,4 -28
4OH145 425 8,70E-03 51,39 -52,161 203,4 -17,3
4OH145 450 8,54E-03 53,13 -46,281 197,5 -19,7
4OH145 475 8,39E-03 50,581 -45,387 197,8 -21,7
4OH145 500 8,41E-03 56,851 -48,48 198,2 -16,4
4OH145 525 9,20E-03 61,674 -48,342 196,5 -13,6
4OH145 550 8,59E-03 63,703 -48,1 195,7 -12,5
4OH145 575 8,70E-03 65,607 -50,389 197,3 -10,4
4OH145 600 8,41E-03 59,161 -48,997 197,9 -14,8
4OH145 625 8,28E-03 69,645 -52,84 198,7 -7,2
4OH145 650 2,74E-03 262,18 -15,028 309,2 9,1
4OH145 675 1,88E-03 303,04 -7,4158 311 -31,6
oh4_8 0 8,64E-03 181,1 -65,2 181,1 -65,2
oh4_8 100 1,30E-02 199,4 -47,7 199,4 -47,7
oh4_8 150 1,81E-02 184,5 -39,8 184,5 -39,8
oh4_8 200 2,08E-02 185,7 -40,1 185,7 -40,1
oh4_8 225 2,06E-02 181,2 -29,1 181,2 -29,1
oh4_8 250 2,35E-02 183,7 -33,2 183,7 -33,2
oh4_8 275 2,22E-02 183,4 -28,1 183,4 -28,1
oh4_8 300 2,56E-02 187,3 -26 187,3 -26
oh4_8 325 2,51E-02 185 -32,2 185 -32,2
oh4_8 350 2,61E-02 182,8 -33 182,8 -33
oh4_8 375 2,62E-02 184,8 -31,6 184,8 -31,6
oh4_8 400 2,74E-02 182,3 -33,9 182,3 -33,9
oh4_8 425 2,45E-02 185,8 -31,9 185,8 -31,9
oh4_8 450 2,30E-02 175 -23 175 -23
oh4_8 475 2,71E-02 184,6 -32,1 184,6 -32,1
oh4_8 500 2,73E-02 178,2 -28,2 178,2 -28,2
oh4_8 525 2,68E-02 175,1 -30,1 175,1 -30,1
oh4_8 550 2,70E-02 176,9 -29,1 176,9 -29,1
oh4_8 575 2,73E-02 176,3 -30 176,3 -30
oh4_8 600 6,47E-03 178,5 1,9 178,5 1,9
oh4_8 625 2,20E-03 200 36,1 200 36,1
oh4_8 650 1,81E-03 115,1 12,2 115,1 12,2
oh4_8 675 2,58E-03 330 63,7 330 63,7
4OH166 0 3,31E-03 243,75 -5,0214 284,3 24,4
4OH166 100 5,47E-03 321,63 -83,579 209,7 -17
4OH166 150 6,49E-03 3,6745 -80,315 204,8 -21,7
4OH166 200 6,98E-03 346,94 -84,172 206,9 -17,7
4OH166 250 8,10E-03 52,001 -84,246 200,8 -15,5
4OH166 300 7,95E-03 84,76 -73,186 188,3 -13
4OH166 350 8,74E-03 48,331 -72,162 191,1 -23,4
4OH166 400 9,08E-03 49,451 -74,884 193,2 -21,5
4OH166 450 9,66E-03 61,715 -74,799 191,4 -18,8
4OH166 475 9,28E-03 52,237 -73,121 191,2 -21,9
4OH166 500 9,55E-03 53,836 -71,162 189,1 -22,5
4OH166 525 1,02E-02 64,627 -72,907 189,2 -18,8
4OH166 550 1,10E-02 64,959 -74,934 191,2 -18
4OH166 575 9,95E-03 66,335 -74,005 190,1 -17,9
4OH166 600 1,04E-02 68,59 -66,858 182,7 -19,4
4OH166 625 1,00E-02 45,264 -72,203 191,7 -24,1
4OH166 650 4,49E-03 325,56 -79,106 212,1 -20,9
4OH166 675 5,84E-03 341,33 -67,033 214,1 -33,6
4OH198 0 4,66E-03 220,27 -39,394 254 28,1
4OH198 100 5,54E-03 36,158 -86,667 217,5 -12,7
4OH198 150 5,86E-03 17,684 -82,907 217,3 -16,7
4OH198 200 7,21E-03 51,384 -73,613 205,9 -19,9
4OH198 250 7,54E-03 61,15 -75,362 206,1 -16,7
4OH198 300 7,76E-03 76,515 -74,938 204,5 -13,1
4OH198 350 7,81E-03 75,051 -74,15 203,7 -13,7
4OH198 400 7,70E-03 69,91 -72,624 202,6 -15,5
4OH198 425 7,12E-03 75,572 -72,63 202,2 -13,8
4OH198 450 7,37E-03 53,302 -63,157 196 -24,9
4OH198 475 7,44E-03 58,072 -71,628 203 -19,2
4OH198 500 7,29E-03 51,216 -60,466 193,9 -27,1
4OH198 525 7,99E-03 50,75 -40,535 172,9 -35,9
4OH198 550 6,53E-03 62,739 -66,763 197,6 -19,7
4OH198 575 7,39E-03 57,717 -61,728 193,6 -23,7
4OH198 600 9,84E-04 301,47 -58,944 248,4 -24,5
4OH198 625 7,17E-04 204,25 26,325 348,2 61,9
oh4_9 0 5,98E-03 300,4 81 300,4 81
oh4_9 100 4,17E-03 195,7 47,1 195,7 47,1
oh4_9 150 4,58E-03 192,5 17,6 192,5 17,6
oh4_9 200 5,67E-03 178,5 4,7 178,5 4,7
oh4_9 225 5,23E-03 190,2 3 190,2 3
oh4_9 250 6,18E-03 184,8 -3 184,8 -3
oh4_9 275 5,95E-03 186,5 1 186,5 1
oh4_9 300 6,51E-03 181,8 -4,4 181,8 -4,4
oh4_9 325 8,11E-03 183,7 -15,9 183,7 -15,9
oh4_9 350 6,93E-03 186,7 -6,5 186,7 -6,5
oh4_9 375 7,32E-03 182,6 0,1 182,6 0,1
oh4_9 400 6,70E-03 181,1 -1,6 181,1 -1,6
oh4_9 425 7,59E-03 178,2 -2,3 178,2 -2,3
oh4_9 450 7,88E-03 188,3 -32,3 188,3 -32,3
oh4_9 475 8,06E-03 179,8 -19,6 179,8 -19,6
oh4_9 500 7,22E-03 172,8 -10 172,8 -10

Table2. Thermal demagnetization data

(1) Sample = sample name

(2) Temperature (°C)

(3) NRM intensity (A/m)

(4) Core Declination (°E)

(5) Core Inclination (°)

(6) Geographic Declination (°E)

(7) Geographic Inclination (°)

oh4_9 525 7,51E-03 173 -14,2 173 -14,2
oh4_9 550 7,85E-03 180,9 -16,1 180,9 -16,1
oh4_9 575 6,95E-03 172,8 -38,2 172,8 -38,2
oh4_9 600 7,81E-03 176,2 -5,6 176,2 -5,6
oh4_9 625 8,31E-03 166,9 -9,8 166,9 -9,8
oh4_9 650 1,69E-03 146,1 -8,8 146,1 -8,8
oh4_9 675 2,64E-03 165,1 27,6 165,1 27,6
4OH237 0 4,82E-03 307,18 -39,105 314,4 -34,8
4OH237 100 5,89E-03 12,867 -46,709 251,2 -51,7
4OH237 150 6,32E-03 22,102 -43,281 239,4 -51,6
4OH237 200 6,38E-03 26,508 -44,836 237,1 -48,4
4OH237 250 6,74E-03 31,491 -44,017 232,5 -46,4
4OH237 300 7,59E-03 33,549 -42,185 229 -46,4
4OH237 350 6,96E-03 48,493 -29,823 206,5 -40,7
4OH237 400 6,98E-03 34,937 -43,091 229,2 -45,1
4OH237 450 7,44E-03 32,826 -39,982 226,9 -48,2
4OH237 475 7,66E-03 29,674 -38,219 227,1 -51,2
4OH237 500 7,51E-03 30,628 -42,274 231,2 -48,1
4OH237 525 7,58E-03 39,161 -34,382 216 -46,7
4OH237 550 7,21E-03 35,88 -33,325 216,4 -49,7
4OH237 575 7,39E-03 45,072 -40,304 220,7 -40
4OH237 600 8,82E-03 33,822 -35,069 220 -50,3
4OH237 625 9,14E-03 34,104 -32,999 217 -51,1
4OH237 650 7,86E-03 39,885 -34,143 215,3 -46,3
4OH237 675 6,45E-03 59,487 -32,309 207,3 -31
4OH263 0 5,32E-03 215,25 25,505 38,5 45,5
4OH263 100 2,38E-03 156,21 24,64 125,1 54
4OH263 150 1,74E-03 167,9 23,354 110 61,1
4OH263 200 3,12E-03 129,46 15,44 155,7 36,7
4OH263 250 2,58E-03 111,68 5,3312 169,6 21,2
4OH263 300 3,04E-03 100,23 27,382 148,4 7,7
4OH263 350 3,68E-03 104,32 21,011 154,2 12,2
4OH263 400 2,08E-03 97,09 13,064 163 6,2
4OH263 425 3,32E-03 101,24 13,568 162,1 10,2
4OH263 450 4,19E-03 97,503 9,4726 166,6 6,9
4OH263 475 4,44E-03 88,956 8,4209 168,1 -1,5
4OH263 500 4,88E-03 88,809 9,9039 166,7 -1,7
4OH263 525 4,63E-03 90,252 11,455 165 -0,3
4OH263 550 4,51E-03 95,255 19,167 157 4
4OH263 575 4,05E-03 91,152 10,67 165,8 0,6
4OH263 600 4,11E-03 100,7 10,516 165,3 9,9
4OH263 625 5,00E-03 98,352 18,289 157,7 7
4OH263 650 2,72E-03 256,13 25,04 22,8 11,2
4OH263 675 1,50E-03 106,91 43,79 131 10
4OH303 0 3,23E-03 236,2 27,229 325,5 35,4
4OH303 100 2,00E-03 251,23 -12,724 283,6 15,1
4OH303 150 2,23E-03 265,72 -38,59 261,9 -4,2
4OH303 200 1,84E-03 264,22 -29,751 270,3 -1
4OH303 250 2,07E-03 297,15 -48,992 251,3 -26,7
4OH303 300 2,04E-03 287,24 -47,416 254,1 -20,4
4OH303 350 1,55E-03 297,4 -51,842 248,2 -26,2
4OH303 400 2,16E-03 305,01 -57,641 240,4 -28,4
4OH303 450 2,09E-03 344,07 -54,487 223,7 -45,7
4OH303 475 1,87E-03 321,71 -55,792 236,4 -37,1
4OH303 500 2,23E-03 330,26 -52,091 235,3 -43,3
4OH303 525 2,15E-03 327,49 -48,846 240,2 -44,4
4OH303 550 2,70E-03 351,52 -64,715 215 -37
4OH303 575 2,49E-03 356,85 -59,274 212,7 -42,7
4OH303 600 2,60E-03 16,526 -43,156 188,9 -55,7
4OH303 625 8,20E-04 346,03 -57,61 220,7 -43,2
4OH303 650 7,07E-04 193,11 4,3777 271,1 75
4OH303 675 1,33E-03 188,04 -17,87 225,5 59,1
4OH363 0 3,10E-02 213,6 53,98 361,2 40,3
4OH363 100 1,77E-02 222,87 66,562 8,6 28,4
4OH363 150 1,30E-02 178,31 45,237 28,7 56,7
4OH363 200 9,97E-03 327,13 77,725 19,9 1,6
4OH363 250 1,11E-02 280,46 83,141 19,6 10,7
4OH363 300 1,20E-02 21,352 65,563 35,3 -10,8
4OH363 350 9,25E-03 4,0567 72,209 27,7 -5,7
4OH363 400 6,90E-03 318,69 82,68 21,6 6,5
4OH363 425 7,78E-03 0,35959 52,099 26,7 -25,9
4OH363 450 6,28E-03 2,5378 54,892 28,1 -23,1
4OH363 475 7,40E-03 0,8443 50,092 27,1 -27,9
4OH363 500 6,43E-03 10,587 70,209 30,1 -7,5
4OH363 525 6,24E-03 26,277 44,481 47,6 -28,7
4OH363 550 7,06E-03 28,183 49,396 46,1 -23,8
4OH363 575 7,44E-03 25,305 44,688 46,8 -28,8
4OH363 600 8,72E-03 18,342 47,609 40,4 -28,2
4OH363 625 6,08E-03 23,732 3,6807 84,3 -61,7
4OH363 650 4,98E-03 329,12 47,111 3,9 -24,8
4OH363 675 4,54E-03 198,35 -13,379 242,7 58,8
4OH403 0 9,80E-03 171,93 -38,217 292,3 46,1
4OH403 100 8,74E-03 109,82 -45,116 259,1 10,2
4OH403 150 1,15E-02 81,495 -32,445 243,6 -9,9
4OH403 200 1,22E-02 85,482 -32,499 243,7 -6,5
4OH403 250 1,27E-02 76,685 -29,834 241 -14
4OH403 300 1,31E-02 71,883 -29,611 241,1 -18,2
4OH403 350 1,28E-02 73,129 -31,947 243,4 -16,9
4OH403 400 1,30E-02 73,814 -30,878 242,3 -16,4
4OH403 425 1,35E-02 67,322 -26,303 237,9 -22,5
4OH403 450 1,30E-02 68,885 -26,425 237,9 -21,1
4OH403 475 1,28E-02 69,574 -27,573 239,1 -20,4
4OH403 500 1,28E-02 67,718 -30,095 242 -21,7
4OH403 525 1,38E-02 60,872 -9,558 219,7 -29,5
4OH403 550 1,35E-02 64,416 -27,062 239,1 -25
4OH403 575 1,24E-02 80,852 -31,947 243,1 -10,4
4OH403 600 2,36E-03 73,202 48,901 160,9 -7,1
4OH403 625 1,86E-03 141,99 50,632 149,8 34,4
4OH403 650 6,11E-03 317,7 57,308 98,9 -18,9
4OH433 0 7,27E-03 106,94 -14,657 359 10,9

Table2. Thermal demagnetization data

(1) Sample = sample name

(2) Temperature (°C)

(3) NRM intensity (A/m)

(4) Core Declination (°E)

(5) Core Inclination (°)

(6) Geographic Declination (°E)

(7) Geographic Inclination (°)

4OH433 100 5,46E-03 350,71 -36,296 91,8 -69,9
4OH433 150 7,32E-03 351,66 -26,463 110,4 -78,6
4OH433 200 7,61E-03 324,64 -23,72 143,5 -56,6
4OH433 250 7,87E-03 337,25 -17,064 158,5 -68,3
4OH433 300 7,17E-03 331,7 -18,121 154,8 -63,1
4OH433 350 9,04E-03 340,31 -7,4991 185,7 -68,1
4OH433 400 8,96E-03 328,04 -12,444 165,1 -58,7
4OH433 425 8,76E-03 320,29 -3,0751 175,8 -48,3
4OH433 450 1,02E-02 321,14 -9,2626 167,3 -51,3
4OH433 475 1,02E-02 324,3 -9,4029 168,6 -54,3
4OH433 500 1,06E-02 325,4 -10,755 166,9 -55,8
4OH433 500 4,10E-03 319,47 5,1839 185,8 -43,8
4OH433 550 9,90E-03 321,11 -14,694 158,7 -52,6
4OH433 575 8,36E-03 325,76 -13,071 163 -56,7
4OH433 600 9,89E-03 327,08 -12,32 164,9 -57,8
4OH433 625 1,02E-02 327,2 -15,616 158,9 -58,6
4OH433 650 7,11E-03 325,14 -23,091 144,6 -57
4OH433 675 3,40E-03 15,973 -32,373 27,5 -69,7
4OH443 0 1,92E-02 356,51 6,964 247,9 -62,8
4OH443 100 9,50E-03 355,64 14,129 248 -55,6
4OH443 150 5,06E-03 328,02 -7,3744 183,1 -56,6
4OH443 200 8,15E-03 338,92 0,91438 208,4 -60,6
4OH443 250 6,18E-03 350,71 10,729 238,1 -57,9
4OH443 300 2,67E-03 315,46 3,6487 188,9 -40,3
4OH443 350 3,96E-03 341,3 -31,7 126,9 -69,6
4OH443 400 5,04E-03 339,95 11,804 222 -52,6
4OH443 425 3,85E-03 346,94 -1,7855 218,9 -67,8
4OH443 450 3,81E-03 325,67 24,174 216,8 -34,6
4OH443 475 3,31E-03 344,89 12,937 230 -53,9
4OH443 550 4,52E-03 331,79 3,9362 203,2 -53,4
4OH443 575 5,39E-03 323,75 -14,943 167,9 -55,1
4OH443 600 5,31E-03 317,19 -12,728 168,8 -48,4
4OH454 0 2,58E-02 130,48 27,069 317,4 38,5
4OH454 100 9,96E-03 122,93 32,628 312,9 30,8
4OH454 150 1,19E-02 95,497 52,888 294,8 8,1
4OH454 200 8,48E-03 98,584 79,074 268,4 7,5
4OH454 250 5,64E-03 116,87 63,459 282,1 17,1
4OH454 300 8,20E-03 75,336 82,243 265 4
4OH454 350 7,29E-03 298,89 87,395 255,2 4,7
4OH454 400 6,92E-03 15,061 65,709 263,9 -17,4
4OH454 425 8,25E-03 323,08 74,066 247,9 -6,8
4OH454 450 8,04E-03 326,82 72,003 247,6 -9,1
4OH454 475 7,60E-03 280,06 74,27 242 3,1
4OH454 500 8,30E-03 294,79 72,789 241,9 -1,3
4OH454 525 7,69E-03 291,7 74,068 242,7 0
4OH454 550 6,56E-03 298,99 66,243 236,8 -5,7
4OH454 575 6,67E-03 278 67,86 235,6 2,6
4OH454 600 6,03E-03 299,55 64,711 235,5 -6,6
4OH454 625 2,36E-03 109,82 39,178 308 19,1
4OH454 650 1,66E-03 255,07 39,757 207,1 15,3
4OH454 675 4,96E-03 275,12 28,283 196,2 -1,6
4OH468 0 1,33E-02 132,59 -15,314 12,7 40,4
4OH468 100 8,46E-03 140,02 -33,749 38,2 38,9
4OH468 150 7,76E-03 142,52 -41,845 47,7 35,4
4OH468 200 6,83E-03 161,89 -41,902 62,7 44,1
4OH468 250 5,59E-03 183,79 -60,812 83,6 28,1
4OH468 300 5,99E-03 208,15 -57,236 98,2 27,5
4OH468 350 6,83E-03 212,13 -69,866 92,5 16
4OH468 400 5,19E-03 201,65 -56,377 95,1 30
4OH468 425 4,69E-03 215,24 -52,131 105,4 29,2
4OH468 450 4,62E-03 217,2 -58,738 101,5 23,5
4OH468 475 5,64E-03 215,12 -63,07 97,7 20,8
4OH468 500 5,06E-03 233,18 -65,045 101,8 13,7
4OH468 550 5,21E-03 188,2 -63,645 85,5 25,1
4OH468 575 5,65E-03 243,97 -59,179 109,6 12,1
4OH468 600 4,84E-03 215,9 -57,632 101,7 24,8
4OH468 625 5,47E-03 213,42 -50,372 105,8 31,3
4OH468 650 3,03E-03 218,1 -37,159 120,2 38,1
4OH468 675 1,18E-03 243,5 -0,82776 170,1 26,5
4OH483 0 5,41E-03 132,06 76,769 354,4 6,8
4OH483 100 3,51E-03 45,599 54,64 11,8 -25,7
4OH483 150 4,19E-03 12,369 56,149 352,9 -34,9
4OH483 200 2,96E-03 340,95 6,2095 267,6 -70,5
4OH483 250 3,04E-03 354,7 4,5244 280,2 -84,1
4OH483 300 2,29E-03 343,01 -9,0563 221,1 -69,8
4OH483 350 3,14E-03 353,03 -27,048 177,1 -60,2
4OH483 400 2,40E-03 9,6599 -6,2246 115 -77,3
4OH483 425 3,63E-03 358,42 -2,2078 185,1 -85,5
4OH483 450 3,02E-03 0,57678 9,3371 348,9 -82,6
4OH483 475 3,56E-03 14,273 -6,9473 106,8 -73,2
4OH483 500 3,11E-03 357,97 5,1579 311,8 -86,2
4OH483 550 3,97E-03 10,913 -2,4571 96,7 -78,2
4OH483 575 3,44E-03 2,6864 7,5094 10,3 -83,9
4OH483 600 3,01E-03 0,3807 0 153,7 -88
4OH484 0 6,04E-03 272,98 -27,086 314,4 -2,7
4OH484 100 3,43E-03 5,1783 -20,479 237,9 -68,9
4OH484 150 3,67E-03 355,28 -7,1978 284,6 -81,4
4OH484 200 4,01E-03 18,957 -17,997 206,5 -64,1
4OH484 250 3,63E-03 27,553 -1,8924 165,6 -62,4
4OH484 300 4,49E-03 29,33 -7,8045 177,1 -59,7
4OH484 350 3,35E-03 40,135 4,628 154,3 -49,6
4OH484 400 4,43E-03 25,753 -4,7863 172,4 -63,8
4OH484 425 4,04E-03 43,191 -2,9811 165,9 -46,7
4OH484 450 3,43E-03 30,935 -6,3693 173,8 -58,5
4OH484 450 3,67E-03 44,007 -0,78046 162,6 -46
4OH484 475 3,33E-03 45,249 -12,145 178,4 -43,5
4OH484 500 3,69E-03 29,482 -17,525 194,2 -56,1
4OH484 525 3,24E-03 41,917 -20,988 191,4 -44
4OH484 550 3,23E-03 27,121 -3,5492 169,2 -62,7
4OH484 575 3,11E-03 34,1 -4,2383 169 -55,7

Table2. Thermal demagnetization data
(1) Sample = sample name
(2) Temperature (°C)
(3) NRM intensity (A/m)
(4) Core Declination (°E)
(5) Core Inclination (°)
(6) Geographic Declination (°E)
(7) Geographic Inclination (°)

4OH484 600 2,85E-03 36,505 -7,6636 174,2 -52,8
4OH484 625 1,03E-03 28,172 8,6327 143,7 -60,6
4OH484 650 1,28E-03 24,825 -19,473 201,6 -58,8
4OH484 675 1,63E-03 328,51 8,7718 358 -57,4
4OH508 0 5,70E-03 258,89 -53,747 286,5 9
4OH508 100 3,00E-03 304,35 -71,379 265,9 -7,5
4OH508 150 3,76E-03 55,088 -71,845 235,6 -7,4
4OH508 200 4,50E-03 41,9 -40,954 214,1 -31,8
4OH508 250 5,95E-03 45,659 -51,676 221,7 -23,1
4OH508 300 5,62E-03 55,849 -47,564 214,1 -19,9
4OH508 350 5,44E-03 60,328 -44,564 209,8 -18,4
4OH508 400 5,34E-03 52,82 -46,289 214 -22,3
4OH508 425 5,96E-03 60,779 -43,214 208,3 -18,6
4OH508 450 6,61E-03 65,124 -38,681 202,7 -17,2
4OH508 475 6,33E-03 64,99 -38,696 202,7 -17,3
4OH508 500 6,48E-03 66,977 -37,475 201 -16,1
4OH508 525 6,65E-03 65,611 -38,754 202,6 -16,8
4OH508 550 6,69E-03 73,593 -35,438 197,6 -11,5
4OH508 575 6,69E-03 69,113 -35,212 198,3 -15,1
4OH508 600 6,56E-03 67,868 -38,254 201,6 -15,3
4OH508 625 6,86E-03 64,045 -37,3 201,6 -18,4
4OH508 650 5,30E-04 289,96 -40,312 297,9 -13,1
4OH528 0 1,68E-02 233,71 -4,857 338,9 36,5
4OH528 100 8,70E-03 248,31 14,586 358,2 19,2
4OH528 150 8,98E-03 256,68 5,3039 347,3 12,6
4OH528 200 4,78E-03 233,86 40,602 29 22,2
4OH528 250 6,07E-03 247,77 18,954 2,9 18,8
4OH528 300 6,14E-03 252,91 19,599 2,4 13,9
4OH528 350 4,37E-03 255,93 -3,8047 338,1 14,4
4OH528 400 5,42E-03 239,48 24,854 11,3 24,5
4OH528 425 4,69E-03 259,63 27,395 9 6,4
4OH528 450 4,08E-03 250,85 29,862 13,2 13,4
4OH528 475 5,14E-03 245,86 27,723 12,3 18,1
4OH528 500 3,85E-03 250,93 27,176 10,5 14
4OH528 550 3,91E-03 250 27,221 10,7 14,8
4OH528 575 3,10E-03 252,61 26,259 9,2 12,7
4OH528 600 3,13E-03 240,09 33,566 19,9 20,8
4OH528 625 3,60E-03 240,1 51,807 37,1 13
4OH548 0 2,25E-02 232,57 -19,158 324,2 35,8
4OH548 100 8,06E-03 252,43 -33,918 311,7 15,7
4OH548 150 6,65E-03 258,94 -36,877 309,4 10
4OH548 200 6,68E-03 260,79 -37,409 309 8,5
4OH548 250 6,98E-03 267,73 -46,66 299,9 3
4OH548 300 6,11E-03 271,18 -37,54 308,9 0,3
4OH548 350 5,22E-03 271,94 -42,73 303,7 -0,1
4OH548 400 5,14E-03 282,47 -37,52 308,1 -8,6
4OH548 425 4,39E-03 276,21 -27,833 318,4 -4,5
4OH548 450 4,12E-03 270,15 -24,513 322 0,7
4OH548 475 4,44E-03 282,53 -31,65 313,9 -9,6
4OH548 500 4,93E-03 272,24 -28,054 318,4 -1
4OH548 525 4,08E-03 290,87 -43,16 301 -13,6
4OH548 550 4,32E-03 268,96 -27,273 319,3 1,8
4OH578 0 2,57E-02 262,11 -20,743 321,8 8,1
4OH578 100 8,53E-03 247,85 -26,77 314,6 20,6
4OH578 150 1,11E-02 277,77 -20,558 321,5 -6,6
4OH578 200 7,03E-03 249,17 -29,368 312 19,1
4OH578 250 5,92E-03 259,53 -55,484 286,7 7,6
4OH578 300 4,39E-03 265,29 -63,708 278,8 3,9
4OH578 350 4,20E-03 234,85 -31,111 307 30,7
4OH578 400 6,28E-03 266,26 -44,874 297,6 4,1
4OH578 425 4,53E-03 259,98 -58,668 283,6 6,9
4OH578 450 3,85E-03 248,65 -68,198 273 9,6
4OH578 475 3,21E-03 239,9 -75,616 265,1 9,1
4OH578 500 3,81E-03 229,88 -72,223 266,4 13,3
4OH578 550 5,44E-03 224,3 -77,68 261,2 10,8
4OH578 575 4,89E-03 211,66 -73,235 261,6 16,2
4OH578 600 2,47E-03 191,69 -61,371 258,9 30
4OH578 625 2,42E-03 222,33 -38,095 294,1 37,1

OH5

5OH130 0 1,79E-02 67,04 63,749 5,1 24,6
5OH130 100 1,03E-02 60,573 58,446 7,3 18,8
5OH130 150 6,68E-03 45,292 51,414 5,1 7,8
5OH130 200 5,04E-03 32,113 55,915 356 7,8
5OH130 250 4,23E-03 38,876 66,928 353,6 19
5OH130 300 3,24E-03 20,045 60,896 348,3 10,2
5OH130 350 1,44E-03 64,867 71,953 357,2 28,8
5OH130 400 2,13E-03 2,596 55,871 340 3,9
5OH130 425 1,90E-03 322 77,684 329,9 28
5OH130 450 1,78E-03 5,69 71,878 340,4 20
5OH130 475 1,67E-03 326,79 63,884 324 15,2
5OH130 500 1,72E-03 303,55 58,405 311,3 17,2
5OH130 525 1,19E-03 265,12 56,401 297,2 33,4
5OH130 550 1,00E-03 300,47 31,681 291,3 -1
5OH130 575 1,21E-03 280,55 57,595 302,5 26,3
5OH130 600 1,30E-03 271,96 42,056 284,7 23,1
5OH130 625 1,31E-03 282,87 59,906 305,4 26,4
5OH130 650 8,21E-04 219,22 45,509 275,7 60,1
5OH130 675 8,65E-04 222,66 48,582 281,5 57,7
5OH181 0 1,46E-02 250,24 42,374 315,4 29,6
5OH181 100 6,75E-03 260,1 39,908 314 21,8
5OH181 150 5,37E-03 258 35,49 309 22,5
5OH181 200 5,21E-03 261,76 35,192 309,4 19,5
5OH181 250 3,02E-03 254,15 33,152 305,7 25,1
5OH181 300 2,52E-03 245,47 34,526 305,9 32,4
5OH181 350 2,12E-03 259,84 29,743 303,4 19,6
5OH181 400 1,76E-03 249,96 28,027 299,3 27,5
5OH181 425 1,44E-03 230,02 16,79 280,5 42,8
5OH181 450 9,74E-04 250,84 22,196 293,2 25,3
5OH181 475 1,23E-03 238,55 29,816 299,3 37,7
5OH181 500 1,04E-03 254,41 -1,214 271,1 13,8

Table2. Thermal demagnetization data

(1) Sample = sample name

(2) Temperature (°C)

(3) NRM intensity (A/m)

(4) Core Declination (°E)

(5) Core Inclination (°)

(6) Geographic Declination (°E)

(7) Geographic Inclination (°)

5OH181 525 1,02E-03 266,68 1,801 278,9 3,8
5OH181 550 1,13E-03 257,41 -3,8174 270 10
5OH181 575 3,30E-04 306,68 42,25 331,6 -8,3
5OH181 600 5,59E-04 222,09 26,323 292,4 51,8
5OH215 0 9,47E-03 136,92 26,669 80,6 44,6
5OH215 100 5,38E-03 142,16 28,896 75,1 48,2
5OH215 150 4,03E-03 139,79 35,112 68,4 43,6
5OH215 200 3,25E-03 132,22 31,706 75,8 39,2
5OH215 250 2,52E-03 148,58 35,656 62,1 49,4
5OH215 300 2,13E-03 133,97 40,603 64,7 37,1
5OH215 350 1,60E-03 143,96 22,864 83 51,9
5OH215 400 1,38E-03 135,58 65,877 39,7 23,6
5OH215 425 1,47E-03 161,76 75,302 26,4 20,9
5OH215 450 1,05E-03 181,42 72,113 21 24,9
5OH215 475 1,12E-03 139,09 55,438 47,4 31,7
5OH215 500 1,40E-03 150,35 70,191 32,1 24
5OH215 550 1,40E-03 245,04 74,083 6,7 13,4
5OH215 575 9,78E-04 334,18 87,981 20,6 5,2
5OH215 600 1,06E-03 259,9 85,983 17,5 7,7
5OH215 625 8,04E-04 20,134 14,337 64,6 -60,8
5OH244 0 5,47E-03 233,54 24,045 320,5 37,6
5OH244 100 2,63E-03 222,55 35,765 338,5 44,3
5OH244 150 2,57E-03 216,44 19,323 316,3 53,9
5OH244 200 1,62E-03 207 39,427 353 52,8
5OH244 250 1,56E-03 171,41 55,456 35,4 45
5OH244 300 1,53E-03 173,09 29,342 46,9 70,6
5OH244 350 1,47E-03 154,83 45,736 55,5 49,2
5OH244 400 1,03E-03 66,267 82,911 35,1 8,1
5OH244 425 9,51E-04 153,91 37,262 65,9 54,8
5OH244 450 9,74E-04 145,09 22,459 95 54,8
5OH244 475 8,71E-04 128,45 33,662 84,2 37,9
5OH244 500 9,46E-04 118,79 31,395 88,4 30,2
5OH244 525 8,77E-04 132,79 16,222 106,5 43,9
5OH244 550 1,22E-03 128,64 22,035 98,9 39,8
5OH244 575 1,03E-03 102,1 5,5956 115,2 12,9
5OH244 600 1,54E-03 115,96 20,631 100,9 28
5OH244 625 1,01E-03 78,304 22,174 94,4 -6,4
5OH244 675 4,98E-04 357,4 74,609 27,8 -4,4
5OH266 0 1,04E-02 249,29 25,712 325,3 24,8
5OH266 100 4,66E-03 247,54 20,218 319 25,8
5OH266 150 3,31E-03 245,24 19,051 317,4 27,8
5OH266 200 3,62E-03 244,11 18,511 316,7 28,8
5OH266 250 2,31E-03 233,55 16,604 313 38,6
5OH266 300 2,09E-03 228,62 25,684 324,9 43,4
5OH266 350 2,01E-03 220,54 17,029 312,2 51,1
5OH266 400 1,23E-03 187,35 19,768 338,8 81,5
5OH266 425 1,23E-03 201 15,019 306,3 69,7
5OH266 450 1,05E-03 180,29 18,366 28,9 86,6
5OH266 475 1,05E-03 193,06 10,127 284,1 76,4
5OH266 500 9,99E-04 188,67 14,202 299,2 81,6
5OH266 525 1,04E-03 197,63 12,478 297,3 72,7
5OH266 550 6,64E-04 177,76 15,827 102,3 87,7
5OH266 575 5,91E-04 237,53 37,41 338,9 34,7
5OH266 600 8,35E-04 273,24 26,928 330,3 3,9
5OH266 625 3,64E-04 206,71 17,587 313 64,3
5OH291 0 1,27E-02 272,53 36,518 332,3 8,1
5OH291 100 4,56E-03 280,44 49,187 346,2 6,2
5OH291 150 3,74E-03 258,76 31,77 325,1 18,2
5OH291 200 3,25E-03 288,68 46,913 346,2 0,2
5OH291 250 2,46E-03 327,38 40,907 359,9 -24,7
5OH291 300 1,85E-03 302,33 65,455 5,9 3,1
5OH291 350 1,85E-03 331,47 55,605 10,4 -13,5
5OH291 400 1,97E-03 337,41 32,588 2,9 -35,9
5OH291 425 2,03E-03 341,62 35,775 8,4 -34,4
5OH291 450 1,42E-03 359,56 24,117 25,9 -48,9
5OH291 475 1,47E-03 19,921 15,638 58,6 -51,9
5OH291 500 1,66E-03 32,013 19,929 68,2 -41,5
5OH291 550 2,07E-03 43,444 14,644 82,6 -36,7
5OH291 575 2,08E-03 26,409 18,304 64,1 -46,2
5OH291 600 1,66E-03 44,469 14,627 83,3 -35,9
5OH291 625 2,15E-03 43,434 8,7599 88,9 -39,9
5OH291 650 6,07E-04 221,76 22,045 310,8 50,4
5OH291 675 4,55E-04 268,34 40,712 335,7 12,2
5OH326 0 1,40E-02 227,13 59,744 314,7 31,9
5OH326 100 8,08E-03 229,83 57,266 311,4 31,9
5OH326 150 5,81E-03 216,27 55,855 315,3 38,8
5OH326 200 3,79E-03 211,34 51,375 313,7 44
5OH326 250 3,85E-03 221,44 55,887 313 36,6
5OH326 300 2,64E-03 210,72 40,601 302 51,5
5OH326 350 1,51E-03 201,51 36,623 305 59,5
5OH326 400 1,60E-03 221,18 44,147 300,2 43,1
5OH326 425 1,50E-03 179,86 37,321 340,8 65,7
5OH326 450 6,97E-04 184,89 46,409 334,4 56,3
5OH326 475 8,50E-04 159,42 37,199 14,1 59,6
5OH326 500 8,76E-04 195,48 29,709 302,3 68
5OH326 525 8,05E-04 174,37 -0,35592 137,4 75,5
5OH326 550 1,05E-03 159,93 -1,5248 105,2 65,4
5OH326 575 6,88E-04 139,55 4,1691 79,3 49,1
5OH326 600 1,15E-03 159,44 -6,0825 112,3 62,1
5OH326 625 8,04E-04 244,58 0,92657 245,4 24,9
5OH326 650 4,56E-04 87,557 34,607 259,9 32,8
5OH326 650 5,47E-04 239,07 14,817 36,2 5,4
5OH326 675 4,42E-04 188,33 25,044 308,6 75,6
5OH351 0 1,96E-02 244,94 56,261 317,8 21,3
5OH351 100 1,04E-02 256,47 61,724 322,1 14,3
5OH351 150 9,36E-03 256,6 60,755 321,1 14,4
5OH351 200 9,33E-03 258,35 60,442 320,7 13,6
5OH351 250 8,41E-03 255,1 58,788 319,2 15,4
5OH351 300 3,87E-03 257,04 68,386 328,9 13,1
5OH351 350 2,74E-03 250,91 72,451 333,4 14,3

Table2. Thermal demagnetization data
(1) Sample = sample name
(2) Temperature (°C)
(3) NRM intensity (A/m)
(4) Core Declination (°E)
(5) Core Inclination (°)
(6) Geographic Declination (°E)
(7) Geographic Inclination (°)

5OH351 400 2,40E-03 263,16 77,905 338,3 10,2
5OH351 425 2,28E-03 259,44 74,741 335,2 11,5
5OH351 450 1,91E-03 240,26 70,286 332,5 18,2
5OH351 475 1,87E-03 254,32 78,246 338,9 12
5OH351 500 1,91E-03 268,22 83,243 343,7 0,2
5OH351 525 1,04E-03 184,45 79,972 349,7 19
5OH351 550 9,78E-04 70,279 49,555 28,3 -5,6
5OH377 0 1,19E-02 243,16 -1,2982 327,6 26
5OH377 100 5,64E-03 245,85 -4,9812 324,3 22,6
5OH377 150 3,79E-03 262,19 8,1839 341,1 9,2
5OH377 200 3,03E-03 257,03 -9,8783 322,1 10,6
5OH377 250 2,40E-03 256,91 -13,223 318,8 9,9
5OH377 300 1,88E-03 245,52 -14,082 314,8 20,4
5OH377 350 1,96E-03 270,3 -11,482 323,3 -2,5
5OH377 400 1,52E-03 259,37 -19,217 313,5 6,2
5OH377 425 1,09E-03 269,68 -0,15784 334,3 0,3
5OH377 450 7,72E-04 255,36 -8,3423 323,3 12,6
5OH377 475 7,63E-04 242,39 -21,046 306,8 20,9
5OH377 500 8,14E-04 268,7 -35,948 298,9 -5,4
5OH377 525 5,55E-04 221,92 -22,438 295,2 37

Rhino Cave

R108 0 5,76E-03 147,05 34,501 295,9 46,8
R108 100 2,68E-03 143,7 47,057 285,2 36,8
R108 150 3,37E-03 68,488 64,08 279,1 -5,6
R108 200 1,74E-03 292,43 70,203 236,7 -3,6
R108 250 2,29E-03 56,937 54,128 285,6 -15,2
R108 300 1,07E-03 23,869 41,021 278,5 -40
R108 350 1,82E-03 39,782 47,861 284 -27,6
R108 400 1,86E-03 37,511 58,744 274,7 -20,5
R108 425 2,10E-03 65,834 32,182 309,3 -18
R108 450 2,19E-03 69,929 46,491 296,1 -10,7
R108 475 2,40E-03 73,464 44,256 299 -8,9
R108 500 1,93E-03 84,947 48,359 296,4 -0,4
R195 0 9,84E-04 199,16 32,595 225,1 64,5
R195 100 1,81E-03 289,71 13,536 193,5 -15,2
R195 150 2,17E-03 298,81 14,494 197,7 -23,1
R195 200 2,14E-03 303,27 12,66 197,8 -27,8
R195 250 2,28E-03 304,53 10,6 196,1 -29,7
R195 300 2,29E-03 302,37 7,3383 191,8 -29
R195 350 2,50E-03 300,77 -1,6025 181,4 -30,2
R195 400 2,80E-03 306,58 10,297 196,8 -31,7
R195 450 2,13E-03 302,46 9,2341 193,8 -28,4
R195 475 2,21E-03 310,48 11,533 200 -34,7
R195 500 2,15E-03 307,39 9,3708 196,1 -32,8
R195 525 1,96E-03 309,08 7,5697 194,9 -35,1
R195 550 1,93E-03 304,38 13,019 198,6 -28,6
R195 575 1,93E-03 305,31 13,157 199,2 -29,4
R195 600 2,22E-03 304,73 11,124 196,8 -29,7
R195 625 1,54E-03 314,48 16,007 207,1 -35,9
R216 0 3,42E-03 144,95 59,023 286,9 29,6
R216 100 1,69E-03 225 64,543 247,8 22,4
R216 150 1,57E-03 258,79 63,306 240,5 9,5
R216 200 1,59E-03 279,83 52,388 230 -2
R216 250 1,21E-03 281,69 38,806 216,9 -5,9
R216 300 1,16E-03 296,38 43,877 225 -15
R216 350 1,25E-03 284,42 40,183 218,7 -7,7
R216 400 8,87E-04 281,56 30,571 208,7 -7,3
R216 425 1,15E-03 278,54 44,539 222,1 -2,5
R216 450 1,25E-03 282,22 47,987 226 -4,4
R216 475 1,21E-03 280,48 45,194 223 -3,8
R216 500 8,78E-04 279,14 55,478 233 -1
R216 525 1,01E-03 273,65 50,225 227,3 1,5
R216 550 7,04E-04 304,11 77,719 256,9 -1,9
R216 575 7,18E-04 277,88 43,878 221,4 -2,2
R246 0 5,34E-03 164 -30,365 53,5 57,8
R246 100 4,73E-04 167,38 -4,2463 0,4 77,2
R246 150 1,56E-03 63,814 -61,501 54,2 -10,4
R246 200 6,29E-04 352,61 -25,435 94,2 -61,6
R246 250 6,57E-04 9,2902 -0,34903 4,1 -80,4
R246 300 4,13E-04 10,925 -23,223 57,7 -62,6
R246 350 5,24E-04 0,24538 -26,907 79,5 -61,1
R246 400 5,86E-04 336,21 -6,3671 150,4 -64,8
R246 450 4,51E-04 349,59 -56,476 86,7 -30,9
R246 475 1,15E-03 15,969 -73,235 75,3 -14,1
R246 500 6,06E-04 355,95 -47,273 83,6 -40,6
R246 525 4,20E-04 84,103 -59,325 49,5 -1,3
R246 550 4,46E-04 94,203 -31,16 21,1 4,6
R246 575 3,47E-04 113,2 9,4431 338,9 22,5
R246 600 5,09E-04 92,396 -19,986 9,9 2,9
R246 625 6,25E-04 91,554 -27,746 17,7 2,3
R246 650 7,50E-04 88,873 -35,55 25,6 0,2
R246 675 9,13E-04 69,157 4,2707 346,2 -20,9
R276 0 5,90E-03 165,3 -31,155 47,1 50,3
R276 100 3,68E-03 273,74 0,46735 157,9 -3,7
R276 150 2,14E-03 331,1 -12,11 142,8 -60,8
R276 200 3,62E-03 296,49 4,2785 164,7 -25,8
R276 250 3,21E-03 310,42 15,161 180,9 -36,5
R276 300 4,03E-03 298,61 6,2624 167,3 -27,5
R276 350 2,71E-03 304,9 22,592 187 -29
R276 400 1,99E-03 291,66 -10,654 147,9 -22,3
R276 425 1,99E-03 320,05 -8,9434 150,2 -50,3
R276 450 1,46E-03 315,59 -7,0358 153,1 -45,9
R276 475 1,57E-03 314,12 -3,6544 157,7 -44,2
R276 500 1,09E-03 316,19 -13,577 143,6 -46,2
R276 525 1,09E-03 305,64 -3,0032 157,6 -35,7
R276 550 1,14E-03 310,38 -19,341 136,7 -40
R276 575 1,54E-03 312,34 -34,581 117,2 -37,7
R276 600 9,29E-04 324,76 -25,497 123 -51,1
R276 625 5,52E-04 343,72 -56,671 78,2 -37,7
R276 650 1,04E-03 130,49 -17,407 3,5 35,8

Table2. Thermal demagnetization data

(1) Sample = sample name

(2) Temperature (°C)

(3) NRM intensity (A/m)

(4) Core Declination (°E)

(5) Core Inclination (°)

(6) Geographic Declination (°E)

(7) Geographic Inclination (°)

R276 675 6,72E-04 149,14 9,5906 328,3 59,2
R316 0 2,70E-03 196,39 -23,136 98,1 44
R316 100 2,82E-03 308,15 9,5801 192,2 -31
R316 150 3,65E-03 315,78 2,6725 189,5 -41,1
R316 200 3,59E-03 323,13 16,318 209,4 -38,7
R316 250 2,94E-03 323,84 -10,172 177,3 -53,8
R316 300 3,00E-03 319,82 11,329 201,9 -39,6
R316 350 3,05E-03 318,13 12,299 201,5 -37,6
R316 400 2,67E-03 322,91 15,65 208,6 -39
R316 450 2,42E-03 311,8 11,209 196,1 -33,2
R316 475 2,04E-03 319,09 27,185 215,5 -28,4
R316 500 2,00E-03 300,02 24,318 201,5 -16,7
R316 525 1,56E-03 286,48 30,431 201,1 -3,2
R316 550 1,68E-03 283,31 26,453 196,3 -2,4
R316 575 1,43E-03 300,14 16,4 194,4 -20,9
R316 600 1,50E-03 281,11 36,813 205,1 3,4
R316 625 1,51E-03 278,88 42,257 209,5 7
R316 650 1,39E-03 256,69 26,782 189,1 20,3
R316 675 1,40E-03 271,79 38,845 204,5 11
R342 0 2,76E-03 143,83 18,132 314,8 52,7
R342 100 1,19E-03 127,19 74,239 260 15,3
R342 150 1,08E-03 344,93 71,076 242,1 -12,3
R342 200 1,10E-03 324,79 75,133 238,4 -6,2
R342 250 6,68E-04 1,5911 86,909 247,1 2,9
R342 300 8,20E-04 351,85 61,785 242,9 -21,9
R342 350 4,50E-04 332,99 49,8 227,3 -29,5
R342 400 8,35E-04 32,082 55,37 266,2 -23,1
R342 400 7,46E-04 34,34 60,515 264 -18,3
R342 450 6,58E-04 62,103 63,978 270 -6,3
R342 475 7,71E-04 76,623 64,057 272,2 -0,4
R342 500 6,24E-04 58,577 46,769 284,5 -16,2
R342 525 8,19E-04 99,97 50,606 286,5 11
R342 550 6,95E-04 93,384 55,921 281,3 6,9
R342 575 8,91E-04 106,44 42,83 294,1 16,1
R342 600 6,68E-04 113,25 44,219 291,8 20,7
R342 625 7,64E-04 111,36 53,619 282,4 17,4
R342 650 4,78E-04 195,84 52,207 234 42
R342 675 2,21E-04 4,316 -15,51 43,3 -79,6
R392 0 2,17E-03 156,21 -20,252 32,8 54,1
R392 100 9,91E-04 125,13 38,564 301,6 31,5
R392 150 1,25E-03 314,49 17,494 192,2 -38,8
R392 200 1,02E-03 313,44 13,751 187,2 -39,3
R392 250 1,10E-03 320,24 6,948 181,6 -48
R392 300 8,86E-04 337,47 12,909 204,6 -60
R392 350 8,49E-04 347,3 -16,494 124,5 -74,4
R392 400 7,83E-04 339,71 -33,3 105,8 -57,7
R392 425 7,14E-04 340,5 -3,0512 173,5 -70,2
R392 450 7,43E-04 337,54 -6,8764 161,9 -67,7
R392 475 7,13E-04 316,8 -11,731 153,3 -47,2
R392 500 4,60E-04 315,11 -37,449 119,3 -39,2
R392 525 4,21E-04 39,995 -34,104 25 -44,3
R392 550 2,31E-04 56,217 -42,399 28,3 -29,3
R417 0 5,06E-03 193,79 26,511 220,7 61,2
R417 100 2,27E-03 229,69 79,017 238,6 8,1
R417 150 1,87E-03 119,25 66,859 267,5 12
R417 200 1,62E-03 252,64 66,008 223,9 7,9
R417 250 1,47E-03 275,12 79,459 236,5 0
R417 300 1,14E-03 223,88 86,366 244,5 3,6
R417 350 1,01E-03 321,6 76,191 238,3 -9,8
R417 400 8,75E-04 254,7 44,39 202,3 11,6
R417 425 6,88E-04 341,57 71,22 240,9 -16,8
R417 450 9,06E-04 34,223 72,756 256,9 -13,2
R417 475 1,08E-03 38,756 69,869 259,9 -14,6
R417 500 9,90E-04 51,757 81,275 253,9 -4,4
R417 525 9,30E-04 58,861 79,581 255,9 -4,4
R417 550 8,77E-04 50,425 73,139 260,1 -9,7
R417 575 1,05E-03 59,21 71,033 263,4 -8,6
R417 600 1,03E-03 75,553 72,88 263,6 -3,3
R417 625 1,12E-03 45,265 65,818 264,6 -15,8
R417 650 4,19E-04 345,82 45,392 233,6 -41,9
R417 675 2,01E-04 183,32 39,282 242,9 51,6
R431 0 3,67E-03 155,07 25,885 291,6 51,6
R431 100 1,93E-03 210,8 9,6367 188,1 56,4
R431 150 2,16E-03 189,64 5,8415 209,6 76,2
R431 200 1,80E-03 210,54 13,224 194,1 55,1
R431 250 1,31E-03 213,8 -23,917 129,4 51,8
R431 300 1,09E-03 209,71 -1,3121 168,4 60,2
R431 350 1,37E-03 205,01 -4,6832 161,5 65,1
R431 400 9,33E-04 207,58 -1,7803 167,8 62,4
R431 425 1,10E-03 193,35 5,0595 198,1 73,9
R431 450 7,76E-04 206,1 -2,069 167,5 63,9
R431 475 1,20E-03 202,02 22,26 215,6 56
R431 500 8,65E-04 186,75 13,235 232,8 71,5
R459 0 3,03E-03 187,58 28,989 242,6 54,3
R459 100 1,91E-03 199,69 18,053 215,4 59,1
R459 150 1,58E-03 201,67 7,2945 195,3 64,6
R459 200 1,39E-03 205,35 0,61638 177,8 63,8
R459 250 1,41E-03 209,29 -1,541 171,5 60,4
R459 300 1,32E-03 202,84 -2,5665 171,6 67
R459 350 1,48E-03 211,95 -12,498 150 57,8
R459 400 1,28E-03 210,11 -6,8932 160,6 60,1
R459 425 1,37E-03 214,32 -6,6164 161,1 55,9
R459 450 1,41E-03 223,5 -11,378 153,8 46,7
R459 475 1,58E-03 222,87 -16,299 146,5 46,8
R459 500 1,40E-03 208,91 -20,902 133,2 58,3

Sidi Abderrahmane

SA1 0 5,53E-04 13,859 -31,493 297,6 -56,8
SA1 100 6,77E-04 15,11 -12,808 268,4 -70,9
SA1 150 7,01E-04 25,68 -7,6259 244,7 -63,6
SA1 200 4,26E-04 13,279 -7,1535 254,8 -75,4

Table2. Thermal demagnetization data
(1) Sample = sample name
(2) Temperature (°C)
(3) NRM intensity (A/m)
(4) Core Declination (°E)
(5) Core Inclination (°)
(6) Geographic Declination (°E)
(7) Geographic Inclination (°)

SA1 250 5,84E-04 27,805 7,9661 211,1 -60,9
SA1 300 6,16E-04 35,603 -3,1646 233,5 -54,4
SA1 350 3,22E-04 345,52 -27,998 345,4 -59,7
SA1 400 1,20E-03 313,75 19,815 76,8 -40,1
SA1 425 3,73E-04 320,28 -25,053 14,1 -44,8
SA1 450 1,59E-04 329,82 -36,943 353,8 -44,5
SA1 475 2,89E-04 332,66 -24,129 6,2 -54,9
SA1 500 3,10E-04 333,94 -7,784 34,1 -63,2
SA1 525 4,03E-04 5,0131 -31,696 311,2 -58,9
SA1 550 5,79E-04 320,67 15,224 73,8 -47,9
SA1 575 2,54E-04 206,9 -72,271 327,7 14,8
SA1 600 3,57E-04 3,4474 21,199 147,9 -67,5
SA1 625 4,94E-04 7,0962 -2,5511 241,9 -82,7
SA1 650 5,45E-04 4,862 27,33 148,5 -61,3
SA2 0 9,06E-04 248,58 7,6737 50,3 20,1
SA2 100 4,34E-04 241,01 13,044 57,8 26,2
SA2 150 8,11E-04 263,91 2,3313 42,6 5,8
SA2 200 8,65E-04 229,47 4,71 51,5 39,3
SA2 250 7,50E-04 261,54 -8,821 31,7 9,4
SA2 300 3,78E-04 190,83 29,284 114 52,2
SA2 350 5,82E-04 255,72 4,4372 45,8 13,6
SA2 400 1,10E-03 193,61 6,244 83,5 71
SA2 425 5,07E-04 235,42 42,258 89,2 19,6
SA2 450 4,64E-04 223,66 11,315 62,1 42,9
SA2 475 5,30E-04 245,62 32,685 76,5 16,2
SA2 500 3,02E-04 279,73 19,929 58,5 -11,5
SA2 525 6,97E-04 249,87 54,291 96,1 5,8
SA2 550 8,82E-04 238,68 26,027 72,2 24,2
SA2 575 6,55E-04 240,27 12,44 57,3 27
SA3 0 7,03E-04 284,38 35,57 67,2 -14
SA3 100 5,52E-04 330,13 4,5731 33,7 -60,2
SA3 150 5,45E-04 335,26 11,972 51 -64,3
SA3 200 5,31E-04 325,93 18,558 57,8 -53,7
SA3 250 6,28E-04 324,79 29,807 73,2 -47,9
SA3 300 6,85E-04 309,43 28,113 63,8 -36,3
SA3 350 7,25E-04 309,7 23,404 58,2 -37,8
SA3 400 5,72E-04 299,09 7,1297 37,4 -29,3
SA3 425 7,86E-04 290,45 22,294 53,8 -20,4
SA3 450 7,62E-04 287,55 14,12 45,1 -18
SA3 475 6,88E-04 307,73 18,286 51,4 -37
SA3 500 6,37E-04 283,16 18,011 49,1 -13,7
SA3 525 6,91E-04 281,85 9,4959 40,4 -12,3
SA3 550 6,27E-04 282,92 7,4227 38,2 -13,3
SA3 575 8,40E-04 296,9 4,029 34 -27,1
SA3 600 1,22E-04 41,673 2,8195 211,8 -48,4
SA3 625 2,14E-04 25,346 38,336 152 -48,6
SA3 650 5,45E-04 295,47 9,4069 40 -25,8
SA4 0 2,23E-03 211,52 -50,88 357,8 29,8
SA4 100 1,08E-03 198,64 -37,272 357 46,2
SA4 150 8,37E-04 202,12 -24,356 12,5 55,2
SA4 200 8,33E-04 205,58 -25,31 15,2 52,4
SA4 250 5,49E-04 212,93 -24,211 23,3 48
SA4 300 6,31E-04 248,2 20,034 85,9 21,5
SA4 350 5,14E-04 205,51 -6,3672 45,3 62,9
SA4 400 5,12E-04 230,49 34,637 105,9 33,5
SA4 450 3,21E-04 269,08 54,521 120 3
SA4 475 7,43E-04 217,22 79,87 149,3 11
SA4 500 4,12E-04 282,33 14,773 81,2 -11,1
SA4 525 7,08E-04 317,09 72,488 143,5 -9,8
SA4 550 8,77E-04 45 82,957 160,5 -2
SA4 575 8,29E-04 341,09 53,196 142,3 -31,6
SA4 600 5,49E-04 231,56 53,287 124,6 24,4
SA4 625 6,74E-04 294,73 74,363 141,3 -3,6
SA4 650 3,77E-04 312,38 25,629 100,3 -35,7
SA4 675 4,12E-04 33,425 81,647 160,1 -4
SA5 0 7,43E-04 210,98 20,082 46,7 59,2
SA5 100 5,91E-04 184,75 50,744 112,7 51,1
SA5 150 5,94E-04 176,04 43,018 123,1 58,8
SA5 200 6,64E-04 177,95 44,127 120,3 57,8
SA5 250 2,50E-04 165,47 63,523 125,6 37,5
SA5 300 4,76E-04 211,56 30,401 64,7 55,5
SA5 350 4,20E-04 250,83 58,015 85,3 20,3
SA5 400 1,00E-03 258,22 36,458 62,3 16,5
SA5 425 4,09E-04 315,55 68,941 102,9 -3,3
SA5 450 5,06E-04 263,9 78,181 105,4 13
SA5 475 5,45E-04 313,75 83,142 112,5 7,2
SA5 500 5,81E-04 70,769 85,503 121,8 10,5
SA5 525 5,55E-04 299,74 76,565 105,8 5,1
SA5 550 7,08E-04 29,796 38,322 145 -32,5
SA5 575 8,00E-04 127,69 69,66 135 23,8
SA5 600 4,90E-04 69,717 84,261 123 10
SA5 625 7,29E-04 13,403 70,652 121,9 -6,8
SA5 650 3,85E-04 58,352 14,125 184,9 -26,5
SA5 675 6,26E-04 208,55 38,543 78,8 53,3
SA6 0 1,83E-03 228,74 -38,434 333,9 31,1
SA6 100 1,22E-03 232,87 -37,683 336,4 28,5
SA6 150 1,00E-03 236,57 -36,777 338,6 26,2
SA6 200 9,44E-04 235,05 -35,346 339,6 27,9
SA6 250 7,92E-04 245,78 -37,973 339,9 18,9
SA6 300 6,69E-04 252,02 -48,845 330,2 11,7
SA6 350 4,64E-04 253,82 -37,144 342,2 12,8
SA6 400 5,71E-04 254,61 -32,309 347,2 13
SA6 450 5,41E-04 269,59 -38,543 342 0,3
SA6 475 4,91E-04 288,69 -4,5521 15,7 -18,6
SA6 500 4,98E-04 337,56 2,7608 27,7 -67,4
SA6 525 4,03E-04 300,74 -7,5649 11,7 -30,4
SA6 550 3,32E-04 297,74 -23,081 354,8 -25,4
SA6 575 4,02E-04 299,37 -0,9985 19,4 -29,4
SA6 600 4,36E-04 3,1798 24,53 117,4 -65,3
SA6 625 5,18E-04 316,78 -14,978 359,2 -44,7

Table2. Thermal demagnetization data

(1) Sample = sample name

(2) Temperature (°C)

(3) NRM intensity (A/m)

(4) Core Declination (°E)

(5) Core Inclination (°)

(6) Geographic Declination (°E)

(7) Geographic Inclination (°)

SA6 650 2,84E-04 210,14 82,756 106,8 6,3
SA6 675 5,93E-04 353,58 5,0309 58,7 -81,9
SA7 0 1,48E-04 190,06 75,22 168,5 32,5
SA7 100 2,57E-04 3,2491 27,026 175,6 -44,9
SA7 150 2,53E-04 4,7636 17,946 179,2 -53,8
SA7 200 1,96E-04 7,7119 8,5126 188,2 -62,4
SA7 250 1,99E-04 2,8293 5,4092 178,6 -66,4
SA7 300 2,30E-04 352,59 11,561 157,1 -59,5
SA7 350 4,00E-04 351,9 40,224 164,3 -31,3
SA7 400 3,78E-04 310 25,567 122 -24,7
SA7 425 2,96E-04 347,42 29,752 157,1 -40,7
SA7 450 2,87E-04 321,25 3,6018 107,2 -46,1
SA7 475 4,18E-04 274,95 23,841 105,7 2,9
SA7 500 3,53E-04 236,64 19,368 92,6 36,6
SA7 525 6,52E-04 315,16 -37,418 45,7 -46,3
SA8 0 7,33E-04 85,314 65,322 155,6 11,7
SA8 100 6,47E-04 87,325 60,239 160,9 11,7
SA8 150 5,60E-04 107,99 49,653 172,5 23
SA8 200 6,16E-04 133,47 30,767 191,8 44,7
SA8 250 6,26E-04 128,19 48,155 171,1 36,2
SA8 300 5,74E-04 118,49 39,965 182,5 31,3
SA8 350 2,84E-04 132,99 -7,8849 243,5 38,1
SA8 400 1,08E-03 133,23 -2,3447 237,1 40,6
SA8 425 3,15E-04 146,92 8,5807 227,9 57
SA8 450 2,44E-04 116,35 16,407 209,8 29
SA8 475 1,23E-04 169,27 -26,747 296,4 47
SA8 500 2,60E-04 145,75 -12,43 257,7 46,4
SA8 525 1,42E-04 47,441 -22,641 237,7 -44,6
SA8 550 2,72E-04 235,51 -17,126 12,2 26,5
SA8 575 5,61E-05 43,675 11,304 191,7 -39,4
SA8 600 1,95E-04 291,16 70,034 111,8 7,1
SA8 625 2,76E-04 217,49 -2,0749 19 49,2
SA9 0 1,92E-04 14,826 -79,458 319,8 0,8
SA9 100 1,93E-04 342,24 -55,942 333,1 -21,4
SA9 150 2,60E-04 54,583 -50,507 290,4 -12,4
SA9 200 3,14E-04 59,487 -13,803 253,9 -26
SA9 250 9,46E-04 57,279 -38,683 279,1 -17,2
SA9 300 3,79E-04 316,67 -50,096 350,1 -18,2
SA9 350 3,10E-04 30,622 -33,266 290,3 -37
SA9 400 6,64E-04 246,57 -39,104 14,3 25
SA9 425 2,53E-04 325,16 -44,63 349,4 -26,1
SA9 450 2,67E-04 21,071 -21,997 290,5 -51,1
SA9 475 2,40E-04 10,192 -67,838 318,6 -10,8
SA9 500 8,07E-04 289,18 -29,391 19,4 -10,8
SA9 525 2,87E-04 19,395 -9,033 277,8 -62,2
SA9 550 1,72E-04 11,788 -47,005 313,1 -31
SA9 575 9,09E-04 27,553 3,2149 246,3 -61,6
SA10 0 1,02E-03 149,12 -53,705 316,5 41,6
SA10 100 7,93E-04 133,3 -55,141 310,5 33,6
SA10 150 7,33E-04 123,47 -54,64 307,1 28,8
SA10 200 7,55E-04 125,01 -55,075 307,9 29,5
SA10 250 6,87E-04 121,04 -56,577 308,6 26,8
SA10 300 6,92E-04 133,55 -49,943 305,1 36,4
SA10 350 5,22E-04 103,42 -49,326 298,8 17,8
SA10 400 5,24E-04 101,89 -58,752 308,6 16,4
SA10 450 4,94E-04 98,215 -54,481 304,1 14,5
SA10 475 3,63E-04 42,675 -39,762 12,6 -58,2
SA10 500 2,39E-04 46,219 -13,065 277,7 -37,8
SA10 525 5,31E-04 73,301 -32,318 285,8 -7,3
SA10 550 5,95E-04 8,111 -44,37 333,6 -33,2
SA10 575 4,49E-04 80,734 -41,623 292,9 1,2
SA10 600 3,39E-04 112,18 -59,944 310,6 21,4
SA10 625 3,50E-04 137,57 -19,183 266 48,6
SA10 650 3,80E-04 50,339 -66,408 322,5 -3,4
SA10 675 3,40E-04 287,1 2,0211 68,9 -17,1
SA11 0 8,67E-03 72,65 10,639 361,3 -1,3
SA11 100 6,91E-03 69,829 10,926 358,8 -2,6
SA11 150 5,26E-03 72,718 9,7416 1,8 -2
SA11 200 5,28E-03 67,422 9,3745 357,7 -5,2
SA11 250 3,37E-03 65,298 11,469 354,8 -4,6
SA11 300 3,38E-03 64,514 10,401 354,7 -5,9
SA11 350 1,76E-03 64,818 21,85 348,8 4
SA11 400 1,24E-03 58,168 16,892 346 -3,5
SA11 450 7,60E-04 359,53 -15,499 290,8 -51,5
SA11 475 9,03E-04 35,07 21,374 324,3 -8,8
SA11 500 2,56E-04 258,34 -29,512 174,6 -17,2
SA11 525 6,48E-04 22,907 5,3157 317,4 -27,7
SA11 550 3,32E-04 307,26 11,465 238,9 -10,8
SA11 575 1,49E-03 342,57 45,133 279,1 10,2
SA11 600 1,80E-04 320,04 12,548 251 -15,3
SA11 625 3,29E-04 165,66 32,127 80,7 65,9
SA11 650 4,65E-04 211,59 32,34 170,3 58,8
SA11 675 1,50E-05 204,66 43,962 179,5 71,1
SA12 0 5,88E-03 63,865 35,892 352,3 -4,3
SA12 100 4,84E-03 59,775 34,361 351,6 -7,9
SA12 150 3,93E-03 55,283 34,23 349,3 -10,9
SA12 200 3,24E-03 53,216 34,406 348 -12,1
SA12 250 2,40E-03 34,29 47,553 328,3 -11,2
SA12 300 1,88E-03 53,307 73,989 318,7 14,9
SA12 350 1,87E-03 29,252 52,97 322,8 -8
SA12 400 3,35E-03 315,95 27,198 263,4 -22,7
SA12 425 9,09E-04 314,03 38,427 270,1 -13,3
SA12 450 8,45E-04 330,78 42,083 283,1 -17,7
SA12 475 7,04E-04 296,68 52,153 272,1 4,8
SA12 500 5,53E-04 317,09 39,569 272,8 -14
SA12 525 8,88E-04 308,37 32,708 262,6 -14,2
SA12 550 9,07E-04 281,13 50,648 265,9 12,5
SA12 575 9,63E-04 329,46 15,409 265,9 -39,8
SA12 600 8,96E-04 320,43 26,877 266,4 -25,6
SA12 625 1,04E-03 302,54 12,781 242,7 -22,5

Table2. Thermal demagnetization data
(1) Sample = sample name
(2) Temperature (°C)
(3) NRM intensity (A/m)
(4) Core Declination (°E)
(5) Core Inclination (°)
(6) Geographic Declination (°E)
(7) Geographic Inclination (°)

SA12 650 7,33E-04 260,33 7,6843 218,5 12
SA13 0 7,64E-03 65,029 27,936 345,5 -8
SA13 100 6,26E-03 61,431 28,612 343,1 -10,3
SA13 150 5,02E-03 65,501 30,137 343,9 -6,5
SA13 200 4,68E-03 65,591 30,284 343,8 -6,3
SA13 250 3,56E-03 61,239 31,645 340,5 -8,6
SA13 300 3,64E-03 57,857 32,051 338,4 -10,6
SA13 350 2,09E-03 30,137 47,384 311,9 -12,7
SA13 400 2,11E-03 38,911 46,324 317,7 -10,4
SA13 450 1,64E-03 12,653 58,734 298,1 -5,6
SA13 475 1,24E-03 12,661 46,683 300,6 -17,4
SA13 500 6,88E-04 340,14 53,802 279,8 -9,3
SA13 525 1,65E-03 332,98 56,545 276,9 -5,3
SA13 550 1,19E-03 27,728 68,315 301,4 5,5
SA13 575 1,64E-03 310,03 59,478 268,6 3,9
SA13 600 1,26E-03 332,11 -6,7388 231,2 -57,7
SA13 625 5,75E-04 226,6 45,308 242,2 47,6
SA13 650 4,93E-04 165,22 44,286 319,7 67,3
SA13 675 3,53E-04 254,39 -1,7847 193,1 13,3
SA14 0 4,98E-03 68,288 17,28 6,3 -8,6
SA14 100 4,09E-03 71,518 18,39 7,2 -5,5
SA14 150 4,05E-03 68,973 18,408 5,8 -7,4
SA14 200 2,61E-03 65,273 15,582 5,9 -11,9
SA14 250 1,56E-03 66,477 14,959 7,1 -11,4
SA14 300 1,55E-03 59,823 14,915 3,1 -16,5
SA14 350 1,48E-03 61,115 11,447 6,7 -17,7
SA14 400 1,56E-03 65,054 13,255 7,7 -13,5
SA14 425 7,31E-04 53,288 -6,3662 17,7 -34,5
SA14 450 8,51E-04 48,048 -0,20195 7,8 -35,1
SA14 475 3,91E-04 352,76 -24,016 258,2 -80,5
SA14 500 2,16E-04 154,28 11,206 66,6 59,1
SA14 525 2,77E-04 279 -18,943 200,3 -17,1
SA14 550 2,86E-04 16,469 -2,0045 333,9 -57,1
SA15 0 4,69E-03 69,631 23,345 1,5 -6,5
SA15 100 3,92E-03 59,903 22,32 357,3 -14,5
SA15 150 2,97E-03 55,125 18,827 357,3 -20,2
SA15 200 3,15E-03 53,092 16,8 357,7 -23
SA15 250 2,40E-03 48,847 19,447 352,7 -24,3
SA15 300 1,67E-03 40,847 17,571 348,2 -31,1
SA15 350 1,67E-03 44,053 18,017 350,4 -28,6
SA15 400 1,50E-03 36,454 20,436 342,3 -31,6
SA15 450 6,83E-04 8,676 2,3482 319,3 -60,4
SA15 475 6,35E-04 344,17 3,6998 271,9 -56,6
SA15 500 1,20E-03 330,43 23,067 268,6 -33,2
SA15 525 6,96E-04 299,88 24,27 247,2 -13,2
SA15 550 6,38E-04 293,66 27,627 246,7 -6,7
SA15 575 6,42E-04 305,2 27,561 253 -14,9
SA15 600 4,23E-04 315,3 16,498 250,9 -29,2
SA15 625 7,96E-04 298,34 10,792 234,8 -19,7
SA15 650 3,65E-04 315,56 37,442 266,5 -14,1
SA15 675 3,60E-04 316,23 34,674 265,1 -16,5
SA16 0 5,32E-03 63,71 29,112 359 9
SA16 100 3,87E-03 62,069 22,954 361,1 3
SA16 150 3,45E-03 61,712 25,207 359,6 4,7
SA16 200 2,89E-03 76,128 28,476 8,4 14,7
SA16 250 4,16E-03 14,036 -66,648 105,1 -74,7
SA16 300 4,57E-03 289,92 43,964 258,7 24
SA16 350 1,31E-03 26,91 42,281 326,3 8,1
SA16 400 4,88E-03 342,79 4,2296 286,4 -31
SA16 425 8,55E-04 317,02 10,035 261,9 -17,1
SA16 450 1,14E-03 301,46 11,89 249 -8,2
SA16 475 8,69E-04 299,91 9,0687 246,2 -9,8
SA16 500 5,96E-04 334,21 -5,8726 273 -38,4
SA16 525 8,29E-04 335,42 4,4255 151,2 -28,9
SA16 550 8,20E-04 277,22 -1,3282 221,5 -5,4
SA16 575 5,97E-04 265,65 21,941 226,8 19,9
SA16 600 5,97E-04 313,08 23,402 264,3 -3,4
SA16 625 3,03E-04 263,47 41,054 240,1 35,2
SA16 650 1,39E-04 208,99 -52,437 144,6 -18,2

Oulad Hamida

oh220 0 2,87E-05 193,81 -60,55 327,4 18,6
oh220 100 5,94E-06 153,34 -31,59 289,8 41,2
oh220 150 1,41E-05 60,25 15,5 207,8 -25,1
oh220 200 1,68E-05 54,28 26,14 194,5 -26,1
oh220 225 1,48E-05 58,5 29,4 193,2 -21,3
oh220 250 1,51E-05 64,27 35,86 189,1 -14,2
oh220 275 9,54E-06 70 48,32 179,2 -5,4
oh220 300 1,31E-05 66,87 58,07 169,4 -3,3
oh220 325 9,00E-06 59,57 66,58 160,3 -2,2
oh220 350 1,16E-05 261,81 79,11 129,3 11,4
oh220 375 4,69E-06 258,33 40,26 89,5 15,3
oh220 400 5,97E-05 63,42 -37,27 267,2 -27,1
oh220 425 8,80E-06 291,66 -7,3 46,5 -22,5
oh220 450 9,80E-06 319,56 -31,92 13,7 -46,7
oh220 475 1,55E-05 14,74 -19,79 266,5 -72,7
oh220 500 1,10E-05 327,91 -16,22 35,6 -58,2
oh220 525 1,46E-05 328,72 -34,03 5,4 -52,6
oh220 550 2,47E-05 1,07 8,05 143,7 -71,9
oh220 575 2,82E-05 8,76 26,73 153,1 -52,3
oh220 600 2,86E-05 345,94 11,32 106,7 -64,5
oh230 25 3,88E-05 227,48 -14,86 14,9 40,1
oh230 100 2,87E-05 250,75 -5,74 29,5 18,9
oh230 150 2,17E-05 264,98 6,46 42,6 5,2
oh230 200 1,96E-05 273,83 9,07 45,5 -3,5
oh230 225 1,72E-05 271,78 15,61 51,9 -1,2
oh230 250 1,57E-05 267,94 4,8 41 2,2
oh230 275 2,13E-05 273,91 2,89 39,3 -3,8
oh230 300 1,84E-05 276,09 -1,13 35,4 -6,1
oh230 325 1,96E-05 268,13 -18,56 17,7 1,1
oh230 350 1,93E-05 259,3 -28,38 7,2 8,4

Table2. Thermal demagnetization data

(1) Sample = sample name

(2) Temperature (°C)

(3) NRM intensity (A/m)

(4) Core Declination (°E)

(5) Core Inclination (°)

(6) Geographic Declination (°E)

(7) Geographic Inclination (°)

oh230 375 1,60E-05 258,95 -43,02 352,5 6,7
oh230 400 1,76E-05 264,1 -46,65 349,4 2,6
oh230 425 1,66E-05 253,92 -48,07 346,9 9,1
oh230 450 1,86E-05 259,06 -26,67 8,9 8,8
oh230 475 1,73E-05 249,22 -21,85 12,4 18,4
oh230 500 2,10E-05 263,02 -22,21 13,7 5,7
oh230 525 2,53E-05 270,31 -9,84 26,5 -0,6
oh230 550 9,41E-06 240,56 -26,83 5,3 25
oh230 575 1,29E-05 241,63 -19,91 13 25,8
oh230 600 9,13E-06 230,76 -71,44 320,8 9,7
oh230 625 2,26E-05 292,69 -20,24 15,2 -21,9
oh230 650 1,69E-05 244,19 -42,45 350,4 17,3
oh230 675 1,93E-05 3,09 -27,02 299,8 -64,8
oh237 0 4,07E-05 197,46 -49,24 320,9 33,7
oh237 100 2,66E-05 151,59 -60,72 292,9 20,6
oh237 150 2,24E-05 106,86 -61,16 279,7 3,6
oh237 200 2,15E-05 82,24 -67,1 284,4 -7,6
oh237 225 2,29E-05 82,44 -67,56 284,8 -7,5
oh237 250 2,22E-05 66,71 -72,35 290,8 -11,7
oh237 275 2,78E-05 90,12 -76,49 293,7 -4,8
oh237 300 3,00E-05 91,32 -76,16 293,4 -4,5
oh237 325 2,99E-05 110,9 -72,06 290,6 1,5
oh237 350 3,41E-05 127,85 -66,31 288,5 9,5
oh237 375 3,48E-05 121,22 -63,34 284,4 8,8
oh237 400 3,74E-05 126,36 -65,63 287,6 9,5
oh237 425 3,30E-05 130,17 -64,77 287,9 11,2
oh237 450 3,24E-05 139,24 -55,89 284,3 20,5
oh237 475 2,51E-05 106,74 -82,52 300,1 -2,8
oh237 500 2,80E-05 122,32 -74,24 294 3,5
oh237 525 2,96E-05 101,18 -75,34 292,9 -2
oh237 550 2,62E-05 23,89 -50,46 287,5 -40,3
oh237 575 3,94E-05 30,28 -50,53 283,3 -37,9
oh237 600 2,69E-05 226,42 -55,11 333,2 18,7
oh237 625 2,91E-05 325,36 -37,62 346,5 -44,6
oh237 650 1,39E-05 297,82 21,48 63,4 -23,6
oh237 675 2,35E-05 274,09 -18,18 19,4 -5,4
oh249 0 4,44E-05 219,13 4,87 9,6 46,7
oh249 100 2,21E-05 214,67 10,6 13,3 53,5
oh249 150 1,36E-05 214,39 19,59 27,5 57,7
oh249 200 1,40E-05 215,21 34,86 56,7 59
oh249 225 1,18E-05 217,96 41,9 69 55,7
oh249 250 1,31E-05 221,75 51,8 83,3 50,2
oh249 275 1,29E-05 316,78 81,14 116,8 20,4
oh249 300 1,76E-05 13,3 68,9 128,1 6,4
oh249 325 1,78E-05 326,18 58,14 106,2 -0,3
oh249 350 2,63E-05 341,3 62,04 114,6 0,3
oh249 375 2,20E-05 291,55 58,52 93,5 12,5
oh249 400 2,39E-05 259,17 35,88 62,9 23,7
oh249 425 2,41E-05 283,22 36,94 71,8 6,3
oh249 450 2,07E-05 268,65 23,7 54,1 11,6
oh249 475 2,30E-05 265,69 -6,15 25,8 1
oh249 500 1,37E-05 327,11 15,25 82,3 -37
oh249 525 1,44E-05 272,74 7,54 41,2 1
oh249 550 3,28E-05 294,78 14,69 58,3 -14,2
oh249 575 3,78E-05 322,66 11,64 75,2 -37
oh249 600 3,50E-05 200,67 0,97 344 57,3
oh279 0 2,73E-05 219,69 -61,06 307,9 28,4
oh279 100 1,19E-05 269,87 -88,39 288,9 7
oh279 150 1,16E-05 35,84 -49,8 262,6 -25,2
oh279 200 1,05E-05 40,15 -41,68 253,9 -29,1
oh279 225 1,04E-05 49,11 -26,25 234,3 -31,9
oh279 250 1,17E-05 46,52 -29,83 239,3 -32,1
oh279 275 9,34E-06 42,91 -37,23 248,4 -30,3
oh279 300 2,28E-05 17,26 -37,36 268,5 -42,8
oh279 325 1,84E-05 15,86 -41,21 271,8 -39,6
oh279 350 2,21E-05 342,42 -37,72 306,2 -42,4
oh279 375 1,75E-05 344,73 4,22 7,7 -74,6
oh279 400 2,70E-05 8,61 -14,14 265,3 -67,2
oh279 425 2,00E-05 315,42 -18,9 346 -39
oh279 450 2,48E-05 341,52 -13,15 329,7 -62,7
oh279 475 2,12E-05 331,7 -21,3 331,1 -50,3
oh279 500 3,09E-05 332,29 -20,06 332 -51,6
oh279 525 7,25E-06 284,3 -42,48 333,2 -5,7
oh279 550 9,49E-06 305,18 -16,42 353,4 -30,9
oh279 575 3,23E-05 338,43 -14,86 331,6 -59,4
oh279 600 1,12E-05 202,44 -0,23 33,2 66,6
oh298 0 1,70E-05 239,2 -23,99 336,7 23
oh298 100 1,17E-05 235,46 -45,33 315,2 15,6
oh298 150 8,82E-06 249,34 -47,15 318,1 6,3
oh298 200 8,90E-06 256,53 -62,25 305,2 -2,7
oh298 225 7,62E-06 270,44 -48,29 320,5 -7,7
oh298 250 6,29E-06 265,48 -40,44 327,7 -3,1
oh298 275 5,87E-06 267,89 -15,33 352,8 -0,6
oh298 300 3,80E-06 237,39 13,56 18 33,8
oh298 325 4,32E-06 232,92 -15,58 342,9 31,7
oh298 350 4,78E-06 257,5 -20,46 345,8 8
oh298 375 6,42E-06 244,56 -6,42 356,7 23,6
oh298 400 6,55E-06 239,64 -5,46 356,4 28,6
oh298 425 4,54E-06 231,93 -21,1 336,5 30,3
oh298 450 5,78E-06 207,04 -33,25 307,9 39,7
oh298 475 6,71E-06 230,58 -25,8 331,1 29,2
oh298 500 9,49E-06 260,15 -36,29 330,9 1,9
oh298 525 1,32E-05 212,87 -22,89 322,3 44
oh298 550 1,72E-05 235,03 -19,56 339,5 28,3
oh298 575 1,70E-05 101,26 -43,37 232,8 1,2
oh298 600 1,94E-05 172,52 4,54 224,1 80,8
oh305 0 3,61E-05 239,81 27,05 25 38,2
oh305 100 3,16E-05 238,5 61,03 69,6 41,9
oh305 150 3,30E-05 276,13 80,2 92,1 29,5
oh305 200 3,42E-05 321,06 78,91 95,8 22,2

Table2. Thermal demagnetization data

(1) Sample = sample name

(2) Temperature (°C)

(3) NRM intensity (A/m)

(4) Core Declination (°E)

(5) Core Inclination (°)

(6) Geographic Declination (°E)

(7) Geographic Inclination (°)

oh305 225 3,79E-05 314,56 77,3 93,6 21,7
oh305 250 4,00E-05 321,45 77,35 94,9 20,8
oh305 275 3,80E-05 336,75 77,64 98,1 19,5
oh305 300 3,37E-05 333,75 67,68 93,4 10,6
oh305 325 3,04E-05 315,05 70,72 89,2 16,6
oh305 350 2,98E-05 318,12 73,81 92 18,5
oh305 375 2,89E-05 315,11 58,35 81,4 6,9
oh305 400 2,94E-05 314,36 56,98 80,2 6
oh305 425 2,85E-05 334,56 58,21 90,2 1,7
oh305 450 2,91E-05 331,54 62,19 90,4 6
oh305 475 2,55E-05 334,23 52,31 87,8 -3,7
oh305 500 1,69E-05 338,33 54,6 90,9 -2,4
oh305 525 2,69E-05 324,76 43,44 78,2 -8,9
oh305 550 1,38E-05 336,25 66,91 94,1 9,6
oh305 575 1,69E-05 237,09 62,63 71,9 42,2
oh305 600 1,27E-05 311,77 70,12 87,9 16,9
oh305 625 2,65E-05 292,6 41,09 59 5,2
oh305 650 9,86E-06 352,21 -14,28 78,4 -71,8
oh305 675 1,11E-05 357,04 72,07 102,3 13,1
oh325 0 1,83E-04 211,33 -29,06 333,1 23,8
oh325 100 1,58E-04 211,96 -34,83 330,6 18,5
oh325 150 1,29E-04 218,12 -35,2 334,9 15,6
oh325 200 1,20E-04 208,81 -34,94 328,1 19,6
oh325 225 1,09E-04 215,93 -31,18 335,6 19,9
oh325 250 1,14E-04 210,98 -31,19 331,7 22,1
oh325 275 1,02E-04 209,6 -30,22 331 23,5
oh325 300 9,27E-05 214,6 -25,36 337,9 25,5
oh325 325 8,70E-05 206,42 -21,5 332,7 32,6
oh325 350 9,40E-05 196,2 -18,66 323,1 38,9
oh325 375 9,94E-05 214,35 -14,83 344,6 34,3
oh325 400 9,27E-05 213,16 -20,08 339,9 30,6
oh325 425 9,37E-05 206,79 -19,02 334,5 34,6
oh325 450 9,73E-05 224,59 -19,64 349,8 24,4
oh325 475 1,05E-04 229,7 -14,87 357,3 24,4
oh325 500 9,26E-05 237,04 -15,32 2 18,8
oh325 525 9,40E-05 229,04 -28,79 346,5 14,9
oh325 550 1,02E-04 254,15 -16,56 11 4,8
oh325 575 9,02E-05 258,14 -32,02 359,9 -6,6
oh325 600 1,17E-04 247,46 -24,16 1,1 5,6
oh325 625 9,42E-05 249,81 -35,21 353,4 -2,5
oh325 650 1,04E-04 246 -24,77 359,9 6,3
oh325 675 1,05E-04 260,25 -18,09 12,8 -0,9
oh345 0 1,43E-04 178,28 -25,2 296 47,8
oh345 100 1,35E-04 176,85 -24,07 293,9 48,8
oh345 150 1,21E-04 172,69 -23,6 288,1 48,8
oh345 200 1,16E-04 172,73 -23,07 288 49,3
oh345 225 1,13E-04 172,37 -23,83 287,7 48,5
oh345 250 1,16E-04 181,21 -19,07 300,2 53,9
oh345 275 1,10E-04 183,16 -14,35 304,1 58,5
oh345 300 1,11E-04 174,19 0,24 278,8 72,3
oh345 325 1,07E-04 172,86 -12,9 284,6 59,3
oh345 350 1,05E-04 180,36 -26,01 298,8 47
oh345 375 1,07E-04 174,55 -13,25 287,9 59,3
oh345 400 1,10E-04 175,25 -16,6 290,1 56,1
oh345 425 1,07E-04 176,65 -3,09 288,6 69,6
oh345 450 9,59E-05 176,28 -3,54 287,8 69,1
oh345 475 1,00E-04 177,59 -10,62 293,2 62,3
oh345 500 9,86E-05 177,74 3,28 288,9 76,1
oh345 525 8,17E-05 180,04 11,55 298,7 84,5
oh345 550 7,68E-05 192,18 -2,29 331,4 67,3
oh345 575 8,33E-05 185,58 11,24 342,2 82,1
oh345 600 8,53E-05 172,19 2,47 269,6 73,6
oh345 625 8,36E-05 175,13 23,93 150,8 81,7
oh345 650 8,53E-05 171,99 5,35 263,4 76
oh345 675 8,81E-05 183,17 16,49 19,2 86,9

Sample = sample name.
cm = elevation of sample from section base in cm.
NRM = natural remanent magnetization of sample at room temperature in mA/m (10E-3 A/m) and 10cc volume.
SUS = volume magnetic susceptibility in 10E-6 SI.
A_LT = low unblocking temperature in °C of magnetic component A.
A_HT = high unblocking temperature in °C of magnetic component A.
A_Dec = mean declination in °E of magnetic component A.
A_Inc = mean inclination in ° of magnetic component A.
C_LT = low unblocking temperature in °C of characteristic magnetic component C.
C_HT = high unblocking temperature in °C of characteristic magnetic component C.
C_MAD = maximum angular deviation of characteristic magnetic component C.
C_Dec = mean declination in °E of characteristic magnetic component C.
C_Inc = mean inclination in ° of characteristic magnetic component C.
C_VGP = virtual geomagnetic pole latitude in ° of characteristic magnetic component C.
Sample cm NRM SUS A_LT A_HT A_Dec A_Inc C_LT C_HT C_MAD C_Dec C_Inc C_VGP
S-41 -41.0 0.300 9.9 100 425 9.2 246.3 -9.0 -22.2
S-62 -62.0 0.311 8.6 0 100 352.9 7.1 100 450 26.5 171.4 -33.5 -72.9
S-77 -77.0 0.252 11.5 0 100 353.4 36.0 100 350 7.0 227.1 -53.8 -51.3
S-91 -91.0 0.159 10.8 S-109 -109.0 0.335 17.7
S-134 -134.0 0.218 13.6 0 100 27.1 22.8
S-180 -180.0 0.376 13.3 0 100 314.4 14.6 100 400 31.1 195.8 -21.5 -63.3
s010 10.0 0.276 132.9 350 575 11.3 176.1 -18.5 -65.6
s014 14.0 0.274 157.1 s040 40.0 0.272 180.3 275 475 10.3 156.0 -21.0 -58.4
s043 43.0 0.333 185.7 s050 50.0 0.375 171.9
s054 54.0 0.134 170.7 150 425 12.7 150.8 -31.1 -58.9
s058 58.0 0.157 160.3 150 500 20.1 187.4 -27.0 -69.6
s061 61.0 0.101 104.1 100 475 17.1 162.7 -33.5 -68.3
s110 110.0 0.230 132.1 0 100 45.0 13.7 150 650 7.5 181.4 1.4 -55.7
s113 113.0 0.140 94.6 250 500 11.6 153.6 10.2 -43.9
s117 117.0 0.244 110.8 150 600 17.5 177.1 14.4 -49.0
s124 124.0 0.123 83.8 150 425 9.9 169.3 12.4 -48.9
s131 131.0 0.157 89.3 225 400 13.6 143.9 -21.0 -49.9
s135 135.0 0.108 87.3 0 100 320.0 67.0 225 325 12.2 173.0 -2.0 -56.8
s140 140.0 0.077 73.6 150 400 14.8 150.8 13.9 -40.8
s146 146.0 0.120 65.4 225 600 18.3 156.2 8.7 -45.9
s152 152.0 0.197 104.9 200 575 16.3 164.6 -8.1 -57.2
s160 160.0 0.183 97.4 150 425 13.6 150.2 4.7 -44.4
s164 164.0 0.117 95.0 150 350 13.2 161.6 3.9 -50.5
s171 171.0 0.146 104.4 150 400 11.9 151.0 8.5 -43.3
s176 176.0 0.176 110.8 225 400 22.9 165.4 -20.5 -63.4
s181 181.0 0.396 111.7 250 500 10.0 181.1 5.6 -53.6
s187 187.0 0.370 128.8 200 525 5.1 156.6 1.9 -49.0
s204 204.0 0.588 181.3 225 400 7.1 159.2 12.7 -45.4
s215 215.0 0.535 182.9 250 400 14.4 167.0 0.9 -53.8
s221 221.0 0.765 214.3 200 425 6.1 171.0 -1.3 -56.0
s230 230.0 0.758 226.4 0 100 33.9 38.3 275 425 7.9 172.5 1.1 -55.1
s234 234.0 0.840 180.4 200 350 5.7 169.2 7.3 -51.4
s240 240.0 1.098 220.1 225 475 7.6 160.7 4.6 -49.8
s253 253.0 1.434 323.9 0 100 336.5 7.5 225 550 4.3 162.2 3.4 -50.9
s268 268.0 2.739 447.2 275 525 2.9 160.9 4.6 -49.8
s273 273.0 2.255 418.5 275 600 5.0 160.2 -0.9 -52.0
s281 281.0 2.658 488.2 0 100 317.4 51.3 250 575 2.2 159.7 6.7 -48.4
s287 287.0 3.634 526.2 275 625 5.3 156.8 -0.8 -50.3
s299 299.0 3.936 549.6 250 650 2.3 159.6 4.6 -49.3
s314 314.0 6.043 669.3 200 550 3.0 160.8 2.5 -50.8 150 525 22.3 163.7 -1.8 -53.9

n011 11.0 0.021 89.0 0 150 8.6 71.2

n015 15.0 0.100 103.8 150 300 20.2 214.3 -3.9 -45.0

n019 19.0 0.114 109.0 0 100 6.7 14.8

n023 23.0 0.050 140.6 0 150 39.5 68.9

n069 69.0 0.250 191.8 250 475 25.3 139.6 -25.2 -48.1

n072 72.0 0.139 183.8 250 450 11.4 134.8 -18.4 -42.1

n074 74.0 0.117 192.9 225 350 17.6 198.6 -39.6 -70.2

n077 77.0 0.159 190.2 0 100 308.8 29.3 225 525 18.9 161.4 -27.7 -64.7

n082 82.0 0.155 188.7 0 100 38.2 0.6 300 400 20.1 148.3 -21.2 -53.2

OH2: s333 333.0 0.798 164.3 200 525 7.5 180.4 -1.3 -57.1

OH2 Hand Sample 03.19 (oh2_3) 347.0 10.980 144.4 100 550 5.6 171.1 -6.7 -58.6

OH2 Hand Sample 04.19 (oh2_4) 351.0 5.885 168.8 0 100 339.2 51.5 150 475 7.6 346.2 15.4 61.3

S352 352.0 10.830 186.0 100 675 7.2 183.5 8.1 -52.2

S372 372.0 6.896 203.9 0 100 49.0 17.1 200 650 18.6 174.2 -34.5 -74.5

OH2 Hand Sample 02.19 (oh2_2) 376.0 19.660 168.1 150 650 10.2 164.8 3.7 -51.8

OH2 Hand Sample 05.19 (oh2_5) 383.0 4.418 161.0 150 425 16.7 205.6 2.3 -47.7

OH1 Bed1 (below trench base):

S-30 -30.0 0.066 10.1

OH1 Bed2 Trench South Wall:

s004 4.0 0.172 153.3

OH1 Bed2 Trench North Wall:

n007 7.0 0.086 108.1

S386 386.0 7.428 194.4 150 675 12.8 155.9 -24.0 -59.6

OH2 Hand Sample 01.19 (oh2_1)

391.0 11.370 131.7 100 500 8.2 162.7 11.2 -47.5

OH2 Hand Sample 06.19 (oh2_6)

401.0 0.319 19.3

S409 409.0 3.177 218.1 100 600 26.7 165.4 16.7 -45.7

S436 436.0 2.855 249.7 100 650 12.5 170.4 -47.9 -80.6

S453 453.0 1.544 91.5 0 150 60.3 20.5 200 425 20.2 130.0 -16.4 -37.6

S471 471.0 0.773 96.2

S486 486.0 1.093 115.3

S510 510.0 0.128 48.0

S520 520.0 1.324 91.8

S548 548.0 1.354 94.3 0 150 35.7 43.2 150 450 23.2 171.2 20.0 -45.3

S565 565.0 0.405 48.1 0 100 52.2 62.7 100 350 19.4 231.6 -12.6 -35.1

S598 598.0 5.212 137.1 100 400 8.3 196.5 2.0 -52.1

S605 605.0 0.957 96.0 0 200 25.5 25.0

S625 625.0 1.181 102.0 0 200 1.4 35.7

S663 663.0 0.770 60.0 0 100 41.0 53.5 150 300 12.9 169.8 5.6 -52.4

S709 709.0 1.067 80.1 0 150 316.9 36.0

S762 762.0 0.783 36.9

S810 810.0 0.580 43.1 0 150 329.8 10.3

S863 863.0 0.615 48.1

S939 939.0 0.738 81.5 0 200 351.9 64.9

S987 987.0 1.077 107.9

S1044 1044.0 1.101 106.8 0 100 5.0 58.9

S1099 1099.0 0.798 125.3 0 100 30.8 82.7 200 525 24.4 172.8 -11.7 -61.5

S1171 1171.0 0.432 25.2

S1238 1238.0 0.272 12.2 0 200 334.1 34.4

S1281 1281.0 0.425 13.8 0 150 22.9 61.9 200 350 17.9 183.0 -36.6 -76.5

S1309 1309.0 0.298 29.0 100 200 35.2 49.4

S1353 1353.0 0.184 22.0

S1375 1375.0 0.640 24.7 0 100 14.1 72.6 100 450 19.0 322.7 23.5 49.9

S1436 1436.0 0.634 30.3

S1525 1525.0 1.367 81.1 0 100 43.5 62.2
S1569 1569.0 3.591 264.5 0 150 354.9 54.4
S1589 1589.0 0.868 43.4 0 100 332.4 13.0
S1599 1599.0 11.770 435.6 0 150 349.6 33.8
S1634 1634.0 20.090 790.1 0 150 347.4 29.9
S1701 1701.0 18.040 714.0 0 150 19.9 77.2

OH3-B:

3BOH30 30.0 1.218 36.8 0 200 327.8 32.5
3BOH57 57.0 0.930 28.3 0 250 339.0 29.2
3BOH94 94.0 1.016 46.2 0 300 320.2 45.7
3BOH136 136.0 1.666 55.2 0 300 347.1 42.2
3BOH178 178.0 1.325 49.3 0 250 325.5 26.1
3BOH221 221.0 1.519 51.2 0 200 341.7 36.5
3BOH281 281.0 0.826 29.0
3BOH308 308.0 1.019 35.4 0 150 16.6 31.3 150 425 24.0 210.6 -3.4 -47.1
3BOH388 388.0 0.999 41.4 0 150 4.9 28.7 350 650 16.5 198.1 36.9 -33.1
3BOH428 428.0 1.055 55.5 0 250 330.4 54.6
3BOH463 463.0 1.765 58.6 100 425 31.1 44.0
3BOH486 486.0 0.510 35.2 100 200 29.8 44.7
3BOH510 510.0 1.326 42.5 0 200 10.5 24.7

OH3-A:

3OH28 28.0 0.600 27.1 0 150 284.7 23.4
3OH51 51.0 0.439 29.3
3OH94 94.0 0.862 37.9 0 150 9.8 18.2
3OH121 121.0 3.505 294.8 0 150 27.8 27.1 300 625 34.4 166.7 -21.0 -64.2
3OH144 144.0 0.328 27.3 0 150 327.0 24.1
3OH172 172.0 0.563 36.6
3OH212 212.0 0.427 23.0 0 150 342.7 27.1
3OH229 229.0 1.156 50.4 0 150 339.3 27.7
3OH246 246.0 1.272 38.5 0 100 284.8 51.4 350 500 10.9 180.5 8.6 -52.1
3OH313 313.0 0.943 35.0 0 100 320.8 33.9 150 300 14.4 150.1 5.2 -44.1
3OH339 339.0 1.251 37.9 0 300 18.1 43.5
3OH379 379.0 0.748 46.5 0 200 333.0 29.9
3OH405 405.0 7.364 42.5 0 200 23.3 45.6 250 475 3.2 34.9 41.6 58.1
3OH462 462.0 4.294 161.7 0 100 10.6 1.4 150 625 31.9 1.9 7.4 60.1
3OH490 490.0 6.235 53.1 0 100 338.3 16.2 150 500 8.8 312.6 28.6 43.6

OH4:

4OH8 8.0 40.350 8380.1 0 150 358.5 25.1 250 675 8.2 178.6 -33.9 -74.9
4OH29 29.0 15.670 2124.6 0 200 0.8 25.5 200 625 3.1 183.0 -48.6 -85.2
4OH59 59.0 25.740 3319.5 0 150 6.4 37.8 300 675 6.9 194.6 -21.5 -63.9
OH4 Hand Sample 07.19 (oh4_7)
91.0 12.580 4049.4 0 250 351.8 22.2 275 675 6.8 182.7 -30.1 -72.4
4OH96 96.0 12.340 2312.6 0 250 10.1 25.1 300 650 12.5 188.7 -18.4 -64.6
4OH116 116.0 3.794 593.8 0 150 10.0 25.5 250 675 8.5 216.8 -43.2 -57.0
4OH145 145.0 1.666 683.8 0 150 25.2 37.8 300 675 15.5 184.3 -13.4 -62.9
OH4 Hand Sample 08.19 (oh4_8)
148.0 8.638 1942.8 0 200 3.7 23.2 275 650 5.3 181.2 -30.0 -72.5
4OH166 166.0 3.313 1103.2 0 200 356.9 29.2 350 675 6.2 189.5 -21.0 -65.7
4OH198 198.0 4.659 723.7 0 200 347.5 44.2 250 625 6.7 199.2 -18.7 -60.2
OH4 Hand Sample 09.19 (oh4_9)
204.0 5.979 1097.0 0 200 353.8 42.1 250 675 9.3 178.9 -8.3 -60.6
4OH237 237.0 4.817 648.6 0 250 6.6 21.9 250 675 7.2 219.4 -46.8 -55.9
4OH263 263.0 5.317 606.9 0 300 11.3 27.2 450 650 11.7 176.4 -2.9 -57.7
4OH303 303.0 3.231 401.3 0 150 13.9 38.1 550 675 20.0 205.7 -47.5 -67.5
4OH363 363.0 31.040 3156.3 0 150 348.7 31.7

4OH403 403.0 9.800 1386.8 0 150 25.6 46.7 250 625 11.3 248.0 -21.0 -24.3
4OH433 433.0 7.275 1324.3 0 200 345.1 39.9 200 675 24.0 174.3 -35.9 -75.4
4OH443 443.0 19.210 1682.5 200 600 16.6 202.2 -58.7 -71.3
4OH454 454.0 25.780 1610.0 0 150 331.9 50.5 425 625 21.6 227.6 -9.5 -37.3
4OH468 468.0 13.260 937.2 0 250 342.4 30.2 4OH483 483.0 5.411 636.0 0 250 2.3 31.0 350 575 32.2 172.4 24.7 -42.9
4OH484 484.0 6.043 573.0 0 150 320.4 28.8 200 675 12.2 173.6 -56.6 -83.7
4OH508 508.0 5.704 631.7 0 250 336.6 29.0 450 650 3.1 199.5 -16.0 -58.8
4OH528 528.0 16.760 836.7 0 150 316.5 53.3 250 625 9.0 8.5 16.2 63.5
4OH548 548.0 22.490 1139.0 0 100 331.6 45.5 100 500 20.9 300.4 35.7 35.7
4OH578 578.0 25.680 1175.0 0 150 322.6 7.8 200 550 31.9 345.3 13.9 60.2
OH5:
5OH130 130.0 17.860 390.7 0 150 3.2 33.9 200 675 19.3 344.4 15.0 60.3
5OH181 181.0 14.570 371.8 0 200 317.5 34.5 250 550 20.0 320.7 29.4 50.4
5OH215 215.0 9.466 270.5 5OH244 244.0 5.479 160.7 0 200 311.7 29.1 250 525 28.3 351.3 43.2 78.7
5OH266 266.0 10.420 272.8 0 150 327.7 23.5 200 500 7.8 315.6 13.2 41.0
5OH291 291.0 9.466 396.6 0 200 328.0 8.0 200 625 17.5 321.4 17.8 46.9
5OH326 326.0 13.970 423.8 0 150 313.8 27.9 200 500 10.9 310.4 45.5 47.1
5OH351 351.0 19.640 566.0 0 150 312.3 27.9 350 525 6.5 335.5 11.8 54.2
5OH377 377.0 11.910 370.9 0 150 321.3 32.2 200 525 9.5 318.0 9.3 41.5
Sidi Abderrhamane:
SA1 177.0 0.553 11.8 0 100 340.5 48.9 SA2 206.0 0.906 35.6 0 100 42.6 14.3
SA3 226.0 0.703 21.5 SA4 276.0 2.231 45.8 0 100 356.8 15.3
SA5 335.0 0.743 23.5 0 100 349.2 23.5
SA6 361.0 1.829 38.4 0 100 327.1 36.1 100 350 12.6 336.0 41.7 67.0
SA7 419.0 0.148 17.9 SA8 434.0 0.733 25.6 SA9 459.0 0.192 17.1 SA10 485.0 1.024 22.9 0 100 347.5 62.0 100 450 16.5 321.9 59.2 59.1
SA11 290.0 8.670 35.7 0 450 5.1 2.3 -0.1 56.3
SA12 304.0 5.882 21.1 0 425 7.0 2.1 -3.9 54.4
SA13 290.0 7.645 30.0 0 450 6.2 355.0 -7.1 52.5
SA14 301.0 4.978 15.9 100 475 3.8 4.8 -0.9 55.7
SA15 303.0 4.697 14.3 100 500 9.7 5.2 -7.1 52.5
SA16 305.0 5.326 20.5
Rhino Cave:
R108 108.0 5.756 443.6 0 150 340.2 73.4 R195 195.0 0.984 190.8 0 150 8.9 46.0 400 575 21.7 195.3 -34.7 -70.1
R216 216.0 3.417 250.7 0 200 318.3 33.5 250 550 20.7 189.0 -10.8 -60.6
R246 246.0 5.341 523.9 250 575 33.0 165.9 -57.4 -77.8
R276 276.0 5.901 655.0 0 100 13.0 37.9 200 625 20.2 181.7 -21.3 -67.4
R316 316.0 2.694 579.4 0 150 46.1 49.7 300 675 14.5 208.4 -67.3 -63.4
R342 342.0 2.761 321.1 0 200 352.1 53.9 250 575 30.7 158.0 -36.8 -66.5
R392 392.0 2.167 262.7 0 150 23.9 49.0 200 550 30.0 196.6 -30.2 -67.1
R417 417.0 5.058 282.0 R431 431.0 3.672 294.1 0 100 313.9 24.8 R459 459.0 3.034 166.2
Oulad Hamida:
oh220 220.0 0.029 59.2 0 100 334.0 12.4
oh230 230.0 0.039 39.0 0 200 335.9 57.6
oh237 237.0 0.041 51.4 0 150 2.3 42.4
oh249 249.0 0.044 58.1 0 275 352.1 37.7
oh279 279.0 0.027 63.8 0 225 330.4 41.1
oh298 298.0 0.017 59.5 0 100 15.4 27.8
oh305 305.0 0.036 81.2 0 200 326.6 14.0
oh325 325.0 0.183 147.4 0 100 353.4 51.4
oh345 345.0 0.143 66.4 0 150 329.2 36.7

Chapter 9: Supplementary Material of

Refining the chronology of ThI-GH interval yielding hominin remains, Thomas Quarry I, Casablanca (Morocco)

Thermal demagnetization and paleomagnetic component analysis

Details of the litho-magnetostratigraphy for Members OH3, OH4, GH-CCC and OH5 of this study and Gallotti et al. (2021) is reported in **Fig. SI2.1** (see also **Fig. 1B** of main text). Vector end-point thermal demagnetization diagrams of 11 new samples from Member OH3 in section OH3-A (**Fig. SI2.2**) revealed the presence in 7 samples of characteristic component (ChRM) directions isolated between ~300-350°C and ~550-625°C and oriented downward (positive inclinations) with northerly declinations (**Fig. SI2.2; Tab. SI2.1**). These ChRM directions were integrated with data from Gallotti et al. (2021), including ChRM directions oriented southerly-and-up from section OH3-B of Member OH3 that were not considered in Gallotti et a. (2021) and that we now place above section OH3-A. Altogether, these ChRM component directions from sections OH3-A and OH3-B, transformed into virtual geomagnetic pole (VGP) latitudes, indicate that the Jaramillo subchron is entirely recorded within Member OH3 (**Fig. SI2.1;** see also **Fig. 1B** of main text).

Vector end-point demagnetization diagrams of 107 samples from OH4-SU6, OH4-SU5, GH-CCC-SU4, and GH-CCC-SU3 show the presence of initial A component directions removed between room temperature and median-maximum values of 350-500°C and oriented downward (positive inclinations) with northerly declinations. ChRM component directions, oriented broadly to the south with negative (up-pointing) inclinations or to the north with positive (down-pointing) inclinations, were isolated in 62 samples up to median-maximum values of 670-690°C (data in **Tab. SI2.1)**. In detail, three types of behaviors were observed upon thermal demagnetization:

(i) Northerly-and-down A component directions continuing their trajectories at high temperatures towards the origin of the demagnetization axes into northerly-and-down ChRM component directions (**Fig. SI2.3**).

(ii) Northerly-and-down A component directions turning at high temperatures to southerly-and-up ChRM end-point component directions which then tend to trend (with large noise-to-signal ratio) to the origin of the demagnetization axes (**Fig. SI2.4**).

(iii) Northerly-and-down A component directions moving along great circles towards the southern-and-up quadrant without however reaching stable end-points (**Fig. SI2.5**). A statistical analysis of the intersection density of the 48 great circles clearly indicates a starting region in the northern quadrant (northerly-and-down A component) and great circle trends toward the southern quadrant (unresolved southerly-and-up ChRM component directions; **Fig. SI2.6A**).

We interpret the ubiquitous A component directions as a pervasive chemical overprint of secondary origin acquired during the Brunhes Chron and carried essentially by magnetite (see also rock magnetic properties below), and the southerly-and-up or northerly-and-down ChRM directions of cases (i) and (iii) samples as primary magnetizations acquired in reverse and normal magnetic polarity, respectively, and carried essentially by hematite (see also rock magnetic properties below)**.** Furthermore, we interpret the tendency of case (ii) samples to turn to the southern quadrant after removal of the A component overprint as due to the presence of unresolved, primary component directions of reverse magnetic polarity, as indicated by great circle analysis. The end-point ChRM directions of cases (i) and (iii) were integrated with ChRM directions from Gallotti et al. (2021) and transformed into VGP latitudes for magnetostratigraphy. We also retained the unresolved ChRM reverse polarity tendencies of case (iii) samples (labelled 'x' in **Fig. 2C** of main text).

The total of 97 ChRM directions obtained with least-square analysis from Members OH3, OH4, GH-CCC and OH5 of this study and Gallotti et al. (2021) (**Sup. Tab. 2**) have maximum angular deviation (MAD) values of 12° ± 7° and appear scattered when analyzed using standard Fisher statistics on an equal-area projection, albeit they display clusters in the northern and southern quadrants, indicative of normal and reverse magnetic polarity, respectively (**Fig. SI2.6B**).

Rock magnetic properties

Rock magnetic analyses were conducted on samples from the calcarenites of OH4-SU5 and the continental sediments of GH-CCC-SU4. Normalized isothermal remanent magnetization (IRM) backfield acquisition curves up to 1500 m T, analyzed with the Gaussian method of Maxbauer et al. (2016), reveal that samples contain large proportions (80-90%) of a low coercivity phase with B1/2 (field required to acquire 50% of the IRM) of 40-60mT, coexisting with smaller proportions (10-20%) of a high coercivity phase with B1/2 of 1000mT (**Fig. SI2.7A**). When coupled with AF decay of the IRM, it appears that ~50% of the IRM is acquired at ~50mT and ~60% of the IRM is removed at ~50mT (**Fig. SI2.7A**). Thermomagnetic experiments performed in Ar atmosphere indicate the presence of sharp decays of magnetization intensity starting above ~500°C (**Fig. SI2.7B**). The first derivatives of these curves (**Fig. SI2.7B inset**) indicate the presence of minima at 550-580°C (f1) marking flexes in magnetization decay, which are taken as evidence of complete unblocking of magnetite (and onset of unblocking of hematite). Sample 4OH493 displays instead two minima (main minimum f2 shown in inset) at temperatures at and above 600°C, indicative of hematite. Stepwise thermal demagnetization of a three-component IRM shows a dominant signal carried by the 0.12T curves with a tendency to drop in intensity in the 540-580°C interval, interpreted as mainly due to magnetite, coexisting with a higher (1.5T) and intermediate (0.4T) coercivity component with maximum unblocking temperatures higher than 600°C, interpreted as hematite (**Fig. 7C**). Hysteresis loops are moderately wasp-waisted whereby they tend to retard closure at high fields between 100 and 500 mT (**Fig. SI2.8A**). This is interpreted as due to the co-occurrence of ferromagnetic (s.l.) minerals with contrasting coercivities such as magnetite and hematite, in agreement with the results outlined above. Low-resolution FORC diagrams show low coercivity asymmetric peaks centered at B_u = 0 and B_c <40 mT, compatible with pseudo-single domain (PSD) magnetite grains (e.g., Roberts et al., 2000), coexisting with higher coercivity tails extending to B_c >100, compatible with hematite (**Fig. SI2.8B**). In summary, samples contain a mixture of low coercivity magnetite and high coercivity hematite, with no detectable differences between the calcarenites of OH4-SU5 and the continental sediments of GH-CCC-SU4.

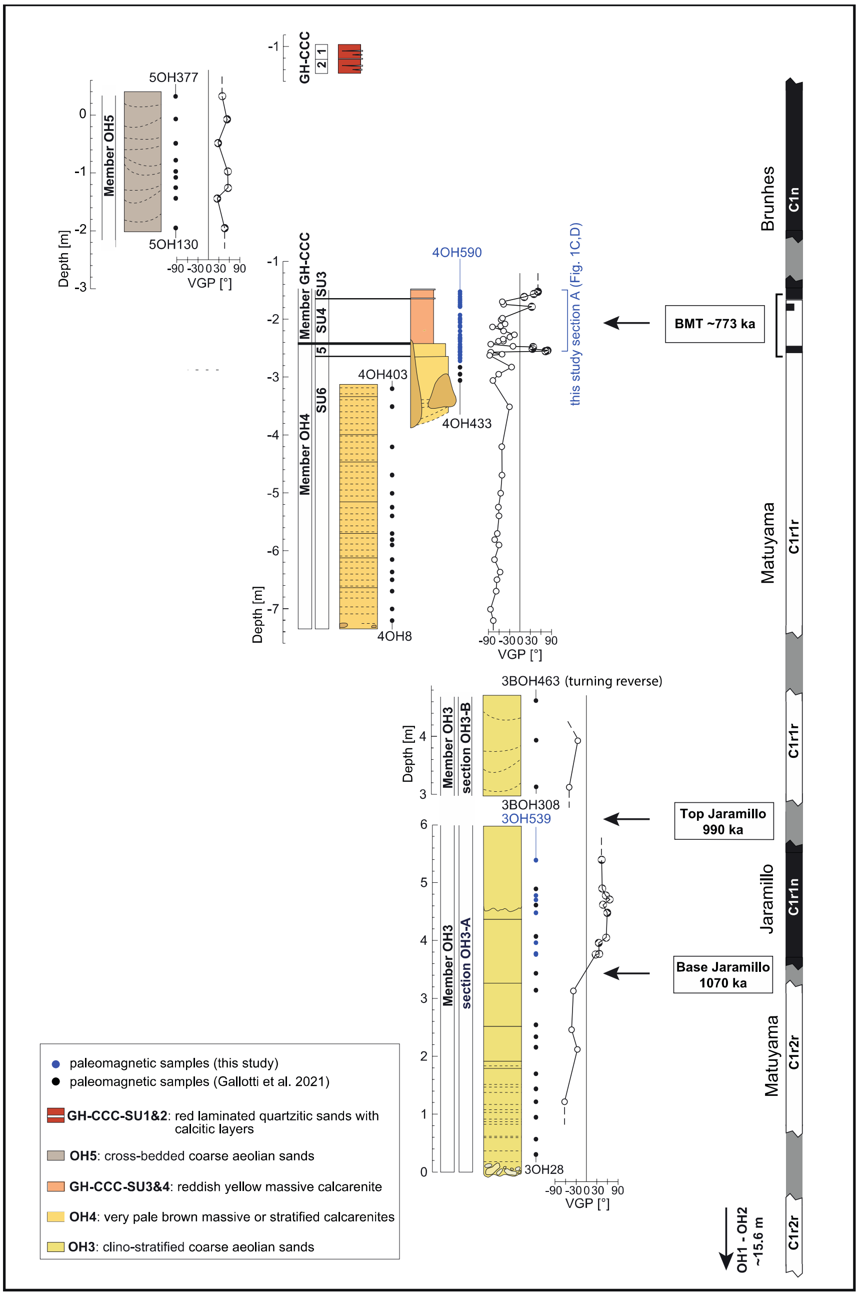

Fig. SI2.1. Litho-Magnetostratigraphy of the Thomas Quarry 1 sequence with lithostratigraphic members arranged in temporal order according to magnetic polarity stratigraphy. Virtual geomagnetic pole (VGP) data (positive values representing normal polarity, negative values reverse polarity) are from Gallotti et al. (2021) and this study. Only section A of Member OH4 and GH-CCC is reported here (see **Fig. 1C** of main text for details). Note that in this study, we re-evaluated the chronostratigraphic position of section OH3-B of Member OH3, which was not considered in Gallotti et a. (2021) and that we now place above section OH3-A thus obtaining a more continuous record across the Jaramillo subchron.

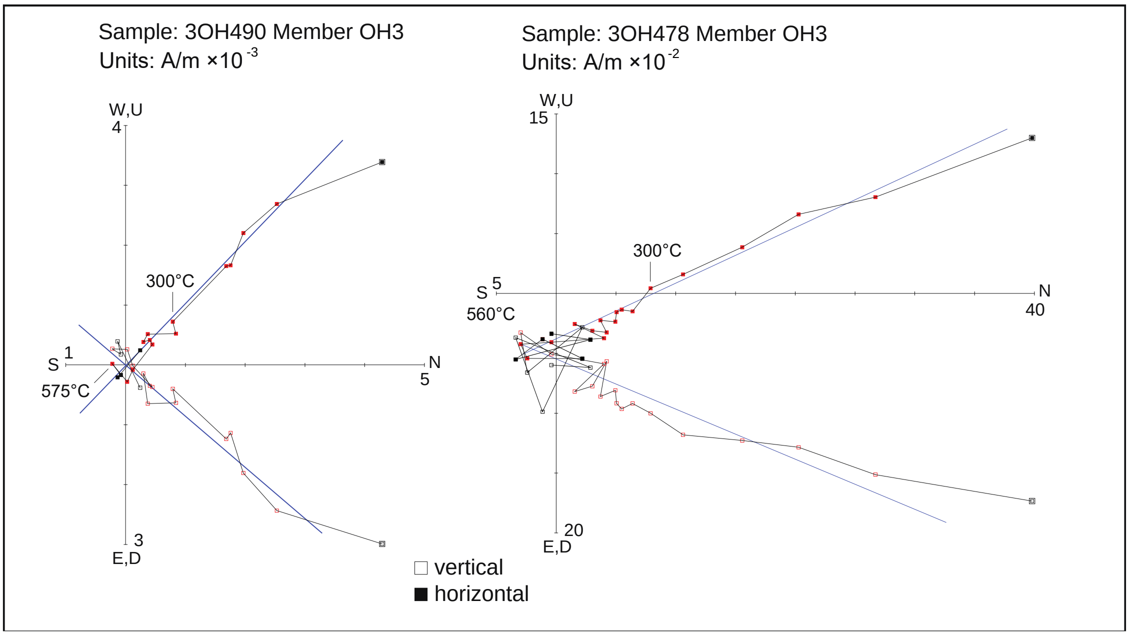

Fig. SI2.2. Vector end-point demagnetization diagrams of representative samples of Member OH3 in section OH3-A. Demagnetization steps highlighted in red are used to extract with the least-square method the characteristic remanent magnetization (ChRM) component directions (blue lines) used to establish magnetic polarity stratigraphy. Filled/open symbols are projections on horizontal/vertical plane. Temperatures are in °C. Made with PuffinPlot (Lurcock and Wilson, 2012).

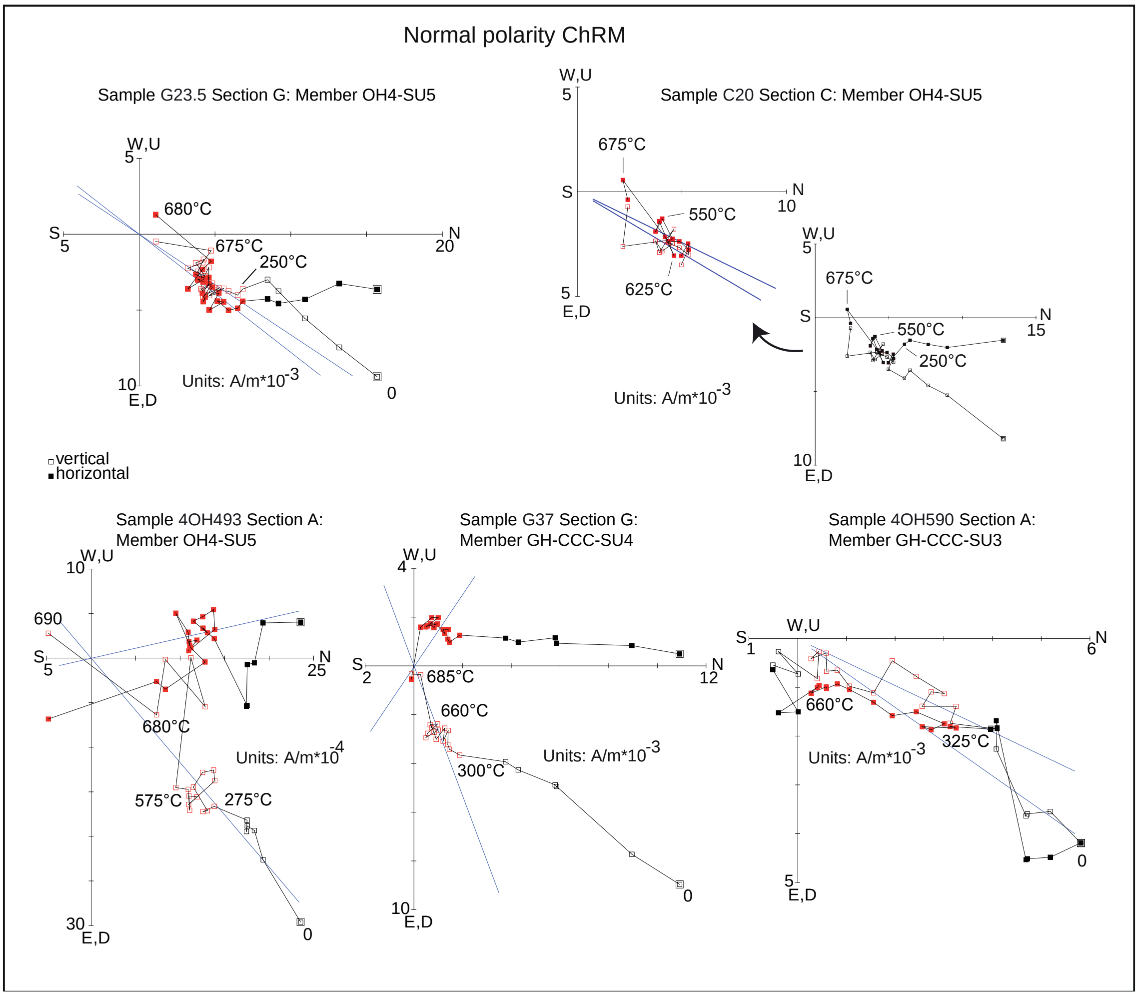

Fig. SI2.3. Vector end-point demagnetization diagrams of representative samples of OH4-SU5, GH-CCC-SU4, and GH-CCC-SU3 interpreted to contain ChRM component directions of normal polarity (case (i) samples). Notes and symbols as in **Fig. SI2.1**.

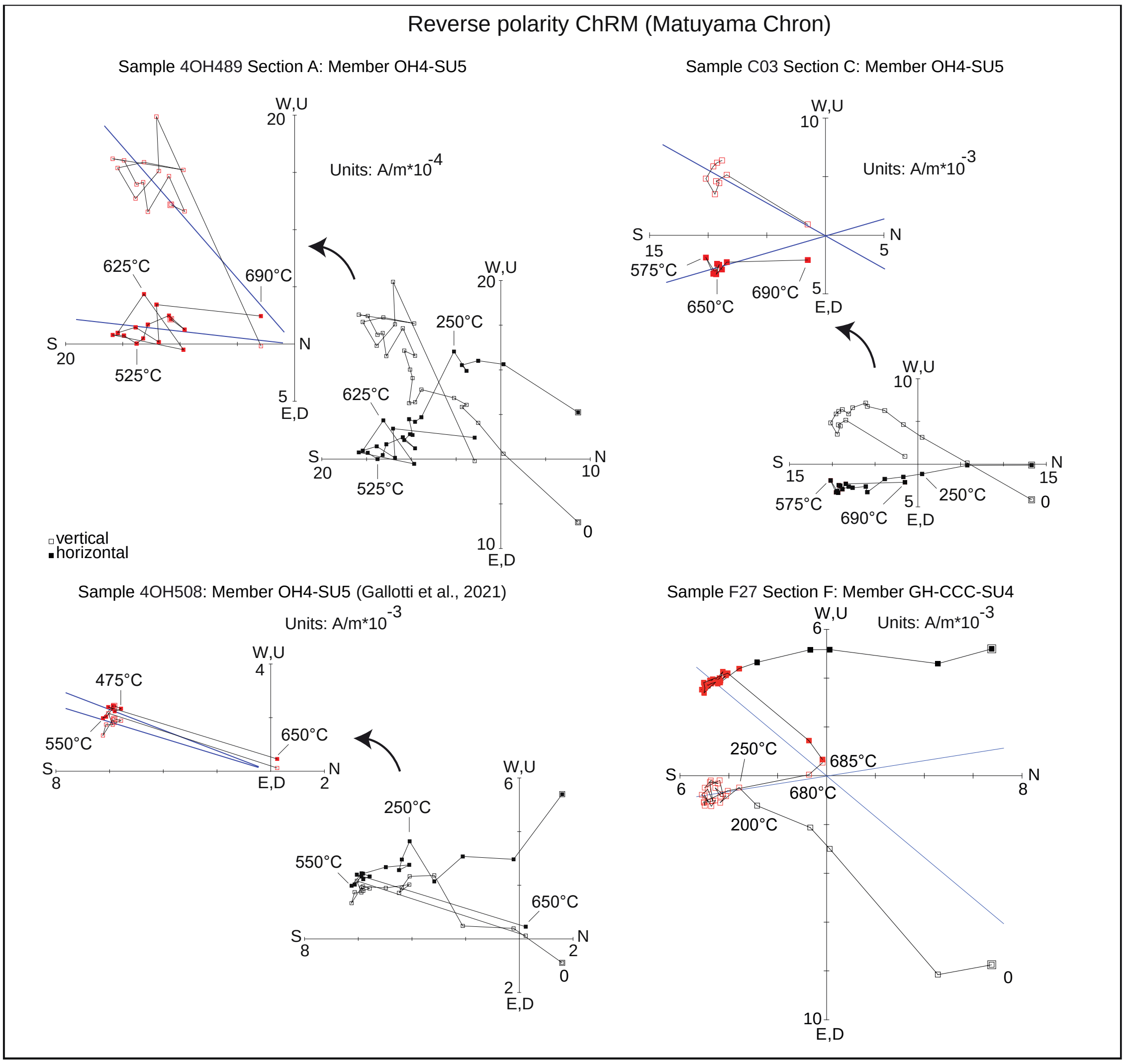

Fig. SI2.4. Vector end-point demagnetization diagrams of representative samples of OH4-SU5 and GH-CCC-SU4 interpreted to contain ChRM component directions of reverse polarity (case (ii) samples). Notes and symbols as in **Fig. SI2.1**.

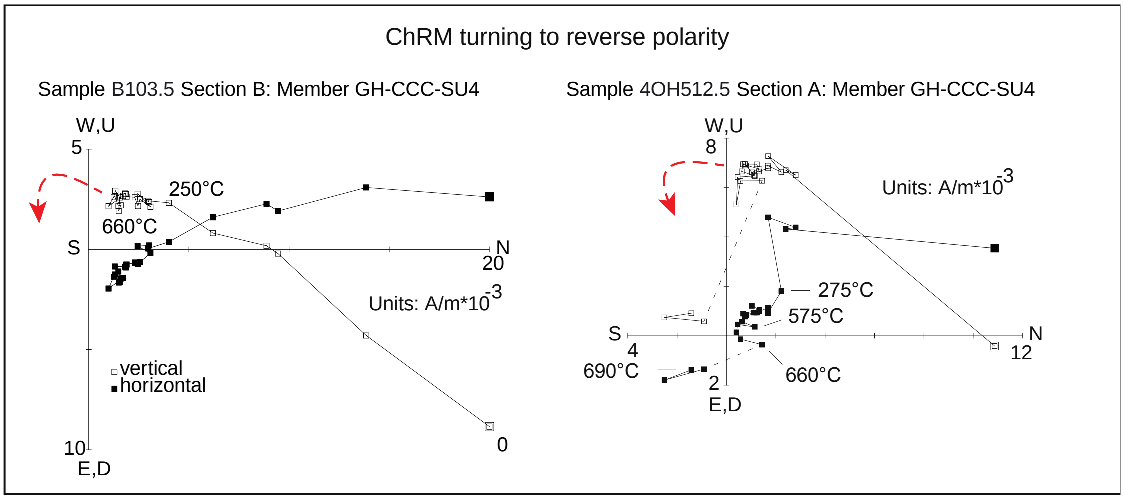

Fig. SI2.5. Vector end-point demagnetization diagrams of representative samples of OH4-SU5 and GH-CCC-SU4 interpreted to contain ChRM component directions showing a tendency to turn to reverse polarity (dashed red arrow), which was assessed qualitatively with great circle analysis (**Fig. SI2.5A**). Notes and symbols as in **Fig. SI2.1**.

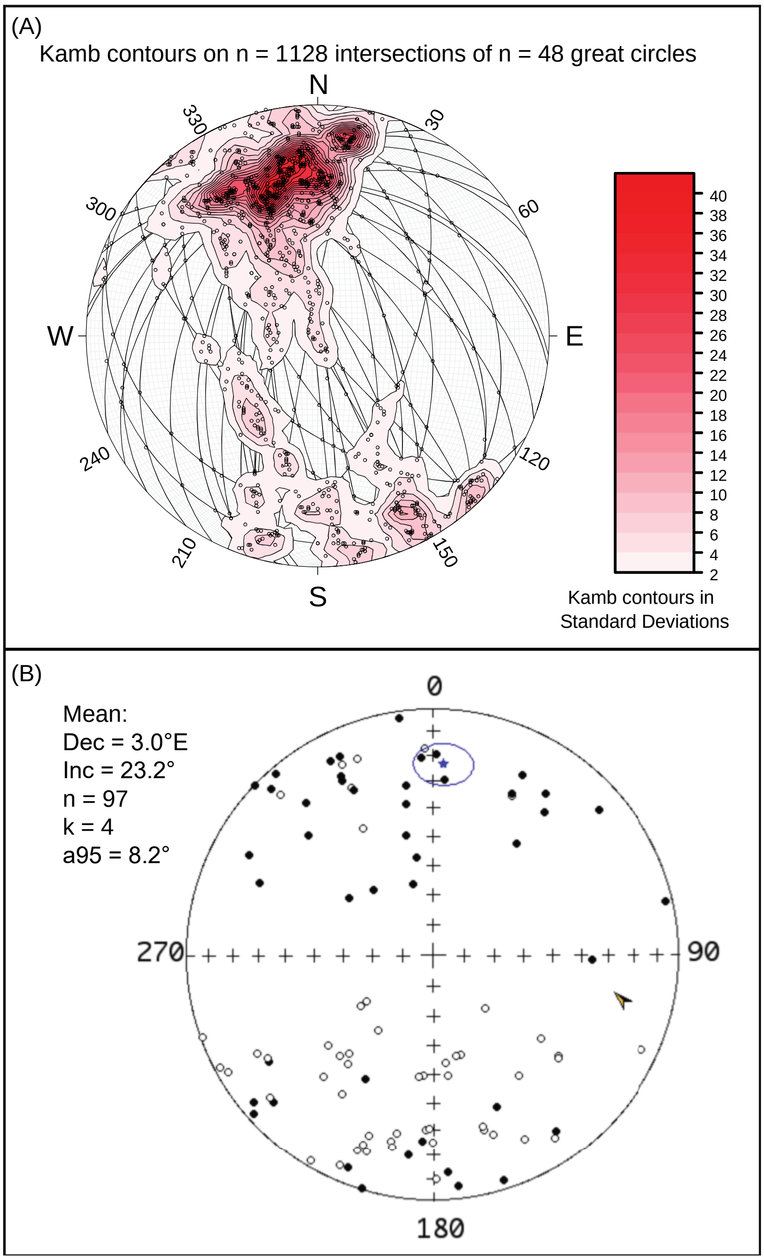

Fig. SI2.6. (A) Great circles of case (iii) samples plotted on an equal-area stereonet with Kamb density contouring of the derived 1128 intersections. Demagnetization trajectories of case (iii) samples tend to move on great circles from the northern quadrant towards the southern quadrant (unresolved ChRM component of reverse polarity). (B) Equal-area projection of the characteristic remanent magnetization (ChRM) component directions for samples of this study and Gallotti et al. (2021) for Members OH3, OH4, GH-CCC, and OH5. Closed symbols are projection onto the lower hemisphere while open symbols onto the upper hemisphere. The star represents the Fisher mean direction and associated cones of 95% confidence.

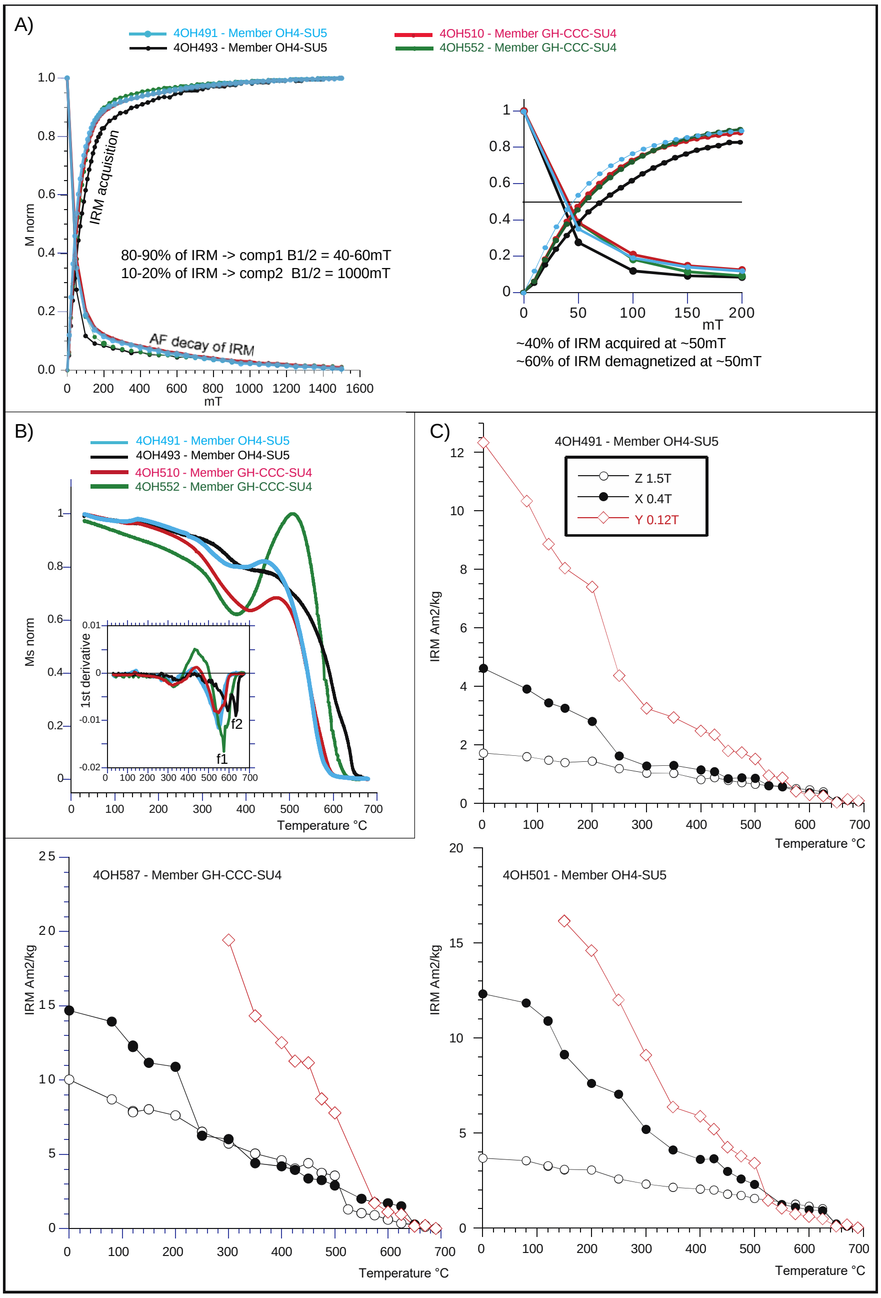

Fig. SI2.7. (A) normalized stepwise acquisition and alternating field (AF) decay of an isothermal remanent magnetization (IRM), (B) thermomagnetic decay of a magnetization induced at 1T in Ar atmosphere, (C) stepwise thermal decay of a three-component isothermal remanent magnetization (IRM) acquired in fields of 1.5T, 0.4T and 0.12T.

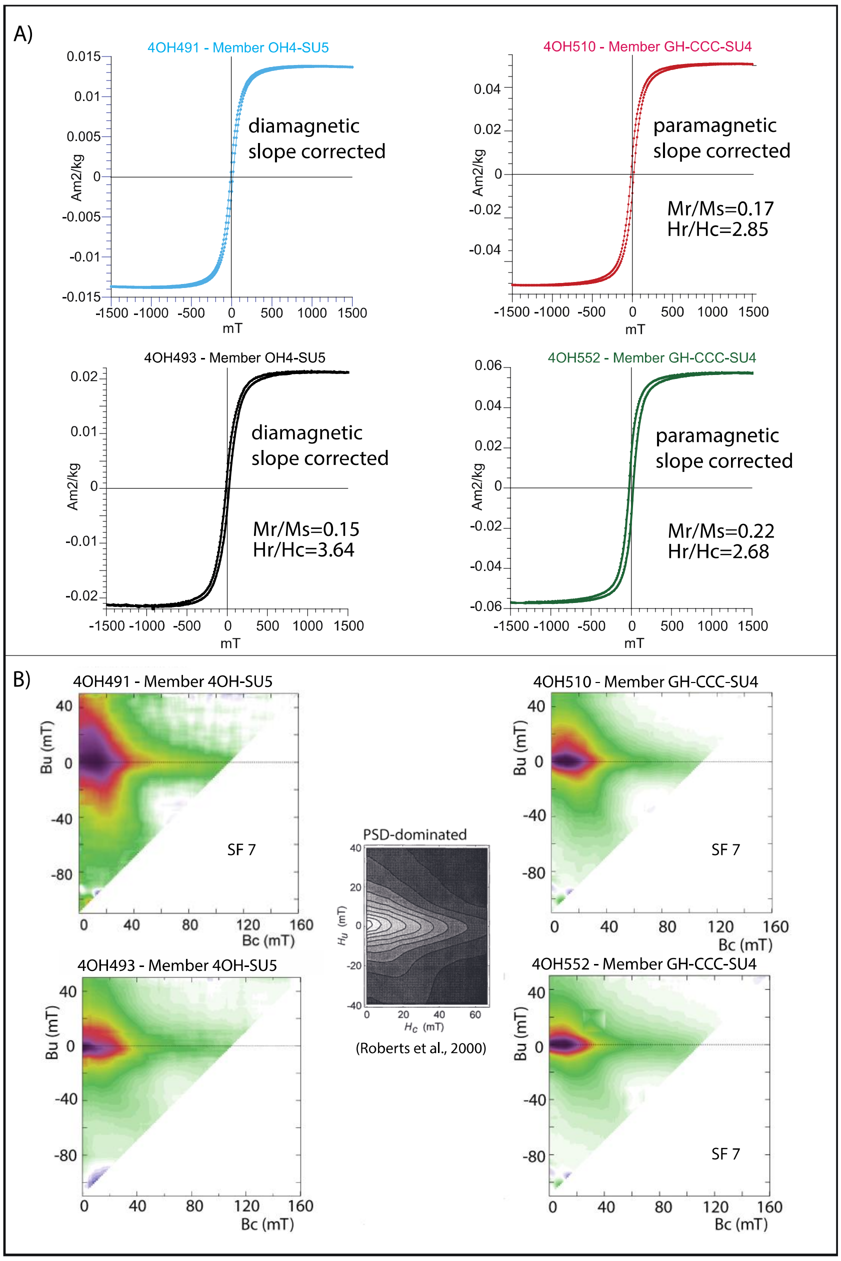

Fig. SI2.8. (A) Hysteresis loops and (B) low-resolution (n=76) FORC diagrams of samples from the calcarenites of OH4-SU5 and the continental sediments of unit GH-CCC-SU4. At the center of panel (B) is an example taken from Roberts et al. (2000) of a FORC attributed to PSD grains.

Tab. SI2.1. Magnetic component data of the studied samples.

SECTION: sampled section; **SAMPLE**: sample ID; **REFERENCE**: magnetostratigraphic data from literature; **DEPTH**: [m]; **COMMENT**; **LT**: minimum temperature of the ChRM component [°C]; HT: maximum temperature of the ChRM component [°C]; **ChRM DEC**: declination of the ChRM component [°E]; **ChRM INC**: inclination of the ChRM component [°]; **MAD**: maximum angular deviation of the ChRM component [°]; **VGP lat**: latitude of the virtual geomagnetic pole [°]; **GC pole DEC**: great cyrcle pole declination [°E]; **GC pole INC**: great cyrcle pole inclination [°]

Section	Sample	Reference	Depth (m	Comment	LT (°C)	HT (°C)	ChRM Dec (°E)	ChRM Inc (°)	MAD3 (°)	VGP lat (°)	GC pole Dec (°E)	GC pole Inc (°)
OH3	3OH28	Gallotti et al. (2021)	28	not interpreted								
OH3	3OH51	Gallotti et al. (2021)	51	not interpreted								
OH3	3OH94	Gallotti et al. (2021)	94	not interpreted								
OH3	3OH121	Gallotti et al. (2021)	121		250	625	161,4733	-23,9178	16,5817	-63		
OH3	3OH144	Gallotti et al. (2021)	144	not interpreted								
OH3	3OH172	Gallotti et al. (2021)	172	not interpreted								
OH3	3OH212	Gallotti et al. (2021)	212		200	575	240,0663	-5,0946	7,4676	-26,1		
OH3	3OH229	Gallotti et al. (2021)	229	not interpreted								
OH3	3OH246	Gallotti et al. (2021)	246		200	625	183,1608	25,2807	19,5851	-43,05		
OH3	3OH308	This Study	308	not interpreted								
OH3	3OH313	Gallotti et al. (2021)	313		100	300	145,1683	13,9887	8,022	-37,61		
OH3	3OH339	Gallotti et al. (2021)	339	not interpreted								
OH3	3OH353	This Study	353	not interpreted								
OH3	3OH376	This Study	376		100	690	331,2536	-41,1219	14,5171	26,64		
OH3	3OH377	This Study	377		150	690	333,9813	-25,6793	14,5109	36,78		
OH3	3OH379	Gallotti et al. (2021)	379	not interpreted								
OH3	3OH385	This Study	385	not interpreted								
OH3	3OH396	This Study	396		600	690	313,635	0,4762	20,0212	35,26		
OH3	3OH401	This Study	401	not interpreted								
OH3	3OH405	Gallotti et al. (2021)	405		100	675	36,9836	42,8703	6,1678	56,77		
OH3	3OH412	This Study	412	not interpreted								
OH3	30H448	This Study	448		150	525	334,4618	27,0695	18,817	59,92		
OH3	3OH462	Gallotti et al. (2021)	462		150	650	357,6416	-17,1479	10,362	47,6		
OH3	3OH471	This Study	471		150	525	1,0555	19,7688	8,0176	66,6		
OH3	3OH478	This Study	478		150	600	332,7556	19,6747	10,6528	55,74		
OH3	3OH490	Gallotti et al. (2021)	490		100	575	313,9487	30,67	5,6886	45,37		
OH3	3OH539	This Study	539		150	680	339,0086	-15,9716	21,7792	43,77		
OH3B	3BOH30	Gallotti et al. (2021)	30	not interpreted								
OH3B	3BOH57	Gallotti et al. (2021)	57	not interpreted								
OH3B	3BOH94	Gallotti et al. (2021)	94	not interpreted								
OH3B	3BOH136	Gallotti et al. (2021)	136	not interpreted								
OH3B	3BOH178	Gallotti et al. (2021)	178	not interpreted								
OH3B	3BOH221	Gallotti et al. (2021)	221	not interpreted								
OH3B	3BOH281	Gallotti et al. (2021)	281	not interpreted								
OH3B	3BOH308	Gallotti et al. (2021)	308		150	425	210,5451	-3,3503	23,9599	-47,18		
OH3B	3BOH388	Gallotti et al. (2021)	388		200	675	208,6201	42,1404	10,4578	-26,01		
OH3B	3BOH428	Gallotti et al. (2021)	428	not interpreted								
OH3B	3BOH463	Gallotti et al. (2021)	463	not interpreted								
OH3B	3BOH486	Gallotti et al. (2021)	486	not interpreted								
OH3B	3BOH510	Gallotti et al. (2021)	510	not interpreted								
OH4	4OH29	Gallotti et al. (2021)	-7,282		350	625	184,5	-49,2	3,1	-84,8		
OH4	4OH59	Gallotti et al. (2021)	-6,982		350	675	191,4	-26,9	3,6	-68,1		
OH4	oh4_7	Gallotti et al. (2021)			325	675	182,1	-29,6	6,9	-72,2		
OH4	4OH96	Gallotti et al. (2021)	-6,612		300	650	192,5	-23,5	4,3	-65,8		
OH4	4OH116	Gallotti et al. (2021)	-6,412		300	675	217,8	-43,5	8,8	-56,3		
OH4	4OH145	Gallotti et al. (2021)	-6,122		300	675	198,6	-16,8	8,7	-59,7		
OH4	oh4_8	Gallotti et al. (2021)			300	675	181,1	-30,2	5,5	-72,6		
OH4	4OH166	Gallotti et al. (2021)	-5,912		350	675	192,0	-21,1	5,9	-64,8		
OH4	4OH198	Gallotti et al. (2021)	-5,592		300	625	200,1	-18,9	6,8	-59,9		
OH4	oh4_9	Gallotti et al. (2021)			325	675	179,2	-9,4	9,0	-61,2		
OH4	4OH237	Gallotti et al. (2021)	-5,202		300	675	220,2	-46,7	7,2	-55,3		
OH4	4OH263	Gallotti et al. (2021)	-4,942		350	675	162,7	4,2	7,3	-50,8		
OH4	4OH303	Gallotti et al. (2021)	-4,542		400	650	222,8	-43,7	15,0	-52,2		
OH4	4OH363	Gallotti et al. (2021)	-3,942	not interpreted								
OH4	4OH403	Gallotti et al. (2021)	-3,542		300	625	240,6	-19,4	6,2	-29,9		
OH4	4OH433	Gallotti et al. (2021)	-3,242		400	675	164,2	-55,6	7,1	-76,8		
OH4	4OH443	Gallotti et al. (2021)	-3,142		200	475	216,1	-59,1	14,5	-60,6		
OH4	4OH454	Gallotti et al. (2021)	-2,829		425	650	242,2	-2,8	9,1	-23,7		
GH: E	4OH458	This Study	-2,790	turning to S quadrant?							241,9	8,7
GH: E	4OH462	This Study	-2,750	jumped to S quadrant								
GH: E	4OH466.5	This Study	-2,684	jumped to S quadrant?							245,9	3,4
GH: E	4OH468	Gallotti et al. (2021)	-2,710	turning to S quadrant?								
GH: E	4OH469.5	This Study	-2,665	not interpreted								
GH: E	4OH470	This Study	-2,686	turning to S quadrant?							244,8	0,5
GH: E	4OH472	This Study	-2,628		500	680	196,8	1,0	24,0	-52,5		
GH: E	4OH475	This Study	-2,597	turning to S quadrant?							291,3	33,2
OH4	4OH483	Gallotti et al. (2021)	-2,622	turning to S quadrant?								
OH4	4OH484	Gallotti et al. (2021)	-2,632		350	650	173,0	-53,8	10,1	-84,1		
GH: A	4OH485	This Study	-2,619		325	670	221,9	-34,0	23,8	-49,8		
GH: A	4OH489	This Study	-2,582		400	690	186,5	-48,8	6,8	-83,3		
GH: A	4OH491	This Study	-2,562		325	680	3,9	29,5	10,9	71,9		
GH: A	4OH493	This Study	-2,551		350	690	347,2	48,8	13,2	78,5		
GH: A	4OH495	This Study	-2,523		325	650	26,5	-28,8	12,9	34,9		
GH: A	4OH497	This Study	-2,492		325	690	48,8	11,6	8,4	37,0		
GH: A	4OH498	This Study	-2,478		275	690	236,7	22,0	7,7	-19,8		
GH: A	4OH503	This Study	-2,441		325	670	173,1	-49,3	16,4	-83,2		
GH: A	4OH505	This Study	-2,415	not interpreted								
GH: A	4OH508	This Study	-2,388		325	690	234,6	-60,8	7,7	-46,8		
GH: A	4OH508	Gallotti et al. (2021)	-2,388		450	650	201,0	-16,0	3,1	-58,1		
GH: A	4OH510	This Study	-2,354		275	680	201,7	7,7	9,6	-47,3		
GH: A	4OH512.5	This Study	-2,332	turning to S quadrant?							226,4	-1,7

GH: A	4OH514	This Study	-2,319		400	680	230,6	6,7	10,3	-29,7		
GH: A	4OH516.5	This Study	-2,290	turning to S quadrant?							62,0	-64,4
GH: A	4OH518	This Study	-2,279		350	650	250,2	-1,0	6,9	-16,7		
GH: A	4OH521.5	This Study	-2,240	turning to S quadrant?							228,6	10,4
GH: A	4OH525	This Study	-2,208		375	690	187,0	19,0	6,4	-46,2		
GH: A	4OH528	Gallotti et al. (2021)	-2,177	not interpreted								
GH: A	4OH532	This Study	-2,140		375	670	167,3	-55,4	15,7	-79,3		
GH: A	4OH532.5	This Study	-2,123		300	680	153,5	-17,8	19,5	-55,5		
GH: A	4OH536	This Study	-2,090		325	670	129,0	-35,1	8,7	-42,7		
GH: A	4OH539	This Study	-2,059	turning to S quadrant?							86,4	16,4
GH: A	4OH543.5	This Study	2,018		325	660	135,7	-65,3	10,9	-54,2		
GH: A	4OH545	This Study	-1,990		350	680	175,9	12,3	12,0	-50,1		
GH: A	4OH548	Gallotti et al. (2021)	-1,971	not interpreted								
GH: A	4OH552	This Study	-1,937	turning to S quadrant?							236,7	-13,4
GH: A	4OH557	This Study	-1,880	turning to S quadrant?							7,1	-54,7
GH: A	4OH561	This Study	-1,842	turning to S quadrant?							36,4	76,3
GH: A	4OH564	This Study	-1,810	turning to S quadrant?							117,2	46,3
GH: A	4OH566	This Study	-1,789		275	660	316,5	-11,7	15,5	33,0		
GH: A	4OH570	This Study	-1,749		325	680	229,0	-43,1	11,0	-46,9		
GH: A	4OH574	This Study	-1,710		450	690	173,6	6,1	9,4	-52,9		
GH: A	4OH575	This Study	-1,700	turning to S quadrant?							38,3	29,9
GH: A	4OH578	Gallotti et al. (2021)	-1,669	turning to S quadrant?							206,0	-62,0
GH: A	4OH583	This Study	-1,620		325	660	77,2	3,7	6,4	11,7		
GH: A	4OH588	This Study	-1,570		275	660	315,8	6,8	11,7	39,0		
GH: A	4OH590	This Study	-1,530		325	660	35,0	21,3	10,3	50,8		
GH: B	B03	This Study	-2,608		450	690	199,3	-23,4	12,6	-62,3		
GH: B	B06	This Study	-2,589		400	690	344,2	65,5	17,4	71,6		
GH: B	B08	This Study	-2,560	not interpreted								
GH: B	B12	This Study	-2,523	not interpreted								
GH: B	B13	This Study	-2,515		400	690	334,7	-15,6	18,2	42,0		
GH: B	B15	This Study	-2,499		350	690	227,2	13,2	18,0	-29,9		
GH: B	B17.5	This Study	-2,480		400	690	114,6	-7,6	12,6	-22,5		
GH: B	B18	This Study	-2,469		350	690	144,4	-39,7	7,0	-56,9		
GH: B	B21	This Study	-2,438	turning to S quadrant?							77,5	28,8
GH: B	B24	This Study	-2,418	turning to S quadrant?							228,9	28,2
GH: B	B26.5	This Study	-2,391		575	675	228,3	3,4	49,0	-32,5		
GH: B	B27.5	This Study	-2,378	turning to S quadrant?							247,1	24,3
GH: B	B29	This Study	-2,362	turning to S quadrant?							211,2	34,9
GH: B	B33	This Study	-2,322	turning to S quadrant?							240,2	-1,5
GH: B	B36	This Study	-2,295	turning to S quadrant?							137,6	61,6
GH: B	B42	This Study	-2,254	turning to S quadrant?							201,0	45,8
GH: B	B45	This Study	-2,225	turning to S quadrant?							284,4	-37,1
GH: B	B49	This Study	-2,188	not interpreted								
GH: B	B53.5	This Study	-2,140	not interpreted								
GH: B	B57.5	This Study	-2,098		500	690	163,7	-27,0	9,5	-65,7		
GH: B	B59.5	This Study	-2,079	turning to S quadrant?							266,3	-17,4
GH: B	B62.5	This Study	-2,050	turning to S quadrant?							254,6	24,4
GH: B	B65	This Study	-2,023		300	690	332,5	21,7	8,2	56,4		
GH: B	B68	This Study	-1,994	turning to S quadrant?							124,6	58,6
GH: B	B70	This Study	-1,971	turning to S quadrant?							231,2	-37,7
GH: B	B82	This Study		not interpreted								
GH: B	B86.5	This Study		turning to S quadrant?							260,2	-13,2
GH: B	B92.5	This Study			325	690	235,3	-63,1	11,8	-46,6		
GH: B	B97	This Study		turning to S quadrant?							265,0	-1,3
GH: B	B100	This Study		turning to S quadrant?							240,0	-36,3
GH: B	B102	This Study			530	680	157,4	33,7	20,6	-33,7		
GH: B	B103.5	This Study		turning to S quadrant?							75,0	28,0
GH: B	B105	This Study		turning to S quadrant?							108,8	38,5
GH: B	B113	This Study			250	680	350,0	38,0	14,2	74,9		
GH: C	C03	This Study	-2,569		500	690	163,7	-28,3	6,0	-66,4		
GH: C	C06	This Study	-2,543		400	690	180,1	-24,6	12,4	-69,3		
GH: C	C10	This Study	-2,511	turning to S quadrant?							105,6	20,2
GH: C	C14	This Study	-2,479		300	690	350,2	57,1	13,0	81,0		
GH: C	C17	This Study	-2,449		350	650	356,8	20,8	29,4	67,0		
GH: C	C20	This Study	-2,419		300	690	26,0	28,0	8,7	60,0		
GH: C	C24.5	This Study	-2,377		550	690	127,9	-44,1	10,8	-44,5		
GH: C	C28.5	This Study	-2,344	turning to S quadrant?							262,5	40,5
GH: C	C32	This Study	-2,311	turning to S quadrant?							97,1	26,6
GH: C	C36	This Study	-2,268	turning to S quadrant?							4,7	-56,2
GH: C	C41	This Study	-2,216		450	690	129,5	-34,6	27,6	-43,0		
GH: C	C46	This Study	-2,173	turning to S quadrant?							104,1	14,5
GH: C	C50	This Study	-2,190		400	690	146,4	-11,6	14,8	-48,3		
GH: C	C57	This Study	-2,068		250	550	351,0	31,3	7,3	71,5		
GH: D	D5.5	This Study	-2,590		350	690	352,0	3,5	32,3	57,3		
GH: D	D11	This Study	-2,513		250	650	332,3	12,2	7,4	52,5		
GH: D	D17.5	This Study	-2,449	turning to S quadrant?							226,9	42,6
GH: D	D21	This Study	-2,415	turning to S quadrant?							230,4	48,4
GH: D	D24	This Study	-2,390	turning to S quadrant?							146,3	52,1
GH: D	D27	This Study	-2,360	turning to S quadrant?							257,4	0,3
GH: G	G6	This Study	-2,635	turning to S quadrant?							100,7	3,3
GH: G	G7	This Study	-2,618		300	690	203,7	-7,2	9,2	-52,8		
GH: G	G10	This Study	-2,620	turning to S quadrant?							260,2	18,5
GH: G	G11	This Study	-2,591		350	690	238,0	-22,4	10,5	-33,0		
GH: G	G14	This Study	-2,559	turning to S quadrant?							264,5	2,3
GH: G	G16	This Study	-2,540		325	690	91,5	35,6	12,0	9,5		
GH: G	G23.5	This Study	-2,464		250	680	37,9	27,6	7,6	50,9		
GH: G	G26	This Study	-2,437		550	620	228,7	-13,2	3,7	-37,6		
GH: G	G28	This Study	-2,409	turning to S quadrant?							102,1	17,1
GH: G	G29	This Study	-2,402	turning to S quadrant?							335,0	-61,2
GH: G	G33	This Study	-2,363		510	690	213,0	-33,4	6,9	-56,8		
GH: G	G37	This Study	-2,314		300	690	304,1	56,2	10,6	44,8		
OH5	5OH130	Gallotti et al. (2021)	2,895		400	675	320,1	21,0	21,7	47,1		
OH5	5OH181	Gallotti et al. (2021)	3,405		350	600	292,5	25,2	16,5	25,9		
OH5	5OH215	Gallotti et al. (2021)	3,745		400	625	26,3	19,9	18,6	56,5		
OH5	5OH244	Gallotti et al. (2021)	4,035	not interpreted								
OH5	5OH266	Gallotti et al. (2021)	4,255		300	625	318,1	60,8	20,1	56,2		

OH5	5OH291	Gallotti et al. (2021)	4,505	not interpreted						
OH5	5OH326	Gallotti et al. (2021)	4,855		350	600	298,4	16,4	27,6	28,2
OH5	5OH351	Gallotti et al. (2021)	5,105		300	550	334,9	12,1	9,4	54,0
OH5	5OH377	Gallotti et al. (2021)	5,365		350	525	319,1	3,1	13,1	40,2